

Methods in  
Molecular Biology 1486

Springer Protocols

Arne Ginnerich  
*Editor*

# Optical Tweezers

Methods and Protocols

**EXTRAS ONLINE**

 Humana Press



# METHODS IN MOLECULAR BIOLOGY

*Series Editor*

John M. Walker

School of Life and Medical Sciences  
University of Hertfordshire  
Hatfield, Hertfordshire, AL10 9AB, UK

For further volumes:  
<http://www.springer.com/series/7651>

# **Optical Tweezers**

## **Methods and Protocols**

Edited by

**Arne Gennerich**

*Department of Anatomy and Structural  
Biology & Gruss-Lipper Biophotonics Center  
Albert Einstein College of Medicine  
Bronx, NY, USA*

 **Humana Press**

*Editor*

Arne Gennerich

Department of Anatomy and Structural  
Biology & Gruss-Lipper Biophotonics Center  
Albert Einstein College of Medicine  
Bronx, NY, USA

ISSN 1064-3745

ISSN 1940-6029 (electronic)

Methods in Molecular Biology

ISBN 978-1-4939-6419-2

ISBN 978-1-4939-6421-5 (eBook)

DOI 10.1007/978-1-4939-6421-5

Library of Congress Control Number: 2016952805

© Springer Science+Business Media New York 2017

This work is subject to copyright. All rights are reserved by the Publisher, whether the whole or part of the material is concerned, specifically the rights of translation, reprinting, reuse of illustrations, recitation, broadcasting, reproduction on microfilms or in any other physical way, and transmission or information storage and retrieval, electronic adaptation, computer software, or by similar or dissimilar methodology now known or hereafter developed.

The use of general descriptive names, registered names, trademarks, service marks, etc. in this publication does not imply, even in the absence of a specific statement, that such names are exempt from the relevant protective laws and regulations and therefore free for general use.

The publisher, the authors and the editors are safe to assume that the advice and information in this book are believed to be true and accurate at the date of publication. Neither the publisher nor the authors or the editors give a warranty, express or implied, with respect to the material contained herein or for any errors or omissions that may have been made.

Printed on acid-free paper

This Humana Press imprint is published by Springer Nature

The registered company is Springer Science+Business Media LLC New York

---

## Preface

Numerous biological processes are dependent on the minute forces and displacements generated by enzymes capable of converting chemical energy into mechanical motion. For example, DNA and RNA polymerases generate forces during DNA synthesis and transcription, while the microtubule motors kinesin and cytoplasmic dynein generate forces that regulate spindle and chromosome positioning during mitosis. Deciphering the molecular mechanisms of these mechanoenzymes has fascinated scientists for more than 150 years since the discovery of muscle myosin. However, it was the invention of optical tweezers in 1986 by Arthur Ashkin that gave researchers the ability to investigate the force-generating molecular mechanisms of single mechanoenzymes. Optical tweezers, which can measure forces of 0.01 to ~1000 pN, have been invaluable in defining the forces and displacements that these biological nanomachines generate. While the optical tweezers of the past have been largely custom-built and used by biophysicists, they are now being more widely employed by nonexperts, owing to a more detailed description of optical tweezers systems and the availability of commercial solutions. However, a thorough description of the theory and design, together with protocols for the calibration and application of optical tweezers to biological systems both *in vitro* and *in vivo*, had not until now been compiled into a single resource.

The aim of this volume is to provide a comprehensive overview of optical tweezers setups, both in practical and theoretical terms, to help biophysicists, biochemists, and cell biologists alike to build and calibrate their own instruments and to perform force measurements on mechanoenzymes both in isolation *in vitro* and in living cells. To aid the reader, this volume has been divided in three parts. The chapters in Part I present the theory and practical design of optical tweezers both without and in combination with single-molecule fluorescence imaging as well as instructions for calibrating and stabilizing optical tweezers. Part II provides detailed protocols for performing force measurements on single DNA- and microtubule/actin-associated mechanoenzymes in isolation as well as protocols for protein unfolding/refolding experiments and the study of protein degradation. Part III describes the recent advances that have opened up quantitative force measurements on actin and microtubule motors in living cells.

It is my hope that, in addition to aiding seasoned users of optical tweezers, this volume will help to further expand the accessibility and use of optical traps by scientists of diverse disciplines. In doing so, may it foster new creative and collaborative approaches for using these exquisitely sensitive instruments to understand how molecular machines in the cell generate force and motion.

*Bronx, NY*

*Arne Gennerich*

---

# Contents

Preface .....	v
Contributors .....	ix

## PART I THEORY AND DESIGN OF OPTICAL TWEEZERS

1 Introduction to Optical Tweezers..... <i>Matthias D. Koch and Joshua W. Shaevitz</i>	3
2 Exact Theory of Optical Tweezers and Its Application to Absolute Calibration .....	25
<i>Rafael S. Dutra, Nathan B. Viana, Paulo A. Maia Neto, and H. Moysés Nussenzveig</i>	
3 Beyond the Hookean Spring Model: Direct Measurement of Optical Forces Through Light Momentum Changes..... <i>Arnaud Farré, Ferran Marsà, and Mario Montes-Usategui</i>	41
4 A Surface-Coupled Optical Trap with 1-bp Precision via Active Stabilization..... <i>Stephen R. Okoniewski, Ashley R. Carter, and Thomas T. Perkins</i>	77
5 Implementation and Tuning of an Optical Tweezers Force-Clamp Feedback System..... <i>Michael Bugiel, Anita Jannasch, and Erik Schäffer</i>	109
6 Custom-Made Microspheres for Optical Tweezers .....	137
<i>Anita Jannasch, Mohammad K. Abdosamadi, Avin Ramaifa, Suman De, Valentina Ferro, Aaron Sonnberger, and Erik Schäffer</i>	
7 Optical Torque Wrench Design and Calibration .....	157
<i>Zhanna Santybayeva and Francesco Pedaci</i>	
8 High-Resolution “Fleezers”: Dual-Trap Optical Tweezers Combined with Single-Molecule Fluorescence Detection .....	183
<i>Kevin D. Whitley, Matthew J. Comstock, and Yann R. Chemla</i>	
9 Versatile Quadruple-Trap Optical Tweezers for Dual DNA Experiments..... <i>Iddo Heller, Niels Laurens, Daan Vorselen, Onno D. Broekmans, Andreas S. Biebricher, Graeme A. King, Ineke Brouwer, Gijs J.L. Wuite, and Erwin J.G. Peterman</i>	257

## PART II OPTICAL TWEEZERS-BASED MANIPULATION AND ANALYSIS OF DNA-DNA INTERACTIONS, PROTEIN UNFOLDING/REFOLDING, AND MOTION/FORCE-GENERATION BY MECHANOENZYMES IN VITRO

10 Probing DNA–DNA Interactions with a Combination of Quadruple-Trap Optical Tweezers and Microfluidics .....	275
<i>Ineke Brouwer, Graeme A. King, Iddo Heller, Andreas S. Biebricher, Erwin J.G. Peterman, and Gijs J.L. Wuite</i>	

11	Probing Single Helicase Dynamics on Long Nucleic Acids Through Fluorescence-Force Measurement . . . . .	295
	<i>Chang-Ting Lin and Taekjip Ha</i>	
12	Mechanically Watching the ClpXP Proteolytic Machinery . . . . .	317
	<i>Juan Carlos Cordova, Adrian O. Olivares, and Matthew J. Lang</i>	
13	Deciphering the Molecular Mechanism of the Bacteriophage φ29 DNA Packaging Motor . . . . .	343
	<i>Shixin Liu, Sara Tafoya, and Carlos Bustamante</i>	
14	Single-Molecule Protein Folding Experiments Using High-Precision Optical Tweezers . . . . .	357
	<i>Junyi Jiao, Aleksander A. Rebane, Lu Ma, and Yongli Zhang</i>	
15	Observing Single RNA Polymerase Molecules Down to Base-Pair Resolution . . . . .	391
	<i>Anirban Chakraborty, Cong A. Meng, and Steven M. Block</i>	
16	Optical Tweezers-Based Measurements of Forces and Dynamics at Microtubule Ends . . . . .	411
	<i>Marian Baclayon, Svenja-Marei Kalisch, Ed Hendel, Liedewij Laan, Julien Husson, E. Laura Munteanu, and Marileen Dogterom</i>	
17	Simultaneous Manipulation and Super-Resolution Fluorescence Imaging of Individual Kinetochores Coupled to Microtubule Tips . . . . .	437
	<i>Ti Deng and Charles L. Asbury</i>	
18	Measurement of Force-Dependent Release Rates of Cytoskeletal Motors . . . . .	469
	<i>Sinan Can and Ahmet Yildiz</i>	
19	Measuring the Kinetic and Mechanical Properties of Non-processive Myosins Using Optical Tweezers . . . . .	483
	<i>Michael J. Greenberg, Henry Shuman, and E. Michael Ostap</i>	
<b>PART III QUANTITATIVE OPTICAL TWEEZERS STUDIES IN VIVO</b>		
20	Quantifying Force and Viscoelasticity Inside Living Cells Using an Active–Passive Calibrated Optical Trap . . . . .	513
	<i>Christine M. Ritter, Josep Mas, Lene Oddershede, and Kirstine Berg-Sørensen</i>	
21	Measuring Molecular Forces Using Calibrated Optical Tweezers in Living Cells . . . . .	537
	<i>Adam G. Hendricks and Yale E. Goldman</i>	
<i>Index</i> . . . . .		553

---

## Contributors

- MOHAMMAD K. ABDOSAMADI • *Center for Plant Molecular Biology, Universität Tübingen, Tübingen, Germany*
- CHARLES L. ASBURY • *Department of Physiology and Biophysics, University of Washington, Seattle, WA, USA*
- MARIAN BACLAYON • *Department of Bionanoscience, Kavli Institute of NanoScience, Faculty of Applied Sciences, Delft University of Technology, Delft, The Netherlands; FOM Institute AMOLF, Amsterdam, Delft, The Netherlands*
- KIRSTINE BERG-SØRENSEN • *Department of Physics, Technical University of Denmark, Kongens Lyngby, Denmark*
- ANDREAS S. BIEBRICHER • *Department of Physics and Astronomy and LaserLab, Vrije Universiteit Amsterdam, Amsterdam, The Netherlands*
- STEVEN M. BLOCK • *Department of Biology and Department of Applied Physics, Stanford University, Stanford, CA, USA*
- ONNO D. BROEKMAN • *Department of Physics and Astronomy and LaserLab, Vrije Universiteit Amsterdam, Amsterdam, The Netherlands*
- INEKE BROUWER • *Department of Physics and Astronomy and LaserLab, Vrije Universiteit Amsterdam, Amsterdam, The Netherlands*
- MICHAEL BUGIEL • *Center for Plant Molecular Biology, Universität Tübingen, Tübingen, Germany*
- CARLOS BUSTAMANTE • *University of California and Howard Hughes Medical Institute, Berkeley, CA, USA*
- SINAN CAN • *Department of Physics, University of California, Berkeley, CA, USA*
- ASHLEY R. CARTER • *Department of Physics and Astronomy, Amherst College, Amherst, MA, USA*
- ANIRBAN CHAKRABORTY • *Department of Biology, Stanford University, Stanford, CA, USA*
- YANN R. CHEMLA • *Center for Biophysics and Computational Biology and Center for the Physics of Living Cells, University of Illinois, Urbana, IL, USA*
- MATTHEW J. COMSTOCK • *Department of Physics and Astronomy, Michigan State University, East Lansing, MI, USA*
- JUAN CARLOS CORDOVA • *Department of Chemical and Biomolecular Engineering, Vanderbilt University, Nashville, TN, USA*
- SUMAN DE • *Center for Plant Molecular Biology, Universität Tübingen, Tübingen, Germany*
- YI DENG • *Department of Physiology and Biophysics, University of Washington, Seattle, WA, USA*
- MARILEEN DOGTEROM • *Department of Bionanoscience, Kavli Institute of NanoScience, Faculty of Applied Sciences, Delft University of Technology, Delft, The Netherlands; FOM Institute AMOLF, Amsterdam, Delft, The Netherlands*
- RAFAEL S. DUTRA • *Instituto Federal de Educação, Ciência e Tecnologia, Paracambi, Brazil; Department of Micro- and Nanotechnology, Technical University of Denmark, Kongens Lyngby, Denmark*
- ARNAU FARRÉ • *Impetux Optics S.L., Barcelona, Spain; Institut de Nanociència i Nanotecnologia, Universitat de Barcelona, Barcelona, Spain*

- VALENTINA FERRO • *Center for Plant Molecular Biology, Universitat Tübingen, Tübingen, Germany*
- YALE E. GOLDMAN • *Pennsylvania Muscle Institute, Perelman School of Medicine, Pennsylvania Muscle Institute, Perelman School of Medicine, Philadelphia, PA, USA; Department of Physiology, Perelman School of Medicine, University of Pennsylvania, Philadelphia, PA, USA*
- MICHAEL J. GREENBERG • *Department of Physiology, The Pennsylvania Muscle Institute, Philadelphia, PA, USA; Department of Biochemistry and Molecular Biophysics, Washington University School of Medicine, St. Louis, MO, USA*
- TAEKJIP HA • *Department of Biophysics and Biophysical Chemistry, Thomas C. Jenkins Department of Biophysics and Department of Biomedical Engineering, Johns Hopkins University, Baltimore, MD, USA; Howard Hughes Medical Institute, Baltimore, MD, USA*
- IDDO HELLER • *Department of Physics and Astronomy and LaserLab, Vrije Universiteit Amsterdam, Amsterdam, The Netherlands*
- ED HENDEL • *FOM Institute AMOLF, Amsterdam, Delft, The Netherlands*
- ADAM G. HENDRICKS • *Department of Bioengineering, McGill University, Montreal, QC, Canada*
- JULIEN HUSSON • *FOM Institute AMOLF, Amsterdam, Delft, The Netherlands*
- ANITA JANNASCH • *Center for Plant Molecular Biology, Universitat Tübingen, Tübingen, Germany*
- JUNYI JIAO • *Department of Cell Biology and Integrated Graduate Program in Physical and Engineering Biology, Yale School of Medicine, New Haven, CT, USA*
- SVENJA-MAREI KALISCH • *Department of Bionanoscience, Kavli Institute of NanoScience, Faculty of Applied Sciences, Delft University of Technology, Delft, The Netherlands*
- GRAEME A. KING • *Department of Physics and Astronomy and LaserLab, Vrije Universiteit Amsterdam, Amsterdam, The Netherlands*
- MATTHIAS D. KOCH • *Joseph Henry Laboratory of Physics and Lewis-Sigler Institute of Integrative Genomics, Princeton University, Princeton, NJ, USA*
- LIEDEWIJ LAAN • *Department of Bionanoscience, Kavli Institute of NanoScience, Faculty of Applied Sciences, Delft University of Technology, Delft, The Netherlands; FOM Institute AMOLF, Amsterdam, Delft, The Netherlands*
- MATTHEW J. LANG • *Department of Chemical and Biomolecular Engineering and Department of Molecular Physiology and Biophysics, Vanderbilt University School of Medicine, Nashville, TN, USA*
- NIELS LAURENS • *Department of Physics and Astronomy and LaserLab, Vrije Universiteit Amsterdam, Amsterdam, The Netherlands*
- CHANG-TING LIN • *Department of Biophysics and Biophysical Chemistry, Johns Hopkins University, Baltimore, MD, USA*
- SHIXIN LIU • *Rockefeller University, New York, NY, USA*
- LU MA • *Department of Cell Biology, School of Medicine, Yale University, New Haven, CT, USA*
- FERRAN MARSÀ • *Impetux Optics S.L., Barcelona, Spain; Institut de Nanociència i Nanotecnologia, Universitat de Barcelona, Barcelona, Spain*
- JOSEP MAS • *School of Physics & Astronomy, University of St Andrews, Scotland, UK*
- CONG A. MENG • *Department of Chemistry, Stanford University, Stanford, CA, USA*
- MARIO MONTES-USATEGUI • *Departamento de Física Aplicada i Óptica, Facultat de Física and Institut de Nanociència i Nanotecnologia, Universitat de Barcelona, Barcelona, Spain*

- E. LAURA MUNTEANU • *FOM Institute AMOLF, Amsterdam, Delft, The Netherlands; Department of Bionanoscience, Kavli Institute of NanoScience, Faculty of Applied Sciences, Delft University of Technology, Delft, The Netherlands*
- PAULO A. MAIA NETO • *Instituto de Física and Instituto de Ciências Biomédicas, Universidade Federal do Rio de Janeiro, Rio de Janeiro, Brazil*
- H. MOYSÉS NUSSENZVEIG • *Instituto de Física and Instituto de Ciências Biomédicas, Universidade Federal do Rio de Janeiro, Rio de Janeiro, Brazil*
- LENE ODDERSHEDE • *Niels Bohr Institute, University of Copenhagen, Blegdamsvej, Copenhagen, Denmark*
- STEPHEN R. OKONIEWSKI • *JILA, National Institute of Standards and Technology and University of Colorado, Boulder, CO, USA; Department of Physics, University of Colorado, Boulder, CO, USA*
- ADRIAN O. OLIVARES • *Department of Biology, Massachusetts Institute of Technology, Cambridge, MA, USA*
- E. MICHAEL OSTAP • *Department of Physiology, The Pennsylvania Muscle Institute, Perelman School of Medicine, University of Pennsylvania, Philadelphia, PA, USA*
- FRANCESCO PEDACI • *Department of Single-Molecule Biophysics, Centre de Biochimie Structurale, Montpellier, France*
- THOMAS T. PERKINS • *JILA, National Institute of Standards and Technology and University of Colorado, Boulder, CO, USA; Department of Molecular, Cellular, and Developmental Biology, University of Colorado, Boulder, CO, USA*
- ERWIN J.G. PETERMAN • *Department of Physics and Astronomy and LaserLab, Vrije Universiteit Amsterdam, Amsterdam, The Netherlands*
- AVIN RAMAIYA • *Center for Plant Molecular Biology, Universität Tübingen, Tübingen, Germany*
- ALEKSANDER A. REBANE • *Department of Cell Biology and Integrated Graduate Program in Physical and Engineering Biology and Department of Physics, Yale University, New Haven, CT, USA*
- CHRISTINE M RITTER • *Niels Bohr Institute, University of Copenhagen, Blegdamsvej, Copenhagen, Denmark*
- ZHANNA SANTYBAYEVA • *Department of Single-Molecule Biophysics, Centre de Biochimie Structurale, Montpellier, France*
- ERIK SCHÄFFER • *Center for Plant Molecular Biology, Universität Tübingen, Tübingen, Germany*
- JOSHUA W. SHAEVITZ • *Joseph Henry Laboratory of Physics and Lewis-Sigler Institute of Integrative Genomics, Department of Physics, Princeton University, Princeton, NJ, USA*
- HENRY SHUMAN • *Department of Physiology, The Pennsylvania Muscle Institute, Perelman School of Medicine, University of Pennsylvania, Philadelphia, PA, USA*
- AARON SONNBERGER • *Center for Plant Molecular Biology, Universität Tübingen, Tübingen, Germany*
- SARA TAFOYA • *Biophysics Graduate Group, University of California, Berkeley, CA, USA*
- NATHAN B. VIANA • *Instituto de Física and Instituto de Ciências Biomédicas, Universidade Federal do Rio de Janeiro, Rio de Janeiro, Brazil*
- DAAN VORSELEN • *Department of Physics and Astronomy and LaserLab, Vrije Universiteit Amsterdam, Amsterdam, The Netherlands*
- KEVIN D. WHITLEY • *Center for the Physics of Living Cells and; Center for Biophysics and Computational Biology, University of Illinois, Urbana, IL, USA*

GIJS J.L. WUITE • *Department of Physics and Astronomy and LaserLab, Vrije Universiteit Amsterdam, Amsterdam, The Netherlands*

AHMET YILDIZ • *Department of Physics and Department of Molecular and Cell Biology, University of California, Berkeley, CA, USA*

YONGLI ZHANG • *Department of Cell Biology, School of Medicine, Yale University, New Haven, CT, USA*

# **Part I**

## **Theory and Design of Optical Tweezers**

# Chapter 1

## Introduction to Optical Tweezers

Matthias D. Koch and Joshua W. Shaevitz

### Abstract

Thirty years after their invention by Arthur Ashkin and colleagues at Bell Labs in 1986 [1], optical tweezers (or traps) have become a versatile tool to address numerous biological problems. Put simply, an optical trap is a highly focused laser beam that is capable of holding and applying forces to micron-sized dielectric objects. However, their development over the last few decades has converted these tools from boutique instruments into highly versatile instruments of molecular biophysics. This introductory chapter intends to give a brief overview of the field, highlight some important scientific achievements, and demonstrate why optical traps have become a powerful tool in the biological sciences. We introduce a typical optical setup, describe the basic theoretical concepts of how trapping forces arise, and present the quantitative position and force measurement techniques that are most widely used today.

**Key words** Optical trap, Optical tweezers, Force measurement techniques, Micron-sized dielectric objects

---

### 1 Overview and Historic Introduction

Historically, the structural properties of living cells were largely inferred from light microscopy images. The subsequent improvement of imaging optics over the centuries and the invention of innovative microscopy techniques [2–6] led to remarkable insights into the blueprint of single cells down to the level of a few hundreds of nanometers, the diffraction limit of light [7, 8]. The innovations seen at the turn of the twenty first century in super-resolution imaging techniques [9–12] overcame this fundamental, physical limit and enabled even greater insight down to the level of individual proteins or protein filaments only a few tens of atoms in diameter [13].

Despite the static picture of life afforded by conventional microscopy, cells are highly dynamic, constantly remodeling themselves and interacting with their chemical and mechanical environment. Driving this vast array of movements are biochemically generated mechanical forces that typically range from femto ( $10^{-15}$ )- to micro ( $10^{-6}$ )-Newtons and vary on timescales between

milliseconds ( $10^{-3}$  s) and hours ( $10^3$  s). It is no surprise then that a variety of techniques have been invented in the last few decades to probe forces and mechanical properties such as rigidity and elasticity of single cells, tissues, and even minute protein machines such as the flagellar motor of sperm or bacteria [14]. By controlled aspiration of a cell membrane using a micropipette, for example, its deformation to an applied pressure can be optically measured and mechanical properties inferred [15]. Another technique, traction force microscopy, measures the deformation of two-dimensional substrates or three-dimensional hydrogels caused by embedded cells [16, 17]. While these techniques probe how large eukaryotic cells interact mechanically with their environment as a whole, they are not accessible to the world of single molecules or small protein compounds generating comparatively small deformation forces.

Atomic force microscopy (AFM) is ideally suited to the small forces and displacements produced by proteins [18, 19]. AFM uses a tiny microfabricated cantilever to measure deflections at atomic resolution caused by surface height changes during a raster scan of the tip, the retraction of a motor protein, or elastic forces of a protein filament (see [20] and references therein). AFMs allow applying relatively large forces in the nanoNewton range. However, probe fabrication techniques currently limit the stiffness range that is achievable, yielding stiff cantilevers that can easily damage soft biological surfaces such as cell membranes. In contrast to AFMs, the stiffness and applied force of an optical trap can be changed instantaneously and flexibly by changing the intensity of the laser beam, as explained in Subheading 3 of this chapter. Depending on the laser source, optical trapping forces range from femtoNewtons to nanoNewtons, a range well-suited to probe the mechanical world of molecular biology. Advanced particle tracking techniques, as introduced in Subheading 4, provide a means to measure nanometer-sized displacements at MHz rates for hours (see also Chapter 4 in this book) and complementary imaging techniques can usually be implemented in a straightforward manner with little complications (see for example Chapters 8, 9 and 17). Further reading and discussion of typical applications of different force probes and measurement techniques can be found in refs. [14, 21].

Although originally intended for the trapping and cooling of atoms [1], the potential applicability of optical tweezers to investigate biological specimens such as bacteria, viruses [22], and whole cells [23] was realized by Ashkin immediately after its invention. Steven Block and colleagues used optical trapping only a few years later to study the flagella of *Escherichia coli* and single kinesin motors [24, 25]. Since then, optical tweezers have been used to investigate biopolymers such as DNA [26–28] (see Chapters 10 and 11), actin [29–31], and microtubules [32–38] (see Chapter 16); molecular motors such as kinesin [25, 39–43] (see Chapter 18), dynein [44, 45], myosin [46–50] (see Chapter 19), RNA

polymerase [51–55] (*see* Chapter 15) and bacteriophage DNA packaging [56] (*see* Chapter 13); protein folding [57] (*see* Chapter 14); mechanical properties of bacteria [58]; bacterial propulsion [59, 60]; surface imaging of single bacteria [61]; filopodia dynamics during phagocytosis [62, 63]; particle interactions, uptake, and diffusion near a lipid bilayer [64, 65]; and micro-rheological properties of polymers [66–68] and whole cells [69]. Further, they have been used as a tool for imaging single bacteria in different orientations [70], to assist during the connection of single neurons by laser pulses [71], for particle sorting [72], to construct and probe artificial cytoskeletal networks [73, 74] and to chemically stimulate and manipulate single cells using drug releasing beads [75].

---

## 2 The Optical Trapping Microscope: Setup and Alignment

Optical tweezers are typically built on top of a commercial microscope. Near infrared wavelengths are most common for the trapping laser as they avoid various kinds of biological photodamage and are easily incorporated into imaging systems that use visible light. At its heart, the trapping apparatus consists of a conventional microscope with brightfield, phase contrast, or DIC illumination through a condenser or detection lens (DL), a high magnification, high numerical aperture (NA) objective lens (OL), and a sensitive camera for image acquisition (Fig. 1). Additionally, fluorescence modalities are often implemented using lasers of different wavelength or a white light source (WLS) with appropriate spectral filters (SF) and dichroic mirrors (DC).

The trapping laser can be coupled to a single mode optical fiber which produces a clean, Gaussian TEM00-mode beam profile (the basis of optical trapping and tracking theories is discussed below). The fiber also reduces mechanical noise so that electronics with fans and other noise-causing elements can be located off the optical table. The beam must be expanded to properly fill (or overfill) the back-focal plane (BFP) of the trapping lens [76] using a beam expander (BE). This can also be accomplished using different focal lengths in a 4f lens relay system ( $L_1, L_2$  in Fig. 1) that images a beam-steering device (BSD) such as a piezo or galvanometric mirror, onto the BFP. Any tilt of the beam by this device results in a tilt of the beam axis in the BFP and hence in a displacement of the laser focus in the focal plane. To achieve high-precision position detection and force measurement, trapping light together with the light scattered at the trapped object is collected by another high NA detection lens (DL) and imaged onto a quadrant photo detector (QPD) by another relay lens system ( $L_4, L_5$ ).

Compared to wide-field optical applications, focused beam and beam scanning technologies such as optical tweezers require extra

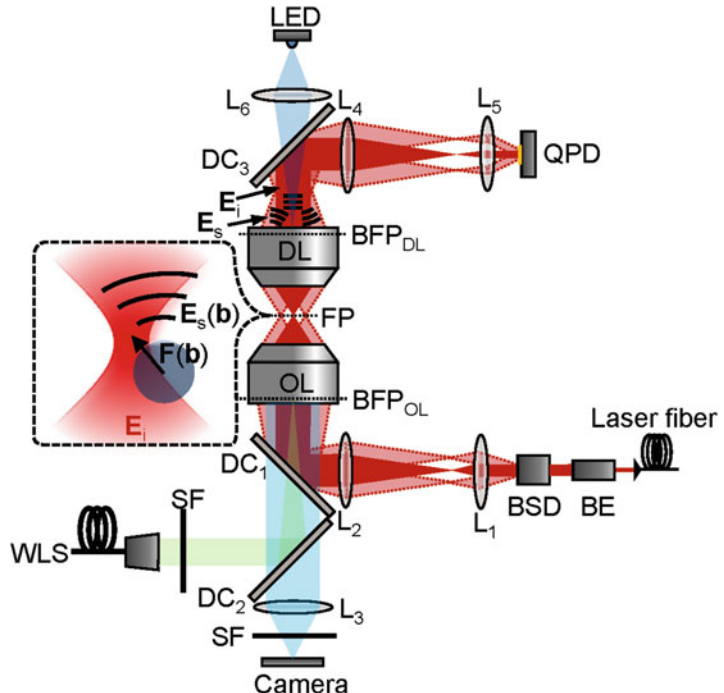


**Fig. 1** Example schematic of an optical trapping microscope

care in aligning the laser relative to the microscope optics. The collimated laser beam must be centered in the back-focal plane of the trapping objective lens and well-aligned with the optical axis. The most reliable mechanism for achieving good alignment is to use a special beam profiling camera, usually sold with appropriate software, to assess the beam quality, ellipticity, and diameter. A dummy back-focal plane aperture can be manufactured to match the exact diameter and position of the objective lens back-focal plane (which can be obtained from the lens vendor). With a good adapter, the beam profiler should be brought close to the BFP. No additional imaging optics should be used between BFP and profiler, since this could alter the beam profile and position. A long, straight threaded tube (~50 cm) to separate the beam profiler from the back aperture position is useful to define the alignment of the beam relative to the optical axis as it leaves the BFP. If using a BSD, it is important to make sure that the beam is still centered in the BFP when the beam is tilted by the BSD. Further, all optical elements (lenses, mirrors, etc.) should be centered on the laser path and beams should hit each surface in a rectangular or 45° angle whenever possible to reduce aberrations. It is a good idea to define a specific beam height above the optical table, to work in 90° angles whenever possible, and to control the profile, position and

orientation after each optical element. Back reflections should be avoided by using wavelength-specific antireflection coated optical elements.

An alternative method to check proper beam alignment is to use the back reflection of the laser focus from a coverslip projected onto the standard microscope camera. By moving the sample along the optical axis with a piezo-driven stage, or by refocusing the objective lens, one can probe the approximate 3D intensity profile of the laser focus. Upon refocusing, the pattern should change symmetrically in the lateral dimensions. Depending on the laser polarization, the reflected intensity pattern is ellipsoidal or cloverleaf shaped. A third method, discussed below, uses a QPD and assess misalignments and problems during the experiment.

### 3 Optical Trapping Forces

Optical trapping forces arise due to an interaction between the focused laser light and the trapped object. An intuitive and simple explanation can be given in the ray optics picture using momentum conservation at the materials surface [77] (Fig. 2). The refraction of the rays is given by Snell's law;  $k_1 = k_0 n_m \sin(\theta_1) = k_0 n_p \sin(\theta_2) = k_2$  with the wave vector or optical momentum in vacuum  $k_0 = 2\pi / \lambda$ , and the refractive indices  $n_m \approx 1.33$  for water and  $n_p \approx 1.5$  for a glass particle. Typically, a laser wavelength of  $\lambda = 1064$  nm is used to minimize the absorption of light by water and biological specimens [78]. Figure 2 illustrates how a trapped

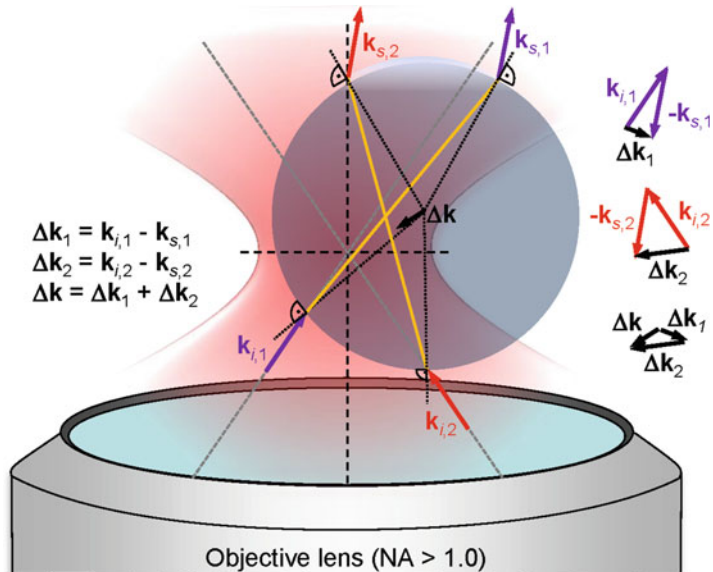


**Fig. 2** Ray optics picture of light momentum transfer

particle at a position  $\mathbf{b}$  relative to the focus refracts two incoming light beams  $k_{i,1}$  and  $k_{i,2}$ , leading to a change of momentum  $\Delta k_1, \Delta k_2$  of the outgoing beams  $k_{s,1}, k_{s,2}$ . By momentum conservation, there is no net change to the total momentum and the trapped particle experiences a compensatory momentum pointed towards the laser focus.

While simple, this picture is only valid for large particles (those with a diameter much larger than the wavelength of light) and neglects the effects of back-scattering and absorption of the trapping laser. Many other factors affect the actual force experienced by a trapped particle. These include the laser power  $P$  [79], numerical aperture  $NA$  [80] of the focusing lens and its illumination [76], polarization  $p$  [81], as well as on the material properties of the trapped particle such as the refractive index  $n_p$  and its size  $D$  [82, 83].

A number of influential groups have developed theories over the last two decades to quantitatively describe optical trapping forces (see [82, 84–86] and references therein). A general description can be given using Mie theory, which is an exact analytical solution of Maxwell's equations for the scattering of light by a spherical particle. However, these calculations can be very complicated. Since most particles used in biological trapping assays are small, they are often assumed to be “Rayleigh particles,” meaning that their diameter  $D$  is much smaller than the wavelength of the trapping laser. This assumption is not formally valid for particles between 500 and 1000 nm in size. However, this simplified theory has proven to give viable results for larger particles and even for helical bacteria with an outer diameter of roughly 600 nm and a length of several held in a rapidly oscillating trap [87, 88].

The Rayleigh approximation treats the dielectric particle as a volume of dipoles, each interacting with the electric  $\mathbf{E}$  and magnetic  $\mathbf{B}$  fields of the laser to produce the Lorentz force

$$\mathbf{F}_d = (\mathbf{p} \cdot \nabla) \mathbf{E} + \frac{\partial \mathbf{p}}{\partial t} \times \mathbf{B} \quad (1)$$

The dipole moment  $\mathbf{p}$  of a small volume element  $V$  in the local electric field  $\mathbf{E} = \mathbf{E}_i + \mathbf{E}_s$  (the superposition of the incident  $\mathbf{E}_i$  and scattered  $\mathbf{E}_s$  field) is given by

$$\mathbf{p} = \epsilon_0 n_m^2 V \alpha \mathbf{E} \quad (2)$$

with the vacuum permittivity  $\epsilon_0 = 8.85 \text{ pF/m}$  and the polarizability  $\alpha = 3(m^2 - 1)/(m^2 + 2)$  according to the Clausius–Mossotti relation with  $m = n_p/n_m$ . Using the vector identity  $(\mathbf{E} \cdot \nabla) \mathbf{E} = \frac{1}{2} \nabla \mathbf{E}^2 - \mathbf{E} \times (\nabla \times \mathbf{E})$  and Faraday's law  $\nabla \times \mathbf{E} = -\frac{\partial}{\partial t} \mathbf{B}$ , the force acting on a dipole can be written as

$$\mathbf{F}_d = \epsilon_0 n_m^2 V \operatorname{Re}(\alpha) \left( \frac{1}{2} \nabla \mathbf{E}^2 + \frac{\partial}{\partial t} \mathbf{E} \times \mathbf{B} \right) \quad (3)$$

The electric field of the monochromatic laser light can be written as  $\mathbf{E}(\mathbf{r}, t) = \mathbf{E}_0(\mathbf{r}) e^{i\omega t}$ . At a wavelength of  $\lambda = 1064$  nm, the wave oscillates at a frequency  $f = c/\lambda \approx 280$  THz, and hence only the temporal average is significant and the second term of Eq. 3 vanishes:

$$\mathbf{F}_d = \frac{\epsilon_0 n_m^2 V \operatorname{Re}(\alpha)}{4} \nabla \mathbf{E}_0^2(\mathbf{r}) \quad (4)$$

This dipole force can be identified with a force density  $\mathbf{f} = \mathbf{F}_d/V$  and the total optical force  $\mathbf{F}_{opt}$  on the particle results from an integration over the complete volume  $V$  of the scatterer. Because the local field  $\mathbf{E}$  is actually the superposition of two fields, the incident and the scattered field, the total force further splits up into two parts that are identified as a gradient force  $\mathbf{F}_{grad}$  (that depends on the gradient of the incident intensity) and a scattering force  $\mathbf{F}_{scat}$  (that mainly describes scattering or radiation pressure) [79]:

$$\mathbf{F}_{opt} = \int_V \mathbf{f} dV = \underbrace{\frac{\epsilon_0 n_m^2 \operatorname{Re}(\alpha)}{4} \int_V \nabla |\mathbf{E}_i|^2 dV}_{= \mathbf{F}_{grad}} + \underbrace{\frac{\epsilon_0 n_m^2 \operatorname{Re}(\alpha)}{4} \int_V \left( \nabla |\mathbf{E}_s|^2 + \mathbf{E}_i \mathbf{E}_s^* + \mathbf{E}_i^* \mathbf{E}_s \right) dV}_{= \mathbf{F}_{scat}} \quad (5)$$

For small objects, the intensity gradient varies only slightly over the particle's diameter and the first integral can be solved:

$$\mathbf{F}_{grad} = \frac{n_m \operatorname{Re}(\alpha) V}{2c} \nabla I(\mathbf{b}) \quad (6)$$

A force profile of  $\mathbf{F}_{grad}$  for all three directions is shown in Fig. 3. For small displacements  $\mathbf{b}$ , the force scales linearly with displacement, expressed by the so-called trap stiffnesses  $\kappa_x$ ,  $\kappa_y$ , and  $\kappa_z$  in each

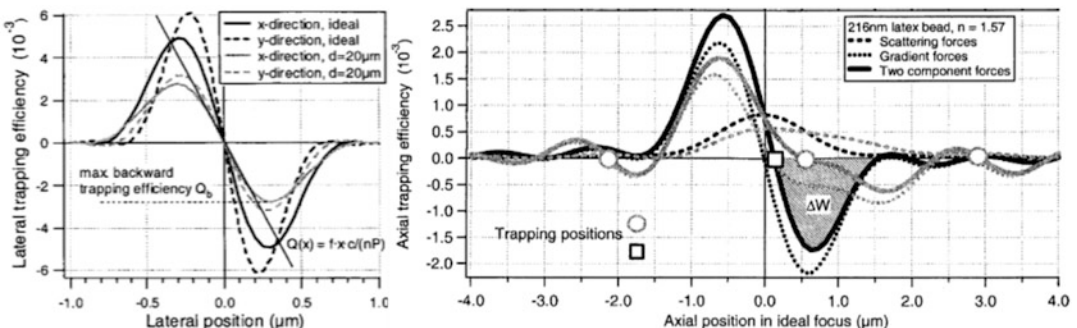


**Fig. 3** Optical forces measured in the lateral (*left*) and axial (*right*) directions relative to the propagation direction of light. Adapted from ref. [142]

direction. This linearity is widely exploited, since it makes calibration (*see* below) easy. Assuming a Gaussian beam profile with width  $\sigma_x = \sigma_y = 0.61 \lambda/\text{NA}$  and  $\sigma_z = 2\lambda/n_m (1-\cos(\alpha))$  from an objective lens with  $\text{NA} = n_m \sin(\alpha)$ , the gradient can be calculated and the linear force relationship, given by the diagonal matrix  $\kappa = (\kappa_x, \kappa_y, \kappa_z)$ , can be found using a Taylor approximation,

$$\begin{aligned} \mathbf{F}_{\text{grad}}(\mathbf{b}) &= \mathbf{F}_{\text{grad}}|_{\mathbf{b}=0} + \nabla \mathbf{F}_{\text{grad}}|_{\mathbf{b}=0} \mathbf{b} + O(\mathbf{b}^2) \\ &\approx \frac{n_m \text{Re}(\alpha) V I_0}{\sqrt{8\pi c}} \begin{pmatrix} \frac{1}{\sigma_x^3} & 0 & 0 \\ 0 & \frac{1}{\sigma_y^3} & 0 \\ 0 & 0 & \frac{1}{\sigma_z^3} \end{pmatrix} \mathbf{b} = -\kappa \cdot \mathbf{b} \quad (7) \end{aligned}$$

The scattering force in Eq. 5 points in axial direction, giving rise to a small force offset as indicated in Fig. 3. A simple calculation of the scattering force cannot be given and detailed calculations are difficult. The scattering force can be formulated as a function of scattering and extinction cross-sections as shown by Rohrbach [79] using an approximation to the exact Mie theory called Rayleigh–Gans theory. However, especially in the linear force regime,  $\mathbf{F}_{\text{scat}}$  is approximately constant for all displacements and can be assumed to only cause a small position offset, which is typically neglected.

## 4 Three-Dimensional Position Tracking of Trapped Particles at Sub-Nanometer Precision and MHz Rates

Displacements of a trapped bead relative to the focus can be measured both to quantify particle motion and to assay the trapping force. The simplest approach is to use video tracking with the camera of the microscope. A 2D Gaussian fit to the intensity image of the bead yields its lateral center position [89]. Automated particle finding and tracking algorithms are freely available as plugins to major scientific image analysis software such as ImageJ (<http://imagej.nih.gov/ij/>). Tracking the axial position of a bead can be done via a look-up table comparing the brightness of a bead, which is dark below the image plane and bright above it (*see* [90]). This method is prone to errors caused by changes in the light level of the illumination, reducing precision and requiring complicated tracking algorithms or strategies [91–93].

More precise systems use BFP interferometry. Small phase changes of the scattered light relative to the incident electric field of the laser caused by tiniest position changes of the bead are amplified tremendously by the incident intensity. For example, even a very weak scatterer that scatters only 1 % of the incoming

light produces an interference signal of 20 %. Although modern scientific cameras become faster and more sensitive nearly every year, the highest frame-rate cameras require a very large number of high incident. Hirvonen et al. [94] recently reported imaging with  $16 \times 64$  pixel arrays at 1 MHz at nontoxic photon levels that would be enough for tracking single beads. However, a high tracking precision has still to be demonstrated and the main power of video-tracking, i.e., simultaneous multi-particle tracking [95], is lost at small pixel number.

BFP tracking usually uses a quadrant photodiode (QPD) or other small position-sensitive detector to evaluate the resulting interference pattern [96, 97]. Alternative methods have been introduced based on polarization [98] or spot measurements in the front-focal plane [99], but these only allow two-dimensional measurements. In contrast to video tracking, BFP tracking with a QPD typically allows tracking rates of several MHz [62, 100] up to 100 MHz [101] and Angstrom level precision (e.g., precise enough to sense displacements of an enzyme along DNA by a single base pair) [102–104].

As illustrated in Fig. 4 and described by Eq. 8, the intensity pattern formed by a coherent superposition of the electric field  $\mathbf{E}_i$  of the incident laser beam and electric field  $\mathbf{E}_s$  scattered at the particle at position  $\mathbf{b}$  is recorded by a QPD placed in the back-focal plane of a detection lens. The phase  $\varphi_i$  of the incident field is constant at the position of the detector, however, the phase  $\varphi_s(\mathbf{b})$  of the scattered field directly encodes its position  $\mathbf{b}$  relative to the focus. These phases can be described in a paraxial beam approximation, also

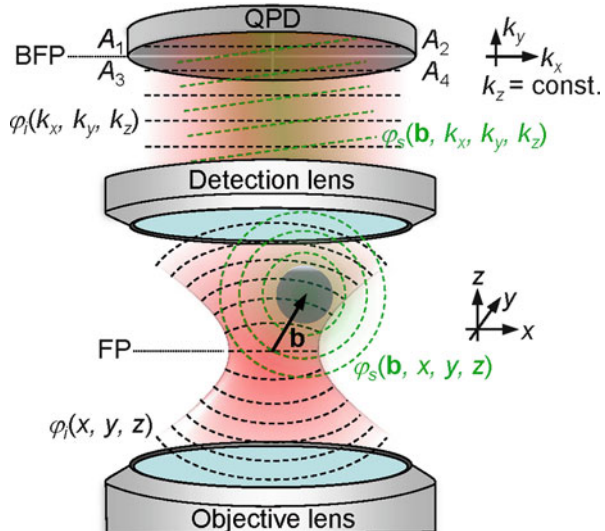


**Fig. 4** Interferometric particle tracking in the back-focal plane

known as Gaussian beam theory [105], which is mathematically relatively simple but strictly speaking only considers slightly focused beams. However, this description has been shown to give viable results even for non-spherical scatterers [87, 88] and highly focused laser beams at  $\text{NA} = 1.49$ . The resultant intensity pattern on the detector is described by

$$\begin{aligned} \left| \tilde{\mathbf{E}}_i + \tilde{\mathbf{E}}_s(\mathbf{b}) \right|^2 &= \left| \tilde{\mathbf{E}}_i(k_x, k_y) \right|^2 + \left| \tilde{\mathbf{E}}_s(k_x, k_y, \mathbf{b}) \right|^2 + 2\text{Re}\left\{ \tilde{\mathbf{E}}_i(k_x, k_y) \cdot \tilde{\mathbf{E}}_s^*(k_x, k_y, \mathbf{b}) \right\} \\ &= I_0(k_x, k_y) + I_s(k_x, k_y, \mathbf{b}) + 2\sqrt{I_0(k_x, k_y)I_s(k_x, k_y, \mathbf{b})} \cos(\varphi_s(\mathbf{b}) - \varphi_i) \end{aligned} \quad (8)$$

According to the Fourier shifting theorem  $\mathbf{E}(x + b_x) \rightarrow \tilde{\mathbf{E}}(k_x)e^{ik_x b_x}$ , such that a lateral displacement  $b_x$  or  $b_y$  in the focal plane leads to a tilt  $k_x b_x$  or  $k_y b_y$  in the BFP. Since the incident phase of a Gaussian beam varies only slowly over the focal extent in the lateral direction [105], the lateral phase difference is given by:

$$\begin{aligned} \Delta\varphi_x(b_x) &= \varphi_{s,x}(b_x) - \varphi_i = \phi_{s,x} = k_x b_x \\ \Delta\varphi_y(b_y) &= \varphi_{s,y}(b_y) - \varphi_i = \phi_{s,y} = k_y b_y \end{aligned} \quad (9)$$

There is a similar, parabolic, phase shift for displacements  $b_z$  in the axial direction, however, which scales with the ratio  $b_z/f \approx 10^{-5}$  and is negligible [106]. Instead, measurement of  $b_z$  relies on another intrinsic feature of a focused (Gaussian) beam called the Gouy phase shift ([107] and references 1–3 therein):  $\phi_{fp}(z) = k_0 z - \tan^{-1}(z/z_0)$  with  $z_0 = 1/a_0 k_z$  and  $a_0 = \text{NA}^2/1.22\pi^2$ . In addition, the scattered field is also retracted by the constant factor  $\pi/2$  relative to the incident field [108]. The complete situation is illustrated in Fig. 5 for a scatterer at three different positions  $b_z$ . In the far field,  $z \rightarrow \infty$ , one obtains again a linear phase dependence with respect to the particle position,

$$\begin{aligned} \Delta\varphi_z(b_z) &= \lim_{z \rightarrow \infty} (\varphi_s - \varphi_i) \\ &= \frac{\pi}{2} - \tan^{-1}(a k_z b_z) \stackrel{a k_z b_z < 0.5}{\approx} \frac{\pi}{2} - a k_z b_z \end{aligned} \quad (10)$$

The simplification on the right side of Eq. 10 holds for  $|b_z| < 0.5/a_0 k_z \approx 1/2\lambda = 532 \text{ nm}$  (for a detection lens with  $\text{NA}_D = 1.2$  and water with  $n_m = 1.33$ ), which is well fulfilled in optical trapping approaches with maximal particle displacements  $b_z < 150 \text{ nm}$  (similar to the limit of the linear detection region discussed in the last section and shown experimentally in the next section).

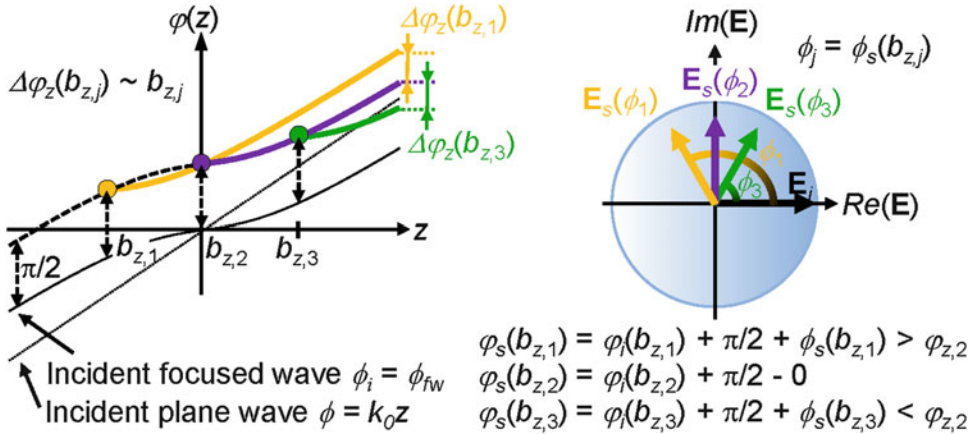


**Fig. 5** Axial phase dependence relative to the scatterer position. Adapted from ref. [87]

In summary, the relevant interference term in Eq. 8 becomes

$$\begin{aligned}
2\operatorname{Re}\left\{\tilde{\mathbf{E}}_i \cdot \tilde{\mathbf{E}}_s^*(\mathbf{b})\right\} &= \left|\tilde{\mathbf{E}}_i + \tilde{\mathbf{E}}_s(\mathbf{c})\right|^2 - \underbrace{\left|\tilde{\mathbf{E}}_i\right|^2}_{\approx \text{const}} - \underbrace{\left|\tilde{\mathbf{E}}_s\right|^2}_{\ll |\tilde{\mathbf{E}}_i|^2} \\
&= 2\left|\tilde{\mathbf{E}}_i\right| \cdot \left|\tilde{\mathbf{E}}_s^*(\mathbf{b})\right| \cdot \cos\left(k_x b_x + k_y b_y - \alpha k_z b_z + \frac{\pi}{2}\right) \\
&= -2\left|\tilde{\mathbf{E}}_i\right| \cdot \left|\tilde{\mathbf{E}}_s^*(\mathbf{b})\right| \cdot \sin\left(k_x b_x + k_y b_y - \alpha k_z b_z\right)
\end{aligned} \tag{11}$$

The incident intensity  $|\mathbf{E}_i|^2$  and the scattered intensity  $|\mathbf{E}_s|^2$  are both constants that can be subtracted electronically from the detection leaving only a sinusoidal dependence to the detector output. Together with the sensitivity,  $s_{PD}$ , of the photodiode measured in Ampere per Watt, the amplification,  $\alpha_{PA}$ , of the pre-amplifier in Volt per Ampere, the polarizability  $\alpha$  of the scatterer and a possible time-dependent laser power  $P(t) = \frac{1}{2}P_0\epsilon_0|\mathbf{E}_i(t)|^2$ , the signal  $\hat{S}_n^{raw}(\mathbf{b})$  of the  $n$ -th quadrant of the QPD is given by:

$$\hat{S}_n^{raw}(\mathbf{b}) = P(t)s_{PD}\alpha_{PA} \left( 1 + \alpha - 2\sqrt{\alpha} \int_{A_n} \sin(k_x b_x + k_y b_y - \alpha k_z b_z) dk_x dk_y \right) \tag{12}$$

The quadrants of the QPD are linearly combined to a signal triplet according to

$$\begin{aligned}
S_x &= (\hat{S}_1^{raw} + \hat{S}_3^{raw}) - (\hat{S}_2^{raw} + \hat{S}_4^{raw}) \\
S_y &= (\hat{S}_1^{raw} + \hat{S}_2^{raw}) - (\hat{S}_3^{raw} + \hat{S}_4^{raw}) \\
S_z &= \hat{S}_1^{raw} + \hat{S}_2^{raw} + \hat{S}_3^{raw} + \hat{S}_4^{raw}
\end{aligned} \tag{13}$$

A straight forward calculation of the resulting integrals, simplified by sine/cosine addition theorems, yields an analytical relation of

the detector signal measured in Volts and the actual particle position for small displacements. Similar to the linear dependence of the force, the position detection is linear for small particle displacements, which can be obtained by a Taylor approximation up to second order,

$$\begin{aligned} S_x &= A_x \text{sinc}\left(\frac{r_{BFP} b_x}{2}\right) \sin\left(\frac{r_{BFP} b_x}{2}\right) \text{sinc}(r_{BFP} b_y) \cos(a_0 k_z b_z) & |b_x| < 100 \text{ nm} \\ &\quad \approx \frac{b_y = b_z = 0}{g_x b_x} & |b_y| < 100 \text{ nm} \\ S_y &= A_y \text{sinc}\left(\frac{r_{BFP} b_y}{2}\right) \sin\left(\frac{r_{BFP} b_y}{2}\right) \text{sinc}(r_{BFP} b_x) \cos(a_0 k_z b_z) & b_x = b_z = 0 \\ &\quad \approx \frac{b_x = b_z = 0}{g_y b_y} & |b_z| < 150 \text{ nm} \\ S_z &= A_z \text{sinc}(r_{BFP} b_x) \text{sinc}(r_{BFP} b_y) \sin(a_0 k_z b_z) & b_x = b_y = 0 \\ &\quad \approx \frac{b_x = b_y = 0}{g_z b_z} & g_z b_z \end{aligned} \quad (14)$$

Here,  $r_{BFP} = k_0 N A_D$  is the radius of the detection lens BFP and  $A_x$ ,  $A_y$ , and  $A_z$  are the maximum signal amplitudes mainly depending on the laser intensity. The constants  $g_x$ ,  $g_y$ , and  $g_z$  are called detector sensitivities with units V/m and are usually determined experimentally together with the trap stiffnesses  $\kappa_x$ ,  $\kappa_y$ , and  $\kappa_z$  in a calibration step prior to any experiment.

## 5 Position and Force Calibration Methods

Theoretically, the calibration constants could be derived analytically from Eqs. 7 and 14. However, most of the constants needed as input parameters to these equations are not known to a sufficient precision and an experimental calibration is often performed. A variety of calibration methods have been reported since the invention of optical tweezers [78, 109–116] (also see Chapters 2 and 3 in this book), among which the most widely used are presented in this introduction. Depending on the experimental design and available hardware, usually a combination of the following methods is chosen.

To obtain the detector sensitivities  $g$ , the easiest method is to attach a bead to the coverslip and move it through the center of the detection focus with a motorized or piezo-driven microscope stage. Fixation can be done using gravity to let beads sediment down and a high salt concentration reducing electrostatic repulsion of the slightly negatively charged glass cover slip and glass or polystyrene bead surfaces, which otherwise shield the attractive short range van der Waals forces (the complete potential is known as the DLVO potential). However, the bead in this method is lost for any further experiment and hence this technique is only desirable as a look-up or control measurement. Using two independent lasers, one with high power generating the actual trap and one at

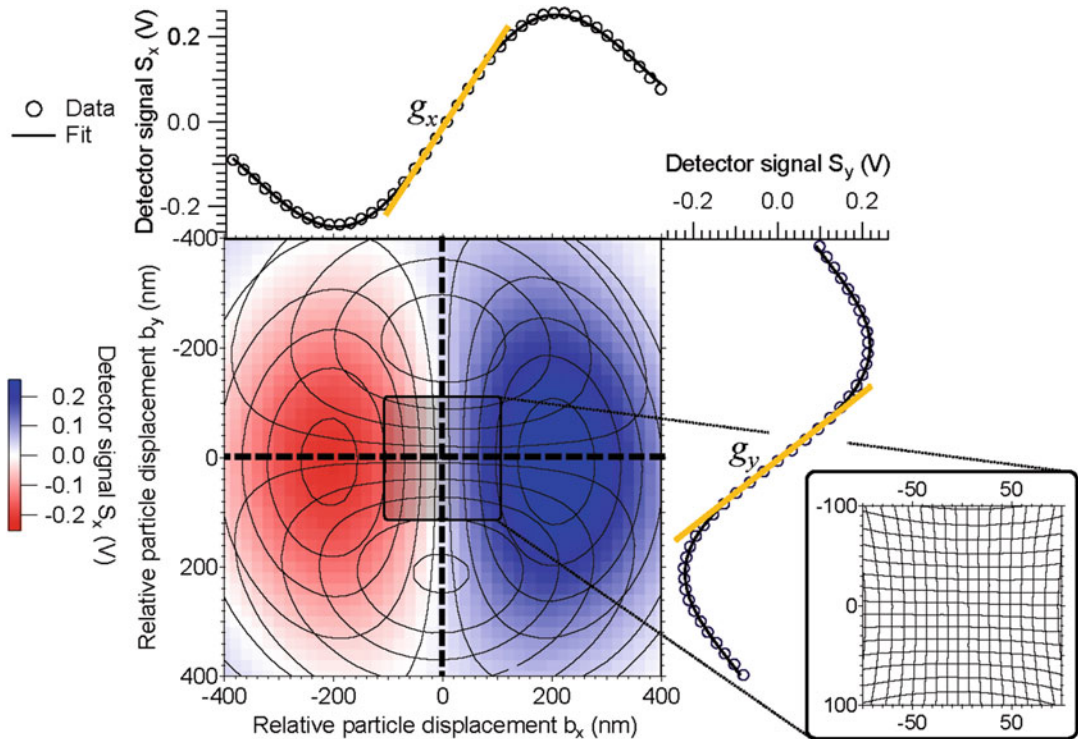


**Fig. 6** Position calibration using a raster scan of a trapped 520-nm polystyrene bead through an independent detection focus. Fits to line scans (*dashed lines*) through the center position yield the detector sensitivities  $g_x$  and  $g_y$ . Isolines are orthogonal around the center (*inset*) indicating that both directions can be considered independent of each other

low power solely for detection, the bead can be moved through the detection focus for calibration while keeping it available for further measurements. The result of a raster scan of the bead position in the  $x$ - $y$  plane is shown in Fig. 6. The amplitude of the signal  $S_x(b_x, b_y)$  in the  $x$ -direction is shown color coded with isolines for  $S_x(b_x, b_y)$  and  $S_y(b_x, b_y)$  in both lateral directions. A cut along  $b_x = 0$  or  $b_y = 0$  and fitting the dramatically simplified version of Eq. 14 yields the detector sensitivities, which typically vary by 10–20 % between both directions due to polarization effects,

$$\begin{aligned} \mathcal{G}_x &= \frac{\partial}{\partial b_x} S_x(b_x, b_y = 0, b_z = 0) \Big|_{b_x=0} = A_x \frac{r_{BFP}}{2} \\ \mathcal{G}_y &= \frac{\partial}{\partial b_y} S_y(b_x = 0, b_y, b_z = 0) \Big|_{b_y=0} = A_y \frac{r_{BFP}}{2} \end{aligned} \quad (15)$$

Similarly, the extent of the linear detection region  $LDR_{10\%}$ , here defined by a maximum deviation from the true slope of 10 %, as well as the unique detection region  $UDR$ , defined by the distance between both extremes of the detection signal, can be obtained by

$$\text{LDR}_{x/y, 10\%} = \frac{2.72}{r_{BFP}} \quad \text{UDR}_{x/y} = \frac{4.6}{r_{BFP}} \quad (16)$$

For the calibration scan shown in Fig. 6:  $\mathcal{g}_x = 1.96 \text{ V}/\mu\text{m}$ ,  $\mathcal{g}_y = -1.66 \text{ V}/\mu\text{m}$ ,  $\text{LDR}_x = 239 \text{ nm}$ ,  $\text{LDR}_y = 248 \text{ nm}$ ,  $\text{UDR}_x = 404 \text{ nm}$  and  $\text{UDR}_y = 420 \text{ nm}$ . As shown by the inset of Fig. 6, isolines are perpendicular on each other for small particle displacements, meaning that  $S_x$  and  $S_y$  are independent. This property is used together with the signal linearity for small displacements to rapidly convert between position signals  $S$  and actual positions  $b$ .

If the position sensitivity is known, the force calibration can be done exploiting the equipartition theorem [117] stating that every harmonic term in the energy function (Hamiltonian) has a mean energy of  $\frac{1}{2}k_B T$ , with Boltzmann constant  $k_B$  and temperature  $T$ . Since bead motions are linear with force for small displacements,  $F = -\kappa b$ , the potential  $V = -\int F db = \frac{1}{2}\kappa b^2$  is harmonic and the position probability distribution  $p(b) = \exp(-V)$  is a Gaussian. The width,  $\sigma_p$ , of the position histogram can be obtained by a Gaussian fit as shown in Fig. 7a for simulated fluctuation data [118, 119] yielding the trap sensitivity

$$\kappa = \sqrt{\frac{k_B T}{\sigma_p^2}} \quad (17)$$

A second approach, called the Langevin or Power-Spectrum approach, analyses the actual motion of a particle in an optical trap. The displacement of a trapped bead is described by the Langevin equation,  $\gamma \dot{b} + \kappa b = F_{th}$  [117, 118], with drag coefficient  $\gamma = 3\pi D\eta$  for a sphere of diameter  $D$  immersed in a fluid with viscosity  $\eta$  moving due to random thermal forces  $F_{th}$ . These forces time-average to zero,  $\langle F_{th}(t) \rangle = 0$ , and have a flat, white noise spectrum  $\langle F_{th}(t)F_{th}(t+\tau) \rangle = 2\gamma k_B T \delta(\tau)$  [117, 120] according to the fluctuation dissipation theorem [117, 118]. Here, inertia is neglected due to the very low Reynolds number for the system [121]. A Fourier transform  $-i\omega\gamma\tilde{b}(\omega) + \kappa\tilde{b}(\omega) = \tilde{F}_{th}(\omega)$  of the Langevin equation directly results in the power-spectral density (PSD) shown in Fig. 7b,

$$\text{PSD}(\omega) = \left| \tilde{b}(\omega) \right|^2 = \frac{2k_B T}{\gamma} \frac{1}{\omega^2 + \omega_c^2} \quad (18)$$

Here,  $\omega_c = \kappa/\gamma$  is the so-called corner frequency, the frequency at which the power is reduced by 50 % compared to  $\text{PSD}(t=0)$ . If the PSD is calculated from calibrated position data  $b(t)$ , the amplitude  $\text{PSD}(t=0) = 2k_B T \gamma / \kappa$ , combined with the corner frequency  $f_c = \omega_c/2\pi$  can be used to determine  $\kappa$  and  $\gamma$ . However, if the detector sensitivity  $\mathcal{g}$  is unknown, prior information about the

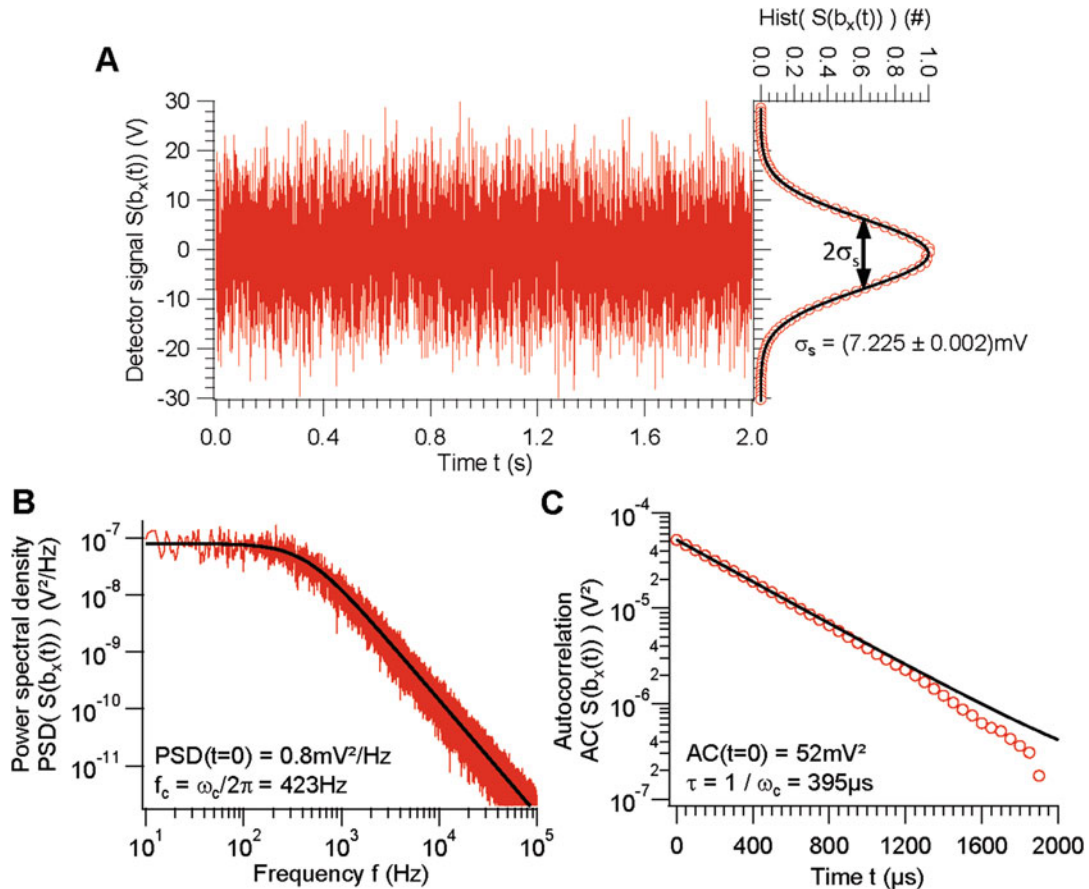


**Fig. 7** Trap calibration for simulated data of a 1062-nm polystyrene bead at a trap stiffness of  $\kappa = 20 \text{ pN}/\mu\text{m}$  and 1 MHz sample rate. (a) The bead is fluctuating inside the optical trap due to Brownian motion driven by thermal forces. The position probability is Gaussian. (b) A Lorentzian fit to the PSD of the confined bead motion yields the corner frequency  $f_c$ . (c) An exponential fit to the autocorrelation of bead positions yields the autocorrelation time  $\tau_c$

bead size and the fluid viscosity ( $\eta \approx 1 \text{ mPas}$  for water at 21 °C), and hence the drag coefficient, can be used to determine  $k$ . The ratio  $\mathcal{G} = \sigma_s/\sigma_p$  of the signal and position histograms then yields the detector sensitivity  $\mathcal{G}$  using Eq. 17. This method is very elegant since it only relies on measurement of fluctuation data. Depending on the trap stiffness, a few seconds of sampled data at several tens to hundreds of kHz is enough for this statistical analysis.

An equivalent method uses the position autocorrelation (AC), which is shown in Fig. 7c and follows from Eq. 18 according to the Wiener–Khintchine theorem,

$$\text{AC}(t) = \text{AC}(b(t)) = \mathcal{F}\left(\left|\tilde{b}(\omega)\right|^2\right) = \frac{k_B T}{\kappa} e^{-\frac{t}{\tau_c}} \quad (19)$$

Here,  $\tau_c = \gamma/\kappa = 1/\omega_c$  is the autocorrelation time. Again, for calibrated position data, the combination of  $\text{AC}(t = 0)$  and  $\tau_c$

gives both the force constant  $k$  and the drag coefficient  $\gamma$ . If the sensitivity is unknown,  $\tau_c$  can still be used to determine  $k$  and the ratio  $g = \sigma_s/\sigma_p$  to determine  $g$ . Years of experience have shown that it is beneficial to have online calibration software evaluating the position histogram, PSD and AC together, mainly to check for systematical errors and anomalous noise and filtering in different frequency bands. On the one hand, these plots can be used during detector and trap alignment, to asses drift of optical components or to identify noisy electronics. On the other hand, a miraculous apparent low frequency drift appearing between different, successive calibrations indicates dirt sticking to the bead or just diffusion in the trap which is too small to be seen in the microscope.

It shall be noted that the raster scan calibration method to determine  $g_x$  and  $g_y$  mentioned above only allows a 2D calibration. Since most biological problems are three dimensional, calibration of the  $z$ -direction is also important. Exploiting pure fluctuation data as described above in the case of unknown detector sensitivity, this is straightforward and the same procedure as for the lateral directions applies, i.e., assuming  $\gamma = 3\pi D\eta$  and using  $AC(t=0)$ ,  $PSD(t=0)$ ,  $\omega_c$  or  $\tau_c$ . In more advanced systems, one can implement 3D beam steering, via slight focusing and defocusing of the trapping beam, to implement a full 3D raster scan of the detection system. Comparing the results of all these methods can be used to estimate error.

All these calibration methods are *in vitro* and rely on clean buffers and dilute particles. For *in vivo* measurements inside a living cell, calibration with a bead outside the cell can normally not simply transferred to a trapped bead inside a cell (where the visco-elastic environment is different and phase distortions due to vesicles, organelles, and proteins can occur). Approaches to tackle these problems are addressed in Chapters 20 and 21 of this book.

## 6 Advanced Optical Trapping: Multiple Traps, Fancy Beams, and Torque

By far the most common application of optical trapping use a single optical trap to pull or push a object or to measure pulling or pushing forces and displacements. In micro-rheology, two spatially separated traps are often generated by two independent laser sources to probe the isotropy or length dependence of a material's viscoelasticity. However, there are more advanced approaches involving line-shaped [87, 122–124] or circular [125] optical traps in combination with temporally or spatially varying optical potentials [88, 126, 127] as well as multiple optical point traps [90, 128–130]. These traps are usually generated by beam steering devices such as spatial light modulators (SLM) [90], acousto-optic deflectors (AOD) [129, 131], electro-optic deflectors (EOD) [132], scan mirrors [133], or combinations thereof

[134, 135]. Spatial light modulators give the unique advantage to nearly arbitrarily shape the wavefront of the laser beam [136], which also allows the user to displace beads in the axial direction or to transfer angular momentum to the trapped particle [137] and any attached biological specimen. Torque has also been applied and measured utilizing polarization dependent optical elements such as half-wave plates and birefringent particles [138–141] (see also Chapter 7 of this book). SLMs, together with camera based particle tracking, give the unique opportunity to trap, move, and track hundreds of beads simultaneously. However, the aforementioned limitations of video-tracking apply and SLMs are technically limited to a maximum refreshing rate of approximately 100 Hz.

Alternatively, AODs or EODs can be used to rapidly switch the laser focus between different positions, thus creating the so-called time-shared or time-multiplexed optical traps. The laser focus moves much faster (typically  $f_{\text{AOD}} \sim 50$  kHz) between different trapping positions than a bead can move away via diffusion (roughly 1–100 ms). This creates an effective, time-averaged potential [87, 129] that allows trapping and moving of tens of particles at the same time, and the creation of line-shaped traps that have been used to probe the viscoelastic properties of microtubules [74] or to trap lengthy helical bacteria [87, 88]. The advantage of this method is that it can be used in combination with BFP interferometry. For multiple point traps, the continuous position trajectory obtained by the QPD only measures one bead at a time. By cutting the detection signal into short pieces corresponding to the time the laser impinges on each bead, and concatenating successive pieces corresponding to the same bead into a long bead trajectory, a single interferometric position trace is obtained for each particle [129]. This, of course, requires that position data from the QPD are sample much faster (typically  $f_{sr} = 1$  MHz) than the jumping frequency of the AOD and the effective sample rate is reduced to  $f_{\text{AOD}}/N$ , where  $N$  is the number of optical traps.

## References

1. Ashkin A, Dziedzic JM, Bjorkholm JE et al (1986) Observation of a single-beam gradient force optical trap for dielectric particles. *Opt Lett* 11(5):288–290
2. Shotton DM (1989) Confocal scanning optical microscopy and its applications for biological specimens. *J Cell Sci* 94 (2):175–206
3. Axelrod D (1981) Cell-substrate contacts illuminated by total internal reflection fluorescence. *J Cell Biol* 89(1):141–145
4. Denk W, Strickler JH, Webb WW (1990) Two-photon laser scanning fluorescence microscopy. *Science* 248(4951):73–76
5. Huiskens J, Swoger J, Del Bene F et al (2004) Optical sectioning deep inside live embryos by selective plane illumination microscopy. *Science* 305(5686):1007–1009
6. Shribak M, Inoué S (2006) Orientation-independent differential interference contrast microscopy. *Appl Optics* 45(3):460–469
7. Abbe E (1873) Beiträge zur Theorie des Mikroskops und der mikroskopischen

- Wahrnehmung. Archiv für mikroskopische Anatomie 9(1):413–418
8. Pawley JB (2006) Handbook of biological confocal microscopy, 3rd edn. Springer, New York
  9. Hell SW, Wichmann J (1994) Breaking the diffraction resolution limit by stimulated emission: stimulated-emission-depletion fluorescence microscopy. Opt Lett 19 (11):780–782
  10. Klar TA, Jakobs S, Dyba M et al (2000) Fluorescence microscopy with diffraction resolution barrier broken by stimulated emission. Proc Natl Acad Sci 97(15):8206–8210
  11. Betzig E, Patterson GH, Sougrat R et al (2006) Imaging intracellular fluorescent proteins at nanometer resolution. Science 313 (5793):1642–1645
  12. Rust MJ, Bates M, Zhuang X (2006) Sub-diffraction-limit imaging by stochastic optical reconstruction microscopy (STORM). Nat Methods 3(10):793–796
  13. Alberts B, Bray D, Hopkin K et al (2004) Essential cell biology, 2nd edn. Garland Science, New York
  14. Suresh S (2007) Biomechanics and biophysics of cancer cells. Acta Mater 55 (12):3989–4014
  15. Hochmuth RM (2000) Micropipette aspiration of living cells. J Biomech 33(1):15–22
  16. Harris AK, Wild P, Stopak D (1980) Silicone rubber substrata: a new wrinkle in the study of cell locomotion. Science 208(4440):177–179
  17. Legant WR, Miller JS, Blakely BL et al (2010) Measurement of mechanical tractions exerted by cells in three-dimensional matrices. Nat Methods 7(12):969–971
  18. Müller DJ, Dufrene YF (2008) Atomic force microscopy as a multifunctional molecular toolbox in nanobiotechnology. Nat Nanotechnol 3(5):261–269
  19. Binnig G, Quate CF, Gerber C (1986) Atomic force microscope. Phys Rev Lett 56 (9):930
  20. Rotsch C, Radmacher M (2000) Drug-induced changes of cytoskeletal structure and mechanics in fibroblasts: an atomic force microscopy study. Biophys J 78(1):520–535
  21. Neuman KC, Nagy A (2008) Single-molecule force spectroscopy: optical tweezers, magnetic tweezers and atomic force microscopy. Nat Methods 5(6):491
  22. Ashkin A, Dziedzic J (1987) Optical trapping and manipulation of viruses and bacteria. Science 235(4795):1517–1520
  23. Ashkin A, Dziedzic J, Yamane T (1987) Optical trapping and manipulation of single cells using infrared laser beams. Nature 330 (6150):769–771
  24. Block SM, Blair DF, Berg HC (1989) Compliance of bacterial flagella measured with optical tweezers. Nature 338:514–518
  25. Block SM, Goldstein LS, Schnapp BJ (1990) Bead movement by single kinesin molecules studied with optical tweezers. Nature 348:348–352
  26. Bouchiat C, Wang M, Allemand J-F et al (1999) Estimating the persistence length of a worm-like chain molecule from force-extension measurements. Biophys J 76 (1):409–413
  27. Wang MD, Yin H, Landick R et al (1997) Stretching DNA with optical tweezers. Biophys J 72(3):1335
  28. Smith SB, Cui Y, Bustamante C (1996) Over-stretching B-DNA: the elastic response of individual double-stranded and single-stranded DNA molecules. Science 271 (5250):795–799
  29. Dupuis DE, Guilford WH, Wu J et al (1997) Actin filament mechanics in the laser trap. J Muscle Res Cell Motil 18(1):17–30
  30. Streichfuss M, Erbs F, Uhrig K et al (2011) Measuring forces between two single actin filaments during bundle formation. Nano Lett 11(9):3676–3680
  31. van Mameren J, Vermeulen KC, Gittes F et al (2009) Leveraging single protein polymers to measure flexural rigidity†. J Phys Chem B 113 (12):3837–3844
  32. Hawkins T, Mirigian M, Selcuk Yasar M et al (2010) Mechanics of microtubules. J Biomed 43(1):23–30
  33. Hawkins TL, Sept D, Mogessie B et al (2013) Mechanical properties of doubly stabilized microtubule filaments. Biophys J 104 (7):1517–1528
  34. Kikumoto M, Kurachi M, Tosa V et al (2006) Flexural rigidity of individual microtubules measured by a buckling force with optical traps. Biophys J 90(5):1687–1696
  35. Kurachi M, Hoshi M, Tashiro H (1995) Buckling of a single microtubule by optical trapping forces: direct measurement of microtubule rigidity. Cell Motil Cytoskeleton 30 (3):221–228
  36. Lansky Z, Braun M, Lüdecke A et al (2015) Diffusible crosslinkers generate directed forces in microtubule networks. Cell 160 (6):1159–1168
  37. Pampaloni F, Lattanzi G, Jonas A et al (2006) Thermal fluctuations of grafted microtubules provide evidence of a length-dependent persistence length. Proc Natl Acad Sci U S A 103

- (27):10248–10253. doi:[10.1073/pnas.0603931103](https://doi.org/10.1073/pnas.0603931103)
38. Kerssemakers J, Janson M, Van der Horst A et al (2003) Optical trap setup for measuring microtubule pushing forces. *Appl Phys Lett* 83(21):4441–4443
  39. Allersma MW, Gittes F, Stewart RJ et al (1998) Two-dimensional tracking of nc6 motility by back focal plane interferometry. *Biophys J* 74(2):1074–1085
  40. Coppin CM, Pierce DW, Hsu L et al (1997) The load dependence of kinesin's mechanical cycle. *Proc Natl Acad Sci* 94(16):8539–8544
  41. Kawaguchi K, Ishiwata S (2000) Temperature dependence of force, velocity, and processivity of single kinesin molecules. *Biochem Biophys Res Commun* 272(3):895–899
  42. Kawaguchi K, Ishiwata S (2001) Nucleotide-dependent single-to double-headed binding of kinesin. *Science* 291(5504):667–669
  43. Visscher K, Schnitzer MJ, Block SM (1999) Single kinesin molecules studied with a molecular force clamp. *Nature* 400 (6740):184–189
  44. Mallik R, Carter BC, Lex SA et al (2004) Cytoplasmic dynein functions as a gear in response to load. *Nature* 427 (6975):649–652
  45. Gennerich A, Carter AP, Reck-Peterson SL et al (2007) Force-induced bidirectional stepping of cytoplasmic dynein. *Cell* 131 (5):952–965
  46. Molloy J, Burns J, Kendrick-Jones J et al (1995) Movement and force produced by a single myosin head. *Nature* 378 (6553):209–212
  47. Rief M, Rock RS, Mehta AD et al (2000) Myosin-V stepping kinetics: a molecular model for processivity. *Proc Natl Acad Sci* 97 (17):9482–9486
  48. Rock RS, Rice SE, Wells AL et al (2001) Myosin VI is a processive motor with a large step size. *Proc Natl Acad Sci* 98 (24):13655–13659
  49. Veigel C, Coluccio LM, Jontes JD et al (1999) The motor protein myosin-I produces its working stroke in two steps. *Nature* 398 (6727):530–533
  50. Veigel C, Wang F, Bartoo ML et al (2002) The gated gait of the processive molecular motor, myosin V. *Nat Cell Biol* 4(1):59–65
  51. Davenport RJ, Wuite GJ, Landick R et al (2000) Single-molecule study of transcriptional pausing and arrest by *E. coli* RNA polymerase. *Science* 287(5462):2497
  52. Forde NR, Izhaky D, Woodcock GR et al (2002) Using mechanical force to probe the mechanism of pausing and arrest during continuous elongation by *Escherichia coli* RNA polymerase. *Proc Natl Acad Sci* 99 (18):11682–11687
  53. Neuman KC, Abbondanzieri EA, Landick R et al (2003) Ubiquitous transcriptional pausing is independent of RNA polymerase backtracking. *Cell* 115(4):437–447
  54. Shaevitz JW, Abbondanzieri EA, Landick R et al (2003) Backtracking by single RNA polymerase molecules observed at near-base-pair resolution. *Nature* 426(6967):684–687
  55. Wang MD, Schnitzer MJ, Yin H et al (1998) Force and velocity measured for single molecules of RNA polymerase. *Science* 282 (5390):902–907
  56. Smith DE, Tans SJ, Smith SB et al (2001) The bacteriophage  $\phi$ 29 portal motor can package DNA against a large internal force. *Nature* 413(6857):748–752
  57. Kellermeier MS, Smith SB, Granzier HL et al (1997) Folding-unfolding transitions in single titin molecules characterized with laser tweezers. *Science* 276(5315):1112–1116
  58. Wang SY, Arellano-Santoyo H, Combs PA et al (2010) Actin-like cytoskeleton filaments contribute to cell mechanics in bacteria. *Proc Natl Acad Sci U S A* 107(20): 9182–9185
  59. Min TL, Mears PJ, Chubiz LM et al (2009) High-resolution, long-term characterization of bacterial motility using optical tweezers. *Nat Methods* 6(11):831–835
  60. Martínez IA, Campoy S, Tort M et al (2013) A simple technique based on a single optical trap for the determination of bacterial swimming pattern. *PLoS One* 8(4):e61630
  61. Friedrich L, Rohrbach A (2015) Surface imaging beyond the diffraction limit with optically trapped spheres. *Nat Nanotechnol* 10(12):1064–1069
  62. Kress H (2006) Cell mechanics during phagocytosis studied by optical tweezers-based microscopy. PhD thesis, University of Heidelberg, Cuvillier Verlag, Göttingen
  63. Kohler F, Rohrbach A (2015) Surfing along filopodia: a particle transport revealed by molecular-scale fluctuation analyses. *Biophys J* 108(9):2114–2125
  64. Meinel A, Tränkle B, Römer W et al (2014) Induced phagocytic particle uptake into a giant unilamellar vesicle. *Soft Matter* 10 (20):3667–3678
  65. Jünger F, Kohler F, Meinel A et al (2015) Measuring local viscosities near plasma

- membranes of living cells with photonic force microscopy. *Biophys J* 109(5):869–882
66. Atakhorrami M, Sulkowska J, Addas K et al (2006) Correlated fluctuations of microparticles in viscoelastic solutions: quantitative measurement of material properties by microrheology in the presence of optical traps. *Phys Rev E Stat Nonlin Soft Matter Phys* 73(6):061501
  67. Guo M, Ehrlicher AJ, Jensen MH et al (2014) Probing the stochastic, motor-driven properties of the cytoplasm using force spectrum microscopy. *Cell* 158(4):822–832
  68. Mizuno D, Head D, MacKintosh F et al (2008) Active and passive microrheology in equilibrium and nonequilibrium systems. *Macromolecules* 41(19):7194–7202
  69. Mizuno D, Bacabac R, Tardin C et al (2009) High-resolution probing of cellular force transmission. *Phys Rev Lett* 102(16):168102
  70. Carmon G, Kumar P, Feingold M (2014) Optical tweezers assisted imaging of the Z-ring in Escherichia coli: measuring its radial width. *New Journal of Physics* 16. doi:10.1088/1367-2630/16/1/013043
  71. Katchinskiy N, Goez HR, Dutta I et al (2016) Novel method for neuronal nanosurgical connection. *Scientific Reports* 6
  72. Landenberger B, Höfmann H, Wadle S et al (2012) Microfluidic sorting of arbitrary cells with dynamic optical tweezers. *Lab Chip* 12 (17):3177–3183
  73. Bergman J, Osunbayo O, Vershinin M (2015) Constructing 3D microtubule networks using holographic optical trapping. *Scientific Reports* 5
  74. Koch MD, Schneider N, Nick P et al (2016) Frequency dependent transport of mechanical stimuli along single microtubules and small networks. Submitted
  75. Kress H, Park J-G, Mejean CO et al (2009) Cell stimulation with optically manipulated microsources. *Nat Methods* 6(12):905–909
  76. Mahamdeh M, Pérez Campos C, Schäffer E (2011) Under-filling trapping objectives optimizes the use of the available laser power in optical tweezers. *Opt Express* 19 (12):11759–11768
  77. Ashkin A (1992) Forces of a single-beam gradient laser trap on a dielectric sphere in the ray optics regime. *Biophys J* 61(2):569–582
  78. Svoboda K, Block SM (1994) Biological applications of optical forces. *Annu Rev Biophys Biomol Struct* 23:247–285. doi:10.1146/annurev.bb.23.060194.001335
  79. Rohrbach A (2005) Stiffness of optical traps: quantitative agreement between experiment and electromagnetic theory. *Phys Rev Lett* 95(16):168102
  80. Kress H, Stelzer EHK, Griffiths G et al (2005) Control of relative radiation pressure in optical traps: Application to phagocytic membrane binding studies. *Physical Review E* 71 (6)
  81. Nieminen TA, Heckenberg NR, Rubinsztein-Dunlop H (2008) Forces in optical tweezers with radially and azimuthally polarized trapping beams. *Opt Lett* 33(2):122–124
  82. Rohrbach A, Stelzer EHK (2001) Optical trapping of dielectric particles in arbitrary fields. *J Opt Soc Am A Opt Image Sci Vis* 18 (4):839–853
  83. Montange RK, Bull MS, Shanblatt ER et al (2013) Optimizing bead size reduces errors in force measurements in optical traps. *Opt Express* 21(1):39–48
  84. Loke VL, Nieminen TA, Parkin SJ et al (2007) FDFD/T-matrix hybrid method. *J Quant Spectrosc Radiat Transfer* 106 (1):274–284
  85. Nieminen TA, Loke VLY, Stilgoe AB et al (2007) Optical tweezers computational toolbox. *J Opt A Pure Appl Opt* 9(8):S196–S203. doi:10.1088/1464-4258/9/8/s12
  86. Malagnino N, Pesce G, Sasso A et al (2002) Measurements of trapping efficiency and stiffness in optical tweezers. *Opt Commun* 214 (1):15–24
  87. Koch M, Rohrbach A (2012) Object-adapted optical trapping and shape-tracking of energy-switching helical bacteria. *Nat Photonics* 6 (10):680–686. doi:10.1038/nphoton.2012.232
  88. Koch M, Rohrbach A (2014) How to calibrate an object-adapted optical trap for force sensing and interferometric shape tracking of asymmetric structures. *Opt Express* 22 (21):25242–25257. doi:10.1364/OE.22.025242
  89. Crocker JC, Grier DG (1996) Methods of digital video microscopy for colloidal studies. *J Colloid Interface Sci* 179(1):298–310
  90. Curtis JE, Koss BA, Grier DG (2002) Dynamic holographic optical tweezers. *Opt Commun* 207(1-6):169–175. doi:10.1016/s0030-4018(02)01524-9
  91. Jesacher A, Bernet S, Ritsch-Marte M (2014) Combined holographic optical trapping and optical image processing using a single diffractive pattern displayed on a spatial light modulator. *Opt Lett* 39(18):5337–5340
  92. Cheong FC, Krishnatreya BJ, Grier DG (2010) Strategies for three-dimensional

- particle tracking with holographic video microscopy. *Opt Express* 18 (13):13563–13573
93. Speidel M, Jonáš A, Florin E-L (2003) Three-dimensional tracking of fluorescent nanoparticles with subnanometer precision by use of off-focus imaging. *Opt Lett* 28(2):69–71
94. Hirvonen LM, Festy F, Suhling K (2014) Wide-field time-correlated single-photon counting (TCSPC) lifetime microscopy with microsecond time resolution. *Opt Lett* 39 (19):5602–5605
95. Tseng Y, Kole TP, Wirtz D (2002) Micromechanical mapping of live cells by multiple-particle-tracking microrheology. *Biophys J* 83 (6):3162–3176
96. Pralle A, Prummer M, Florin EL et al (1999) Three-dimensional high-resolution particle tracking for optical tweezers by forward scattered light. *Microsc Res Tech* 44(5):378–386
97. Gittes F, Schmidt CF (1998) Interference model for back-focal-plane displacement detection in optical tweezers. *Opt Lett* 23 (1):7–9
98. Svoboda K, Schmidt CF, Schnapp BJ et al (1993) Direct observation of kinesin stepping by optical trapping interferometry. *Nature* 365(6448):721–727
99. Rice SE, Purcell TJ, Spudich JA (2003) Building and using optical traps to study properties of molecular motors. *Methods Enzymol* 361:112–133
100. Göglar M, Betz T, Käs JA (2007) Simultaneous manipulation and detection of living cell membrane dynamics. *Opt Lett* 32 (13):1893–1895
101. Chavez I, Huang R, Henderson K et al (2008) Development of a fast position-sensitive laser beam detector. *Rev Sci Instrum* 79(10):105104
102. Abbondanzieri EA, Greenleaf WJ, Shaevitz JW et al (2005) Direct observation of base-pair stepping by RNA polymerase. *Nature* 438(7067):460–465
103. Perkins TT (2014) Ångström-precision optical traps and applications\*. *Annu Rev Biophys* 43:279–302
104. Carter AR, Seol Y, Perkins TT (2009) Precision surface-coupled optical-trapping assay with one-basepair resolution. *Biophys J* 96 (7):2926–2934
105. Saleh BEA, Teich MC (1991) Fundamentals of Photonics. Wiley, New York
106. Goodman JW (2005) Introduction to fourier optics. In: JW Goodman Englewood. Introduction to Fourier optics, 3rd edn. CO: Roberts & Co Publishers, 2005 1
107. Feng S, Winful H (2001) Physical origin of the Gouy phase shift. *Opt Lett* 26 (8):485–487
108. Rohrbach A, Stelzer EHK (2002) Three-dimensional position detection of optically trapped dielectric particles. *J Appl Phys* 91 (8):5474–5488
109. Berg-Sørensen K, Flyvbjerg H (2004) Power spectrum analysis for optical tweezers. *Rev Sci Instrum* 75(3):594–612
110. Neuman KC, Block SM (2004) Optical trapping. *Rev Sci Instrum* 75(9):2787–2809
111. Richly MU, Türkcan S, Le Gall A et al (2013) Calibrating optical tweezers with Bayesian inference. *Opt Express* 21(25):31578–31590
112. Tolić-Nørrelykke SF, Schäffer E, Howard J et al (2006) Calibration of optical tweezers with positional detection in the back focal plane. *Rev Sci Instrum* 77(10):103101
113. Ghislain LP, Switz NA, Webb WW (1994) Measurement of small forces using an optical trap. *Rev Sci Instrum* 65(9):2762–2768
114. Vermeulen KC, van Mameren J, Stienen GJ et al (2006) Calibrating bead displacements in optical tweezers using acousto-optic deflectors. *Rev Sci Instrum* 77(1):013704
115. Lang MJ, Asbury CL, Shaevitz JW et al (2002) An automated two-dimensional optical force clamp for single molecule studies. *Biophys J* 83(1):491–501
116. Farré A, Marsà F, Montes-Usategui M (2012) Optimized back-focal-plane interferometry directly measures forces of optically trapped particles. *Opt Express* 20 (11):12270–12291
117. Coffrey WT, Kalmykov XYP, Waldron JT (2004) The Langevin Equation, vol 14, 4th edn, World Scientific Series in Contemporary Chemical Physics. World Scientific, Singapore
118. Kress H (2006) Cell mechanics during phagocytosis studied by optical tweezers-based microscopy. PhD thesis, University of Heidelberg, Cuvillier Verlag, Göttingen
119. Kress H (2006) Cell mechanics during phagocytosis studied by optical tweezers-based microscopy. pHD thesis, University of Heidelberg
120. Wang MC, Uhlenbeck GE (1945) On the theory of the Brownian motion II. *Rev Mod Phys* 17(2-3):323–342
121. Purcell EM (1977) Life at low Reynolds-number. *Am J Physics* 45(1):3–11
122. Brunner M, Dobnikar J, von Grunberg HH et al (2004) Direct measurement of three-body interactions amongst charged colloids. *Phys Rev Lett* 92(7):078301. doi:[10.1103/PhysRevLett.92.078301](https://doi.org/10.1103/PhysRevLett.92.078301)

123. Crocker JC, Matteo JA, Dinsmore AD et al (1999) Entropic attraction and repulsion in binary colloids probed with a line optical tweezer. *Phys Rev Lett* 82(21):4352–4355. doi:[10.1103/PhysRevLett.82.4352](https://doi.org/10.1103/PhysRevLett.82.4352)
124. Tränkle B, Speidel M, Rohrbach A (2012) Interaction dynamics of two colloids in a single optical potential. *Phys Rev E Stat Nonlin Soft Matter Phys* 86(2):021401
125. Faucheux LP, Stolovitzky G, Libchaber A (1995) Periodic forcing of a Brownian particle. *Phys Rev E* 51(6):5239–5250
126. Faucheux LP, Bourdieu LS, Kaplan PD et al (1995) Optical thermal ratchet. *Phys Rev Lett* 74(9):1504–1507. doi:[10.1103/PhysRevLett.74.1504](https://doi.org/10.1103/PhysRevLett.74.1504)
127. Nambiar R, Gajraj A, Meiners JC (2004) All-optical constant-force laser tweezers. *Biophys J* 87(3):1972–1980. doi:[10.1529/biophysj.103.037697](https://doi.org/10.1529/biophysj.103.037697)
128. Guilford WH, Tournas JA, Dascalu D et al (2004) Creating multiple time-shared laser traps with simultaneous displacement detection using digital signal processing hardware. *Anal Biochem* 326(2):153–166
129. Ruh D, Traenkle B, Rohrbach A (2011) Fast parallel interferometric 3D tracking of numerous optically trapped particles and their hydrodynamic interaction. *Opt Express* 19(22):21627–21642
130. Visscher K, Gross SP, Block SM (1996) Construction of multiple-beam optical traps with nanometer-resolution position sensing. *IEEE Journal of Selected Topics in Quantum Electronics* 2(4):1066–1076
131. Visscher K, Block SM (1998) Versatile optical traps with feedback control. *Methods Enzymol* 298:460–489
132. Valentine MT, Guydosh NR, Gutiérrez-Medina B et al (2008) Precision steering of an optical trap by electro-optic deflection. *Opt Lett* 33(6):599–601
133. Fällman E, Axner O (1997) Design for fully steerable dual-trap optical tweezers. *Appl Optics* 36(10):2107–2113
134. Akselrod G, Timp W, Mirsaidov U et al (2006) Laser-guided assembly of heterotypic three-dimensional living cell microarrays. *Biophys J* 91(9):3465–3473
135. Čížmár T, Dalgarno H, Ashok P et al (2011) Optical aberration compensation in a multiplexed optical trapping system. *Journal of Optics* 13(4):044008
136. Grier DG (2003) A revolution in optical manipulation. *Nature* 424(6950):810–816
137. Padgett M, Bowman R (2011) Tweezers with a twist. *Nat Photonics* 5(6):343–348
138. Oroszi L, Galajda P, Kirei H et al (2006) Direct measurement of torque in an optical trap and its application to double-strand DNA. *Phys Rev Lett* 97(5):058301
139. La Porta A, Wang MD (2004) Optical torque wrench: angular trapping, rotation, and torque detection of quartz microparticles. *Phys Rev Lett* 92(19):190801
140. Friese M, Nieminen T, Heckenberg N et al (1998) Optical alignment and spinning of laser-trapped microscopic particles. *Nature* 394(6691):348–350
141. Pedaci F, Huang Z, van Oene M et al (2011) Excitable particles in an optical torque wrench. *Nat Phys* 7(3):259–264
142. Rohrbach A, Stelzer EH (2002) Trapping forces, force constants, and potential depths for dielectric spheres in the presence of spherical aberrations. *Appl Optics* 41(13):2494–2507

# Chapter 2

## Exact Theory of Optical Tweezers and Its Application to Absolute Calibration

Rafael S. Dutra, Nathan B. Viana, Paulo A. Maia Neto,  
and H. Moysés Nussenzveig

### Abstract

Optical tweezers have become a powerful tool for basic and applied research in cell biology. Here, we describe an experimentally verified theory for the trapping forces generated by optical tweezers based on first principles that allows absolute calibration. For pedagogical reasons, the steps that led to the development of the theory over the past 15 years are outlined. The results are applicable to a broad range of microsphere radii, from the Rayleigh regime to the ray optics one, for different polarizations and trapping heights, including all commonly employed parameter domains. Protocols for implementing absolute calibration are given, explaining how to measure all required experimental parameters, and including a link to an applet for stiffness calculations.

**Key words** Optical tweezers, Optical trap forces, Absolute calibration

---

### List of Symbols

$a$	Radius of trapped particle
$F$	Trapping force
$b$	Distance from microsphere center to coverslip
$k_z, k_\rho$	Axial and transverse trap stiffness, respectively
$\lambda, \lambda_0$	Generic and vacuum wavelength, respectively
NA	Objective numerical aperture
$n$	Generic refractive index
$n_g, n_p, n_w$	Refractive indices of glass, trapped particle and water, respectively
OT	Optical tweezers
$P$	Incident laser beam power
$Q_z, Q_\rho$	Axial and transverse dimensionless efficiency factors, respectively
$\theta_o$	Focused laser beam opening angle
$\omega$	Laser beam angular frequency
$z_{eq}$	Axial equilibrium position

---

## 1 Introduction

In the preceding chapter, the history, design, and approximate theory of optical tweezers (OT) are introduced and discussed. In the present chapter, we outline the formulation of a theory based on first principles and its application to an absolute calibration, including instructions for how to measure all required experimental parameters. For indirect calibration methods, see refs. [1, 2] and references therein.

Why should one seek an absolute calibration? A basic rationale is to seek a full understanding of the physics of trapping forces, enabling one to predict the quantitative behavior of generated forces in various circumstances. Other benefits are possible design improvements and an extended spatial range of applicability.

In typical applications in cell biological and biophysical experiments, a  $\text{TEM}_{00}$  near infrared laser beam (vacuum wavelength  $\lambda_0$ ) goes through a beam expander and is focused by a high numerical aperture (NA) oil immersion objective of an inverted microscope, through a glass coverslip, into a water-filled sample chamber, to trap a transparent microsphere (radius  $a$ ). Usually,  $\lambda_0$  is neither  $\gg a$  (Rayleigh range) nor  $\ll a$  (ray optics range) so that neither the Rayleigh nor the ray optics approximation is appropriate. We therefore developed a theory based on first principles that permits an accurate calibration of OTs even in cases where  $\lambda_0$  and  $a$  are similar. The theory is based on an optical (electromagnetic) representation of the highly focused laser beam produced by the objective and includes the defocusing effects of the glass/water interface (interface spherical aberration), and effects resulting from optical aberrations. To be of use in practice, its implementation must also provide procedures for the experimental determination of all requisite parameters.

Taking into account the wave diffraction phenomena associated with the physical processes described above, we are able to formulate an exact theory. For example, to calculate the forces acting on the microsphere, we employ the Mie scattering theory, which is an exact solution of the electromagnetic scattering problem [3, 4], and use Debye's exact representation of a converging beam in free space, which is based on a superposition of plane waves in all directions  $\theta$  within the beam solid angle (angular spectrum of plane waves) [5]. However, to be of practical use, we will require its electromagnetic generalization, describing diffraction of the incident laser beam by the microscope objective.

This diffraction effect is treated by classical diffraction theory. This is a very good approximation in the domain to which it will be applied [6]. We exemplify this, for simplicity, by scalar diffraction by an aperture  $A$  in an opaque plane screen  $S$  (Fig. 1).

Rayleigh's formula [7] yields an exact result for the diffraction amplitude in the direction defined by unit vector  $\hat{s}$ ,

$$f(\hat{s}) = \frac{\hat{s} \cdot \hat{s}_0}{i\lambda} \int \exp[-ik(\hat{s} - \hat{s}_0) \cdot \mathbf{x}] u(\mathbf{x}) d^2x, \quad (1)$$

where  $\hat{s}_0$  defines the direction of incidence,  $k = 2\pi/\lambda$  is the wave number, the integral is extended over the full plane of the screen  $S$ , and  $u(\mathbf{x})$  is the (generally unknown) *exact* wave function on this plane.

For short wavelengths  $\lambda \ll D$ , where  $D$  is the aperture diameter, and for not too large diffraction angles  $\theta$  (i.e., not  $\gg \lambda/D$ ), we have in the domain where  $|u(\mathbf{x})|$  is appreciable,

$$k(\hat{s} - \hat{s}_0) \cdot \mathbf{x} \leq kD \sin \theta = k_\perp D \text{ not } \gg 1, \quad (2)$$

where  $k_\perp$  is the transverse wave number. Thus, for not too large diffraction angles for which the intensity is mostly concentrated, the diffraction pattern reflects only Fourier components of the aperture distribution associated with broader features, rather than very fine details.

Classical diffraction theory is based on Kirchhoff's approximation. Applying Eq. 1 to the plane immediately beyond the screen (depicted by the dashed line in Fig. 1), Kirchhoff's approximation replaces  $u(\mathbf{x})$  by the incident wave over the aperture  $A$  and sets it to vanish over the geometrical shadow, the blocked part of the screen  $S$  (shadowed area in Fig. 1). For not too large diffraction angles defined by Eq. 2, this blocking effect is a good approximation, explaining why classical diffraction theory works so well; in the

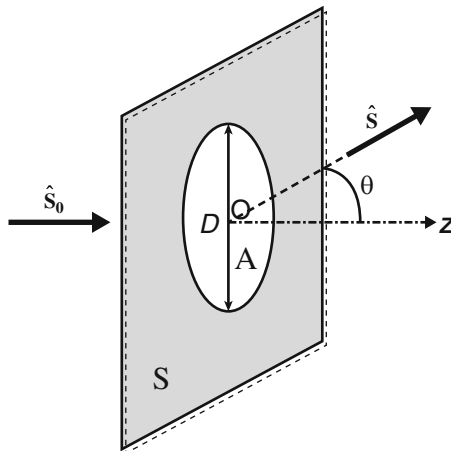


**Fig. 1** Diffraction by an aperture on an opaque plane screen. On a plane immediately beyond the screen (shown by the *dashed line*), Kirchhoff's approximation replaces the wave function by its geometrical optics distribution (incident wave beyond the aperture and zero in the shadow region blocked by the opaque screen)

forward direction, the average of  $u(\mathbf{x})$  over the aperture dominates the amplitude. This insensitivity of classical diffraction patterns to fine details in the aperture distribution is related to the principle of stationary phase and to stationary properties of the patterns [6].

### 1.1 Mie–Debye Approximation to the Axial Force

We outline the theory of absolute calibration as it was developed by successive approximations, incorporating new features as their needs were recognized. The first attempt was for the simpler case of the axial force, disregarding aberrations [8]. It employs Mie theory and represents the focused beam by the Richards and Wolf electromagnetic generalization [9] of the Debye model based on classical diffraction theory, which we call MD (Mie–Debye) approximation. Importantly, the Abbe sine condition [9] is taken into account.

The beam is generated by an incident Gaussian TEM<sub>00</sub> mode overfilling the microscope high NA objective (circular aperture), producing the diffracted highly focused beam. Each plane wave in this angular spectrum is Mie scattered by the microsphere, the center of which is aligned with the beam axis, defined as the  $z$  direction, leading to an axial trapping force. This force  $F$  can be obtained by computing the Maxwell stress tensor for the total (incident + scattered) field and integrating over the surface of the microsphere. It is usually expressed in terms of a dimensionless efficiency factor  $Q_z$ , the ratio of  $F$  to one half the force  $2P/v$  exerted on a perfectly reflecting mirror by a perpendicularly incident light beam of power  $P$  in a medium of refractive index  $n$ , where  $v = c/n$ ,

$$Q_z = \frac{cF}{nP}. \quad (3)$$

The result [8] is a partial-wave series in terms of the Mie coefficients. For size parameters  $\omega a/c \gg 1$ , where  $\omega$  is the laser beam angular frequency and  $a$  is the microsphere radius, one finds that the efficiency factor at the position of the geometrical focus ( $z = 0$ ) is asymptotically given by

$$Q_z(z = 0) = \frac{8r \sin^2(\Delta/2)}{1 + r^2 - 2r \cos \Delta} \langle \cos \theta \rangle \quad (4)$$

where  $\Delta \equiv 4n_p \omega a / c$ ,  $n_p$  is the microsphere refractive index, and the angular brackets denote an average over the intensity distribution of the focused laser beam. This expression has a simple physical interpretation. It represents the radiation pressure efficiency factor of an infinite set of Fabry–Perot interferometers of width  $2a$ , refractive index  $n_p$ , and with round-trip phase  $\Delta$ , each one oriented at angle  $\theta$ , traversed at normal incidence by the respective angular spectrum component [10]. This near-sinusoidal oscillatory behavior was the first wave interference effect found in OT performance [11]. While its direct observation would demand a hard-to-attain

resolution, a closely related effect has been observed with water droplets trapped by a supercontinuum laser source [12].

At an axial equilibrium position  $z_{\text{eq}}$ , the axial stiffness is given by

$$\kappa_z = -\frac{n_w P}{c} \left( \frac{\partial Q_z}{\partial z} \right)_{z=z_{\text{eq}}}, \quad (5)$$

in which  $n_w$  is the refractive index of water in which the microsphere is immersed. In the geometrical optics limit,  $Q_z$  only depends on the dimensionless parameter  $\zeta \equiv z/a$ , so that

$$\frac{\partial Q_z}{\partial z} = \frac{1}{a} \frac{dQ_z}{d\zeta}. \quad (6)$$

In this limit, the stiffness must therefore decay hyperbolically as a function of the microsphere size  $a$ , which provides an important validation test.

Plotting the predicted  $\kappa_z$  versus  $a$ , one finds [8] the expected cubic power law growth in the Rayleigh region ( $\omega a/c \ll 1$ ), going through a peak at  $\omega a/c \approx 2.5$ , followed by an oscillatory decay for  $\omega a/c \gg 1$ , where the small interference oscillations follow the pattern of the oscillations in Eq. 4. Averaging over the oscillations, one recovers the geometrical-optic hyperbolic decay (Eq. 6). This is the typical expected behavior of the (semiclassical) limiting transition from wave optics to geometrical optics [10].

## 1.2 MDSA Approximation to the Transverse Force

The next step in the development of absolute calibration was to extend the results to the transverse trapping force (relevant for cell biology applications), which began with a direct extension of the axial approach [13]. The microsphere center is no longer on the beam axis and the efficiency factor is a vector  $\mathbf{Q}$ , with  $(Q_\rho, Q_\phi, Q_z)$  being the vector components in cylindrical coordinates. The transverse stiffness was first evaluated for circular polarization of the incident beam, and later extended to linear polarization [14].

The essential check that the partial-wave series expansions yield the correct results in the geometrical-optic limit is highly nontrivial, requiring the derivation of WKB (Wentzel–Kramers–Brillouin) approximations for the rotation matrices (Appendix B in [13]). An important feature of the transverse force evaluation was that the equilibrium position in the presence of a transverse pulling force was obtained by solving an implicit equation expressing the condition of a vanishing  $Q_z$ .

The results for the transverse trap stiffness as a function of microsphere radius  $a$  were similar to those for the axial case, showing growth to a peak followed by oscillatory decay, with size average over the oscillations asymptotically approaching the geometrical-optic results. Few experimental results were available at the time [13] was published, but they indicated a sizable

displacement of the peak position. This was attributed to neglect of interface spherical aberration, which stretches the paraxial focus into an axial strip and increasingly degrades the trapping force as one moves away from the interface.

The effects of interface spherical aberration on the Richards and Wolf representation of the focused beam were treated in ref. [15]. The main effect is the introduction within the angular spectrum integral representation of an additional phase factor  $\exp(i\Psi)$ , where

$$\Psi(z, \theta) = kL \left( \cos \theta_1 - \frac{\cos \theta}{N^2} \right). \quad (7)$$

is the interface spherical aberration function,  $L$  is the distance between the interface and the paraxial focal plane,  $N = n_w/n_g$ , where  $n_w$  and  $n_g$  are the refractive indices of water and glass, respectively, and  $\theta_1 = \arcsin(\sin \theta / N)$  is the angle of refraction on the interface. The microsphere center coordinates are  $(\rho, \phi, z)$ , with origin at the paraxial focus. One must also multiply the integrand by the Fresnel transmission amplitude, here given for perpendicular polarization,

$$T(\theta) = \frac{2 \cos \theta}{\cos \theta + N \cos \theta_1}. \quad (8)$$

The dependence of  $T(\theta)$  on polarization is neglected, since  $N$  is close to unity, so that the results for parallel and perpendicular polarizations are very close.

Introducing these additional factors into the angular spectrum components and the associated terms of the partial-wave expansion, we get the MDSA approximation. The transverse trap stiffness  $\kappa_\rho$  is determined by

$$\kappa_\rho = -\frac{n_w P}{c} \left( \frac{\partial Q_\rho}{\partial \rho} \right)_{z=z_{eq}}, \quad (9)$$

where the axial equilibrium position  $z_{eq}$  is obtained by solving the implicit equation  $Q_z(z_{eq}) = 0$ .

A thorough experimental test of the MDSA approximation was performed independently by two laboratories using OT setups with an underfilled and an overfilled objective lens, respectively [16]. The experimental results show good agreement with the MDSA predictions, over a broad bead size range, for the following features:

1. *Trapping threshold.* For the case of an underfilled objective, the minimum bead size that can be trapped is signaled by a scattering of the experimental results over a range of different values (no stable equilibrium position).

2. *Location of the stiffness peak*, which is very sensitive to beam shape.
3. *Trap stiffness variation with height*, arising from interface spherical aberration.
4. *Multiple equilibria*. Although OT forces are in general not conservative, forces along the axis may be derived from an optical potential [17]. By plotting this potential for a typical configuration, one finds that the most stable axial equilibrium position changes with the height, and that the bead may hop between them as the objective is displaced. This is quantitatively confirmed by the experiment. In spite of these successful accomplishments, the MDSA approximation fails badly just at the stiffness peak, where the observed value is about  $\frac{1}{4}$  of the predicted one. This was ascribed to additional optical aberration effects not included in MDSA [16].

### 1.3 MDSA+ and Absolute Calibration

Absolute calibration was finally achieved (*see Note 1*) by taking into account additional aberrations of the optical system [18], arising from the microscope objective and from other elements, such as the beam expander. The diffraction theory of optical aberrations [19] is employed to deal with them. They represent corrections to the Gaussian paraxial theory, which assumes that propagation angles  $\theta$  around the beam axis are  $\ll 1$ .

The Seidel aberrations (the primary optical aberrations) introduce new phase corrections, associated with the lowest powers of an expansion in terms of  $\sin\theta/\sin\theta_o$ , where  $\theta_o$  is the opening angle of the laser beam. Two of them, field curvature and distortion, do not affect the intensity distribution around the focus and can therefore be ignored. We refer to [18] for a systematic treatment of the other aberrations, as well as for images of some typical aberration effects. It reveals that coma does not strongly affect the trap stiffness and the system spherical aberration only introduces a correction to the interface spherical aberration discussed in the Methods Sect. 3. However, astigmatism has a very strong effect in the neighborhood of the stiffness peak, so that it is essential to take it into account.

This requires a diagnostic procedure to determine the astigmatism parameters. The method employed is an adaptation of that described in ref. [20]. Instead of being directed to the sample chamber after going through the microscope objective, the laser beam is reflected by a plane mirror placed near the focal plane. The laser light travels back through the objective, beam splitter and microscope tube lens to produce a recorded image for analysis. The relation with the astigmatism parameters is based upon Kirchhoff's approximation and the principle of stationary phase (see also the comments following Eq. 2).

Introducing the correction phase factors originating from optical aberrations into the MDSA approximation, one obtains the

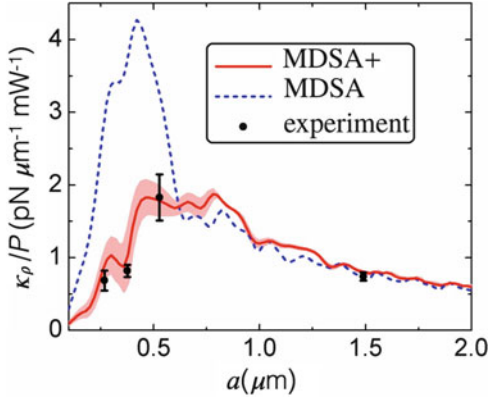


**Fig. 2** Transverse OT stiffness per unit power  $\kappa_p/P$  vs. microsphere radius  $a$  for an objective lens displacement  $d = 3.0 \pm 0.5 \mu\text{m}$ . No adjustable parameters are employed. *Solid red line*: MDSA+ with measured astigmatism parameters  $A_{\text{ast}} = 0.56 \pm 0.03$  and  $\phi_{\text{ast}} = 55 \pm 5^\circ$ . The *red shaded* theoretical uncertainty band is bounded by the curves for  $A_{\text{ast}}$ ,  $\phi_{\text{ast}}$ , and  $d$ , with their respective uncertainties. *Black circles*: experimental points. *Blue dashed line*: MDSA

“MDSA+” result for the trap stiffness (Appendix A in [18]). Comparison with experimental results for the transverse trap stiffness [18] shows that it corrects the MDSA overestimate of the peak height by a factor of order 4 and leads to an overall agreement within error bars, with no fitting needed, for microsphere radii ranging from the Rayleigh domain to the ray optics one, for all polarizations and trapping heights commonly employed in cell biology. Typical results for the transverse trap stiffness per unit power as a function of bead radius are shown in Fig. 2.

It also predicts a previously undetected window of instability around the peak region within a height range of a few microsphere radii. Indeed, plots of the axial optical potential at different heights show that it goes through a region of indifferent equilibrium. This is confirmed by experiment, which reveals appreciable dispersion of data taken within this region.

The height range where MDSA+ can be applied is bounded below, on account of some effects that are disregarded. They include optical reverberation (multiple light scattering between the microsphere and the interface), surface interactions, and contributions from evanescent waves beyond the critical angle [21]. For these reasons, it is not advisable to perform absolute calibration below distances of the order of the wavelength or the microsphere size from the interface.

## 2 Materials

An applet in Computable Document Format (CDF), for direct evaluation of the OT stiffness from experimentally measured input parameters, is described below. It contains instructions for its use and can be downloaded from <http://sites.if.ufrj.br/lpo/en> and employed after downloading the application Wolfram CDF Player (*see Note 2*).

The MDSA+ Applet for Absolute Calibration (Fig. 3) evaluates the axial equilibrium position, as well as axial and transverse optical trap stiffness values, for a microsphere of given radius, trapped by a circularly polarized laser beam, using MDSA+ theory [18]. Absolute calibrations require input data about the OT components and the optical setup, including the desired microsphere height above the coverslip, as well as seed values for numerical computations. It employs the MDSA+ partial-wave series for simulating the results for the calibration experiment: starting from the configuration with the trapped bead just touching the coverslip at the bottom of the sample chamber, one moves the objective lens upward by a desired distance  $d$ . The outputs of the applet are the height  $h$  of the actual equilibrium position (distance from the microsphere center to the coverslip) and the axial and transverse stiffness values,  $\kappa_z$  and  $\kappa_\rho$ . After entering the input parameters (*see Methods Sect. 3*), the following steps are internally performed:

File Edit Window Help

Wolfram CDF Player™ Find 100%

**Legend:**

Blue: parameters to control the numerical calculations  
 Red: parameters measured in the lab  
 Brown: other important input parameters  
 Black Bold: output parameters with 3 significant digits

**Inputs (Blue):**

- $L_0 = \text{initial seed for numerical root-finding algorithm that calculates the initial focal position, in units of microsphere radius}$
- $z_0 = \text{initial seed for numerical root-finding algorithm that calculates the axial equilibrium position } h \text{ after objective displacement, in units of microsphere radius}$
- $P_L = \text{laser power at objective entrance, in mW}$
- $w = \text{waist of laser beam at objective entrance, in mm}$
- $t = \text{mean transmittance of the objective}$
- $A_{\text{ap}} = \text{astigmatism parameter}$
- $\phi_{\text{ax}} = \text{astigmatism angle with respect to x direction, in degrees}$
- $d = \text{objective displacement, in } \mu\text{m}$
- $\phi = \text{direction of microsphere displacement with respect to x direction, in degrees}$
- $R_{\text{obj}} = \text{radius of objective entrance, in mm}$
- $n_{\text{w}} = \text{refractive index of immersion medium (usually water)}$
- $a = \text{microsphere radius, in } \mu\text{m}$
- $\text{Re}(n_p) = \text{real part of microsphere refractive index}$
- $\text{Im}(n_p) = \text{imaginary part of microsphere refractive index}$
- $\lambda_0 = \text{laser wavelength in vacuum, in } \mu\text{m}$
- $\text{NA} = \text{objective numerical aperture}$
- $N_{\text{tot}} = \text{number of terms retained in Mie series}$
- $h = \text{equilibrium position height between the microsphere center and the glass slide surface, in } \mu\text{m}$
- $\kappa_z = \text{axial trap stiffness, in pN}/\mu\text{m}$
- $\kappa_\rho = \text{transverse trap stiffness, in pN}/\mu\text{m}$

**Start**

**Fig. 3** Picture of Applet for OT Calibration

1. Evaluation of the initial focal position  $L_i$ , imposing the equilibrium condition that the axial force vanishes when the microsphere touches the glass surface. Here the applet calculates the root of an equation involving partial wave series.
2. After performing an objective lens displacement  $d$ , evaluation of the corresponding equilibrium position height  $h$ , imposing again the equilibrium condition that the axial force vanishes for the new focal position  $L = L_i + Nd$ , where  $N = n_w/n_g$ . Here the applet calculates the root of an equation involving partial wave series.
3. Evaluation of axial trap stiffness  $\kappa_z$ .
4. Evaluation of transverse trap stiffness  $\kappa_\rho(\phi)$ , corresponding to the direction on the  $xy$ -plane defined by the azimuth angle  $\phi$  chosen by the user.

To proceed, choose the seed values  $(L_0, z_0)$  required for the applet to perform the computation. The speed, and sometimes also the success of a computation, depends on how close the seed parameters are from the true root values. The seed parameter  $L_0$  is employed to evaluate the initial focus position  $L_i$ , and  $z_0$  is employed to evaluate the final equilibrium bead height  $h$ . Both are measured in units of microsphere radius. For a given microsphere radius  $a$ ,  $L_0$  is a fixed parameter and  $z_0$  is a function of the objective lens displacement  $d$  (*see Note 3*).

All output values are given with three significant figures. For accuracy consistent with this number it is recommended to set the input accuracy control parameter  $\alpha$  to  $\alpha = 10$ , as illustrated in Fig. 3. The computational time increases with  $\alpha$  (*see Note 4*). It also increases with the microsphere radius  $a$ . For large microsphere sizes (far beyond those usually employed in biophysical experiments), convergence of the Mie series is slow, but geometric optics is then a good approximation.

### 3 Methods

In this section, we explain what data need to be collected as input parameters in order to employ the MDSA+ Applet for Absolute Calibration described in Materials Sect. 2, including instructions for how to obtain them. The required input parameters are listed below. For each of them, a protocol or a reference is provided.

1. Laser vacuum wavelength  $\lambda_0$ : provided by the laser manufacturer.
2. Input beam waist  $w$  at the objective entrance. The laser is usually employed in a  $\text{TEM}_{00}$  spatial mode. This mode has a

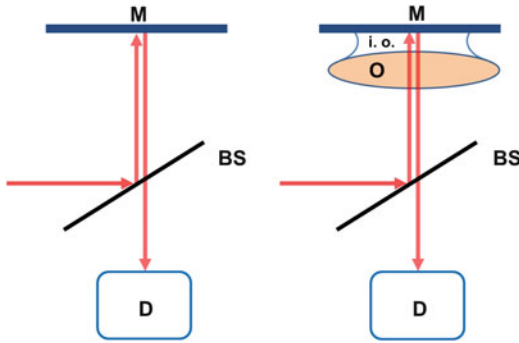


**Fig. 4** Schematic representation of the measurement of the microscope objective's mean transmittance. *Left:* measurement without objective. *Right:* measurement with objective attached to mirror with immersion oil. *M* mirror, *D* Detector (power meter), *BS* Beam Splitter, *O* Objective, *i.o.* immersion oil

Gaussian intensity profile. Its waist  $w$  is determined by using a diaphragm and a power meter, measuring the laser power before ( $P_{\text{in}}$ ) and after ( $P(R_d)$ ) passing the diaphragm, as a function of the radius  $R_d$  of the diaphragm aperture [22], and fitting the results to Eq. 10:

$$P(R_d) = P_{\text{in}} \left[ 1 - \exp(-2R_d^2/w^2) \right]. \quad (10)$$

3. The refractive indices of water ( $n_w$ ), glass ( $n_g$ ), and of the trapped microsphere ( $n_p$ ), at the temperature of the sample chamber, for vacuum wavelength  $\lambda_0$ , which can be found in tables of physical constants. Microsphere absorption is represented by the imaginary part of  $n_p$ .
4. Microsphere radius  $a$ : provided by manufacturer (*see Note 5*).
5. The objective numerical aperture NA (provided by the manufacturer) and back entrance radius  $R_{\text{obj}}$  (measured using a caliper).
6. The laser power at the objective entrance  $P_E$  and the objective mean power transmittance  $t$  [16, 22]. The objective transmittance can be determined by a procedure inspired by the double lens method [23]: one employs a beam splitter (BS), a plane mirror (M), and a power meter (Fig. 4). A laser beam, with power  $P_{\text{in}}$  and radius  $R$  less than or equal to the objective entrance radius  $R_{\text{obj}}$  (to avoid overfilling), is first directed to the BS. The reflected part of the beam is then back-reflected by M at normal incidence and redirected to the BS. After passing through the BS (transmitted light), the power  $P_r$  is measured with the power meter. It is given by  $P_r = r_{\text{BS}} t_{\text{BS}} P_{\text{in}}$ , where  $r_{\text{BS}}$  and  $t_{\text{BS}}$  are the reflectance and transmittance of the BS, respectively (the reflectance of the mirror is assumed to be 100 %). The same procedure is then repeated, but now with the

objective lens placed in front of M, with a thin layer of immersion oil, to bring the objective lens and M in close contact (Fig. 4) (*see Note 6*). Finally, after passing through the BS, the power  $P_r'$  is measured. It is given by  $P_r' = r_{BS} t^2 t_{BS} P_{in}$ , with the transmittance  $t$  squared since the original beam now passes twice through the objective lens. The mean transmittance of the objective can then be obtained from the relation between  $P_r'$  and  $P_r$ :  $P_r'/P_r = t^2$ .

7. In the OT sample chamber, the trapped microsphere center is located at a distance  $h$  from the glass coverslip. The parameter  $h$  depends on the position of the system paraxial focus as well as on the sphere equilibrium position within the beam. The distance is experimentally determined by the following procedure. One traps a microsphere with the OT and one employs the microscope knob to determine when the microsphere touches the coverslip, by decreasing the distance between the surface of the trapped bead and the surface of the cover glass until the image of the microsphere undergoes a sudden large change [16]. This defines the microsphere radius  $a$ , since in this particular case  $h = a$ . Displacing the objective lens upward by a distance  $d$ , one reaches a height  $h$  that can be determined by employing the absolute calibration applet.
8. The primary aberrations of the optical system are astigmatism, coma, field distortion and spherical aberration. The microscope objective is built to avoid coma (*see Note 7*). Among the other three, only astigmatism and spherical aberration must be determined, since field distortion does not affect trapping stiffness. To verify whether the system has astigmatism, take a look at the focused laser beam by reflecting it on a mirror after passing through the objective, as in step 6. Astigmatic systems display two ellipsoidal spots at different axial positions. They can be observed [18] by slightly defocusing the system (Fig. 5) and are

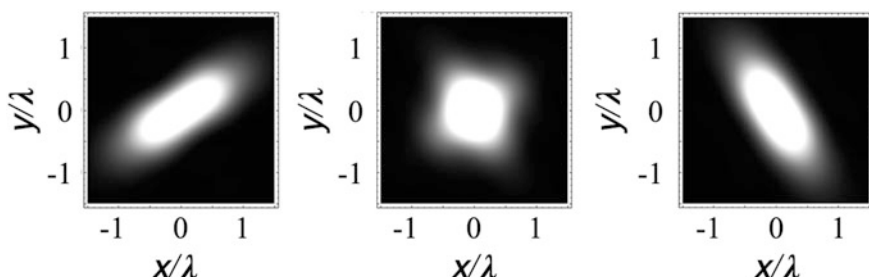


**Fig. 5** Calculated energy density for three different planes along the optical axis in the presence of astigmatism with  $A_{ast} = 0.4$  and  $\phi_{ast} = 33^\circ$ . Coordinates  $(x,y)$  define the position in the image plane and  $\lambda$  is the wavelength in the medium. The image in the *middle* corresponds to the *circle of least confusion* of an astigmatic system. The image on the *left* corresponds to the *tangential focus* and the image on the *right* to the *sagittal focus*

characterized by the amplitude  $A_{\text{ast}}$  and the angle  $\phi_{\text{ast}}$ . They can be measured [18] by analyzing the reflected light intensity when the image of the spot is defocused near the focus of the optical system (*see Note 8*). If needed, the ellipsoidal spots can also be corrected by employing a spatial phase modulator [24, 25].

## 4 Notes

1. For a review of previous attempts to achieve absolute calibration, *see* ref. [16].
2. This application is freely available at the site: [education.wolfram.com/cdf-player-download.html](http://education.wolfram.com/cdf-player-download.html)
3. Some reference values for the seed parameters  $L_0$  and  $z_0$  (in units of the microsphere radius) that optimize the numerical root-finding algorithm for typical OT setups are exemplified below. The values for  $z_0$  are optimized for objective displacements  $d$  in the range from 3 to 5  $\mu\text{m}$ . When employing larger values of  $d$  (so as to have a larger focal height), multiple equilibrium positions appear [16]. They can be found by using different seed values  $z_0$ . Each root  $h$  represents a stable equilibrium position when the corresponding value found for the axial stiffness  $k_z$  is positive.  
Example (1)  $\alpha = 0.27 \mu\text{m}$ :  $L_0 = 0.63$ ,  $z_0 = -0.4$  (no astigmatism);  $L_0 = -1.6$ ,  $z_0 = 1.9$  (moderate astigmatism).  
Example (2)  $\alpha = 0.53 \mu\text{m}$ :  $L_0 = 0.76$ ,  $z_0 = -0.2$  (no astigmatism);  $L_0 = -0.23$ ,  $z_0 = 0.96$  (moderate astigmatism)
4. To illustrate typical computing times, the following numerical examples are based on the MDSA+ theory with the astigmatism parameters  $A_{\text{ast}} = 0.56$  and  $\phi_{\text{ast}} = 55^\circ$ , the same used in ref. [18]. The  $\alpha$  parameter was proposed in ref. [26] to control the number of Mie series terms retained and consequently the truncation error of the evaluation. The Wiscombe's criterion [27] is recovered for  $\alpha = 15$ . For a given  $\alpha$ , the applet runs more slowly for large microspheres, because the number of Mie terms grows with microsphere radius. The calculations were performed using a standard notebook with an Intel® Core™ i5 processor and 8 Gb RAM. The average time spent with the applet to obtain  $h$ ,  $\kappa_z$  and  $\kappa_\rho$  for four typical values of  $\alpha$  with  $\alpha = 10$ , was:  
Example (1)  $\alpha = 0.268 \mu\text{m}$ : 9 s,  
Example (2)  $\alpha = 0.376 \mu\text{m}$ : 13 s,  
Example (3)  $\alpha = 0.527 \mu\text{m}$ : 20 s,  
Example (4)  $\alpha = 1.49 \mu\text{m}$ : 120 s.

5. For precision work, one can order NIST traceable microspheres.
6. One must ensure that, after reflection by M, the beam passes again through the objective lens and leaves it collimated, to recover the original beam as closely as possible, which can be done by adjusting the distance between M and the objective lens.
7. This can readily be checked by observing the image of the focused spot reflected by a mirror, noting the absence of coma features [18].
8. A simpler method to obtain a rough estimate of the astigmatism parameter is based on the measurement of the distance  $s$  between the tangential and sagittal foci around the diffraction focus [19]. This distance can be measured by displacing the mirror, using the microscope knob or a piezoelectric positioning system.  $A_{\text{ast}}$  is obtained employing a formula derived from the scalar diffraction theory of optical aberrations, valid in the paraxial regime ( $\sin\theta_o \ll 1$ ) [19]:

$$s = 4 \left( \frac{A_{\text{ast}}}{\sin^2\theta_o} \right) \lambda_g, \quad (11)$$

where  $\lambda_g$  is the laser wavelength in glass and  $\theta_o$  is the objective angular aperture. The other important parameter to characterize the astigmatism is the angle,  $\phi_{\text{ast}}$ , formed by the major axis of the ellipses that characterizes the astigmatic focus, with respect to the  $x$  axis, on the tangential focus region (see Fig. 4), first spot from left to right.

## Acknowledgments

This work was supported by the Brazilian agencies CNPq, FAPERJ, and INCT Fluidos Complexos.

## References

1. Neuman KC, Block SM (2006) Optical trapping. *Rev Sci Instrum* 75:2787–2809
2. Le Gall A, Perronet K, Dulin D et al (2010) Simultaneous calibration of optical tweezers spring constant and position detector response. *Opt Express* 18:26469–26474
3. Lorenz L (1890) Sur la lumière réfléchie et réfractée par une sphère (surface) transparente. *Kongel Danske Vidensk Selskabs Skrifter* 6:1
4. Mie G (1908) Beiträge zur Optik trüber Medien, speziell kolloidaler Metallösungen. *Ann der Phys* (Leipzig) 25:377–445
5. Debye P (1909) Das Verhalten von Lichtwellen in der Nähe eines Brennpunktes oder einer Brennlinie. *Ann der Phys* (Leipzig) 89:755–776
6. Nussenzveig HM (1959) Diffraction theory in the k-representation. *An Acad Bras Cienc* 31:515–521, Reproduced in Oughston K E (editor) (1992) *Selected Papers on scalar wave diffraction*. SPIE Press, NY
7. Bouwkamp CJ (1954) Diffraction theory. *Rep Prog Phys* 17:35–100

8. Maia Neto PA, Nussenzveig HM (2000) Theory of optical tweezers. *Europhys Lett* 50:702–708
9. Richards B, Wolf E (1959) Electromagnetic diffraction in optical systems II. Structure of the image field in an aplanatic system. *Proc Roy Soc Lond A* 253:358–379
10. Nussenzveig HM (1992) Diffraction effects in semiclassical scattering. Cambridge University Press, Cambridge
11. Ashkin A (2006) Optical trapping and manipulation of neutral particles using lasers. World Scientific, Singapore, pp 201–202, 204
12. Guillou M, Dholakia K, McGloin D (2008) Optical trapping and spectral analysis of aerosols with a supercontinuum laser source. *Opt Express* 16(11):7655–7664
13. Mazolli A, Maia Neto PA, Nussenzveig HM (2003) Theory of trapping forces in optical tweezers. *Proc Roy Soc Lond A* 459:3021–3041
14. Dutra RS, Viana NB, Maia Neto PA et al (2007) Polarization effects in optical tweezers. *J Opt A Pure Appl Opt* 9:S221–S227
15. Török P, Varga P, Laczik Z et al (1995) Electromagnetic diffraction of light focused through a planar interface between materials of mismatched refractive indices: an integral representation. *J Opt Soc Am A* 12 (2):325–332
16. Viana NB, Rocha MS, Mesquita ON et al (2007) Towards absolute calibration of optical tweezers. *Phys Rev E* 75:021914-1–021914-14
17. Roichman Y, Sun B, Stolarski A et al (2008) Influence of nonconservative optical forces on the dynamics of optically trapped colloidal spheres: the fountain of probability. *Phys Rev Lett* 101:128301-1–128301-4
18. Dutra RS, Viana NB, Maia Neto PA et al (2014) Absolute calibration of forces in optical tweezers. *Phys Rev A* 90:013825-1–013825-13
19. Born M, Wolf E (1999) Principles of optics, 7th edn. Cambridge University Press, Cambridge
20. Novotny L, Grober RD, Karrai K (2001) Reflected image of a strongly focused spot. *Opt Lett* 26:789–791
21. Schäffer E, Norrelykke SF, Howard J (2007) Surface forces and drag coefficients of microspheres near a plane surface measured with optical tweezers. *Langmuir* 23:3654–3665
22. Viana NB, Rocha MS, Mesquita ON et al (2006) Characterization of objective transmittance for optical tweezers. *Appl Opt* 45:4263–4269
23. Misawa H, Koshioka M, Sasak K et al (1991) Three-dimensional optical trapping and laser ablation of a single polymer latex particle in water. *J Appl Phys* 70:3829–3836
24. Roichman Y, Waldron A, Gardel E et al (2006) Optical traps with geometric aberrations. *Appl Opt* 45:3425–3429
25. López-Quesada C, Andilla J, Martín-Badosa E (2009) Correction of aberration in holographic optical tweezers using a Shack-Hartmann sensor. *Appl Opt* 48:1084–1090
26. Neves AAR, Pisignano D (2012) Effect of finite terms on the truncation error of Mie series. *Opt Lett* 37:2418–2420
27. Wiscombe WJ (1979) Mie scattering calculations: advances in technique and fast, vector-speed computer codes. Atmospheric Analysis and Prediction Division, National Center for Atmospheric Research, Boulder, CO

# Chapter 3

## Beyond the Hookean Spring Model: Direct Measurement of Optical Forces Through Light Momentum Changes

Arnau Farré, Ferran Marsà, and Mario Montes-Usategui

### Abstract

The ability to measure forces in the range of 0.1–100 pN is a key feature of optical tweezers used for biophysical and cell biological studies. Analysis of the interactions between biomolecules and the forces that biomolecular motors generate at the single-molecule level has provided valuable insights in the molecular mechanisms that govern key cellular functions such as gene expression and the long-distance transport of organelles. Methods for determining the minute forces that biomolecular motors generate exhibit notable constraints that limit their application for studies other than the well-controlled *in vitro* experiments (although recent advances have been made that permit more quantitative optical tweezers studies insight living cells). One constraint comes from the linear approximation of the distance vs. force relationship used to extract the force from the position of the bead in the trap. This commonly employed “indirect” approach, although usually sufficiently precise, restricts the use of optical tweezers to a limited range of displacements (typically up to  $\pm 150$  nm for small beads). Measurements based on the detection of the light-momentum changes, on the other hand, offer a “direct” and precise way to determine forces even when the generated displacements reach the escape point, thus covering the complete force range developed by the trap. In this chapter, we detail the requirements for the design of a force-sensor instrument based on light-momentum changes using a high-numerical-aperture objective lens and provide insights into its construction. We further discuss the calibration of the system and the main steps for its routine operation.

**Key words** Optical trap, Optical tweezers, Force measurements, Back-focal plane interferometry, Light momentum method

---

### 1 Introduction

Optical tweezers have become a valuable tool for studying biomolecular forces and molecular interactions at the single-molecule level owing to their ability to measure piconewton forces at high bandwidth. A mechanical force,  $F$ , can be derived from the displacement,  $x$ , through a calibrated spring. The linearization of the relation between the two parameters,  $F = -\kappa \cdot x$ , provides a direct conversion law for a certain range of displacements. This idea has been often successfully translated into the microscopic realm, due

in part to its simplicity, and it is undoubtedly the standard approach in optical tweezers [1]: the earlier methods based on the measurement of escape forces [2, 3] were soon left aside as they could not provide the dynamic range required by biomolecular experiments and were replaced by schemes where positional measurements are performed with a calibrated optical trap. Back-focal-plane interferometry (BFPI) [4, 5] quickly became the de facto standard in order to determine short displacements of the trapped sample, a method whereby the output voltage,  $V$ , of a photodiode is used to track the deflections of an auxiliary detection laser (or, most often, of the trapping beam itself) as the particle shifts from its equilibrium position at the center of the trap. Unfortunately, this approach, which considers the trap as a microscopic Hookean spring, demands a specific calibration prior to any experiment in order to determine the trap stiffness  $\kappa$ , which is rather cumbersome (*see* ref. [6] for a more detailed discussion). Furthermore, as the linear relation between force and displacement is a first-order approximation of a more general law [7, 8], the approach can only be used in the region close to the trap center where the error is sufficiently small. Contrary to the escape force method, this leaves a substantial part of the force that the trap can develop unused (i.e., the escape force is often larger than the maximum force measurable with this method, *see* ref. [9]) and thus implies the use of more laser power than actually required if one did not have this limitation, with possible deleterious effects on the sample [10, 11]. In addition, we often have only vague ideas about the linear force vs. distance range of the optical trap as most calibration methods only provide a value for the trap stiffness  $\kappa$ . Only a drag-force experiment that tracks the sample in response to applied known forces [12–15], a well controlled DNA-pulling assay [16] or a dual-beam optical tweezers setup can provide this information [17].

For small silica and latex beads ( $r < 500$  nm), a linear behavior for displacements in the range of 100–200 nm has been consistently reported [12–14] and it is often used as a reference. However, this may grossly underestimate the amplitude of the linear region for certain bead sizes, as we show in Fig. 1. We computed the electromagnetic force generated by a Gaussian optical trap on polystyrene spherical particles of variable radii ( $r = 0.1\text{--}2.0$   $\mu\text{m}$ ) by means of a T-matrix scattering code [18]. Figure 1a shows the radius of the linear region (as defined by three different error levels) in absolute values. In the Rayleigh regime, the force profile is determined by the characteristics of the beam (e.g., the beam waist, *see* ref. [8]) and not by the size of the bead so that the amplitude of the linear region is roughly constant and of approximately  $\pm 120$  nm (within an error of 10 %) for small beads ( $r < 320$  nm) regardless of the trapping wavelength or the relative index of refraction (Fig. 1a, shaded area and inset; *see* also Fig. 1d), in good agreement with previous experimental results [12–14]. However, for larger beads

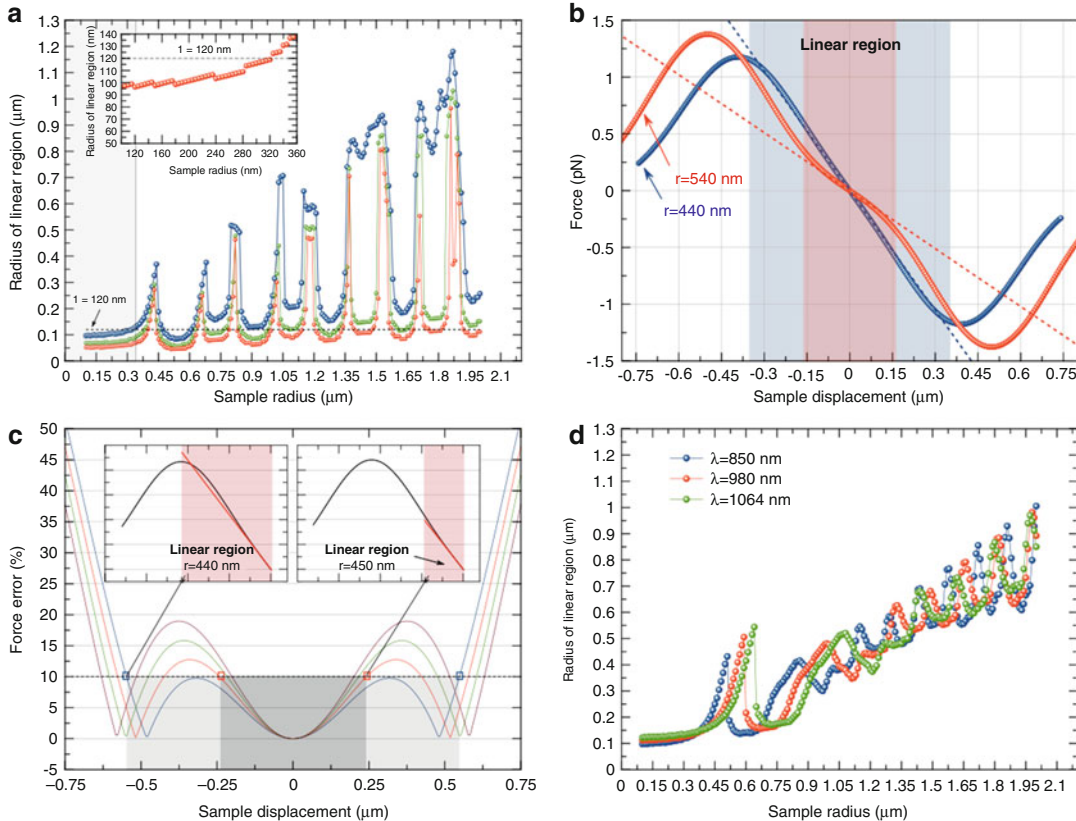


**Fig. 1** (a) Radius of the linear region as a function of sample radius. The linear region is defined as the displacement at which the error between the force and the linear approximation is less than 3 % (red solid line), 5 % (green solid line), and 10 % (blue solid line), respectively, and has been computed for polystyrene particles with a refractive index of  $n = 1.59$ , circularly polarized laser light at  $\lambda = 1064$  nm and a trapping objective lens with an NA of 1.3. For small samples ( $r < 350$  nm), the linear region is approximately 120 nm (shaded area, black dashed line, and inset). The linear region presents alternating maxima and minima due to resonance effects. (b) Force vs. displacement curves for two sample sizes,  $r = 440$  nm (blue open circles) and  $r = 540$  nm (red open circles). The dashed lines are linear fits to the corresponding force curves in the small central region indicated by the blue and red shaded areas and are therefore representatives for the force-distance relationships (and therefore the spring constants) one would obtain from thermal calibrations. The 540-nm curve presents a double harmonic potential that limits the linear region to  $\sim 150$  nm (light-red shaded area). On the contrary, the 440-nm curve is well described by a pure harmonic function up to the extreme points, with a linear region of  $\sim 350$  nm (light-blue shaded area). (c) Force error vs. sample displacement around the discontinuity at  $r = 440$  nm. The force error curve that corresponds to  $r = 440$  nm (blue solid line) crosses the 10 % ordinate (open blue square) at a much larger displacement than the curve corresponding to  $r = 450$  nm (red solid line and red open square respectively). The linear region is thus wider in the former case (insets and shaded areas). (d) Linear region for particles of  $n = 1.5$  at  $\lambda = 1064$  nm (green line),  $\lambda = 980$  nm (red line), and  $\lambda = 850$  nm (blue line). The curves notoriously differ from the ones in (a)

( $r > 320$  nm), and similarly to what is known about the trap stiffness and/or the maximum trap strength [19], the linear region shows sharp maxima and minima due to interference and resonance phenomena.

It has been reported for particles outside the Rayleigh regime that the optical potential cannot be described by a single harmonic function and that a considerable stiffening of the force curve can be observed for large lateral displacements [15]. This effect is sensitively dependent on particle size [17] as shown in Fig. 1b. The force vs. displacement curve for a 540 nm-radius bead shows a significant stiffening of the potential for lateral displacements greater than  $\sim 150$  nm whereas the one for a 440 nm-radius bead does not. Thus, the harmonic approximation is significantly better in this latter case (light-red shaded area), which explains the maximum at 440 nm and the minimum at 540 nm in Fig. 1a. On the other hand, the discontinuities at the maxima are the product of the fixed error threshold and a fast changing force curve for these sample sizes. Figure 1c depicts the calculated error between the actual force and its linear approximation at both sides of a discontinuity in the linear region (here defined by a 10 % error). The intercept of the error curve corresponding to a particle size of  $r = 440$  nm (blue line) with the 10 % ordinate (blue open square) takes place at a much larger displacement than the one (red open square) corresponding to a particle size only 10 nm larger (red line). Even precision commercial microspheres can show a coefficient of variation in diameter of  $\sim 5$  % between nominally identical beads so that a sample preparation may contain bead sizes at both sides of the discontinuity. However, in practical terms, the effect is not as important as the difference in the extent of the linear regions may suggest: within the linear range of the 440-nm bead, the 450 nm bead would cause a maximum force error of  $\sim 13$  % (instead of  $\sim 10$  %). Therefore, experiments done with bead sizes around these maxima may benefit from a greatly extended linear region, which may reach values above 1  $\mu\text{m}$  for the largest sizes, but are more delicate as the error quickly changes with size in these regions.

The measuring range is also a function of several variables, such as the acceptable error (Fig. 1a), the trapping wavelength or the relative index of refraction (Fig. 1d). Taken together, these observations indicate that a simple rule-of-thumb, except for small samples, cannot anticipate the stretch of the linear region, which should be determined by other means. A further difficulty, which is more evident for large beads, is that the commonly employed calibration based on the power spectrum method only sample a small part of the optical potential and may not produce the best linear fit for the force vs. displacement curve. For example, a misrepresentative stiffness is responsible for the small linear regions around  $r \approx 1.95$   $\mu\text{m}$  in Fig. 1a.

However, in the nature itself of BFPI lays a possible solution to these issues. Ironically, for a method that is at the heart of the Hookean spring approach, BFPI does not directly measure positions. When the trapping beam is used for the BFPI measurement and not an auxiliary laser, the asymmetries in the far-field

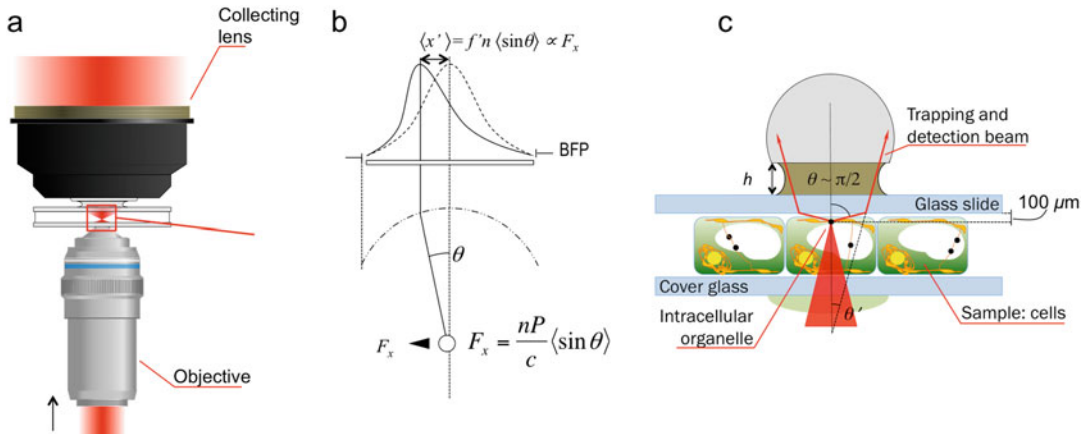


**Fig. 2** (a) The momentum method can be used with high-NA traps by capturing the entire forward-scattered light. (b) A particle pulled out of the equilibrium position by the force  $F_x$  deflects the trapping beam by an angle  $\theta$ , which can then be measured at the back-focal plane of a collecting lens as a displacement of the center of mass of the light distribution  $\langle x' \rangle$ . (c) As the method involves a calibration factor that neither depends on the size nor the refractive index of the trapped bead, it can be applied to measuring optical forces in complex media such as the interior of cell

distribution of the scattered light carry information on the photon momentum change. It is through this connection that BFPI can relate to sample displacements (*see* Subheading 1.1), yet, under concrete conditions, as shown by Smith et al. [20] a decade ago, this information can be used instead to derive the force directly, without intermediate steps.

The momentum method, originally developed for traps with two counter-propagating lasers [20], has been successfully implemented by our group in the more frequently used single-beam configuration (optical tweezers, Fig. 2) [21] and its relation with BFPI has been demonstrated experimentally [22]. This approach has been recently employed in single-beam optical tweezers to measure forces of motor proteins in cells [23, 24], in the study of enhanced trapping with complex beams [25] and in the characterization of synthetic nanomotors [26]. We describe the momentum method in some detail in the following, analyzing its relation to BFPI and discussing how it can resolve issues inherent to the harmonic approximation.

### 1.1 Relation Between Back-Focal Plane Interferometry and the Momentum Method

After interacting with the bead, the trapping beam is re-scattered, changing its direction of propagation (that is, the components of the momentum). The change in momentum is due to a transfer of a part of it to the particle, which gives rise to the pulling force. The momentum information is contained in the angular intensity distribution,  $I(\theta, \phi)$ , of the scattered light in such a way that the force on a particle can be written as [20]:

$$\vec{F} = \frac{n}{4\pi c} \oint I(\theta, \phi) \hat{r} d\gamma, \quad (1)$$

where  $n$  is the refractive index of the suspension medium,  $c$  the speed of light,  $\hat{r}$  the unit vector from the focus,  $\gamma$  represents a solid angle, and the integration is done on the surface of a sphere of large radius surrounding the particle. The optical tweezers instrument required to determine light momentum changes has a similar design to the one used for BFPI-based position measurements. Briefly, a collecting lens captures the laser light from the trap, and the light pattern at its back-focal plane is projected onto a photodetector. The photodetector generates voltage signals that always indicate the force exerted by the beam of light on the trapped bead, as the procedure will effectively compute the integral in Eq. 1, provided that:

- (a)  $\sim 100\%$  of the scattered light is captured by the collecting lens,
- (b) The projection of the captured light onto a plane (the back-focal-plane of the lens) maintains its momentum structure by fulfilling the Abbe sine condition [20, 21],
- (c) The momentum distribution is transferred without loss of light to the detector,
- (d) The detector performs the appropriate integration of the light signals (i.e., a Lateral Effect Position-Sensing Detector, PSD, must be used instead of a quadrant photodiode, QPD), and
- (e) The conversion factor between detector voltages and force units is fixed and known.

However, the conditions a) through e) are not explicitly enforced in BFPI. For example, the optical field that is captured in BFPI is often an arbitrary small section of the scattered light (Fig. 3). In this case, the relation between the detector signals and force is also arbitrary and dependent on the scattering properties of the bead. As this relation cannot be easily established by means of general electromagnetic principles, known forces, either thermal or viscous, have to be applied as a reference prior to any experiment. In contrast, the momentum method provides an output voltage that can be directly converted into units of force through a constant,  $R_D/f'\varphi T_c$ , which neither depends on the bead size nor on any other specific experimental property and only depends on the parameters of the detection instrument, i.e., the radius and responsivity of the detector,  $R_D$  and  $\varphi$ , the focal length and the optical transmittance of the instrument,  $f'$  and  $T$ , and the speed of light,  $c$  [20–22]. Despite these differences, the layout of the instrument is identical in the two cases (a lens capturing the scattered laser light and a position-sensitive detector placed conjugate to its back-focal

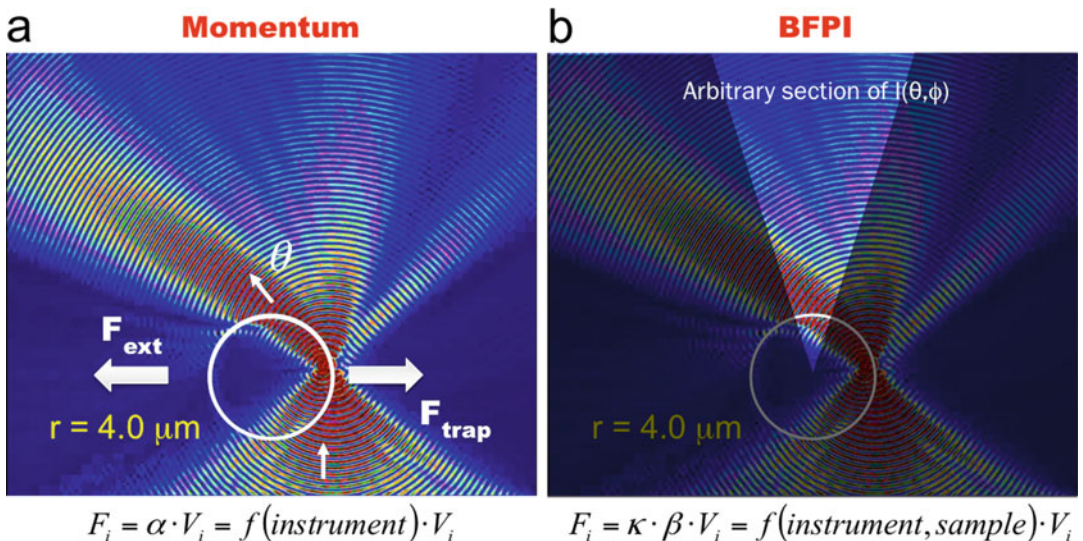


**Fig. 3** (a) A trapped bead is displaced from the equilibrium position by an external force until the restoring force of the trap re-equilibrates the system; the light of the trap is scattered at large angles. In the momentum method, all forward-scattered light is collected and analyzed, in such a way that the relation between the output signals and the force only depends on macroscopic properties of the detection instrument. (b) By contrast, a BFPI instrument captures an arbitrary section of the scattered light so that the relation between the output signals and the force is also arbitrary. In general, this relation also depends on the scattering properties of the sample so that a unique calibration factor does not exist

plane measuring its deflection) and the BFPI signals provide approximate representations of the corresponding force curves, which is illustrated in Fig. 4 (see ref. [21] for equivalent experimental results). We have carried out the simulation with the OTGO package [27], which uses the geometrical optics approximation, valid for large particles ( $r > > \lambda$ ). The upper row of images shows, for different sample displacements (indicated by arrows), the appearance of the back-focal plane of a collecting lens with a numerical aperture of  $\text{NA} = 1.33$ , which is capable of capturing the entire forward-scattered light [21, 22]. By contrast, the inner white circle indicates the light collected by a lens of  $\text{NA} = 1$ .

The trapped bead acts as a refractive lens in this regime, progressively tilting the beam as the off-axis displacement increases. At large displacements, the pattern displays a remarkable astigmatism since the sagittal and meridional curvatures of the bead at the impact point differ greatly in this case. The center-of-mass of these back-focal plane distributions,  $S_j = \int r_j I(\hat{r}) d\hat{r}$ , has been computed numerically by simulating the operation of the PSD in a momentum-based instrument (Fig. 4). With the known calibration factor ( $R_D/f' \varphi T_c$ ), the result is the green solid line that closely follows the true force curve (black solid line) well beyond the trap's linear region (compare the light green and light orange-shaded areas). For large bead displacements, increased back-scattered

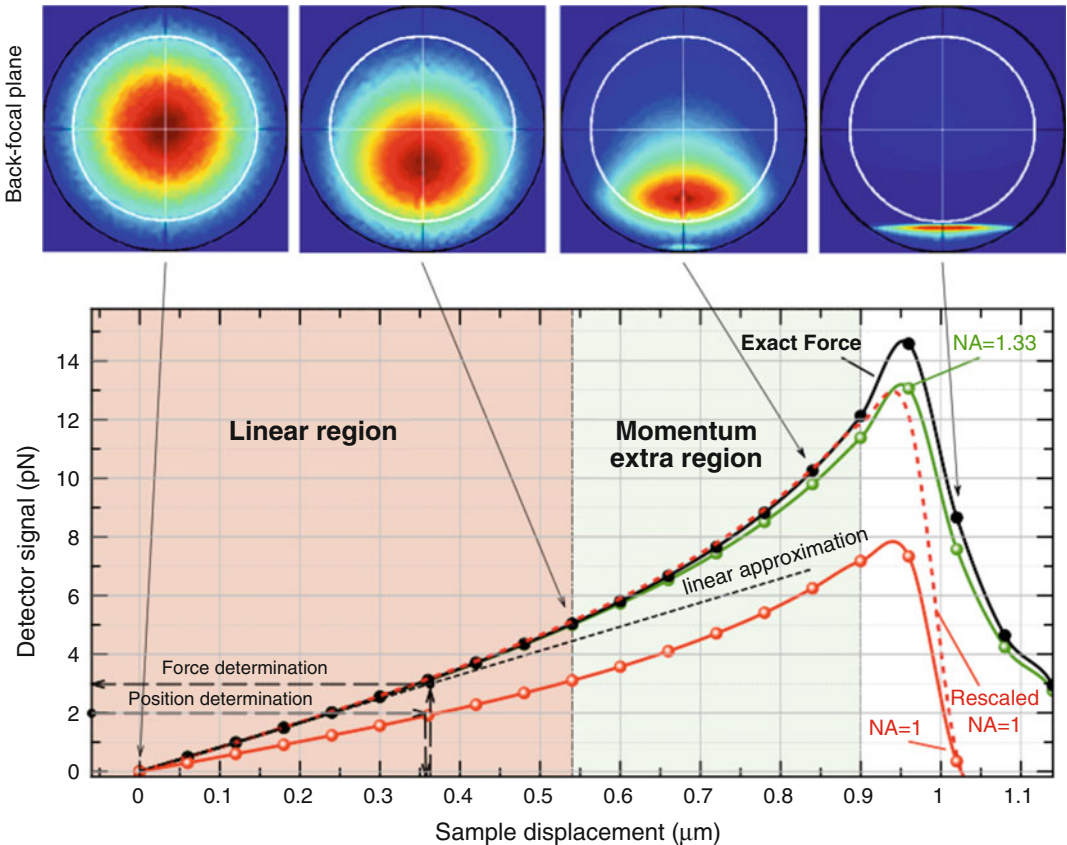


**Fig. 4** Simulation showing the image of the back-focal-plane of a collecting lens of  $NA = 1.33$  capturing the light scattered in the forward direction by a microsphere of  $r = 1 \mu\text{m}$  and  $n = 1.5$  for different microsphere displacements, in the geometrical optics regime (upper row) (NA of trapping objective: 1.3). Only the light that is scattered by the microsphere and therefore produces force is shown for clarity. The light patterns integrated by a PSD generate a signal that scaled through the known factor  $\alpha_{\text{sensor}} = R_D/f'\gamma c$  (solid green line) closely resembles the force curve (black solid line) for all displacements, enabling force measurements in an extended region (light-green shaded area). By contrast, when the scattered light is collected by a lens of  $NA = 1$ , the signal in the same scale does not match the force curve (solid red line). However, when used as a position indicator, it enables the measurement of forces in the reduced region shaded in light red (region where  $F \approx \kappa x$ ). In fact, the signal scaled by the calibration factor  $\kappa \cdot \beta$  (dashed red line) closely follows the force curve in a much wider region, showing that it retains considerable information about the momentum change of the trapping beam

light, which is not collected in the simulation (nor in our instrument), produces a growing error ( $\sim 10\%$  at its maximum). By contrast, the red solid line represents the output of the PSD coupled to a collection optics of  $NA = 1$ , and thus simulates the behavior of an instrument in which conditions a) or c) above are not fulfilled. With the same calibration factor as before, the curve does not overlap the force plot at any displacement so that the output signal needs to be accurately related back to force in order to measure under these experimental conditions. BFPI does so by

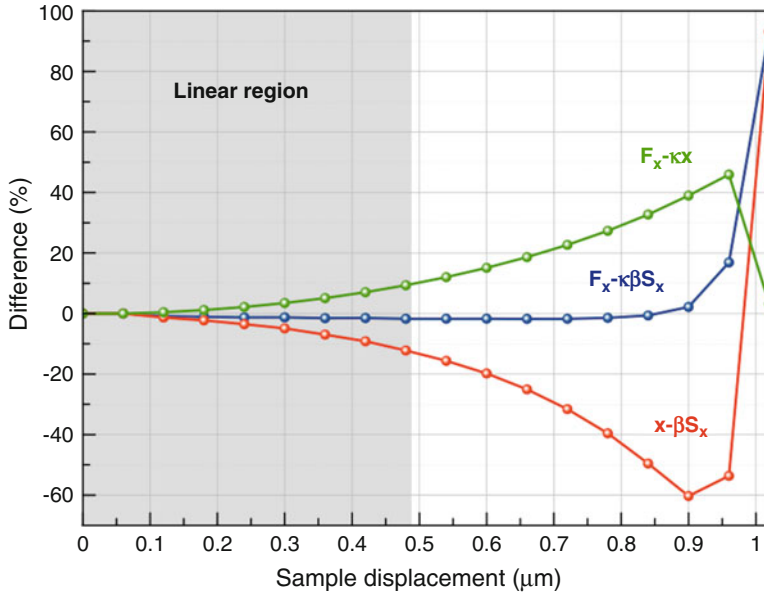


**Fig. 5** The BFPI signals are proportional to the optical force in a range much larger than the one in which they are proportional to displacements under the conditions simulated in Fig. 4: the *blue line* indicates the difference between the force and the scaled BFPI signal and the red line shows the difference between the sample position and the scaled BFPI signal. The *green line* shows the error between the force and its linear approximation. The linear region (shaded in gray) is where this difference is sufficiently small. The BFPI signal correctly indicates the force in a larger region

converting the voltage signal first into displacements and then subsequently recovering the force information by means of harmonic approximation (black dashed arrows).

As BFPI still preserves force information, once the PSD output,  $S_x$ , is rescaled by the factor  $\kappa\beta$  ( $\beta$  is the position sensitivity, i.e.,  $x = \beta S_x$ ), the curve closely matches the force curve (Fig. 4, dashed red line). In fact, as observed experimentally [17, 22] and illustrated in Fig. 5, the range over which BFPI signals are proportional to force (blue line) can be larger than the one in which they are proportional to displacements (red line). The force is measured accurately well beyond the linear region (green line and dashed area), without many of the problems discussed above, unbeknownst to the user. Thus, when the position information is not simultaneously required, optimizing BFPI to be able to measure accurately through the momentum information is a great alternative: because of the more direct approach to determining forces the method measures accurately in a greater range (up to the escape force in our experience) and without the need for recurrent calibrations. This makes the momentum approach ideal where the power at the sample cannot be high or when the conditions required for the application of the harmonic approximation of the force cannot be guaranteed. Important examples are the measurement of forces

in a non-viscous medium such as the cellular interior [23, 24], while minimizing laser damage, or measurements made on unusual samples [6, 23, 28] or beams.

Below, we provide the keys for building a system to measure forces based on this approach, as well as the protocol to calibrate its force response (*see Note 1*). Compared to the narrower cone of light emanating from a trap with counter-propagating lasers, the use of high-NA optics, required here for the detection of the whole scattered beam, demands some specific, thorough analyses and also complicates the construction of the system. First, we describe the determination of the effective focal length, the responsivity and the detector radius, which are needed to for the macroscopic calibration (i.e., for the determination of the calibration factor  $\alpha_{\text{sensor}} = R_D/f'\phi T_c$ ), and then explain the complementary microscopic approach based on the power-spectrum method. The agreement between the results of the two calibration methods allows the verification of the correct construction and calibration of the system. Finally, we describe the procedure to measure forces with the setup and then how to derive positions from forces whenever trap stiffness calibration is possible.

## 2 Materials

### 2.1 Detection Setup

The elements required for the basic optical setup are:

1. Aplanatic, long focal length lens with a numerical aperture (NA) larger than the refractive index of the suspension medium in which the experiment is performed (*see Notes 2 and 3*). This lens operates simultaneously both to capture the scattered light and as an illumination condenser.
2. Relay lens corrected for spherical aberrations to project the light pattern at the back-focal-plane (BFP) of the collecting lens onto the active area of the PSD (*see Notes 4 and 5*).
3. Bandpass filter (*see Note 6*).
4. Neutral density (ND) filter with antireflective coating for the trapping wavelength (*see Note 7 and 8*).
5. PSD (*see Notes 9–11*).
6.  $x$ - $y$  translation stage for the PSD (*see Note 12*).
7. Data acquisition board with adjustable voltage range and 16 bit minimum resolution.
8. Linear power supply for the PSD with low output noise and ripple (a few mV).
9. Dichroic mirror for separating the trapping wavelength from the visible light used to illuminate the samples.

## 2.2 Force Calibration

- The material for the force calibration of the instrument comprises:
1. Iris diaphragm with a diameter larger than the entrance pupil of the trapping objective and minimum clear aperture of 1 mm.
  2. Auxiliary lens for imaging the iris on the PSD.
  3. Translation stage with graduated scale (1 mm marks minimum) to calibrate the PSD radius. Its maximum travel should be larger than the diameter (or size) of the active area of the PSD.
  4. Laser power meter, with accuracy better than 3–5 %. The power meter is used to determine the optical transmittance of the instrument and therefore its error directly determines the accuracy of the macroscopic calibration.
  5. Ronchi ruling with  $\sim 100$  lines/mm (thickness  $\sim 1$  mm).
  6. Small video camera with an active area larger than the size of the light pattern at the PSD (capable of capturing the whole momentum distribution).
  7. Bertrand lens.
  8. Two identical high-numerical aperture microscope objectives.
  9. Thermometer.
  10. Microscope glass slides ( $26 \times 76$  mm, thickness  $\sim 1$  mm).
  11. Microscope coverslips #1.0 or #1.5 ( $22 \times 22$  mm).
  12. Double-sided scotch tape or Nescofilm.
  13. Nail polish or correction fluid (such as Tipp-Ex).
  14. Plastic microspheres. The microspheres should be selected according to the trapping wavelength in order to produce both Rayleigh and Mie scattering, as well as intermediate sizes between these two extremes (approx. 0.5, 1, 2, and 3  $\mu\text{m}$  diameter for 1064 nm trapping wavelength).
  15. Purified water.
  16. High viscosity immersion oil (Cargille Type B).

## 3 Methods

The construction and calibration of the instrument proceeds as shown in Fig. 6.

### 3.1 Characterization of the PSD Spatial Response

This step is part of the macroscopic calibration. Although not mandatory, it is advisable to start by characterizing the PSD before building the setup (see Note 13).

The following steps describe how to eliminate residual offsets from force signals and center the PSD detector (see Note 12).

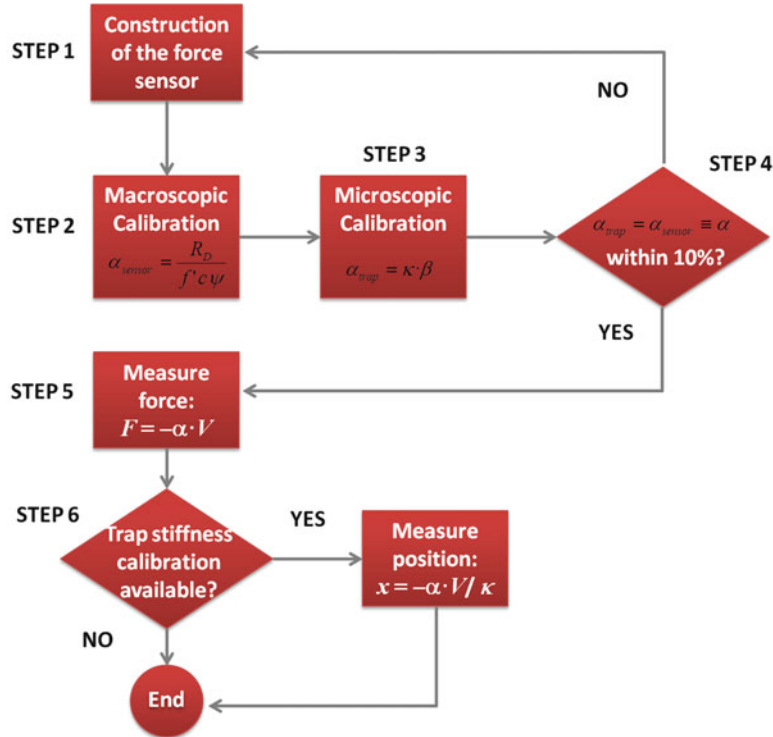


**Fig. 6** Flow diagram of the construction, calibration, and validation protocols

1. Mount the PSD on the translation stage with the graduated scale directly in front of the laser and place an iris in front of the laser output to reduce the beam diameter to 1 mm.
2. Adjust the auxiliary lens to form the image of the iris on the active area of the PSD.
3. Place an antireflection-coated ND filter (with transmittance  $T_{\text{ND}}$ ) in front of the detector to avoid damage from the laser light. Responsivity of silicon at 1064 nm is around 0.3 A/W and the typical gain and typical maximum output voltage of PSDs are 10 kΩ and 10 V, respectively. Therefore, as a rule of thumb, the maximum laser power should be kept below the PSD saturation level of  $10/3T_{\text{ND}}$  mW, i.e., at  $\sim 1/T_{\text{ND}}$  mW.
4. First, remove the electronic offsets of the PSD (which vary from device to device) for a proper centering of the beam on the PSD: in total darkness (with the laser off and no ambient light), record 1000 data points.
5. Compute the mean for the four output signals (*see Note 10*):  $V_{0,x}$ ,  $V_{0,y}$ ,  $V_{\text{sum},0,x}$ , and  $V_{\text{sum},0,y}$
6. Subtract these offset values from the measured voltages (Fig. 7a). Note that these offsets depend on temperature ( $\sim 1\text{ }^{\circ}\text{C}$ ) so that they should be recalculated whenever the ambient temperature changes significantly.

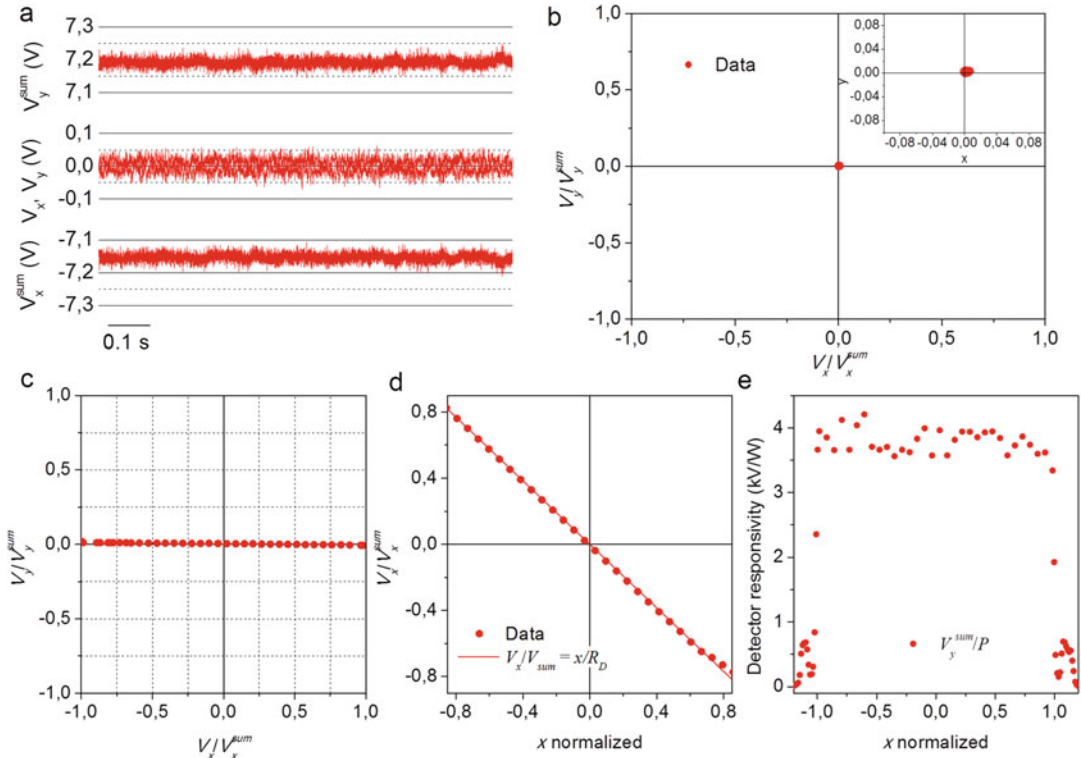


**Fig. 7** (a) PSD signals  $V_x$  and  $V_y$  with offsets removed. Signals  $V_{\text{sum},x}$  and  $V_{\text{sum},y}$  are also recorded for normalization purposes. (b) Two-dimensional map of normalized position signals with offsets removed showing a well-centered PSD. The *inset* is a magnified view of the center. (c) Scan in the *horizontal* direction of the PSD to calibrate the effective radius of the detector. (e) Data in (c) plotted against the true displacements of the detector obtained through the graduated scale of the stage; the slope is the radius in the *horizontal* direction. (e) Final check of the uniformity of the PSD response. The *plot* shows the result for a high quality detector. Low-quality PSDs have regions of different responsivity within the usable area and should be avoided

7. Compute the normalized position  $(V_x - V_x^0)/(V_x^{\text{sum}} - V_x^{\text{sum},0})$  for both channels. Unless stated otherwise, throughout the text we consider that electronic offsets are removed from the output voltages.
8. Turn the laser on and set the laser power so that the output voltage is, approximately, half its maximum value (around 5 V).  $V_{\text{sum},x}$  and  $V_{\text{sum},y}$  should provide the same result with the opposite sign (as they come from currents in the PSD of the opposite direction).
9. Plot the two normalized signals on an x–y chart. The data should appear at the center of the plot.
10. If this is not the case, adjust the PSD translation mount to cancel them out (*see* Fig. 7b). Then, the laser beam is centered on the detector.

Below we describe how to measure the effective radius,  $R_D$ , of the PSD (*see Note 14*):

1. Make sure that when the laser spot is centered on the active area of the PSD that the screw of the translation stage is, more or less, at the mid-point of the graduated scale. Then, move the stage to one end until the light spot reaches an edge of the active area of the PSD.
2. For a fixed laser power,  $P$ , record its value with the power meter and the PSD output voltages  $V_x$ ,  $V_y$ ,  $V_{\text{sum } x}$  and  $V_{\text{sum } y}$  with the detector. Move the stage toward the other edge in 20 steps and measure the five quantities in each position (Fig. 7c).
3. Plot  $V_x/V_{\text{sum } x}$  against the position of the PSD,  $x$ . The slope corresponds to the inverse of the detector radius  $R_D$  (Fig. 7d and *see Note 15*).
4. Also plot the ratio  $V_{\text{sum } x}/P$  against the position of the PSD (Fig. 7e),  $x$ , and check that you obtain a constant value (close to 3000 V/W for a 1064 nm laser) within >90 % of the size of the PSD. This is the maximum size that the light pattern projected onto the PSD should have. Low quality detectors may exhibit large nonuniformities across their surfaces and should be avoided.

### 3.2 Construction of the Instrument

As described in the introduction, the instrument needed to determine light-momentum changes is similar to the one used for position measurements in BFPI (Figs. 8 and 9), but its construction explicitly enforces certain requirements, such as that the light scattered by the sample in the forward direction is fully captured.

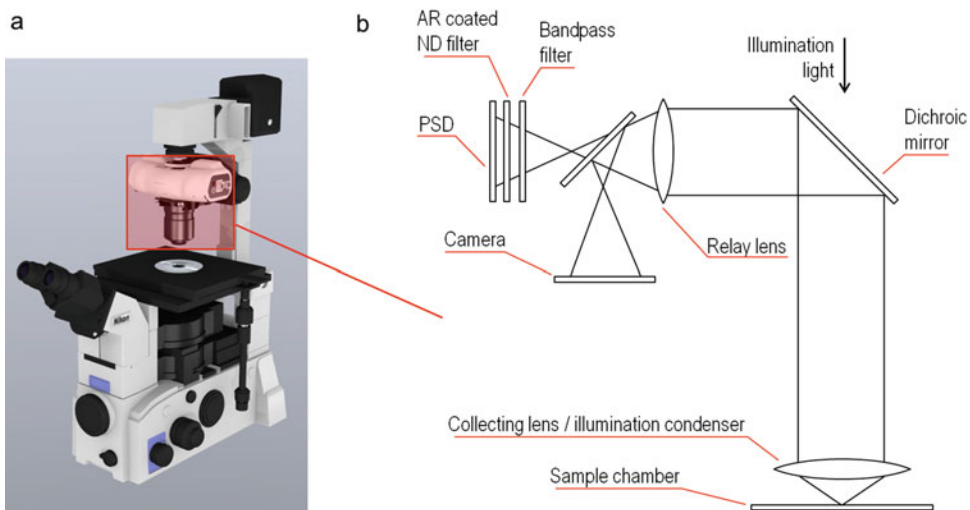


**Fig. 8** (a) View of a commercial instrument based on light momentum changes and (b) optical layout. The camera allows observation of the light distribution at the back-focal plane, which is essential in several steps of the protocol. The PSD can be removed to allow this observation but a permanent location for the camera, as in the drawing, is more convenient

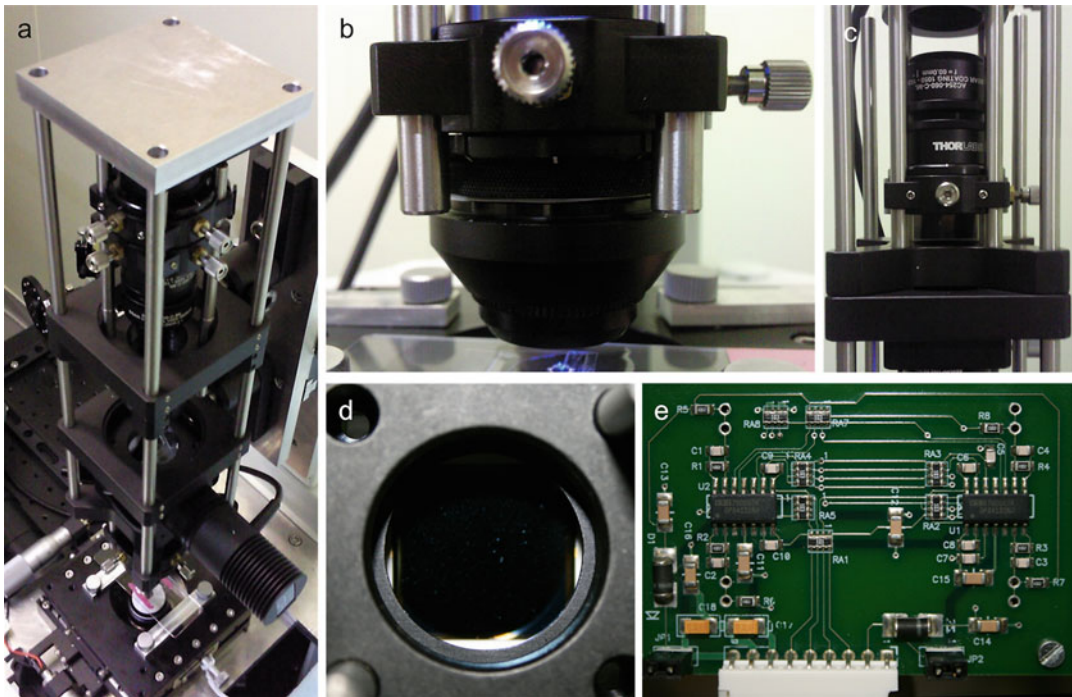


**Fig. 9** Main elements of a force sensor instrument based on light momentum changes. (a) General view. (b) Oil-immersion detection lens with high NA. (c) Relay lens system composed of two achromatic doublets working at infinity conjugates. (d) PSD's sensitive surface and (e) PSD electronic circuitry incorporating transimpedance amplifiers, reverse bias, sum and difference op-amps

Good step-by-step protocols for constructing BFPI instruments are available in the literature [29, 30]. These can be used as a starting point to build a system that can then be tuned and calibrated according to our protocols, in order to measure the light momentum. However, as a consequence of the requisites of the momentum method, the technical characteristics of many elements in the setup, including the microchamber that holds the samples, should be carefully considered (and not solely the detector). The additional requirements are discussed at length in Notes 1–17, and are referenced when pertinent.

### 3.3 Macroscopic Calibration

The main step of the macroscopic calibration is the determination of the calibration parameter  $\alpha_{\text{sensor}} = R_D/f'\psi c$ . The procedure for obtaining the effective radius,  $R_D$ , has been discussed in Subheading 3.1. The following protocol describes how to adjust the location of the camera and the PSD, and how to determine the focal length of the instrument,  $f'$ . Finally, determination of the instrument's responsivity,  $\psi$ , is described in Subheading 3.7.

All system elements should be mounted at this stage as follows:

1. Remove the trapping objective and the sample.
2. Add an iris diaphragm with a diameter  $\phi \leq 1$  mm to minimize any aberration introduced by the Ronchi ruling.
3. Place the Ronchi ruling on the stage with the surface that contains the diffraction grating facing the incoming light and put a droplet of oil on top of it. Bring the detection lens in contact with the oil. The working distance of the detection lens is about 2 mm (here defined as the distance between the front surface of the lens and the trapped bead when working at its maximum numerical aperture) and thus the thickness of the ruling's substrate should be also  $\sim 1$  mm, to reduce the amount of oil necessary for the detection lens to operate at its optimal working distance (*see* Subheading 3.4 for further details).
4. Place the video camera at the detector plane.
5. Turn on the laser and move the camera (or, alternatively the relay lens system) until the diffraction peaks are in sharp focus (Fig. 10). This corresponds to the image of the BFP of the collecting lens. The PSD should then be placed carefully in this same plane.
6. To calibrate the focal length of your detection system and, therefore, of the conversion between positions and momenta, take an image of the diffraction pattern.
7. Measure the distance in millimeters of the different diffraction orders to the central order. For this you will need the inter-pixel distance of your camera, provided by the manufacturer. To determine the 0th order, rotate the Ronchi ruling. All light spots should move except for this one.
8. Then, plot the position of the first  $m$  diffraction orders as a function of  $n \cdot \sin \theta_m$ . This value can be computed from the laser

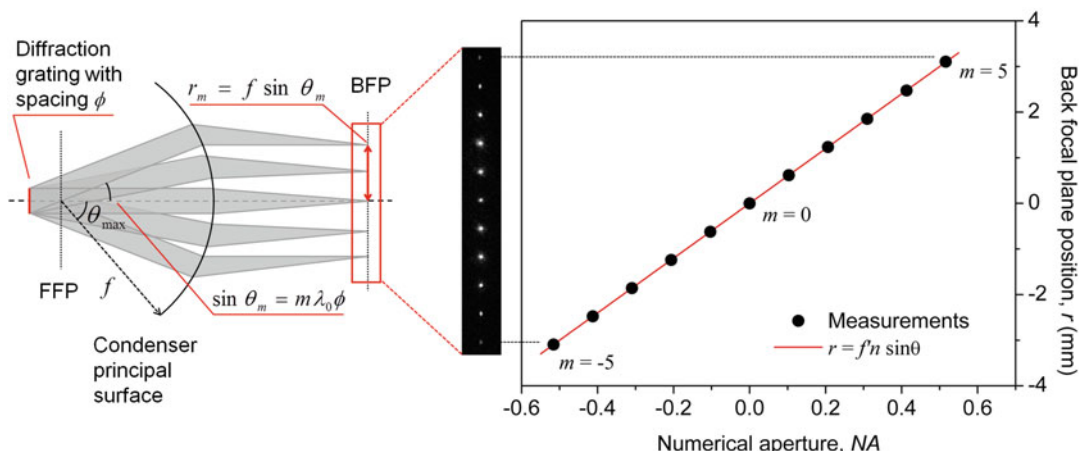


**Fig. 10** Determination of the equivalent focal length,  $f'$ , of the system composed of detection and relay lenses. A Ronchi ruling generates plane waves by diffraction traveling at known angles. The optical system focuses the diffraction orders on a camera in a scale that is determined by  $f'$

wavelength in vacuum,  $\lambda_0$ , and the frequency  $\phi$  (in lines/mm) of the Ronchi ruling as  $m\lambda_0\phi$ . If the design of the instrument is correct, the result should be a straight line, whose slope corresponds to the focal length of the instrument,  $f'_{\text{sensor}}$ . In general, only the central orders are easy to observe so that the condition of aplanaticity can only be confirmed for small angles (typically  $<30^\circ$ ).

### 3.4 Sample Chamber Characteristics

The following step is the construction of a microchamber to suspend the sample.

The momentum method introduces some requirements for this. As the detection lens has a large NA, immersion oil will be needed for its correct operation. This implies that the sample will have to be sandwiched between two glass elements (a glass slide and a cover glass, respectively). Since a long focal length detection lens is preferable (see Note 2), the working distance will also be large (typically 1–2 mm). In this case, a thick glass slide (1 mm) should be placed on the top to reduce the amount of oil between the slide and the lens. A thick glass also prevents chamber bending when contact with the bulky detection lens is made. In addition, the amount of captured light decreases when the trap is moved away from the top glass of the chamber deep into the sample, so the thickness of the spacer should not typically exceed 100  $\mu\text{m}$ .

The sample chamber can be simply built by sticking two small strips of double-sided Scotch tape, which will work as spacers, to a glass slide. Place a standard #1.0 or #1.5 coverslip over the spacers and gently press on the glass covering the tape until an enclosed chamber is formed. The chamber is filled with a suspension of microspheres in deionized water by carefully placing the tip of a micropipette at one of the open ends and gently pipetting in the solution ( $\sim 50 \mu\text{l}$ ). Dilute the sample enough so that one observes on average one bead in the field of view of the microscope. Finally, apply nail polish or correction fluid (such as Tipp-Ex) to the open ends in order to seal the chamber. Tips for dealing with the beads sticking to the glass surfaces are described in ref. [29].

The lateral dimensions of the microchamber should also be considered to prevent vignetting of the light scattered at high angles, especially when working away from the top glass. Light scattered by a sample at the bottom of the chamber that travels close to  $90^\circ$  to the normal may reach the top glass as far as  $\sim 1 \text{ cm}$  away from its origin in the  $X$ – $Y$  plane. For this reason, loss of high-NA rays can sometimes be seen in the BFP when working close to the edge. Make sure that no air islets reduce the effective working region and try to work in the central region of your chamber.

The capture of all the forward-scattered light requires the correct axial positioning of the assembled instrument, i.e., the front lens should be set at a specific distance from the top surface of the

### 3.5 Height Positioning of the Instrument

sample chamber while keeping the relative distances between the different components unchanged. The preservation of the calibration constant that converts volts into pN also relies on this adjustment; misplacement of the instrument by only 0.2 mm in the axial direction can change the effective focal length by 4 % (altering the calibration), and misplacement by  $\sim 1$  mm may significantly affect light collection. It is therefore critical to perform the following steps:

1. Put a chamber on the stage containing a diluted sample of beads of 1–2  $\mu\text{m}$  diameter (preferably polystyrene microspheres).
2. Turn on the laser and trap a single microsphere.
3. Adjust the axial position of the water-immersion objective lens to push the trapped bead slightly against the top glass to enhance the scattering at large angles (Fig. 11a).
4. Check the intensity pattern with the camera. Adjust the laser power if necessary. If the instrument is set at the correct height, two clear concentric disks must appear (*see* Fig. 11). The first should have a size of  $2 \cdot f'_{\text{sensor}} \cdot \text{NA}_{\text{objective}}$  (light non-scattered by the sample), whereas the second one should have

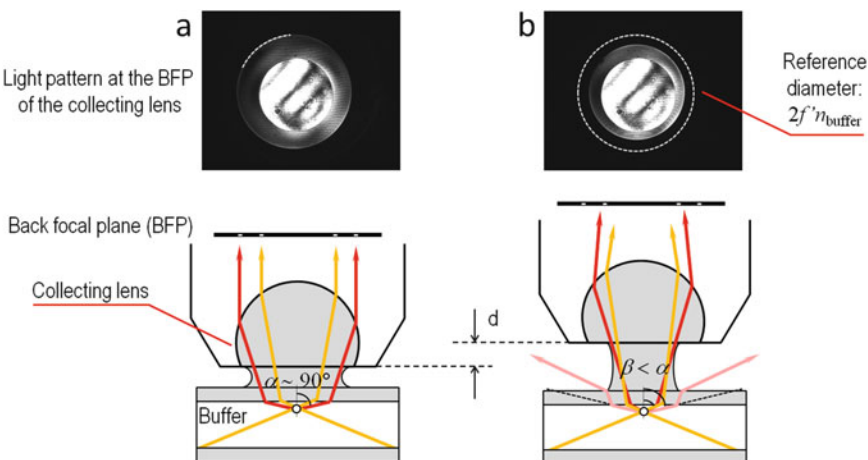


**Fig. 11** (a) Adjustment of the axial position of the detection instrument. This step is critical for capturing all forward-scattered light as well as for preserving the calibration constant at a known value. The figure shows the back-focal plane of the detection lens as well as a sketch of the trajectories of scattered (red) and unscattered (yellow, coming directly from the trap) light rays. When the trap is empty, the BFP would show an illuminated disk with a numerical aperture  $\text{NA} = \text{NA}_{\text{objective}}$ . However, with a trapped bead, and in agreement with the Gittes-Schmidt interference model (5), an outer ring of light that has been scattered by the particle can be appreciated in the image. Inside this region where the scattered and unscattered light cones overlap (region with  $\text{NA} \leq \text{NA}_{\text{objective}}$ ), interference fringes are formed. When the instrument is at the correct height, the faint disk of scattered light reaches a numerical aperture  $\text{NA} = n_{\text{buffer}}$  (corresponding to angles within the buffer of  $\sim 90^\circ$ ). (b) When the height is incorrect, internal and external light losses and deviations from the sine condition make the scattering disk smaller

a size of  $2 \cdot f'_{\text{sensor}} \cdot n_{\text{buffer}}$  (light re-scattered by the sample in the upper hemisphere, *see also Notes 3 and 16*).

5. Replace the camera with the PSD. Make sure that the PSD surface lies on the same plane of the camera chip, and proceed to characterize its linearity range.

### **3.6 Characterization of the PSD Power Linearity**

The PSD power linearity should be checked with light patterns similar to those registered when doing force measurements, as the PSD power response depends to a certain extent on the shape of the light distribution (avoid focused light spots, as the detector response will become nonlinear). Perform the following steps *in situ* with light coming from a trapped bead:

1. Set the sampling frequency at 1 kHz.
2. Record the sum voltage,  $V_{\text{sum}}$ , for 1 s and compute the mean.
3. Repeat the process for 20 increasing laser powers,  $P$ , until the detector signal saturates. The powers should be evenly spaced and cover the total dynamic range of the sensor.
4. Plot  $V_{\text{sum}}$  against  $P$  and check that the output voltage is linear within typically 1 % or less. The value at which the sensor starts saturating determines the maximum output signal  $V_{\text{max}}^{\text{sum}}$ .

### **3.7 Characterization of the Instrument's Responsivity**

The efficiency is determined in two steps. It is important to characterize the optical transmission of the instrument under experimental conditions (*see Note 17*). To do so, and with the instrument adjusted according to the previous instructions, perform the following steps:

1. Calibrate the transmittance of an objective of high-NA used for trapping. To do this, use the dual-objective method [31], which requires two identical objectives. Place one of the objectives in the microscope and replace the detection lens with the second objective. For this you may need to adapt the diameters with a custom mechanical part.
2. Put a sample chamber on the stage. This chamber is specifically built for the measurement of the responsivity, and consists of a droplet of water between two identical thin coverslips (the same ones used in order to close the bottom of the experimental microchamber described in Subheading 3.4). After some time, you may need to check that the liquid has not dried out.
3. Put the objectives in contact with the chamber through the appropriate immersion fluid (oil/water) and set the height of the bottom objective so that the sample is in sharp focus.
4. Place an iris diaphragm at an optical equivalent of the entrance pupil of the first objective and center it so it is on axis with the laser beam.

5. Turn the laser off and look through the Bertrand lens of the microscope to center the second objective with the optical axis of the first one (coinciding with that of the whole microscope). If you use oil-immersion objectives, check that no air bubbles are trapped in the oil. If there are bubbles, gently remove the oil with a lens tissue and apply a new drop of oil.
6. Turn on the laser and make the laser beam come out of the second objective collimated (the laser beam is also assumed to enter the first objective collimated). To do this, move the second objective in the axial direction.
7. Next, measure the transmittance of the lenses using a powermeter to determine the power at the back aperture of both objectives. Make sure that you measure the whole beam. The transmittance of a single objective lens is then obtained as the ratio  $(P_{\text{out}}/P_{\text{in}})^{1/2}$ .
8. Repeat the measurement for different diameters of the diaphragm and obtain a curve T vs. r (Fig. 12a). For diameters

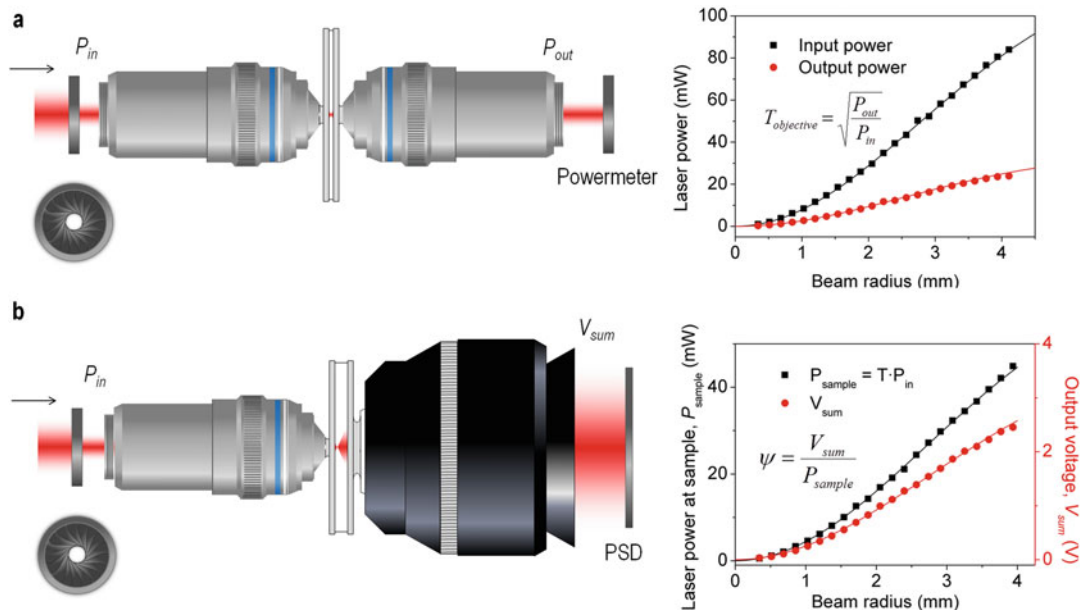


**Fig. 12** Characterization of the instrument's responsivity by a two-step process. (a) First, the transmittance of a trapping objective is obtained through the dual-objective method. A totally symmetric setup allows one to obtain the optical transmission by measuring powers at the input and output sides. (b) Once the transmission of the objective is known, the process is repeated for the detection instrument, now measuring the output of the PSD for a known power at the sample, which finally renders the parameter  $\psi$  in V/W. A nonuniform transmission as a function of the beam radius may be observed in these high-NA lenses

of the iris smaller than 1 mm, the measurements are inaccurate (due to decentering and noncircularity of the iris and PSD nonlinearities) and should not be used (observe the different slope of the curves in Fig. 12a for the smaller beam radii).

9. For more accurate measurements, refer to ref. [12].
10. The second part of the calibration provides the instrument's responsivity. Replace the upper objective with the detection lens (Fig. 12b).
11. Replace the *ad hoc* chamber built with the two thin coverslips by a regular sample chamber built according to the instructions in Subheading 3.4.
12. Set the height of the instrument according to the protocol detailed in Subheading 3.5.
13. Use the Bertrand lens again to center the instrument with the first objective.
14. Determine the power in the sample,  $P_{\text{sample}}$ , from measurements of the input power and the transmittance of the objective, and simultaneously obtain recordings of the total output voltage,  $V_{\text{sum}}$ .
15. The responsivity of the instrument is given by the ratio:  $\psi = \varphi \cdot T \equiv V_{\text{sum}}/P_{\text{sample}}$ .
16. Repeat the process for different diameters of the beam as a consistency check by changing the aperture of the iris diaphragm. The resulting curve should be smooth and similar to the one in Fig. 12b, without outliers or any other indications for inaccurate measurements (as a result of an imperfect iris centering, for example). Calculate the responsivity value that corresponds to the numerical aperture of your trapping objective.

### 3.8 Microscopic Calibration

The microscopic calibration is performed by determining the calibration factor  $\alpha_{\text{trap}} = \kappa \cdot \beta$ . With the PSD centered and the instrument adjusted in height for correct momentum measurements, trap a microsphere of known size in a medium of known viscosity (preferably water); use different sizes as detailed in Subheading 2.2.

1. Measure the room temperature with a precise thermometer.
2. Set the laser power at the sample to 50 mW. Remember that low laser powers decrease the cut-off frequency of the power spectrum, shifting the relevant information to a region where low-frequency noise will increasingly affect the measurement, which results in errors in the calibrated  $\kappa \cdot \beta$ .
3. Set the sampling frequency to the maximum attainable value (see Note 18).

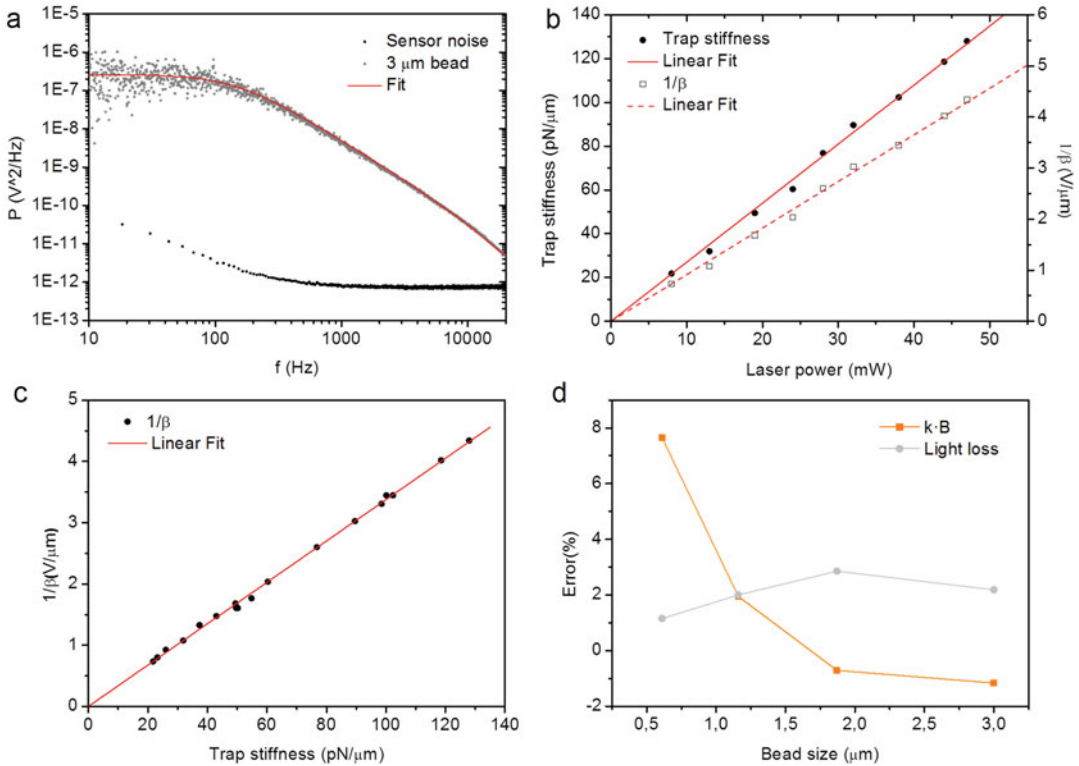


**Fig. 13** (a) Power spectrum of a  $3\text{-}\mu\text{m}$  microsphere and fit to a Lorentzian function. The data allows us to extract the parameters  $\kappa$  and  $\beta$ , which are necessary for the microscopic calibration. The plot also shows the dark noise of our instrument. (b) Both  $\kappa$  and  $1/\beta$  should be proportional to the laser power. (c) The two microscopic calibration constants are not independent from each other in a light momentum change instrument (since  $\alpha_{\text{trap}} = \kappa \cdot \beta$ ); plotting  $1/\beta$  vs.  $\kappa$  should produce a straight line. Here, microspheres of four different diameters at different laser powers have been used to calibrate the traps. (d) Residual light losses (for example through back scattering) and other effects produce errors of up to 10 % that correlate with bead size. However, the amount of light captured is not a good indicator of measurement precision

4. Record a trace of typically  $10^6$  data points [32]. If the detector bandwidth is low, it may be preferable not to record long time series to avoid recording of low-frequency drift.
5. Obtain the power spectrum of the signal and fit the data to a (corrected) Lorentzian (see Note 19 and Fig. 13a).
6. Use the corner frequency,  $f_c$ , and the fitted diffusion constant,  $D^V$ , to determine the product  $\kappa \cdot \beta$  (see Note 20).
7. Repeat the process for several beads to cancel out the error associated with the polydispersity of its size.

### 3.9 Evaluation of Instrument Design and Calibration

The agreement of the two force calibrations,  $\alpha_{\text{trap}} = \alpha_{\text{sensor}} \equiv \alpha$ , is a strong indication that the instrument is correctly placed and that there are no reflections or other alterations of the light patterns. The system is set and forces should then be correctly measured for

any bead size. However, even in this case, the force response of the instrument calibrated *in situ*,  $\alpha_{\text{trap}}$ , may differ from  $\alpha_{\text{sensor}}$  by up to 10 % due to internal light losses and other effects that we have not covered here (*see Fig. 13* and **Notes 21–23**). To optimize the capture and detection of the laser beam and thus improve the ultimate accuracy of the system, some cumbersome additional procedures are required. With this, the error can be lowered to 5 % for a wider range of experimental conditions (**Note 24**).

In the case of large discrepancies between calibrations, the setup should be reexamined in search of artifacts causing these errors (*see Note 25*). Then, both  $\alpha_{\text{trap}}$  and  $\alpha_{\text{sensor}}$  should be recalibrated and compared again. This recursive procedure should be continued until the two values agree, within the accepted tolerance. As discussed in **Note 26**, this is the only available indicator of correct instrument design, construction and calibration; indicators such as the total recorded power may be misleading and should therefore be considered only as additional sources of information (*see Note 21*). In any case, instrument calibration through a single route, particularly the power-spectrum method, may be an attractive option because of its simplicity and familiarity, but should not be used as the only source of calibration in order to minimize potential errors in the final experiments. In our experience, benchmarking the microscopic and macroscopic calibrations with each other constitutes the only reliable strategy for true force results.

### **3.10 Measurement of Forces and Positions**

1. Turn on the laser power supply and let it warm up for 30 min.
2. Meanwhile, prepare a sealed slide chamber with the sample inside, as described in Subheading **3.4**.
3. Mount the chamber on the microscope and put both the objective and the assembled and calibrated detection arm in contact with it through the corresponding immersion medium (oil, Cargille Type B, for the detection lens). Set the correct height of the detection instrument (as described in Subheading **3.5**) and center it on the axis with the Bertrand lens.
4. Turn on the PSD power supply.
5. Remove the voltage offsets as described in Subheading **3.1**.
6. Turn on the laser and set the laser power at 100 mW in the sample chamber (a large power will minimize Brownian motion). For this, use the total output voltage of the PSD divided by the calibrated responsivity of the instrument,  $V_{\text{sum}}/\psi$ . Remember that the laser power should never exceed the maximum voltage of the PSD defined in Subheading **3.6**. If necessary, add extra ND filters (AR coated if placed close to the PSD) and compensate the force calibration accordingly (i.e.,  $\alpha/T_{\text{ND}}$ ).
7. Trap a bead.

8. Center the light pattern on the PSD according to the indications given in Subheading 3.1.
9. Reset the laser power and the sampling frequency to the desired value.
10. Start measuring the force using the force calibration parameter  $\alpha$  to convert the output voltages  $V_x$  and  $V_y$  into pN. Figure 14a

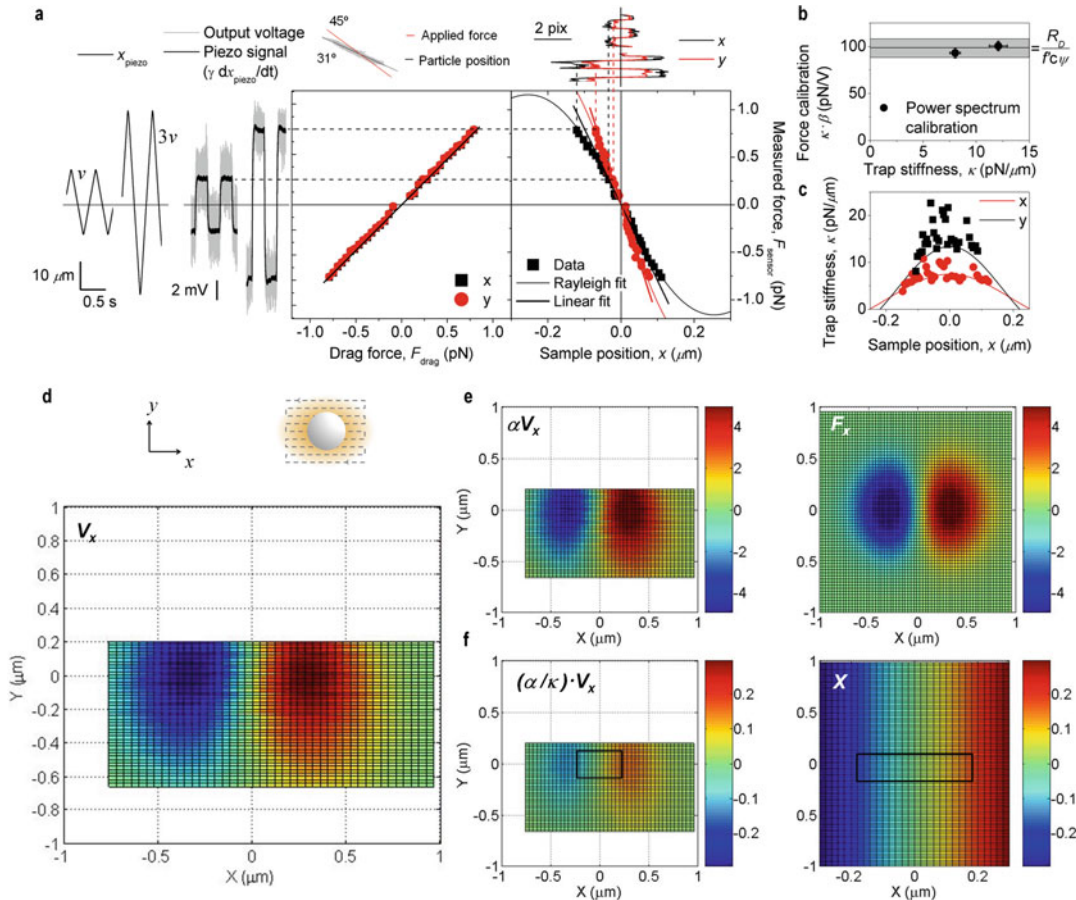


**Fig. 14** (a) A piezoelectric stage was used to apply small forces on a trapped microsphere ( $d = 0.49 \mu\text{m}$ ,  $P = 9 \text{ mW}$ ). The flow of buffer generated around the trapped particle was used to exert hydrodynamic forces, given by Stokes' law,  $F_{\text{drag}} = 3\pi d\eta v$ , with controlled magnitude and direction. Using this method, we explored the measurement of forces outside the linear regions of the trapping and detection signals. The particles were oscillated at  $45^\circ$  to simultaneously produce equal forces along the two principal directions of the trap with different stiffness (the trapping laser was linearly polarized). The flow velocity was increased up to the escape force,  $F_{\text{esc}}$ , while both the momentum change and the position of the sample were measured. The particle displacement was obtained with a video camera. We observe that the force is correctly measured in both channels simultaneously with a single calibration factor  $\alpha$ , even though the stiffness differs for the two directions. The two PSD signals are always proportional to the Stokes force and are thus of equal magnitude

shows a measurement example of the hydrodynamic force applied to a trapped microsphere using a piezoelectric stage to generate fluid flows with controlled velocities.

If the optical tweezers setup also allows extraction of the trap stiffness, the following steps can be performed to measure positions (*see Note 27*):

11. Set the laser power at the value used to track the sample displacements.
12. Calibrate the trap stiffness as described in Subheading 3.8. Since  $\beta = \alpha/\kappa$ , the measured power spectrum is now given by  $S_{xx}(f) = 4\gamma k_B T \kappa^2 / [\alpha^2 (4\pi^2 \gamma^2 f^2 + \kappa^2)]$ , where the two free parameters are the stiffness and the drag coefficient. This means that when momentum measurements are used to determine forces, positions can also be determined without prior knowledge of either the particle size or the medium viscosity.
13. Measure the  $x$  and  $y$  positions of the particle as the products of the factor  $\alpha/\kappa$  and the output voltages  $V_x$  and  $V_y$  (*see Fig. 14f* for an example).



**Fig. 14** (continued) (oscillation at 45°). On the other hand, the motion of the particle occurs with an angle of 31° due to the two different stiffnesses, indicating that the system does not intrinsically measure displacements (which would have components of unequal magnitude). When the same PSD signals are plotted against the displacement of the sample, the two curves corresponding to the two different stiffnesses appear. A fit to Rayleigh force expressions represents the experimental data well (as a result of the small bead used) (b) The product of the trap stiffness and the position sensitivity barely changes for the two components and equals the macroscopic calibration, whereas the associated stiffness varies by more than 50 %. The trap stiffness obtained from the slope of the F-x curve at zero displacement (*thick solid line*) was found to match the calibration from the power-spectrum analysis. Furthermore, the particle moves away from the harmonic region and enters a domain where the stiffness changes in a continuous fashion. (c) The slope of the curve changes from point to point so that the calibration is only valid at the vicinity of each position. The stiffness was computed from the standard deviation of the position at each force plateau,  $\kappa = k_B T / \langle x^2 \rangle$ . (d) PSD signal in the  $x$  channel,  $V_x$ , when the particle was scanned in the  $x-y$  plane with the piezo stage through a stationary trap. (e) When  $V_x$  is multiplied by the calibration constant  $\alpha$ , the result is a good match for the force map computed using Rayleigh expressions for the whole range of values, similar to panel (a) but in two dimensions. The Rayleigh force map for a Gaussian beam at the experimental laser power,  $F_x$ , was computed for  $w_0 \approx 0.5 \mu\text{m}$ , which is comparable to the beam waist obtained for our water-immersion objective using a microscopic version of the knife-edge scanning method ( $w_0 \approx 0.6 \mu\text{m}$ ). (f) In contrast to the relation to force, PSD signals are more difficult to relate to particle displacements. When multiplied by the positional calibration factor  $\beta$ , the result is only single valued and close to the theoretical values within a small region around the trap center (*rectangle*). Furthermore, the value of  $\beta \cdot V_x$  is not independent of the value of the  $y$ -coordinate [35, 41] (*see Note 28*)

---

## 4 Notes

1. The method naturally provides measurements of transverse forces. Thus, experiments are, in principle, limited to a plane perpendicular to the optical axis. There exists the possibility of extending the detection to the full volume by introducing a second detector [35]. Nevertheless, most optical trapping experiments are usually performed in 2D, or even in 1D, so the setup described here should cover most of the interesting configurations. Even in the more complex and uncontrolled environment of cells, the problems under study can often be considered to be confined to a plane; for example, transport of organelles or vesicles in axons of cultured neurons or in highly spread, flat cells occurs typically in 2D.
2. The aplanatic condition ensures that light propagating with an angle  $\theta$  at the sample (i.e., with the transverse component of the momentum  $p_x = (h/\lambda) \cdot \sin\theta$ ), ends up at a position in the BFP of the collecting lens that is proportional to  $p_x$ , regardless of the value of the angle  $\theta$ . This guarantees that the beam at the BFP is separated in its fundamental momenta, in such a way that a twofold increase, for example, in the transverse component of the beam momentum is reflected as a change by a factor of two in the position of the light pattern at the BFP. This means that only if every ray from the beam hits the BFP at a position proportional to the momentum with the same conversion constant will the change in the light pattern correspond to the deflection of the beam caused by the transfer of momentum:  $\langle x' \rangle = \langle f' n \cdot \sin\theta \rangle = f' n \langle \sin\theta \rangle = (f' n \lambda / h) \langle p_x \rangle$ . Aplanatic lenses are designed to fulfill the Abbe sine condition across the whole BFP. This means that rays propagating parallel to the optical axis at a distance  $f' n \cdot \sin\theta$  are focused with an angle  $\theta$  at the focal plane, or, in the opposite direction, all rays with a propagation angle  $\theta$  at the sample plane are focused at the same position  $f' n \cdot \sin\theta$  at the BFP ( $f'$  and  $n$  being the focal length of the lens and the refractive index of the immersion liquid respectively). In other words, the Abbe sine condition allows the natural extension of the optical Fourier transform to large angles. This condition seems difficult to fulfill with oil-immersion lenses, because spherical aberrations rapidly degrade their imaging performance. This problem has been widely studied due to its impact in the trapping efficiency of optical tweezers for distances of some tens of microns [33]. The problem can be eliminated with the use of water-immersion objectives. However, we face a similar problem in the opposite direction, when the lens is used for detection. The design of aplanatic lenses, in principle, fulfills the Abbe sine condition only in a specific plane, placed at the working distance of the lens; any

displacement of the trap to another plane introduces deviations from the Abbe condition. However, the use of long focal length lenses (the front lens group of immersion condensers) can overcome this limitation to some extent. A lens with a typical focal length of 10 mm and NA = 1.4 experiences a maximum deviation from the Abbe sine condition of 2 % for displacements of the trap by 70  $\mu\text{m}$ . In contrast, the use of oil-immersion objectives with short focal length lenses can lead to a severe deterioration of the optical properties even for axial displacements of the trap by 20–30  $\mu\text{m}$ , so they should not be used for this purpose. On the other hand, water-immersion objectives, less affected by losses of the Abbe sine condition at large distances, should also be avoided for detection since they can only capture a small fraction of the scattered beam (discussed in **Note 3**).

3. The capture of the entire  $4\pi$  solid angle of scattered light for the correct measurement of the momentum transfer is the most challenging step in this method. Furthermore, the beam has to be analyzed without introducing relative changes in the intensity pattern of scattered light. Global attenuations of the beam will have no effect on the precision of our measurements, since they will only change the calibration. What must be maintained intact are the relative intensities of the scattering pattern. As discussed in **Note 26**, the backscattered light typically represents a small fraction of the beam and has a moderate impact on the force error. This means that our efforts should be focused only on the  $2\pi$  solid angle of light re-scattered in the forward direction, i.e., on the light propagating up to  $90^\circ$  with respect to the normal (i.e., parallel to the glass surface of the microchamber). The condition for ensuring proper collection of all this light is that the acceptance angle of the detection lens must be larger than the angle of refraction of the ray in the glass. This can be synthesized in the equation:  $\text{NA}_{\text{lens}} > n_{\text{medium}}$ . The worst-case scenario corresponds to rays propagating in the suspension medium (typically water) almost parallel to the glass surface of the microchamber ( $\theta \approx \pi/2$ ). When they enter the glass, the direction of propagation changes to  $\theta' = \arcsin(n_{\text{medium}}/n_{\text{glass}})$ . If the acceptance angle of the lens is given by  $\theta_{\text{lens}} = \arcsin(\text{NA}_{\text{lens}}/n_{\text{glass}})$ , then the aforementioned condition guarantees that  $\theta_{\text{lens}} > \theta'$ . As a rule of thumb, the front lens group of oil-immersion condensers with NA = 1.4 are a good choice for the detection lens. The main microscope manufacturers sell these lenses as parts, so there is no need to buy the entire condenser. When using these long-working-distance lenses, high viscosity oil is needed to keep the entire front lens immersed in the fluid. However, viscous oil tends to incorporate air bubbles that modify the optical properties of the

interface. Cargille Type B is a good compromise solution for this issue.

4. As discussed above, the construction of a system based on the momentum method does not differ much from that of a BFPI instrument. The central idea is that the detection lens must be used for both illumination of the sample and capture of the trapping beam. To do so, we use a dichroic mirror (or equivalent) to separate the two light sources. The dichroic mirror reflects the laser wavelength away from the optical axis of the microscope and allows the illumination light to pass through. The other important element is the relay lens system, which projects the BFP of the detection lens onto the PSD. To choose the correct lens (*see also Note 5*), consider the lateral magnification,  $\beta$ , and the total length of the optical path of the detection system, D. These two magnitudes are connected; if the lateral magnification is small, the total optical path length increases. If one wants a small D while keeping  $\beta$  fixed, the relay lens will have to be more powerful, i.e., with a shorter focal length. Short focal length lenses are more prone to aberrations (and critical deviations from the Abbe condition), if not carefully designed. The magnification should be chosen so that the light pattern fits into 80–90 % of the active area of the detector (since outside this region most PSDs become noticeably nonlinear with position),  $\beta = 0.85r_{\text{PSD}}/r_{\text{BFP}}$ , and the total length should be measured (or simply estimated). The chosen magnification should also permit the camera to capture a complete image of the BFP. Quite often, the size of the camera's sensor chip is the most limiting parameter. Then, the distance between the lens and the PSD,  $s'$ , is given by  $D \cdot \beta/(\beta + 1)$ , the distance between the lens and the BFP is  $-D/(\beta + 1)$  ( $s < 0$ ) and the focal length is  $D \cdot \beta/(\beta + 1)^2$ . The final choice should be the focal length closest to the obtained value such that the lens can be mounted after the dichroic mirror. The distances s and  $s'$  should be recalculated. *See Note 5* for further information on the positioning of the relay lens along the optical path.
5. As explained in Subheading 3.3, the calibration of the BFP of the detection lens plays a fundamental role in this method. It imposes a stringent condition on the quality of the relay lens. Any kind of distortion introduced in the light pattern due to spherical aberration of the relay lens will lead to errors in the focal length of the system, the correct axial position of the detection lens (and, therefore, in the amount of captured light), and ultimately in the measurements of force. A good solution for the relay lens system is the use of a pair of achromatic doublets (with focal lengths  $f'_1$  and  $f'_2$ ) working at infinite conjugate ratios, for which these lenses are optimized

(see Fig. 9c), with their focal lengths such that  $D_{\text{pattern}} \cdot f'_2/f'_1$  is smaller than the active area of the PSD. The diameter of the lenses is another important question. To avoid vignetting of the laser, the diameter of the lenses should be larger than the size of the light pattern at the BFP of the collecting lens. For long-focal-length detection lenses of high NA (immersion condensers), this can sometimes be an added difficulty as they have large diameters. A solution is to defocus the detection lens in such a way that the light beam is no longer collimated, but slightly converging. As the lens is not working at its design specifications in this situation, it may deviate from the sine condition. A controlled spherical aberration introduced by the relay lens can restore the aplanaticity of the compound system.

6. Bandpass filters based on destructive interferences should be avoided, since transmittance may then change greatly with the incident angle, modifying the relative distribution of light.
7. The ND filter should be selected to maximize the output signal of the PSD. In addition, the filter should be antireflection-coated for the trapping wavelength, as the surface of the PSD retroreflects as much as 20–25 % of the light incident on its surface. If the ND filter is placed close to the PSD, part of that light may again be redirected back into the detector, producing spurious signals.
8. One of the differences with regard to BFPI is that here the trapping and the detection lasers are always the same. An advantage is the inherent alignment of the detection, which simplifies the task of building and centering the system. On the other hand, it does not allow uncoupling of the two processes so no fine tuning of the detection laser properties and the positional sensitivity [36] can be achieved.
9. The PSD is, along with the detection lens, the central element of the method. This photodetector ultimately measures the deviation of the light pattern at the BFP, which is directly proportional to the momentum transfer between the laser beam and the sample. This is achieved through the operation performed by this type of silicon detector. PSDs are designed so that the photocurrents generated in the depletion region of the PN junction increase with the distance from the electrodes placed on the edges of the active area (typically of  $10 \times 10$  mm). This means that the output voltage is always linear with the position of a laser spot on the detector, and the conversion from volts to mm is the same regardless of its size or shape. By contrast, the more common QPDs provide a signal linear with the position of the light spot only for small displacements and which changes whenever the characteristics of this distribution are modified. These segmented photodiodes are

not truly position detectors for large displacements, but rather “centering” or “nulling” devices. Their main advantages are that the sensitivity can be tuned by changing the diameter of the laser spot and that the response time is faster since the rise time is dominated by the RC circuit, with the load resistance being typically lower than the interelectrode resistance of PSDs. However, the latter advantage is only for short wavelengths. As shown in previous studies [37, 38], PSDs turn out to be faster at the infrared region of the spectrum. This is due to their different design. PSDs are typically built with a thick depletion layer (typically some hundreds of  $\mu\text{m}$ ), which is where electrons and holes are accelerated to produce the photocurrent; QPDs, by contrast, exhibit a narrow depletion layer (typically  $\sim 10\text{s }\mu\text{m}$ , *see* ref. [39]). At IR wavelengths, most of the electron–hole pairs are created outside this region, where charges can only move due to diffusion, a much slower process. As a result, the response of the photodetector decreases dramatically from MHz to some kHz. The effect is less severe in PSDs, as the distance traveled by diffusive charges from the N-layer to the depletion region is shorter. A possible solution for QPDs is the use of other materials, such as InGaAs.

10. Duo-lateral PSDs are the most typical kind of position detector. They use two different resistive layers to obtain the 2D positional information. Typically, the four photocurrents generated by the device are converted into voltages by transimpedance amplifiers and processed by sum and difference circuits in order to provide four different signals:  $V_x$ ,  $V_y$ ,  $V_{\text{sum } x}$ , and  $V_{\text{sum } y}$ . The two sum voltages are equal,  $V_{\text{sum } x} = -V_{\text{sum } y}$ , and correspond to the total intensity measured through either electrons or holes currents. A cheaper option, although at the expense of a lower linearity, are tetra-lateral PSDs, which use a single layer to produce the signals. In this case, only three outputs are given,  $V_x$ ,  $V_y$ ,  $V_{\text{sum}}$ . PSDs can be purchased as modules that already incorporate amplifiers and processing circuits (Fig. 9e).
11. An alternative detector is a video camera [40]. In this case, the centroid of the light distribution is computed numerically. The advantage is that this approach is extensible to any other operation, which may be convenient in certain situations. Furthermore, the calibration of the light patterns and the focal length is performed with the same instrument as the one used for the measurement. However, its higher cost and weight, its reduced bandwidth, and the handling of the large volume of generated data are factors that one should consider before using it.
12. An  $x$ – $y$  translation stage may help in centering the laser beam on the PSD. This avoids sending part of the light pattern outside the active area when their size is similar and also

allows elimination of the offsets from the force before an experiment.

13. The reverse bias applied to the PN junction of a PSD is an important parameter, as it determines power and spatial linearity, and rise time. The upper limit of the linear range of the response to power strongly depends on the reverse voltage, as in any other photodiode. On the other hand, reverse voltage also increases the saturation photocurrent, making the PSD more linear in position at high incident powers. Finally, a large reverse voltage also decreases the rise time of the device, increasing the bandwidth. The price to pay is a higher dark current and increased noise.
14. Calibration of the radius of the PSD is not strictly necessary and can be skipped. Typically, the nominal size given by the manufacturer is enough for the force calibration of the instrument. At 1064 nm, however, we have found discrepancies of up to 9 % between seemingly identical detectors, and differences of 5 % between the  $x$  and  $y$  directions have been observed for nominally square detectors.
15. The positional output voltage of PSDs is given by  $V_x/V_x^{\text{sum}} = x/R_D$  within typically,  $>90$  % of their active area. Here,  $x$ , is the position of the light spot on the sensor and  $R_D$  is the detector radius (half width) for circular (square) PSDs. This normalized position varies between  $-1$  and  $1$ .
16. The camera should be larger than the diameter of the intensity distribution,  $2 \cdot f'_{\text{sensor}} \cdot n_{\text{medium}}$ . If a water-immersion objective is used, lift the trap up until the particle reaches the top surface of the microchamber and push it against the glass. This will modify the relative intensities of the pattern, making it possible to observe the second outer disk.
17. Many optical elements can respond to the polarization of the laser beam along the optical train of the instrument and change its intensity. The determination of the instrument's responsivity,  $\psi$ , takes all these effects into account. However, if the user changes the polarization of the trapping laser, the calibration of  $\psi$  must be repeated.
18. Although tempting, the use of fast photodetectors (with MHz bandwidths) may not be the best option for many biological experiments. Typical conformational changes of molecules take place at timescales much slower than frequencies that can be reached for current photodiodes. At these speeds, recordings of seconds or minutes translate into huge amounts of data that are difficult to process and handle. In these cases, detectors running at tens of kHz may be enough to obtain meaningful information. However, high-speed photodiodes may be useful for power-spectrum calibration of the trap. In this case, thermal

noise is, by contrast, the desired information so the use of large bandwidths provides more reliable results. A typical sampling frequency of 50 kHz allows the use of high corner frequencies (avoiding contamination from low-frequency drift). Aliasing and the parasitic low-pass filtering from the PSD, which affect the power spectrum at high frequencies, can be modeled and thus accounted for in the fitting procedure to obtain the calibration constants (*see Note 9* and ref. [41]).

19. The MATLAB software [41] includes several effects to obtain a precise calibration of the trap stiffness and the position sensitivity.
20. The one-sided power spectrum is obtained as  $S_{xx}(f) = D / [\pi^2(f^2 + f_c^2)]$ , where  $D = k_B T / \gamma$  is the diffusion constant,  $k_B$  the Boltzmann constant,  $T$  the sample temperature, and  $\gamma = 3\pi\eta(T)d_{\text{bead}}$  the drag coefficient, obtained from the dynamic viscosity of the medium,  $\eta$ , and the particle size,  $d_{\text{bead}}$ . The instrument provides voltages, so the computed power spectrum contains a factor  $1/\beta^2$ . The product of  $\kappa = 2\pi\gamma f_c$  and  $\beta = \sqrt{D/D^V}$  is determined from the corner frequency,  $f_c$ , and the fitted diffusion constant,  $D^V$ . To correctly measure the force calibration in situ, the key parameter, besides the size of the microsphere, is the sample temperature, which is the sum of the lab temperature and temperature increase due to the laser heating. The latter may change between particles of different sizes and should be derived in each case. Given its complexity, an alternative solution is to obtain the power spectrum at relatively low laser powers, always taking into account that low frequency noise tends to favor the introduction of errors in the force calibration. A good choice may be the use of 1  $\mu\text{m}$  microsphere at 20 mW ( $f_c \approx 700\text{--}800$  Hz). The error of the stiffness due to heating under these conditions should be less than 1 %.
21. Unfortunately, there is, in principle, no indicator to quantify these errors. As suggested in refs. [21, 22], for most typical samples in optical trapping, backscattering represents a small fraction of the light. Latex or glass microspheres of different sizes generally exhibit a faint scattering in the opposite direction of the incident laser (1–3 %), so that one may be tempted to conclude that, with this method, the error in the force is always small as long as the backscattering is kept low. Furthermore, the analysis of the results shows a typical standard deviation of the data of ~5 % (*see* ref. [21, 22]), which is similar to the light loss. However, if we take a closer look at the discrepancies between measured and theoretical forces for particles with different properties, we observe that errors for individual samples can be much larger than the lost intensity (*see* Fig. 13).

The reason is that the two magnitudes, the direction of the ray and the associated irradiance, are, in fact, uncoupled, so that just “a few” photons can produce significant errors in the global momentum. For general particles (e.g., non-spherical), it may be difficult to anticipate the effect of the uncertainties introduced in the measurements.

22. The additional decrease in captured light by the reduction of the acceptance solid angle of the detection system, for example, which could happen in BFPI, would ultimately lead to the loss of a single force calibration factor. Then, the *in situ* determination of  $\kappa$  and  $\beta$ , using, for instance, the power-spectrum method, would be the only possibility left.
23. However, with the instructions and hints given here for the design and calibration of the instrument, the capture of the forward-scattered beam in full is guaranteed. Also, the results may not differ by more than 10 % from the theoretical values for a wide range of conditions, including microspheres of silica or polystyrene and biological objects, of sizes between some hundreds of nanometers to some microns, trapped with both water- and oil-immersion objectives, with laser powers up to some hundreds of mW. While large for certain experiments, in which *in situ* calibration provides higher accuracy, these errors can be low enough for most of the main applications of this method, i.e., in those situations where trap stiffness calibration cannot be ensured or has large associated errors, as in cells or with complex samples [6]. Moreover, these errors represent an upper bound.
24. For higher accuracy, additional effects must be taken into account. This is beyond the scope of this chapter, but we mention it here for the sake of completeness. A first question that one must address in order to improve the robustness of the force calibration is the nonuniform transmittance of the detection lens. At high numerical apertures, the Fresnel reflection factors of the internal surfaces become markedly different for on-axis and marginal rays. The factors modulate the back-focal plane distribution (attenuating more toward the periphery of the lens), introducing an error in the computation of the momentum. A further cause of concern is that this effect depends on the angular composition of the scattering pattern and therefore on the physical properties of the sample, something to which the momentum method is supposed to be immune. Another issue is the dependence of the PSD responsivity on temperature. At infrared wavelengths the responsivity of silicon becomes notably dependent on temperature; at 1064 nm, we have measured a variation as great as 1 %/°C. As this parameter has a direct impact on the calibration through

the factor  $\psi$ , room temperature changes introduce perceptible errors in the measurements.

25. The use of two calibrations following completely different and complementary routes (one based on the microscopic description of the motion of a trapped particle in a fluid, and the other relying upon the macroscopic description of the detection instrument) allows us to detect possible artifacts on the basis of the mismatch between them. Deviations larger than 10 % can be attributed to incorrect instrument design since typical uncertainties in the determination of  $R_D/f'\psi c$  never exceed this value. Possible cause of these errors may be: (1) Incorrect position of the elements along the optical path that modify the effective focal length of the instrument; (2) Vignetting of the beam that changes the momentum structure of the light pattern at the BFP of the detection lens; (3) Presence of significant reflections that change the amount of light reaching the PSD; 4. Incorrect computation of some of the parameters required for force calibrations (sample temperature, bead size, responsivity, etc.)
26. In this method, the main source of error comes from laser light scattered by the trapped bead, which, as its momentum is transferred to the trapped object, is not recorded by the detector; therefore, its contribution to the net force is overlooked, leading to an underestimation/overestimation of the momentum change. Among the main causes of these light losses (*see Note 25*), the capture of the forward-scattered photons alone for the detection of the beam deflection is the most evident problem, but it is inherent to this detection configuration. This problem can only be solved by the use of a second PSD placed at the BFP of the trapping objective, which would then be simultaneously used for detection of the backscattering [20]. Therefore, even when all the other effects are controlled, the dispose of the lower  $2\pi$  solid angle of the beam should be analyzed to delimit its impact on the final force error.
27. As noted in the introduction, the momentum method derives the force from general electromagnetic principles and Newton's laws, and does not rely on a linear relation with the particle's displacement. Thus, the method can be applied advantageously when this relation does not exist or cannot be easily established experimentally. This does not mean that the sample position is merely an auxiliary magnitude in BFPI; quite often, the positional information is as important as the force itself. A momentum-based instrument can provide positional information if the stiffness of the optical trap is known (the displacements in the linear region of the trap can be obtained from the force data by diving the force data by the trap stiffness). The advantage with respect to BFPI is the additional information represented by the equation  $\alpha = \kappa \cdot \beta$ , which avoids

the necessity of knowing the sample size or the buffer viscosity (*see also* Subheading 3.10). The disadvantage is that the positional sensitivity factor  $\beta$  is fully determined by the need to image the full BFP on the PSD and cannot be changed.

28. The experiment in Fig. 14 summarizes the main barriers overcome by the method: (1) Measurements were correct up to the escape force of the trap, clearly beyond the linear region of the force; (2) The stage was oscillated at 45° moving outside the region where the position response of the instrument is linear [34]; (3) Forces were correctly measured regardless of the trap stiffness. The laser beam was linearly polarized, so that the trap had different spring constants along  $x$  and  $y$  but the total force, computed as a sum of the two components, was still correct; and (4) Force readings were correct in a region where no trap stiffness was even defined since the slope of the force curve was continuously changing.

---

## Acknowledgements

We would like to thank Frederic Català and Estela Martín-Badosa for fruitful discussions. This work was funded by the Spanish Ministry of Education and Science, under grants FIS2007-65880 and FIS2010-16104. A. Farré and F. Marsà are the recipients of research grants from the INNCORPORA program from the Ministerio de Economía y Competitividad (Spain).

## References

1. Verdeny I, Farré A, Mas J et al (2011) Optical trapping: a review of essential concepts. *Opt Pura Apl* 44:527–551
2. Block SM, Blair DF, Berg HC (1989) Compliance of bacterial flagella measured with optical tweezers. *Nature* 338:514–518
3. Ashkin A, Schuetze K, Dziedzic JM et al (1990) Force generation of organelle transport measured *in vivo* by an infrared laser trap. *Nature* 348:346–348
4. Visscher K, Gross SP, Block SM (1996) Construction of multiple-beam optical traps with nanometer-resolution position sensing. *IEEE J Sel Top Quantum Electron* 2:1066–1076
5. Gittes F, Schmidt CF (1998) Interference model for back-focal-plane displacement detection in optical tweezers. *Opt Lett* 23:7–9
6. Farré A, Mas J, Marsà F et al (2015) Force measurements in complex samples with optical tweezers, in optics in the life sciences, OSA Technical Digest, paper OtT1D.1
7. Ashkin A (1992) Forces of a single-beam gradient laser trap on a dielectric sphere in the ray optics regime. *Biophys J* 61:569–582
8. Harada Y, Asakura T (1996) Radiation forces on a dielectric sphere in the Rayleigh scattering regime. *Opt Commun* 124:529–541
9. Bui AAM, Stilgoe AB, Khatibzadeh N et al (2015) Escape forces and trajectories in optical tweezers and their effect on calibration. *Opt Express* 23:24317–24330
10. Liang H, Vu KT, Krishnan P et al (1996) Wavelength dependence of cell cloning efficiency after optical trapping. *Biophys J* 70:1529–1533
11. Neuman KC, Chadd EH, Liou GF, Bergman K et al (1999) Characterization of photodamage to *Escherichia coli* in optical traps. *Biophys J* 77:2856–2863
12. Kuo SC, Sheetz MP (1993) Force of single kinesin molecules measured with optical tweezers. *Science* 260:232–234

13. Finer JT, Simmons RM, Spudich JA (1994) Single myosin molecule mechanics: piconewton forces and nanometre steps. *Nature* 368:113–119
14. Svoboda K, Block SM (1994) Force and velocity measured for single kinesin molecules. *Cell* 77:773–784
15. Richardson AC, Reihani SNS, Oddershede LB (2008) Non-harmonic potential of a single beam optical trap. *Opt Express* 16:15709–15717
16. Greenleaf WJ, Woodside MT, Abbondanzieri EA et al (2005) Passive all-optical force clamp for high-resolution laser trapping. *Phys Rev Lett* 95:208102
17. Jahnel M, Behrndt M, Jannasch A et al (2011) Measuring the complete force field of an optical trap. *Opt Lett* 36:1260–1262
18. Nieminen TA, Loke VLY, Stilgoe AB et al (2007) Optical tweezers computational toolbox. *J Opt A-Pure Appl Opt* 9:S196–S203
19. Stilgoe AB, Nieminen TA, Knöner G et al (2008) The effect of Mie resonances on trapping in optical tweezers. *Opt Express* 19:15039–15051
20. Smith SB, Cui Y, Bustamante C (2003) Optical-trap force transducer that operates by direct measurement of light momentum. *Methods Enzymol* 361:134–162
21. Farré A, Montes-Usategui M (2010) A force detection technique for single-beam optical traps based on direct measurement of light momentum changes. *Opt Express* 18:11955–11968
22. Farré A, Marsà F, Montes-Usategui M (2012) Optimized back-focal-plane interferometry directly measures forces of optically trapped particles. *Opt Express* 20:12270–12291
23. Mas J, Farré A, López-Quesada C et al (2011) Measuring stall forces in vivo with optical tweezers through light momentum changes. *Proc SPIE* 8097:809726
24. Jun Y, Tripathy SK, Narayanareddy BRJ et al (2014) Calibration of optical tweezers for in vivo force measurements: how do different approaches compare? *Biophys J* 107:1474–1484
25. Taylor MA, Waleed M, Stilgoe AB et al (2015) Enhanced optical trapping via structured scattering. *Nat Photon* 9:669–673
26. Ma X, Jannasch A, Albrecht U et al (2015) Enzyme-powered hollow mesoporous janus nanomotors. *Nano Lett* 15:7043–7050
27. Callegari A, Mijalkov M, Gököz AB et al (2015) Computational tollbox for optical tweezers in geometrical optics. *J Opt Soc Am B* B11–B19
28. Català F, Marsà F, Farré A et al (2014) Momentum measurements with holographic optical tweezers for exploring force detection capabilities on irregular samples. *Proc SPIE* 9164:91640A
29. Lee WM, Reece PJ, Marchington RF et al (2007) Construction and calibration of an optical trap on a fluorescence optical microscope. *Nat Protocols* 2:3226–3238
30. Nicholas MP, Rao L, Gennerich A (2014) An improved optical tweezers assay for measuring the force generation of single kinesin molecules. *Methods Mol Biol* 1136:171–246
31. Viana NB, Rocha MS, Mesquita ON et al (2006) Characterization of objective transmittance for optical tweezers. *Appl Opt* 45:4263–4269
32. Berg-Sørensen K, Flyvbjerg H (2004) Power spectrum analysis for optical tweezers. *Rev Sci Instrum* 75:594–612
33. Lang MJ, Asbury CL, Shaevitz JW et al (2002) An automated two-dimensional optical force clamp for single molecule studies. *Biophys J* 83:491–501
34. Pralle A, Prummer M, Florin E et al (1999) Three-dimensional high-resolution particle tracking for optical tweezers by forward scattered light. *Microsc Res Tech* 44:378–386
35. Bustamante C, Smith SB (2006) Light-force sensor and method for measuring axial optical-trap forces from changes in light momentum along an optic axis US Patent 7133132 B2
36. Ke PC, Gu M (1998) Characterization of trapping force in the presence of spherical aberration. *J Mod Opt* 45:2159–2168
37. Neuman KC, Block SM (2004) Optical trapping. *Rev Sci Instrum* 75:2787–2809
38. Huisstede JHG, Rooijen BD, van der Werf KO et al (2006) Dependence of silicon position-detector bandwidth on wavelength, power, and bias. *Opt Lett* 31:610–612
39. Berg-Sørensen K, Oddershede L, Florin E-L et al (2003) Unintended filtering in a typical photodiode detection system for optical tweezers. *J Appl Phys* 93:3167–3176
40. Thalhammer G, Obmascher L, Ritsch-Marte M (2015) Direct measurement of axial optical forces. *Opt Express* 23:6112–6129
41. Tolić-Nørrelykke I-M, Berg-Sørensen K, Flyvbjerg H (2004) MatLab program for precision calibration of optical tweezers. *Comput Phys Comm* 159:225–240

# Chapter 4

## A Surface-Coupled Optical Trap with 1-bp Precision via Active Stabilization

Stephen R. Okoniewski, Ashley R. Carter, and Thomas T. Perkins

### Abstract

Optical traps can measure bead motions with Å-scale precision. However, using this level of precision to infer 1-bp motion of molecular motors along DNA is difficult, since a variety of noise sources degrade instrumental stability. In this chapter, we detail how to improve instrumental stability by (1) minimizing laser pointing, mode, polarization, and intensity noise using an acousto-optical-modulator mediated feedback loop and (2) minimizing sample motion relative to the optical trap using a three-axis piezo-electric-stage mediated feedback loop. These active techniques play a critical role in achieving a surface stability of 1 Å in 3D over tens of seconds and a 1-bp stability and precision in a surface-coupled optical trap over a broad bandwidth ( $\Delta f = 0.03\text{--}2$  Hz) at low force (6 pN). These active stabilization techniques can also aid other biophysical assays that would benefit from improved laser stability and/or Å-scale sample stability, such as atomic force microscopy and super-resolution imaging.

**Key words** Optical trap, Optical tweezers, Single molecule, Active stabilization, Force spectroscopy

---

### 1 Introduction

Optical traps can apply controlled forces to individual biomolecular complexes and measure motions of molecular motors along their substrates with exquisite precision. As a result, advances in the precision and stability of optical traps have yielded many landmark results in single-molecule biophysics, including resolving the steps of kinesin [1], myosin [2], RNA polymerase [3], and the ribosome [4]. A number of excellent articles review the construction and application of optical traps [5–9].

While optical traps can resolve Å-scale bead displacements in a millisecond [5, 10, 11], reaching a similar level of precision and stability in a biophysical assay is much more challenging. Consider the surface-coupled optical trap depicted in Fig. 1a. A DNA molecule is stretched between a surface and an optically trapped bead. Unwanted motion in the surface or trap position degrades the positional precision of the single-molecule assay. However, by

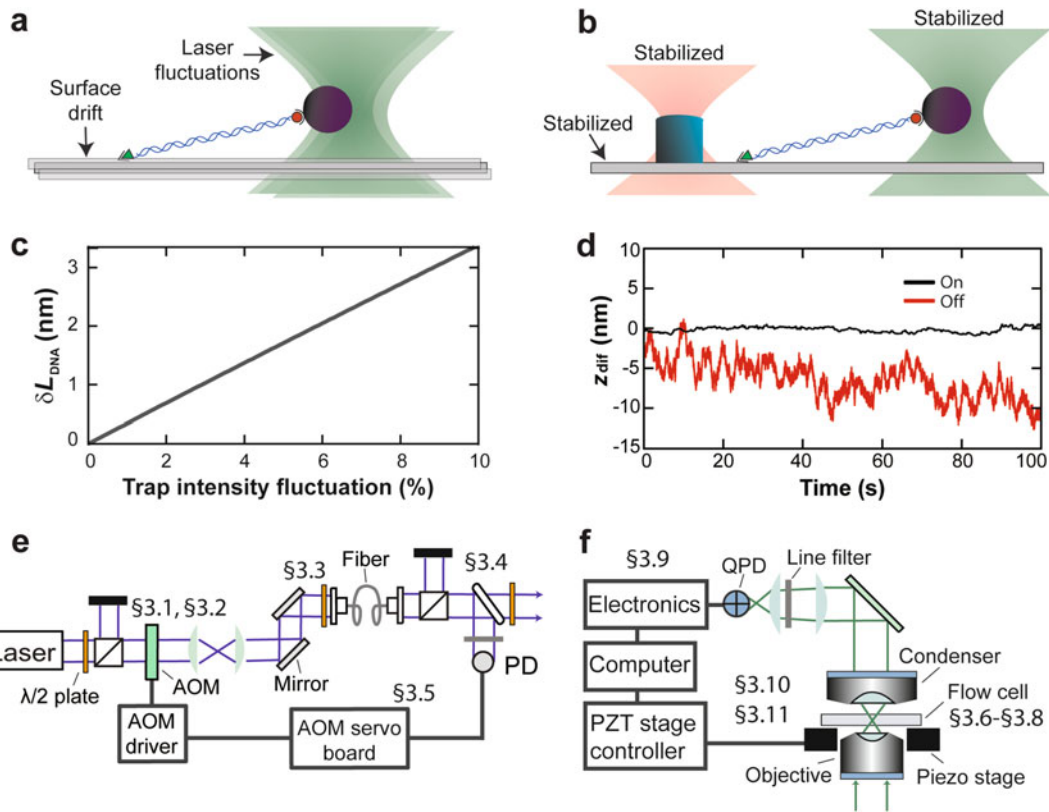


**Fig. 1** (a) Schematic of a surface-coupled optical-trapping assay used to measure motion of an enzyme along DNA. A DNA molecule is anchored to a glass coverslip at one end and to an optically trapped bead at the other. Surface drift and laser pointing fluctuations corrupt measurements of DNA length. (b) An actively stabilized surface-coupled optical-trapping assay where the sample surface is stabilized by keeping the position of a fiducial mark fixed relative to a detection laser. Each laser is stabilized with an acousto-optic modulator (AOM)-mediated feedback loop. Not shown: a third laser that is collinear with the trapping laser for independent bead detection. The assay precision arises from excellent differential-pointing stability between the three lasers' foci. (c) Intensity noise affects trapped bead position under load and thereby measurements of DNA contour length ( $L_{DNA}$ ). For a typical DNA length in a surface-coupled assay ( $L_{DNA} = 1,000$  nm) under 6 pN of load, variations in contour length ( $\delta L_{DNA}$ ) increase linearly with fluctuations in the trapping laser intensity. Intensity fluctuations of a few percent result in nm-scale apparent variations in  $L$  that can mask bp-sized motions (reprinted with permission from ref. [13]; © 2009 Elsevier). (d) The difference in the vertical position of a common object ( $z_{diff}$ ) measured by two detection lasers plotted as a function of time. In three-dimensional back-focal-plane detection [10], the vertical position signal is proportional to the total light on the detector. Hence, a measurement of  $z_{diff}$  using unstabilized lasers shows significantly more noise than a measurement where both lasers are stabilized and their sum signals are offset amplified (see Subheading 3.9). (Reprinted with permission from ref. [12]; © 2007 The Optical Society). (e) Optics diagram of the trapping laser with its stabilization feedback loop (PD: photodiode;  $\lambda/2$ : half-wave plate). Construction and tuning of this feedback loop is covered in Subheadings 3.1–3.5. (f) Schematic of a surface-stabilization feedback loop where the optical signal is electronically processed and a computer-based feedback loop moves the sample surface via a piezo-electric (PZT) stage. Construction and implementation of this feedback loop is covered in Subheadings 3.6–3.11 (QPD: quadrant photodiode)

actively stabilizing the sample surface [12] and the trapping laser (Fig. 1b) [13], one can more precisely measure the extension and tension of the DNA [14]. Ideally, this measurement is limited by the Brownian motion of the bead. Since such thermal motion has a zero mean, spatial precision is often increased at the cost of temporal resolution by time-averaging the bead motion. This strategy does not yield increased precision if instrumental noise sources—like drift in the sample surface or pointing noise in the laser—dominate the measured motion. These noise sources corrupt the measurement process. For example, variations in the stiffness of the optical trap due to laser-intensity fluctuations cause apparent changes in the DNA length (Fig. 1c). Intensity fluctuations also degrade the precision with which one can measure the vertical position of the bead, or, more relevant to this chapter, the vertical position of a fiducial mark on the sample surface with a detector beam (Fig. 1d). To obtain 1-bp (base pair) precision along DNA, the adverse effects of instrumental noise on bead-position measurements must be reduced to  $\leq 1 \text{ \AA}$  [3, 9].

These instrumental noise sources are typically reduced through a combination of passive and active stabilization techniques. Passive techniques tend to reduce noise by isolating the experiment from the noise source. For example, a floating optical table isolates the experiment from environmental vibrations, and an enclosure around the optics minimizes beam-pointing fluctuations by reducing air currents. An excellent example of passive stabilization is the dual-beam optical trap, which decouples the single-molecule assay from the surface and thereby isolates it from surface noise [15]. Active techniques use feedback; they measure the amount of noise in the system, and modulate some parameter(s) of the system in real time to reduce that noise.

In this chapter, we detail how to apply active-stabilization techniques to minimize laser noise in a surface-coupled optical-trapping instrument and to stabilize the surface relative to the optical-trapping laser (Fig. 1b) as a means to achieve 1-bp precision and stability in single-molecule assays. To minimize a variety of sources of laser noise, we first pass the laser through an acousto-optic modulator (AOM) and a single-mode, polarization-maintaining optical fiber. Coupling the laser into the fiber transforms pointing and mode noise into intensity noise. We then measure the intensity after the laser exits the fiber and use that signal to stabilize the laser intensity via the AOM (Fig. 1e). To minimize surface motion, we attach fiducial marks to the coverslip so that unwanted sample motion can be measured using a lower-powered “detector” laser. The coverslip is then mounted on a three-axis piezo-electric (PZT) stage, which can move with Å-scale precision to compensate for the unwanted surface motion (Fig. 1f). This combination of active laser and surface stabilization enables our instrument to achieve 1-bp stability ( $\Delta f = 0.03\text{--}2 \text{ Hz}$ )

at a relatively low load (6 pN), with higher precision and larger bandwidth achieved at higher forces.

In the first five sections of this chapter, we detail how to create the laser stabilization feedback loop (Fig. 2). Subheading 3.1 explains the installation of an AOM system, and Subheading 3.2 details the AOM-laser alignment needed to achieve the best performance. Subheading 3.3 discusses coupling the resulting first-order AOM-diffracted laser beam into a single-mode, polarization-maintaining optical fiber. Subheading 3.4 details sampling 10 % of the laser intensity after a subsequent fiber launch onto a photodiode for intensity stabilization, and Subheading 3.5 provides the details on building and testing an AOM servo-circuit board; these electronics transform the photodiode's intensity signal into a control signal for the AOM.

The last six sections of this chapter detail how to create the surface-stabilization feedback loop. Subheadings 3.6, 3.7, and 3.8 detail creating a sample chamber with an array of fiducial marks fabricated onto the interior of a coverslip. Subheading 3.9 provides the schematic for building an offset-amplifier, so that the vertical position of a fiducial mark can be more precisely detected and thereby stabilized. Subheading 3.10 explains vertically aligning multiple lasers to maximize sensitivity and aligning a detector laser to a fiducial mark (*see Note 1*). Finally, Subheading 3.11 discusses the software design and implementation of the surface-stabilization feedback loop and testing the performance of the stabilization using an out-of-loop monitor.

---

## 2 Materials

### 2.1 Installing an AOM System

1. Near-infrared (NIR) laser (for either trapping or detection).
2. Single-beam NIR AOM (Isomet, model 1205C-2, PbMoO<sub>4</sub> crystal. Anti-reflection coated).
3. Fixed-frequency analog-modulation driver (Isomet, our model: 232A-2, new model: 532C-2).
4. Four-axis tilt aligner (Newport, model 9071, 3 mm & 8° travel).
5. Machined mount for tilt aligner.
6. +28 V 1 A DC (direct current) power supply (Isomet).
7. Electrical soldering iron.
8. Heat sink for modulation driver.
9. Thermal paste.
10. BNC cables and SMA-to-BNC, SMB-to-BNC converters (Isomet).
11. Controllable DC-voltage source.
12. Optics table.

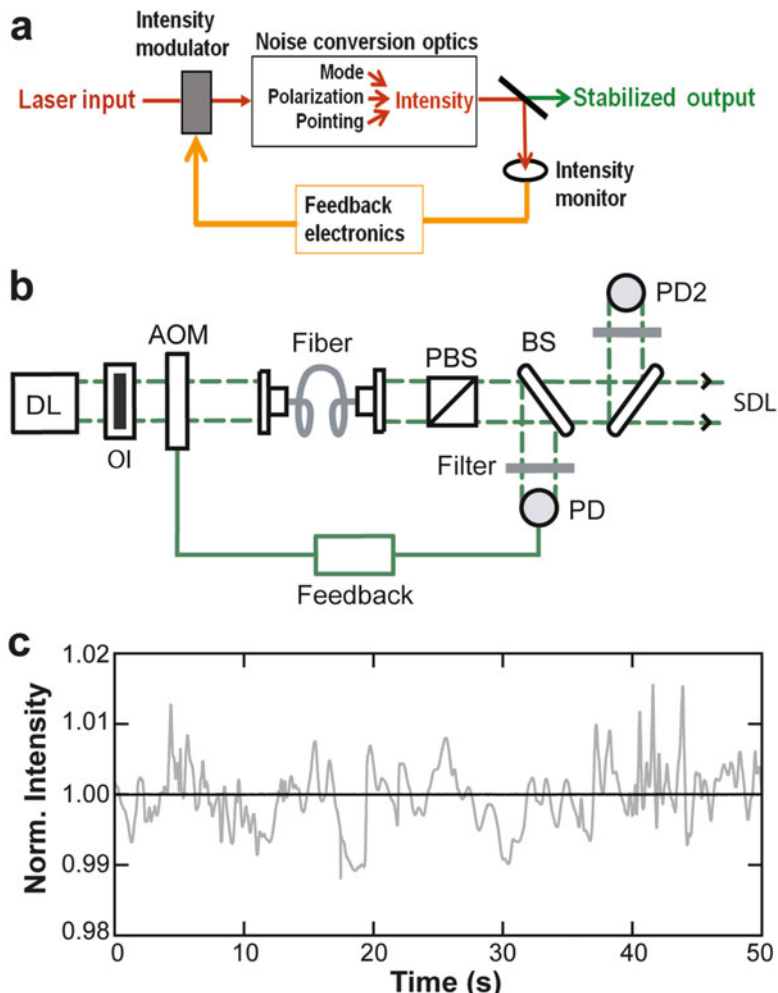


**Fig. 2** (a) Conceptual diagram of the laser stabilization feedback loop where several types of laser noise are converted into intensity noise. The intensity noise is measured and then minimized using a feedback loop. The advantage of this scheme is the exact magnitude of different types of laser noise does not need to be known. (b) Optics diagram for implementing the laser stabilization feedback loop shown in (a). A second photodiode (PD) is shown and is used to characterize the performance of the feedback loop using an out-of-loop monitor (DL diode laser, OI optical isolator, BS beam splitter). (c) A plot of normalized laser intensity versus time, prior to stabilization (gray) and after stabilization (black) for a 785-nm detection laser. Data were averaged to 100 Hz (reprinted with permission from ref. [12]; © 2007 The Optical Society)

## 2.2 Maximizing the Diffraction Efficiency of a Laser through an AOM

1. The AOM system from Subheading 3.1.
2. Two plano-convex lenses (Thorlabs, N-BK7 material, focal lengths determined by available space).
3. Fiber bench (Thorlabs, model FB-38).

4. Half-wave plate, fiber bench mountable (Thorlabs, model RABH-980).
5. PBS cube, fiber bench mountable (Newport, model 05FC16PB.5).
6. Beam block (Thorlabs, model LB1).
7. Power meter (Thorlabs, model PM100D with S130C detector).
8. NIR detection card.
9. Laser safety glasses.

**2.3 Coupling  
the First-Order AOM  
Diffraction into  
an Optical Fiber**

1. The optical system from Subheading 3.2.
2. Beam block or iris.
3. Two plano-convex lenses (Thorlabs, N-BK7 material, focal lengths determined by available space).
4. Two NIR mirrors (Thorlabs, model BB1-E03).
5. Fiber bench with wall plates and dust cover (Thorlabs, model FB-38W).
6. Half-wave plate, fiber bench mountable (Thorlabs, model RABH-980).
7. Fiber coupler (Thorlabs, FiberPort model PAF-X-5-B).
8. Polarization-maintaining fiber-optic patch cable, panda style, one FC/APC and one FC/PC connector (OZ Optics).
9. Machined clamp for patch cable stabilization.
10. Laser pointer for fiber-optic testing (FC male head).

**2.4 Launching the  
Laser and Monitoring  
the Fiber Output  
Intensity with a  
Photodiode**

1. Fiber-optic patch cable from Subheading 3.3.
2. Machined clamp for patch cable stabilization.
3. Fiber-launch system, free space (Thorlabs, model KT110).
4. Mounted aspheric lens (Newport, model 5723-H-B;  $f = 8$  mm, anti-reflection coated).
5. Asphere adapter (Newport, model 5709).
6. Beam profiler (or razor blade and power meter).
7. Plano-convex lens (focal length calculated during aspheric lens installation).
8. PBS cube (Newport, model 10FC16PB.5).
9. 90/10 beam sampler (Newport, model 10B20NC.2).
10. Neutral density filter (Thorlabs, e.g., model ND20A).
11. Analog PIN photodiode (Excelitas, model YAG-444AH).
12. Power supply for photodiode.
13. NIR laser-line filter (e.g., Thorlabs, model FL1064-10).

14. Machined mount for photodiode and line filter.
15. XY translator (Thorlabs, model ST1XY-D).
16. 10-k $\Omega$  gain trans-impedance amplifier, *see* circuit diagram at <https://jila.colorado.edu/perkins/research/resources>.
17. Machined housing for photodiode mount and amplifier.

## **2.5 Completing the Feedback Loop with an AOM Servo Board and Checking Performance**

1. The completed setup from Subheading 3.4.
2. *See AOM Servo Parts List* at <https://jila.colorado.edu/perkins/research/resources>.
3. Spectrum analyzer (SRS, model SRSR780) or oscilloscope (>80 MHz bandwidth).

## **2.6 Cleaning Glass Coverslips**

1. Magnetic stir plate with large stir bar.
2. Ultrasonic bath (Branson 5200).
3. 18-M $\Omega$  purified water (e.g., from a Thermo Scientific Barnstead Nanopure).
4. Microwave.
5. Four 1-L beakers.
6. One purified water squirt bottle and one ethanol squirt bottle.
7. 250 mL completely denatured ethanol (Macron, product number 7018-16).
8. 300 mL acetone (Fisher).
9. 80 g KOH pellets (Fisher, 0.4 % potassium carbonate).
10. Glass coverslips (22×40 mm, thickness 1 1/2).
11. Custom-machined Teflon coverslip rack with handle.
12. Container for coverslip rack (such as an empty pipette tip box).
13. Parafilm.
14. Diamond scribe.

## **2.7 Fabricating Fiducial Marks onto Coverslips**

1. Cleaned coverslips from Subheading 3.6.
2. Teflon coverslip rack.
3. Container for coverslip rack (such as an empty pipette tip box).
4. Gloves.
5. Tweezers.
6. Hot plate.
7. FOx 16 Flowable Oxide (Dow Corning).
8. Spin coater.
9. Scanning electron microscope (FEI, Nova NanoSEM 630).
10. Fume hood.
11. Two 50-mL beakers.

12. Filtered water.
13. TMAH solution (Dow Electronic Materials, MicroPosit MF CD-26, 2.4 % tetramethylammonium hydroxide).
14. Nitrogen gas spray gun.
15. O<sub>2</sub> plasma etcher (PlasmaSTAR, AXIC).

## **2.8 Assembling Flow Cells with Fabricated Coverslips**

1. Fabricated coverslips from Subheading 3.7.
2. Microscope slides (Corning, 75 × 25 × 1 mm<sup>3</sup>).
3. Double-sided tape (Scotch, ½ inch wide).
4. Scissors.
5. Razor blade.
6. 5-min epoxy (Devcon).
7. Disposable dish (e.g., a weigh boat).
8. Pipette tip.
9. Custom-machined Teflon mount.

## **2.9 Processing a QPD Voltage Signal with an Offset Amplifier Circuit Board**

1. See Offset Amplifier Parts List at <https://jila.colorado.edu/perkins/research/resources>.
2. LabVIEW software.
3. PCI board to send computer-controlled voltages (National Instruments, NI-PCI-6703).
4. PXI Data Acquisition System (National Instruments) (see Note 2).
  - (i) NI PXIE-1082 PXIE chassis/controller.
  - (ii) NI PXIE-PCIe8375 computer to chassis boards (compatible with Dell and HP PCs).
  - (iii) NI PXIE-6368 Simultaneous X-series data acquisition board.
5. Three shielded cables (National Instruments, two SHC68-68-EPM and one SH68-68-D1).
6. Three connector blocks (National Instruments, model SCB-68).

## **2.10 Preparing the Instrument for Surface Stabilization**

1. The flow cell from Subheading 3.8.
2. The setup from Subheading 3.9.
3. Three-axis, closed-loop PZT stage (Physik Instrumente, model P-517.3CD).
4. PZT stage controller (Physik Instrumente, model E-710. P3D).
5. GPIB to USB cable (National Instruments, NI GPIB-USB-B).
6. Monolithic slide holder (to be screwed into the piezo stage).
7. Mounting accessories for PZT stage (dependent on individual setup).

---

## 3 Methods

### 3.1 Installing an AOM System

To actively stabilize a near-infrared (NIR) laser, we convert its pointing, mode, and polarization noise into intensity noise and then mitigate intensity noise using an AOM-mediated feedback loop (Fig. 2). To create this feedback loop, we first need to install a single-beam NIR AOM system (Fig. 3a). This system is composed of three devices: the AOM, a modulation driver for the AOM (Fig. 3b), and a power supply. The AOM has an SMA input, and two apertures for laser input and output. When an oscillating voltage is applied to the SMA input, a piezoelectric transducer inside of the AOM rapidly expands and contracts in response. These vibrations create a traveling sound wave that varies the refractive index in an attached crystal. If a beam of light passes through the crystal, these index variations act as a diffraction grating (Fig. 3c), diffracting some of the light intensity (Fig. 3d). The amount of diffracted intensity will depend on the amplitude of the sound wave. This amplitude is controlled by a voltage applied to the input of the modulation driver. The angle between the zeroth and first order beams is set by the frequency of the sound wave (*see Note 3*).

Our modulation driver has three connection points: a power supply input labeled “+Vdc”, a voltage input labeled “MOD”, and a voltage output labeled “RF”, for radio frequency. It also has a control screw labeled “PWR ADJ”, and an optional control screw labeled “BIAS ADJ”. The output RF signal’s amplitude is set by the “MOD” input voltage. The “MOD” and “RF” connectors can be BNC, SMA, or SMB, depending on the driver model; the driver manufacturer should be contacted for purchasing the best cables or converters. To keep the diffracted beam’s position fixed in space, we use a fixed-frequency (80 MHz) modulation driver. To power the modulator, we connect the “+Vdc” terminal to a 28 V DC (direct current) power supply regulated to  $\pm 1\%$  (*see Note 4*). In addition, the driver *must* be connected to an external heatsink, which can either be machined or bought. A driver’s heatsink requirements are given in its manual.

1. Choose the height you wish to set the optical axis at above the optics table. This is the height at which the laser will propagate. The laser propagation height will determine the height of many of the optics in this system. This height is largely a matter of convenience, but shorter is generally better, as it will make the optics less susceptible to mechanical vibrations. Denote this height as  $y_0$ , in a coordinate system with  $z$  pointing along the optical axis (*see Note 5*).

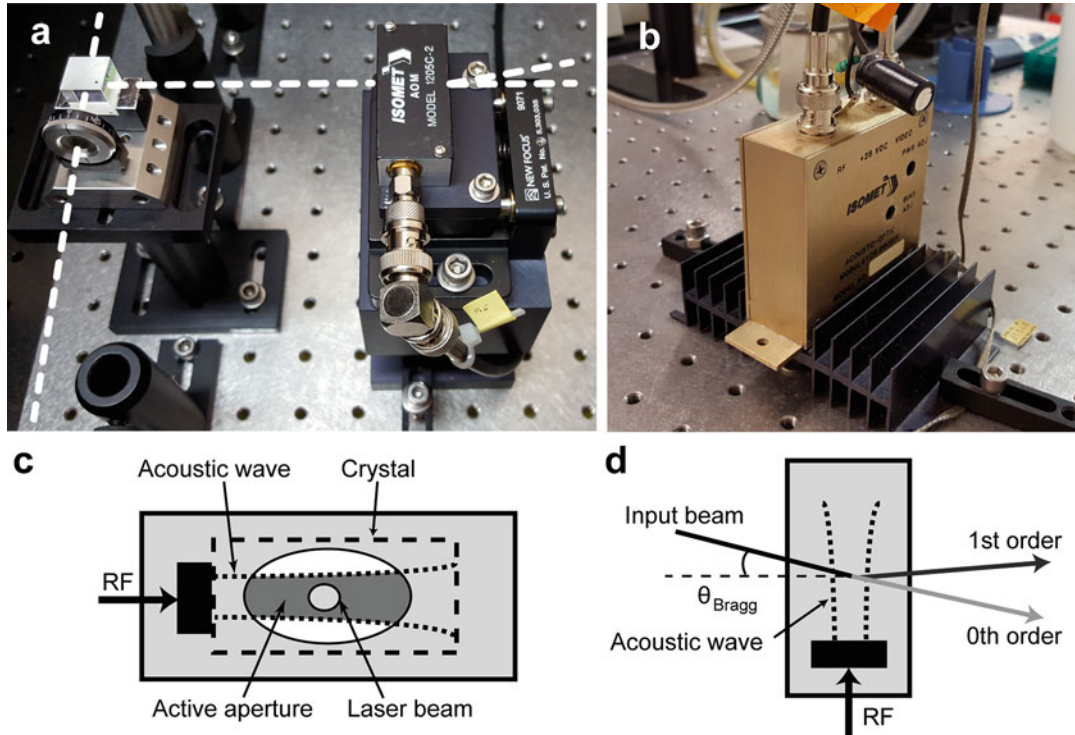


**Fig. 3** (a) Photograph showing the AOM setup for the 1064-nm trapping laser (the *white dashed line* indicates the laser path). (b) Photograph showing the AOM driver with low-pass DC power filter and heat sink anchored to the optical table. (c) Cartoon depicting the operation of an AOM. The radio frequency (RF) voltage signal drives the transducer (*black*) to produce an acoustic wave in the attached crystal. The nodes and anti-nodes of the sound wave form a diffraction grating in the crystal. Note that changes in the acoustic wave's amplitude have to spatially propagate from the transducer to the far side of the laser beam to fully affect the first order beam's intensity. (d) Top view of the AOM's operation. Beams higher than first order are not shown, since they typically have very low intensity

2. Mount the AOM to the Tilt Aligner, and calculate the distance between the center of the AOM's aperture and the bottom of the Tilt Aligner stage. Call this distance  $y_A$ .
3. If  $y_0$  and  $y_A$  are different, machine a monolithic block to serve as a mount for the Tilt Aligner and AOM. If necessary, a machine shop can help with this task. Make the block height  $y_0 - y_A$ , so that the center of the AOM's aperture is located at the optical axis. The block should be machined so that it can be securely anchored using table clamps (e.g., Thorlabs, CL5) (Fig. 3a).
4. Machine or purchase a finned heat sink for the modulation driver. Our design is shown in Fig. 3b. Secure the driver to the heat sink using a thermal transfer paste, and clamp the heat sink down to the table.
5. Solder the power supply output to the “+Vdc” input of the driver. Connect the driver’s “MOD” input to a controllable DC voltage source (note the “MOD” input has a 0–1 V range). Connect the “RF” output to the AOM.

### 3.2 Maximizing the Diffraction Efficiency of a Laser through an AOM

An AOM system can efficiently diffract incident laser intensity into the first order beam. Higher-order beams exist, but have very weak intensities. Our feedback design couples the first order beam into an optical fiber, because the intensity in the first order beam can be reduced to zero. Therefore, to make the most effective use of limited trapping laser power, we maximize the intensity of the first order beam. Diffraction Efficiency (DE) is the ratio of laser power in the first order beam when the RF power is on over the power in the zeroth order beam when the RF power is off. DE depends on the RF power applied to the AOM, the height and angle at which the beam enters the AOM, and the width of the beam inside of the AOM. For NIR lasers, the DE will increase with increasing RF power (though not always linearly). This power dependency is in contrast to visible wavelengths, where the DE decreases after some wavelength-dependent saturation power  $P_{\text{sat}}$ . The  $P_{\text{sat}}$  values for NIR wavelengths are past the safe-operating limit of the AOM.

DE is maximized when a laser enters the AOM in the center of its “active aperture” at a specific angle called the Bragg angle (Fig. 3c, d). The active aperture is defined as the exposed part of the crystal where the acoustic wave is present (as opposed to the material aperture, which is just the exposed part of the crystal), and is specified by the length of its shortest axis. The material and active apertures of the AOM are not in general the same, and any laser power that fails to pass through the active aperture is lost. Therefore, the incident beam diameter should not be larger than the short axis of the active aperture; DE is maximized when these two widths are equal. While smaller beam widths reduce the DE, they improve the rise time of modulations, since acoustic wave propagation across smaller beams takes less time (*see Note 6*). We set the beam width of our trapping laser equal to the active aperture to maximize DE. We kept the detection lasers at their initial beam widths, since their DE was not critical because only a few mW of laser power was needed. We angularly aligned the AOM by manually turning its mounting block until the DE was maximized. Finally, for aligning any near-IR laser, laser safety goggles should always be worn.

1. Turn the driver’s “PWR ADJ” control screw all the way to the right, then back  $\frac{1}{4}$  of a turn. If a “BIAS ADJ” control screw is present, turn it all the way to the left. These adjustments will increase the DE.
2. Find the active aperture specification in the AOM’s data sheet, and measure your initial beam width.
3. For a trapping laser, determine the ratio in beam size needed to change the initial beam diameter to match the active aperture width and then calculate the pair of focal lengths needed to

achieve this change in beam size using a telescope. Install that telescopic lens system between the laser and the AOM. In general, this step can be skipped for detection lasers. For high-power lasers, be sure to check that the expected maximum laser intensity does not exceed the damage threshold of the AOM.

4. Install the half-wave plate, PBS cube, and beam block as shown in Fig. 1e, so that the majority of the light is directed into the AOM in a pure polarization state.
5. Use the half-wave plate to reduce the laser power into the AOM until its output beam (with the “RF” off) is barely visible on an IR detector card.
6. Read the power in the output beam with a power meter, and turn the half-wave plate back until the detected power is ~5 mW. Remember to work within the linear range of the power meter.
7. Turn on the power supply to the driver, and set the “MOD” input to an intermediate value (we use 0.4 V). Use the IR card to find the zeroth and first order beams, and move the power meter so that it only detects the first order beam (or simply block the zeroth order beam).
8. Slightly unclamp the AOM mount block so that it can be rotated. Slowly rotate the block and watch how the power in the first order beam changes. Clamp the block at the position that gives the largest power.
9. Perform the same alignment with the tilt aligner, and measure the final output power in the 1<sup>st</sup> order beam. Calculate the DE by dividing this value by the power you used in **step 6**.
10. For more detection sensitivity, turn the half-wave plate to increase laser intensity into the AOM. Then repeat **steps 6–9**. We typically align until the DE is above 0.75.

### **3.3 Coupling the First-Order AOM Diffraction into an Optical Fiber**

When a laser is coupled into a single-mode, polarization-maintaining optical fiber, its pre-fiber mode and pointing noise are converted into intensity noise (Fig. 2a, b). We couple the AOM’s first order beam into such a fiber and use an AOM-mediated feedback loop to stabilize the post-fiber intensity noise. An angle-cleaved connector (FC/APC) at the fiber input mitigates back reflections, and a flat connector (FC/PC) at the fiber output ensures that the post-fiber beam emerges in a circular TEM<sub>00</sub> mode. To couple the laser into the fiber, we use an ultrastable, micro-positioning fiber coupler with an embedded focusing lens. The efficiency of this fiber coupling is maximized when the diameter of the collimated input beam  $D$  satisfies the following equation:

$$D = 2f(NA_{\text{fiber}}) = f \frac{4\lambda}{\pi\omega}, \quad (1)$$

where  $f$  is the focal length of fiber-coupler lens,  $NA_{\text{fiber}}$  is the numerical aperture of the fiber ( $NA_{\text{fiber}} \equiv 2\lambda/\pi\omega = 0.11$  for  $\lambda = 850$  nm),  $\lambda$  is the beam wavelength, and  $\omega$  is the mode-field diameter (MFD) of the fiber at the laser wavelength. Note this  $NA_{\text{fiber}}$  is based upon the MFD, not the manufacturer's specified NA, which is typically 20–30 % larger. We use a 5-mm fiber coupler ( $f = 4.6$  mm), and NIR fibers will typically have MFD values of 5–8  $\mu\text{m}$ .

The  $D$  value for maximum coupling efficiency will probably not equal the diameter needed for maximal DE in the AOM. Thus a two-lens telescope is needed to change the beam diameter. For trapping lasers, this two-lens system can also be used to mitigate the thermally induced pointing noise that arises from large RF power changes to the AOM. Specifically, when the modulation signal to the transducer changes, there is a transient temperature gradient in the AOM crystal that distorts the diffraction grating and leads to pointing noise in the diffracted beam [13]. A two-lens system reduces the severity of the thermally induced pointing noise so that the feedback loop can fully remove this adverse effect from the output beam. To determine the parameters for this system, a ray matrix equation for two thin lenses and two free-space propagations must be solved. Solving this matrix equation, one finds that:

$$D = d \left( 1 + \frac{l_1 l_2}{f_1 f_2} - \frac{l_1 + l_2}{f_1} - \frac{l_2}{f_2} \right); \quad l_1 = f_1 + f_2, \quad (2)$$

where  $f_1$  and  $f_2$  are the focal lengths of the first and second lenses,  $l_1$  is the distance between the two lenses,  $l_2$  is the distance between the second lens and the fiber coupler lens, and  $d$  is the diameter of the beam before the first lens (ideally the same as the diameter in the AOM).

1. Block the zeroth order beam with either an iris (for milliwatt-scale beams) or a beam block (for watt-scale beams).
2. If the laser will only be used at a fixed intensity (such as the detection lasers), skip this step. For beams that require a dynamic intensity—namely the trapping beam—solve Eq. (2).  $D$  and  $d$  will be fixed, and the ranges of  $l_1$  and  $l_2$  will depend on the available space. We use  $f_1 = 200$  mm and  $f_2 = 300$  mm plano-convex lenses. Note that Eq. (2) does not need to be a strict equality, but differences should be kept below 20 %. Install the two lenses at their corresponding distances, putting the second lens on a translation stage.

3. Install two turning mirrors before the fiber coupler. We use these mirrors as a 2-mirror beam walk, to align the beam into the fiber coupler.
4. Screw the fiber coupler into one end of the fiber bench, and install the fiber bench half-wave plate.
5. Align the two turning mirrors such that the power through the half-wave plate and fiber coupler (without any patch cable attached) is maximized.
6. To make preliminary alignments to the fiber coupler, attach the patch cable to it, and attach a handheld fiber optic tester to the other end of the cable. A visible red laser should now run backwards through the system. Adjust the fiber coupler's five degrees of freedom such that the test beam overlaps the laser (going as far back upstream as possible). Note that a pair of irises uniquely defines a beam path. So by aligning both the visible and near-IR lasers to such a pair of irises, one can facilitate this process.
7. Remove the fiber-optic tester. Use a power meter to detect whether laser light is emerging from the cable's output connector; if there is no light, redo steps 5 and 6. Otherwise, adjust the fiber coupler screws slowly to maximize the transmitted power (*see Note 7*). A good alignment will give ~75 % or more transmission.
8. For trapping lasers, jump the AOM driver "MOD" voltage from a low value to a high value (e.g., 0.1 V to 0.6 V). Observe the intensity stability after the fiber in response to a large, abrupt change in RF power. If unacceptable, translate the position of the second lens along the  $z$ -axis—the laser propagation axis—so that  $D$  decreases, and try again. Iterate this process until you reach an optimum compromise between baseline fiber-coupling efficiency and pointing stability for your application. By changing the position of the lens, the diameter and cone-angle of the laser is altered at the fiber input. This process sacrifices coupling efficiency for stability in response to a large change in laser power induced by a change in the AOM.
9. When satisfied with the alignment, cover the fiber coupler with its dust cover and gently clamp a length of cable near the fiber coupler such that it does not sag or bend near the coupler (sharp bends reduce transmission efficiency). We use two machined blocks that can be screwed snuggly together, and have grooves down their middles in which the cable can securely sit. Figure 4a shows our finished fiber input setup.

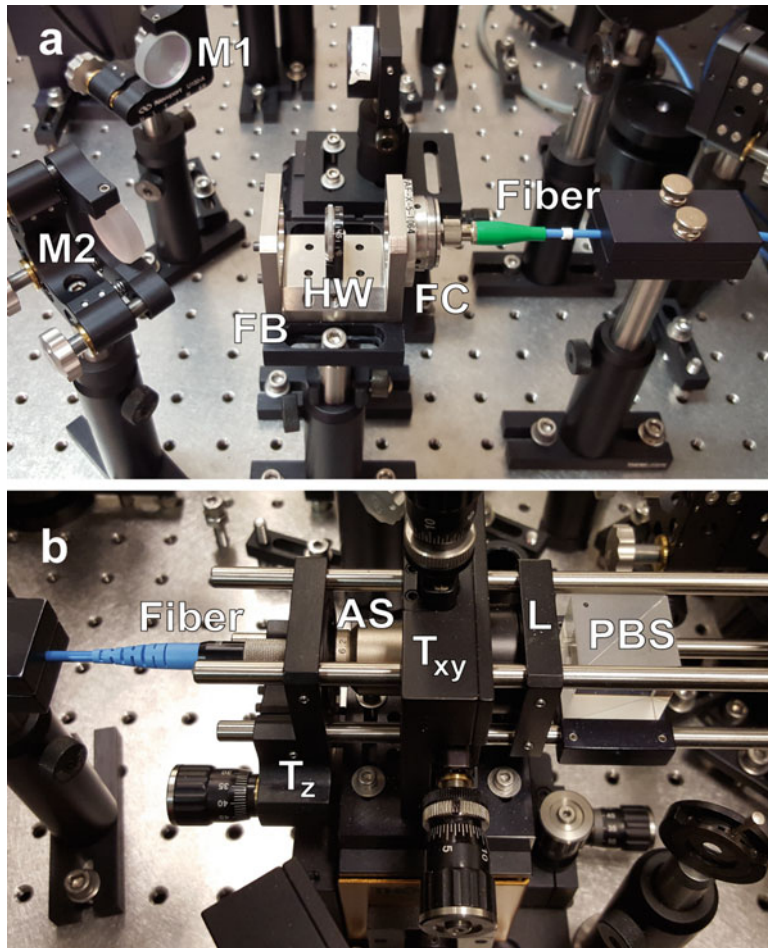


**Fig. 4** (a) Photograph showing our setup for coupling a laser into an optical fiber. M1 and M2 are turning mirrors, FB is a fiber bench, HW is a half-wave plate, FC is a fiber coupler, and Fiber is a polarization-maintaining, single-mode optical fiber. (b) Photograph showing our fiber output setup. T<sub>z</sub> is a fiber-cage Z translator, AS is an aspheric lens, T<sub>xy</sub> is a fiber-cage XY translator, L is a plano-convex lens, and PBS is a polarizing-beam splitter

### 3.4 Launching the Laser and Monitoring the Fiber Output Intensity with a Photodiode

To launch the laser out of the fiber and feedback on its intensity for the stabilization feedback loop, we construct a fiber launch system that expands and collimates the fiber output beam (*see Note 8*). We use a stable multi-axis translation stage underneath to aid in subsequent beam alignment. Specifically, *x* and *y* motion of the fiber launch translation stage maps to pure rotations in the imaging plane of the microscope; *z*-axis motion of the fiber tip relative to an aspheric lens provides for fine control of laser collimation. A PBS cube in the fiber launch is used to re-polarize the laser after the fiber, since small rotations in polarization can occur over time, even with a polarization-maintaining fiber. The PBS cube turns this polarization noise into intensity noise, which is mitigated by the feedback loop. Figure 4b shows our finished fiber launch setup.

To measure the intensity of the laser after the fiber launch, we use a 90/10 beam sampler that diverts 10 % of the output laser intensity onto a photodiode. The photodiode's current signal is converted to a voltage that is input into an analog AOM-servo circuit board that, in turn, outputs a voltage signal to the AOM driver. The rest of the laser light is sent into a microscope objective to serve as either a trapping or a detection laser.

We use silicon analog photodiodes in a TO-36 packaging for all of our lasers (YAG-444AH). These photodiodes have a 60-MHz bandwidth and 5-ns rise time for a  $50\text{-}\Omega$  load at  $\lambda = 1064\text{ nm}$  when applying a large ( $-180\text{ V}$ ) reverse bias. Reverse biasing eliminates a wavelength-dependent filtering in silicon photodiodes, including quadrant photodiodes, when using 1064-nm light [16]. By reducing the reverse bias, we tradeoff increased thermal stability of the photodiode during large-laser power changes for decreased detection bandwidth. We find that  $-30\text{ V}$  is a good compromise between signal stability and response time for this feedback loop (see Note 6).

1. Install a fiber-launch cage system on an optics table (we use the KT110 by Thorlabs). Put the FC/PC fiber adapter plate in the Z translator, and slide the mount onto the XY translator's back assembly rods. Make sure the adaptor plate's center is at your set optical-axis height  $y_0$ , and that its key slot is vertical (so that the output polarization is vertical). Connect the fiber optic patch cable (FC/PC end) to the adaptor plate.
2. Mount an aspheric lens into the XY translator, with the planar side facing the fiber's adaptor plate. We use a mounted aspheric lens with an anti-reflection coating (Newport 5723-H-B) and an RMS-threaded asphere adaptor (Newport 5709). We then use the RMS-to-SM1 adaptor ring from the fiber launch kit to install the aspheric lens into the XY translator.
3. Screw the SM1 iris diaphragm into the cage plate, and mount it on the assembly rods downstream of the XY translator. Open the iris fully, and slide it to the end of the cage assembly. Now adjust the distance between the Z translator mount and the aspheric lens so that the diverging output beam passes through the iris unclipped. Screw-tighten the Z translator to the assembly rods at this position. Remove the iris from the cage.
4. Determine the beam diameter you wish to send into the rest of the optical-trapping setup. Call this diameter  $d_0$ . A plano-convex lens needs to be added to the cage assembly to collimate the fiber output beam to this diameter. To determine the required focal length for this lens, measure the beam diameter at a position close to the XY translator (using either a beam profiler or a razor blade and power meter). Use a ruler and a piece of tape to mark the location of this measurement on the optics table. Repeat this process at a position farther away from the translator. Call the smaller beam diameter  $d_1$ , the larger

diameter  $d_2$ , and the distance between them  $\Delta z$ . If we imagine the beam emerging from the XY translator as a cone of light from a point source, simple geometry says that  $\theta$ , the angle between the optical axis and the cone's edge, must obey  $\tan(\theta) = (d_2 - d_1)/2\Delta z$ . From here, a ray matrix calculation shows that the focal length needed to collimate the beam at diameter  $d_0$  is  $f = d_0/2\theta$ .

5. Add this lens to the cage system at the location that collimates the beam. Install a PBS cube after the lens, so that polarization noise introduced by the fiber is turned into intensity noise and mitigated (*see Note 9*).
6. Place a 90/10 beam splitter after the cube. If the power in the 10 % beam is larger than 1 mW, install a reflective neutral-density filter to reduce the incident power.
7. Machine or purchase a photodiode mount that can screw into the XY translator. Install the photodiode into the mount, with a line filter placed in front of the photodiode at the laser's wavelength. Machine a protective casing with two BNC connectors to house the photodiode mount and a 10-k $\Omega$  trans-impedance amplifier.
8. Assemble transimpedance amplifier based on the provided circuit diagram (*see* [\*https://jila.colorado.edu/perkins/research/resources\*](https://jila.colorado.edu/perkins/research/resources)*). Connect the photodiode's current output to the trans-impedance amplifier (to turn it into a voltage), and connect the amplifier to one of the two BNC connectors. Connect the photodiode's bias input to the other BNC connector, and attach to the photodiode's power supply. Install the photodiode into an XY translator and align the photodiode in the 10 % beam path (*see Note 10*).*

### **3.5 Completing the Feedback Loop with an AOM Servo Board and Checking Performance**

The final component of the intensity stabilization feedback loop is a proportional-integral servo circuit board. This board takes the photodiode voltage and a user-determined reference voltage as inputs, and outputs a voltage to the AOM driver's "MOD" connector. The board tries to keep the photodiode voltage equal to the reference voltage by changing the AOM driver's modulation voltage. For example, if the photodiode voltage is above the reference, the board lowers the modulation voltage to decrease the DE of the AOM and thereby lowers the incident power on the photodiode. The parts list, schematic, and circuit board layout for this AOM servo board can be found at [\*https://jila.colorado.edu/perkins/research/resources\*](https://jila.colorado.edu/perkins/research/resources), and this circuit board layout can be sent out for manufacture (e.g., at PCB Unlimited). The board is designed to fit into a single slot NIM case, and we use a NIM bin rack as its ±15 V power supply. Once built, the servo board must be tuned to maximize its low frequency gain and minimize its gain at frequencies larger than the inverse of the AOM's response time. If the gain

in that bandwidth is not zero, the servo loop will try to servo itself and will start oscillating.

1. Assemble the circuit board using the schematic, circuit-board layout, and parts list. Install into a single-slot NIM case. Power the board with  $\pm 15$  V (*see Note 11*).
2. Connect the photodiode's output to "PD INPUT (J13)," connect a cable carrying 5 V DC to "COMPUTER /INTERNAL CONTROL (J10)," connect "OUT TO AOM (J50)" to the AOM driver's "MOD" input, and connect "COMPUTER (EXTERNAL) INTENSITY CONTROL (J12)" to a controllable DC-voltage source. The laser-intensity servo loop is now complete.
3. Use a T-connector to simultaneously read the "PD INPUT" on a real-time spectrum analyzer (1-MHz bandwidth), and turn the coarse gain, fine gain, and PI corner controls all the way counter-clockwise (*see Note 12*).
4. Set "INTENSITY CONTROL" to a low voltage (such as 1 V), and see whether the green board LED lights up. If it does, the servo loop is working and "locked" at the set voltage. If the "under" LED lights up, the photodiode's voltage is less than the reference. Check your optical system to make sure laser light is making it through the fiber, and onto the photodiode. If the "over" LED lights up, the photodiode voltage is larger than the reference, and the servo is trying to reduce the power in the AOM's first order beam. If the "over" status persists, check the optics and try turning the power to the board and AOM driver off and on.
5. Once the servo is locked, turn the coarse gain up until the signal on the spectrum analyzer starts to peak, then back down one notch. Do the same for the fine gain, turning it back half a screw turn, and repeat for the PI corner. The servo is now tuned. If a spectrum analyzer is not available, this procedure can be done with an oscilloscope where the signal will start to oscillate with too much gain.
6. The best way to check the performance of a feedback loop is to monitor the control variable using an out-of-loop detector. To check this servo's performance, take another beam sampler and monitor the fiber output intensity on a second, out-of-loop photodiode, as shown in Fig. 2b. A plot of normalized laser intensity vs. time when the servo is off (gray) and on (black) is shown in Fig. 2c.

### **3.6 Cleaning Glass Coverslips**

To stabilize the position of the sample surface, we fabricate fiducial marks onto the surface, monitor their position with a detection laser, and counter any observed drift with a three-axis PZT stage. Before fabrication begins, the coverslips must first be cleaned.

We use the following protocol for typical glass cleaning, and O<sub>2</sub> plasma if more rigorous cleaning is needed. Note that a base-etch, such as KOH, should not be used to clean the coverslips *after* fabrication, as it will etch the HSQ posts off of the glass.

1. Use a diamond scribe to write a small “X” into the lower right corner of each of the coverslips (on one side only). This will be the side onto which we fabricate fiducial marks.
2. Place 80 g of potassium hydroxide (KOH) pellets and 250 mL of completely denatured ethanol into a 1-L beaker, and dissolve using a magnetic stir bar and plate (*see Note 13*). This gives a 5.7 M KOH solution.
3. Place this beaker into an empty ultrasonic bath. Place two half-filled 1 L beakers of filtered (0.2 µm) water and one 1 L beaker of 300 mL acetone in the bath, as well, for a total of four beakers.
4. Fill the ultrasonic bath with water (up to 3 in. high), and turn on.
5. Load coverslips into a Teflon coverslip rack (shown in Fig. 5a) and submerge into acetone solution for 3 min.
6. Rinse coverslips and rack with ethanol, and then submerge into the KOH solution for 3 min.
7. Rinse all of the KOH solution off with filtered water, and submerge into the first beaker of water for 3 min.
8. Rinse again with filtered water, and submerge into the second beaker of water for 3 min.
9. Rinse with filtered water and then with ethanol. Dry the ethanol-rinsed coverslips and rack by placing them into a microwave for 2 min on high heat.
10. Store in a sealed container, such as an empty pipette tip box with Parafilm covering.

### **3.7 Fabricating Fiducial Marks onto Coverslips**

We fabricate fiducial marks onto coverslips using a hydrogen silsesquioxane (HSQ) negative resist and e-beam lithography. HSQ crosslinks to form a low-index glass when exposed to EUV or e-beam radiation, and non-cross-linked HSQ can be removed from glass using tetramethylammonium hydroxide (TMAH). To make fiducial marks, we therefore spin-coat a coverslip with a 0.4–1-µm thick layer of HSQ, and then e-beam pattern an array of ~600-nm diameter circular dots onto the HSQ layer in a low-vacuum environment. The excess, non-irradiated HSQ is then removed (*i.e.*, “developed”) using a solution of TMAH and water. This procedure creates an array of glass posts covalently attached to the coverslip, as shown in Fig. 5b. Other fabricated fiducial marks, such as silicon disks, can also be used, as detailed in a previously published protocol [17]. Non-fabricated fiducial marks, such as beads stuck or

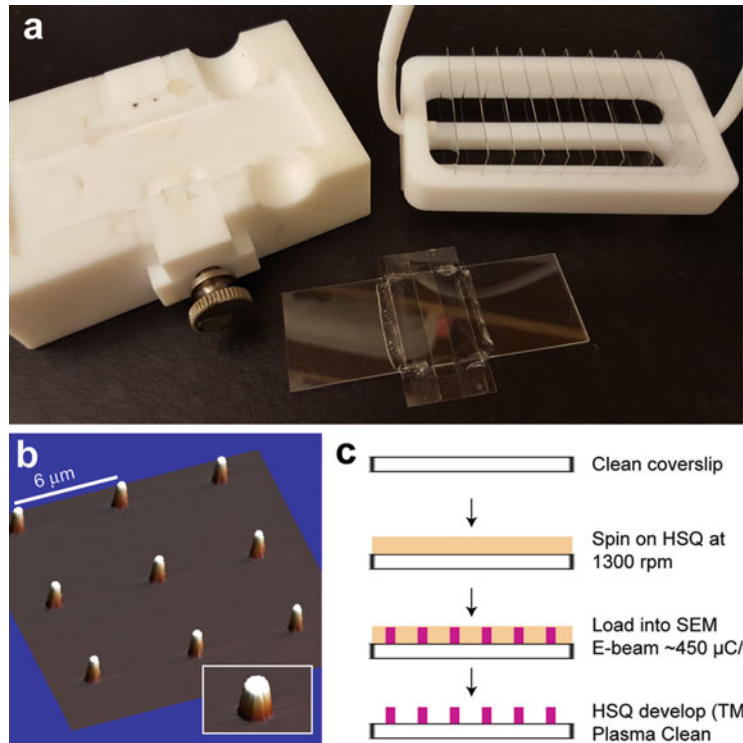


**Fig. 5** (a) Photograph showing a custom-machined Teflon block for reproducibly placing coverslips containing fiducial marks onto a microscope slide (*left*), an example flow cell (*middle*), and a Teflon rack and handle for cleaning coverslips in acids or bases (*right*). (b) Atomic-force-microscope image of a coverslip surface patterned with fabricated fiducial marks. Note these posts are spaced 6 by 6  $\mu\text{m}$  apart. Optimum spacing depends on the length of DNA, the size of the bead, and the range of the electronically steerable mirror. We often use a 15- $\mu\text{m}$  spacing for 2- $\mu\text{m}$  long DNA when using 0.7- $\mu\text{m}$  diameter beads. (c) Cartoon of the fiducial mark fabrication process

melted onto the surface, will, in general, not suffice for Å-scale stabilization [12], since they are not covalently attached to the surface and typically move relative to the coverslip with  $>1$  Å motion. Such motion tends to get worse after multi-hour exposure to an aqueous environment.

This procedure requires the use of a spin coater, an O<sub>2</sub>-plasma reactive-ion etcher, and a scanning-electron microscope (SEM) with a low-vacuum sample chamber (to prevent harmful charging effects, *see Note 14*). Such equipment is often housed in shared clean room facilities, with different models having different capabilities and limitations. Since your equipment will most likely differ from ours, we provide only general instructions for this part of the protocol. Likewise, the fabrication parameters given below were optimized for our specific equipment; treat our values as

representative ones from which to start your own optimization process.

1. Design an automated SEM procedure to pattern a  $1.5 \times 1.5 \text{ mm}^2$  area in the center of the coverslip with 600-nm diameter dots, spaced 15  $\mu\text{m}$  apart vertically and horizontally. We use DesignCAD and NPGS software for this purpose, with the following parameters: dosage = 450  $\mu\text{C}/\text{cm}^2$ ; current = 25 pA; center-to-center = 6.82 nm; line spacing = 50.02 nm; magnification = 1000 $\times$ .
2. Prepare a coverslip for spin coating by placing it on a 200 °C hotplate for 2 min, diamond-scribed side up. Ensure that in all subsequent steps, the coverslip is always placed scribed side up.
3. Place the coverslip onto the spinner and pipette 200  $\mu\text{L}$  of HSQ (FOx 16) onto it. Spin at 1000–5000 rpm for 50 s at an acceleration of 5.5 krpm/s to make 0.4–1- $\mu\text{m}$  tall posts (1000 rpm makes 1- $\mu\text{m}$ -tall posts).
4. Post-heat the coverslip on a hotplate at 180 °C for 4 min.
5. Load the coverslip into the SEM and pump the sample chamber down to low vacuum [0.075–1 Torr (10–130 Pa)]. Ensure that a low-vacuum detector (LVD) is in place. Set voltage to 30 keV, align and focus the SEM, and run your exposure program.
6. Once the program is complete (~20 min), turn off the voltage and bring the chamber to atmosphere.
7. In the fume hood, fill a 1 L beaker with the TMAH development solution CD-26 (enough to comfortably submerge the coverslip), and fill another 1 L beaker with distilled water. Using tweezers or a Teflon coverslip holder, submerge the coverslip in the TMAH solution for 12 min., then remove and immediately submerge in the distilled water beaker for 1 min.
8. Remove coverslip, rinse off with filtered-water squirt bottle, and dry with nitrogen gas. Use a microscope capable of observing micron-scale features to check whether development is complete. If not, repeat step 8.
9. Once the coverslip is completely developed, it must be cleaned in an O<sub>2</sub>-plasma etch. We perform our etch in a PlasmaSTAR etcher at <25 mTorr (3 Pa) vacuum with the mass-flow controller set to 100 sccm and the power set to 550 W. At these conditions, we run two 180-s etches. Between etches we rotate the metal holder containing the coverslip.

### **3.8 Assembling Flow Cells with Fabricated Coverslips**

The single-channel flow cells we use have a simple design and can be made by hand in a few minutes. They have dimensions of  $25 \times 5 \times 0.15 \text{ mm}^3$  corresponding to a 15- $\mu\text{L}$  volume. More

complicated microfluidic designs exist [18], and can be integrated with coverslips containing fiducial marks. Fig. 5a shows a finished flow cell.

1. Place a microscope slide onto a clean surface. This can be a simple tabletop, or something more complicated like a machined Teflon mount (*see* Fig 5a). Such a mount improves the repeatability of flow cell construction by having pre-marked locations for tape and coverslip placement (*see steps 3 and 4*), ensuring that the post array is located in the same part of the microscope slide, and thus can be easily located under the microscope.
2. Take a ~5-cm-long piece of double-sided tape and stick it lengthwise by its edge to the top edge of the table. Use scissors or a razor blade to cut the tape in half.
3. Take the two tape halves and stick them onto the slide, perpendicular to the slide's long axis, 5-mm apart.
4. Take a fabricated coverslip from Subheading 3.8 and lay it mark-side down on the two tape halves, again perpendicular to the slide's long axis. Make sure the fiducial mark array is centered and that the coverslip overhangs the slide on both sides equally. Using the tip of a Pipetman (or something similar), gently press the coverslip into the tape to ensure a firm, uniform bond (*see Note 15*).
5. Use a razor blade to cut off any tape overhanging the coverslip.
6. Repeat the above steps until you have the number of flow cells you plan to use that day.
7. To rigidify the flow cells, mix together 5-min epoxy in a disposable cup and apply it to the gaps between the coverslip and the slide (except for the fluid channel). Pipette tips are our preferred tool for this task.

### **3.9 Processing a QPD Voltage Signal with an Offset Amplifier Circuit Board**

Back-focal-plane detection is widely used to measure bead motions in an optical trap from a change in light distribution on a quadrant photodiode (QPD) [5], either directly with the trapping laser or with a weaker detection laser. To process the voltage signal from a QPD, we use electronics to amplify the normalized difference signals (typically referred to as  $V_x$  and  $V_y$ ) and to offset-amplify the sum signal, the total light falling on the QPD ( $V_z$ ). By calculating a normalized difference signal, the lateral motion is approximately independent of laser intensity variations. However, since vertical motion of the bead or the fiducial mark is detected as a change in the total light incident upon the QPD, variations in the laser intensity used to detect such vertical motion is indistinguishable from actual vertical motion. Indeed, a variation in intensity of just 1 % appears as ~30-nm-scale axial motion. Additionally, these

small voltage changes make it difficult to precisely measure axial motion. Hence, we amplify the initial QPD's sum signal ( $V_z$ ) by  $\mathcal{G}(V_z - V_0)$ , where  $\mathcal{G}$  is the gain and  $V_0$  a fixed offset voltage. The resulting amplification leads to a larger signal variation per unit displacement (i.e., the sensitivity in V/nm). To do this, we use an analog offset-amplifier to match the variable portion of the sum signal to the  $\pm 10$ -V range of a standard 16-bit data-acquisition (DAQ) system. For simplicity, we also refer to the offset-amplified sum signal as  $V_z$ .

1. Use the schematic and parts list provided at <https://jila.colorado.edu/perkins/research/resources> to assemble the offset amplifier, and install it into a single slot NIM case. Power the board with  $\pm 15$  V (see Note 11).
2. If necessary, install a data-acquisition system. Split the QPD signals into  $V_x$ ,  $V_y$  and  $V_z$  components, and send them through an anti-aliasing filter set to half of your data-acquisition system's sampling frequency. Send the resulting  $z$  signal into an offset amplifier, and then all three signals into the DAQ system.
3. Test that the system can collect voltages from the QPD, process them, and record them onto a computer.

### **3.10 Preparing the Instrument for Surface Stabilization**

Since it is outside the scope of this chapter to detail the installation of common optical-trapping components, this section and all following sections will assume that the experimenter has: installed two detection diode lasers and one trapping laser, and stabilized them using the methods of Subheadings 3.1–3.5, installed computer-controllable 2-axis PZT mirrors (or equivalent beam-steering optics) in the trapping and detection lasers' beam paths, combined beam paths of all three lasers, coupled the lasers into an objective lens, installed a condenser lens and three QPDs to collect the scattered and transmitted laser light from the sample plane, projected a visible light source into the sample plane, and installed a CCD camera and monitor to image the sample plane. In addition, we will not cover the common passive-stabilization techniques used to mitigate environmental noise [5, 6, 19]. These include: enclosures for all optical components, mounting all optics on vibration-isolation tables, housing the instrument in a temperature-stabilized, acoustically quiet room (we use NC30), and mechanically stabilizing instrument components to reduce their susceptibility to environmental vibrations.

1. Connect and install the PZT stage and controller into the existing optical-trapping setup. Be sure to mechanically stress relieve the cable from the controller to the PZT stage, so inadvertent cable motion (i.e., swinging) does not introduce mechanical noise. We use a Nikon TE2000-S inverted

microscope. Alternative trapping designs in the absence of a commercial microscope frame are also used [20].

2. Connect the stage controller to a computer. The three communication protocols are available for our PZT stage: serial (RS-232), GPIB (IEEE-488.2), and PIO. We find that GPIB suffices for most applications (*see Note 16*). Stage manufacturers typically provide LabVIEW software for communicating with the controller. Install that software and ensure its functionality.
3. Install a microscope slide adaptor plate that screws into the top of the piezo stage. Read the stage manual carefully for proper installation procedures, as screws that are too long can damage the stage.
4. Mount the sample slide into the holder, and align the objective and condenser lenses.
5. Focus the objective until the CCD camera's imaging plane aligns with the sample surface. If the center of the fabricated sample cell is aligned with the objective's field of view, you should see a regular array. If not, adjust the lateral position of the sample.
6. Next, the focus of each laser beam must be appropriately placed in space. To set the vertical position of the trap relative to the imaging plane, first fill the sample chamber with a dilute solution of beads. Trap a bead, and then move the stage in  $z$  until the coverslip contacts the bead (which can be detected by an abrupt change in the trap's QPD  $z$  voltage signal [21]). We then change the collimation of the trapping laser beam until the sum signal ( $V_z$ ) of the bead does not change when retracting the trapped bead away from the coverslip surface by changing the vertical position of the stage. Nonideal collimation will result in a  $V_z$  signal that drops linearly in  $z$  (note, in both cases,  $V_z$  is modified by oscillatory Fabry–Perot interference [21]). Collimation of the trapping beam is adjusted by changing the position of the tip of the single-mode fiber (as detailed in Subheading 3.4). We then move the position of the CCD camera to bring the image of a trapped bead into focus.
7. The vertical position of the detection lasers' foci should be set to maximize their detection sensitivity (in V/nm). To this end, we vertically position the bead detection laser's focus ~50 nm past the beam waist of the trap laser so that the detector beam focus is in the center of the trapped bead (which is displaced past the trapping beam waist due to radiation pressure). The fiducial mark detection laser is most sensitive when its beam waist is centered vertically with respect to the post. In our setup, the post detection laser's beam waist is ~400 nm upstream of the trap's focus (i.e., closer to the surface).

8. With the  $z$  positions of the lasers set, move the post detection beam onto a nearby post using the manual turnscrews of the PZT mirror. If the low-power detection beam cannot be imaged in the water-filled cell, use real-time voltage readings from the QPD to tell when the beam passes over a post. Generally, a color filter can be positioned in front of the CCD camera to attenuate the trapping-beam wavelength but still allow visualization of the much weaker detection lasers.
9. LabVIEW software is used to precisely center the beam over a post. To do so, we use a closed-loop tip-tilt PZT mirror to electronically steer the laser across the post in the  $x$  and  $y$  directions ( $\pm 300$  nm), while its QPD voltages are recorded as a function of beam position. The resulting signals are nearly the derivatives of Gaussians, with the center of the post corresponding to the lateral center point of this function: its antisymmetry point. We therefore fit a derivative of a Gaussian to each of these signals, and extract the fit parameters. One of those parameters is the “center offset,” the distance between the antisymmetry point (the post’s center) and the center of the scanned range. We convert that position into a PZT voltage and use it to reposition the beam’s PZT mirror, centering the beam. We typically repeat this process again to fine-tune the position (see Note 17).

### **3.11 Coding a Surface-Stabilization Feedback Loop and Testing Final Performance**

To complete the surface-stabilization feedback loop, we use a LabVIEW program to monitor the surface position and move the PZT stage to compensate for any unwanted surface movement. We first calibrate the detector so that  $V_x$ ,  $V_y$ , and  $V_z$  can be converted to the  $x$ ,  $y$ , and  $z$  spatial positions of the post. Once that is done, we choose a set position ( $x_{\text{set}}$ ,  $y_{\text{set}}$ ,  $z_{\text{set}}$ ) for the post. We then continuously measure the post’s position. Every 10 ms (100 Hz bandwidth), the program computes the mean current position of the post over the previous 10-ms window and takes the difference between this measurement and the set position. The software-based feedback loop then moves the stage a portion of that difference in the opposite direction (we use  $-0.2$  as our proportionality constant). More complex control schemes, such as differential or integral feedback, are also possible, but we find that proportional control is enough to stabilize the surface to 1 Å in 3D over 1-s intervals (1–25 Hz bandwidth) and keep the drift sub-nm over 50-s intervals [12].

The resonance frequency of the PZT stage limits how fast this feedback loop can operate. For our PI P-517.3CD, it is  $\sim 500$  Hz. Hence, the minimum loop closure time is  $\sim 2$  ms. The response time of the stage to software commands also affects the loop closure time, but the software can be tuned to minimize this delay. A more robust (though more complex) version of this stabilization can be found in ref. [22], which achieves 1 Å in 3D stability over 1000 s.

The best way to test the performance of a feedback loop is to measure the control variable using an out-of-loop detector. To that end, we routinely test the performance of the surface-stabilization loop by monitoring the position of a second fiducial mark on the surface with a second, out-of-loop detection laser (Fig. 6a). This gives us a much more accurate measure of stability, since noise sources hidden from the feedback loop (such as positional drift of the in-loop laser) can be measured. Using this out-of-loop laser test, we find that the ultimate limit on our stability is set by the differential-pointing stability between the lasers.

1. Once a detection beam is centered over a post (see Subheading 3.9), the voltage output from the detection electronics must be calibrated into a position. To calibrate the voltage signal, scan the post through the laser focus in all three axes using the stage. Record the stage position vs. detected voltage curve for each axis. Fit a seventh order polynomial to each curve, *using voltage as the independent variable*, and extract the eight fit coefficients. These coefficients are our calibration. To go from detected voltage to post position, just form a voltage polynomial with these coefficients and take the sum. We typically scan  $\pm 200$  nm in 1-nm steps, and for each step average 30 points taken at 4000 Hz.
2. For the stabilization algorithm, create a while loop that performs buffered continuous data acquisition on the position of the post. We take 1200 samples per iteration at 120 kHz and average them, giving us a loop update time of 10 ms.
3. At the start of the while loop, store the initial post position as the “Set Position.” Every following iteration, take the difference between the current position and the set position. Multiply that difference by  $-0.2$  and send a move command to the stage controller to move the stage by that amount. Let this while loop run during your experiment, and algorithmically or manually stop it when you are finished.
4. To test stabilization performance, modify the above program so that a second out-of-loop detector beam can simultaneously measure the position of a second post. Center that beam over the post, scan the post through the beam so that its voltage signal is calibrated, and then perform the same data acquisition. Results from this kind of experiment are shown in Fig. 6b, c.

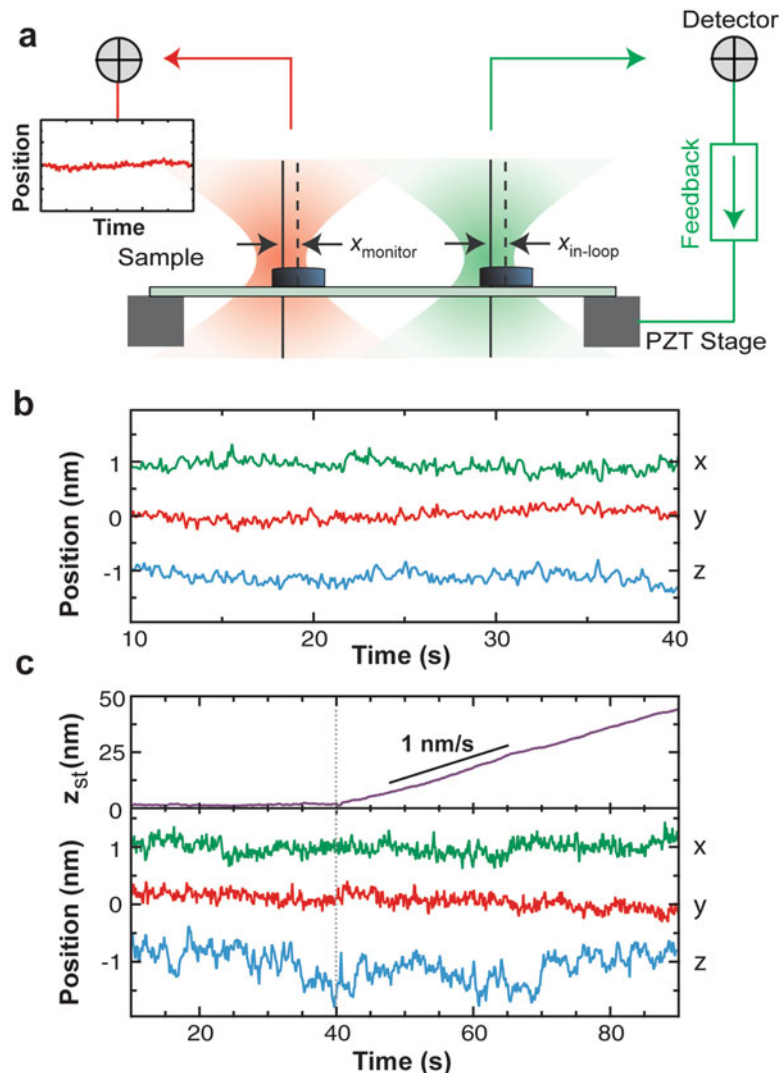


**Fig. 6** (a) Diagram for characterizing the performance of the surface-stabilization feedback loop using an out-of-loop detector. Note that any well-performing feedback loop necessarily drives the in-loop signal to zero over long timescales. Hence, characterizing sample stability based on an in-loop measurement leads to incorrect conclusions. For instance, it cannot distinguish laser-pointing noise from lateral sample motion. (b) Sample position vs. time measured by the independent, out-of-loop laser. Traces offset from zero for clarity; x: top trace, y: middle trace, z: bottom trace. (c) As in (b), but at  $t = 40$  s, the intensity of the trapping laser was increased from 50 to 150 mW, leading to heating and expansion of the objective. The stabilization feedback loop compensated for this significant vertical drift by moving the stage in z (top curve). RMS stability in the short term (1 s) remained 1 Å, while long term RMS stability (50 s) was 1.5 Å in x and y, 2.6 Å in z (reprinted with permission from ref. [12]; © 2007 The Optical Society)

---

## 4 Notes

1. There are excellent video-based methods for stabilizing a microscope sample surface with nm precision [23]. Our laser-based technique is best suited to those applications that require sub-nm stability.
2. This data-acquisition system is the one we currently use for our instrument, but less expensive options are available which will work just as well for the stabilization protocols detailed in this chapter.
3. A more detailed explanation of these components and how they function can be found in the support section of Isomet's website at [isomet.com/appnotes.html](http://isomet.com/appnotes.html).
4. Adding a low-pass filter to this connection can help filter stray AC signals.
5. It is helpful to use a calibrated standard, such as a post-mounted iris, to set height  $y_0$ . With this standard, one can easily check whether a new optical element keeps the laser propagating at constant height  $y_0$ .
6. The time it takes for a sound wave to propagate from the transducer to the far side of the laser beam is the ultimate limit in the response time of the servo loop. We find that the response time at 2-mm beam diameter is small enough for our optical-trapping purposes (giving us a ~200 kHz servo bandwidth).
7. Fiber-coupler alignment can be a tedious and frustrating process; this coupler was chosen for its stability, not its user friendliness. Align the coupler in  $x$  and  $y$  first, and then leave those screws fixed. Optimize the positions of the three  $z$  screws one at a time. One of the  $z$  screws should improve the coupling much more than the others: this screw tilts the fiber coupler to accommodate the angle-cleaved fiber connector. Note that slightly adjusting the two turning mirrors during this alignment can provide surprisingly large results.
8. Our setup uses an aspheric lens and plano-convex lens to quickly collimate and expand the beam within a cage system. Other optical elements, such as triplet collimators, now exist which can perform the same task using only one component [24]. The cost of this simplicity is a loss of customizability and ease of access.
9. The reflectivity of dichroic mirrors is polarization dependent. If dichroic mirrors are used to combine multiple lasers beams into a single-beam path (as widely done in many optical-trapping setups), any polarization noise in the incident beam will be transformed into intensity noise when it reflects off of the

dichroic mirror. This source of noise is mitigated by the PBS cube and the intensity feedback loop.

10. Depending on the size of the incident beam, you may need to install an iris before the photodiode. The edge of the silicon chip is typically inhomogeneous, so it is good practice to not use this area for sensitive readings. An iris will also block any stray beam reflections from reaching the photodiode. A lens can help minimize the diameter of the beam before reaching the PD.
11. We position the power supply 1–2 m away from the board, after finding stray fields generated by the power supply coupled into the board’s electronics and produce unwanted line (60 Hz) noise. Albeit very small (~90 nV), this noise is especially deleterious since it coupled into the reference voltage used in the offset-amplifier, where the small noise was multiplied by a large gain and inferred as vertical motion.
12. PI corner is technically a misnomer in this design. The corner is actually between a single integrator (20 dB/decade) and a double integrator (40 dB/decade).
13. We have found it difficult to completely dissolve KOH pellets with more than 0.4 % potassium carbonate content.
14. An alternative way to prevent charging of an insulating substrate is to cover the substrate with a thin film of metal; we did this in early versions of the protocol. Specifically, we thermally evaporated a 15-nm layer of aluminum onto the resist, used the SEM to expose dots as usual, and then etched off the aluminum by soaking it in a solution composed of 80 mL phosphoric acid, 5 mL acetic acid, 5 mL nitric acid, and 10 mL distilled water for 10 s. After rinsing the coverslip with distilled water and nitrogen drying, we developed as usual.
15. We colloquially refer to this technique as “coloring in the slide,” since a firm bond will make the tape look darker. If the slide is not colored in, fluid in the channel can leak out through the air gaps between the tape and one of the glass surfaces. Also color the tape that overhangs the slide on one side of the coverslip, to make sure that fluid does not leak between the tape and the glass during buffer exchanges.
16. Faster communication can be achieved by using a protocol based on a field-programmable gate array (FPGA), as demonstrated in ref. [25].
17. If after centering the laser precisely with respect to the post, you move a post in  $z$  through the laser focus and observe large voltage changes in  $x$  and  $y$ , the beam is tilted with respect to the  $z$ -axis of the stage. Adjust the XYZ translator that is supporting the full fiber launch system from Subheading 3.4 to align the

optical axis to the  $z$ -axis of the stage, and so reduce this cross talk. Note this is not the same as moving the XY-position of the aspheric lens with respect to the fiber tip, which would not have the desired effect.

## Acknowledgments

We thank Carl Sauer for providing detailed electronic diagrams and associated files for the circuit boards. This work is supported by a National Science Foundation Graduate Research Fellowship (Grant No. DGE 1144083 to S.R.O.), a National Institute of Health Molecular Biophysics Training Grant awarded to S.R.O. (T32 GM-065103), the NSF (Phys-1125844), and NIST. Mention of commercial products is for information only; it does not imply NIST recommendation or endorsement, nor does it imply that the products mentioned are necessarily the best available for the purpose. T.T.P. is a staff member of NIST's quantum physics division.

## References

1. Svoboda K, Schmidt CF, Schnapp BJ, Block SM (1993) Direct observation of kinesin stepping by optical trapping interferometry. *Nature* 365:721–727
2. Finer JT, Simmons RM, Spudich JA (1994) Single myosin molecule mechanics: piconewton forces and nanometre steps. *Nature* 368:113–119
3. Abbondanzieri EA, Greenleaf WJ, Shaevitz JW, Landick R, Block SM (2005) Direct observation of base-pair stepping by RNA polymerase. *Nature* 438:460–465
4. Wen JD, Lancaster L, Hodges C, Zeri AC, Yoshimura SH, Noller HF, Bustamante C, Tinoco I (2008) Following translation by single ribosomes one codon at a time. *Nature* 452:598–603
5. Visscher K, Gross SP, Block SM (1996) Construction of multiple-beam optical traps with nanometer-resolution position sensing. *IEEE J Sel Top Quant Electron* 2:1066–1076
6. Neuman KC, Block SM (2004) Optical trapping. *Rev Sci Instrum* 75:2787–2809
7. Moffitt JR, Chemla YR, Smith SB, Bustamante C (2008) Recent advances in optical tweezers. *Annu Rev Biochem* 77:205–228
8. Lee W, Strumpfer J, Bennett V, Schulten K, Marszalek PE (2012) Mutation of conserved histidines alters tertiary structure and nanomechanics of consensus ankyrin repeats. *J Biol Chem* 287:19115–19121
9. Perkins TT (2014) Angstrom-precision optical traps and applications. *Annu Rev Biophys* 43:279–302
10. Pralle A, Prummer M, Florin E-L, Stelzer EHK, Horber JKH (1999) Three-dimensional high-resolution particle tracking for optical tweezers by forward scattered light. *Microsc Res Tech* 44:378–386
11. Denk W, Webb WW (1990) Optical measurement of picometer displacements of transparent microscopic objects. *Appl Opt* 29:2382–2391
12. Carter AR, King GM, Ulrich TA, Halsey W, Alchenberger D, Perkins TT (2007) Stabilization of an optical microscope to 0.1 nm in three dimensions. *Appl Opt* 46:421–427
13. Carter AR, Seol Y, Perkins TT (2009) Precision surface-coupled optical-trapping assays with 1 base-pair resolution. *Biophys J* 96:2926–2934
14. Wang MD, Yin H, Landick R, Gelles J, Block SM (1997) Stretching DNA with optical tweezers. *Biophys J* 72:1335–1346
15. Shaevitz JW, Abbondanzieri EA, Landick R, Block SM (2003) Backtracking by single RNA polymerase molecules observed at near-base-pair resolution. *Nature* 426:684–687
16. Peterman EJG, van Dijk MA, Kapitein LC, Schmidt CF (2003) Extending the bandwidth

- of optical-tweezers interferometry. *Rev Sci Instrum* 74:3246–3249
17. Paik DH, Perkins TT (2012) Single-molecule optical-trapping measurements with DNA anchored to an array of gold nanoposts. *Methods Mol Biol* 875:335–356
18. Candelli A, Wuite GJL, Peterman EJG (2011) Combining optical trapping, fluorescence microscopy and micro-fluidics for single molecule studies of DNA-protein interactions. *Phys Chem Chem Phys* 13:7263–7272
19. Bustamante C, Chemla YR, Moffitt JR (2008) High-resolution dual-trap optical tweezers with differential detection. In: Selvin PR, Ha T (eds) Single-molecule techniques. Cold Spring Harbor, New York
20. Moffitt JR, Chemla YR, Izhaky D, Bustamante C (2006) Differential detection of dual traps improves the spatial resolution of optical tweezers. *Proc Natl Acad Sci U S A* 103:9006–9011
21. Neuman KC, Abbondanzieri EA, Block SM (2005) Measurement of the effective focal shift in an optical trap. *Opt Lett* 30:1318–1320
22. Walder R, Paik DH, Bull MS, Sauer C, Perkins TT (2015) Ultrastable measurement platform: sub-nm drift over hours in 3D at room temperature. *Opt Express* 23:16554–16564
23. Capitanio M, Cicchi R, Pavone FS (2005) Position control and optical manipulation for nanotechnology applications. *Eur Phys J B* 46:1–8
24. Janshoff A, Neitzert M, Oberdorfer Y, Fuchs H (2000) Force spectroscopy of molecular systems - single molecule spectroscopy of polymers and biomolecules. *Angew Chem Int Ed Engl* 39:3213–3237
25. Churnside AB, King GM, Carter AR, Perkins TT (2008) Improved performance of an ultra-stable measurement platform using a field-programmable gate array for real-time deterministic control. *Proc SPIE* 7042:704205

# Chapter 5

## Implementation and Tuning of an Optical Tweezers Force-Clamp Feedback System

Michael Bugiel, Anita Jannasch, and Erik Schäffer

### Abstract

Feedback systems can be used to control the value of a system variable. In optical tweezers, active feedback is often implemented to either keep the position or tension applied to a single biomolecule constant. Here, we describe the implementation of the latter: an optical force-clamp setup that can be used to study the motion of processive molecular motors under a constant load. We describe the basics of a software-implemented proportional-integral-derivative (PID) controller, how to tune it, and how to determine its optimal feedback rate. Limitations, possible feed-forward applications, and extensions into two- and three-dimensional optical force clamps are discussed. The feedback is ultimately limited by thermal fluctuations and the compliance of the involved molecules. To investigate a particular mechanical process, understanding the basics and limitations of the feedback system will be helpful for choosing the proper feedback hardware, for optimizing the system parameters, and for the design of the experiment.

**Key words** Optical tweezers, Force clamp, PID controller, PID tuning, Kinesin, Single-molecule biophysics, Force spectroscopy

---

### 1 Introduction

Optical tweezers are frequently used to probe the mechanics of single biomolecular machines. To investigate their conformational changes, which are often fueled by and coupled to nucleotide hydrolysis, the molecules are immobilized on microspheres, which are trapped in the tightly focused laser beam of the optical tweezers (Fig. 1). For small microsphere displacements from the trap center, the force is proportional to the displacement according to Hooke's law. The proportionality constant—the spring constant—is called the trap stiffness. Thus, keeping on average the displacement constant results in a constant applied force: the molecule is under constant tension—the force is clamped. Such experiments are also called *isotonic* based on the terminology from muscle physiology where an isotonic contraction refers to a muscle's length change under constant tension as opposed to an isometric exercise, in

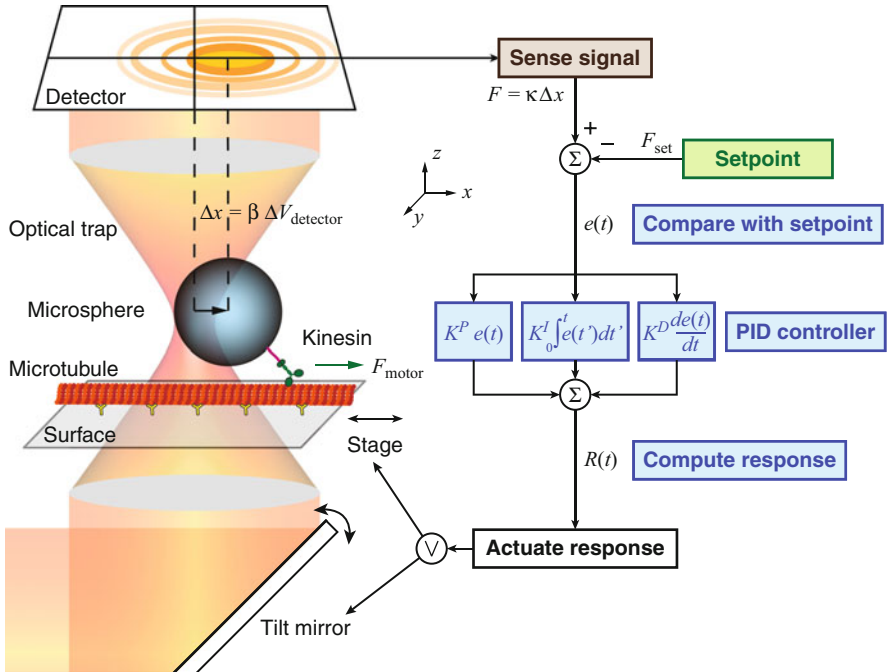


**Fig. 1** Schematic of a force-clamp feedback cycle for a kinesin-motor-protein experiment. The kinesin motor generates a force  $F_{\text{motor}}$ , which displaces the microsphere from the trap center. This displacement  $\Delta x$  causes the detector to generate a voltage  $\Delta V_{\text{detector}}$  proportional to the displacement with a displacement sensitivity  $\beta$ . In this manner, the trapping force  $F = \kappa \Delta x$  is sensed, where  $\kappa$  is the trap stiffness. The measured force is compared with the setpoint force  $F_{\text{set}}$  and the difference, the error  $e$ , is determined. Based on the error, the feedback response  $R$  is calculated by a PID controller (see text for details). Finally, any change in the desired force or displacement is compensated by moving the trap and microsphere relative to each other, e.g. by actuating a tilt mirror, an acousto-optic deflector, or a sample translation stage

which a muscle generates tension against an immobile object (e.g., [1]). Thus, during an *isometric* experiment the position of a molecular machine, such as a non-processive myosin, is clamped (see, e.g., [2–6]). Here, we will not consider isometric clamps further, but rather focus on the implementation of feedback loops for isotonic force clamps.

A feedback loop consists of the system under control with a desired system variable setpoint, a sensor, a controller, and an actuator that can change the state of the system (Fig. 1). To keep the applied force constant, the microsphere displacement is measured typically by a position-sensitive photodiode and multiplied by the calibrated displacement sensitivity and trap stiffness. This measured force  $F$  is compared with the desired setpoint force  $F_{\text{set}}$ . Based on their difference, the error signal  $e = F - F_{\text{set}}$ , a response is calculated by the controller to minimize the difference in the next measurement cycle. In the simplest case, the error is multiplied by a constant, the proportional gain  $K^P$ , and used as input for the actuator response such that  $F(e) = K^P e$ . Interestingly,

for such a simple controller, the error  $e$  can never be zero because otherwise the actuator response would result in a zero force  $F(e = 0) = 0 \neq F_{\text{set}}$ . Thus, the measured force can never reach the desired non-zero setpoint force. The remaining error is called the steady-state error—here it would be  $F_{\text{set}}/(1 + K^P)$ —and can be eliminated by adding an integral gain. In addition to avoiding a steady-state error, the response should be ideally as fast as possible. The response time is influenced by the choice of the controller, how it is tuned, the intrinsic delay of the feedback loop, and most importantly by the thermal noise of the system. Below, we discuss these feedback-loop related issues.

The first optical tweezers-based feedback systems have been applied to measure the movement and force production of muscle myosin in an isometric position clamp [2, 7]. Subsequently, instead of moving the laser beam, an isometric position clamp has been realized by modulating the laser power [8]. This system has been applied to study DNA mechanics and the translocation of RNA polymerase [8, 9]. The first isotonic force clamps have been used to measure the force–velocity relation of conventional kinesin (kinesin-1) [10] and soon afterwards of myosin-V [11]. Later on, the technology was applied to cytoplasmic dynein [12]. One advantage of a force clamp compared to a stationary trap is that under constant force, the size of molecular steps can be directly measured: the motor extension does not change during translocation, i.e. the compliance of the microsphere-filament linkage does not need to be accounted for [13, 14]. The first force clamps were implemented in one dimension with loads being applied in a direction opposing or assisting the motion of the molecular motor. Later on, the one-dimensional feedback has been extended to two [12, 15, 16] and three dimensions [16, 17]. One-dimensional force clamps have also been used to characterize RNA hairpin unfolding [18] and protein unfolding [19]. Since active feedback systems introduce extra noise, a passive force-feedback was developed [20] to resolve the single-base pair steps of RNA polymerase [21]. In the passive mode, the trap separation in a dual-trap was kept constant with one trap being operated at its maximum force for which the force-sensitivity, i.e. the derivative with respect to position, is zero. A constant trap separation—not under constant force—has been successfully applied for small conformational changes during protein unfolding [22, 23]. In recent years, faster feedback systems have been realized using field-programmable gate arrays (FPGAs). FPGAs are utilized to time-share traps, interlace them with fluorescence excitation, account for feedback delay times, or track fiducial markers for surface-stabilization and applications requiring ultra-stable instrumentation [24–26].

The remaining chapter is organized as follows: in Subheading 2, we first discuss the essential hardware components necessary for a force clamp and then briefly outline the optical tweezers setup and

experimental reagents for the employed single-molecule assays. In Subheading 3, we then explain the basic operation and implementation of a PID controller, how to determine the optimal feedback rate, and how to adjust the PID parameters. We conclude by discussing the extension of the one-dimensional feedback system into two- and three-dimensional force clamps and discuss more advanced controllers that make use of feed-forward control.

---

## 2 Materials

### 2.1 Essential Force-Clamp Components

Optical tweezers range from single-beam gradient traps (e.g., [27, 28]) via sophisticated dual-beam systems combined with various microscopy techniques (e.g., [24, 29]) to holographic optical tweezers (e.g., [30–33]). Here, the force clamp is implemented in a single-beam optical tweezers. The essential elements for a force-clamp feedback system are a detection unit, steering optics or a fast piezo-electric translation stage for the sample, and either an analog or digital feedback controller:

1. **Position detection.** Three-dimensional position detection may be achieved by (1) back-focal-plane interferometry [34, 35] or by direct imaging of the trapped particle on (2) a camera [36] or on a position-sensitive photodiode like a quadrant photo diode (QPD) [37]. The time response and position sensitivity is a key parameter when deciding on a detection method. While video detection has permitted the three-dimensional tracking of trapped microspheres in real time with sub-nanometer precision at more than 1 kHz bandwidth [36], it requires programming of a graphics processing unit (GPUs) and may not be fast enough for certain applications using FPGA-based controllers. Back-focal-plane interferometry is often the method of choice [34, 35]. Care needs to be taken in the choice of the photodiode when using infrared lasers so that unintended filtering does not reduce the desired bandwidth [38]. With a special detector, sub-nanometer position detection with more than 30 MHz bandwidth has been demonstrated [39].
2. **Sample movement and beam steering.** To create a relative movement between the sample and the trap, there are two possibilities: (1) moving the sample while keeping the laser trap stationary or (2) steering the laser focus relative to the stationary sample. To test and tune the feedback system, it is advantageous to have both possibilities available. Fast and precise three-dimensional sample movement is mostly realized by piezoelectric translation stages. The stage resolution depends on the scan range because a larger scan range is often achieved by a lever, which also amplifies the intrinsic noise of the piezoelectric transducer. Therefore, sub-nanometer resolution is often only

available for stages with a smaller scan range. Smaller scan-range stages are also mechanically stiffer, which results in a faster response time. For such stages, response times typically range between 1 and 10 ms. The working range of piezo stages is usually higher than that of beam-steering solutions.

Two-dimensional beam steering can be achieved by several technologies: galvanometric scanning mirrors (GSMs) [40, 41], piezo-tilt mirrors [27, 28, 42], acousto-optic deflectors (AODs) [12, 15, 43, 44], or electro-optic deflectors (EODs) [45]. All of these techniques have in common that they alter the angle of incidence of the laser beam when it enters the back aperture of the objective lens. If the device is positioned in a conjugate telecentric plane to the back-focal plane of the trapping objective, the pivoting of the beam around the back-focal plane is translated into lateral displacements of the optical trap focus in the sample plane without power loss. Apart from the costs (GSMs are cheaper compared to the other steering technologies), the devices differ in terms of their bandwidth, optical efficiency, and steering precision. The bandwidths of GSMs and piezo-tilt mirrors are on the order of 1 kHz and much slower compared to AODs and EODs, which can be operated up to a few 100 kHz. Nevertheless, a 1 kHz bandwidth is sufficient for most applications. While mirror-based systems hardly lose power, about 20 % and 50 % of power is lost when EODs and AODs are used, respectively [46]. Compared to AODs, EODs have a higher steering precision and their transmittance depends less on the angle of the incident light [44, 46]. A change in power as a result of a change in the angle of incidence leads to a variation in trap stiffness [44]. For mirror-based systems, the trap stiffness and displacement sensitivity hardly vary with angle (Fig. 2, *see Note 1*). Any deviation could potentially be corrected for, which for most practical applications is not necessary. Trapping parameter variation can also be avoided by using the sample stage as the actuator. Compared to AODs and EODs, GSMs have the lowest spatial precision and piezo-tilt mirrors the highest with a resolution of a few nrad. Independent of the device used for trap steering, if the actuation is controlled by a computer-controlled analog signal, the bit resolution of the analog output may limit the resolution (*see Note 2*).

3. **Feedback controller.** Feedback controllers can be either analog or digital. Analog controllers are mostly PID controllers, which have a high bandwidth and hardly any delay times. However, tuning of the controller and switching it from open to closed loop may be more complicated. Digital controllers or programmable logic controllers are software based and can, therefore, be more advanced than a simple PID controller. The digital control requires the communication with an analog-to-digital converter

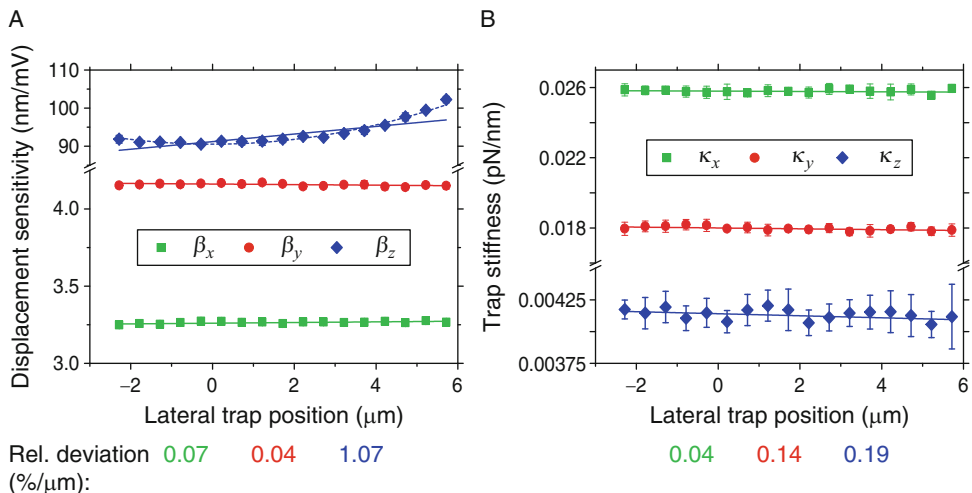


**Fig. 2** Dependence of the calibration factors on the lateral trap position. **(a)** Displacement sensitivity and **(b)** trap stiffness for a 590 nm polystyrene microsphere as a function of the lateral trap position for the  $x$  (squares),  $y$  (circles) and  $z$  (diamonds) direction. The lateral trap position was controlled by changing the beam steering angle using a tilt mirror. The *solid lines* are linear fits. All slopes were small but statistically different from zero. Data points are mean values of six measurements; error bars are standard deviations. A parabola was fit to  $\beta_z$  (*dotted line*), its minimum position defining the zero position. The relative deviations for  $x$ ,  $y$ , and  $z$  (based on the linear fits) in percent per  $\mu\text{m}$  in absolute values are given below the graphs

for the input and a digital-to-analog converter for the output. The communication and conversion may lead to delay times, which are minimized for real-time or FPGA-based systems. Many feedback applications do not require a real-time system. Using standard software like LabVIEW (National Instruments, Austin, TX) with no dedicated real-time hardware running on a general-purpose operating system like Windows or Linux, feedback rates of a few kHz can be achieved.

Another factor that may limit the overall performance and feedback rate is the dead time. The dead time is caused by transport effects, e.g. the conduction or diffusion of heat for a temperature control [28], instrument lag, or the time it takes to sample and analyze the data. The latter may be limiting for video-based particle tracking [36]. For photodiode-based detection, using state-of-the-art components, force-clamp systems typically have a dead time on the order of a few tens of microseconds or less. Because this dead time is small compared to the typical response time of the system (*see* Subheading 3.3 for how fast the response time is), it is negligible and we will not consider it further.

## 2.2 Optical Tweezers Setup

The force-clamp measurements shown in this chapter are performed with a single-beam gradient trap described in detail in [28, 47]. A brief description follows:

1. Expand an infrared laser (5 W at 1064 nm) and guide it through various optics to the trapping objective (CFI S Fluor 100×/0.7–1.3 oil objective, Nikon).
2. The detection of the trapped microsphere is realized by an identical objective and a quadrant photodiode (QP154-Q-HVSD, Pacific Silicon Sensors, Westlake Village, CA) placed in a plane conjugate to its back-focal plane.
3. The temperature of the two objectives is kept constant at  $29.200 \pm 0.001$  °C [28].
4. The sample position is controlled in three dimensions by two piezo translation stages: (a) a long-range travel, piezo-inertial drive ( $8 \times 8 \times 3.5$  mm in  $x$ ,  $y$ , and  $z$ , respectively; MS30,15, MechOnics) and (b) a nanopositioning stage ( $30 \times 30 \times 10$  μm, P-733.3DD, Physik Instrumente, Karlsruhe, Germany).
5. The laser focus can be controlled dynamically relative to the imaging plane of the objective in two dimensions. The movement is performed by a two-axis piezo tilt-mirror (Nano-MTA2/2X, MadCity Labs, Madison, WI) placed in a conjugate telecentric plane to the back-focal plane of the objective.
6. The whole setup is controlled via custom-written software programmed in LabVIEW (National Instruments, Austin, TX).
7. Calibration procedures were described previously [27, 48].

In surface-coupled assays, the setup has near Å resolution in three dimensions [28].

### **2.3 Single-Molecule Assay**

Some of the force-clamp tuning experiments were performed with kinesin motors under single-molecule conditions. Kinesin-coated microspheres, microtubules, and flow cells were prepared following standard procedures with established protocols [16, 49, 50]:

1. Attach GFP-tagged kinesins to polystyrene microspheres via anti-GFP antibodies and a polyethylene glycol (PEG) linker. The PEG linker helps to preserve functionality of the motor and prevent non-specific interactions. The detailed protocol is described in [50].
2. Prepare taxol-stabilized microtubules: mix 4.8 mg/ml tubulin, 1 mM GTP, 4 mM MgCl<sub>2</sub>, and 4.8 % DMSO in BRB80 (80 mM PIPES/KOH pH = 6.9, 1 mM MgCl<sub>2</sub>, 1 mM EGTA) and incubate the mixture for 1 h at 37 °C.
3. Afterwards, dilute the microtubules in BRB80 containing 10 μM taxol (BRB80T) and spin them down in a Beckman Airfuge with 100,000 g-force.
4. Incubate the flow cell with tubulin antibodies.
5. Block the rest of the surface by 1 % Pluronic F-127.

6. Resuspend the microtubules in BRB80T and immobilize them on the sample surface via the tubulin antibodies in the flow cell.
7. Dilute kinesin-coated microspheres in motility solution and flush them into the flow cell channel. The motility solution for yeast kinesin-8, Kip3, consisted of BRB80 with 112.5 mM KCl, 0.1 mg/ml casein, 1 mM Mg-ATP, and an anti-fade cocktail (0.5 %  $\beta$ -mercaptoethanol, 20 mM glucose, 20  $\mu$ g/ml glucose oxidase, 8  $\mu$ g/ml catalase).
8. Using the optical tweezers, a trapped microsphere was placed on top of a microtubule to await a kinesin–microtubule interaction. Single-molecule conditions were achieved by following Poisson statistics [51].
9. For tuning experiments of the feedback, bind the kinesin-coated microspheres to the microtubule using the non-hydrolyzable ATP analogue AMPPNP in the motility solution instead of ATP. AMPPNP binds kinesins to microtubules very tightly [52].

### 3 Methods

In this section, we describe the basics of a PID controller, the tuning procedure for good feedback parameters, and provide a rough guideline for programming the controller. Implementing and tuning a feedback system are crucial requirements for working with an optical tweezers force clamp. The following explanations are for a one-dimensional feedback, but can be expanded to two and three dimensions in a similar fashion.

#### 3.1 Basics of a PID Controller

A PID controller is one of the most common feedback loop control mechanisms. Related controllers are less common (*see Note 3*). There is a vast amount of articles, reviews, and books on the topic (for an introduction *see*, e.g., [53–57]). A PID controller continuously calculates a response from the error  $e$ —the difference between the desired setpoint and process variable. The process variable in an optical tweezers-based force clamp is the force experienced by the microsphere in the laser focus. Over a limited range, this force is proportional to the microsphere displacement, which can be measured with high accuracy (*see Subheading 2.1*). For a quantitative analysis, a calibration of the optical trap, which depends on the microsphere size, its composition, the laser power, and the proximity to nearby surfaces [27, 48], is essential. In case of the commonly used back-focal-plane detection, the photodiode voltage needs to be converted to displacement units and the corresponding force. Once the process variable—the measured force—is known, the PID controller response is calculated as a sum of three components:

1. The proportional response  $r^P(t)$  is proportional to the error

$$r^P(t) = K^P \cdot e(t), \quad (1)$$

where  $K^P$  is the coefficient for the proportional gain. If  $K^P$  is too small, the error is only slowly compensated. Thus, the controller has a slow response. If  $K^P$  is too large, the error is overcompensated. In the subsequent feedback cycle, the error will have changed its sign and the controller will overcompensate the error in the opposite direction and so on. In this manner, the system will start to oscillate. As pointed out in the introduction, using solely a proportional controller—even with an optimal value of  $K^P$ , the desired setpoint is never reached. There always remains a finite difference between the setpoint and the process variable, the so-called steady-state error. Therefore, proportional control is usually not used alone.

2. For the integral response  $r^I(t)$ , all errors are summed up from the beginning until the time  $t$

$$r^I(t) = K^I \cdot \int_{t_0}^t e(t') dt', \quad (2)$$

where  $K^I$  is the coefficient for the integral gain. For a positive error, this error sum response increases with time unless the error becomes zero. Therefore, this response is able to eliminate the steady-state error. If  $K^I$  is too small, the elimination is slow, increasing the overall response time of the feedback loop. If  $K^I$  is too large, an overshoot and/or oscillations develop. Large overshoots and/or output limitations of the controller can cause a long relaxation time before the setpoint is reached. In particular for situations that cause a large error (a large setpoint change or a large and fast movement of the molecular machine), the integral error may wind up to such a large integral response value that even when the error has switched sign it will take a long time until the overshoot is compensated by the controller. This phenomenon is called integral windup. It can be avoided by anti-windup filters [56].

3. For the derivative response  $r^D(t)$ , the time derivative of the error is calculated according to

$$r^D(t) = K^D \cdot \frac{de(t)}{dt}, \quad (3)$$

where  $K^D$  is the coefficient for the derivative gain. The derivative response gives information on how fast the error is changing and can therefore be used for an extrapolation of how the error will change. Because this extrapolation predicts the state of the system for the next cycles of the feedback loop, a correctly tuned  $K^D$  value can speed up the response of the controller in the sense that it reduces the amplitude of both the overshoot

and subsequent oscillations that occur after a step response. To understand this behavior intuitively, it is useful to consider that the error is equal to the (constant) setpoint minus the process variable. Therefore, the error's time derivative is equal to the negative derivative of the process variable (the derivative of the setpoint is zero). Thus, the derivative term counteracts large slopes or changes in the process variable, which occur after a step response or during oscillations. In this manner, the overshoot and oscillations are damped out faster, reducing the overall settling time. However, since derivatives are susceptible to noise, a large  $K^D$  value can amplify the system noise or even destabilize the controller. Thus, in particular for single-molecule assays, for which Brownian motion is a dominant noise source, derivative control needs to be carefully tuned. Derivative control may not be useful for every feedback system. Alternatively, to reduce the impact of noise, a derivative filter can be added to the controller [58].

The overall response of a PID controller is summed up to

$$\begin{aligned} R(t) &= r^P(t) + r^I(t) + r^D(t) \\ &= K^P \cdot e(t) + K^I \cdot \int_{t_0}^t e(t') dt' + K^D \cdot \frac{de(t)}{dt}, \end{aligned} \quad (4)$$

or in another notation

$$R(t) = K^P \left( e(t) + \frac{1}{T_I} \cdot \int_{t_0}^t e(t') dt' + T_D \cdot \frac{de(t)}{dt} \right) \quad (5)$$

with an overall gain factor  $K^P$  and time constants  $T_I$  and  $T_D$  for the integral and derivative term. In the following, we use the first notation (Eq. 4). How to set “good” values for  $K^P$ ,  $K^I$ , and  $K^D$  is explained in Subheading 3.4. Prior to this, we will discuss the implementation of the controller and the choice of the optimal feedback rate.

### 3.2 Implementing a PID Controller

A digital PID controller can be implemented in any software that can communicate with the required hardware. Many hardware-control platforms (e.g., LabVIEW) provide ready-made subroutines that enable the user to quickly use PID control. Independent of the choice of software, Fig. 3 illustrates the basic flowchart for a force clamp briefly described below:

1. First, the user needs to provide some system parameters such as the sampling and feedback rates (*see Note 4*) and the sensitivities for the actuator (here a piezo-tilt mirror).
2. Before engaging the feedback, the user also needs to input a number of parameters that are specific to the trapped particle

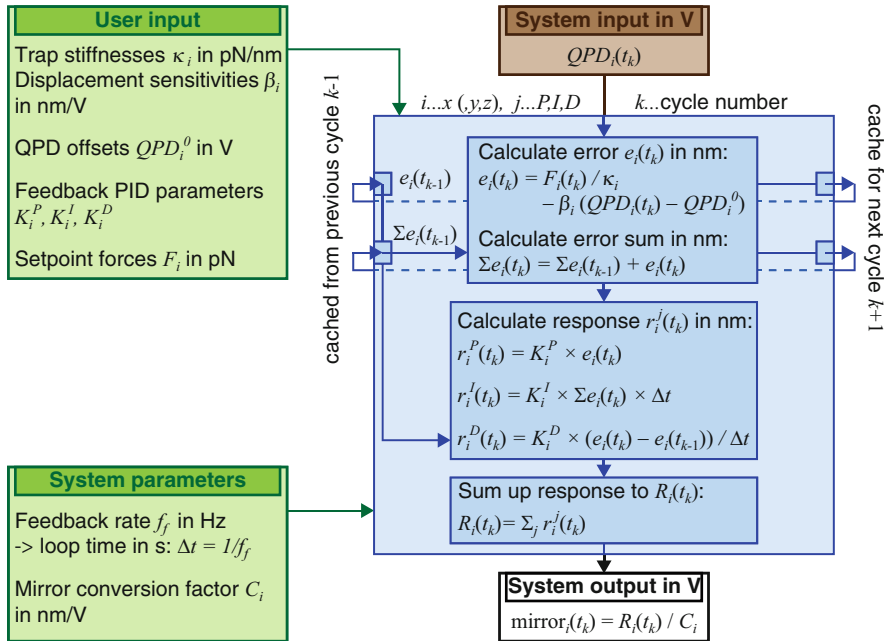


**Fig. 3** Program flowchart for one feedback cycle. The chart includes input parameters and calculations for a digital controller. Color coding is the same as in Fig. 1. Here, a piezo-tilt mirror is used as actuator and a quadrant photodiode (QPD) as a position sensor. The index  $i$  stands for the directions ( $x, y, z$ )

and experiment. For each dimension, here indicated by the subscript  $i$ , the following parameters are needed: the trap stiffness, the displacement sensitivity, any offsets that the position detector, here a QPD, may have (in particular when using the  $z$ -direction), the PID parameters, and the setpoint force. By choosing different values for  $F_x$  and  $F_y$ , one can apply loads in the  $xy$ -plane with an arbitrary angle.

3. Once all parameters are given, the force clamp can be activated. The activation can be done manually or automatically once the molecular machine has generated a user-defined threshold force.
4. During one cycle of the closed-loop operation, first, the process variable—here the QPD voltage—is read in. Whether the error is calculated in units of voltage, displacement, or force is arbitrary. We chose to calculate it in displacement units because the information we are interested in are the displacements that the molecular machine generates under a constant force. To this end, we subtract the QPD offset voltage from the current QPD value and multiply this difference by the respective displacement sensitivity to convert the voltage to a displacement. We convert the force setpoint to a displacement setpoint by dividing it by the trap stiffness. The difference between the displacement setpoint and the current QPD displacement reading is the error in nanometers.

5. In addition to the current error, we calculate the cumulative error by an addition to the previous sum of errors that was passed on from the previous feedback cycle.
6. Then, the response of the PID controller is calculated as outlined in Subheading 3.1.
7. Finally, the response is converted to a voltage, which is sent as output to the actuator, here to adjust the mirror position (*see Note 5*).

The loop usually repeats until the molecular machine detaches, the actuator reaches its maximal range, or the user terminates the clamp. After termination, it is advisable that the trap is automatically returned to its starting position by a user-defined speed that is small enough so that the drag force does not cause a loss of the trapped particle.

For the subsequent data analysis, the actual microsphere position for the direction  $i$  in nm is calculated according to

$$\begin{aligned} \text{microsphere position}_i &= \text{mirror position}_i - \text{displacement}_i \\ &= C_i \cdot \text{mirror}_i^{\text{sensor}} + e_i - F_i/\kappa_i \\ &= C_i \cdot \text{mirror}_i^{\text{sensor}} - \beta_i \cdot (\text{QPD}_i - \text{QPD}_i^0), \end{aligned} \quad (6)$$

where  $\text{mirror}_i^{\text{sensor}}$  is the actual mirror position read from its monitor signal in volts,  $C_i$  the mirrors' volts-to-nm converting factor, and  $\text{QPD}_i^0$  are the offsets on the QPD. The displacement term should on average be a constant. When large deviations occur, such as a large step, the applied force is not constant. During these times, care must be taken as motor displacements may be attenuated if length changes of the compliant motor-microsphere linkage occur. However, the microsphere position is always accurately known according to the above equation and sharp steps and transitions can be observed even for slow feedback loops (*see Note 6*).

### 3.3 Feedback Rate

For an optimal feedback performance, the choice of the feedback rate  $f_f$  or the loop time  $\Delta t = 1/f_f$  at which the actuator is updated is important. If the feedback rate is too low, the force clamp may be too slow to follow the motion of the molecular machine, leading to a deviation from the force setpoint. If the feedback rate is too fast, the force clamp tracks the Brownian motion of the microsphere. Even though the force fluctuations are still reduced if the Brownian motion is tracked, the reduction occurs at the cost of larger positional fluctuations of the actuator [25], resulting in an overall higher noise on the experimental readout (Eq. 6). Thus, there must be an optimal feedback rate.

The optimal rate is primarily determined by the response time of the microsphere. If the molecular motor performs a step, the

drag on the microsphere prevents an instantaneous response. The response of the microsphere and, therefore, of the feedback is limited by the autocorrelation time constant  $\tau_c = \gamma/\kappa = 1/(2\pi f_c)$  of the trapped and filament-tethered microsphere, where  $\gamma$  is the drag coefficient of the microsphere,  $f_c$  the corner frequency of the microsphere's Lorentzian-like power spectral density [48], and  $\kappa$  the effective spring constant—approximately the sum of the trap stiffness and inverse linker-motor compliance [59, 60]. If the motor takes a step, the microsphere has reached  $1 - 1/e \approx 63\%$  of its new equilibrium position after one correlation time. The user needs to decide how aggressive the feedback should run. Generally, a conservative feedback loop is operated with  $\Delta t \approx 10\tau_c$ , a moderate with  $\Delta t \approx \tau_c$ , and an aggressive one with  $\Delta t \approx 0.1\tau_c$  [58]. For single-molecule assays, feedbacks are usually desired to track the molecules as fast as possible with the lowest amount of noise. For lowest-noise performance, the feedback should be operated with a rate about equal to the corner frequency  $f_f \approx f_c$  [25], which is between moderate and conservative tuning. For fast motors, a more aggressive tuning might be desirable such that the actuator response does not have large steps between feedback cycles. In addition to a more aggressive tuning, it is advisable to reduce the autocorrelation time constant by increasing the trap stiffness as much as possible and decreasing the drag coefficient by using smaller microspheres. Optimal feedback rates are often in the lower kHz range. The combined stiffness of the motor and linkage to the microsphere depends on the applied load and is typically in the range of 0.01–0.1 pN/nm [16, 60]. The chosen trap stiffness for many single-molecule assays has a similar range. Using this range, the corner frequency for a 1-μm-diameter microsphere is about 0.2–1.7 kHz. To increase the bandwidth and decrease the response time, smaller microspheres, which have a smaller drag coefficient, are often used. However, when working close to a surface, e.g. during a kinesin experiment, the drag coefficient parallel to the surface can increase more than twofold [27]. Taking an increased drag into account even when using smaller microspheres, the corner frequency and, therefore, the optimal feedback rate during a single-molecule experiment is typically a few hundred Hz up to a few kHz. Figure 4 illustrates the decrease in corner frequency when working close to a surface. In Fig. 4a, an example of the power spectral density of a trapped microsphere far away from a surface is shown. When the same kinesin-decorated microsphere is bound to a surface-immobilized microtubule via the kinesin, the corner frequencies for the lateral directions are smaller and for the axial direction larger compared to the free microsphere far away from the surface, making all three corner frequencies nearly equal (Fig. 4b). The power spectral density of the microsphere movement in Fig. 4b was acquired in the absence of a force. Thus, the lower lateral frequencies are mainly due to the increased

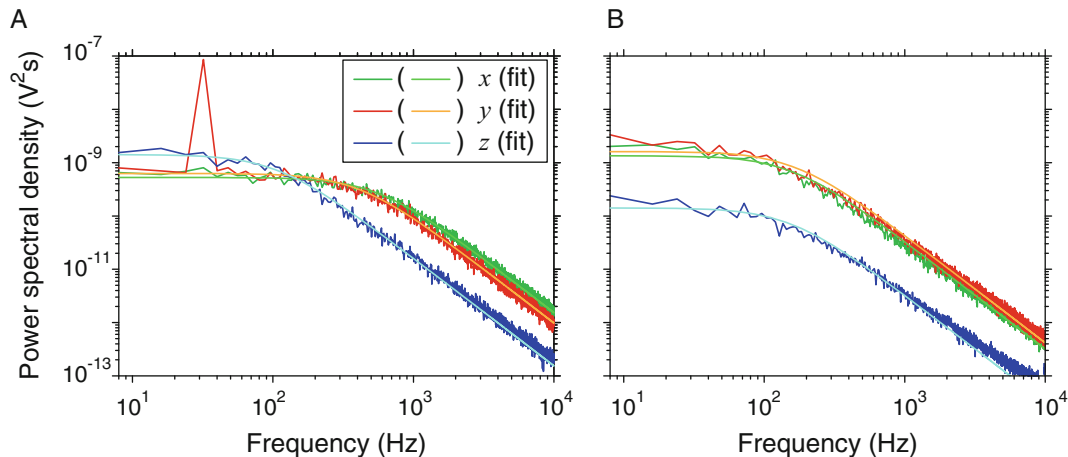


**Fig. 4** Power spectral densities for a free and filament-tethered microsphere. A 590 nm-diameter, kinesin-8-decorated [16, 49] polystyrene microsphere was, first, (a) trapped at a height of 2  $\mu\text{m}$  above the surface. Subsequently, the power spectral density of its motion was recorded featuring a peak for calibration purposes [27, 48]. Afterwards, (b) the same microsphere was bound via kinesin to a surface-immobilized microtubule in the presence of AMPPNP. According to the increase in the drag, the height of the bound microsphere can be estimated to be 53 nm above the surface. The trap stiffness was 0.023 pN/nm, 0.018 pN/nm, and 0.006 pN/nm for x, y, and z, respectively. For the respective directions, the Lorentzian fits resulted in corner frequencies of 673 Hz, 530 Hz, and 138 Hz in (a) and 159 Hz, 165 Hz, and 153 Hz in (b)

drag close to the surface and in part due to a rotational coupling. The kinesin-tethered microsphere performs a pendulum motion in the lateral direction for which the pendulum motion is limited by the trapping potential similar to magnetic tweezers experiments with DNA-tethered microspheres. The coupling increases the effective drag given by the sum of the translational and rotational contributions [61]. The increased axial corner frequency is a result of a larger motor-linker stiffness, which over-compensates the increase in the axial drag coefficient. The increase in the axial drag is significantly larger compared to the lateral direction [27]. A higher corner frequency and faster response time is reached in high-force assays. For example, increasing the laser power and, therefore, the trap stiffness by about sixfold to  $\approx 0.1$  pN/nm results in a corner frequency of about 1 kHz. Also, the corner frequency increases when an applied load pulls the motor-microsphere linkage taut as a result of the nonlinear compliance (*see* Subheading 3.4.2 below). Thus, a feedback rate smaller or about equal to 1 kHz is sufficient for many single-molecule assays. For these feedback rates, fast acousto- or electro-optic modulators may not be necessary. Once the optimal feedback rate is determined, one can proceed with the tuning of the PID parameters.

### 3.4 PID-Parameter Tuning

There are many ways to tune and choose PID parameters and the best choice usually depends on the application. For most single-

molecule assays, a fast response is often desired. However, a fast response typically implies a larger overshoot and less stability against disturbances or nonlinearities that may be caused by changes in the setpoint. Initial tuning and testing of the controller and force clamp can be done by tracking the motion of surface-immobilized microspheres. Fine-tuning should be done under conditions that mimic the experiment by using, for example, conditions that lead to a rigor binding of the molecular machine to its substrate; the linker that connects the motor to the microsphere adds compliance to the system and increases the overall response time. The motion of the rigor-bound machine can then be mimicked by computer-controlled movements of the sample using, for example, a piezo-electric translation stage with nanometer precision. If such a stage is not available, the feedback loop can be tested by stepwise changes of the setpoint.

For the tuning of the PID loop, we use the Ziegler–Nichols tuning method [62], which is a heuristic method and one of the most frequently used methods of tuning PID controllers, supplemented by trial-and-error fine-tuning. Because the response times are typically on the millisecond time scale, this fine-tuning is a fast way to achieve the desired feedback behavior (*see Note 7*). In the Ziegler–Nichols method, the parameters  $K^I$  and  $K^D$  are set to zero and  $K^P$  is increased until a critical value is reached for which the system maintains an oscillation with a constant amplitude after a step response. Subsequently, optimal PID parameter values are calculated from the critical proportional gain and the period of the oscillation. In the literature, different improvements and expansions of the Ziegler–Nichols method can be found [55, 63]. For systems that have relatively large dead times, other methods like the Cohen–Coon method [58, 64] are in use.

### 3.4.1 Tuning with Immobilized Microspheres

1. Microspheres can be immobilized on unmodified glass surfaces as a result of attractive van-der-Waals interactions, which outweigh electrostatic repulsions if surface charges are sufficiently screened [27]. To this end, microspheres should be suspended in deionized water supplemented with a high salt concentration, e.g. of 100 mM KCl.
2. Subsequently, a microsphere is trapped and calibrated near the surface [27, 48] to determine the following user input parameters (Fig. 3): the trap stiffness, the displacement sensitivity, and the QPD offsets.
3. Then, the microsphere-surface distance is reduced until the microsphere makes a sudden jump towards the surface. Once in contact, the microsphere and surface tightly interact, immobilizing the microsphere (*see Note 8*).
4. Apply a stepwise motion to the sample using the piezo-electric translation stage. Alternatively, change the setpoint periodically.

Ideally, the step size and stepping rate should be similar to the expected behavior of the molecular machine. For example, the velocity of the kinesin-8 Kip3 that we use here as an example motor is known from single-molecule fluorescence measurements to be about 40 nm/s [65]. For kinesin with a step size of 8 nm [13], this speed corresponds to an average stepping rate of 5 Hz. It is convenient to apply the stepwise motion in form of a square wave instead of a continuous series of mono-directional steps. In this manner, the testing range does not exceed the range of the optical trap and the actuator.

5. Set the value for  $K^I$  and  $K^D$  to zero and gradually increase  $K^P$  until the system becomes unstable. While increasing  $K^P$ , the overdamped response to the step first becomes faster. Then, an overshoot develops until the response eventually starts to oscillate. Ideally, increase  $K^P$  until the oscillations neither increase nor decrease in amplitude. We call this  $K^P$  value the critical gain  $K_c$ .
6. Determine the oscillation period  $t_c$  for  $K^P = K_c$ .
7. Reduce the proportional gain by about 30–50 % to  $K^P \approx 0.6K_c$ , set the integral gain to  $K^I \approx K_c/t_c$  and the derivative gain to  $K^D \approx \frac{1}{16}K_c t_c$ .
8. Check whether the step response is as desired. If not, vary the individual parameters by about  $\pm 20\%$ . A higher variation may be necessary for the integral and derivative gain.
9. For a multidimensional feedback, repeat this procedure separately for the other directions.

Figure 5 illustrates the effect of fine-tuning the parameters using a rather large step of 50 nm. For initial testing, a larger step has the advantage of a higher signal-to-noise ratio. If the proportional gain  $K^P$  is too high, the system oscillates. If the value is too small, the response is very slow (Fig. 5a). The oscillation period is comparable to the oscillation period with the critical gain. For the data shown, the critical gain was  $K_c \approx 1.5$  with an oscillation period of  $t_c \approx 0.01$  s. With these values, the optimal parameters, according to the Ziegler–Nichols method, are:  $K^P \approx 1$ ,  $K^I \approx 150\text{ s}^{-1}$ , and  $K^D \approx 0.001$  s. The integral control eliminates the steady-state error. The optimal  $K^I$  value causes an overshoot (Fig. 5b). Because the feedback performance is stable over a broad range of  $K^I$  values with only a small compromise with respect to the response time, we typically reduce the integral gain significantly until the overshoot disappears. As pointed out in Subheading 3.1, the derivative gain reduces the amplitude of the oscillatory response (Fig. 5c). If the derivative gain is too high, noise and oscillations are amplified. In summary, the choice of the optimal parameters, in particular the integral gain, depends on the experimental conditions and can be

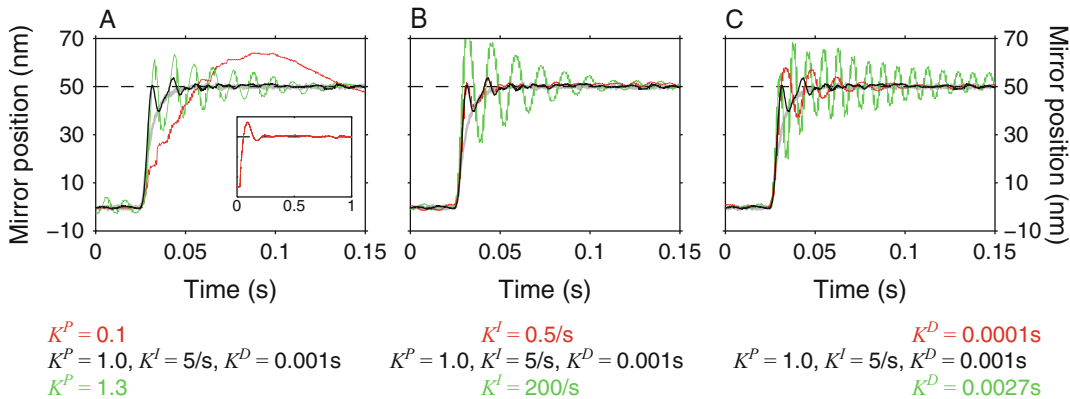


**Fig. 5** Tuning of PID parameters. The feedback response to a 50 nm step of a 590 nm-diameter microsphere is plotted for different PID parameters. The step (gray dashed line) with a rise time of 15 ms (time between 10 and 90 % of the step amplitude) was generated by a 50-nm displacement of the sample stage. Relative to the optimal parameters (response in black), parameters were decreased (red curve) or increased (green, oscillatory curve). Parameter values are indicated below the graphs. (a)  $K^P$ , (b)  $K^I$ , and (c)  $K^D$ . Inset in (a): Feedback response at a longer time scale for the low  $K^P = 0.1$  value showing that the system eventually settles to the new position

quickly fine-tuned by gradually changing the individual parameters until the desired response is achieved.

Note that the values for the integral and derivative gain depend on the feedback rate. Thus, if, for example, a different microsphere size is used or a different amount of tension is applied such that the corner frequency and optimal feedback rate change,  $K^I$  and  $K^D$  need to be adapted. In the discrete calculation of Fig. 3, the integral and derivative gain are proportional and inverse proportional, respectively, to the loop time  $\Delta t$ . If  $K_1^I$  and  $K_1^D$  are optimized for the feedback rate  $f_{f,1}$  as described in Subheading 3.3, new values  $K_2^I$  and  $K_2^D$  can be calculated for a new rate  $f_{f,2}$  according to

$$K_2^I = K_1^I \frac{f_{f,2}}{f_{f,1}} \quad \text{and} \quad K_2^D = K_1^D \frac{f_{f,1}}{f_{f,2}}. \quad (7)$$

For example, if the feedback rate is increased twofold, the parameters  $K^I$  and  $K^D$  should be increased and decreased twofold, respectively, to have a well-tuned force clamp.

Once the trial-and-error fine-tuning is finished, the force clamp is operational and can be tested. Figure 6 shows an example in which 5 nm-large steps were followed with a zero load. The individual steps were clearly resolved. The force was constant with an rms noise of 0.01 pN. Because the overall system is eventually nonlinear, the optimal PID parameters may depend on the step size and vary with time [58]. The displacement sensitivity and trap stiffness depend on the displacement from the trap center and may depend on the position of the actuator. Drift may also affect these

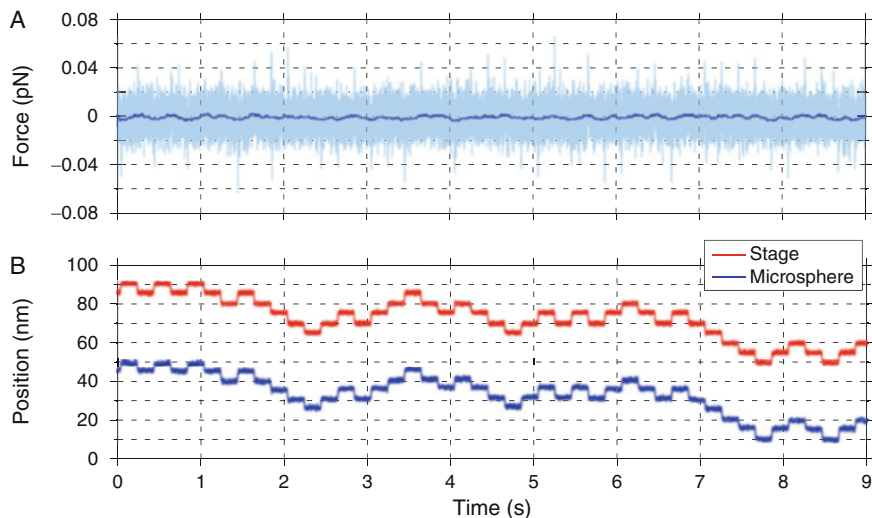


**Fig. 6** Test experiment with surface-immobilized microspheres. The optical trap follows successfully an immobilized microsphere that moved in 5 nm steps with a random direction and stepping rate of 5 Hz. (a) Force based on QPD signal (*light-blue*: 4 kHz, filtered by a running median filter to 8 Hz). (b) Applied motion of the stage (*red*, top trace) and actuator response of the mirror minus displacement (Eq. 6, *blue*, bottom trace). The traces are depicted with an offset for clarity and displayed with a 4 kHz sampling rate. PID values:  $K^P = 0.9$ ,  $K^I = 0.5 \text{ s}^{-1}$  and  $K^D = 0.0025 \text{ s}$

parameters. These effects lead to a variation in the response time of the feedback system. To prevent instabilities, parameters should be tuned accordingly, i.e. the most aggressive tuning might not be optimal. In our system, lower  $K^P$  values were required for smaller step sizes with a reduction of the  $K^P$  value of about 10–30 % when reducing the step size from 50 to 5 nm. Since surface-immobilized microspheres have a much smaller response time compared to the response time in single-molecule experiments with compliant biomolecular motors, tuning needs to be repeated under conditions that mimic the experiment, in our case a kinesin assay.

### 3.4.2 Tuning with Kinesin-Bound Microspheres

1. Prepare a sample as described in Subheading 2.3 using the non-hydrolyzable ATP analog AMPPNP instead of ATP. In the presence of AMPPNP, kinesin binds to microtubules in a rigor state.
2. To ensure single-molecule conditions, the ratio between microspheres and kinesins should be chosen such that according to Poisson statistics only 1 out of 3–4 microspheres shows motility in the presence of ATP (Subheading 2.3).
3. Trap a microsphere, calibrate the trap, and determine the QPD offsets as before (Subheading 3.4.1).
4. Place the microsphere on an immobilized microtubule until it binds. If it does not bind, choose another microsphere.

5. Choose the desired force setpoint and move the sample relative to the trap to apply the desired load.
6. Measure the corner frequency of the microsphere's power spectral density or its autocorrelation time and set the optimal feedback rate (Subheading 3.3).
7. While applying the desired force, tune the PID parameters in the same manner as for surface-immobilized microspheres (Subheading 3.4.1). For the kinesin assay, we typically have a two- to tenfold smaller proportional gain compared to surface-immobilized microspheres. The optimal PID parameters may depend on force. Also, if the feedback rate is too fast, the noise on the error signal may be too large. In this case, the derivative gain may have to be set to zero.

Once the optimal parameters are found, the force clamp can be tested. Figure 7 shows an example in which a 1D force clamp followed simulated steps of 8 nm and a random direction at a stepping rate of 5 Hz. Most steps could be still resolved under a load of 1.1 pN using an unbiased step detector [66]. The average detected step size was  $8.2 \pm 0.3$  nm (SEM,  $N = 47$ ). For a better resolution, the applied force can be increased to decrease the compliance of the linker.

The compliant linker between the microtubule-bound kinesin-motor heads and the microsphere increases the

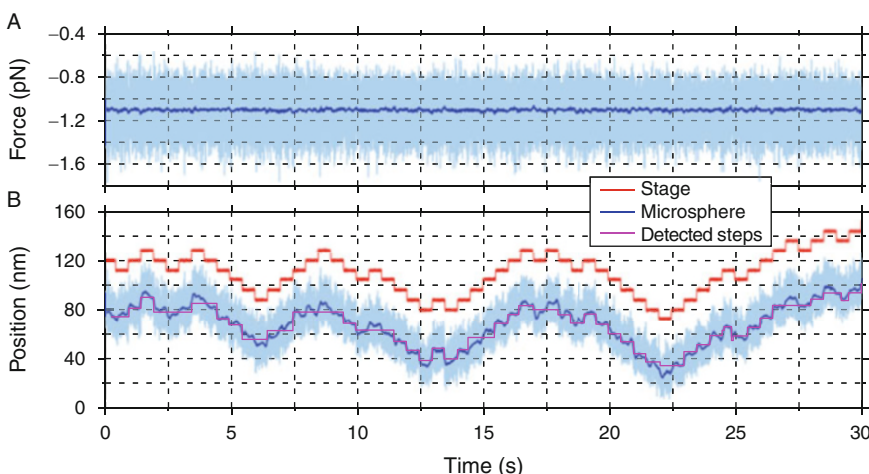


**Fig. 7** Test experiment that mimics experimental conditions. The force clamp successfully followed a microsphere—anchored to a surface-bound microtubule via a kinesin motor in the presence of AMPPNP—that was moved in 8 nm steps in a random direction by the sample stage with a stepping rate of 5 Hz. (a) Force as a function of time (light-blue: 4 kHz, filtered by a running median filter to 8 Hz). The setpoint was 1.1 pN. (b) Applied motion of the stage (red, top trace) and actuator response of the mirror added to the positional signal from the QPD (Eq. 6, blue, bottom trace) overlaid with the detected steps (magenta line). The traces are depicted with an offset for clarity and displayed with a 4 kHz and 8 Hz bandwidth. PID values:  $K^P = 0.1$ ,  $K^I = 0.1 \text{ s}^{-1}$ , and  $K^D = 0$

autocorrelation time of the trapped microsphere and therefore the overall response time thereby reducing the feedback rate (see Subheading 3.3). However, since the linker is an entropic spring, the compliance decreases with load, which in turn reduces the response time and the fluctuations both on force and position. Thus, the resolution of the force clamp improves with load. We demonstrate this behavior in Fig. 8. As the setpoint force is increased, the fluctuations of the force setpoint decrease (Fig. 8a). With loads up to 4.5 pN, the standard deviation of the fluctuations was reduced by more than tenfold compared to the zero-force value. The reduction in the force fluctuations is correlated with a reduction in positional fluctuations such that steps—invisible at low force—are resolved at a higher force (Fig. 8b). The higher positional resolution is due to the increased linker stiffness. Long compliant linkers like DNA [67] or PEG [50] reduce the positional resolution. To achieve the highest resolution, linkers should be kept short and, as pointed out in Subheading 3.3, microspheres as small as possible.

### 3.5 Two-Dimensional Feedback, Fast Alternating Loads and Feed-Forward Control

The extension to a two-dimensional (2D) force clamp is straightforward and broadens the scope of the experiments. Typically, optical traps are equipped with 2D laser and stage position control. For a digital controller, the software may be adapted to apply forces in an arbitrary direction as indicated in Fig. 3, i.e. in two actively

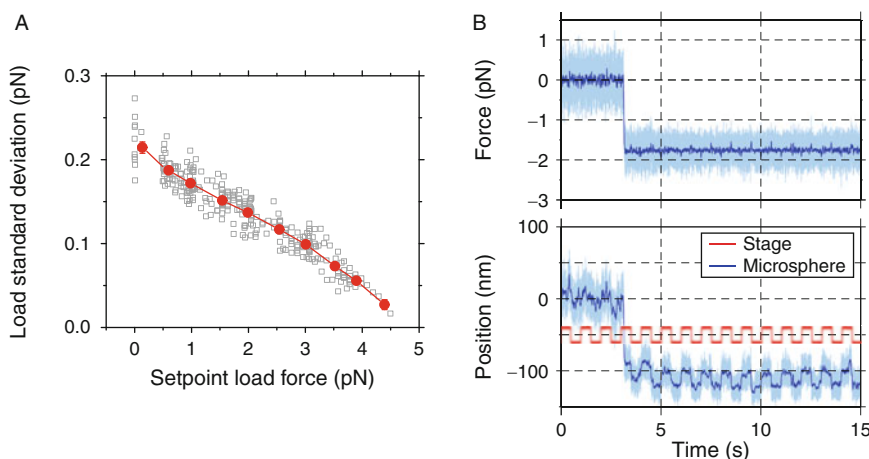


**Fig. 8** Positional resolution improves with load. **(a)** Standard deviation of the applied load (open squares) as a function of the force setpoint. Data were obtained by applying constant loads on microspheres ( $N = 277$  from 34 data sets, trap stiffness was 0.02–0.03 pN/nm) in the presence of ATP [16]. The line connecting the binned data (red solid circles) is a guide to the eye. **(b)** Force and position of a kinesin-bound microsphere as a function of time. A square wave of 20 nm amplitude and 1 Hz was applied on the stage. Steps could only be resolved with an applied load, here about 1.85 pN (light-blue: 4 kHz, dark-blue: median filtered to 8 Hz, red: steps of the stage (the signal was offset for clarity),  $\kappa = 0.024$  pN/nm). PID values:  $K^P = 0.18$ ,  $K^I = 0.1 \text{ s}^{-1}$  and  $K^D = 0$ . Data were acquired in the presence of AMPPNP

controlled independent directions. In this manner, molecular motors can be followed on arbitrarily oriented filaments [15]. Also, sideward loads can be applied to measure the directional bias of conventional kinesin-1 and its asymmetric sideward-load dependence [68], or the random sideward stepping of kinesin-8, which is also asymmetrically biased by force [16]. Apart from misalignment artifacts, note that if a linearly polarized laser is used for trapping, the trap stiffnesses in the two lateral directions usually differ [69, 70]. This difference may lead to artifacts for a 2D force clamp that operates in a direction that is not parallel or perpendicular to the polarization direction (*see Note 9*).

To change the direction of a sideward load, the load needs to be changed quickly over a large distance compared to the molecular stepping distance. The large movement is necessary because the microsphere acts as a lever amplifying the motion [16]. Large sudden changes in the setpoint require different PID parameters compared to a concatenation of small steps. For a fast response, a higher proportional gain is necessary. For example, for a load reversal, we increase the optimal  $K^P$  for following slow, low-force, 10-nm kinesin-bound microsphere steps in the presence of AMPPNP (Fig. 7) from 0.1 to 0.3 (Fig. 9). While the increased  $K^P$  value reduces the rise time more than twofold, it introduces an overshoot to small steps. The user therefore needs to decide whether a smaller overshoot or a fast rise time is preferred.

If even faster load changes are required, one can use *feed-forward* to accelerate the response. As opposed to feedback that responds to past changes as fast as possible, feed-forward uses foreknowledge about changes in the difference between the set-point and process variable (the error  $e$ ) to pre-act accordingly. In this manner, a faster, more accurate tracking of a fast event is possible. For example, for scanning applications, like atomic force microscopy, the location and time of a change in the scanning direction is known. This information can be used to minimize errors at the turning point [71]. In Fourier space, a turning point has components of all frequencies and its sharpness is always limited by the response time of the system. Feed-forward can increase the bandwidth of the scanning speed nearly tenfold [71].

For optical tweezers, feed-forward is less common. In one implementation for alternating loads [68], the feedback is stopped and the trap is moved to the new location that is predicted to result in the desired sideward load of the opposite polarity. The prediction can be based on a prior measurement or knowledge of the geometry, trapping parameters, and force-extension curve of the linker. Once the new position is reached, the feedback is reactivated. In this manner, the settling time for reaching the new position is solely determined by the rise time of the actuator and not by the larger response time of the feedback. Therefore, an overall faster response is possible. In another application [25, 72],

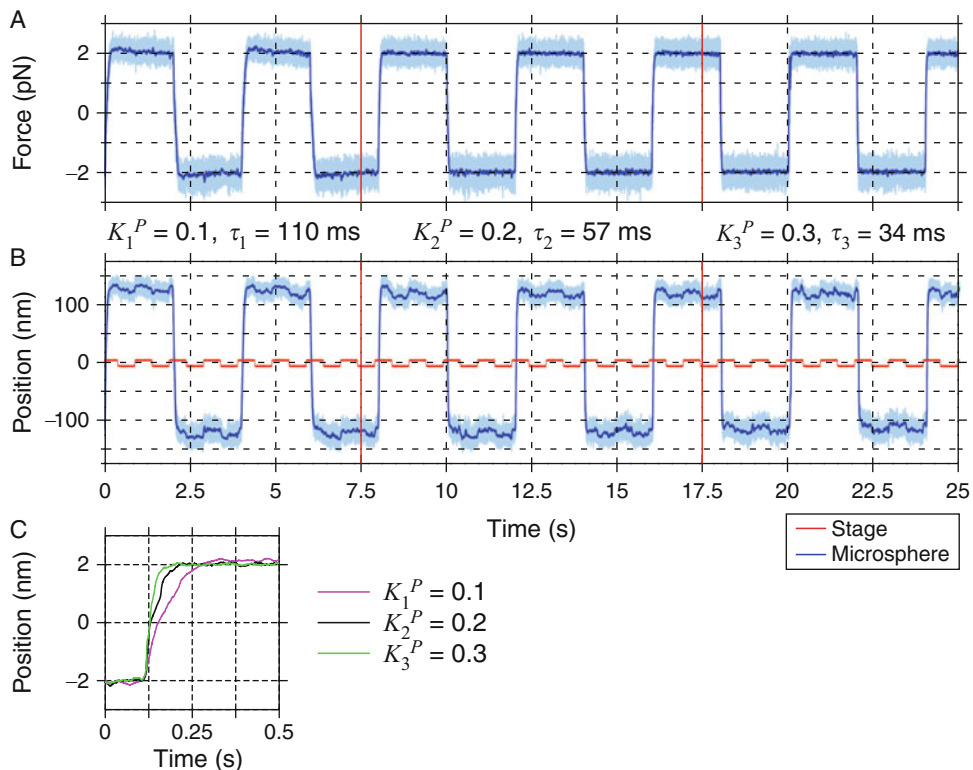


**Fig. 9** Alternating sideward load tuning experiment that mimics experimental conditions. **(a)** Force and **(b)** position versus time of a kinesin-bound microsphere in the presence of AMPPNP. A square wave of 10 nm amplitude and 1 Hz was applied to the stage. The sideward load of  $\pm 2$  pN switched the direction every 2 s. The proportional gain  $K^P$  was increased at 7.5 and 17.5 s. Its value and the rise time  $\tau$  (time for 10–90 % rise) are given.  $K^I = 0.1 \text{ s}^{-1}$  and  $K^D = 0$ . **(c)** Plot of three representative step responses from **(b)** with different  $K^P$

the motion of a trapped particle is predicted based on its current position and the expected relaxation in a harmonic potential during the feedback-loop time. This predictive control loop can be used to artificially increase the trap stiffness by reducing the Brownian motion and force fluctuations. In this manner, the corner frequency is increased and a larger bandwidth and higher resolution is possible. An excessive increase in gain comes at the cost of increased positional fluctuations.

### 3.6 Three-Dimensional Force Clamping

Since optical tweezers are three-dimensional (3D) position and force transducers, force clamps can also be extended to three dimensions [16, 17]. Using back-focal-plane interferometry, the axial information, here the  $z$  direction (Fig. 1), is extracted from the sum signal of the QPD [27, 35] after subtracting the offset voltage. The  $z$  position is then linearly proportional to the power on the QPD. Since the offset for the  $z$  direction is large compared to the signal, it is essential that the laser power has low power fluctuations [27]. As actuator, either a 3D piezoelectric

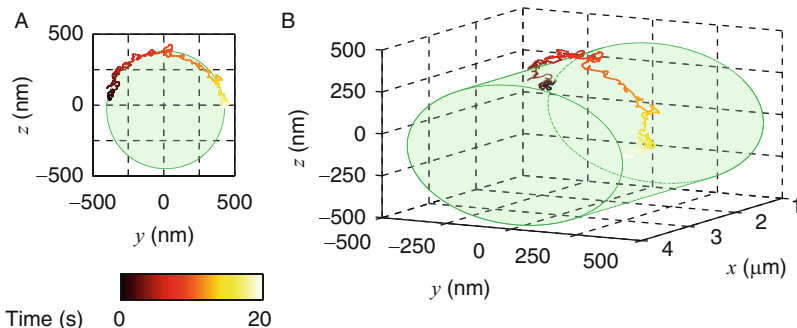


**Fig. 10** 3D force clamp. Three-dimensional trace of a microsphere transported by a kinesin-1 motor along a microtubule under zero load. The microtubule was freely suspended on a topographic structure. (a) The  $y$ - $z$  projection shows a circular path with a diameter corresponding to the microsphere plus microtubule diameter in addition to the kinesin-microsphere linkage length. (b) The 3D trajectory shows a helical path. We measured a pitch of about  $5.6\ \mu\text{m}$ . The left-handedness and pitch is consistent with the supertwist of a 14-protofilament microtubule grown in the presence of GTP and stabilized by taxol, which has a pitch of  $5.8 \pm 0.3\ \mu\text{m}$  [73]. The ATP concentration was  $10\ \mu\text{M}$

translation stage, a piezo-driven objective mount, or a deformable mirror [74] can be used (see Note 10). Using setpoint changes, tuning of the PID controller can be performed analogously to the lateral feedback (Subheading 3.4). For 3D experiments close to the surface, the input parameters (trap stiffness, displacement sensitivity, and QPD offset) depend on the microsphere-surface distance, in particular when using an oil immersion objective for trapping [27]. This dependence may have to be measured prior to and corrected for during a 3D clamping experiment. In addition, when using oil immersion objectives, the focal shift  $\delta_f$  needs to be accounted for. If the sample surface is moved relative to the trapping objective by an amount  $\Delta z$ , the microsphere-center–surface distance changes only by  $\delta_f \Delta z$ , where  $\delta_f \approx 0.8$  for a glass–water interface [27, 75]. Accounting for the above effects, we can track conventional kinesin in 3D, here under zero load, as it moves along a single protofilament of a supertwisted microtubule (Fig. 10). 3D tracking enables one to faithfully reconstitute the three-dimensional cellular environment, circumventing artifacts that may arise from interactions with the cover glass surface. Furthermore, a 3D force clamp broadens the scope of feasible experiments that require the high precision of optical tweezers.

#### 4 Notes

1. We noticed that when the system is not well aligned, i.e. if the trapping laser is not perfectly centered on the optical axis of the trapping objective and/or if the tilt mirror is not in a

conjugate telecentric plane to the back-focal plane of the trapping objective, that larger variations in trap stiffness and displacement sensitivity up to a few percent per micrometer do occur. This deviation might be used as a sensitive means to align the system.

2. If a 16 bit,  $\pm 10$  V output voltage controls a  $0\text{--}30$   $\mu\text{m}$  scan range with a  $0\text{--}10$  V signal, 1 bit corresponds to  $10 \mu\text{m}/2^{15} = 0.9$  nm (1 bit accounts for the sign). Because most actuator devices have a much slower response compared to the output rate of the digital-to-analog converter, one can circumvent the limited bit resolution by the use of “dithering”—i.e., a fast modulation of the least significant bit. The actuator cannot follow the fast modulation and will be positioned at an intermediate value between the two bits.
3. The PI control lacks the D control of the PID system. Although the response time for PI control is faster than I-only control, it is still up to 50 % slower than P-only control. Therefore, in order to decrease the response time, PI control is often combined with D control. In PI-DP control, the feedback is combined with an additional proportional response, to constrain the derivative response to sudden changes in the setpoint [53]. For our optical tweezers force clamp, we only used PI or PID control.
4. The sampling rate  $f_s$  can be higher than the feedback rate  $f_f$ . To minimize artifacts and noise, the full alias-free bandwidth should be used and subsequently  $N = f_s/f_f$  data points averaged for one feedback cycle. For example, if data is sampled with 40 kHz and the feedback loop is updated with 1 kHz, 40 data points would be averaged per cycle.
5. To operate the force clamp properly, the polarity of the actuator needs to be correct. If the actuator has the opposite polarity, the response needs to be negated. Also, for motor proteins that interact with a polar substrate, its directionality might not be known a priori. In this case, the setpoint may have to be negated to account for the filament polarity.
6. If transient deviations from a constant force are permissible, slower hardware might be considered, which may have certain advantages with respect to precision, steering range, or price.
7. For a force-clamp feedback system, one can manually test many sets of feedback parameters without having to wait long before the system has settled to a new state. Such an approach may be cumbersome for systems that have response times on the minute time scale, e.g. a temperature feedback, because for each set of parameters one has to wait for a period of several response times before the system has settled. Thus, for such systems, trial-and-error tuning can be very time consuming.

8. To achieve rigidly immobilized microspheres, it may be necessary to wash the microspheres a few times by centrifugation and resuspension in deionized water. After washing, remnant motion of the microsphere is below 1 Å for all directions at time scales below 1 s [28].
9. Cross-talk for a 2D force clamp may be caused by tilted samples, by a misalignment of the detector, and/or by deviations of the trapping laser from the optical axis. Even for a well-aligned system, a mismatch between an imposed angle that the feedback controller follows and the actual angle at which the filament track is oriented (e.g., for assays that use microtubule or actin filaments) may cause deviations from the force setpoint (Fig. 11a). An additional artifact may arise when switching load directions (Fig. 11b). Optical tweezers systems often use linearly polarized trapping lasers, for which the trap stiffnesses  $\kappa$  between the two lateral axes ( $x, y$ ) differ. This difference depends on the diameter and refractive index of the microsphere. For example, for a 500 nm-diameter polystyrene microsphere the difference between  $\kappa_x$  and  $\kappa_y$  is  $\approx 25\%$  [69, 70]. Therefore, the direction of the force vector differs from that of the position vector and can lead to artificial displacements upon a force reversal as illustrated in Fig. 11b. For example, for a

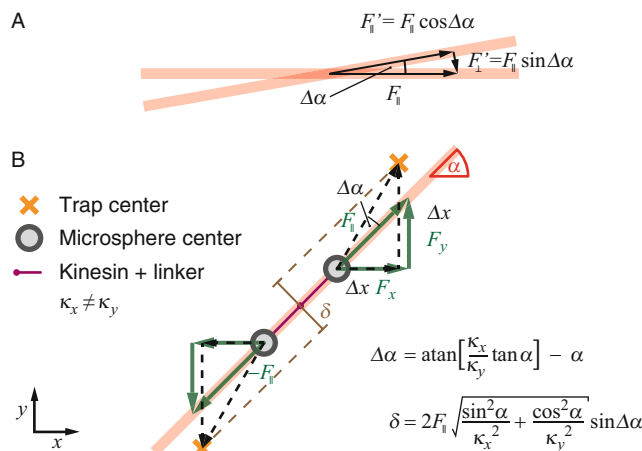


**Fig. 11** Potential artifacts of a 2D force clamp. (a) An angular mismatch  $\Delta\alpha$  between the imposed direction  $F_\parallel$  and actual orientation of a track reduces the load along the filament axis to  $F'_\parallel = F_\parallel \cos \Delta\alpha$  and more importantly causes an off-axis load  $F'_\perp = F_\parallel \sin \Delta\alpha$ . (b) Switching load directions may cause an artificial off-axis displacement. An asymmetric optical trapping potential (trap stiffness  $\kappa_x \neq \kappa_y$ )—common for linearly polarized trapping lasers—leads to a misalignment of the force axis  $F_\parallel$  (green arrows pointing from the gray circle along the red filament) compared to the line connecting the microsphere center with the trap center (dashed black lines pointing from the gray circle to the orange cross). The additional angle  $\Delta\alpha$  is related to the lateral forces and microsphere displacements  $\Delta x$  and  $\Delta y$  by:  $\tan(\alpha + \Delta\alpha) = \Delta y / \Delta x$  and  $\tan \alpha = F_y / F_x$  with  $F_x = \kappa_x \Delta x$  and  $F_y = \kappa_y \Delta y$ . When the load direction is reversed (e.g., in a kinesin assay), the switching causes the off-axis displacement  $\delta$ . Equations for  $\Delta\alpha$  and  $\delta$  are given

590 nm-diameter polystyrene microsphere, we measured  $\kappa_x = 0.030$  pN/nm and  $\kappa_y = 0.025$  pN/nm. If the force clamp would track a motor along a microtubule oriented at  $\alpha = 45^\circ$ , the angular deviation between the force and position vector would be  $\Delta\alpha \approx 6^\circ$ . With a load reversal from plus to minus 1 pN along the microtubule axis, the trap center experiences an off-axis displacement of  $\delta \approx 7$  nm. This displacement is not due to a sideward motion of the molecular motor itself, but purely due to the geometry and asymmetric trapping potential.

10. Piezoelectric steering for the  $z$  direction is slower compared to the steering by a deformable mirror and may be associated with the following artifact: when using oil-immersion objectives, the immersion oil between the coverslip and the objective lens needs to be displaced. Because of the immersion oil's high viscosity, this displacement may lead to a transient bending or lifting of the coverslip. Using thicker coverslips and/or less viscous immersion oil may be beneficial.

## Acknowledgements

We thank Gero Hermsdorf and Mayank Chugh for comments on the manuscript. This work was supported by the European Research Council (ERC Starting Grant 2010, Nanomech 260875), the Rosa Luxemburg Foundation, the Technische Universität Dresden and the Universität Tübingen.

## References

1. Huxley AF, Niedergerke R (1954) Interference microscopy of living muscle fibres. *Nature* 4412:971–973
2. Finer JT, Simmons RM, Spudich JA (1994) Single myosin molecule mechanics: piconewton forces and nanometre steps. *Nature* 368:113–119
3. Veigel C, Coluccio L, Jontes J et al (1999) The motor protein myosin-I produces its working stroke in two steps. *Nature* 398:530–533
4. Takagi Y, Homsher EE, Goldman YE et al (2006) Force generation in single conventional actomyosin complexes under high dynamic load. *Biophys J* 90:1295–1307
5. Laakso J, Lewis J, Shuman H et al (2008) Myosin I can act as a molecular force sensor. *Science* 321:133–136
6. Capitanio M, Canepari M, Maffei M et al (2012) Ultrafast force-clamp spectroscopy of single molecules reveals load dependence of myosin working stroke. *Nat Methods* 9:1013–1019
7. Molloy JE, Burns JE, Kendrick-Jones J et al (1995) Movement and force produced by a single myosin head. *Nature* 378:209–212
8. Wang MD, Yin H, Landick R et al (1997) Stretching DNA with optical tweezers. *Biophys J* 72:1335–1346
9. Wang MD, Schnitzer MJ, Yin H et al (1998) Force and velocity measured for single molecules of RNA polymerase. *Science* 282:902–907
10. Visscher K, Schnitzer MJ, Block SM (1999) Single kinesin molecules studied with a molecular force clamp. *Nature* 400:184–189
11. Rief M, Rock RS, Mehta AD et al (2000) Myosin-V stepping kinetics: a molecular model for processivity. *Proc Natl Acad Sci USA* 97:9482–9486
12. Gennerich A, Carter AP, Reck-Peterson SL et al (2007) Force-induced bidirectional stepping of cytoplasmic dynein. *Cell* 131:952–965

13. Svoboda K, Schmidt CF, Schnapp BJ et al (1993) Direct observation of kinesin stepping by optical trapping interferometry. *Nature* 365:721–727
14. Svoboda K, Block SM (1994) Force and velocity measured for single kinesin molecules. *Cell* 77:773–784
15. Lang M, Asbury C, Shaevitz J et al (2002) An automated two-dimensional optical force clamp for single molecule studies. *Biophys J* 83:491–501
16. Bugiel M, Böhl E, Schäffer E (2015) The kinesin-8, Kip3, switches microtubule protofilaments in a sideward random walk asymmetrically biased by force. *Biophys J* 108:2019–2027
17. Ander M, Subramaniam S, Fahmy K et al (2015) A single-strand annealing protein clamps DNA to detect and secure homology. *PLOS Biol* 13:e1002213
18. Liphardt J, Onoa B, Smith SB et al (2001) Reversible unfolding of single RNA molecules by mechanical force. *Science* 292:733–737
19. Cecconi C, Shank EA, Bustamante C et al (2005) Direct observation of the three-state folding of a single protein molecule. *Science* 309:2057–2060
20. Greenleaf WJ, Woodside MT, Abbondanzieri EA et al (2005) Passive all-optical force clamp for high-resolution laser trapping. *Phys Rev Lett* 95:208102
21. Abbondanzieri EA, Greenleaf WJ, Shaevitz JW et al (2005) Direct observation of base-pair stepping by RNA polymerase. *Nature* 438:460–465
22. Gebhardt JCM, Bornschlögl T, Rief M (2010) Full distance-resolved folding energy landscape of one single protein molecule. *Proc Natl Acad Sci USA* 107:2013–2018
23. Stigler J, Ziegler F, Gieseke A et al (2011) The complex folding network of single calmodulin molecules. *Science* 334:512–516
24. Comstock MJ, Ha T, Chemla YR (2011) Ultrahigh-resolution optical trap with single-fluorophore sensitivity. *Nat Methods* 8:335–340
25. Wallin AE, Ojala H, Ziedaite G et al (2011) Dual-trap optical tweezers with real-time force clamp control. *Rev Sci Instrum* 82:083102
26. Walder R, Paik DH, Bull MS et al (2015) Ultrastable measurement platform: sub-nm drift over hours in 3D at room temperature. *Opt Express* 23:16554–16564
27. Schäffer E, Nørrelykke SF, Howard J (2007) Surface forces and drag coefficients of microspheres near a plane surface measured with optical tweezers. *Langmuir* 23:3654–3665
28. Mahamdeh M, Schäffer E (2009) Optical tweezers with millikelvin precision of temperature-controlled objectives and base-pair resolution. *Opt Express* 17:17190–17199
29. Heller I, Sitters G, Broekmans OD et al (2013) STED nanoscopy combined with optical tweezers reveals protein dynamics on densely covered DNA. *Nat Methods* 10:910–916
30. Liesener J, Reicherter M, Haist T et al (2000) Multi-functional optical tweezers using computer-generated holograms. *Opt Commun* 185:77–82
31. Lyng Eriksen R, Daria VR, Glückstad J (2002) Fully dynamic multiple-beam optical tweezers. *Opt Express* 10:597–602
32. Grier DG, Roichman Y (2006) Holographic optical trapping. *Appl Opt* 45:880–887
33. Gibson GM, Bowman RW, Linnenberger A et al (2012) A compact holographic optical tweezers instrument. *Rev Sci Instrum* 83:113107
34. Gittes F, Schmidt CF (1998) Back-focal-plane detection of force and motion in optical traps. *Biophys J* 74:A183–A183
35. Pralle A, Prummer M, Florin EL et al (1999) Three-dimensional high-resolution particle tracking for optical tweezers by forward scattered light. *Microsc Res Tech* 44:378–386
36. Huhle A, Klaue D, Brutzer H et al (2015) Camera-based three-dimensional real-time particle tracking at kHz rates and Ångström accuracy. *Nat Commun* 6:5885
37. Carter N, Cross R (2001) An improved microscope for bead and surface-based motility assays. In: Kinesin protocols. Methods in molecular biology, book section 8, vol 164. Humana Press, Totowa, NJ, pp 73–89
38. Berg-Sørensen K, Oddershede L, Florin EL et al (2003) Unintended filtering in a typical photodiode detection system for optical tweezers. *J Appl Phys* 93:3167–3176
39. Chavez I, Huang R, Henderson K et al (2008) Development of a fast position-sensitive laser beam detector. *Rev Sci Instrum* 79:105104
40. Rohrbach A, Tischer C, Neumayer D et al (2004) Trapping and tracking a local probe with a photonic force microscopes. *Rev Sci Instrum* 75:2197–2210
41. Gennerich A, Schild D (2005) Sizing-up finite fluorescent particles with nanometer-scale precision by convolution and correlation image analysis. *Eur Biophys J* 34:181–199
42. Moffitt JR, Chemla YR, Izhaky D et al (2006) Differential detection of dual traps improves the spatial resolution of optical tweezers. *Proc Natl Acad Sci USA* 103:9006–9011
43. Simmons RM, Finer JT, Chu S, Spudich J (1996) Quantitative measurements of force

- and displacement using an optical trap. *Cold Spring Harb Protoc* 70:1813–1822
44. Brouhard GJ, Schek HT III, Hunt AJ (2003) Advanced optical tweezers for the study of cellular and molecular biomechanics. *IEEE Trans Biomed Eng* 50:121–125
  45. Valentine MT, Guydosh NR, Gutiérrez-Medina B et al (2008) Precision steering of an optical trap by electro-optic deflection. *Opt Lett* 33:599–602
  46. Huang Y, Wan J, Cheng MC et al (2009) Three-axis rapid steering of optically propelled micro/nanoparticles. *Rev Sci Instrum* 80:599–602
  47. Mahamdeh M, Campos CP, Schäffer E (2011) Under-filling trapping objectives optimizes the use of the available laser power in optical tweezers. *Opt Express* 19:11759–11768
  48. Tolić-Nørrelykke SF, Schäffer E, Howard J et al (2006) Calibration of optical tweezers with positional detection in the back focal plane. *Rev Sci Instrum* 77:1–11
  49. Jannasch A, Bormuth V, Storch M et al (2013) Kinesin-8 is a low-force motor protein with a weakly bound slip state. *Biophys J* 104:2456–2464
  50. Bugiel M, Fantana H, Bormuth V et al (2015) Versatile microsphere attachment of GFP-labeled motors and other tagged proteins with preserved functionality. *J Biol Methods* 2:e30
  51. Block SM, Goldstein LSB, Schnapp BJ (1990) Bead movement by single kinesin molecules studied with optical tweezers. *Nature* 348:348–352
  52. Lasek R, Brady S (1985) Attachment of transported vesicles to microtubules in axoplasm is facilitated by AMP-PNP. *Nature* 316:645–647
  53. Åström KJ (2002) Control system design. Department of Mechanical and Environmental Engineering, University of California
  54. Bechhoefer J (2005) Feedback for physicists: a tutorial essay on control. *Rev Mod Phys* 77:783–836
  55. Åström KJ, Häggglund T (2006) Advanced PID control. ISA - The Instrumentation, Systems, and Automation Society
  56. Åström KJ, Murray RM (2008) Feedback systems: an introduction for scientists and engineers. Princeton University Press, Princeton
  57. McMillan GK (2012) PID control in the third millennium: lessons learned and new approaches, chap. 14 Springer, Berlin, pp 415–461
  58. Cooper DJ (2005) Practical process control. Control Station, Inc.
  59. Gittes F, Schmidt CF (1998) Signals and noise in micromechanical measurements. In: Methods in cell biology, vol 55. Academic Press, New York, pp 129–156
  60. Gittes F, Schmidt FC (1998) Thermal noise limitations on micromechanical experiments. *Eur Biophys J* 27:75–81
  61. Daldrop P, Brutzer H, Huhle A et al (2015) Extending the range for force calibration in magnetic tweezers. *Biophys J* 108:2550–2561
  62. Ziegler J, Nichols N (1942) Optimum settings for automatic controllers. *Trans ASME* 64:759–768
  63. Hang C, Åström K, Ho W (1991) Refinements of the Ziegler-Nichols tuning formula. *Control Theory Appl IEE Proc D* 138:111–118
  64. Shahrokhi M, Zomorodi A (2003) 8th national Iranian chemical engineering congress. In: Comparison of PID controller tuning methods, pp 1–12
  65. Varga V, Leduc C, Bormuth V et al (2009) Kinesin-8 motors act cooperatively to mediate length-dependent microtubule depolymerization. *Cell* 138:1174–1183
  66. Bormuth V, Varga V, Howard J et al (2009) Protein friction limits diffusive and directed movements of kinesin motors on microtubules. *Science* 325:870–873
  67. Guydosh NR, Block SM (2009) Direct observation of the binding state of the kinesin head to the microtubule. *Nature* 461:125–128
  68. Block S, Asbury C, Shaevitz J et al (2003) Probing the kinesin reaction cycle with a 2D optical force clamp. *Proc Natl Acad Sci USA* 100:2351–2356
  69. Bormuth V, Jannasch A, Ander M et al (2008) Optical trapping of coated microspheres. *Opt Express* 16:13831–13844
  70. Jannasch A, Bormuth V, van Kats CM et al (2008) Coated microspheres as enhanced probes for optical trapping. *Proc of SPIE* 7038:70382B 1–8
  71. Li Y, Bechhoefer J (2007) Feedforward control of a closed-loop piezoelectric translation stage for atomic force microscope. *Rev Sci Instrum* 78:1–8
  72. Ojala H, Korsbäck A, Wallin AE et al (2009) Optical position clamping with predictive control. *Appl Phys Lett* 95:181104
  73. Howard J (2001) Motor proteins and the cytoskeleton. Sinauer Associates, Sunderland, MA
  74. Ota T, Kawata S, Sugiura T et al (2003) Dynamic axial-position control of a laser-trapped particle by wave-front modification. *Opt Lett* 28:465–467
  75. Neuman KC, Abbondanzieri EA, Block SM (2005) Measurement of the effective focal shift in an optical trap. *Opt Lett* 30: 1318–1320

# Chapter 6

## Custom-Made Microspheres for Optical Tweezers

Anita Jannasch\*, Mohammad K. Abdosamadi\*, Avin Ramaiya\*, Suman De, Valentina Ferro, Aaron Sonnberger, and Erik Schäffer

### Abstract

Due to their high position and force sensitivity and the ability to remotely apply forces and torques, optical tweezers are widely used in diverse fields, such as biology, material science, and physics. Often, small dielectric particles are trapped and used as probes, which for experimental convenience are mostly spherical and composed of silica or polystyrene. The optical properties of these materials together with the microsphere size determine the trapping efficiency, and the position and force resolution. However, using only a single, homogeneous, isotropic, and unstructured material limits the range of trapping properties and thereby the applications of optical tweezers. Here, we show how custom-made microspheres composed of coated high-refractive-index materials—titania and nanodiamonds—and birefringent, liquid crystals extend the range and combination of desired trapping properties. These custom-made microspheres either enable the generation of high forces, a high force or time resolution, or the applications of torques. Custom-made probes expand the range of possible experiments and approaches broadening the scope and applicability of optical tweezers.

**Key words** Optical tweezers, Core–shell particles, Anti-reflection coating, Nanonewton, Microspheres, Titania, Nanodiamonds, TEOS, MCM-41, Liquid crystalline birefringent particles, Angular trapping, Rotation, Optical torque

---

### 1 Introduction

In this chapter, we describe three different approaches how to make custom-made microspheres: (1) anti-reflection coated titania microspheres for high-force applications, (2) silica-coated nanodiamonds for high-resolution measurements, and (3) liquid-crystalline, birefringent microspheres for rotational measurements. Each approach stands on its own and can be read independent of the others by following the corresponding subsections of the Introduction, Materials, Methods, and Notes.

---

\* These three authors contributed equally to this work.

## **1.1 Anti-reflection**

### **Coated Titania**

### **Microspheres for High-Force Applications**

The force range of optical tweezers is limited by the trapping efficiency and the available laser power. Typical trapping forces range from sub-picowatt to hundreds of picowatts [1–3]. This range is sufficient to characterize the mechanics of individual, biological molecular machines. The mechanical characterization of more complex cellular processes like cell adhesion and contraction, mitosis, the beating of cilia, or the disruption of amyloid fibrils requires larger forces [4]. Increasing the laser power to increase trapping forces leads to heating and potentially photo-damage, which precludes this option for many applications in particular in biology. The only other parameter that can increase the trapping force with a given laser power is an increase of the trapping efficiency. Therefore, we developed anti-reflection coated, high-refractive-index titania core–shell particles that have a very high trapping efficiency [5–9]. Using these particles in an optimized optical tweezer setup [10, 11], one can generate optical forces in excess of 1 nN with a trap stiffness exceeding 5 pN/nm [9]. The high trap stiffness is useful for demonstrating that the noise that drives Brownian motion has a color [8]. Enhanced optical manipulation of cells [12] demonstrates that the anti-reflection coated particles are also bio-compatible.

Here, we will describe how to produce monodisperse, spherical, anti-reflection coated, high-refractive-index titania microspheres. We use anatase titania with a high refractive index of  $n_{\text{core}} = 2.3$  as a core, coated with amorphous titania with a refractive index of  $n_{\text{shell}} = 1.8$  resulting in a total microsphere diameter of about 1  $\mu\text{m}$ . To achieve an anti-reflective effect, the core size and coating thickness need to be accurately matched with the ones predicted by Mie theory calculations [9]. The calculations are specific for the setup—mainly for the trapping wavelength  $\lambda$  (for more details see Subheading 3.1). For our setup ( $\lambda = 1064 \text{ nm}$ ), we improved the trapping efficiency twofold compared to polystyrene microspheres (fourfold compared to silica) of similar sizes, achieving a quality factor  $Q$  of 0.25, i.e. up to 25 % of the laser power can be converted to perform mechanical work [9].

In Subheading 3, we will describe the synthesis of these photonically structured titania microspheres, including details for both the core synthesis (Subheading 3.1.1) and the shell growth (Subheading 3.1.2) (Fig. 1a). The refractive indices of the core and the shell are determined with static light-scattering measurements and holographic microscopy. Transmission electron microscopy (TEM) revealed homogeneous core sizes and coatings (Fig. 1b). We can successfully trap the titania core–shell microspheres. By using our calibration method [13], we are able to confirm the high trapping efficiency. The high corner frequency in the power spectral density is consistent with the expected high lateral trap stiffness of 3.8 pN/nm/W<sub>focus</sub> (Fig. 1c). In summary, these custom-made particles enable (1) high-force, (2) high-trap-stiffness, or (3) low-photo-damage measurements.

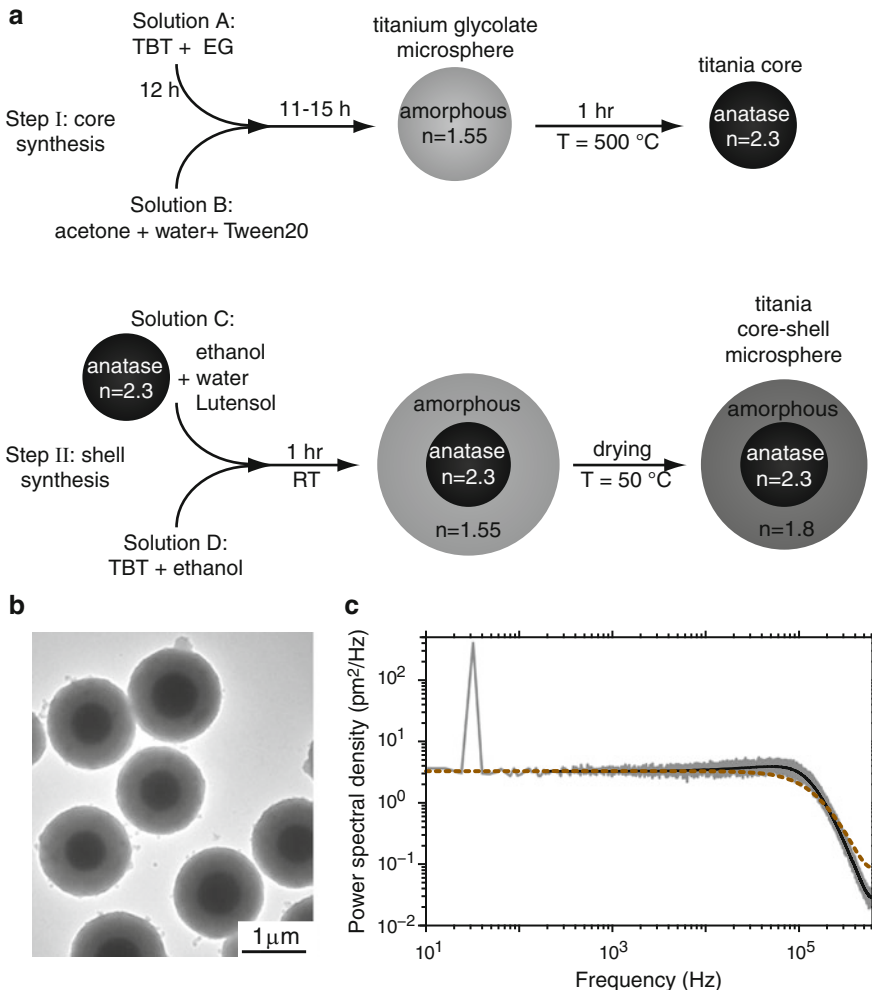


**Fig. 1** Fabrication scheme and characterization of anti-reflection coated titania microspheres. **(a)** Schematic of the reaction. In Step I, anatase titania cores are synthesized. In Step II, a layer of amorphous titania is produced surrounding the cores. **(b)** TEM image of coated titania microspheres showing the core–shell structure. The synthesized microspheres have a diameter of  $1.00 \pm 0.02 \mu\text{m}$  (mean  $\pm$  SEM unless noted otherwise,  $N = 6$ ). **(c)** Power spectral density (PSD) of a trapped, coated titania microsphere. The high-precision spectrum is shown in black (averaged over 100,000 spectra,  $\Delta f = 200 \text{ Hz}$ ). The calibration spectrum features a calibration peak at 32 Hz (gray line, averaged over 100 spectra,  $\Delta f = 8 \text{ Hz}$ ) [13]. The dashed-line shows a Lorentzian. The PSD deviates from a Lorentzian because of a hydrodynamic resonance [9]. The trapped titania core–shell microsphere had a diameter of  $1.02 \mu\text{m}$  with a trap stiffness of  $5.4 \text{ pN/nm}$  with  $1.4 \text{ W}$  laser power in the focus

### 1.2 Silica-Coated Nanodiamonds for High-Resolution Measurements

Brownian motion of a trapped particle ultimately limits the force and position resolution of optical tweezers. The resolution limit is proportional to the square root of the thermal energy, the particle size, and the measurement bandwidth. Thus, for a given temperature and bandwidth, the resolution can only be improved by significantly reducing the size of the trapped object. For example, a

tenfold reduction in size from typically used microsphere diameters of 0.5–1.0  $\mu$ m to 50–100 nm improves the force resolution about threefold. Unfortunately, the trapping efficiency strongly depends on the microsphere size such that the maximum force that can be reached with small particles becomes limiting for single-molecule force measurements. For particles that are smaller than the wavelength of the trapping light, the trapping efficiency is roughly proportional to the volume: for example, a polystyrene microsphere with a diameter of  $\sim$  150 nm has a 20 $\times$  smaller trapping efficiency than a  $\sim$  600 nm-diameter microsphere. As a consequence, to achieve the same trap stiffness, a 20 $\times$  higher laser power is required. Therefore, for small conventional polystyrene or silica microspheres, the maximal trapping forces are only a few piconewtons for a high laser power trap (1 W in the focus), which may limit certain applications.

To increase the trapping efficiency, we use high-refractive-index particles—nanodiamonds with a refractive index of 2.4. Nanodiamonds are most well known for their nitrogen-vacancy centers, which can be introduced to nanodiamonds making them fluorescent with exceptional properties: they do not blink nor bleach [14, 15]. Here, we will not make use of their fluorescent properties and instead exploit their high refractive index. Because nanodiamonds are bio-compatible, they are suited for biological applications. Furthermore, nanodiamonds are birefringent, enabling torque measurements with optical tweezers (*see Subheading 1.3*).

Nanodiamonds can be readily purchased in different sizes. However, the surface of nanodiamonds is chemically not very reactive, which makes modifications more difficult. In addition, pure, untreated nanodiamonds tend to aggregate in aqueous solutions. Also, nanodiamonds are not spherical and have an asymmetric shape. To overcome these challenges, we describe a protocol to coat nanodiamond cores with a mesoporous silica shell of about 30 nm thickness. The silica shell renders the nanodiamonds stable in water solutions, enables functional coupling of target proteins to the surface, and makes the blocky particle shape more spherical [16, 17].

In Subheading 3, we will describe the synthesis of silica-coated nanodiamonds (Fig. 2a). We first characterized the coated nanodiamonds using transmission electron microscopy (TEM) and found a silica coating of uniform thickness (Fig. 2b). These  $\sim$ 130 nm-diameter silica-coated nanodiamonds can be stably trapped. In agreement with our calculations, we can confirm the high trapping efficiency of the coated nanodiamonds. In Fig. 2c, the corner frequency in the power spectral density corresponds to a lateral trap stiffness of 0.28 pN/nm/W. Based on our calculations, this trap stiffness is 7 $\times$  higher compared to polystyrene microspheres of the same size. Trapped nanodiamonds of this size have a high force resolution, i.e. an rms noise of about 5 fN Hz $^{-0.5}$  [18] and would require about 180 mW of laser power in the focus to achieve a trap stiffness of 0.05 pN/nm suitable, for example, for a

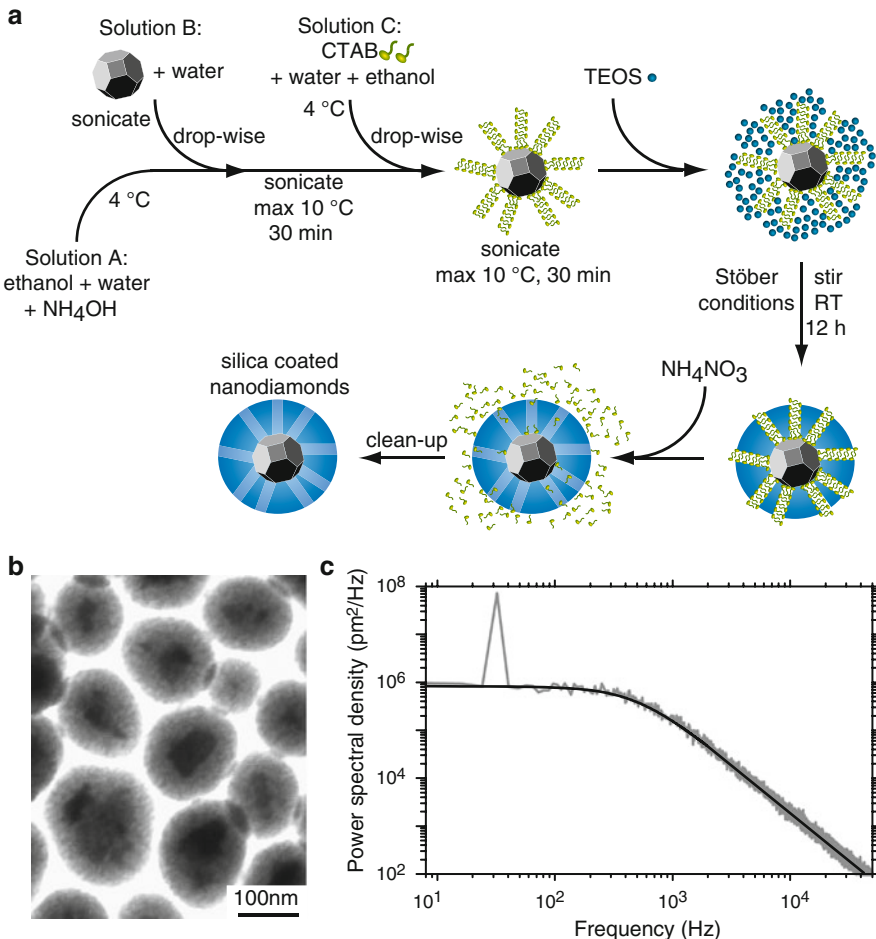


**Fig. 2** Fabrication scheme and characterization of silica-coated nanodiamonds. **(a)** Schematic of the reaction. **(b)** TEM image of silica-coated nanodiamonds. The coated nanodiamonds have an average total diameter of  $150 \pm 8$  nm ( $N = 41$ ). The bare nanodiamonds have a median diameter of 90 nm. The shell thickness is  $31 \pm 1$  nm ( $N = 17$ ). **(c)** Power spectral density of a silica-coated nanodiamond trapped in an optical tweezers. The calibration spectrum (gray line, averaged over 40 spectra,  $\Delta f = 8$  Hz) features a calibration peak at 32 Hz [13]. The black line shows a Lorentzian fit. The trapped silica-coated nanodiamond had a diameter of 133 nm. The trap stiffness was 5.5 fN/nm at 20 mW laser power in the focus

kinesin assay. To summarize, silica-coated nanodiamonds are ideal probes for measurements that require high force and/or time resolution.

### 1.3 Liquid-Crystalline, Birefringent Microspheres for Rotational Measurements

Optical tweezers are most widely used for measuring linear motion. Optical tweezers are equally well suited as transducers for rotational motion and torque [19–24]. However, convenient, stable, and small probes for rotational experiments are often lacking [20, 22, 25]. Rotational motion often occurs in biology such as in the bacterial rotary motor [26, 27], during DNA transcription of supercoiled DNA [28], in the ATP synthase [29], and during the locomotion of molecular motors [30, 31]. Thus, novel rotational

probes applied to study such processes may broaden the scope of optical tweezers.

An optical torque can be exerted onto trapped particles that either have a shape anisotropy or are birefringent. Here, we will concentrate on birefringent microspheres. For a linearly polarized laser, a birefringent microsphere aligns with the plane of polarization [21]. Thus, rotation of the plane of polarization causes a rotation of the trapped microsphere. Alternatively, using a quarter-wave plate in the laser path, the linear polarization can be converted to circular polarization. In such a trap, a birefringent microsphere spins with a constant rotation frequency. The rotation frequency depends on the ellipticity of the laser polarization, the microsphere diameter, the birefringence, and the laser power.

In Subheading 3, we will describe the synthesis of birefringent liquid-crystalline microspheres based on an established protocol [32] (Fig. 3a). The microsphere sizes can be varied from about

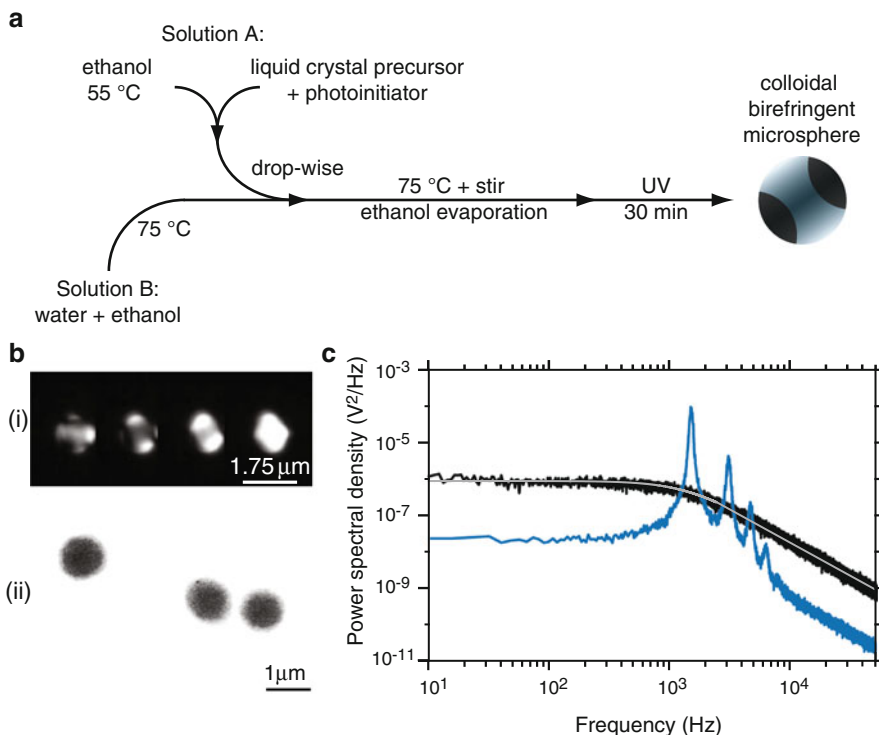


**Fig. 3** Fabrication scheme and characterization of birefringent, liquid crystalline microspheres. (a) Schematic of the synthesis of birefringence microspheres. (b) (i) Differential interference contrast (DIC) and (ii) TEM image of birefringence microspheres. The birefringent microspheres have a diameter of  $630 \pm 40$  nm ( $N = 30$ ). (c) Power spectral density of an 830 nm-diameter, birefringent microsphere trapped in an optical tweezers with circularly polarized light (peaked line). The rotational peak is at about 1350 Hz, corresponding to a rotation rate of the microsphere of 675 Hz. For comparison, the black line shows that a 600 nm-diameter, optically isotropic polystyrene microsphere does not rotate in circularly polarized light (Lorentzian fit in light gray; data averaged over 40 spectra,  $\Delta f = 8$  Hz). The laser power in the focus was 110 mW

0.2 to 2.0  $\mu\text{m}$ . In Fig. 3b, an example TEM image is shown of microspheres with a diameter of  $630 \pm 40 \text{ nm}$  ( $N = 30$ ). These birefringent microspheres can be stably trapped and rotated using circularly polarized trapping light (Fig. 3c). In summary, these microspheres are ideal probes to detect rotations or exert torques.

## 2 Materials

### 2.1 Anti-reflection

#### *Coated Titania Microspheres*

##### Chemicals

- Titanium butoxide (TBT); Sigma-Aldrich.
- Ethylene glycol (EG); Merck.
- Tween20; Sigma-Aldrich.
- Lutensol ON50; BASF (free sample from the company).
- Analytic acetone.
- Analytic ethanol.
- Denatured ethanol.
- Deionized water.

##### Equipment

- Heidolph Type 50300 magnetic mixing plate.
- Thermo Scientific Furnace Type M104, 230 V, 11 A.
- Bath sonicator: VWR Ultrasonic Cleaner USC-THD (*see Note 1*).
- Tip sonicator: Bandelin Sonopuls.
- Labnet Enduro minimax shaking plate.
- Bottles: Rotilab-screw-neck ND24, 20 ml with screw caps (PP, white).
- Round bottom glass flask with a ground glass stopper with a volume of 500 ml.
- Erlenmeyer flask with a volume of 300 ml.
- Falcon tubes with a volume of 15 and 50 ml.

### 2.2 Silica-Coated Nanodiamonds

##### Chemicals

- Analytical ethanol.
- 30 % ammonium hydroxide ( $\text{NH}_4\text{OH}$ ) solution; Sigma-Aldrich.
- Nanodiamonds (MSY 0–0.2  $\mu\text{m}$  with a median diameter of 90 nm produced by high-pressure, high-temperature (HPHT) synthesis); Microdiamant.
- Cetrimonium bromide:  $(\text{C}_{16}\text{H}_{33})\text{N}(\text{CH}_3)_3\text{Br}$  also called cetyltrimethylammonium bromide or hexadecyltrimethylammonium bromide often abbreviated by CTAB; Sigma-Aldrich.

- Tetraethyl orthosilicate (TEOS); Sigma-Aldrich.
- Ammonium nitrate solution ( $\text{NH}_4\text{NO}_3$ ); 15 g/l in ethanol.
- Deionized water.

#### Equipment

- VWR Ultrasonic Cleaner USC-THD.
- Heidolph Type 50300 magnetic mixing plate.
- Laboratory glass bottles with crew cap (PP, blue, integral lip seal) and a volume of 100 ml.
- TEM grids: 400 Mesh, hexagonal, Cu (G400H-Cu, Science Services) subsequently coated with Pioloform and carbon.

### **2.3 Liquid-Crystalline, Birefringent Microspheres**

#### Chemicals

- Mesogen/liquid crystal precursor RM257; Merck.
- Photoinitiator Darocur 1173; BASF.
- Analytic ethanol.
- Deionized and degassed water.

#### Equipment

- ULTRA-VITALUX ultraviolet high-pressure lamp (13.6 W at UVA).
- IKA C-MAG-HS7, magnetic stirrer with heating plate.
- Glass beakers with a volume of 250 and 1000 ml.
- Laboratory glass bottles with screw cap (PP, blue, integral lip seal) and a volume of 250 or 500 ml.

## **3 Methods**

### **3.1 Synthesis of Anti-reflection Coated Titania Microspheres**

Anti-reflection coated titania microspheres consist of a crystalline titania, anatase core with a refractive index of 2.3, and an amorphous shell with a refractive index of  $\sim 1.8$ . First, the anatase titania cores are synthesized. Subsequently, a layer of amorphous titania is produced on top of the cores. The protocol for both steps is similar to the method described in Demirörs et al. [7] with a few important changes that make the procedure more reproducible. The two independent protocols for the core and shell synthesis provide separate means to vary the core and shell size. The core and shell diameter are deduced from Mie theory calculations using the *Optical Tweezers Computational Toolbox* by Nieminen et al. [5, 9, 33, 34] by adjusting the following parameters:

- Refractive indices of the microsphere core, shell, and the medium.
- Size of the core and shell.
- Wavelength and polarization of the trapping laser.
- Numerical aperture of the trapping objective.
- Filling ratio of the trapping objective.

For our optical tweezers setup (wavelength  $\lambda = 1064$  nm, linearly polarized, numerical aperture NA = 1.3, filling ratio 0.9), we achieved the highest trapping efficiency for an  $\sim 450$  nm diameter anatase titania core with an  $\sim 300$  nm amorphous titania coating [9]. Below, we describe the protocol for microspheres with a core size of  $\sim 450\text{--}500$  nm anatase titania with a shell thickness of  $\sim 300\text{--}400$  nm amorphous titania, resulting in  $\sim 1050\text{--}1300$  nm monodisperse titania core–shell microspheres.

### 3.1.1 Anatase Titania Core Synthesis

The titania core synthesis is based on a nucleation-growth approach. A reactivity-reduced titania precursor solution is prepared by mixing titanium butoxide with ethylene glycol (Solution A) [35]. As surfactant, an acetone solution with Tween20 is used (Solution B). The titanium glycolate precursor hydrolyzes in acetone with a controlled water content to produce spherical titanium glycolate microspheres (also referred to as amorphous titania microspheres). Unreacted precursors and acetone are removed via solvent exchange. After the cleaning process, the titanium glycolate microspheres are dried and calcined at 500 °C, promoting a structural change from amorphous to fully crystalline, anatase titania microspheres with a refractive index of 2.3. To achieve amorphous titania microspheres with different sizes, the concentrations of titanium butoxide and the surfactant in acetone can be adjusted (*see Note 2*). The water in acetone is assumed to control the hydrolysis rate of the glycolated precursor and, therefore, influences the microsphere size and size dispersion [36].

#### Solution A: Precursor Titanium Butoxide (TBT) Solution

1. Mix 0.46 ml TBT with 100 g ethylene glycol (EG) in an Erlenmeyer flask and incubate the solution overnight at room temperature while slowly shaking the flask on a shaking plate. During the incubation, the flask is covered with aluminum foil to keep light out. The resulting solution should be clear and colorless. It is recommended not to use the solution if it is older than a week.

#### Solution B: Surfactant Acetone Tween20 Solution

1. Mix 0.6 g Tween20 with 240 ml acetone (2.04 mM Tween20) in an Erlenmeyer flask.
2. Add 240  $\mu$ l water.

3. Mix the solution with a magnetic stirrer ( $\sim 700$  rpm) for at least half an hour.
4. After mixing, the solution should be used within a few hours.

Reaction: Titanium Glycolate Microspheres

1. Fill 100 ml of Solution B in a clean round bottom flask.
2. Add 13 ml of Solution A, close the lid and immediately shake the flask vigorously in the vertical direction for 5 s.
3. Let the solution react in the closed flask overnight for at least 11 h and at most 15 h without any mixing or stirring.
4. Centrifuge the solution for 10 min at  $3000 \times g$ .
5. Collect the microsphere pellet and resuspend the microspheres in 200 ml denatured ethanol.
6. Sonicate the solution using a bath sonicator (full power, unless noted otherwise, *see Note 1*) for 10 min and centrifuge it for 10 min at  $3000 \times g$ .
7. Collect the microsphere pellet and resuspend it in 2 ml fresh, denatured ethanol.
8. Sonicate the resuspension for 2 min to redisperse the microspheres.
9. The resulting titanium glycolate microspheres will have a diameter of 650–700 nm (*see Note 2*).

Calcination of Titanium Glycolate Microspheres to Form Anatase Titania Cores

1. Transfer the 2 ml titanium-glycolate-microsphere–ethanol suspension to a 20 ml screw neck glass bottle and sonicate the solution for 30 min.
2. Dry the titanium glycolate microspheres at  $70^\circ\text{C}$  until all the ethanol is evaporated.
3. Put the glass bottle in a furnace and heat up the microspheres to  $500^\circ\text{C}$ . Once the temperature has reached  $450^\circ\text{C}$ , the microspheres are calcined for 1 h. Do not preheat the furnace, otherwise the glass bottle can break.
4. Let the bottle cool down for 30 min at room temperature.
5. Disperse the microspheres in 2 ml fresh analytic ethanol, close the bottle with a cap, and sonicate it for 10 min.
6. Calcinated anatase titania cores are chemically stable particles and can be stored for extended periods. To prevent evaporation of the ethanol, the bottles are sealed with Parafilm and stored at  $4^\circ\text{C}$ .

7. The final calcined anatase titania microspheres that serve as cores for the subsequent steps will have a diameter of 400–500 nm and a refractive index of 2.3 (*see Note 2*).

### *3.1.2 Amorphous Titania Shell Coating*

The coating of the amorphous titania shell onto the anatase titania cores is based on a seeded-growth mechanism [37]. The cores, dispersed in ethanol, serve as nucleation centers for the titania precursor (Solution C). The resulting size and shape of the shell coating is controlled by the use of the surfactant Lutensol ON50 (Solution D) diluted in the cores solution (*see Note 3*). The refractive index of the amorphous shell can be changed from  $n = 1.55$  to  $n \sim 1.8$  by drying and resuspension of the core–shell microspheres.

#### Solution C: Precursor TBT Solution

1. Dissolve 0.2 ml TBT in 9.8 ml analytic ethanol in a 10 ml falcon tube.
2. Shake the tube vigorously in the vertical direction by hand for 1 min.
3. The solution should be used within a few hours.

#### Solution D: Surfactant Core Solution

1. Add 0.4 ml Lutensol ON50 in 10 ml deionized water (0.1 M aqueous Lutensol ON50 solution) in a 20 ml glass bottle with cap.
2. Add 80  $\mu$ l of the 0.1 M aqueous Lutensol ON50 solution to 8.92 ml analytic ethanol.
3. Sonicate the anatase titania core solution (anatase titania cores stored in analytical ethanol) for 10 min.
4. Add 1 ml anatase titania core solution to the above-prepared, 9 ml Lutensol ethanol solution by dripping continuously the 1 ml anatase titania core solution to the Lutensol ethanol solution spread over a period of at least 2 min without any stirring or mixing. After adding the cores, the solution is mixed by pipetting up and down ten times with a 1 ml pipette. Try to avoid air bubbles.
5. Let the mixture rest for 5–10 min.
6. Subsequently, sonicate the mixture for 2 min. The use of a tip sonicator with 60 % power is advisable. To prevent heating, tip-sonication should be carried out in an ice bath.

#### Reaction: Amorphous Titania Shell Coating

1. Add the entire TBT precursor (10 ml of Solution C) to the glass bottle containing the 10 ml of the surfactant core mixture (Solution D) and shake the flask vigorously in the vertical direction for 5 s.

2. Stir the solution with a magnetic stirrer with 700 rpm for 1 h.
3. Stop the reaction by centrifuging the solution for 5 min at  $3000 \times g$  and resuspend the pellet in 20 ml denatured ethanol.
4. Sonicate the microsphere solution for 10 min and repeat the centrifugation step.
5. Resuspend the core–shell microspheres in 1 ml denatured ethanol and sonicate it for 2 min.
6. To increase the refractive index of the shell from 1.55 to 1.8, dry the core–shell microspheres at 50 °C. After the ethanol is evaporated, keep the microspheres at 50 °C for an additional  $\sim 30$  min.
7. Resuspend the core–shell microspheres in 2 ml analytic ethanol and sonicate it for 10 min.
8. The titania core–shell microspheres will have diameter of 900–1300 nm with a shell refractive index of  $\sim 1.8$  (*see Note 3*).

### **3.2 Synthesis of Silica-Coated Nanodiamonds**

To optimize nanodiamonds for optical trapping and functionalization with bio-molecules, we coated the nanodiamonds with a silica shell following an established procedure [17]. The shell is produced with a conventional base-catalyzed, sol–gel reaction via the hydrolysis and condensation of tetraethyl orthosilicate (TEOS) in ethanol according to the Stöber method [38] modified by using nanodiamonds as negatively charged cores and using the surfactant hexadecyltrimethylammonium bromide (CTAB) as a template for mesopores, which are formed through the self-assembly of CTAB.

The coating method was originally based on the formation of polydisperse, mesoporous silica microspheres [39] of type MCM-41 [40]. The pores with a diameter of about 3–4 nm result from worm-like micelles (with a persistence length of about 15 nm) that CTAB forms at concentrations well above its critical micelle concentration (CMC  $\sim 1$  mM; we use about 10 mM) [41, 42] in particular in the presence of negatively charged molecules. The surfactant and ethanol are also crucial for a monodisperse coating on negatively charged, nanometer-sized cores [43–45]. Ethanol segregates to the micelles and swells them. In addition, ethanol slows down the hydrolysis and condensation reaction of TEOS promoting the growth of spherical particles via a reaction-limited monomer-cluster growth, also called Eden growth, in combination with Ostwald ripening (pp. 199–201 in [46]). Interestingly, the pores are oriented in a radial fashion, which allows the use of these particles for drug-delivery systems once CTAB is removed by washing with an ammonium nitrate solution. The shell thickness is determined by the amount of both, CTAB and TEOS [17]. To avoid clustering and to resuspend the nanodiamonds after washing

steps, the solutions are sonicated several times. All sonication steps are performed in a bath sonicator at maximum power. The bath sonicator is filled with ice-water and located in 4 °C room (*see Note 4*).

#### Solution A: Reaction Mixture

1. Cool ethanol and deionized water to 4 °C.
2. Mix 6 ml ethanol, 8.5 ml deionized water in a glass bottle with cap and store the solution at 4 °C.
3. Add 50 µl ammonium hydroxide solution (NH<sub>4</sub>OH) just before the addition of the nanodiamonds (*see Note 5*). Work under a hood!

#### Solution B: Nanodiamond Solution

1. Add 10 mg of nanodiamond powder in 10 ml deionized water (1 g/l) in a glass bottle with cap.
2. Sonicate the nanodiamond-water mixture for 10–20 min until the solution is milky and has no more visible particles.

#### Solution C: CTAB Solution

1. Dissolve 80 mg CTAB in 1.32 ml deionized water and 600 µl analytic ethanol in a glass bottle with a cap.
2. Stir the solution using a magnetic stirrer (600 rpm) until it gets clear. Note that a bit of foam can form.
3. Before use, cool the solution down to 4 °C.
4. We typically prepare a stock solution with a total volume of about 14 ml (using 10× the amounts stated above).
5. The solution can be stored for several weeks at room temperature. Do not use the solution anymore if it has turned milky.

#### Solution D: Washing Solution

1. Dissolve 1.5 mg ammonium nitrate (NH<sub>4</sub>NO<sub>3</sub>) in 100 ml analytic ethanol in a glass bottle with a cap.
2. Stir the solution using a magnetic stirrer until it gets clear.
3. The solution can be stored for several weeks at room temperature.

#### Reaction: Silica Coating

1. Put the glass bottle containing the freshly made Solution A into a sonicator with ice water.
2. Add drop-wise 5 ml of Solution B to Solution A while sonicating at maximum power.
3. Close the glass bottle with a cap and further sonicate it for 30 min in an ice water bath to maintain a temperature below 10 °C. Check the temperature from time to time. The temperature should not exceed 10 °C (*see Note 4*).

4. Add 2 ml of Solution C in a drop-wise manner to the reaction bottle containing the mixture of Solution A and B, close the bottle, and sonicate again for 30 min in ice water.
5. Remove the bottle from the sonicator and stir the solution with a magnetic stirrer (600 rpm) under the hood at room temperature.
6. Add 40  $\mu$ l TEOS to the bottle (*see Note 6*). With this amount, a shell thickness of 20–30 nm is expected at the end of the reaction (*see Note 7*).
7. The solution is stirred with a magnetic stirrer (600 rpm) at room temperature for 10–14 h (overnight). The solution should be milky. Foam might form.

#### Cleaning and Storage

1. Sonicate the reaction mixture for 10 min.
2. To remove CTAB, wash the mixture 3× with the washing solution (Solution D; use about 3–5 ml per step). Start by centrifuging the nanodiamond solution at  $20,850 \times g$  for 30 min.
3. Discard the supernatant.
4. Add 3–5 ml of Solution D and resuspend the pellet completely by sonication.
5. Repeat **steps 2 – 4** two more times.
6. Repeat **steps 2** and **3** once.
7. Add 3–5 ml of ethanol and resuspend the pellet completely by sonication.
8. Repeat **steps 2** and **3**.
9. Finally, resuspend the pellet from the last washing step in 5 ml ethanol (100 %) and sonicate until the solution is milky without visible particles.
10. Store the solution at 4 °C in glass bottles.
11. Before use, sonicate for 30 min until the solution is milky. To exchange the solvent, centrifuge at  $20,850 \times g$  for 30 min. Discard the supernatant and resuspend the pellet with the desired solvent. Sonicate until the solution is milky.

#### Preparation for TEM Imaging

1. Sonicate the nanodiamond solution until the solution is milky.
2. Dilute 1  $\mu$ l of nanodiamond solution in 9  $\mu$ l ethanol (100 %).
3. Add a drop of 3  $\mu$ l of diluted nanodiamond-ethanol solution onto the grid.
4. Wait until the drop evaporates and then add additional 3  $\mu$ l.

5. Wait until the drop evaporates.
6. Image the nanodiamonds using a TEM.
7. You can store grids in a Petri dish.

### **3.3 Preparation of Liquid-Crystalline, Birefringent Microspheres**

To make birefringent microspheres, we use a liquid crystal, called RM257, which has an ordinary and extraordinary refractive index of  $n_o = 1.508$  and  $n_e = 1.687$ , respectively, resulting in a very high birefringence of  $\Delta n = 0.179$  (quartz has  $\Delta n = 0.009$ ). Presumably due to a distortion of the nematic order, microspheres have a lower birefringence of 0.083 for unpolymerized particles and 0.031 for polymerized particles [32]. The fabrication procedure starts by dissolving the nematic liquid crystal precursor in an organic solvent at elevated temperatures. Subsequently, evaporation of the solvent causes a precipitation of spherical particles into the aqueous solution [32]. The microsphere size and polydispersity can be precisely controlled by varying the amount of the liquid crystal precursor, the volume of the organic solvent, and the evaporation rate. At room temperature, the microspheres are solid. Addition of a photoinitiator to the reaction mix before the precipitation enables the cross-linking of the mesogen. In this manner, a fixed orientation can be locked, which makes the microspheres more robust at higher temperatures and increases their shelf life. The birefringence of polymerized microspheres is lower than that of non-polymerized ones. However, polymerized microspheres remain suspended for a longer time and can be suspended in ethanol for centrifugation (*see Notes 8 and 9*). The microspheres can be functionalized using silica chemistry once a silica coating has been added as in the nanodiamond section above or by acrylate chemistry (*see Note 10*).

#### Solution A: Liquid-Crystal–Precursor Solution

1. Heat 50 ml ethanol to 55 °C in a glass beaker of 100 ml volume.
2. Add 25 mg of the mesogen RM257 to the preheated ethanol and stir the solution with a magnetic stirrer (300 rpm) while maintaining the temperature.

#### Solution B: Heated Ethanol Solution

1. Add 200 ml water to 300 ml ethanol in a glass beaker of 750 ml volume.
2. Heat the solution to 75 °C while stirring with a magnetic stirrer (300 rpm).

#### Reaction: Birefringent Microspheres

1. Once Solution B has reached 75 °C, add Solution A in a drop-wise manner while stirring the solution with a magnetic stirrer. The stirring speed should be as high as possible without forming bubbles. The ethanol–water mixture has to be maintained

above 69 °C since this is the nematic transition temperature for the mesogen RM257, above which it forms a nematic liquid crystal.

2. Let the solution evaporate at 75 °C until only 200 ml of the solution remain. The solution should have turned milky by then. The rate of evaporation can be controlled by sealing the beaker with a perforated aluminum foil. An increase in the area of perforation increases the evaporation rate, thus resulting in smaller particles and, vice versa, a decrease in the area of perforation decreases the rate of evaporation resulting in larger particles.
3. Let the solution cool down to room temperature.
4. The microspheres can be stored in a glass bottle with cap at 4 °C for several weeks with shaking once every week (*see Note 9*).

#### Polymerization and Cross-Linking the Liquid Crystal

To make polymerized microspheres, change the following steps:

1. Solution A: Additionally add 250 mg photoinitiator Darocur 1173 to Solution A. The concentration of the photoinitiator is 10× higher than the mesogen.
2. Reaction: Do not cool down the solution in the last step of the reaction. Instead, cover the whole beaker containing the milky microsphere solution with an aluminum foil and expose the sample to UV-light for 30 min at 75 °C while constantly stirring it (300 rpm). The distance of the lamp to the microsphere solution is 15 cm (*see Note 11*).
3. Let the solution cool down to room temperature.
4. The microspheres can be stored in a glass bottle sealed with a cap at room temperature for several months (*see Note 8*).

---

## 4 Notes

1. The sonication steps are important to avoid clustering of the microspheres and are performed with a bath sonicator at maximum power unless stated otherwise. We did not observe any alterations in the core and shell size and shapes for longer sonication times.
2. The size of the titanium glycolate microspheres and the anatase titania cores depend on the ratio of Solution A:B and changes linearly with the molar concentration of TBT in the final solution.
3. The amorphous shell thickness depends on the amount of TBT in Solution C. A TBT concentration higher than 2.5 % in Solution C increases the possibility of secondary nucleation and the occurrence of non-spherical microspheres. For intended shell coatings of more than 400 nm, the coating procedure can be repeated several times.

4. Using sonication may increase the reaction temperature significantly, which promotes the evaporation of ammonia, essentially removing the ammonium hydroxide from the reaction mixture.
5. Due to the high volatility of ammonia at room temperature, the effective concentration of the ammonium hydroxide solution can be drastically decreased, which hinders the completion of the formation of silica from the precursor. Therefore, ammonium hydroxide should be added freshly to the solution. Furthermore, always keep the cap of the flask with the solution closed at all times. Only open the cap when a new component should be added.
6. In the presence of water or humidity, TEOS can hydrolyze very fast to form silica. Therefore, it is advisable to store TEOS in an inert gas atmosphere.
7. The nanodiamond cores are highly heterogeneous and polydisperse. Therefore, assuming the core to be a sphere in calculations to determine the required amount of reagents may not be accurate. By trial and error, we found a minimum amount of 20 µl of TEOS is required to form a silica shell of 10–20 nm thickness. By using 160–200 µl of TEOS, a shell thickness of 80–100 nm can be achieved.
8. Polymerized microspheres are extremely stable and may remain suspended for months depending on the size. The microspheres can be concentrated by centrifugation.
9. Unpolymerized microspheres are less stable and remain suspended for 3–4 weeks depending on the microsphere size. The microspheres can be concentrated by evaporation as mentioned above.
10. It is possible to couple biomolecules to these microspheres via a silica coating of the particles. Alternatively, acrylate polymerization of exposed acrylate groups of the crystal precursor RM257 can be covalently coupled to polyethylene glycol (PEG). For example, PEG is used as a linker to attach functional single molecules to surfaces [47].
11. The UV-light exposure time and distance to the sample is optimized by a test series.

---

## Acknowledgements

We thank K. Sandomirski and T. Gisler for a detailed protocol how to make birefringent microspheres, Basudev Roy for help with the rotational power spectrum, and Sven A. Szilagyi, Melanie Eckert, Michael Bugiel, and Mayank Chugh for comments on the manuscript. This work was supported by the European Research Council (ERC Starting Grant 2010, Nanomech 260875), the Rosa Luxemburg Foundation, the Technische Universität Dresden and the Universität Tübingen.

## References

1. Neuman KC, Block SM (2004) Optical trapping. *Rev Sci Instrum* 75:2787–2809
2. Perkins T (2009) Optical traps for single molecule biophysics: a primer. *Laser Photon Rev* 3:203–220
3. Zhang H, Liu Kk (2008) Optical tweezers for single cells. *J R Soc Interface* 5:671–690
4. Fazal F, Block S (2011) Optical tweezers study life under tension. *Nat Photon* 5:318–321
5. Bormuth V, Jannasch A, Ander M et al (2008) Optical trapping of coated microspheres. *Opt Express* 16:423–427
6. Jannasch A, Bormuth V, van Kats CM et al (2008) Coated microspheres as enhanced probes for optical trapping. *Proc SPIE* 7038:70382B
7. Demirörs AF, Jannasch A, van Oostrum PDJ et al (2011) Seeded growth of titania colloids with refractive index tunability and fluorophore-free luminescence. *Langmuir* 27:1626–1634
8. Jannasch A, Mahamdeh M, Schäffer E (2011) Inertial effects of a small Brownian particle cause a colored power spectral density of thermal noise. *Phys Rev Lett* 107:228301
9. Jannasch A, Demirörs AF, van Oostrum PDJ et al (2012) Nanonewton optical force trap employing anti-reflection coated, high-refractive-index titania microspheres. *Nat Photon* 6:469–473
10. Mahamdeh M, Schäffer E (2009) Optical tweezers with millikelvin precision of temperature-controlled objectives and base-pair resolution. *Opt Express* 17:17190–17199
11. Mahamdeh M, Campos CP, Schäffer E (2011) Under-filling trapping objectives optimizes the use of the available laser power in optical tweezers. *Opt Express* 19:11759–11768
12. Craig D, McDonald A, Mazilu M et al (2015) Enhanced optical manipulation of cells using antireflection coated microparticles. *ACS Photon* 2:1403–1409
13. Tolić-Nørrelykke SF, Schäffer E, Howard J et al (2006) Calibration of optical tweezers with positional detection in the back focal plane. *Rev Sci Instrum* 77:103101
14. Yu SJ, Kang MW, Chang HC et al (2005) Bright fluorescent nanodiamonds: no photo-bleaching and low cytotoxicity. *J Am Chem Soc* 127:17604–17605
15. Fu CC, Lee HY, Chen K et al (2007) Characterization and application of single fluorescent nanodiamonds as cellular biomarkers. *Proc Natl Acad Sci USA* 104:727–732
16. Bumb A, Sarkar SK, Billington N et al (2013) Silica encapsulation of fluorescent nanodiamonds for colloidal stability and facile surface functionalization. *J Am Chem Soc* 135:7815–7818
17. von Haartman E, Jiang H, Khomich AA et al (2013) Core-shell designs of photoluminescent nanodiamonds with porous silica coatings for bioimaging and drug delivery I: fabrication. *J Mater Chem B* 1:2358
18. Gittes F, Schmidt CF (1998) Signals and noise in micromechanical measurements. In: *Methods in cell biology*, vol 55. Academic Press, New York, pp 129–156
19. Bishop A, Nieminen T, Heckenberg N et al (2003) Optical application and measurement of torque on microparticles of isotropic non-absorbing material. *Phys Rev A* 68:033802
20. Bishop AI, Nieminen TA, Heckenberg NR et al (2004) Optical microrheology using rotating laser-trapped particles. *Phys Rev Lett* 92:198104
21. La Porta A, Wang MD (2004) Optical torque wrench: angular trapping, rotation, and torque detection of quartz microparticles. *Phys Rev Lett* 92:190801
22. Deufel C, Forth S, Simmons CR et al (2007) Nanofabricated quartz cylinders for angular trapping: DNA supercoiling torque detection. *Nat Methods* 4:223–225
23. Gutiérrez-Medina B, Andreasson JOL, Greenleaf WJ et al (2010) An optical apparatus for rotation and trapping. *Methods Enzymol* 475:377–404
24. Pedaci F, Huang Z, van Oene M et al (2012) Calibration of the optical torque wrench. *Opt Express* 20:3787–3802
25. Vogel R, Persson M, Feng C et al (2009) Synthesis and surface modification of birefringent vaterite microspheres. *Langmuir* 25:11672–11679
26. Chen X, Berg HC (2000) Torque-speed relationship of the flagellar rotary motor of *Escherichia coli*. *Biophys J* 78:1036–1041
27. Xing J, Bai F, Berry R et al (2006) Torque-speed relationship of the bacterial flagellar motor. *Proc Natl Acad Sci USA* 103:1260–1265
28. Ma J, Bai L, Wang MD (2013) Transcription under torsion. *Science* 340:1580–1583
29. Toyabe S, Watanabe-Nakayama T, Okamoto T et al (2011) Thermodynamic efficiency and mechanochemical coupling of F1-ATPase. *Proc Natl Acad Sci USA* 108:17951–17956

30. Hua W, Chung J, Gelles J (2002) Distinguishing inchworm and hand-over-hand processive kinesin movement by neck rotation measurements. *Science* 295:844–848
31. Andrecka J, Ortega Arroyo J, Takagi Y et al (2015) Structural dynamics of myosin 5 during processive motion revealed by interferometric scattering microscopy. *eLife* 4:e05413
32. Sandomirski K, Martin S, Maret G et al (2004) Highly birefringent colloidal particles for tracer studies. *J Phys Condens Matter* 16:S4137
33. Nieminen TA, Loke VLY, Stilgoe AB et al (2007) Optical tweezers computational toolbox. *J Opt A: Pure Appl Opt* 9:S196–S203
34. Hu Y, Nieminen TA, Heckenberg NR et al (2008) Antireflection coating for improved optical trapping. *J Appl Phys* 103:093119
35. Yu HK, Yi GR, Kang JH et al (2008) Surfactant-assisted synthesis of uniform titania microspheres and their clusters. *Chem Mater* 20:2704–2710
36. Pal M, Serrano JG, Santiago P et al (2007) Size-controlled synthesis of spherical TiO<sub>2</sub> nanoparticles: morphology, crystallization, and phase transition. *J Phys Chem C* 111:96–102
37. Eiden-Assmann S, Widoniak J, Maret G (2005) Synthesis and characterization of hollow and non-hollow monodisperse colloidal tio2 particles. *J Disper Sci Technol* 25:535–545
38. Stöber W, Fink A, Bohn E (1968) Controlled growth of monodisperse silica spheres in the micron size range. *J Colloid Interface Sci* 26:62–69
39. Grün M, Unger KK, Matsumoto A et al (1999) Novel pathways for the preparation of mesoporous MCM-41 materials: control of porosity and morphology. *Micropor Mesopor Mater* 27:207–216
40. Kresge CT, Leonowicz ME, Roth WJ et al (1992) Ordered mesoporous molecular sieves synthesized by a liquid-crystal template mechanism. *Nature* 359:710–712
41. Shikata T, Hirata H, Kotaka T (1988) Micelle formation of detergent molecules in aqueous media. 2. Role of free salicylate ions on viscoelastic properties of aqueous cetyltrimethylammonium bromide-sodium salicylate solutions. *Langmuir* 4:354–359
42. Cates ME, Candau SJ (1990) Statics and dynamics of worm-like surfactant micelles. *J Phys: Condens Matter* 2:6869–6892
43. Liu S, Cool P, Collart O et al (2003) The influence of the alcohol concentration on the structural ordering of mesoporous silica: cosurfactant versus cosolvent. *J Phys Chem B* 107:10405–10411
44. Yoon SB, Kim JY, Kim JH et al (2007) Synthesis of monodisperse spherical silica particles with solid core and mesoporous shell: mesopore channels perpendicular to the surface. *J Mater Chem* 17:1758–1761
45. Kim JH, Yoon SB, Kim JY et al (2008) Synthesis of monodisperse silica spheres with solid core and mesoporous shell: morphological control of mesopores. *Colloids Surf A* 313–314:77–81
46. Brinker CJ, Scherer GW (1990) Sol-gel science. Academic Press, San Diego
47. Bugiel M, Fantana H, Bormuth V et al (2015) Versatile microsphere attachment of GFP-labeled motors and other tagged proteins with preserved functionality. *J Biol Methods* 2:e30

# Chapter 7

## Optical Torque Wrench Design and Calibration

Zhanna Santabayeva and Francesco Pedaci

### Abstract

Expanding the capabilities of optical traps with angular control of the trapped particle has numerous potential applications in all fields where standard linear optical tweezers are employed. Here we describe in detail the construction, alignment, and calibration of the Optical Torque Wrench, a mode of function that can be added to linear optical tweezers to simultaneously apply and measure both force and torque on birefringent microscopic cylindrical particles. The interaction between the linear polarization of the laser and the birefringent cylinder creates an angular trap for the particle orientation, described by a periodic potential. As a consequence of the experimental control of the tilt of the periodic potential, the dynamical excitability of the system can be observed. Angular optical tweezers remain less widespread than their linear counterpart. We hope this technical guide can foster their development and new applications.

**Key words** Torque, Optical tweezers, Polarization, Birefringence, Single-molecule biophysics

---

### 1 Introduction

The ability of optical tweezers to manipulate microscopic objects has been instrumental in the advance of several fields of scientific research. In particular, the biophysics community has benefited from the high spatio-temporal resolution of optical tweezers in its ability to elucidate the dynamical behavior of several biological systems, probing them at the single-molecule level and overcoming the limitations of standard bulk techniques [1]. This has been possible due to the ability to simultaneously apply force and measure the position of an object within the optical trap with resolutions within and below the nanometer range. Together with magnetic tweezers and atomic force microscopes, optical tweezers are now a frequently used instrument in the field of force-spectroscopy [2]. In typical implementations, the trapped micron-sized particle bridges the gap between the macroscopic scale of the instrumentation and the molecular scale of the system under study. Force is transmitted to the molecular level via specific surface functionalizations and attachment methods that are used to bind

the molecule of interest to the trapped particle in several different geometries.

In special configurations of optical tweezers, it is possible to control and measure not only position and force, but also *angle* and *torque* of the trapped particle. This can provide control of all the degrees of freedom of the trapped particle [3]. The possibility to align the trapped object by transferring torque has been recognized early in the development of optical tweezers [4, 5], but until present it remains less developed and employed than the standard linear mode of operation. This is mainly due to the increased technical complexity associated with the transfer of optical torque (which we will briefly describe in the next section). Overcoming these difficulties will make angular optical tweezers more accessible to a broader audience. Such an advance would positively impact fields in which linear optical tweezers find applications, and would very likely give rise to novel research possibilities.

In single-molecule studies, in particular, application and measurement of torque (via angular control of the trapped particle) provides information about important biological processes not available by solely measuring linear displacements [6–8]. Torque and rotation are in fact relevant physical parameters in fundamental molecular and cellular mechanisms. A good example is the double stranded coiled structure of DNA which, under the effect of torque, undergoes large topological modifications that the cell finely controls during processes such as replication and transcription [9–11]. Also, continuous rotation around one axis is found in at least three molecular motors. ATP synthesis and bacterial motility are based on rotary motors ( $F_0F_1$ , flagellar and gliding motors, respectively [12–14]), which produce rotation from different energy sources. The flagellar motor in particular is an extremely powerful example: using the ion motive force as an energy source, it can produce torque and speed in the nN nm and kHz range, respectively [15].

### **1.1 Transfer of Optical Torque**

The transfer of torque from the trapping beam to the trapped particle can be accomplished by different mechanisms. Using optical vortices and higher order Gauss–Laguerre transverse laser modes, *orbital* angular momentum can be transferred to homogeneous particles [16]. In these configurations, the Poynting vector of the optical mode carries angular momentum around the optical axis. Torque can be also transferred in a symmetric laser transverse mode employing special chiral particles which scatter light asymmetrically, modifying the orbital angular momentum of the beam [17, 18].

In the following, we focus on the mechanism of *spin* angular momentum (SAM) transfer, which produces torque using the symmetric TEM<sub>00</sub> laser mode on trapped *birefringent* particles. Birefringence (i.e., the anisotropy of the medium polarizability

and refractive index) implies that the electric field and the particle polarization induced by the electric field are not parallel. When the angle  $\theta$  between the field  $\vec{E}$  and the particle dipole  $\vec{p}$  is nonzero, a torque  $\vec{\tau}$  is generated according to  $\vec{\tau} = \vec{E} \times \vec{p}$ . In the implementation we discuss here, termed Optical Torque Wrench (OTW) [5, 19–21], a linearly polarized focused laser traps a cylindrical particle of quartz, a positive-uniaxial birefringent crystal. After the propagation through the medium, the linear polarization of the laser is slightly modified at the trap output, increasing its ellipticity. Using the circular polarization base, this modification can be described as an imbalance between the left and right circular components at the trap output with respect to the balanced linear input. The left and right circular polarization components correspond to photons with positive and negative angular momentum, respectively ( $L = \pm h/2\pi$ , where  $h$  is Plank's constant). An imbalance of circular components at the trap output therefore reflects a change in the beam's angular momentum which leads to torque transfer from the photons to the particle. Relying on the polarization state of the trapping beam, SAM transfer also gives the interesting possibility to measure the torque applied to the particle by polarimetry: the difference between the two circular components measured at the trap output is proportional to the torque transferred to the particle. Based on this principle, angular calibration is possible for absolute torque measurements [22], as described in Subheading 3.8.

To optimize both force and torque transfer, as mentioned above, the particles employed in an OTW are shaped by nano-fabrication to microscopic cylinders (*see* Subheading 2.3). Similarly to silica beads, linear forces of several tens of pN can be applied to these particles at reasonable laser intensities (10–100 mW in CW operation). Minimization of the scattering force acting on a cylinder, with an aspect ratio of  $\sim 2$ , forces the geometrical axis of the cylinder to align parallel to the laser propagation direction [23]. In order to maximize torque transfer, the birefringent crystals are fabricated such that their geometrical axis is perpendicular to their optical axis. If the trapped cylinder is free to rotate about its axis, the linear polarization of the laser and the extraordinary axis of the crystal tend to align. The extraordinary axis of the cylinder is therefore angularly trapped in a potential well defined by the laser polarization. The degrees of freedom of the trapped particle ( $X, Y, Z$  and two angles) are all constrained as a result of its geometry, the laser intensity gradient, and the linear polarization of the laser light (Fig. 1a).

## 1.2 Dynamics of the Optical Torque Wrench

We give here a short overview of the theory describing the angular dynamics of the trapped particle in an OTW. The interested reader can find more details in refs. [5, 19, 21, 22, 24].

The torque transferred to the positive uniaxial birefringent particle can be written in terms of the angle  $x = \theta_{\text{cyl}} - \theta_{\text{pol}}$  between the linear laser polarization  $\theta_{\text{pol}}$  and the extraordinary axis  $\theta_{\text{cyl}}$  according to

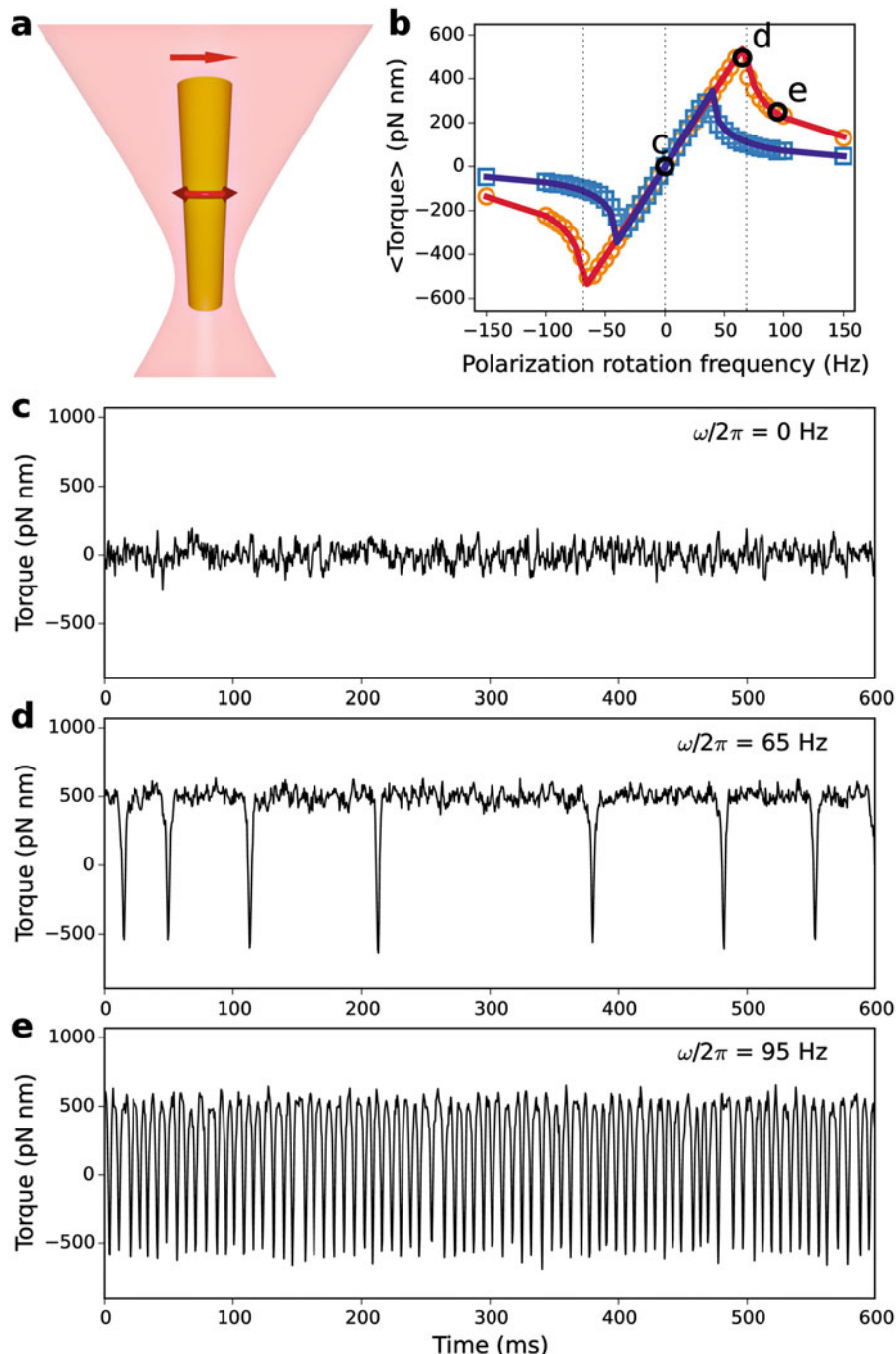


**Fig. 1** (a) Schematic representation of the trapped birefringent cylinder in its stable vertical alignment in the trap (laser coming from below), where the linear polarization (top arrow) controls the rotation of the cylinder around its geometrical axis. (b) Average optical torque  $\langle \tau \rangle$  transferred to the cylinder as a function of the polarization rotation frequency  $\omega$  for two laser intensities ( $I_1 = 55$  mW blue points,  $I_2 = 92$  mW orange points). The lines fit the data using Eq. 5 with  $\gamma = 1.3$  pN nm s,  $\omega_c = 40$  Hz for  $I_1$ , and  $\omega_c = 69$  Hz for  $I_2$ .

$$\tau = \tau_o \sin(2x), \quad (1)$$

where  $\tau_o$  is the maximum optical torque, which depends on laser intensity, particle size, and birefringence [5]. In the over-damped limit, the angular equation of motion for the particle can be written as

$$-\gamma(\dot{x} + \dot{\theta}_{\text{pol}}) - \tau_o \sin(2x) + \eta(t) = 0 \quad (2)$$

where  $\gamma$  is the angular drag coefficient of the particle and  $\eta(t)$  is the Langevin force, a Gaussian-distributed white noise term obeying

$$\langle \eta(t)\eta(t') \rangle = 2k_B T \gamma \delta(t - t').$$

For small  $x$ , linearizing the optical torque at the equilibrium point  $\tau \simeq 2\tau_o x$  leads to an angular stiffness  $\kappa = 2\tau_o$ . If the laser polarization rotates at a constant frequency  $\omega$  (i.e.  $\theta_{\text{pol}} = \omega t$ ), the equilibrium point is shifted, and the equation of motion can be written in terms of a periodic potential  $V(x) = -\frac{\tau_o}{2} \cos(2x)$ , tilted by an external force  $F = -\gamma\omega$  as

$$\gamma\dot{x} = -(V - Fx)' + \eta(t). \quad (3)$$

The net result of the drag force induced by the rotation of the laser polarization is a tilt of the sinusoidal potential.

The dynamical behavior of such a system, first described by Adler [25], depends nonlinearly on the polarization rotation frequency  $\omega$ . Two regimes exist, separated by a saddle-node bifurcation occurring at  $\omega = \omega_c = \tau_o/\gamma$ . In the first regime ( $|\omega| < \omega_c$ ), the polarization rotation speed, and consequently the drag torque on the particle, is low enough to allow the particle to follow in phase with the polarization rotation. In this regime, a strong potential barrier separates two successive stable states. As  $\omega$  approaches  $\omega_c$ , the tilt of the periodic potential increases and the energy barrier decreases. Thermal noise can now trigger an escape over the barrier, and the resulting trajectory of the system to the new equilibrium is measured as a pulse or spike in the torque signal. This is a characteristic feature of the *excitability* of the Adler system [19]. Physically, a torque spike corresponds to a transient out-of-phase rotation of the particle with respect to the rotating polarization. In the second regime, where  $|\omega| > \omega_c$ , the potential barrier

---

**Fig. 1** (Continued) Panels **c**, **d**, and **e** show the torque time traces at the frequencies indicated in panel **b**. **(c)** For  $\omega = 0$  and for all the frequencies below the critical frequency ( $\omega_c/2\pi = 69$  Hz for the intensity of 92 mW), the torque signal fluctuates around the mean value  $\gamma\omega$ . **(d)** Close to the critical frequency, noise-triggered excitable spikes start to appear, indicating transient out of phase rotation of the polarization and cylinder. **(e)** For larger  $\omega > \omega_c$  the particle remains quasi-static under the action of the quickly rotating polarization: the signal becomes more periodic, and the average torque drops to zero. Sampling rate: 20 kHz (no filter applied)

disappears, which results in the appearance of a limit cycle, a closed trajectory in the phase space, characterized by a periodic torque signal with period given by

$$T_o = \frac{\pi}{\sqrt{\omega^2 - \omega_c^2}}. \quad (4)$$

The actual period  $T_s$  of the experimental torque signal thermally fluctuates around this mean value so that  $\langle T_s \rangle \approx T_o$  [19].

The time-averaged value of the torque  $\langle \tau \rangle$  transferred from the laser to the particle can be expressed as a function of  $\omega$  in the different dynamical regimes as

$$\langle \tau \rangle = \begin{cases} \gamma(\omega - \sqrt{\omega^2 - \omega_c^2}) & \omega > \omega_c \\ \gamma \omega & |\omega| < \omega_c \\ \gamma(\omega + \sqrt{\omega^2 - \omega_c^2}) & \omega < -\omega_c \end{cases} \quad (5)$$

where the sign of  $\omega$  indicates clockwise and counterclockwise rotation. The different regimes are visible from the measurement of the mean torque as a function of  $\omega$ , as shown in Fig. 1b for two laser intensities. In Fig. 1c–e we show three typical torque traces one can measure in the different regimes. For frequencies below  $\omega_c$  (Fig. 1c), and particularly for  $\omega = 0$ , the torque signal reflects the fluctuations in a single potential well. Close to the critical frequency (Fig. 1d), excitable spikes indicate single thermally induced escape events from one potential minimum to the following. For higher frequencies (Fig. 1e), the barriers between minima disappear and the torque trace becomes more periodic. In Table 1 we review the main parameters used to describe the theory of the OTW, together with their typical experimental values and ranges.

**Table 1**  
**Parameters used to describe the OTW and their typical value or range**

Symbol	Description	Typical value(s)
$\tau_o$	Maximum torque	1000 pN nm
$\tau(t)$	Instantaneous torque transferred to the particle (Eq. 1)	$(-\tau_o, \tau_o)$
$\tau_m$	Torque measured	(−50, 50) mV
$\delta \tau_m$	standard deviation of $\tau_m$ (Eqs. 6, 7)	5–25 mV
$\gamma$	Particle drag coefficient	1 pN nm s
$\beta_\tau$	Sensitivity	0.05 mV/(pN nm)
$\kappa$	Angular stiffness ( $\simeq 2\tau_o$ )	2000 pN nm/rad
$\omega$	Polarization rotation frequency (CW and CCW)	$\omega/2\pi = (-\text{kHz}, \text{kHz})$
$\omega_c$	Critical polarization rotation frequency	$\omega_c/2\pi \sim 50 - 100 \text{ Hz}$
$T_o$	Period of the periodic solution of $\tau(t)$ for $ \omega  > \omega_c$ (Eq. 4)	$(\infty, 0)$ for $\omega = (\omega_c, \infty)$

## 2 Materials

### 2.1 Instrumentation

Experimentally, one can consider the angular system as a set of modules that can be added to standard optical tweezers setups. We focus here on the construction, alignment, and calibration of these modules, and we will not describe in detail the development of the linear optical tweezers. Refer to the excellent existing literature and Chapters 5 and 9 of this book, for detailed insights into the designs of optical tweezers [1, 26–29].

A schematic of the optical setup used in our experiments is shown in Fig. 2. The optical trap is formed between two identical microscope objectives (“objective” and “condenser”). Water immersion objectives (1.2 numerical aperture) are chosen to minimize aberrations that depend on the Z-position of the trap [30]. Before the laser light enters the objective, the beam shape, intensity, and polarization are controlled by different components. The 1064 nm laser is linearly polarized. The size of its TEM<sub>00</sub> mode is adjusted by a variable beam expander in order to fill the circular rear aperture of the objective. Coarse control of the intensity is achieved by a manual polarizer-waveplate system at the laser output (not shown), while the active adjustment of the intensity and fast

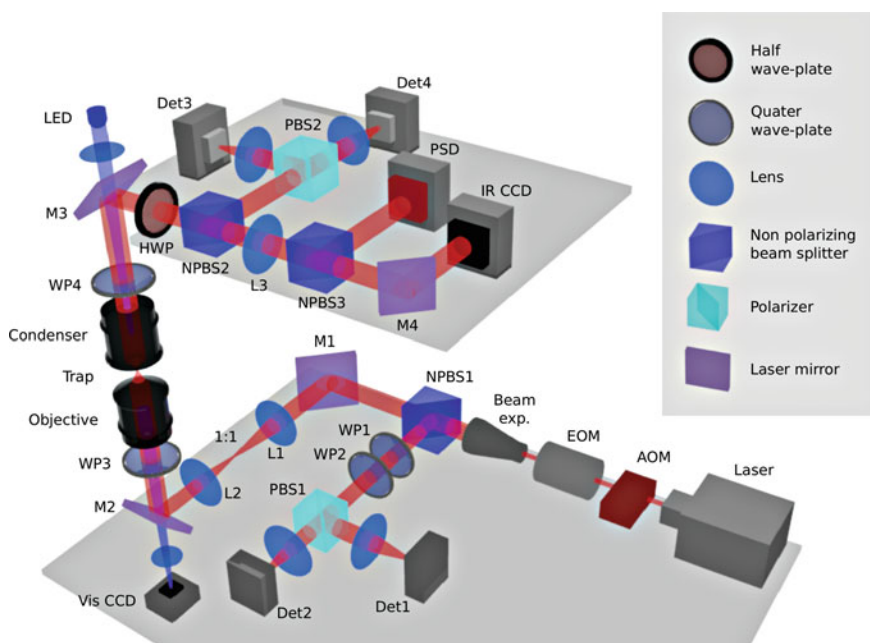


**Fig. 2** Schematic Optical Torque Wrench setup (see text for description). AOM: acousto-optic modulator. EOM: electro-optic modulator. NPBS<sub>n</sub>: non-polarizing beam splitters. WP<sub>n</sub>: quarter waveplate. HWP: half waveplate. PBS<sub>n</sub>: polarizing beam splitters. Det<sub>n</sub>: photo-detectors. L<sub>n</sub>: lenses. M<sub>n</sub>: laser line mirrors. IR and Vis CCD: infrared and visible CCD cameras. PSD: position sensitive detector. LED: light emitting diode

intensity noise reduction are performed by an acousto-optic modulator (AOM) controlled by a PID feedback loop implemented in an FPGA (detector not shown) [31].

The polarization control is based on an electro-optic modulator (EOM) [21]. Its mechanical support allows the adjustment of 4 degrees of freedom ( $x, y$ , and two angles). To maximize the EOM performance, the laser polarization purity (100:1) is improved by a Glan Laser Polarizer ( $10^5:1$  extinction ratio) inserted before the EOM (not shown). The role of the EOM is to produce, combined with the quarter waveplate WP3, a linear polarization at the trap with an orientation that depends on the EOM driving voltage (*see* Subheading 3.1). To achieve this, the EOM design allows a maximum phase shift between the two polarization components of  $\lambda$  (this maximum phase shift is the double of that obtained by standard Pockell cells). Using an EOM allows electro-optical high speed (MHz) polarization modulation with a single laser beam. The polarization state is measured before the laser light enters the objective lens by the optics included between the non-polarizing beam splitter PBS1 and the two photo-detectors Det1 and Det2. This “reference” torque measurement is necessary to remove small spurious effects of the EOM on the ellipticity of the polarization at the trap (*see* Subheading 3.3). The torque measurement is performed by detecting the polarization state at the trap output, with the optics included between the quarter waveplate WP4 and the photo-detectors Det3 and Det4.

The 1:1 telescope formed by lenses L1 and L2 is such that the plane of L1 is imaged by L2 in the back focal plane of the objective. This standard 4f configuration allows the displacement of the trap at the sample plane simply by a mechanical displacement of L1. Bright field illumination of the sample plane is achieved by a visible LED focused on the back focal plane of the condenser (i.e., the condenser focal plane closer to the LED) through the mirror M3, and collected by a tube lens and a visible CCD camera through the mirror M2 (*see Note 1*). At the trap output, the lens L3 images the back focal plane of the condenser onto a position sensitive detector (PSD) and an infrared CCD camera (IR CCD). The PSD signals can be calibrated to give the XYZ position of the center of mass of the trapped particle. The image of the laser light distribution at the condenser back focal aperture (conjugate to the plane of the trap), recorded by the IR CCD, is useful during alignment of the linear trap and gives visual clues about the presence and position of the trapped particle.

## 2.2 Components

We list here the components used in our setup (*see* Fig. 2 for the abbreviations used), together with their main characteristics and specifications.

1. The room hosting the setup is temperature controlled at 22  $\pm$  0.2 °C at equilibrium. The optical table M-RS2000 is

mounted on pneumatic legs S-2000A-428 (Newport) for vibration damping (*see Note 2*).

2. Electro-optical modulator (EOM): LM0202 LT, 1064 nm (Linos), with a maximum phase shift of  $\lambda$  between the two polarization components. EOM driver: high-voltage power amplifier PZD350A (Trek), bandwidth from DC to 90 kHz. The EOM is mounted on the 4-axis mechanical stage 902082-02 (Newport) for alignment.
3. Objective and condenser: Zeiss C-Apochromat 63x/1.2NA Water Corr, M27m wd 0.28 mm at 0.17 mm. Immersion oil: Zeiss Immersol W 2010.
4. Piezo-stage: P-517.3CD,  $100 \times 100 \times 20 \mu\text{m}$ , resolution 0.3 nm ( $X, Y$ ) 0.1 nm ( $Z$ ). Driver: E712-3CD (Physik Instrumente).
5. Laser: ALS-IR-1064-3-SF (Azur Light Systems), 3W CW, rms  $< 0.03\%$  (20 Hz–20 MHz),  $1064 \pm 0.5 \text{ nm}$ , 100:1 linear polarization purity,  $\text{TEM}_{00}$  with  $M^2 < 1.1$ , pointing stability  $< 1 \text{ rad}/^\circ\text{C}$ . As a secondary laser, we use SDL-1064-LN-2000T, 1064 nm, 2W CW (Shanghai Dream Lasers Technology Co Ltd). Bright field illumination (LED): M660L3, 660 nm, 640 mW (Thorlabs).
6. Acousto-optical modulator (AOM): AOM MT80-A1,5-1064. AOM driver: MODA80 fixed frequency driver (AA-Optoelectronic).
7. Optical components. Mirrors: Y1S-1025-45,  $R_s - R_p \sim 2\%$  and Y1-1025-45-P,  $R_s - R_p \sim 0.01\%$  (CVI Melles Griot). Beam expander: 2-8x 4401-256-000-20 (Linos Qioptiq). Lenses: PLCX 1064 nm (CVI Melles Griot).
8. Polarization optics. Nonpolarizing beam splitters (NPBS): 10 BC16NP.9 (Newport), 1064 nm,  $R/T = 50/50 \pm 3\%$ . Half and quarter waveplates: QWPO 1064-10-2 and QWPO 1064-10-4 (CVI Melles Griot). The waveplates are mounted on precision mechanical rotary mounts PRM1/M (Thorlabs), *see Note 3*. Glan laser polarizer: CPAD 10.0-670-1064 5 (CVI Melles Griot),  $10^5:1$  extinction ratio. Polarizers (PBS): XEP-1064.0-25.0M (CVI Melles Griot)  $10^4:1$  extinction ratio.
9. Detection systems. Photo-detectors (Det): DET 10N/M, InGaAs Detector, 500–1700 nm, 5 ns rise time (Thorlabs). Position sensitive detector (PSD): DL100-7-PCBA3 (First sensor Inc). Video cameras (VisCCD and IRCCD): DCC1545M CMOS Camera (Thorlabs). I/O cards: PXI-7852R FPGA, 750 kHz analog input, 1 MHz analog output (National Instruments).
10. Software. The hardware is controlled by a program developed in LabVIEW (National Instruments), while the analysis of the acquired data is performed in Python (*see Note 4*).

### 2.3 Birefringent Cylinder Fabrication

The first realizations of SAM transfer and measurement in an optical tweezers were performed on microscopic birefringent crystals with irregular shapes [5, 20]. It was then realized that the uniaxial positive birefringence is advantageous to uniquely align the extraordinary axis of the particle with the linear polarization [20]. The cylindrical geometry of the particle was later finely tuned during nano-fabrication [32] to precisely define the aspect ratio [23] and the orientation of the optical axis which fixed all the degrees of freedom of the particle in the optical trap.

Different protocols for cylinder fabrication have been developed, all based on the etching of cylindrical posts from a quartz substrate that has the correct alignment of the optical axis (Z-cut). After etching, the crystalline posts are mechanically cleaved from the substrate, collected and stored in solution (*see Note 5*). Masking of the substrate prior to etching has been achieved by different strategies. Optical lithography [21, 32] requires the fabrication of a mask to be used during the exposure, but has the advantage of being a parallel process (the entire pattern is written at the same time). Electron lithography [33] is the most accurate procedure, but is serial (the pattern is written by a scanning electron beam) and costly. Nano-sphere lithography of cylinders [34] has also been developed with the aim to reduce complexity and costs.

Recently, we have succeeded in producing micro-cylinders for the OTW by laser interference lithography, a simple, inexpensive and fast method [42]. Figure 3 shows the final result of our method, depicting a region of the substrate where the cylinders have been mechanically cleaved. The following results presented in this chapter are based on experiments with these particles.

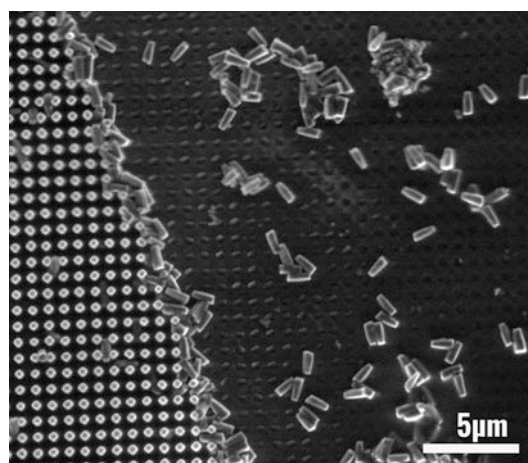


**Fig. 3** Quartz birefringent cylinders used in this work, obtained by laser-interference lithography. The image is taken in a region of the wafer where the particles have been partially mechanically cleaved from the substrate

### 3 Methods

#### 3.1 Polarization Design

In optical setups, fine control of the polarization is usually not trivial. Optical components, even if optimized, have different amplitude and phase responses for  $s$  and  $p$  reflections, which can lead to polarization degradation. Therefore, the ellipticity and orientation of the polarization are generally kept fixed along the beam propagation, often to have mainly  $s$  reflections. Torque transfer by SAM requires fine polarization control because the ellipticity and orientation dynamically change along the beam path (*see Note 6*). We start by describing the basic design of the polarization system we use for torque transfer and measurement. We will then show how this design can lead to artifacts in the torque signal due to imperfections and residual birefringence in the EOM and other optical elements. Finally, we will describe how one can correct for such systematic errors to get accurate torque measurements.

In Fig. 4a we schematically show the optical elements involved in the preparation of the laser polarization (at the trap input) and torque measurement (at the trap output). In Fig. 4b, we show how the polarization is affected by the EOM voltage along the same optical elements depicted in Fig. 4a, and how the final torque measurement depends on voltage and angle between the particle axis and the rotating polarization. The goal of the polarization preparation is to obtain at the trap position a polarization with minimal ellipticity where the angle is linearly proportional to the voltage  $V$  driving the EOM. The EOM can be described as a birefringent crystal sandwiched between two electrodes perpendicular to its extraordinary axis. In this geometry, the application of voltage between the electrodes uniquely changes the refractive index of the extraordinary axis and thereby “dephases” the polarization component propagating parallel to it while leaving the perpendicular component unaltered.

1. The laser polarization, filtered by a GL polarizer, is linear and vertical with respect to the optical table. All reflective optical parts are optimized for  $45^\circ$  reflection.
2. The EOM axis is aligned at  $45^\circ$  (Fig. 4) with respect to the input vertical polarization. The ellipticity of the EOM output is a function of the applied voltage.
3. The axis of the subsequent quarter waveplate (WP3, as in Fig. 2) is aligned at  $45^\circ$  with respect to the EOM axis. The two linear components parallel to the EOM axis have the same amplitude and voltage-dependent phase difference, and are transformed by WP3 into two opposite (L–R) circular components.

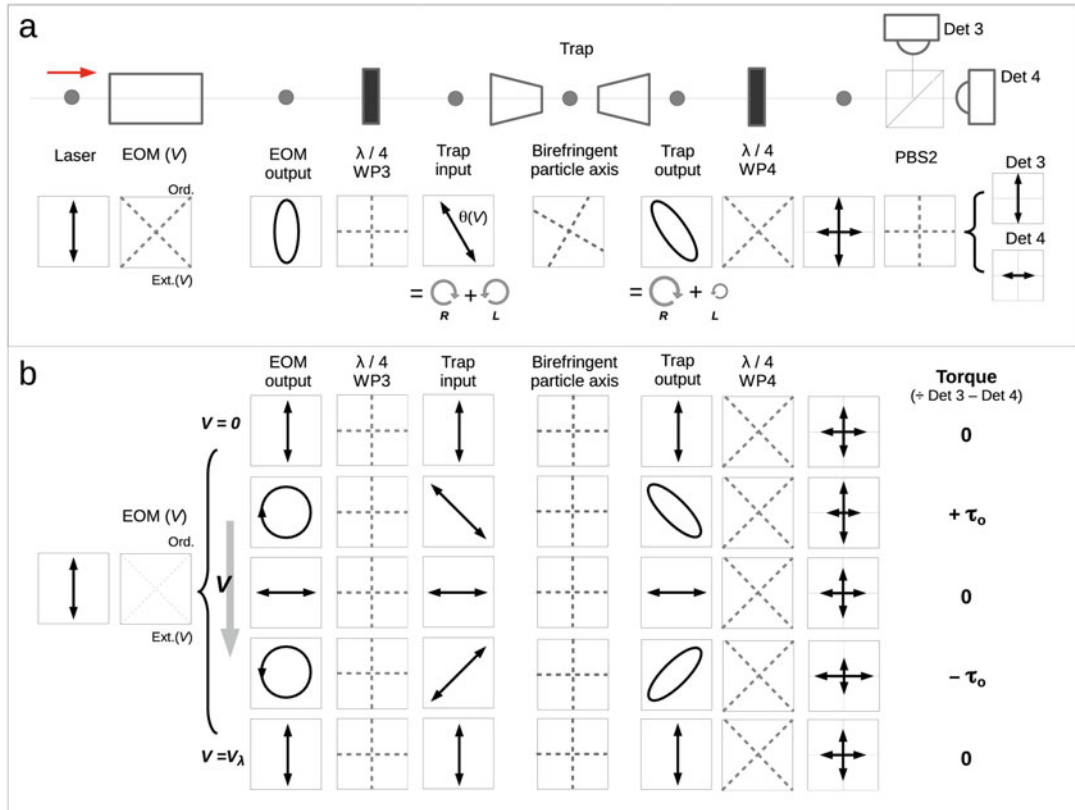


**Fig. 4** Schematic polarization path. **(a)** The optical components used to control the polarization are indicated (*upper row*, compare with Fig. 2) together with their optical axis and the corresponding polarization states (*lower row*) along the beam path. **(b)** The effect on the polarization state of increasing the EOM driving voltage  $V$  is schematically indicated at the position of the same optical components shown in **(a)**. The net effect at the trap is to rotate a linear polarization, similar to what a single half waveplate would do if mechanically rotated. Continuous rotation of the linear polarization at the trap is achieved by a sawtooth signal  $V$  of amplitude  $V_\lambda$  (the voltage required to obtain a phase shift of  $\lambda$  between the two EOM components). In the trap, the axis of the birefringent particle is considered fixed. The polarization state at the trap output is analyzed by the quarter waveplate WP4 and polarizer PBS2. The difference between the signals recorded by detectors Det3 and Det4 is proportional to the torque transferred to the particle

4. The circular components have identical amplitudes, while their relative phase is voltage-dependent. Their sum has therefore a linear polarization at the trap input with the orientation linearly dependent on the EOM voltage.
5. To obtain a continuously rotating linear polarization at the trap, the EOM voltage has to be modulated by a sawtooth voltage with peak-to-peak amplitude equal to  $V_\lambda$  in order to obtain smooth rotations of the polarization between  $0^\circ$  and  $180^\circ$  followed by fast transitions from  $180^\circ$  to  $0^\circ$ . The EOM driver should allow voltage transitions between  $V = 0$  and  $V = V_\lambda$  which are much shorter than the characteristic time of the particle in the optical angular trap (1–10 ms), in order not to

perturb the effective steady rotation of the polarization experienced by the particle during the voltage jump. The symmetry of the sawtooth (e.g., either the signal slowly increases from  $V = 0$  to  $V = V_\lambda$  then quickly jumps back to  $V = 0$ , or the opposite) sets the direction of rotation (CW or CCW) of the polarization, while its frequency controls the polarization rotation speed  $\omega$  (*see Note 7*).

### 3.2 Torque Measurement

The polarization at the output of the trap, after propagation through the birefringent crystal, acquires an amount of ellipticity which depends on the angle  $x$  between the extraordinary axis of the particle and the input linear polarization, and on the particle's dimensions and birefringence. This ellipticity increase is small but measurable.

1. The elliptical polarization at the trap output can be decomposed into two opposite circular components, whose amplitudes are no longer identical (Fig. 4a).
2. The quarter waveplate WP4 is aligned at  $45^\circ$  with respect to WP3, and transforms these two circular components into two linear components (parallel and perpendicular to the original laser polarization).
3. The following polarizer (PBS2) separates the two linear components and the two photo-detectors Det3 and Det4 record their intensities. The difference between the two signals is proportional to the torque transferred to the particle.

### 3.3 Correction of Spurious Ellipticity

Due to the finite efficiency of the EOM and possibly to other residual birefringence in the optical path, the polarization at the trap retains a small spurious amount of ellipticity, with a small dependence on the applied voltage (1–5 % in our setup). During steady rotation of the polarization, this voltage dependent ellipticity leads to a torque signal which is deterministically modulated at the frequency of the EOM (*see*, for example, Fig. 6).

1. To dynamically correct for this artifact, we perform a torque background measurement which we subtract from the torque measurement performed at the trap, using the optics included between the non-polarizing beam splitter NPBS1 and the detectors Det1–Det2 (Fig. 2). This *reference* signal is equivalent to the torque signal measured using an empty trap. It is acquired simultaneously to the actual torque transferred at the trap, and automatically removed from it.
2. As we measure the reference as the reflection from a beam splitter (NPBS1), this could introduce extra phase and amplitude variations between the two polarization components (the nominal intensity difference between reflection and transmission is 3 %). To compensate both, at the trap output, we also measure

the torque from the reflection of an identical beam splitter (NPBS2).

3. The use of the periscope (M2–M3) inverts the horizontal and vertical polarization components at the output of the trap with respect to the input. The half waveplate HWP (placed between M3 and NPBS2) rotates the polarization by  $90^\circ$ , and therefore restores the symmetry between the torque measurement at the trap output and the reference measurement (i.e., the same components are reflected and transmitted by PBS1 and PBS2).

### 3.4 Alignment of the EOM Axis

The following instructions describe how to optimize the alignment of the EOM axis with respect to the linear polarization of the input beam (Fig. 5a).

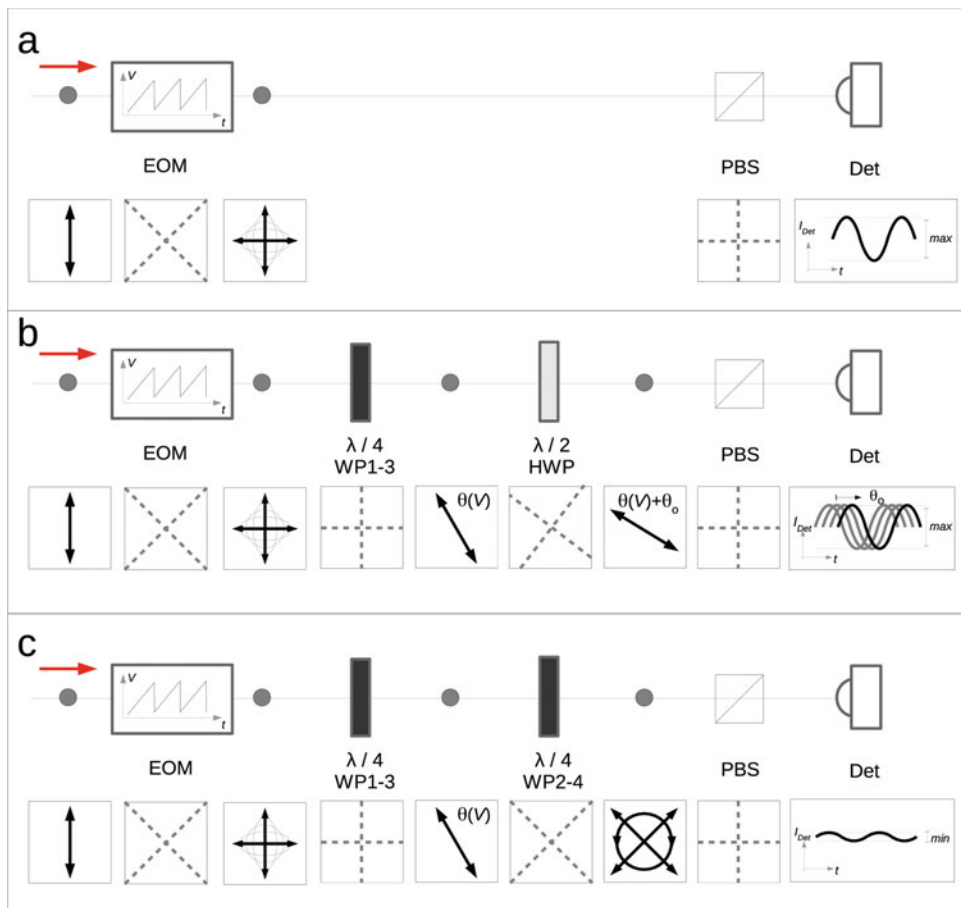


**Fig. 5** Schematic alignment procedure for the polarization path and torque measurement (see Subheading 3.4 for details). For each panel, the *first row* shows the optical components employed (compare with Fig. 2), while the *second row* displays the optical axis of each component, their input–output polarization states, and a schematic time trace measured by the detector (Det) following the polarizer PBS. (a) EOM axis alignment. (b) Alignment of the first quarter waveplate (WP1 or WP3), using a half waveplate (HWP) and the PBS as analyzer. (c) Alignment of the second quarter waveplate (WP2 or WP4)

1. Position the EOM, followed by a polarizer and a photo-detector. The polarization at the EOM input is set linear and vertical with respect to the plane of the table. The axes of the polarizer are horizontal and vertical.
2. Maximize the transmission of the EOM by adjusting the rotation around its geometrical axis to align the EOM position and angles.
3. Apply a sawtooth voltage signal to the EOM, using the nominal amplitude  $V_\lambda$  of the device (at any frequency within its bandwidth). With an oscilloscope, monitor both the EOM voltage and the signal from the photo-detector.
4. Rotate the EOM axis to maximize the contrast of the sinusoidal signal recorded by the photo-detector. In this condition, the axis of the EOM will be at  $45^\circ$  with respect to the input polarization.
5. Precisely adjust the amplitude of the sawtooth voltage signal  $V_\lambda$ , by observing and minimizing the discontinuity of the sinusoidal signal recorded by the detector in response to the jump in voltage of the sawtooth.

### **3.5 Trap and Reference Polarization**

In Fig. 5b we show how to achieve the alignment of the quarter waveplates WP1–WP3, which convert the polarization from the EOM into a linear polarization for the reference and trap torque measurements, respectively. In Fig. 5c, we show the alignment of the quarter waveplates WP2–WP4, which are used, together with the polarizers PBS1 and PBS2, to measure the torque in the reference (by Det1 and Det2) and in the trap (by Det3 and Det4), respectively.

1. In the configuration described above (Subheading 3.4), place a quarter waveplate and a half waveplate between the EOM and polarizer (Fig. 5b).
2. Align the quarter waveplate axis to be horizontal and vertical. After the quarter waveplate, the polarization should be linear and rotating as a function of the EOM voltage. This can be checked by rotating the half waveplate, which simply introduces an extra rotation angle  $\theta_o$  to the rotating linear polarization. The angle of the quarter waveplate is optimized when a rotation of the half waveplate produces only a temporal shift in the photo-detector sinusoidal signal without affecting its contrast.
3. The quarter waveplate can now be used as WP3 at the trap input. A similar procedure can be used for WP1 in the reference arm at the reflection of NPBS1.
4. From the previous configuration, exchange the half waveplate with the second quarter waveplate WP4 (Fig. 5c).
5. Align the axis of WP4 to be at  $45^\circ$  with respect to the first quarter waveplate. When this condition is achieved, the

components parallel to the polarizer axis have identical intensity and do not depend on the EOM voltage. This can be optimized by minimizing the contrast of the signal of the photo-detector.

6. The same procedure is used for the reference arm, with waveplates WP1 and WP2.

### **3.6 Optimization of Torque Measurement in an Empty Trap**

The torque transferred to a trapped particle ( $\tau_{\text{trap}}$ ) is proportional to the difference between the signals recorded by photo-detectors Det3 and Det4, and corrected by the reference torque  $\tau_{\text{ref}}$  measured by the difference between the signals of Det1 and Det2. To optimize the alignment, we use here the fact that the reference torque signal must be equal to the torque signal obtained when the optical trap is empty.

1. Use a sample solution with no particles, to prepare for a measurement with an empty trap (see Note 8).
2. Apply the optimized sawtooth voltage to the EOM (see Subheading 3.4) to rotate the linear polarization at the trap.
3. Optimize the alignment of the photo-detectors (Det1 to Det4) to obtain signals with similar amplitude. Ideally all signals should be constant in time, but as discussed in Subheading 3.3, a modulation will likely be visible due to spurious birefringence in the optical path. Obtain the same peak-to-peak value in the reference signals (Det1 and Det2) and in the trap output (Det3 and Det4). If needed, use filters to reduce the intensities measured by Det2 and Det3, which record higher intensities than Det3 and Det4.
4. Compute the difference signals  $(\text{Det3} - \text{Det4}) = \tau_{\text{trap}}(t)$  and  $(\text{Det1} - \text{Det2}) = \tau_{\text{ref}}(t)$ . Precisely align the quarter waveplates WP3 and WP4 to match the torque measurement at the trap output with the reference measurement (see Notes 3 and 9).
5. Compute and display the time trace of the signal  $\tau(t) = \tau_{\text{trap}} - \alpha \tau_{\text{ref}}$ , where  $\alpha$  is a control parameter that accounts for a possible constant difference in amplitude between the signals recorded in the reference arm and at the trap output.
6. Choose a value of  $\alpha$  that produces a constant trace for  $\tau(t)$  (see Note 10).
7. Repeat from point 4, until the trace  $\tau(t)$  is constant, as expected from the torque transferred to an empty trap.

### **3.7 Optimization of Torque Measurement with a Trapped Particle**

1. Use a sample with a concentration of birefringent particles such that on average no more than one particle is present per field of view of the microscope, in order to avoid trapping of multiple particles. Trap one birefringent particle.
2. Apply the sawtooth EOM voltage at low frequency. The polarization rotation frequency  $\omega$  should be below the critical

frequency  $\omega_c$  of the trapped particle (expect  $\omega_c \sim 50\text{--}200$  Hz), in order for the particle to rotate in phase with the polarization (*see* Subheading 1.2).

3. The signal  $\tau(t)$  reflects the angular fluctuations of the trapped particle in the sinusoidal potential defined by the (slowly rotating) polarization (*see* Subheading 1.2), similarly to the fluctuations around the equilibrium position of a bead trapped in a moving trap. Therefore, the trace  $\tau(t)$  should not display any deterministic modulation at the EOM frequency. In case a modulation is present, minimize it as described in point 4 of Subheading 3.6 above (*see* Notes 11 and 12).
4. When  $\omega$  is increased further, spikes in the torque trace  $\tau(t)$  should appear when  $\omega_c$  is reached and passed. This behavior is the fingerprint of the dynamic *excitability* of the angularly forced system [19], and is the final test for a proper alignment. In Fig. 6a we show both the reference and trap output torque measurements for  $\omega$  close to the critical frequency  $\omega_c$ . Even if minimized according to the procedure described above, the spurious modulation at the EOM sawtooth frequency is clearly

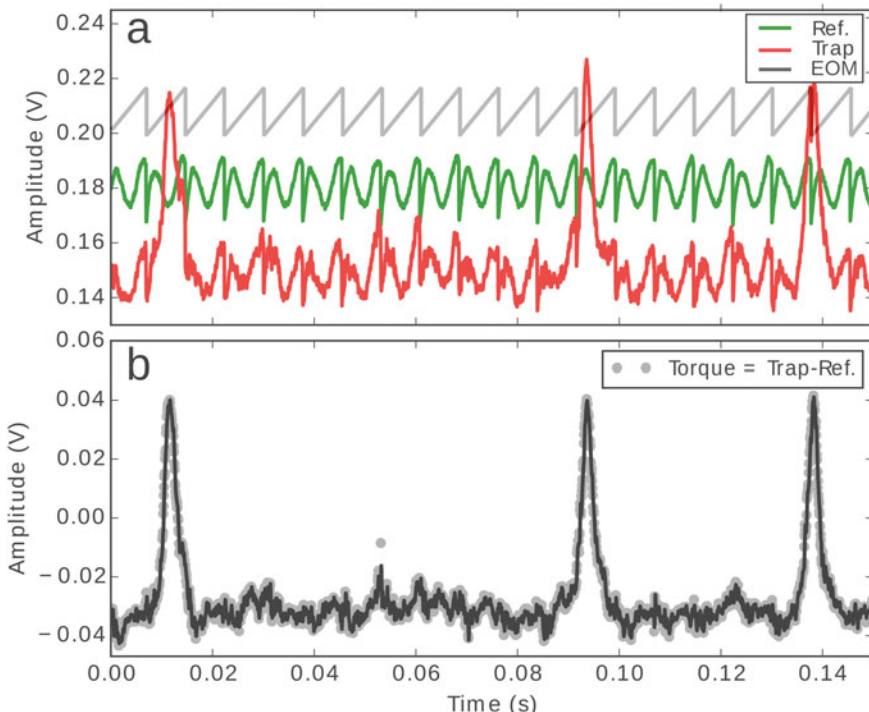


**Fig. 6** Torque measurement close to the critical point ( $\omega \sim \omega_c$ ). (a) Time traces of the torque measured at the trap output (red), the torque reference (green) showing the deterministic modulation at the EOM frequency, and the EOM sawtooth driving voltage (gray), with peak-to-peak amplitude of 1.4 V (rescaled for convenience) and frequency of 128 Hz (therefore  $\omega/2\pi = 64$  Hz). (b) Trace of the torque transferred to the particle, resulting from the subtraction of the reference torque from the trap torque of panel a. Excitable spikes are visible. The sampling rate is 20 kHz (gray points), low-pass filtered at 5 kHz (dark line).  $I = 92$  mW

visible in the two signals. In Fig. 6b, their weighted difference  $\tau(t)$  is plotted (see Subheading 3.6). In the resulting torque trace, the amplitude at the EOM modulation frequency is minimized below the level of the thermal noise acting on the particle.

### 3.8 Methods of Angular Calibration

Many similarities exist between the calibration procedures for linear and angular traps. One important difference is the underlying optical potential, which is periodic in the angular system. This leads, among other effects, to the possibility that the particle explores the full angular potential without physically escaping from it, contrary to what happens in linear optical tweezers when the non-parabolic extremities of the potential well are visited. This feature is exploited during calibration. Different experimental methods to calibrate the angular trap exist [20, 22]. We review here three of them which have been described in more detail in [22].

As in linear optical tweezers, three parameters need to be quantified during the calibration of an OTW:

1. The *torque sensitivity*  $\beta_\tau$  [in units of V/(pN nm)], which is used to transform the torque signal measured in Volts into torque physical units.
2. The *angular stiffness* of the trap  $\kappa$  (in units of pN nm/rad), or equivalently, the *maximum torque*  $\tau_o$  (in units of pN nm).
3. The *angular drag coefficient*  $\gamma$  of the particle (in units of pN nm s).

During calibration, the only control parameter that is varied is the polarization rotation frequency  $\omega$ , while the other parameters (laser intensity, position of the trap, etc.) are kept fixed. A positive (negative) value of  $\omega$  indicates rotation in the CCW (CW) direction. In general, the number of points in the measured torque trace  $\tau_m(t)$  should be large enough to record several spikes when  $\omega$  approaches  $\omega_c$ , while the sampling frequency should allow full resolution of their shape (200 kHz sampling rate is used in the following).

#### 3.8.1 Torque Standard Deviation

Starting from Eq. 1, it is possible to analytically express the standard deviation  $\delta \tau_m$  of the experimentally measured torque signal  $\tau_m$  as a function of the polarization rotation frequency  $\omega$  as

$$\delta \tau_m = \beta_\tau \sqrt{2\tau_o k_B T} \left[ 1 - (\omega/\omega_c)^2 \right]^{\frac{1}{4}} \quad \text{for } \omega < \omega_c \quad (6)$$

$$= \beta_\tau \tau_o \left[ \frac{\sqrt{(\omega/\omega_c)^2 - 1}}{(\omega/\omega_c) + \sqrt{(\omega/\omega_c)^2 - 1}} \right]^{\frac{1}{2}} \quad \text{for } \omega > \omega_c \quad (7)$$

1. After alignment, record the torque signal  $\tau_m(t)$  for a set of different values of  $\omega$  (controlled by the EOM sawtooth

frequency), covering the range from  $\omega \ll -\omega_c$  to  $\omega \gg \omega_c$ . The sign of  $\omega$  is controlled by the symmetry of the sawtooth signal driving the EOM.

2. The critical frequency  $\omega_c$  can be simply estimated from the lowest EOM frequency at which spikes in the torque trace are visible.
3. Plot the standard deviation of the torque signal  $\delta \tau_m$  as a function of  $\omega$  (Fig. 7a). The fit of the experimental values, using Eqs. 6 and 7, yields the three calibration parameters  $\beta_\tau$ ,  $\tau_o$ , and  $\gamma = \tau_o/\omega_c$ .

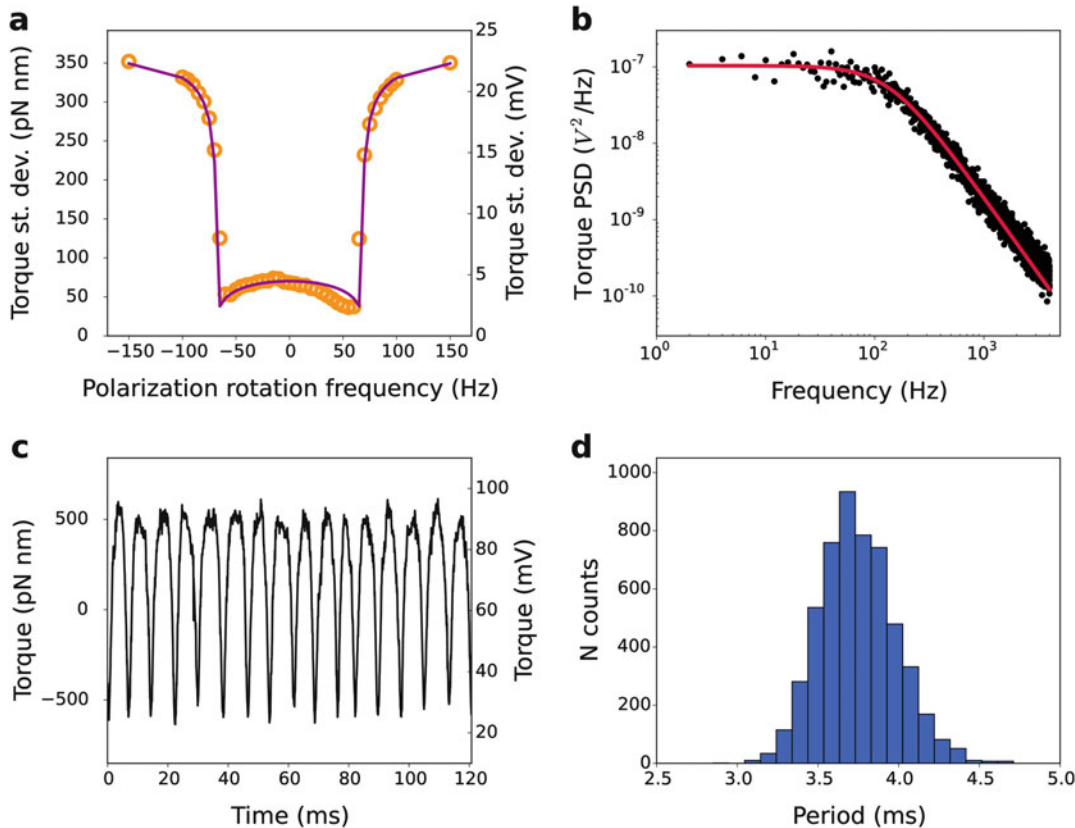


**Fig. 7** Calibration of the OTW, performed at a laser power of 92 mW (see Fig. 1). (a) Torque standard deviation  $\delta \tau_m$  (points) measured as a function of polarization rotation frequency  $\omega$  (Subheading 3.8.1). The line represents the fit of the data using Eqs. 6 and 7, giving  $\tau_o = 432$  pN nm,  $\gamma = 1.0$  pN nm s, and  $\beta_\tau = 0.080$  mV/(pN nm). (b) Power spectral density of the measured torque  $\tau_m$  (points) at  $\omega = 0$  Hz (Subheading 3.8.2). The Lorentzian fit (line) yields the parameters  $A_o = 1.93$  mV<sup>2</sup> Hz (Eq. 8) and  $f_c = 135$  Hz (Eq. 9). One extra measurement (as in panel c) is required for full calibration. (c) Torque trace for  $\omega$  in the periodic regime with  $\omega/2\pi = 95$  Hz and  $\omega_c/2\pi = 69$  Hz (see also Fig. 1e). Here the measurement of  $V_o = 36.7$  mV (half peak-to-peak amplitude), together with the measurements of  $A_o$  and  $f_c$  from panel b, gives  $\tau_o = 495$  pN nm,  $\gamma = 1.2$  pN nm s, and  $\beta_\tau = 0.074$  mV/(pN nm) (Subheading 3.8.2, Eqs. 10–12). (d) From the single trace shown in panel c, one can extract the three quantities which provide full calibration (Subheading 3.8.3) measuring the moments of the distribution of the period  $T_S$  between spikes (mean  $\langle T_S \rangle = 3.7$  ms and variance  $\delta T_S^2 = 0.05$  ms<sup>2</sup>) and the standard deviation of the signal ( $\delta \tau_m = 26$  mV). Using Eqs. 16–18 we obtain  $\tau_o = 464$  pN nm,  $\gamma = 1.1$  pN nm s, and  $\beta_\tau = 0.083$  mV/(pN nm)

### 3.8.2 Power Spectrum and Maximum Torque Amplitude

- Setting  $\omega = 0$ , record a sufficiently long torque trace  $\tau_m$ . If linearization around the particle's stable point is possible (i.e.,  $\tau_o \gg k_B T$ ), the power spectral density of  $\tau_m$  is described by a Lorentzian  $P_o(\tau_m, f) = A_o/(f^2 + f_c^2)$ , with amplitude

$$A_o = 4\beta_\tau^2 \tau_o^2 k_B T / (\pi^2 \gamma) \quad (8)$$

and corner frequency [20, 21]

$$f_c = \tau_o / (\pi \gamma) = \omega_c / \pi. \quad (9)$$

- Fitting the experimental spectrum to the Lorentzian function yields the two independent variables  $A_o$  and  $f_c$  (Fig. 7b, see Note 13).
- A third independent variable is obtained by a torque measurement performed at  $\omega > \omega_c$ , by measuring the amplitude  $V_o$  (defined as half of the peak-to-peak value in Volts) of the periodic torque trace (Fig. 7c).
- The value of  $V_o$  can vary along the torque trace due to the small spurious modulation discussed in Subheading 3.3. An accurate average value of  $V_o = \beta_\tau \tau_o$  can be obtained inverting Eq. 7 and measuring the standard deviation  $\delta \tau_m$  of the entire recorded torque signal.
- Using the measured three variables  $A_o, f_c$ , and  $V_o$ , the calibration parameters are given by

$$\gamma = 4k_B T V_o^2 / (\pi^2 A_o) \quad (10)$$

$$\tau_o = \pi \gamma f_c \quad (11)$$

$$\beta_\tau = V_o / \tau_o. \quad (12)$$

### 3.8.3 Diffusion in a Tilted Potential

As shown in Subheading 1.2, the OTW angular dynamics correspond to the motion of a particle in a sinusoidal potential tilted by the drag torque for  $\omega \neq 0$ , and subject to thermal noise. The effective diffusion coefficient  $D_{eff}$  for a particle diffusing in a tilted periodic potential is different from that described by the Einstein relation  $D_o = k_B T / \gamma$  [37, 38]. For the OTW, the effective diffusion coefficient for  $\omega > \omega_c$  can be expressed as

$$D_{eff} = \frac{\pi^2 \delta T_s^2}{2 \langle T_s \rangle^3} = \frac{k_B T}{\gamma} f(r) \quad (13)$$

where  $\delta T_s^2$  is the variance of the torque period and  $f(r)$  is the function

$$f(r) \approx \frac{1}{\sqrt{1 - r^2}} + \frac{2\sqrt{1 - r^2}}{1 + \sqrt{1 - r^2}} \left[ r^2 + \frac{5}{4} r^4 \left( 1 + \frac{1}{1 + \sqrt{1 - r^2}} \right) \right] \quad (14)$$

where  $r = \omega_c / \omega$  (for more details, see ref. [22]).

1. Fix  $\omega > \omega_c$  and record the resulting torque signal  $\tau_m$ . In this regime, the analytical solution predicts a periodic torque signal with deterministic period  $T_o$  given by Eq. 4 (Fig. 7c). Experimentally, the measured period  $T_s$  is statistically distributed around  $T_o$ . The recorded trace should be long enough to correctly sample the distribution of  $T_s$ .
2. Measure the average value of the torque period  $\langle T_s \rangle$  and its variance  $\delta T_s^2$  in the temporal domain (see Fig. 7d).
3. From Eq. 4, calculate the critical frequency

$$\omega_c = \tau_o / \gamma = \sqrt{\omega^2 - (\pi / \langle T_s \rangle)^2}. \quad (15)$$

4. From the value of  $\omega$  and  $\omega_c$  calculate the corresponding values of  $r$  and  $f(r)$  (Eq. 14).
5. The drag coefficient of the particle is calculated from Eq. 13 as

$$\gamma = \frac{2k_B T \langle T_s \rangle^3}{\pi^2 \delta T_s^2} f(r). \quad (16)$$

6. The maximum optical torque can now be calculated from  $\gamma$  and  $\omega_c$  by

$$\tau_o = \gamma \omega_c. \quad (17)$$

7. Measure the standard deviation  $\delta \tau_m$  of the torque trace, and find the angular sensitivity  $\beta_\tau$  from Eq. 7

$$\beta_\tau = \frac{\delta \tau_m}{\tau_o} \sqrt{\frac{(\omega / \omega_c) + \sqrt{(\omega / \omega_c)^2 - 1}}{\sqrt{(\omega / \omega_c)^2 - 1}}}. \quad (18)$$

### 3.8.4 Calibration Accuracy and Precision

The precision of the parameters  $(\tau_o, \gamma, \beta_\tau)$  resulting from a given calibration procedure can be quantified by  $N$  iterations of the same procedure, allowing one to find the mean and error of each parameter. However, the error of each parameter can also be estimated from a single iteration by standard error propagation in the analytical expression used. The major source of measurement error is the spurious torque modulation discussed in Subheading 3.3. When such a systematic error is minimized below the level of the thermal noise (as in Fig. 6), we find that the relative errors of the three parameters are of the order of 10 % [22].

The accuracy of the calibration can be verified by comparing the measured drag coefficient  $\gamma$  with the expected theoretical value  $\gamma_{\text{th}}$  of a cylindrical particle of a given size [39]. The particle dimensions can be determined from EM images as shown in Fig. 3 (average the two diameters in case of a conical shape). For the cylinders used

here, with an average length of  $1.5 \pm 0.1 \mu\text{m}$  and a diameter of  $550 \pm 50 \text{ nm}$ , the theoretical angular drag coefficient can be estimated as  $\gamma_{\text{th}} \sim 1.7 \pm 0.4 \text{ pN nm s}$ , which is reasonably close with the values obtained by the different methods ( $\gamma = 1.0, 1.2, 1.1 \text{ pN nm s}$ ).

## 4 Notes

1. It is not advisable to use standard dichroic mirrors (such as the ones used in fluorescence experiments) in the laser path (e.g., as M2 and M3), as they would compromise the intensity and phase balance of the two *p-s* polarization components. Using laser grade mirrors has the advantage of having a narrow band of high reflection for both polarization components, so that other wavelengths can be used in transmission for sample illumination (specifically here through M2 and M3).
2. We find it convenient to build the microscope from modular parts, instead of using a commercial solution. The modularity allows for modifications of the setup and gives access to all internal components. The optical trap is vertical in our setup, in order to leave the sample plane horizontal. The trap output is sent to the detection systems, located on a horizontal plane (as in Fig. 2). This is convenient for access, alignment, and stability. The laser pointing stability, especially critical for the measurement of linear displacement, can be substantially improved by placing tubes around the beam to minimize airflow. This is especially important where the beam is focused in air (e.g., in the 1:1 telescope formed by L1 and L2).
3. The precise alignment of the quarter waveplates WP3 and WP4 is particularly critical to obtain a good torque signal (free from the spurious modulation at the EOM frequency). Mount these waveplates on rotary stages, which can be controlled with micrometer resolution by manual actuators. Physical access to the waveplates in the microscope body should be possible and simple, as they need to be aligned most frequently. Alternatively, the waveplates could be controlled by rotary motorized stages.
4. We use LabVIEW to program the hardware–software interface, especially because several vendors provide compatible plug-and-play drivers and software for their hardware. In particular we use a LabVIEW controlled FPGA card to acquire and to process output signals. For data analysis, we opted for Python which is free, open source, and vastly used. We suggest the use of the command shell IPython, together with the extensions NumPy (arrays and matrices), SciPy (scientific computing),

matplotlib (scientific graphics), mayaVi (3D visualization), and the IDEs Spyder or Anaconda.

5. Once the cylinders are cleaved from the surface of the wafer, they can be stored in pure water. Cylinders tend to stick to the walls of a plastic cuvette. This does not happen in a glass cuvette. BSA or alcohol can also be added to the solution to avoid cylinder clustering.
6. We assume that the polarization state at the focus of the objective during our experiments is linear. This explains the behavior of the birefringent particle, which can be fitted reasonably well by the theoretical model. However, the actual polarization state at the trap can be modified once the beam is focused by a large NA objective. Therefore, a more detailed model of the polarization of a tightly focused beam is required to better approximate the real polarization state of the OTW [40].
7. The frequency of the EOM sawtooth signal is equal to  $2\omega$ , where  $\omega$  indicates the rotation frequency of the linear polarization at the trap. The polarization rotates  $360^\circ$  in two periods of the sawtooth signal.
8. The flow cell hosting the cylinders is made of two glass cover slips (170  $\mu\text{m}$  thickness) separated by a rectangular piece of melted parafilm with a hand-cut channel ( $\sim 3$  mm wide). The top slide is prepared by drilling two small holes ( $\sim 1$  mm diameter) for inlet and outlet using a sandblaster. A manual syringe is used to pump the solution in the flow cell.
9. To match the reference and trap torque signals while fixing  $\omega < \omega_c$ , sequentially acquire traces of less than 1 s and dynamically display  $\tau_{\text{trap}}$  as a function of  $\tau_{\text{ref}}$ . Optimize the angle of WP3 and WP4 in order to obtain a linear plot. Any systematic deviation from a linear relation in such a graph is the result of the spurious modulation at the EOM frequency.
10. Another useful plot to display during the alignment is  $\tau(t) = \tau_{\text{trap}} - \alpha\tau_{\text{ref}}$  as a function of the EOM sawtooth voltage. For  $\omega < \omega_c$ , this plot should be as flat as possible. This allows to optimize the alignment and the value of  $\alpha$ .
11. It is also possible to minimize the spurious modulation with the alignment described in Subheading 3.3 while displaying the spectrum of the trace  $\tau$ . In the spectrum, a peak at the EOM frequency ( $2\omega$ ), together with its harmonics, is well visible and should be minimized.
12. For  $\omega < \omega_c$ , the torque trace  $\tau(t)$  should be noisy with a DC component that linearly depends on  $\omega$ . Check the dependency of the DC component of  $\tau(t)$  on  $\omega$  (see Fig. 1b). If not observed, the alignment of the wave plates probably needs to be improved.

13. The procedure to fit the angular spectrum with a Lorentzian is identical to that performed in linear optical tweezers for the position of the particle. Therefore, the analysis developed for linear optical tweezers can be readily applied here, *see*, for example, ref. [41] for a deeper analysis of the data.

## Acknowledgements

We are grateful to B. Charlot (IES Montpellier, France) for the novel nano-fabrication protocol of the particles and their SEM image, and to A. Nord for critical reading of the manuscript. We acknowledge funding from the European Research Council under the European Union's Seventh Framework Programme (FP/2007-2013)/ERC Grant Agreement n.306475.

## References

1. Neuman KC, Block SM (2004) Optical trapping. *Rev Sci Instrum* 75:2787–2809
2. Neuman KC, Nagy A (2008) Single-molecule force spectroscopy: optical tweezers, magnetic tweezers and atomic force microscopy. *Nat Methods* 5:491–505
3. Padgett M, Bowman R (2011) Tweezers with a twist. *Nat Photon* 5:343–348
4. Ashkin A, Dziedzic JM (1987) Optical trapping and manipulation of viruses and bacteria. *Science* 235:1517–1520
5. Friese MEJ, Nieminem TA, Heckenberg NR, Rubinsztein-Dunlop H (1998) Optical alignment and spinning of laser-trapped microscopic particles. *Nature* 394:348–350
6. Bryant Z, Oberstrass FC, Basu A (2012) Recent developments in single-molecule DNA mechanics. *Curr Opin Struct Biol* 22:304–312
7. Forth S, Sheinin MY, Inman J, Wang MD (2013) Torque measurement at the single-molecule level. *Ann Rev Biophys* 42:583–604
8. Lipfert J, van Oene M, Lee M et al (2015) Torque spectroscopy for the study of rotary motion in biological systems. *Chem Rev* 115:1449–1474
9. Gilbert N, Allan J (2014) Supercoiling in DNA and chromatin. *Curr Opin Genet Dev* 25:15–21
10. Forth S, Deufel C, Sheinin MY et al (2008) Abrupt buckling transition observed during the plectoneme formation of individual DNA molecules. *Phys Rev Lett* 100:148301
11. Ma J, Bai L, Wang MD (2013) Transcription under torsion. *Science* 340:1580–1583
12. Yoshida M, Muneyuki E, Hisabori T (2001) ATP synthase - a marvellous rotary engine of the cell. *Nat Rev Mol Cell Biol* 2:669–677
13. Sowa Y, Berry RM (2008) Bacterial flagellar motor. *Q Rev Biophys* 41:103–132
14. Shrivastava A, Lele PP, Berg H (2015) A rotary motor drives flavobacterium gliding. *Curr Biol* 25:338–341
15. Magariyama Y et al (1994) Very fast flagellar rotation. *Nature* 371:752–752
16. Lavery MPJ, Speirits FC, Barnett SM, Padgett MJ (2013) Detection of a spinning object using light's orbital angular momentum. *Science* 341:537–540
17. Galajda P, Ormos P (2001) Complex micro-machines produced and driven by light. *Appl Phys Lett* 78:249–251
18. Normanno D, Capitanio M, Pavone F (2004) Spin absorption, windmill, and magneto-optic effects in optical angular momentum transfer. *Phys Rev A* 70:053829
19. Pedaci F, Huang Z, Oene Mv et al (2011) Excitable particle in an optical torque wrench. *Nat Phys* 7:259–264
20. La Porta A, Wang MD (2004) Optical torque wrench: angular trapping, rotation, and torque detection of quartz microparticles. *Phys Rev Lett* 92:190801
21. Gutierrez-Medina B, Andreasson JOL, Greenleaf WJ et al (2010) An optical apparatus for rotation and trapping. *Methods Enzymol* 475:377–404
22. Pedaci F, Huang Z, van Oene M, Dekker NH (2012) Calibration of the optical torque wrench. *Opt Exp* 20:3787–3802

23. Cao Y, Stilgoe AB, Chen L et al (2012) Equilibrium orientations and positions of non-spherical particles in optical traps. *Opt Exp* 20:12987–12996
24. Inman J, Forth S, Wang MD (2010) Passive torque wrench and angular position detection using a single-beam optical trap. *Opt Lett* 35:2949–2951
25. Adler R (1946) A study of locking phenomena in oscillators. *Proc IRE* 34:351–357
26. Moffitt JR, Chemla YR, Smith SB, Bustamante C (2008) Recent advances in optical tweezers. *Annu Rev Biochem* 77:205–228
27. Nicholas MP, Rao L, Gengerich A (2014) An improved optical tweezers assay for measuring the force generation of single kinesin molecules in mitosis. In: *Mitosis*, vol. 1136. Springer, New York, pp 171–246
28. Svoboda K, Block SM (1994) Biological applications of optical forces. *Annu Rev Biophys Biomol Struct* 23:247–285
29. Mameren J v, Wuite GJL, Heller I (2011) Introduction to optical tweezers: background, system designs, and commercial solutions. In: *Single molecule analysis*. Humana Press, pp 1–20
30. Lee WM, Reece PJ, Marchington RF, Metzger NK, Dholakia K (2007) Construction and calibration of an optical trap on a fluorescence optical microscope. *Nat Protoc* 2:3226–3238
31. Schwettmann A, Sedlacek J, Shaffer JP (2011) Field-programmable gate array based locking circuit for external cavity diode laser frequency stabilization. *Rev Sci Instrum* 82:103103
32. Deufel C, Forth S, Simmons CR et al (2007) Nanofabricated quartz cylinders for angular trapping: DNA supercoiling torque detection. *Nat Methods* 4:223–225
33. Huang Z, Pedaci F, Wiggin M et al (2011) Electron beam fabrication of micron-scale birefringent quartz particles for use in optical trapping. *ACS Nano* 5:1418–1427
34. Li P-C, Chang J-C, La Porta A, Yu ET (2014) Fabrication of birefringent nanocylinders for single-molecule force and torque measurement. *Nanotechnology* 25:235304
35. Forth S, Deufel C, Sheinin MY et al (2008) Abrupt buckling transition observed during the plectoneme formation of individual DNA molecules. *Phys Rev Lett* 100:148301
36. Tolić-Nørrelykke SF, Schäffer E, Howard J et al (2006) Calibration of optical tweezers with positional detection in the back focal plane. *Rev Sci Instrum* 77:103101
37. Reimann P, den Broeck CV, Linke H et al. (2001) Giant acceleration of free diffusion by use of tilted periodic potentials. *Phys Rev Lett* 87:010602
38. Asakia KS, Mari SA (2005) Diffusion coefficient and mobility of a Brownian particle in a tilted periodic potential. *J Phys Soc Jpn* 74:2226–2232
39. Tirado MM, de La Torre JG (1980) Rotational dynamics of rigid, symmetric top macromolecules. Application to circular cylinders. *J Chem Phys* 73:1986
40. Kang H, Jia B, Gu M (2010) Polarization characterization in the focal volume of high numerical aperture objectives. *Opt Exp* 18:10813–10821
41. Berg-Sørensen K, Flyvbjerg H (2004) Power spectrum analysis for optical tweezers. *Rev Sci Instrum* 75:594
42. Santybayeva Z, Meghit A, Desgarceaux R et al (2016) Fabrication of quartz microcylinders by laser interference lithography for angular optical tweezers. *J Micro/Nanolith MEMS MOEMS* 0001;15(3):034507.

# Chapter 8

## High-Resolution “Fleezers”: Dual-Trap Optical Tweezers Combined with Single-Molecule Fluorescence Detection

Kevin D. Whitley, Matthew J. Comstock, and Yann R. Chemla

### Abstract

Recent advances in optical tweezers have greatly expanded their measurement capabilities. A new generation of hybrid instrument that combines nanomechanical manipulation with fluorescence detection—fluorescence optical tweezers, or “fleezers”—is providing a powerful approach to study complex macromolecular dynamics. Here, we describe a combined high-resolution optical trap/confocal fluorescence microscope that can simultaneously detect sub-nanometer displacements, sub-piconewton forces, and single-molecule fluorescence signals. The primary technical challenge to these hybrid instruments is how to combine both measurement modalities without sacrificing the sensitivity of either one. We present general design principles to overcome this challenge and provide detailed, step-by-step instructions to implement them in the construction and alignment of the instrument. Lastly, we present a set of protocols to perform a simple, proof-of-principle experiment that highlights the instrument capabilities.

**Key words** Optical tweezers, Optical trapping, Single-molecule fluorescence, Förster resonance energy transfer, FRET, Confocal microscopy, Fleezers

---

### 1 Introduction

Optical traps—or “optical tweezers”—utilize the momentum of light to exert forces on microscopic objects. By tightly focusing a laser beam, a dielectric object such as a micron-sized polystyrene bead can be trapped stably in three dimensions near the focus of light [1]. Beyond its ability to manipulate microscopic objects, an optical tweezer setup is a sensitive quantitative tool. The trap behaves as a linear, “Hookean” spring near its center, and can be used to measure displacements of a trapped bead and the forces exerted on it with sub-nanometer and sub-piconewton (pN) resolution, respectively. This sensitivity range has made optical tweezers a powerful tool to study biological macromolecules at the single molecule level. Optical traps have been used to stretch nucleic acids and proteins, probing their mechanical properties and how secondary and tertiary structures unravel under force [2, 3]. Stretching

individual molecules of DNA or RNA has also become a powerful approach to study protein–nucleic acid interactions [4, 5]. Optical tweezers are particularly amenable to the study of molecular motors, which generate forces on pN scales. They have been instrumental in deciphering the mechanism of a wide range of molecular motors involved in cytoskeletal transport, the central dogma, and beyond (reviewed in refs. [6, 7]). Recent advances in design have improved the resolution of these instruments to where it is now possible to observe directly molecular motion on the scale of a single base pair (bp) of DNA. *High-resolution* optical tweezers [8, 9] now provide unprecedented access to the stepping dynamics of nucleic acid motors (reviewed in ref. [10]): transcription by RNA polymerase with 1 bp resolution [8, 11], translation codon by codon by the ribosome [12], RNA and DNA unwinding by helicases at the bp scale [13, 14], and hierarchical bp-scale stepping in translocases [15].

Despite such advances, optical traps have important limitations. Macromolecular dynamics involve conformational changes that are inherently three-dimensional in nature. Most optical trap measurements are ill-equipped to capture this complexity of motion, projecting all movement onto a single axis, along the direction of applied force [16]. As a result, only a limited view of the underlying dynamics is provided. In addition, optical trap measurements have often been limited to investigating systems involving few components, examined in isolation. Many cellular processes, however, involve highly coordinated, multicomponent assemblies. Optical trap assays can be ill-suited to study larger complexes because they typically measure only a single dynamical observable, which does not reveal internal dynamics or coordination within these complexes. These limitations have motivated the development of new single-molecule techniques that can measure complex macromolecular dynamics.

A new generation of *hybrid* optical tweezers has allowed simultaneous measurement of multiple observables. Optical *torque* traps exert and measure force and torque simultaneously [17], and several fluorescence optical tweezers (or *fleezers*) combining fluorescent imaging capabilities with mechanical manipulation have been developed [18–21]. In this chapter, we describe the design of an instrument that combines high-resolution optical tweezers with single-molecule fluorescence microscopy (Fig. 1) [16]. A unique aspect of this instrument, which contrasts with other optical trap/fluorescence designs, is that neither fluorescence detection nor optical trap sensitivity is sacrificed in combining the techniques. The high-resolution fleezers can simultaneously detect fluorescence signals with single-molecule sensitivity, mechanical displacements with sub-nm resolution, and forces with sub-pN resolution [16].

Figure 1 displays three examples of measurements feasible with this instrument. The confocal microscope can either be used to

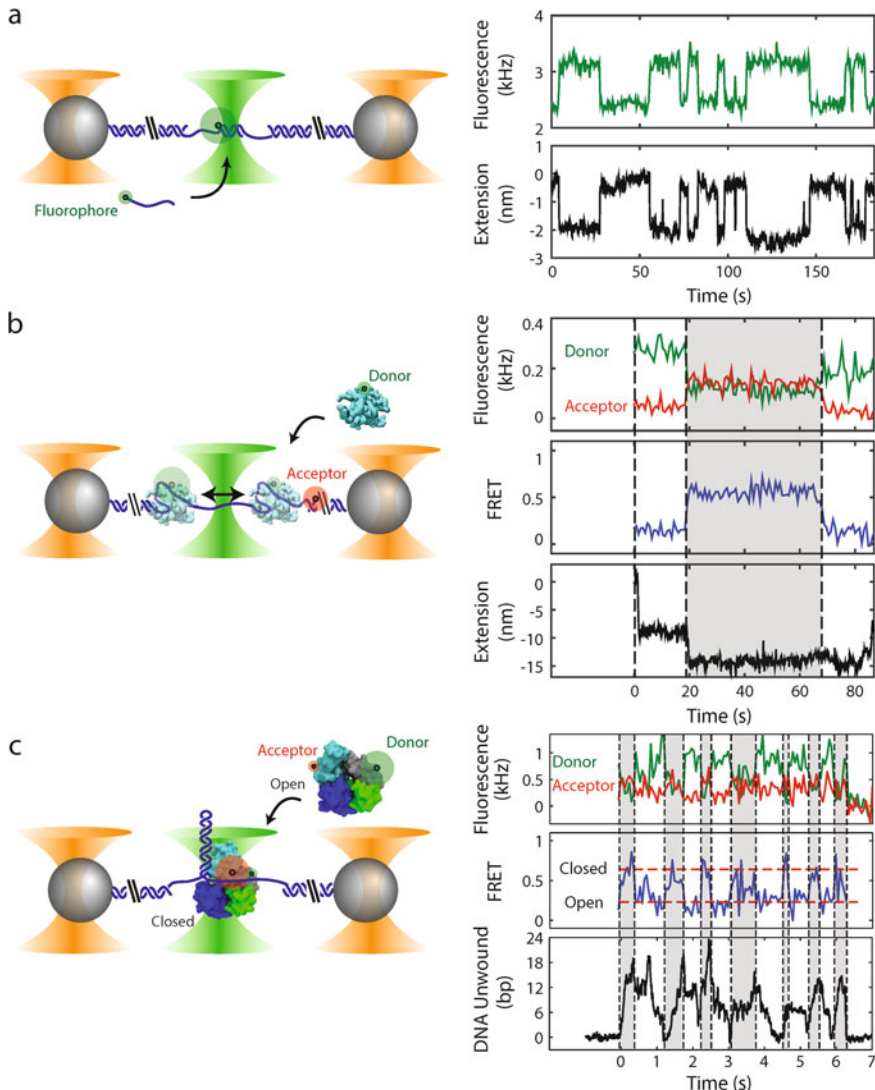


**Fig. 1** Examples of experiments with combined high-resolution optical trap and fluorescence (not to scale). *Left panels:* Polystyrene microspheres (grey) are held in optical traps (orange cones), tethered by an engineered DNA molecule (blue) containing a variable central segment flanked by long double-stranded DNA (dsDNA) handles. Fluorophores are excited by a green laser (green cone). *Right panels:* Time traces showing simultaneous measurement of fluorescence and tether extension. **(a) Oligonucleotide hybridization.** Short oligonucleotides (blue line) labeled with a fluorophore (green disk) bind and unbind to a complementary ssDNA section in the center of the tethered DNA. The fluorescence and change in tether extension upon hybridization are recorded simultaneously. **(b) Single-stranded DNA binding protein wrapping dynamics.** A tethered DNA molecule containing a short ssDNA region is labeled with a FRET acceptor at the ss-dsDNA junction (red disk). An *E. coli* single-stranded DNA binding protein (SSB, cyan) labeled with a FRET donor (green disk) binds to and wraps ssDNA around itself. Simultaneous measurement of FRET efficiency and tether extension enables determination of both the position of SSB along the tether and the amount of ssDNA wrapped. The SSB can transiently wrap and unwrap ssDNA under tension (e.g.,  $t = 20$  s), and can diffuse one-dimensionally along the ssDNA by reptation ( $t = 70$  s) (data reproduced from ref. [22] with permission

count dye-labeled molecules or to detect dynamics by single-molecule Förster Resonance Energy Transfer (smFRET), while the traps detect mechanical displacements and forces from the DNA molecule stretched between the two trapped beads. In the first example (Fig. 1a), fluorescence is used to detect a dye-labeled oligonucleotide binding to a complementary DNA sequence tethered between trapped beads, while the trap detects the change in extension upon hybridization, as single-stranded (ss)DNA is converted to double-stranded (ds) DNA [16]. In the second (Fig. 1b), *E. coli* single-stranded DNA binding protein labeled with a single donor fluorophore wraps ssDNA labeled with an acceptor dye. The combination of trap and smFRET is used to distinguish between protein wrapping/unwrapping ssDNA and its diffusion along ssDNA [22]. Finally (Fig. 1c), internal conformational dynamics of *E. coli* UvrD helicase labeled with a donor and acceptor dye are detected by smFRET simultaneously with detecting its unwinding of a DNA hairpin by optical trap [23].

Stability and sensitivity are key to this instrument's performance. We use a *dual trap* design (Fig. 1), in which both traps are formed from the same laser, as it provides exceptional stability [9]. As a consequence, trapping is done away from the sample chamber surface, and we detect fluorescence using *confocal microscopy* (as opposed to total internal reflection microscopy often used in surface-based assays). An important technical challenge is that fluorophores photobleach very quickly near an optical trap. This results from the fluorophore absorbing trap infrared photons while in the excited state, leading to a transition into a dark state [24]. Since this mechanism requires absorption of both fluorescence excitation and trap light, one solution is to separate the optical trap and fluorophore by a large distance, preventing simultaneous exposure of the dye to both light sources [19]. However, this approach is not conducive to high-resolution measurement. It necessitates long molecules to tether to the trapped beads, which are compliant and poor transducers of mechanical signals. High resolution requires close proximity between trap and fluorophore, and the solution is to separate the two light sources *in time* [25].

---

**Fig. 1** (continued) from eLife Sciences Publications. (c) UvrD helicase conformational and unwinding dynamics. A tethered DNA molecule contains a hairpin and short ssDNA protein loading site. *E. coli* UvrD helicase (cyan, blue, grey, and green) is labeled with FRET donor and acceptor pair to differentiate between two possible conformational states: "Open" and "Closed." Simultaneous measurement of FRET efficiency and number of DNA base pairs of the hairpin unwound by the helicase enables correlation of the conformation with the activity of the helicase. Changes in UvrD conformational state correspond to switches between unwinding and rezipping of the DNA hairpin (reproduced from ref. [23] with permission from AAAS). The proteins in this figure were prepared with VMD [48] using PDB entries 1EYG, 2IS2, and 3LFU

### a Instrument setup

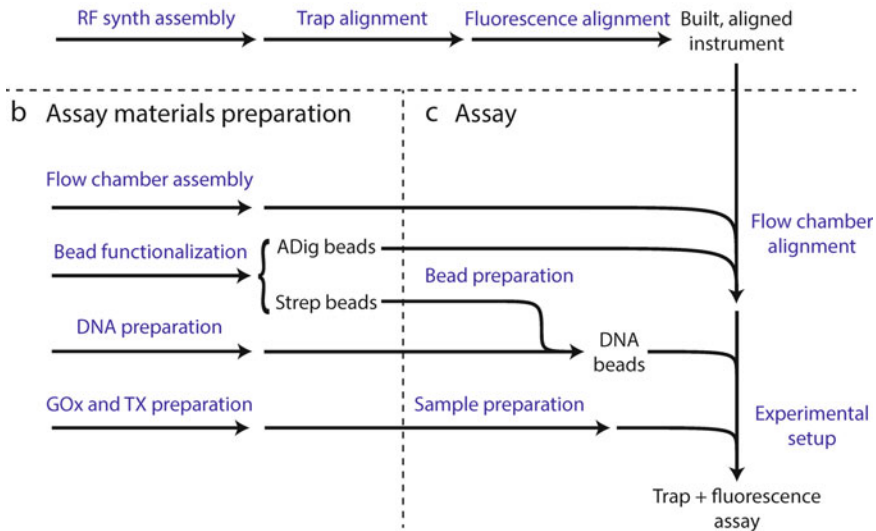


**Fig. 2** Protocol summary. (a) Sequence of major steps involved in assembling and aligning the instrument. (b) Materials for the trap + fluorescence assay are prepared in parallel, including two sets of functionalized beads: anti-digoxigenin (ADig) beads and streptavidin (Strep) beads, and stock solutions of glucose oxidase + catalase (GOx) and trolox (TX). (c) Major steps involved in setting up a trap + fluorescence assay

By *interlacing* the two light sources at a high rate, i.e., turning them on and off out of phase, it is possible to attain a 20-fold improvement in photobleaching lifetime over exposing the fluorophore simultaneously to fluorescence excitation and trapping light [25].

In this chapter, we describe in detail the design and construction of our hybrid high-resolution optical trap/confocal microscope (for an overview, see Fig. 2). We note that many protocols for building and aligning optical traps have been discussed elsewhere [26–28], and we do not repeat these here. Instead, we focus on the complexities specific to combining single-molecule fluorescence detection with optical traps. We provide a detailed parts list, optical layout, and general design principles to build the instrument. Since interlacing is an essential feature of the instrument, we devote much of the chapter to the materials and protocols for precise timing and synchronization of the light sources and data acquisition. We also provide detailed protocols for aligning the confocal microscope to the optical traps. Lastly, materials and protocols are given for doing a simple, proof-of-principle experiment to measure the binding of a fluorescently labeled oligonucleotide to a complementary single-stranded DNA molecule tethered between trapped beads (Fig. 1a).

---

## 2 Materials

### 2.1 Optical Trap Setup

There are many considerations in designing and constructing an optical trap, many of which are beyond the scope of this chapter. We refer the reader to the many excellent resources on this topic [26, 28, 29]. The combined optical trap/confocal microscope layout relies on general design principles that maximize stability, spatial and temporal resolution, and control. The instrument is housed in a temperature-regulated, acoustically isolated room, and built on a thick optical table levitated on pneumatic isolators. All optical components that the trap or fluorescence lasers impinge on are mounted to the optical table by 1"-thick pedestals. Wherever possible, high-performance optomechanical components (e.g., kinematic mirror mounts, translation stages) are used and are equipped with locking screws so that they can be fixed after alignment. We also adhere to the general philosophy of "less is more," i.e., the fewest components should be used to achieve a specific purpose. Our experience is that more components increase the coupling of noise into the instrument. In contrast to many optical trap designs, we also do not integrate the traps into an inverted microscope body. This provides us with complete control over all instrument components and more flexibility in design.

The overall optical layout consists of three separate "modules": one for the optical trap, one for the fluorescence confocal microscope, and one for the bright-field imaging system (Fig. 3 and 4). We discuss the optical trap module first. General construction and alignment procedures are not discussed in detail, as these can be found elsewhere [26, 27]. Instead, we focus only on those features unique to the instrument and on its essential components: (1) trapping laser, (2) acousto-optic modulator, (3) objective, and (4) detectors.

The traps are generated by a 5-W, 1064-nm fiber laser. The advantage of this type of laser is that the single-mode, polarization-maintaining fiber is also the laser cavity, which provides an optimal (Gaussian) beam profile and pointing stability. The emitted infrared (IR) light first passes through an optical isolator (ISO1), which eliminates back-reflection into the laser cavity, followed by a power modulation stage consisting of a half-wave plate (HW1) on a rotary stage and polarizing beamsplitter (PBS1) cube. These components are used to divert power from the trapping beam by rotating its polarization axis prior to the PBS. Excess light is reflected into a high-power beam dump (BD). This stage is used for coarse adjustment of the laser power as needed typically for initial alignment protocols. The trap acousto-optic modulator (AOM1) controls the laser power once the trap laser is aligned.

The AOM is used in the next stage to switch the IR light on and off for interlacing with the fluorescence excitation, as described

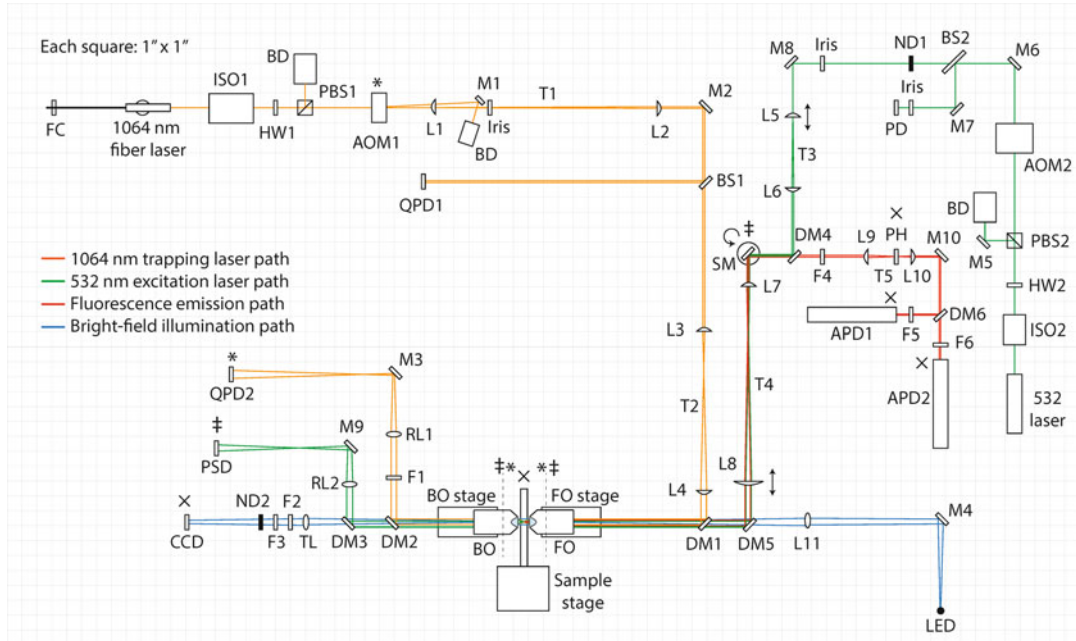


**Fig. 3** Detailed layout of the instrument (to scale). *FC* fiber clamp; *ISO* optical isolator; *HW* half-wave plate; *PBS* polarizing beam-splitting cube; *BD* beam dump; *AOM* acousto-optic modulator; *L* lens; *M* mirror; *BS* beam-splitter; *QPD* quadrant photodiode; *DM* dichroic mirror; *FO* front objective; *BO* back objective; *F* filter; *RL* relay lens; *TL* tube lens; *ND* neutral density filter; *PD* photodiode; *SM* steerable mirror; *PSD* position-sensitive detector; *PH* pinhole; *APD* avalanche photodiode. Planes conjugate to *AOM1* are indicated by an asterisk (\*), those conjugate to *SM* are indicated by a double cross (‡), and those conjugate to the sample plane are indicated by an *x* (X). Double-sided arrows at *L5* and *L8* indicate adjustable translational stages. The circular arrow at *SM* indicates a steerable mirror. Dotted lines indicate the front and back focal planes of *FO* and *BO*

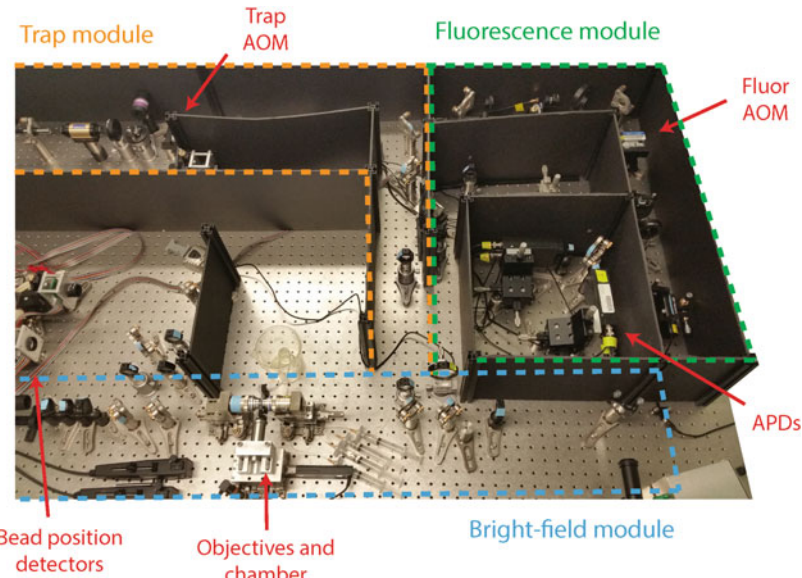


**Fig. 4** Photograph of instrument. The instrument is organized into three separate “modules” (Trap, Fluorescence, and Bright-field), indicated by the colored dotted lines. Major components of the instrument (AOMs, objectives, bead position detectors, and APDs) are labeled

above. The rate of switching is an important design consideration. If a trap is turned off for too long, forces on the once-trapped bead will pull the bead away from its initial position, out of the trapping region, and the bead may escape. Thus, it is necessary to modulate at a high rate, comparable to or faster than the relaxation timescales of the bead under tension ( $>10$  kHz; we interlace at 66 kHz) to maintain a viable trap [25]. This is possible using AOMs, which function by diffracting the incident laser beam by a sound wave propagating in a crystal. The sound wave is produced by a piezo element adhered to the crystal oscillating via a radio frequency (RF) source. The first diffraction beam (First order) is used for trapping, and the amplitude of the sound wave determines its intensity. When using an AOM to control the trap intensity, one important factor to consider is the trapping beam diameter. The beam must be small enough to fit into the AOM “active area,” defined by the size of the sound field in the crystal (3 mm in this setup). If the beam diameter is too large, additional lenses will be required to shrink it to the appropriate size, which occupy unnecessary space on the optical table and introduce extraneous components. In addition, the rate at which an AOM can modulate the trap intensity is ultimately limited by the speed of sound in the crystal divided by the beam diameter (~2 MHz for a 1.5 mm beam waist). Therefore, smaller beam diameters are advantageous; we chose a fiber laser with 1.5-mm diameter beam collimation for these reasons.

Since the sound wave in the AOM crystal acts as a diffraction grating for the incident trapping beam, the sound *frequency* determines the angle at which the beam diffracts. We exploit the ability to modulate the beam angle in this instrument for two purposes: (1) to steer the trapping beam, and (2) to form two traps by *time-sharing*, in which the trapping beam is deflected rapidly (faster than the relaxation time of trapped beads) between two angles, generating stable traps at two positions in the specimen plane [30, 31]. This design provides notable advantages. In some dual trap layouts, the two traps are formed by splitting the IR laser beam into two orthogonally polarized beams, with the angle of one beam controlled by a steerable mirror [9]. Previous work showed that any differential optical path between the two trapping beams increases the noise in the instrument, because each beam travels through different environments susceptible to local fluctuations [26]. In the polarization-based design, the two beams must be spatially separated, leading to residual noise even when the differential path is kept to a minimum. However, in the time-sharing approach, beams share identical optical elements and an almost identical beam path, and the instrument is much less sensitive to environmental noise. Thus, during one interlacing cycle, the two traps are formed by timesharing for 1/3 of the cycle each, then turned off for the remaining 1/3 cycle (Fig. 5).

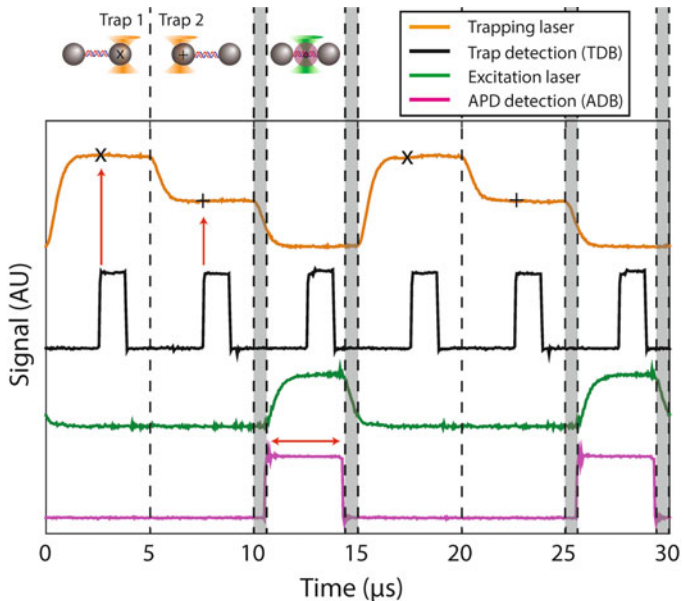


**Fig. 5** Interlacing and timesharing of optical trap and fluorescence excitation lasers, and synchronization of lasers with data acquisition timing. Two optical traps (orange) are created in sequence during two thirds of the interlacing period by time-sharing. The trap AOM (AOM1) switches between two deflection angles (traps in each interval are set to different intensities for clarity in the figure). Trap data acquisition occurs at time points centered on each trap interval. “ $\times$ ” and “ $+$ ” denote the time points for the first and second trap, respectively. The rising edge of a digital pulse (black) is synchronous with the trap data acquisition timing (red vertical arrows). The fluorescence excitation (green) is only ON during the last third of the interlacing period while the trap is OFF. There are 625-ns delays (grey shaded regions) between turning OFF (ON) the optical traps and turning ON (OFF) the fluorescence excitation. A digital pulse (magenta) synchronous with the APD data acquisition timing is centered on the excitation laser interval. Fluorescence emission signals are only collected during this third time interval (red horizontal arrow). Laser intensities in the plot are measured by feedback photodetectors QPD1 and PD (see Fig. 3), and digital pulses synchronous with data acquisition timing are output directly from the DAQ card trap input timing debug (TDB) and APD gate timing debug (ADB) lines (see Fig. 10). All are recorded using a digital oscilloscope

We note that acousto-optic *deflectors* (AOD) are more commonly used for beam steering than modulators. AODs work by the same principle as AOMs, but have been optimized to provide a larger deflection range. However, we have found that AODs adversely affect the quality of the trapping beam and also introduce fluctuations in beam power over small deflection angles. These can affect trap performance. We thus use an AOM to control temporally both the trapping beam intensity and deflection angle. The price of using an AOM is a smaller beam deflection range. We note

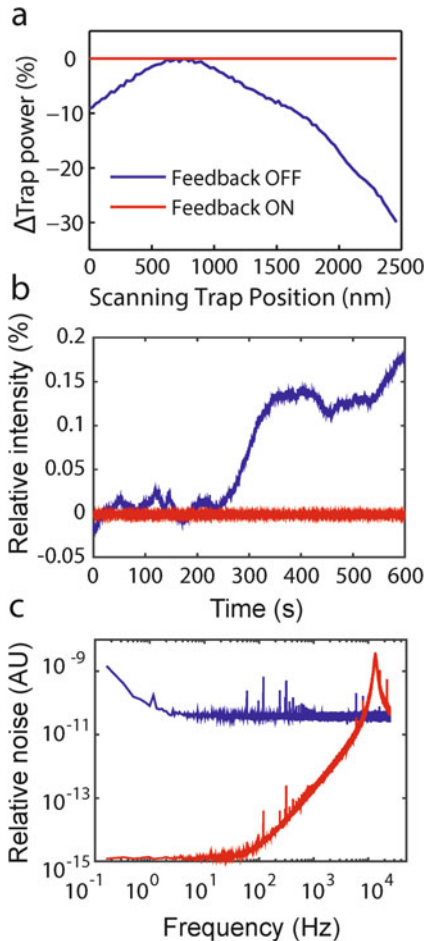


**Fig. 6** Effect of intensity feedback on trap performance. (a) The trapping beam power changes significantly as the trapping AOM deflects the beam over a range of distances in the specimen plane (*blue*), but remains constant with feedback ON (*red*). (b) Feedback stabilizes the trap laser intensity against drift over long time periods (*red*, feedback ON; *blue*, feedback OFF). (c) Noise power spectrum of laser intensity. Use of feedback reduces low-frequency noise from the trapping laser by up to six orders of magnitude (*red*, feedback ON; *blue*, feedback OFF) (reproduced from ref. [16] with permission from Nature Publishing Group)

that all acousto-optic devices exhibit some degree of variation in diffraction efficiency with deflection angle (Fig. 6a). This is problematic as it means that trap stiffness varies with trap position. To counteract this effect, we implement a feedback system to keep the beam intensity within a narrow range for optimal trap performance. Picking off a small fraction (1–2 %) of the trapping beam after the AOM using a high quality wedged beam sampler (BS1), an IR enhanced photodiode (QPD1) monitors the laser intensity (*see Note 1*). The signal from QPD1 is passed to the

instrument control system, which then uses a standard Proportional-Integral-Derivative (PID) feedback loop to modulate the RF sound wave amplitude driving the AOM to maintain constant beam intensity no matter where the traps are positioned (*see* Subheading 2.5). This feedback system is effective in stabilizing laser power fluctuations regardless of source, reducing intensity noise by up to six orders of magnitude (Fig. 6b and c) [16].

The trapping light next passes through two telescopes (T1 and T2), which expand the beam (by 3 $\times$  and 2 $\times$ , respectively) to overfill slightly the aperture of the front objective (FO, adjusted to approximately 9 mm beam waist at FO aperture) [29]. The telescopes also make the plane about which the trapping beams pivot inside the AOM conjugate telecentric to the back-focal plane of the objective (denoted by \* in Fig. 3). This ensures that deflection of the trapping beam by the AOM produces a displacement of the focused traps in the specimen plane while not clipping the beam on the FO aperture (*see Note 2*).

Next, a dichroic mirror (DM1) reflects the trapping light into the front objective (FO). We recommend using a high-quality dichroic that reflects trapping light and transmits fluorescence light efficiently and has a flat surface ( $<\lambda/10$ ) and thick ( $>3$  mm) substrate to avoid trap beam distortions prior to entering the objective. FO focuses the IR light, forming the optical traps inside the sample chamber. Considerations for selecting objectives for optical trapping have been described at length elsewhere [26, 29]. Here, we note the use of water-immersion objectives. Oil-immersion objectives generate traps close to the coverslip surface, and the trap stiffness is dependent on the depth of the trap within the chamber. As a result, drift of the surface or focal depth couples to the trap stiffness. An advantage of water- over oil-immersion objectives is that the traps are formed far away from the surface of the flow chamber, where the trap stiffness is decoupled from surface drift, improving stability [26, 32]. However, this comes at a price of a smaller numerical aperture (NA), which leads to moderately weaker traps and affects fluorescence detection (*see* Subheading 3.5). An identical back objective (BO) is used as a condenser to collect the trapping light. Although an objective is not essential for this purpose, we also use BO as the objective in the bright-field imaging system as it allows directly imaging the traps, which is convenient for alignment (*see* Subheadings 2.3 and 3.3). An identical dichroic (DM2) reflects the trap light into the detection stage after BO.

Finally, the positions of the beads in the optical traps are monitored by *back-focal plane interferometry* of the trapping light [33, 34]. In contrast to other groups, we do not use a separate detection laser during normal operating procedures. A relay lens (RL1) collects the light forward-scattered by the trapped beads at the back-focal plane of BO and images it onto a position-sensitive

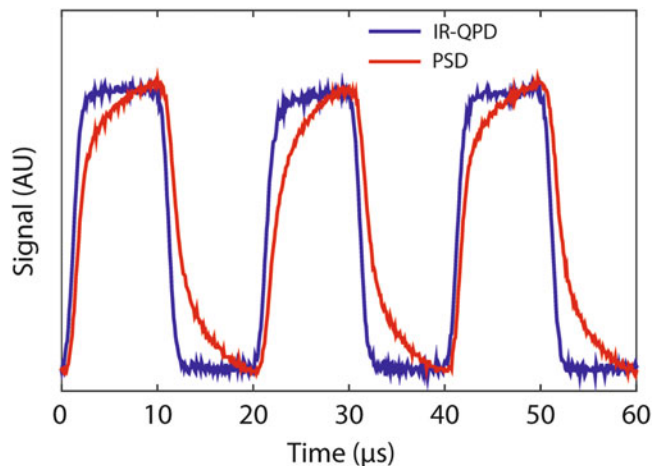


**Fig. 7** Comparison of IR-enhanced QPD to PSD for IR laser detection. The trapping laser power measured by an IR-enhanced QPD (blue) and PSD (red) during its ON/OFF interlacing cycle is shown. The PSD exhibits parasitic low-pass filtering, characterized by long rise and fall times (reproduced from ref. [16] with permission from Nature Publishing Group)

quadrant photodetector (QPD2). QPD2 outputs voltages proportional to the lateral position,  $x$  and  $y$ , of the centroid of the collected light and to the total light intensity. The positions of the beads in both traps are monitored *with the same* QPD; which signal comes from which trapped bead is resolved temporally by the data acquisition system (*see* Subheadings 2.5 and 3.2). The choice of photodetector is an important consideration in the design of this instrument. At the 1064-nm trapping wavelength, widely used silicon-based position-sensitive detectors (PSD) exhibit parasitic filtering above  $\sim 10$  kHz [35]. This low-pass filtering leads to signal inaccuracies during interlacing and timesharing at 66 kHz (Fig. 7). We have found that IR-enhanced quadrant photodetectors are accurate at rates  $> 100$  kHz at 1064 nm and are essential for proper operation of the instrument.

#### Components of interest

1. 5-W, 1064-nm fiber laser (IPG Photonics, YLR-5-1064-LP) (*see Note 3*).
2. Fiber clamp (FC; Newport, CCL-1 cable clamp).
3. 1064 nm optical isolator (ISO1; Thorlabs, item formerly from Optics for Research, IO-3-1064-VHP).
4. 1064 nm zero-order half-wave plate (HW1; Newport, 05RP-02-34).
5. Continuous rotation mount for wave plate (Thorlabs, RSP1).

6. 1064 nm laser line polarizing beam-splitting cube, 12.7 mm (**PBS1**; Newport, 05BC16PC.9).
7. Three-axis optic tilt mount for PBS cube (Newport, UGP-1).
8. Laser beam dumps (2 each: **BD**; Kentek, ABD-075NP).
9. 1064 nm acousto-optic modulator (AOM) (**AOM1**; IntraAction, ATM-803DA6B).
10. Five-axis alignment stage for AOM (Newport, item formerly from New Focus, 9081).
11. Lenses (all are 1064 nm anti-reflection coated, 25.4 mm diameter):
  - (a) Plano-convex lens, 88.3 mm EFL (**L1**; Newport, KPX091AR.33).
  - (b) Plano-convex lens, 250 mm EFL (**L2**; Newport, KPX109AR.33).
  - (c) Plano-convex lens, 100 mm EFL (**L3**; Newport, KPX094AR.33).
  - (d) Plano-convex lens, 200 mm EFL (**L4**; Newport, KPX106AR.33).
  - (e) Bi-convex lens, 150 mm EFL (**RL1**; Newport, KBX070AR.33).
12. Iris (Thorlabs, SM1D12C).
13. Laser line dielectric mirrors, 1064 nm (2 each: **M1** and **M2**; Newport 10Z40DM.10).
14. Broadband beam sampler, 1010–1550 nm (**BS1**; Newport, 10Q20NC.3).
15. Short-pass dichroic beamsplitters, reflected wavelength = 1064 nm, transmitted wavelength = 415–700 nm (2 each: **DM1** and **DM2**; CVI, SWP-45-RP1064-TUVIS-PW-1025-UV) (*see Note 4*).
16. IR-enhanced quadrant photodiodes (QPDs) (2 each: **QPD1** and **QPD2**; First sensor, formerly Pacific Silicon, QP154-Q-HVSD).
17. Precision stages for QPDs (2: Newport, 460A-XYZ).
18. 60× water-immersion microscope objectives, NA = 1.2 (2 each: **FO** and **BO**; Nikon, CFI Plan APO VC 60XWI).
19. Precision stages for microscope objectives (2 each; Newport, Ultralign 561D-XYZ [right-handed] and 561D-XYZ-LH [left-handed]).
20. 1064 nm laser line filter (**F1**; Newport, 10LF25-1064).

## 2.2 Fluorescence Confocal Microscope

Much of the fluorescence confocal microscope module layout is similar to that of the trap, with some important distinctions. A 532-nm 30-mW laser is used for excitation. Although only micro-watts of power are necessary for typical single-molecule confocal microscopy, we also use the excitation laser for alignment (*see* Subheadings 3.3 and 3.4), which requires increased power.

As shown in Fig. 3, the excitation beam passes through an optical isolator, power stage, and AOM. Here, the AOM only modulates the laser intensity for interlacing with the optical trap. As in the optical trap module, a fraction (approximately 1 %) of the excitation light intensity is diverted (pellicle beam splitter BS2) and monitored by a photodiode (PD) and stabilized via a feedback loop.

Two telescopes (T3 and T4) expand the beam by  $4\times$  and  $1.3\times$ , respectively (approximately 6 mm final beam waist, slightly less than the FO aperture, to ease the co-alignment of trap and fluorescence beams) (*see Note 5*). We recommend using achromatic doublet lenses for all fluorescence imaging in this module to maintain consistent focusing across the fluorescence spectrum. The excitation beam next enters the front objective FO. There are a few important characteristics for the objectives to keep in mind when trapping simultaneously with fluorescence. First, since water-immersion objectives have a lower NA than oil-immersion objectives, the fluorescence collection efficiency in this setup will be slightly lower than that for standard confocal microscopes. Second, chromatic aberrations in FO require adjusting the fluorescence excitation beam collimation so that it is focused in the same plane as the trapped beads. This is achieved via two translation stages that displace the first and second lenses of T3 and T4, respectively, along the optical axis. These provide coarse and fine control over the focal depth of the fluorescence excitation, respectively (*see* Subheading 3.4). In addition, a piezo-actuated tip-tilt mirror stage (SM) between T3 and T4 is used to adjust the lateral position of the excitation relative to the traps in the specimen plane. The pivot plane of the mirror is made conjugate with the back-focal plane of FO (denoted by  $\ddagger$  in Fig. 3) by T4.

Fluorescence emission from the excitation focus at the specimen plane is collected by FO, traveling back along the same path as the excitation, but passing through a long-pass dichroic mirror (DM4) and into the confocal pinhole stage. This consists of a telescope (T5), the first lens of which focuses the emission light onto the pinhole (PH, generally 20–100  $\mu\text{m}$  diameter, depending on lens selection and background rejection requirements) (*see Note 6*) that rejects out-of-focus light, and the second of which collects the transmitted light. The fluorescence signals are monitored by two avalanche photodiodes for measuring donor (APD1) and acceptor fluorescence (APD2). These detect individual photons and output a single digital pulse per photon to the data acquisition system (*see* Subheading 3.4).

The 532-nm excitation light transmitted through the sample chamber is also collected by BO and imaged onto a position-sensitive detector (PSD). This detection system is used during alignment, utilizing the excitation as a detection beam for a trapped bead for accurate positioning of the confocal spot laterally in relation to the trapped beads (*see Subheadings 3.3 and 3.4*).

In general, it is best to keep fluorescence and trap modules well-separated and partitioned to prevent stray trap light from reaching the fluorescence detectors and producing a background signal. We recommend enclosing the instrument modules in blackout boxes containing multiple turns to maximize absorption of stray light (Fig. 4).

Components of interest:

1. 532 nm laser (World Star Tech, TECGL-30) (*see Note 7*).
2. 532 nm laser mount and coarse adjustment stage (Newport, VB-1).
3. 532 nm optical isolator (**ISO2**; Thorlabs, item formerly from Optics for Research, IO-3-532-LP).
4. 532 nm zero-order half-wave plate (**HW2**; Newport, 05RP02-16).
5. Continuous rotation mount for wave plate (Thorlabs, RSP1).
6. 532 nm PBS cube (**PBS2**; Newport, 05BC16PC.3).
7. Three-axis optic tilt mount for PBS cube (Newport, UGP-1).
8. Laser beam dump (**BD**; Kentek, ABD-075NP).
9. 532 nm AOM (**AOM2**; IntraAction, AOM-802AF1).
10. AOM driver electronics for excitation laser (IntraAction, ME-801.5-6).
11. Pellicle beamsplitter (**BS2**; Newport, PBS-2C).
12. Iris (2 each; Thorlabs, SM1D12C).
13. QPD or non-position-sensitive photodiode (**PD**; QPD: First sensor, QP154-Q-HVSD. Non-position sensitive photodiode: Thorlabs, PDA36A).
14. Motorized filter flip mount (**ND1**; Thorlabs, MFF101).
15. Assortment of neutral density filters (**ND1** and **ND2**; e.g., Thorlabs, NE05A).
16. Laser line dielectric mirrors, 532 nm (5 each: **M5**, **M6**, **M7**, **M8**, and **M9**; Newport, 10Z40DM.11).
17. Compact linear lens positioning stages for coarse and fine positioning of fluorescence confocal depth (2 each; Newport, item formerly from New Focus, 9066-COM) (*see Note 8*)
18. Lenses (all are 430–700 nm anti-reflection coated, 25.4 mm diameter unless otherwise stated):

- (a) Visible achromatic doublet lens, 100 mm EFL (**L5**; Newport, PAC052AR.14).
- (b) Plano-convex lens, 100 mm EFL (**L6**; Newport, KPX094AR.14).
- (c) Visible achromatic doublet lens, 150 mm EFL (**L7**; Newport, PAC058AR.14).
- (d) Visible achromatic doublet lens, 50.8 mm diameter, 200 mm EFL (**L8**; Newport, PAC087AR.14).
- (e) Bi-convex lens, 150 mm EFL (**RL2**; Newport, KBX070AR.14).
- (f) Visible achromatic doublet lens, 50.80 mm EFL (**L9**; Newport, PAC040AR.14).
- (g) Plano-convex lens, 25.4 mm EFL (**L10**; Newport, KPX076AR.14).

19. Dichroic mirrors:

- (a) 532 nm long-pass dichroic mirror (**DM4**; Semrock, LPD02-532RU-25).
- (b) 532 nm short-pass dichroic mirror (**DM5**; CVI, SWP-43-RU532-TUVIS-PW-1025-C) (*see Note 9*).
- (c) 590 nm edge dichroic mirror (**DM6**; Chroma, 590dcxr).

20. Two-axis piezoelectric mirror tip/tilt actuator (**SM**; Mad City Labs, Nano-MTA2 Invar).

21. Three-axis tip/tilt mount for piezoelectric mirror (**SM**; Newport, item formerly from New Focus, 9411).

22. QPD or position-sensitive detector (PSD) (**PSD**; QPD: First Sensor, formerly Pacific Silicon, QP154-Q-HVSD. PSD: First Sensor, DL100-7-PCBA3).

23. Precision stage for **PSD** (Newport, 460A-XYZ).

24. Filters:

- (a) Notch filter to further remove 532 nm excitation laser (**F4**; Chroma, HQ545lp) (*see Note 10*).
- (b) Cy3-based emission filter (**F5**; Chroma, HQ580/60 m) (*see Note 11*).
- (c) Cy5-based emission filter (**F6**; Chroma, HQ680/60 m) (*see Note 12*).

25. Mounted precision pinhole (**PH**; e.g., Thorlabs, P100S).

26. Precision three axis translation stage for pinhole (Newport, 461-XYZ-M).

27. Avalanche photodiodes (APDs) (2 each: **APD1** and **APD2**; Excelitas, formerly PerkinElmer, SPCM-AQRH-14).

28. Precision stages for APDs (2 each; Newport, 460A-XYZ).

### 2.3 Bright-Field Imaging System

The instrument is equipped with a bright-field imaging system (Fig. 3 and 4) that serves two purposes: (1) to visualize directly the sample chamber and beads during experiments, and (2) to image the trap and fluorescence excitation laser beams during some alignment protocols. The specimen plane is imaged by an IR-enhanced CCD camera using Kohler illumination from a blue LED (*see Note 13*). Band-pass filters on flip mounts are used to cut out IR trapping and green excitation light during normal instrument operation. The camera signal is recorded and displayed on the instrument computer using a frame-grabbing PC card. PCI-express video cards such as the one listed below should be used, as they provide sufficient data bandwidth to maintain a continuous video stream without interfering with other instrument measurements and control operations.

1. 465 nm blue LED (LED; e.g., Kingbright, 604-WP7113VBC/D).
2. Visible mirror (M4; Thorlabs, PF10-03-P01).
3. Bi-convex lenses, 25.4 mm diameter, 200 mm EFL (2 each: L11 and TL; Newport, KBX076).
4. 1000 nm shortpass filter (F2; Thorlabs, FES1000).
5. 532 nm single-notch filter (F3; Semrock, NF01-532U-25).
6. IR-enhanced CCD camera (CCD; Watec, WAT-902-B).
7. Frame-grabbing PC card (Matrix Vision, mvDELTAE-BNC).
8. Video monitor with BNC inputs for viewing inside instrument room (e.g., Ganz, ZM-L17A, distributed by Reytec).
9. Reticle calibration stage micrometer (Edmund Optics, 59-280).

### 2.4 Trap AOM RF Synthesis

The trap laser intensity and deflection angle are both controlled via AOM. Since the sound wave that determines both is driven by an RF source, precise and stable RF generation is key for stable, high-resolution trapping. Although the AOM RF signal can be produced from an integrated commercial source, we have found that an RF synthesizer custom-built from a direct digital synthesis (DDS) RF source chip provides much lower noise [16] (Fig. 8). The frequency of the RF output is referenced to a clock signal that must be supplied to the board. The stability of the clock directly affects the stability of the RF output frequency and therefore the stability of trap positioning. The synthesizer itself generates a variable low power signal that we amplify by a low-noise, fixed-gain RF power amplifier to drive the AOM. Care must be taken not to exceed the damage threshold of the AOM with RF power >2–3 W (Fig. 9). A DC-block is inserted inline between the RF synthesizer and amplifier as the amplifier is very susceptible to damage by a DC input. We recommend the following parts to assemble such an RF synthesizer

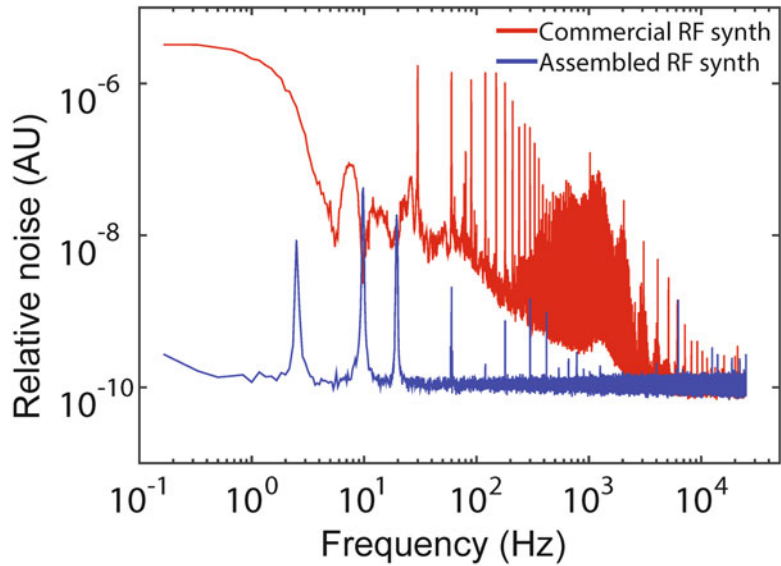


**Fig. 8** Noise power spectra from commercial and custom-built RF synthesizers. The custom-built RF synthesizer (blue) exhibits lower noise than the commercial synthesizer (red) by up to four orders of magnitude (reproduced from ref. [16] with permission from Nature Publishing Group)

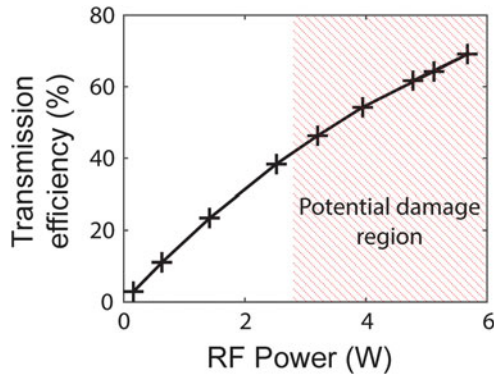


**Fig. 9** Transmission efficiency of trapping AOM as a function of input RF power. The intensity of the first-order diffracted beam relative to the total intensity input to the AOM increases with RF power. High input RF power can damage the AOM (red hatched region)

and amplifier. The specifications for the AOM modulating the fluorescence intensity are less stringent, and a commercial RF source is sufficient in this case.

1. Direct digitally synthesized (DDS) integrated circuit (IC) RF source chip on “evaluation” PC board (Analog Devices, AD9852/PCBZ or AD9854/PCBZ).

2. 14-pin DIP, 49.152 MHz fixed output, HCMOS logic, temperature compensated crystal oscillator (TCXO) with 1 ppm stability (Conner-Winfield, HTFL5FG5-049.152 M) (*see Note 14*).
3. 14-pin DIP socket.
4. 3.3 V regulated linear power supply for RF synthesizer (Acopian, A3.3NT350).
5. Standoffs to mount RF board to chassis, 4-40, f-f, 0.375" long (4 each; e.g., Mouser, 534-2202).
6. #4 flat insulating washers to mount RF board to chassis (4 each; e.g., Mouser, 534-3368).
7. 40 line ribbon cable (e.g., Mouser, 517-3302/40FT).
8. 40 pin ribbon cable plug (e.g., Mouser, 517-3417-7000).
9. 12" long SMB plug coaxial test cable (2 each; e.g., Allied, 528-0255).
10. SMB to BNC adaptor (2 each; e.g., Allied, 319-0409).
11. BNC jack to jack isolated bulkhead adaptor (2 each; e.g., Allied, 713-8028).
12. RF synthesizer chassis, 19" rack box (e.g., Mouser, 563-NHC-14155).
13. Low-noise, fixed-gain RF power amplifier, 5 W maximum output, 40 dB gain (Mini-Circuits, ZHL-5 W-1) (*see Note 15*).
14. 24 V linear regulated power supply for RF power amplifier (Acopian, 24PHI15AM) (*see Table 1*).
15. Low-noise RF cables (Mini-circuits, CBL-25FT-SMSM+).
16. DC-block (Mini-circuits, BLK-89 S+).
17. RF RMS power meter (Mini-circuits, ZX47-40-S+) (*see Note 16*).
18. Assortment of RF attenuators (e.g., Mini-circuits, HAT-10+) (*see Note 17*).
19. Combined DPO oscilloscope and RF spectrum analyzer (Tektronix, MDO4000B) (*see Note 18*).

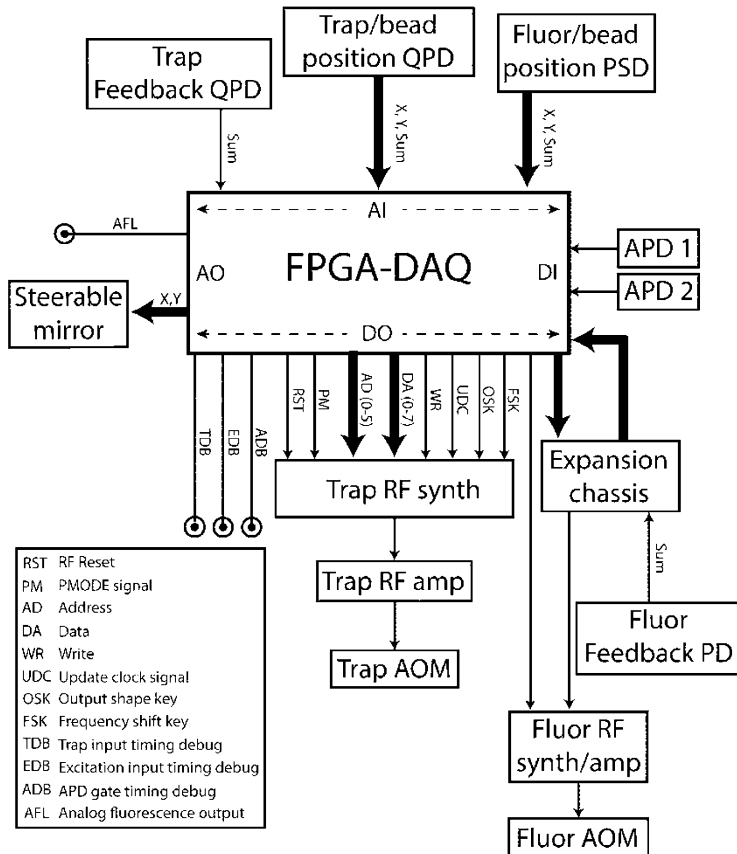
**Table 1**  
**Linear regulated low noise DC voltage sources from Acopian**

DB15-10	+/- 15 V, 100 mA	For the QPD/PSD detectors
5EB50	5 V, 500 mA	For wide-field microscope LED
A24MT210-M	24 V, 2.1 A	For NI current analog out control
50EB03	50 V, 30 mA	For QPD reverse bias
A3.3NT350	3.3 V, 3.5 A	For RF DDS synthesizer board supply
24PH15AM	24 V, 15 A	For RF power amplifier supply

## 2.5 Data Acquisition and Instrument Control System

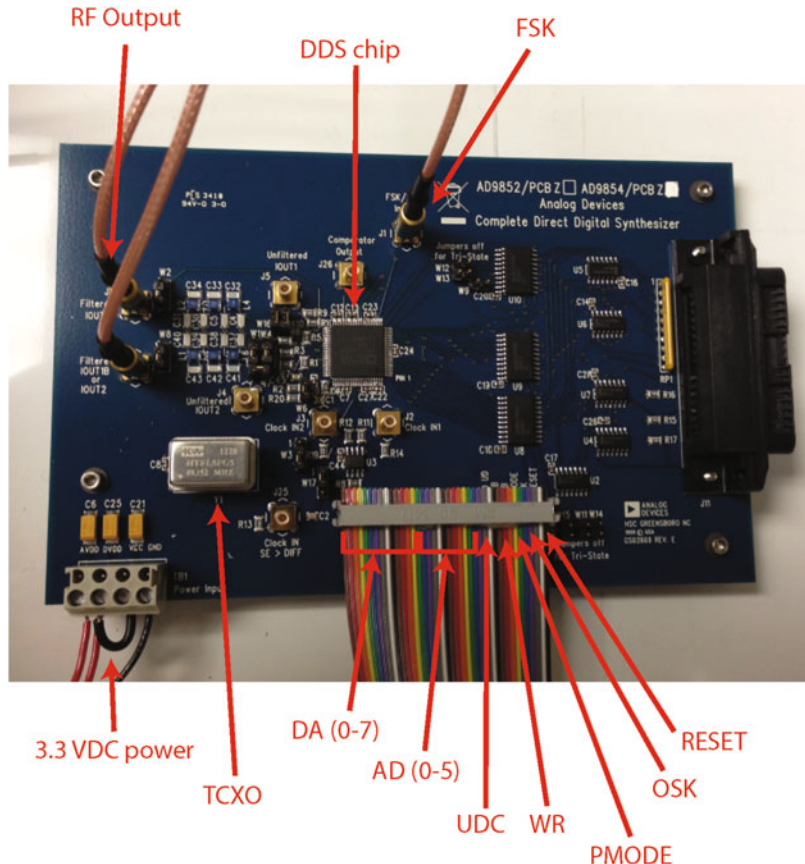
Key components of the instrument, including the trap and fluorescence excitation AOMs, single-photon counting APDs, the bead position measuring QPD, and laser feedback detectors, must be controlled and synchronized to trap interlacing with  $\mu\text{s}$ -level precision. PC-based data acquisition (DAQ) cards have historically been unable to achieve this level of timing and control easily, suffering from operating system interference. However, recent Field Programmable Gate Array (FPGA)-based PC DAQ cards circumvent this problem by moving all key timing operations from the PC “host” to a programmable chip on the DAQ card. The FPGA chip runs precisely and consistently as programmed with 40 MHz (25 ns) timing resolution and is isolated from interference from the PC. The FPGA is the “brain” behind all time-sensitive instrumentation control and data acquisition. Data are transferred from the FPGA to the host PC for non-time critical operations such as data analysis, plotting, and saving (*see Note 19* for computer build). Custom LabVIEW (National Instruments) software is used to control the instrument and is separated into FPGA and host PC portions (*see Note 20*).

Figure 10 displays the input/output architecture of the FPGA and all the components with which it communicates. There are eight synchronously sampled analog input (AI) channels in total: the  $x$ ,  $y$ , and *sum* voltages of QPD2 that monitors the trapped bead positions; the  $x$ ,  $y$ , and *sum* voltages of PSD that monitors the fluorescence excitation beam during alignment protocols; and two *sum* voltages from the trap and fluorescence feedback detectors QPD1 and PD. Note that the first seven channels are measured directly by the FPGA DAQ card AI. However, the fluorescence feedback detector intensity is measured by an additional AI card installed in an expansion chassis. This additional AI card is directly controlled by the FPGA and adds four more independently sampled AI. This design eases future expansion of the number of fluorescence excitation lasers and data channels. Two digital inputs (DI) collect photon pulses from APD1 and APD2. Two analog outputs (AO) control the two-axis steering mirror (SM) that scans the fluorescence excitation laterally in  $x$  and  $y$  at the specimen plane. A number of digital output (DO) channels are used to communicate with the custom-built RF source that drives the trap AOM (Figs. 10 and 11). Three additional “debugging” DO are used to indicate APD gating (ADB), trap laser (TDB), and fluorescence excitation laser (EDB) AI timing during interlacing synchronization protocols (*see Subheadings 3.2, 3.3, and 3.4*). One digital output controls a motorized flip mount to insert or remove a neutral density (ND) filter from the excitation beam path to easily switch between fluorescence excitation (low beam intensity) and bead detection beam (high beam intensity) methods (*see Subheading 3.3*).



**Fig. 10** Input/output architecture of the FPGA-based DAQ card. Thicker lines refer to groups of wires. The FPGA uses 20 DO lines to communicate with the trap RF synthesizer, including six for individual bits denoting the address byte (AD) and eight for individual bits denoting the data byte (DA). The output RF signal from the synthesizer goes to an amplifier and then to the trap AOM. Three separate debugging DO lines (TDB, EDB, and ADB) are used for synchronizing detection input timing with the interlacing cycle (see Subheadings 3.2, 3.3, and 3.4). One of the FPGA-controlled AO lines is used to output an analog fluorescence signal (AFL) for aligning the instrument (see Subheading 3.4). The FPGA controls an additional set of AI lines in an expansion chassis. This chassis has one AI line used for the fluorescence feedback PD, and one AO line that is used, along with a DO line from the FPGA, to control the fluorescence RF synthesizer

The trap AOM RF synthesizer chip is configured in part (e.g., the RF frequency and amplitude output values) by writing digital bytes (data) to specific locations (addresses) in the chip memory (Fig. 12). We utilize the high-speed parallel data communication method (set by PMODE signal (PM) DO line) of the RF synthesizer board. With this method, a single 8-bit byte of information is sent to a single 6-bit address location in a single data transfer cycle.



**Fig. 11** Assembled RF synthesizer board. A ribbon cable (*bottom*, digital lines labeled) and a coaxial cable (*top*) carry digital signals to the board directly from the FPGA (see Fig. 10). The temperature-compensated crystal oscillator (TCXO) is mounted to a 14-pin DIP socket on the board. A coaxial cable carries the filtered RF output signal from the board to the amplifier (*top left*, labeled IOUT1 on board; the second cable is ignored). Power is supplied to the board from a single 3.3 VDC source (*bottom left*)

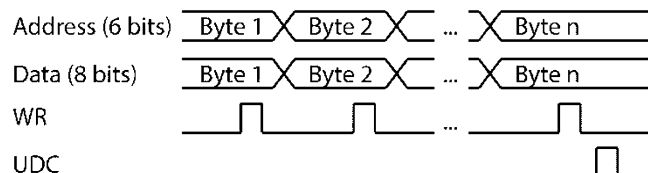


**Fig. 12** Scheme for writing data to RF synthesizer board. Multiple bytes of data are sequentially transferred to a buffer by setting data and address DO lines and then sending a TTL pulse to the write (WR) line. After all necessary changes are made, they are all activated simultaneously by sending a pulse to the update clock (UDC) signal line, which initiates a simultaneous transfer of the buffer memory to the active memory

In general, multiple bytes must be sent in sequence to specify the RF synthesizer board configuration fully (e.g., 6 bytes fully determine the RF frequency). Therefore, in order for all RF chip properties to change synchronously, the board employs a buffered memory process whereby changes are made first to an inactive copy of the chip memory (the buffer). Multiple bytes of data are sequentially transferred to the buffer. This is done by first setting data and address DO lines and then sending a TTL pulse to the write (WR) line. After all necessary changes are made, they are all activated simultaneously by sending a pulse to the update clock (UDC) signal line, which initiates a simultaneous transfer of the buffer memory to the active memory (Fig. 12). The reader should refer to the RF synthesizer chip manual for a complete table of address/configuration settings (Table 9 of ref. [36]) for a more detailed description of operation.

There is one key exception to the above. It turns out that changes in RF amplitude and frequency output from a simultaneous UDC-initiated buffer transfer are not timed sufficiently synchronously for our high-resolution trapping requirements. To compensate for this time delay, we devised a method by which we can invoke two independent FPGA DO lines to time and synchronize RF frequency and amplitude switching independently. We utilize the frequency shift keying (FSK) method of the RF synthesizer chip, whereby two separate RF frequencies can be stored on the chip (serving as the “active” and “inactive” trap) and the RF output can be switched between the two frequencies using the RF chip FSK digital input. We specify the next trap frequency in the “inactive” memory location and the amplitude in the usual buffer and control the switching of frequency via the RF chip FSK input and the amplitude via the usual RF chip UDC input. By specifying a delay in the FPGA timing between the switching of the FSK and UDC, we can synchronize RF frequency and amplitude switching (*see* Subheading 3.1).

The fluorescence excitation AOM driver is controlled by one AO channel (analog scaling) and one DO (digital gating) channel. Using both the analog and digital controls together allows maximally extinguishing the fluorescence beam when it should be off. The analog input of the IntraAction AOM driver we use is low impedance and the analog out channels built into the FPGA DAQ card cannot provide sufficient current to drive it. Therefore we use a special high current analog out card installed in the expansion chassis to provide the analog signal to the fluorescence AOM driver.

It is helpful to use a robust desktop computer with up-to-date multi-core processors (e.g., Intel quad-core i7) and as much memory as possible (32 GB suggested). We also highly recommend using at least two storage drives: a small (e.g., 512 GB) fast solid state drive containing the operating system and all software used (including LabVIEW) and a larger (e.g., 2 TB) conventional hard

disk drive (*see Note 21*) for saving data. Separating these two drives prevents conflicts during high-speed data acquisition and streaming from the FPGA to the PC and saving to the hard disk.

1. 750 kHz sampling rate FPGA-based multi-function DAQ PC card (National Instruments, NI PCIe-7852R).
2. C-series expansion chassis (National Instruments, NI 9151).
3. C-series high current analog output card (National Instruments, NI 9265).
4. C-series analog input expansion card (National Instruments, NI 9215).
5. Breakout box (2 each; National Instruments, SCB-68).
6. Cable to mixed IO breakout box (National Instruments, SHC68-RMIO).
7. Cable to digital IO breakout box (National Instruments, SHC68-68-RDIO).
8. Cable to expansion chassis (National Instruments, SH68-C68-S).
9. Custom LabVIEW software (download here: <http://www.pamsu.edu/people/comstock/software.html>).

## **2.6 Optical Tweezers and Confocal Microscope Alignment**

1. 10  $\mu\text{m}$  fluorescent polystyrene microspheres, excitation max = 540 nm, emission max = 560 nm (Thermo, F-8833).
2. 1.0  $\mu\text{m}$  fluorescent polystyrene microspheres, excitation max = 540 nm, emission max = 560 nm (Thermo, F-8820).
3. 1.0  $\mu\text{m}$  fluorescent polystyrene microspheres, excitation max = 535 nm, emission max = 575 nm (Thermo, F-8819).

## **2.7 Sample Flow Chamber Assembly**

1. Laser engraver (Universal Laser Systems, VLS2.30).
2. CorelDRAW X4 (CorelDRAW).
3. 1.5 HP portable dust collector motor blower (Penn State Industries, DC3XX).
4. Dust collection hose and clamps (Penn State Industries, D50C and DBC4).
5. Movable stage for chamber (Newport, Ultralign 562-XYZ).
6. Movable stage controller (Newport, ESP301-3N).
7. Closed loop DC servo stage motors (3 each; Newport, TRA12CC).
8. Joystick (Newport, ESP300-J).
9. Remote infuse/withdraw syringe pumps for bead channels (2 each; Harvard, PHD Ultra Nanomite 703601).
10. Remote infuse/withdraw syringe pump for sample channels (Harvard, PHD Ultra Remote Infuse/Withdraw Programmable 703107).

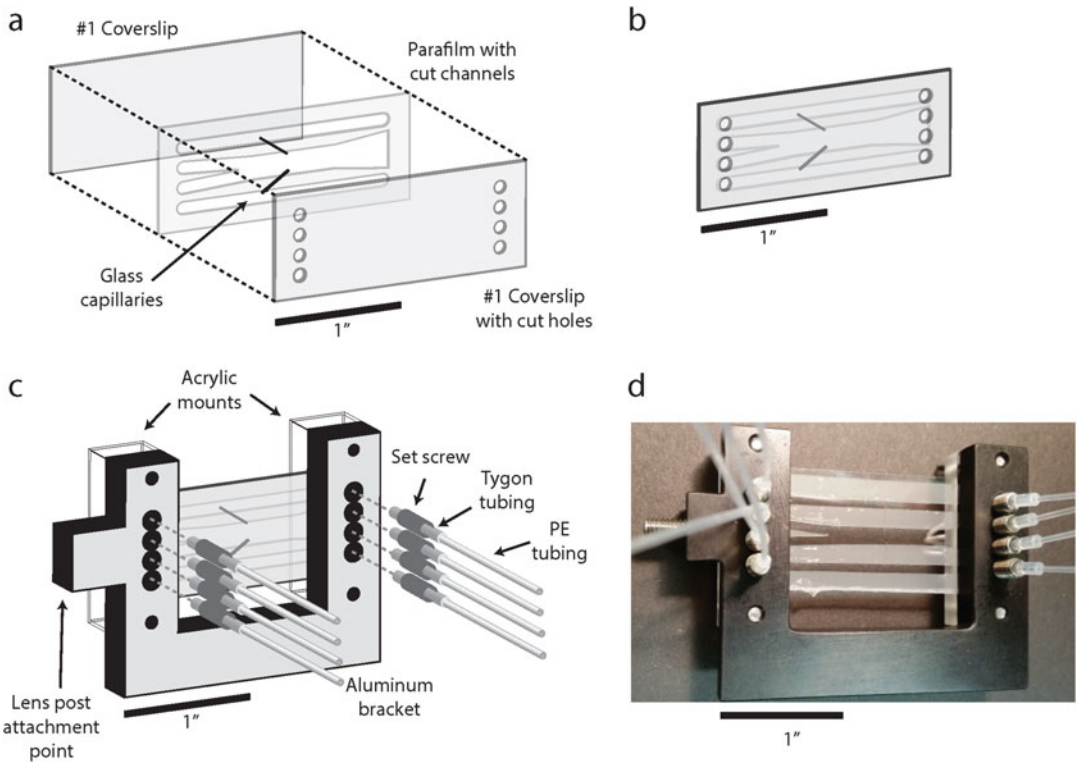


**Fig. 13** Assembly of laminar flow chamber. (a) Expanded view of the “Parafilm sandwich” that comprises the chamber. A piece of Parafilm with flow channels cut into it is placed on a coverslip with eight holes cut into it. Two glass capillaries span the Parafilm to connect the bottom and top channels to the large central channel. A coverslip with no holes is then placed on top of the Parafilm to form the assembled chamber. (b) A fully assembled flow chamber. (c) A flow chamber mounted on an anodized aluminum bracket, held in place by two acrylic mounts. Four holes on either side of the mount are aligned with the holes of the coverslip. A short length of Tygon tubing is threaded through a set screw, and a longer stretch of polyethylene (PE) tubing is inserted into the Tygon tubing. Eight threaded set screws are prepared and screwed into the eight holes in the aluminum bracket to serve as inlet and outlet channels for the flow chamber. (d) Photograph of an assembled and mounted flow chamber

11. Microscope coverslips (Fisher, 12-548-5P).
12. Parafilm M (Pechiney Plastic Packaging, PM996).
13. Glass capillaries with ID = 0.0250 mm, OD = 0.10 mm (King Precision Glass, custom order).
14. Anodized aluminum bracket (machined in house, *see* Fig. 13).
15. Polished acrylic mounts (2 each; machined in house, *see* Fig. 13).
16. 4/40 × 1/2" screws for assembling bracket and acrylic mounts (4 each; *see* Fig. 13).
17. 8/32 × 3/8" set screws with 1/16" holes drilled through centers (8 each; McMaster, *see* Fig. 13).

18. 26G × 3/8 in intradermal bevel needles (BD, 305110).
19. Tygon tubing with ID = 1/32", OD = 3/32", Wall = 1/32" (Fisher, ABW00001).
20. Polyethylene tubing with ID = 0.015", OD = 0.043" (BD, 427406).
21. N-(2-aminoethyl)-3-aminopropyltrimethoxysilane (United Chemical Technologies, A0700).
22. Methoxy-PEG-succinimidyl valerate, MW 5000 (Laysan Bio, MPEG-SVA-5000-1g).

### **2.8 Functionalization of Beads**

1. Standard benchtop microcentrifuge with Rotor FA-45-30-11 (Eppendorf, 022620601).
2. Sample rotator (e.g., VWR, 10136-084).
3. Analog vortex mixer (Fisher, 02-215-365).
4. 1× PBS buffer (10 mL): 137 mM NaCl, 2.7 mM KCl, 4.3 mM Na<sub>2</sub>HPO<sub>4</sub>, 1.47 mM KH<sub>2</sub>PO<sub>4</sub>, pH = 7.4.
5. Protein G-coated polystyrene microspheres, 880 nm nominal diameter (Spherotech, PGP-08-5).
6. Anti-digoxigenin (Roche, 11333089001).
7. Streptavidin-coated polystyrene microspheres, 810 nm nominal diameter (Spherotech, SVP-08-10).

### **2.9 Construction of DNA**

1. Standard thermal cycler for DNA PCR reactions (e.g., Bio-Rad T100, 1861096).
2. Electrophoresis cell with power supply, 8- and 15-well combs, gel caster, and 7 × 10 cm tray (Bio-Rad Mini-Sub Cell GT Cell and PowerPac Basic Power Supply, 1640300).
3. UV lamp (Laboratory Products Sales, ENF-240C).
4. Blue light source gel transilluminator (Clare Chemical Research, Dark Reader Transilluminator DR89X).
5. Nanodrop 2000 UV-Vis spectrophotometer (Thermo Scientific).
6. pBR322 vector (New England Biolabs, N3033S).
7. Lambda phage DNA template (NEB, N3011S).
8. Primers (Integrated DNA Technology) (*see* Table 2).
9. Phusion high-fidelity polymerase PCR master mix (NEB, M0531S).
10. QIAquick PCR purification kit (Qiagen, 28104).
11. 5× stock of TBE buffer (1 L): 400 mM Tris-HCl, 450 mM boric acid, 10 mM EDTA, pH = 8.3.
12. 6× gel loading dye (NEB, B7021S).

**Table 2**  
**Oligonucleotides used in example experiment**

Oligonucleotide	Sequence (IDT format, 5' to 3')
LH forward primer	/5Biosg/TGA AGT GGT GGC CTA ACT ACG
LH reverse primer	CAA GCC TAT GCC TAC AGC AT
RH forward primer	/5DigN/GGG CAA ACC AAG ACA GCT AA
RH reverse primer	CGT TTT CCC GAA AAG CCA GAA
Ins	/5Phos/CCT GGT TTT TAG GAC TTG TTT CCC ACT GGC
Probe	ACA AGT CCT/3Cy3Sp/

13. 1 kb DNA ladder (NEB, N0468S).
14. Pre-cast 1 % agarose gels in TBE with ethidium bromide (Bio-Rad, 1613010).
15. PspGI restriction enzyme (NEB, R0611S).
16. TspRI restriction enzyme (NEB, R0582S).
17. UltraPure low melting point agarose (ThermoFisher, 16520-050).
18. GelGreen nucleic acid gel stain, 10,000× in water (Biotium, 41005).
19. QIAEX II gel extraction kit (Qiagen, 20021).
20. T4 DNA ligase (NEB, M0202S).

### **2.10 Oxygen Scavenging System/Fluorescence Imaging Buffer**

There exist numerous methods for improving fluorescence signal quality in single-molecule experiments, and many of these can be easily adapted for use in these experiments. In particular, oxygen scavenger systems such as the glucose oxidase/catalase mixture are known to increase the photobleaching lifetime of fluorophores [37]. Since singlet oxygen species also tend to cause tether breakage [38], such a system has the effect of improving both tether and fluorophore quality. Additionally, a triplet state quencher like Trolox can be used to both prevent fluorophore blinking and photo-bleaching [39].

1. T50 buffer (50 mL): 10 mM Tris-HCl, 50 mM NaCl, pH = 8.0.
2. Glucose oxidase from *Aspergillus niger* (Sigma, G7141).
3. Pyranose oxidase from *Coriolus* sp. (Sigma, P4234).
4. Catalase from *Aspergillus niger* (EMD Millipore, 219261).
5. Trolox (Sigma-Aldrich, 238813).
6. 0.22 µm centrifugal filters (EMD Millipore, UFC30GV0S).
7. 0.22 µm syringe filters (EMD Millipore, SLMP025SS).

**2.11 Preparation of Beads and Sample for DNA Hybridization Experiment**

1. Gastight glass syringes, 1 mL, PTFE Luer Lock (4 each; Hamilton, 81320).
2. Fluorescently labeled probe DNA (Integrated DNA Technology) (*see Table 2*).

### 3 Methods

**3.1 Setup of RF Synthesizer for Trapping AOM**

The first component to be assembled and configured is the RF synthesizer that drives the trapping AOM (Fig. 11). An important step in this process is synchronizing the times at which the frequency and amplitude of the RF signal switch. A delay between the RF amplitude and frequency switch will result in a sudden change in one trap stiffness, effectively “kicking” the trapped bead. To avoid this, we require direct and independent timing control of both the RF amplitude and frequency in order to make small timing adjustments to make them synchronous. We do this by tuning a delay into the FPGA timing between the triggering of these two inputs. The proper delay time can be determined by visualizing the RF signal switching directly on an oscilloscope with a sufficient time resolution to resolve individual RF oscillations clearly. This delay time is robust, so this procedure only needs to be performed once.

The following steps describe the assembly of the RF synthesizer board:

1. Prepare chassis by drilling holes in bottom panel for RF board standoffs and holes in front panel for signal (RF output and FSK input) and power (3.3 VDC) feedthroughs. We find that the ribbon cable used for digital communication between the FPGA and the RF board can be easily slid out underneath the chassis lid (i.e., no need for a feedthrough).
2. Install standoffs on bottom panel of chassis.
3. Install BNC signal feedthroughs and banana jack power feedthroughs on front panel.
4. Ground yourself with an anti-static strap and perform all RF board assembly work on top of a grounded, anti-static mat. Handle all components by their edges and do not touch component pins or exposed circuitry.
5. Mount RF board onto chassis standoffs. Do not over tighten screws.
6. Install 14-pin DIP socket onto RF board. Most sockets we have found have all 14 pins, whereas the board only has the 4 corner holes. In this case trim off the inner 10 pins with a wire cutter. Given the tight fit of the socket pins we have installed, we have not needed to solder this connection.

7. Install the 14-pin DIP TCXO directly into the 14-pin DIP socket now on the board (*see Fig. 11*) (*see Note 22*).
8. Set the jumpers on the board to the following:
  - (a) W9, W11, W12, W13, W14, W15 jumpers OFF (tri-state jumpers are only set to ON when using the printer port for communication).
  - (b) W7, W10, W16 jumpers ON (to enable filtered output).
  - (c) W1, W2, W3, W4, W8 jumpers on the bottom two pins (to enable filtered output).
  - (d) W17 jumper on the upper two pins (to use the TCXO clock chip).
  - (e) W6 OFF (to use a single resistor for the output).
9. Connect coaxial signal cables between RF board and panel feedthroughs (2 each for RF output and FSK input, use adaptors).
10. Connect RF board power inputs to chassis front panel power feedthroughs: first solder wires to panel banana jack feedthrough, then screw wires into board inputs. We use a single 3.3 VDC source for all three RF board power inputs.
11. Start the RF board by turning on its power supply.
12. Initialize (configure) the RF board once after turning it on. This begins with a reset of the board (RESET) followed by a series of digital data transfers using the parallel communications method all performed by the custom LabVIEW software (*see Note 23*). Set the following on the board:  $6\times$  system clock, phase locked loop (PLL) range low, PLL enabled, output shape keying (OSK) enabled, unramped frequency shift keying (FSK) mode, manual update clock. This RF board reset and initialization is performed whenever the custom LabVIEW software is restarted. The board can remain powered on.

The following steps describe how to synchronize the switching of RF amplitude and frequency for precise interlacing:

13. Connect the RF synthesizer output directly to an oscilloscope. Set the scope input impedance to  $50\ \Omega$  OR use a “T” divider to split the signal between a  $50\ \Omega$  terminator and the scope set to high input impedance (typically 1–10 M $\Omega$ ) (*see Note 24*).
14. Set two easily distinguishable frequencies and amplitudes, corresponding to the two traps. It is easiest to set the second trap amplitude to be  $\sim 2\times$  larger or smaller than the first.
15. With no programmed delay between the frequency and amplitude triggers, either the frequency or amplitude will typically switch before the other (Fig. 14 middle and bottom

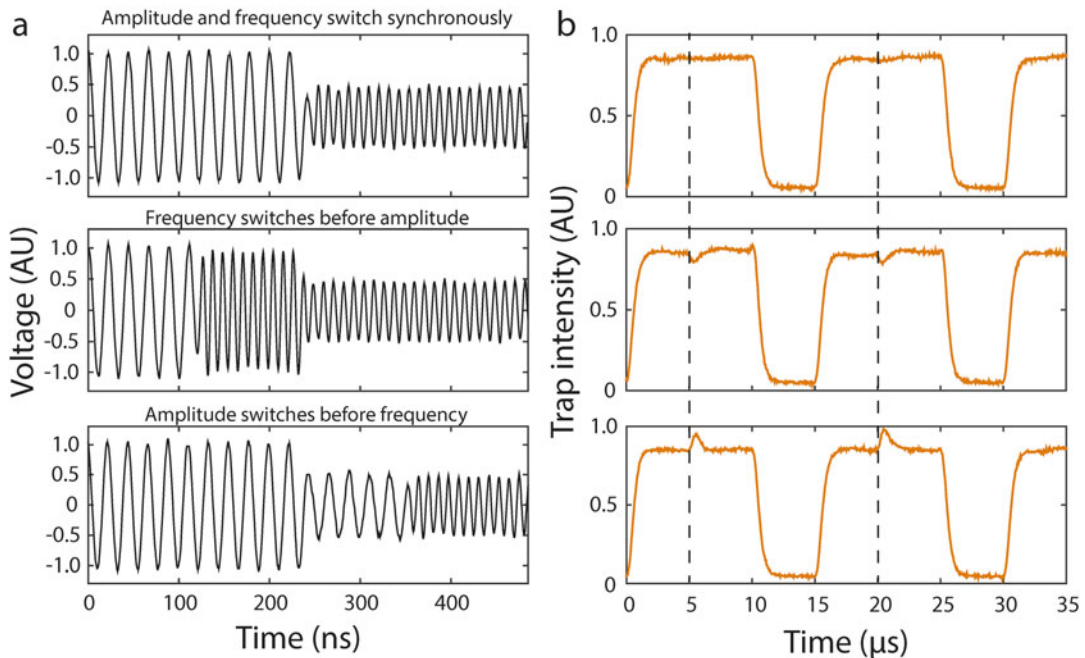


**Fig. 14** Synchronization of frequency and amplitude switching of the RF signal. **(a)** RF signals for the two traps are shown with both frequency and amplitude different by a factor of 2 for clarity (trap 1, 45 MHz; trap 2, 90 MHz). With an appropriately programmed delay between amplitude and frequency signals from the FPGA, the switch happens synchronously (*top panel*). When there is no programmed delay, the frequency can switch before (*middle panel*) or after (*bottom panel*) the amplitude. **(b)** Traps 1 and 2 during the interlacing cycle, where the RF amplitude is chosen such that both traps have the same intensity. The dotted line indicates when the transition between trap 1 and trap 2 occurs. With the programmed delay between amplitude and frequency switching, the change from trap 1 to trap 2 occurs without any change in intensity (*top panel*). With no programmed delay, the intensity of trap 2 either drops (*middle panel*) or rises (*bottom panel*) to effectively “kick” the bead held in this trap

panels). Adjust the delay between amplitude and frequency switching until amplitude and frequency switching occur simultaneously (Fig. 14 top panel). 125–250 ns is a typical delay (or 5–10 FPGA clock cycles, for a 40 MHz clock).

16. Make this delay the default value in LabVIEW. On startup of the instrument, the amplitude and frequency will be now be synchronized. We have found that this delay remains constant for a given RF board.

### 3.2 Setup of Optical Trap Module

Most of the alignment procedures for the optical trap module have been described in detail previously [26], so we will not repeat these protocols here. The reader can use Fig. 3, which displays a schematic of the instrument drawn to scale, to guide construction of the module. We also refer the reader to the excellent resources on general considerations for aligning optical traps [26, 27, 29]. Here, we focus instead on special considerations required by the

use of an AOM and interlacing: how to align the AOM with the trapping beam, how to synchronize trap signal acquisition with the interlacing cycle, and how to locate the plane conjugate to the AOM for positioning the objectives.

Synchronizing data acquisition with interlacing is a particularly important protocol. Since the AOM switches the two traps ON/OFF during the interlacing cycle, measurements of bead positions in each trap must be synchronized with this cycle. Moreover, each bead will be displaced away from the trap center during the OFF cycle of its trap, and will be displaced toward the trap center during the ON cycle (*see Note 25*). The pair of trapped beads thus oscillate during interlacing. It is necessary to sample the bead position in the *center* of each trap ON interval, as it provides the true *average* bead position (and force) [16] (Fig. 5).

The following steps describe the alignment procedure for the trap AOM. It is important to keep in mind that the first-order diffracted beam coming out of the AOM is the one that will ultimately form the traps, so all alignment must be done for this first-order beam:

1. Mount the AOM on the five-axis stage. We recommend machining an adapter plate made of invar or stainless steel to attach the AOM rigidly to the stage, and to minimize drift due to heating of the AOM.
2. Elevate the stage using two 1" height adjustable pedestals for extra stability. Choose pedestal heights such that the trapping beam will pass approximately through the center of the AOM aperture.
3. Set the stage to the middle of its range of motion.
4. Connect the RF output signal from the synthesizer to a DC block. A DC offset can damage the RF amplifier, so it is important to filter DC signals out.
5. Connect this RF signal to the low-noise, fixed-gain RF amplifier.
6. Connect the amplified RF output to the trapping AOM using a low-noise RF cable.
7. Clamp down the RF cable to the optical table in such a way as to relieve any strain on it. Any shaking of this cable will in turn shake the AOM to which it is attached, so it must be firmly set in place.
8. Drive the AOM in the center of its scan range (80 MHz) at low power (~1 W) (*see Note 26*).
9. Align the AOM by hand such that the trapping beam is roughly centered on the input and output apertures. The beam will pass straight through.

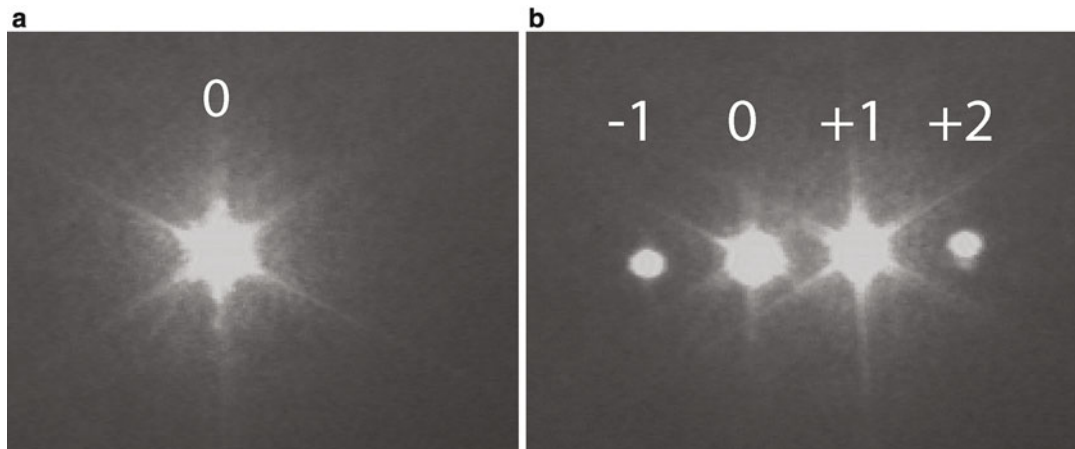


**Fig. 15** Diffraction pattern produced by an AOM (either trap or fluorescence AOM). **(a)** When the AOM is OFF, only the zeroth order (undiffracted) beam is observed. **(b)** When the AOM is ON, several orders of diffracted beams are observed. The +1 order beam is the one used for trapping

10. To achieve an approximate alignment, slowly rotate the angle of the AOM in either direction by hand until a diffraction pattern can be observed coming out of it (*see Fig. 15*). There are numerous angles that will produce a diffraction pattern, but the optimal angle is the one that produces a pattern with highest intensity. This will be the first angle beyond an incidence angle of  $0^\circ$  as the AOM is rotated either clockwise or counter-clockwise (Other sets of diffraction spots will appear if you continue rotating the AOM, and they will be less intense than the first set.).
11. Clamp down the base of the AOM stage when this optimal (but still approximate) diffraction pattern appears.
12. Place an iris downstream of the AOM to block out all but the first-order diffracted beam. Keep in mind that it is this first-order beam that will ultimately form the traps. Failure to block out the other orders may result in the creation of additional interfering traps.
13. Using either a power meter or photodetector to record the output beam intensity, rotate the AOM using the fine-adjustments of the stage until the intensity of the first-order beam reaches a maximum.
14. In order to align with the center of the AOM active area, translate the AOM in one of the directions orthogonal to the beam path, finding the two stage positions at which the intensity of the first-order beam reaches half of its maximum intensity (*see Note 27*).
15. Position the stage in the middle of these two positions.
16. Repeat **steps 14** and **15** for the other direction.

17. Adjust the rotation again to maximize intensity (it is easy to change the angle slightly while translating).
18. Attach a  $\frac{1}{2}''$  diameter 1064-nm laser line mirror (with very high reflection efficiency) to a post, and deflect the zeroth order beam to a high power beam dump (Fig. 3) (*see Note 28*).

The steps below describe how to synchronize the input timing of the DAQ card with the trap interlacing cycle using the feedback QPD (QPD1 in Fig. 3):

19. After the AOM has been aligned, continue to align optics up to the feedback detector QPD1 (Fig. 3).
20. Send the total intensity signal of QPD1 to an oscilloscope, and turn on interlacing with both traps ON (*see Note 29*). It is best to adjust the amplitudes for each trap to be different so that the center of each can more easily be distinguished (Fig. 5, orange).
21. Output from the DAQ card a digital pulse that is synchronous with the analog input timing (TDB line, Fig. 10), and visualize this pulse on the oscilloscope together with the trapping laser intensity signal (Fig. 5, black).
22. In LabVIEW, adjust the phase of the analog input timing until it is centered on the trapping laser intervals (*see Note 30*).
23. Record this phase shift, and set the “initial phase” to this value in the instrument software (make it a default value).
24. Upon startup of the instrument, this phase will always be automatically adjusted to the correct value (*see Note 31*).
25. Trap laser intensity feedback can now be turned on.

The following steps locate the plane conjugate to the trapping laser AOM deflection axis (Fig. 3). The conjugate planes will not be as well-defined when the beam is steered by an AOM instead of a movable mirror. Because there is no true single pivot plane for the deflected beam in the AOM, the conjugate plane will be smeared over a certain distance, typically  $\frac{1}{2}''$  for our optics:

26. Connect a QPD  $x$ , or horizontal, output to an oscilloscope, and center the QPD on the beam near the location you expect the conjugate plane to be.
27. Turn off interlacing, and oscillate one trap in the  $x$  direction.
28. Turn on trap intensity feedback or else the  $x$  signal will be difficult to interpret.
29. Translate the QPD in the  $z$  or axial direction until the oscillations on the scope reach a minimum. They will not reach zero. The conjugate plane will not be sharply defined, so it is sufficient to find the minimum.

### **3.3 Setup of Fluorescence Confocal Microscope Module: Excitation Laser Path**

The following protocol describes the alignment of the fluorescence excitation and emission paths and the synchronization of the excitation and the trapping interlacing cycles (Figs. 3 and 5). It is important to note that all the synchronization and alignment is done *relative to the trapping laser*, so it is important that the trapping module be optimally aligned before continuing.

The synchronization steps are essential for proper interlacing. Not only must the fluorescence excitation be switched ON during the OFF interval of the traps, but the excitation intensity signal from the feedback detector (PD) and the fluorescence emission signals from the APDs must also be sampled at the appropriate times in the interlacing cycle (Fig. 5). Since fluorescence is only emitted during the excitation laser ON interlacing period, photons should only be counted during this period to reject background. One way to do this is to “gate” the APDs ON/OFF using the APD gate digital inputs. However, we have found that this method often produces false counts, which grow increasingly worse as the APDs age. A preferable option is to keep the APDs ON continuously and instead program the FPGA to record photon counts only during the excitation laser ON interval. The FPGA “recording interval” must still be aligned temporally with the excitation laser ON interval.

The optical alignment procedures include adjusting the lateral ( $x$  and  $y$ ) and axial ( $z$ ) position of the confocal excitation spot relative to the optical traps in the specimen plane. For a preliminary, coarse adjustment, we use the CCD camera from the visible bright-field imaging system to image the trapping and fluorescence beams. Fine adjustments are made in one of two ways: (1) imaging a trapped fluorescent bead by raster-scanning the confocal excitation across it and using the APDs to record the fluorescence emission, or (2) using the fluorescence excitation as a “detection beam” [29], scanning it across a trapped bead and recording the beam deflection with the PSD. We provide protocols for each option.

The following steps describe how to synchronize the switching of the fluorescence excitation to the trapping laser to achieve precise time-sharing:

1. Align the excitation beam path initially without regard to the trapping beam up to the excitation intensity feedback detector (PD, Fig. 3).
2. As done previously with the feedback detector for the trapping laser, send the total intensity signal of PD to an oscilloscope (see Note 29), and turn on interlacing with both the excitation laser and trapping laser ON (Fig. 5, green and orange).
3. In LabVIEW, adjust the phase of the AOM interlacing timing until it is positioned between the trapping intervals as in Fig. 5. We set additional 625-ns delays between turning OFF (ON)

the optical traps and turning ON (OFF) the fluorescence excitation (Fig. 5, grey shaded regions).

4. Record this phase shift, and set the “initial phase” to this value.
5. Make this initial phase value the default in LabVIEW. Upon startup of the instrument, this phase will then always be adjusted to the correct value (*see Note 31*).

The following steps describe the synchronization of the feedback detector (PD) signal acquisition with the excitation laser during interlacing. Although the excitation laser and trapping laser are synchronized in **steps 1-5**, the DAQ card will not sample PD at the appropriate time. This problem arises because the analog output of this detector is connected to an expansion input card with a time delay. The procedure is similar to that described above:

6. Send the total intensity signal of PD to the oscilloscope, and turn on interlacing with the excitation laser ON (Fig. 5, green).
7. Output from the DAQ card a digital pulse that is synchronous with the analog input timing (EDB line, Fig. 10), and visualize this pulse on the oscilloscope together with the excitation laser intensity signal (Fig. 5, green).
8. In LabVIEW, adjust the phase of the excitation laser feedback detector analog input timing until it is centered on the excitation laser ON interval.
9. Record this phase shift, and set the “Initial phase” to this value.
10. Make this initial phase value the default in LabVIEW. Upon startup of the instrument, this phase will then always be adjusted to the correct value (*see Note 31*).
11. Excitation laser intensity feedback can now be turned on.

These steps describe the coarse alignment of the excitation laser path in x, y, and z relative to the trapping beam using an image of the beam profile on the CCD camera:

12. Immediately after the pellicle beam-splitter (BS2), insert a motorized flip mount for adding neutral density (ND) filters. The flip mount is motorized so that the filters can be flipped out of the beam path when the excitation laser is used as a detection laser, which requires high intensity. Adding ND filters here will roughly control the excitation laser intensity. The AOM along with the feedback system provide fine control over the intensity.
13. When setting up the steerable mirror (SM), make sure it is set to the center of its scan range (5 V in both *x* and *y* directions).
14. Center the excitation beam on the front objective (FO) back aperture and make certain it is collimated.

15. Translate the front objective stage until the front apertures of both objectives are a few millimeters apart, and place a few drops of water between them.
16. Adjust the trap intensity and camera location to visualize the trap in the CCD image as a focused spot.
17. Adjust the first movable lens (L5) of the telescope T3 to adjust the excitation laser collimation and roughly focus the fluorescence excitation beam with the trap.
18. Roughly co-align the trapping and excitation beams laterally in the *x* and *y* directions by observing them on the CCD camera and adjusting the excitation beam angle (using the coarse adjustment stage beneath the steerable mirror) until it is approximately at the same location as the trapping beam. The fluorescence excitation and trap lasers are now roughly focused to the same sample chamber location (laterally and axially).
19. Set up the remaining components of the excitation laser path (RL2, M9, and PSD).
20. Place the PSD at a plane conjugate to that of the steerable mirror. The procedure for this is essentially the same as that for the trapping laser AOM (Subheading 3.2, steps 26–29), except in this case the procedure must be repeated for both the *x* and *y* directions. The conjugate plane should be at the same location for both.

### **3.4 Setup of Fluorescence Confocal Microscope Module: Emission Path**

The following steps describe the alignment of the fluorescence emission path. This requires trapping a fluorescent bead in a flow chamber. Refer to the protocols on assembling laminar flow sample chambers (Subheading 3.9) and mounting the chamber in the instrument (Subheading 3.12) below for details:

1. Set up a flow chamber and trap a large fluorescent bead (~10  $\mu\text{m}$ ).
2. Roughly position the lateral focal spot of the excitation laser on the trapped bead by scanning in the *x* and *y* directions with the steerable mirror (SM) and observing the bright spot from fluorescence emission on the CCD camera.
3. Adjust the excitation intensity (adjust ND filters and AOM) so that the bead fluorescence emission can be visualized directly by eye. If the room is dark, we have found we can directly observe the emission path for many minutes before the bead photobleaches.
4. Align all optics involved in fluorescence detection (everything downstream of dichroic mirror DM4) using the visible fluorescence emission beam from this bead. Leave the pinhole out for now. It may be necessary to trap more than one bead if they bleach too quickly.

The steps below describe the alignment procedure for the APDs. APDs require special care, as the ambient light in a room is intense enough to damage them. As a general rule, APDs should remain off until it is time to make fine adjustments to them, at which point the lights in the instrument room must be turned off:

5. Mount the APDs on three-axis precision stages.
6. Align the APDs until the fluorescence emission spot from the large beads is visible near the middle of the detector. The APDs must remain off during this step to prevent damage.
7. Output an analog signal from the DAQ card that is proportional to the measured fluorescence to the oscilloscope (AFL line, Fig. 10), so the fluorescence signal can be observed in the instrument room during fine adjustment.
8. Add ND filters to the motorized flip mount in the excitation laser path, and be sure the filters are flipped in. The intensity of the fluorescence can be high enough to damage the APDs, so it is best to begin with lower intensity (higher ND) and increase it carefully as the need arises. Keep the intensity well below the damage threshold (~1 MHz count rate) at all times (*see Note 32*).
9. With the lights off in the room, observe the fluorescence signals from the APDs on the oscilloscope. In each direction ( $x$ ,  $y$  and  $z$ ) separately, scan the APD across the range of stage positions over which you can observe the fluorescence signal, from minimum to maximum to minimum again. Do not gate the APD: leave it continuously ON.
10. For each direction, record the position of the APD stage when the fluorescence signal is at the half-maximum on either side of the range.
11. Set the stage halfway between the two half-maxima.
12. Once this has been done for the large beads, trap smaller beads (i.e., a bead size that will be used in experiments, typically 1  $\mu\text{m}$ ) and repeat APD alignment. This will give a more precise alignment (*see Note 33*).

The following steps describe the synchronization of fluorescence signal detection by the APDs with the excitation laser interlacing cycle:

13. Create a digital pulse synchronous with the APD measurement ON time (ADB line, Fig. 10) and visualize this on the oscilloscope (Fig. 5, magenta line).
14. Trap a 1  $\mu\text{m}$  fluorescent bead, and roughly position the confocal spot in the middle of it using the bright emission spot on the CCD camera.

15. Observe the fluorescence signal in LabVIEW, and adjust the phase of the APD measurement ON time until the fluorescence signal just begins to increase. This is the start time of the excitation laser.
16. From this point, shift the phase of the APD measurement forward by 3.75  $\mu$ s (25 % of the interlacing cycle) (*see Note 34*).
17. Record this phase shift, and set the “Initial phase” to this value.
18. Make this initial phase value the default in LabView. Upon startup of the instrument, this phase will then always be adjusted to the correct value (*see Note 31*).

The following steps describe how to make fine adjustments to the confocal lateral position relative to the optical traps in the specimen plane. The steerable mirror (SM, Fig. 3) is used to position the confocal spot laterally. The mirror position drifts slowly over time relative to the trap, however, so this procedure must be repeated at the beginning of every experiment (or every 4 h or so). There are two options for this alignment. The detection beam method is usually preferred as it generates a robust image of beads that do not bleach, and is unaffected by particular experimental conditions:

19. Set up a flow chamber (*see Subheading 3.9*) and trap either one bead or a pair of beads, as needed.

Option 1: The following steps use the fluorescence excitation laser as a detection beam and detect its deflection via the PSD as it is scanned across the trapped bead(s).

20. Flip out the ND filters to increase the excitation laser intensity. APDs should be OFF!
21. Image the trapped bead(s) onto the PSD by scanning the confocal spot in  $x$  and  $y$  using the steerable mirror (Fig. 16a, b).
22. Flip in the ND filters.

Option 2: The following steps describe an alternate alignment method using the fluorescence signal from the APDs.

23. Image the trapped bead(s) by recording fluorescence using the APDs as the steerable mirror scans in the  $x$  and  $y$  directions (Fig. 16c) (*see Note 35*).

Both options:

24. Position the confocal spot laterally with respect to the imaged bead(s) as desired using the steerable mirror (e.g., centered between a pair of beads as for the experiments in Fig. 1).

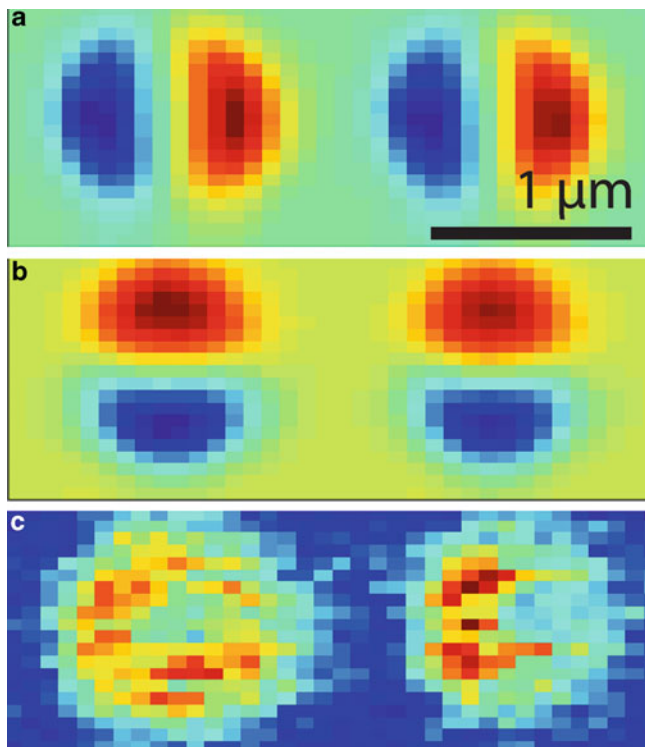


**Fig. 16** Images of trapped polystyrene beads using fluorescence imaging and detection laser scan. (a) Deflection in the  $x$  direction of the fluorescence excitation laser as it is scanned across the two trapped beads. (b) Deflection in the  $y$  direction of the excitation laser as it is scanned across the beads (blue denotes negative values; red, positive values). (c) Image of fluorescence intensity of two beads in Trap 1 and 2 recorded by the APDs. The signals result from autofluorescence of the beads (adsorbates can also give a signal)

The axial position (focal depth) of the excitation laser is roughly aligned to that of the trapping laser in Subheading 3.3, steps 12–20. The steps below describe how fine adjustments are made to the focal depth by translating the second movable lens (L8 in Fig. 3) using the translational stage on which it is mounted. Unlike the lateral alignment described above, we find that the axial position does not vary appreciably in time. It is not necessary to repeat these steps before every experiment. There are two ways to find the optimal axial position.

Option 1: Using the fluorescence signal from a fluorescent bead.

25. Trap a 1  $\mu\text{m}$  fluorescent bead.
26. Set the confocal spot lateral position at the center of the bead by taking a fluorescence image (see step 23).

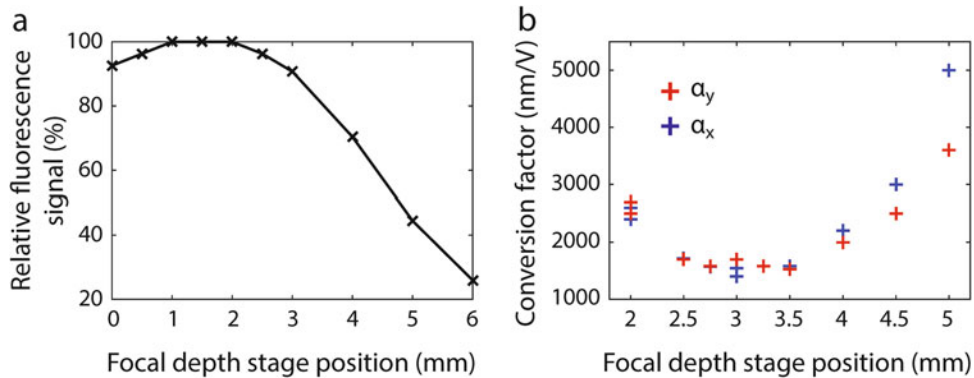


**Fig. 17** Adjustment of confocal spot focal depth. **(a)** Relative fluorescence intensity from a trapped fluorescent bead as the focal depth of the confocal spot is scanned (by scanning lens L8 along beam path). The fluorescence intensity drops significantly as the spot is moved away from the plane of the trapped beads. **(b)** PSD voltage-to-bead position conversion factors,  $\alpha$ , derived from calibration using the excitation laser as a detection laser as the focal depth of the confocal spot is scanned. The conversion factors  $\alpha$  are minimized when the confocal spot lies in the same plane as the trapped beads. Note: **(a)** and **(b)** were not performed for the same instrument alignment and disagree slightly

27. Record the fluorescence intensity of the bead at this stage position.
  28. Adjust the stage position incrementally (usually by 1 mm) and repeat **step 27** for each position.
  29. Plot fluorescence intensity vs. stage position. The optimal stage position is the one that maximizes the fluorescence signal (Fig. 17a).
- Option 2: Using the excitation laser as the detection laser to measure the Brownian fluctuations of a nonfluorescent bead.
30. Trap a 1  $\mu\text{m}$  bead (nonfluorescent).
  31. Set the confocal spot lateral position at the center of the bead by taking a detection laser scan (*see steps 20–21*).
  32. Leave the ND filters flipped out.
  33. Perform a trap calibration (*see Subheading 3.12, steps 24–25*) using the excitation laser as a detection beam, and record the power spectrum of the bead position.
  34. Determine the conversion factors  $\alpha_x$  and  $\alpha_y$  between bead position (in nm) and QPD output (in V) from fitting the power spectrum.
  35. Plot  $\alpha_x$  and  $\alpha_y$  vs. stage position. The optimal stage position is the one that minimizes  $\alpha_x$  and  $\alpha_y$  (Fig. 17b). This position will correspond to the highest detection sensitivity, when the confocal spot is aligned in the same plane as the trapped bead.

The following steps describe the protocol for aligning the confocal pinhole:

36. Trap a large ( $10\text{ }\mu\text{m}$  diameter) fluorescent bead.
37. Set the confocal spot lateral position by taking a fluorescence image (see **step 23**).
38. Attach the mounted pinhole to its precision three-axis stage.
39. Adjust the intensity of the excitation laser so that the fluorescence emission beam is visible by eye on the pinhole mount.
40. Shine a small flashlight behind the pinhole so that its location can be easily seen on the other side. The pinhole and fluorescence spot should both be visible.
41. Adjust the pinhole stage until the two spots overlap. It may help to start with the pinhole far away from the fluorescence focus so that the beam spot will be large enough to see. The APDs should now be able to detect the fluorescence.
42. As done previously (see **steps 5–12**), output an analog signal from the DAQ card that is proportional to the measured fluorescence to the oscilloscope (AFL line, Fig. 10), so the fluorescence signal can be observed in the instrument room during the fine-adjustment.
43. Add ND filters to the motorized flip mount in the excitation laser path, and be sure the filters are flipped in. The intensity of the fluorescence can be high enough to damage the APDs, so it is best to begin with lower intensity (higher ND) and increase it carefully as the need arises. Keep the intensity well below the damage threshold ( $\sim 1\text{ MHz}$  count rate) at all times.
44. With the lights off in the room, observe the fluorescence signals from the APDs on the oscilloscope. In each direction ( $x$ ,  $y$ , and  $z$ ) separately, scan the pinhole stage across the range of positions over which you can observe the fluorescence signal, from minimum to maximum to minimum again (see **Note 36**).
45. For each direction, record the position of the pinhole stage when the fluorescence signal is at the half-maximum on either side of the range.
46. Set the stage halfway between the two half-maxima.
47. Once this has been done for the large beads, trap smaller beads (i.e., a bead size that will be used in experiments, e.g.,  $1\text{ }\mu\text{m}$ ) and repeat **steps 43–46**. This will give a more precise alignment.

### **3.5 Adjustment of the Front Objective Correction Collar**

Water immersion objectives contain an adjustable “correction collar” to correct for spherical aberrations at the water-cover glass interface. The collar should be adjusted for the sample chamber cover glass thickness to give optimal focus. However, objectives are

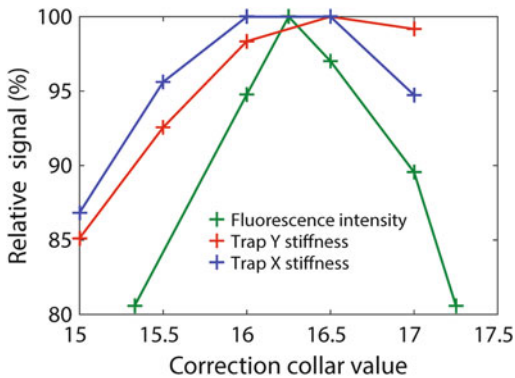


**Fig. 18** Adjustment of front objective (FO) correction collar (collar shown in Fig. 20a). Relative fluorescence intensity and trap stiffnesses in the *x* and *y* directions from a trapped fluorescent bead as the correction collar is adjusted. The fluorescence intensity and trap stiffness do not reach a maximum at the same collar position likely due to chromatic aberrations in the objectives

not perfectly achromatic, such that the optimal settings for the IR trapping laser (1064 nm) will not be quite the same for the excitation lasers (typically 488–633 nm). For high resolution trapping, the correction collar is typically adjusted to minimize the spherical aberration of the trapping laser and to optimize trapping efficiency. Adjusting the correction collar for the trapping laser will, however, ensure that the fluorescence excitation lasers retain some spherical aberration, and thus will decrease the collection efficiency of the fluorescence (Fig. 18). Thus, a compromise is needed between trapping efficiency and fluorescence detection efficiency. We have found that optimizing for trapping or fluorescence efficiency does not usually substantially affect the other. However it is prudent to check both the trapping efficiency and the fluorescence detection efficiency as a function of correction collar setting.

1. Set the correction collar to 16.25. #1 coverslips are ~130–170  $\mu\text{m}$  thick, so this is a good starting point.
2. Trap a small fluorescent bead the same size as used in experiments (1  $\mu\text{m}$  diameter typical).
3. Set the confocal spot lateral position to the center of the bead by taking a fluorescence image and adjusting the confocal spot (*see Subheading 3.4, step 23*). If the collar is close to its optimal position for fluorescence detection, the image of the bead will appear circular. If not, the image will be distorted, appearing diagonally elliptical.
4. Record the fluorescence intensity at this collar position, and save the fluorescence image of the bead.
5. Perform a calibration of the trap (*see Subheading 3.12, steps 24–25*) and record the trap stiffness in the *x* and *y* directions.

6. Repeat steps 4 and 5 as correction collar position is varied.
7. Plot the resulting fluorescence intensity and trap stiffness vs. collar position (Fig. 18) (*see Note 37*).
8. Set the collar position to optimize either the trap stiffness or the fluorescence signal, depending on the demands of the experiment being done. Our typical setting for #1 coverslips is 16.25.

### **3.6 Calibration of Trap and Confocal Spot Positioning**

In the following protocol, we describe how to determine the separation between the traps and the confocal excitation location in the specimen plane in nanometers.

The following steps calibrate the visible imaging system:

1. Place a stage micrometer (a linear, constantly spaced 10  $\mu\text{m}$  grid works well) between the objectives in the location usually occupied by the sample chamber.
2. Record an image of the grid using the CCD camera.
3. Determine the grid spacing in units of image pixels:
  - (a) Using thresholding, convert the image into a binary image (grid bars and the gaps in between convert to black and white bars, respectively).
  - (b) Find the centroids of each white bar.
  - (c) Plot the measured centroid positions (in pixels) vs. the known centers of the bars (e.g., 10  $\mu\text{m}$  between bars).
  - (d) Fit a line to the data. The slope of the line is the best value of the pixels-to-distance ( $\mu\text{m}$ ) conversion factor.
4. Rotate the stage micrometer 90° and repeat for the orthogonal direction.

The following steps describe how to calibrate the fluorescence steerable mirror (SM) position:

5. Set up a flow chamber (*see Subheading 3.9*).
6. Take images of the fluorescence excitation beam on the CCD camera at different SM  $x$  and  $y$  positions.
7. Using image analysis software, locate the beam center in each of the images as a function of SM  $x$  and  $y$  voltage; e.g., crop the image around the beam spot, threshold to produce a binary image, find the centroid of the bead image.
8. Determine the V-to-nm conversion factor from the slope of a linear fit of the beam center positions vs.  $x$  and  $y$  mirror voltage. Typical values are ~1000 nm/V in  $x$ , ~500 nm/V in  $y$ .

The following steps describe how to calibrate the trap position:

9. Set up a flow chamber (*see Subheading 3.9*) and trap a 1  $\mu\text{m}$  bead.

10. Take images of the trapped bead using the CCD camera at different trap positions.
11. Using image analysis software, locate the centers of the trapped bead in each of the images as a function of RF frequency (as above).
12. Determine the MHz-to-nm conversion factor from the slope of a linear fit of the bead center positions vs. RF frequency. A typical value for our instrument build is 123 nm/MHz. This value will vary with the specific optical alignment.

### **3.7 Construction of DNA for Oligonucleotide Hybridization Experiment**

This protocol describes how to reproduce experiments described in Comstock et al. [16] (Fig. 1a), which test the fluorescence and trapping capabilities of the instrument by detecting the hybridization of a fluorescently labeled oligonucleotide to DNA tethered between two trapped beads. For this experiment, we synthesize a DNA construct consisting of a short segment of ssDNA flanked by long dsDNA “handles” (Fig. 19). All oligonucleotides used to assemble this construct can be purchased from Integrated DNA Technology (IDT) and are listed in Table 2. We synthesize three DNA segments separately and then ligate them together: left handle (“LH,” 1.5 kb), insert (“Insert,” 19-nt long), and right handle (“RH,” 1.7 kb). LH and RH are made by PCR amplification of sections of the pBR322 plasmid and  $\lambda$  phage DNA using forward primers functionalized with 5' biotin and 5' digoxigenin, respectively (Fig. 19). The “probe” that hybridizes to Insert is a 9-nt complementary ssDNA oligonucleotide, labeled with a Cy3 fluorophore on the 3' end. It is possible to purchase this labeled oligonucleotide directly from IDT. Alternately, labeling can be done in-house using standard amine/NHS ester chemistry [40].

Steps 1–4 below describe the synthesis and purification of LH and RH:

1. For PCR synthesis of LH, mix 35  $\mu$ L of nuclease-free water, 5  $\mu$ L of forward primer (10  $\mu$ M concentration), 5  $\mu$ L of reverse primer (10  $\mu$ M), 2  $\mu$ L of pBR322 template DNA (10 ng/ $\mu$ L), 3  $\mu$ L DMSO, and 50  $\mu$ L 2 $\times$  Phusion HF Master Mix for a final volume of 100  $\mu$ L.
2. For PCR synthesis of RH, mix 35  $\mu$ L of nuclease-free water, 5  $\mu$ L of forward primer (10  $\mu$ M concentration), 5  $\mu$ L of reverse primer (10  $\mu$ M), 2  $\mu$ L of  $\lambda$  DNA (10 ng/ $\mu$ L), 3  $\mu$ L DMSO, and 50  $\mu$ L 2 $\times$  Phusion HF Master Mix for a final volume of 100  $\mu$ L.
3. Run PCR on both reaction mixes, using the following program: (1) 98 °C for 30 s, (2) 98 °C for 10 s, (3) 59 °C for 10 s, (4) 72 °C for 33 s, (5) repeat steps 2–4 30 $\times$ , (6) 72 °C for 5 min, (7) 4 °C forever.

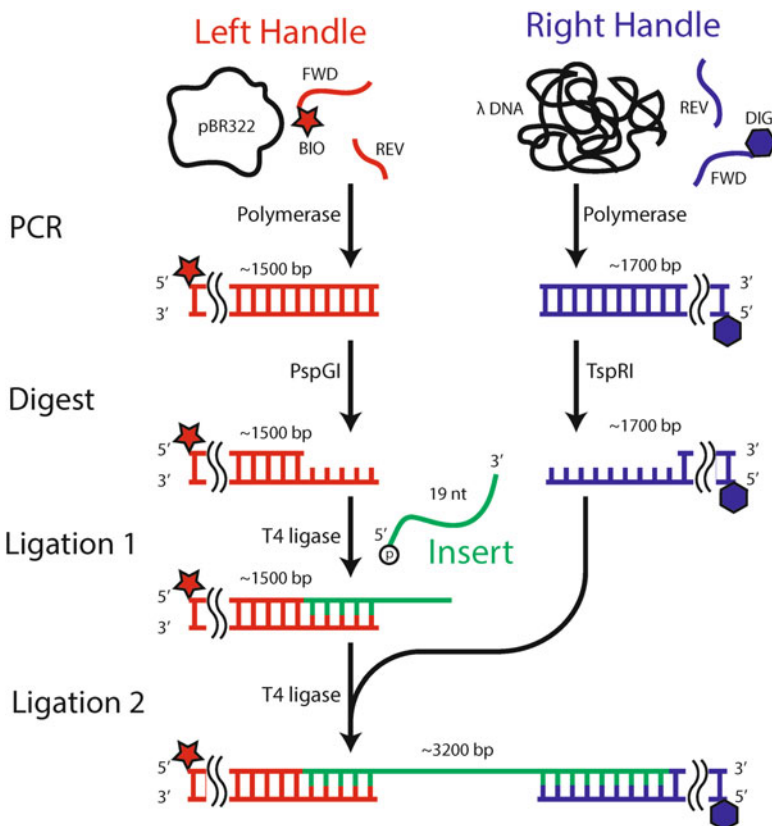


**Fig. 19** Construction of DNA substrate. Schematic depicting the major steps involved in preparing the DNA construct. The handles are first prepared by PCR of template DNA (pBR322 and  $\lambda$  DNA) using primers (FWD and REV) with either a biotin moiety (BIO, *Left Handle*) or a digoxigenin moiety (DIG, *Right Handle*) attached to the 5' ends of the FWD primers. The two handles are digested by restriction enzymes (PspGI and TspRI) to produce 5' and 3' overhangs. The digested Left Handle is then ligated using T4 ligase to the short Insert containing a phosphate group on its 5' end. Finally, the Right Handle is ligated to this product (Left Handle + Insert) to produce the final construct

4. Purify PCR products following the QIAquick PCR purification kit “spin protocol.” Add 30  $\mu$ L of elution buffer instead of 50  $\mu$ L for a more concentrated solution.

Steps 5–9 below describe the verification of PCR products by gel electrophoresis. These steps are optional:

5. Mix 1  $\mu$ L of each PCR product with 4  $\mu$ L nuclease-free water and 1  $\mu$ L 6x gel loading dye.
6. Place a pre-cast 1 % agarose gel (in TBE) with ethidium bromide in an electrophoresis cell, and cover it with 0.5  $\times$  TBE (see Note 38).

7. To this gel, add 5  $\mu$ L of a 1 kb DNA ladder to lane 1, then 5  $\mu$ L of the LH PCR product to lane 2, and 5  $\mu$ L of RH PCR product to lane 3.
8. Run at 70 V for ~1 h.
9. Image using UV lamp to verify the size of the PCR products.

**Steps 10–12** below describe the digestion of LH and RH with restriction enzymes to produce 5' and 3' overhangs, respectively. The overhangs are used to base pair to Insert:

10. Add to 30  $\mu$ L of LH: 2  $\mu$ L of PspGI restriction enzyme and 3.5  $\mu$ L of CutSmart 10 $\times$  buffer.
11. Add to 30  $\mu$ L of RH: 2  $\mu$ L of TspRI restriction enzyme and 3.5  $\mu$ L of CutSmart 10 $\times$  buffer.
12. Incubate the LH reaction mix at 75 °C for 1 h and the RH reaction mix at 65 °C for 1 h. For convenience, we suggest using a PCR thermal cycler with a temperature gradient of 65–75 °C, so both reactions can be done simultaneously. We program the PCR cycler to 4 °C after 1 h to stop the reaction.

**Steps 13–22** below describe the purification of the digestion products using gel electrophoresis. Optionally, these steps can be replaced by purifying the digestion products with a PCR cleanup kit following the QIAquick PCR purification kit spin protocol, adding 30  $\mu$ L of elution buffer for a more concentrated solution (*see Note 39*):

13. Add 60 mL of 0.5 $\times$  TBE to a flask and then add 0.6 g of agarose. Dissolve by briefly heating to a boil in a microwave and swirling.
14. Add 6  $\mu$ L of GelGreen to the solution and mix well (*see Note 40*).
15. Pour this solution into a gel cast with a 7  $\times$  10 cm gel tray and 8-well comb. Remove any bubbles (dab with the corner of a Kimwipe), then allow it to cool. The solution will solidify into a 1 % agarose gel.
16. Place the gel into the electrophoresis cell, and pour 0.5 $\times$  TBE into the cell until the entire gel is submerged.
17. Add 5  $\mu$ L of 7 $\times$  gel loading dye to each digestion product, and mix well.
18. Add 10  $\mu$ L of 1 kb DNA ladder to lane 1 of the gel, then all 35  $\mu$ L of LH digestion product to lane 2, then all 35  $\mu$ L of RH digestion product to lane 3.
19. Run at 70 V for ~1 h.
20. Weigh a set of 1.5 mL tubes (write the weights on the tubes).
21. Image the gel using the Dark Reader Transilluminator, and cut out the appropriate bands 1.5 and 1.7 kb (for LH and RH respectively) using a clean razor blade. Place these gel slices in the previously weighed 1.5 mL tubes.

22. Purify the digestion products from the agarose gel slices using QIAEX II gel extraction kit. Add 30  $\mu$ L of elution buffer instead of 50  $\mu$ L for a more concentrated solution.

**Steps 23–29** below describe the ligation of LH and RH to Insert. This ligation is done in two steps (LH + Insert first, followed by RH) so that agarose gel purification can be avoided (*see Note 41*):

23. Measure the concentrations of LH and RH using a Nanodrop, which requires only 1  $\mu$ L of each solution (*see Note 42*).
24. Add 4  $\mu$ L of 10 $\times$  T4 DNA ligase buffer and 4  $\mu$ L of T4 DNA ligase to the entire ~30  $\mu$ L volume of LH. Based on the concentration measured in the previous step, add a 10x excess of Insert. Add nuclease-free water up to a final volume of 40  $\mu$ L.
25. Ligate LH to Insert at RT (~22 °C) for 1 h, and then heat to 65 °C for 15 min to inactivate T4 ligase.
26. Purify ligation product with a PCR cleanup kit following the QIAquick spin protocol, adding 30  $\mu$ L of elution buffer.
27. Make a solution of this ligation product (LH + insert) and a 2 $\times$  excess of RH with a final volume of 32  $\mu$ L, based on the concentrations measured in **step 23**. Add 4  $\mu$ L of 10 $\times$  T4 DNA ligase buffer and 4  $\mu$ L of T4 DNA ligase to this for a final volume of 40  $\mu$ L.
28. Ligate RH to LH + Insert at RT (~22 °C) for 1 h, and then heat to 65 °C for 15 min to inactivate T4 ligase.
29. *Optional:* gel purify the final ligation product as described in **steps 13–22**.

### 3.8 Preparation of Oxygen Scavenging and Anti-blinking Solutions

This protocol describes how to prepare two different oxygen scavenging systems we typically use: one using glucose oxidase (for GOx) [37] and the other using pyranose oxidase (for POx) [41] (*see Note 43*). The full oxygen scavenging system includes one of these two enzymes plus catalase and glucose. For long-term storage, glucose is left out of the mixture. We use Trolox (TX) as a triplet-state quencher to reduce fluorophore blinking and photo-bleaching [39].

The following steps describe preparation of the oxygen scavenging systems:

1. Dissolve 20 mg of glucose oxidase (for GOx) or 5.8 mg of pyranose oxidase (for POx) and 1.3 mg of catalase into 200  $\mu$ L T50 buffer (*see Subheading 2.10*).
2. Centrifuge the solution at 13,000 rpm (18,000 rcf) for 1 min to spin down bubbles and any undissolved material.

3. Centrifuge solution through a 0.22- $\mu\text{m}$  centrifuge filter at 13,000 rpm for 1 min.
4. Store at 4 °C for short-term use (typically a few weeks, watching out for possible precipitation), or aliquot and flash freeze in liquid nitrogen and store at –20 °C for long-term storage (typically months).

The following steps describe preparation of Trolox:

5. Add ~8.5 mL of water (*see Note 44*) and 50  $\mu\text{L}$  of 1 M NaOH to 10 mL conical tube. The high pH helps the Trolox dissolve.
6. Add 10 mg Trolox powder.
7. Wrap tube in foil and rotate for ~1 h to dissolve.
8. Add 1.10 mL of 1 M Tris–HCl, pH = 8.0 for a final concentration of 110 mM Tris.
9. Add water to a total volume of 10 mL.
10. Filter the buffer through a 0.22- $\mu\text{m}$  syringe filter.
11. Store the Trolox solution in the dark at 4 °C.

### **3.9 Bead Functionalization**

The following protocol describes how to prepare anti-digoxigenin-antibody- and streptavidin-coated beads that link to the digoxigenin and biotin ends of the DNA (Fig. 19). Although the beads come stored in PBS buffer with sodium azide to prevent bacterial contamination, we store beads in aliquots without azide and do not encounter problems with bacteria. These functionalized bead aliquots can be stored for weeks to months at 4 °C. They should never be frozen.

The following steps describe preparation of the anti-digoxigenin (ADig) beads:

1. Add 40  $\mu\text{L}$  of 1.0 % Protein G-coated microspheres into 160  $\mu\text{L}$  1× PBS with 0.01 % Tween 20 (*see Note 45*).
2. Centrifuge at 7500 rpm (6000 rcf) for 1 min.
3. Pipette off the supernatant, taking care not to remove beads.
4. Add 200  $\mu\text{L}$  1× PBS + 0.01 % Tween 20.
5. Resuspend pellet by vortexing for 10–30 s.
6. Repeat steps 2–5.
7. Add 10  $\mu\text{L}$  of 1 mg/mL anti-digoxigenin antibody dissolved in 1 × PBS.
8. Rotate on a tube shaker/rotator for 30 min to keep beads in suspension.
9. Repeat steps 2–5 twice.

The following steps describe preparation of the streptavidin (Strep) beads:

10. Add 40  $\mu\text{L}$  of 1.0 % w/v streptavidin-coated microspheres into 160  $\mu\text{L}$  1 $\times$  PBS.
11. Spin at 7500 rpm for 1 min.
12. Remove supernatant, being careful not to remove beads.
13. Add 200  $\mu\text{L}$  1 $\times$  PBS.
14. Resuspend pellet by vortexing 10–30 s.
15. Repeat steps 11–14.

### **3.10 Assembly of Laminar Flow Sample Chambers**

An underappreciated component of optical trap experiments is the sample chamber. A well-designed chamber can significantly improve the throughput of an experiment and allow better control over the system of study. The protocol below describes the design and assembly steps for making laminar flow chambers.

Sample chambers consist of two No. 1 microscope coverslips that sandwich a layer of sealing film into which the channels have been cut (Fig. 13). The top and bottom channels usually contain streptavidin and anti-digoxigenin beads, respectively, and are each shunted to the central channel by thin glass capillaries. Flow in the top and bottom channels causes beads to flush into the central channel, where they are captured by the optical traps. In this protocol, we describe a chamber design in which the central channel contains two adjacent flow streams (Fig. 21). Since the flow is *laminar*, the two streams do not mix but rather maintain a narrow, stationary interface limited only by diffusion [42]. This chamber design allows rapid exchange of solution conditions by translating the optical traps across the flow interface [43]. This can be used to assemble protein–nucleic acid complexes *in situ* [14, 22, 23, 44]; for example, loading a motor protein on DNA, then adding ATP in a controlled temporal sequence.

We utilize a computer-controlled CO<sub>2</sub> laser engraver to etch inlet and outlet holes into the front coverslip and to cut channels into the film. Although it is possible to do the latter manually with a razor blade, the engraver system allows more elaborate chamber designs that would be difficult to render otherwise. The hole and channel designs are input into a drawing program (e.g., Corel-DRAW) and then “printed” to glass and Parafilm by the engraver, respectively. The details of this process are discussed in the protocol.

Once assembled, the sample chamber is mounted on a custom-built U-shaped aluminum bracket (Fig. 13). Two acrylic mating pieces press the chamber against the two edges of the bracket, aligning holes tapped for 8–32 screws with the inlet and outlet holes of the front coverslip surface. Short pieces of Tygon silicone tubing are fed through machined 8–32 set screws in which the cores have been removed; these are gently screwed into the sample

mount, pressing the silicone tubing end onto the inlet and outlet holes of the chamber, forming a seal. Polyethylene tubing is fed into the exposed silicone tubing end and used to flow solutions into the chamber.

The bracket is in turn mounted to a motorized precision  $x$ - $y$ - $z$  linear translation stage. The motors allow the translation of the chamber relative to the traps and the positioning of the traps anywhere within the flow channels. The motors also allow this positioning remotely from outside the instrument room. Key sample chamber locations, e.g., the exits of the capillaries out of which beads are flushed, are saved in the instrument software. The chamber can be translated to those recorded positions automatically. We also utilize a joystick to move the chamber relative to the traps manually, e.g., when capturing individual beads in the traps.

The following steps describe how to cut inlet and outlet holes in a coverslip:

1. Prepare a batch of coverslips for engraving. It is convenient to prepare ~15 coverslips at a time using a jig that holds an array of coverslips.
2. In CorelDRAW, make a blueprint of the arrayed coverslips with holes like the one shown in Fig. 13.
3. Set the following settings for the engraver: Power 15 %, Speed 10 %, PPI 250, Z-Axis 4" (*see Note 46*).
4. Connect the exhaust from the laser engraver to the portable dust collector blower motor, and the output of this into a fume hood. Turn on the motor.
5. Align the engraver vertically: insert jig, place vertical alignment tool onto jig, and adjust stage height.
6. Align the engraver laterally:
  - (a) Load the jig with a single coverslip in the upper left corner location.
  - (b) Run the engraver program and print a single copy of the blueprint. This will etch the glass and reveal the printing offset.
  - (c) Measure the  $x$ - $y$  offset from the desired location using a micrometer (a few mm could occur).
  - (d) Translate the blueprint to correct for the offset.
  - (e) *Optional:* perform another test run on a single coverslip to verify alignment.
7. Load the jig with the full set of coverslips.
8. Run the engraver program and print 15–20 copies. It will take ~30 min.
9. After engraving is finished, clean all coverslips by carefully wiping them by hand with acetone. Check to make sure there are no fingerprints or pieces of dust.

Some biomolecules will tend to adsorb to the surfaces of the chamber. Adsorption may be particularly important if the molecules are fluorescently labeled, as this may increase fluorescence background. To keep molecules in solution, chambers should be passivated with polyethylene glycol (PEG) [23], using a protocol adapted from ref. [45]. **Steps 10–14** should follow if the chambers are to be passivated with PEG. Otherwise these steps may be skipped:

10. Sonicate the coverslips in acetone for 30 min.
11. Rinse the coverslips with water 3× to remove excess acetone.
12. Sonicate the coverslips in 3 M KOH for 20 min.
13. Rinse with water 5× to remove excess KOH.
14. Rinse once with methanol, and dry with nitrogen gas.

The following steps describe cutting channels into Parafilm:

15. Cut a 4" × 4" square of Parafilm and place it taut over a frame. We use a machined square metal frame and tape the Parafilm over it.
16. In CorelDRAW, make a blueprint of the flow channels as shown in Fig. 13.
17. Set the following settings for the engraver: Power 9 %, Speed 10 %, PPI 500, Z-Axis 4".
18. Connect the exhaust from the laser engraver to the portable dust collector motor, and the output of this into a fume hood. Turn on the motor.
19. Run the engraver program and print one copy.
20. After engraving is finished, use tweezers to pull off carefully any loose segments of Parafilm that may be still attached to the channel structure.

The following steps describe how to assemble a flow chamber:

21. Use tweezers to carefully lay down the cut Parafilm on the “hole” coverslip, aligning the Parafilm channels with the coverslip holes (Fig. 13). It is important to attempt to do this correctly the first time, as moving the Parafilm around tends to leave residue on the coverslips.
22. Use a fresh, clean razor blade to cut two glass capillaries to a length such that they will span the Parafilm between the outer channels and the inner channel (*see Note 47*).
23. Use tweezers to place the two capillaries at the appropriate positions on the Parafilm (*see Note 48*).
24. Lay the uncut coverslip on top of the Parafilm to form a “Parafilm sandwich” between the two coverslips (*see Fig. 13*).

25. Preheat a hot plate and a ~0.5 kg weight before use to ~100–130 °C (*see Note 49*).
26. Melt the Parafilm by laying the assembled chamber on the hot plate between two Kimwipes (to prevent melted Parafilm from sticking to the hot plate) with the weight on top of it. Wait ~2–3 min for the Parafilm to melt. It is important that the weight is well centered to apply a uniform pressure over the chamber, otherwise one side will become flatter than another.
27. Take the chamber off the hot plate and allow it to cool for ~1 min.
28. Mount the chamber onto its bracket, lining up the chamber holes with the bracket holes (*see Fig. 13*). Gently screw the mounts into place to secure the chamber position (*see Note 50*).
29. Cut a sufficient length of Tygon tubing for all input/output interfaces (typically 5/8" per input/output), cutting one end of it diagonally into a point to ease the next step.
30. Thread the Tygon tubing into the set screw, leaving sufficient space between the tubing ends.
31. Carefully cut the Tygon tubing between the set screws using a new razor blade, making sure the cut is straight (*see Note 51*).
32. Cut a sufficient length of PE tubing (7–10" typically), and push it into the Tygon tubing.
33. Gently screw the set screws into the chamber bracket until the Tygon tubing is flush up against the chamber (*see Note 52*).
34. Insert 26-gauge 3/8" intradermal bevel needles (brown package) to the input PE tubing (*see Note 53*).

**Steps 35–48** should follow if the chambers are to be passivated with PEG. Otherwise these steps may be skipped:

35. Sonicate a 125 mL Erlenmeyer flask in 1 M KOH.
36. Rinse the flask with water 3× to remove excess KOH.
37. Sonicate the flask in methanol for 20 min.
38. Rinse the flask with methanol and dry with nitrogen gas.
39. In the flask, make a solution of 1 % (v/v) *N*-(2-aminoethyl)-3-aminopropyltrimethoxysilane and 5 % (v/v) acetic acid in methanol.
40. Assemble the flow chamber, then flow 1 mL of the amino-silane mixture through the channels.
41. Allow the amino-silane mixture to incubate for 15 min.
42. Flow another 1 mL of the mixture, and incubate for 15 min.
43. Flush out the amino-silane mixture with 1 mL methanol.

44. Flush out the methanol with 3 mL water.
45. Make a solution of 25 % (w/v) methoxy-PEG-succinimidyl valerate in 0.1 M sodium bicarbonate.
46. Flow ~200 µL of this PEG solution into each channel.
47. Allow the chamber to incubate for ~4 h, then rinse with copious amounts of water and dry with nitrogen gas.
48. Store PEG chambers in 4 °C in the dark.

### **3.11 Preparation of Beads for Experiment**

In this section we describe how to prepare DNA beads. We find that the DNA does not remain very stable on these beads, and so typically perform a fresh incubation at the start of each experiment.

1. Add 1 ng of the DNA construct to ~8 ng of Strep beads.
2. Incubate at RT for ~1 h for biotin-streptavidin bonds to form.
3. When Strep + DNA beads are ready, prepare four sample syringes by wetting the plunger and syringe interior with distilled water and then inserting the plunger. Attach needles to the ends.
4. Dilute ADig beads ~1000× into T50 buffer (*see Subheading 2.10*), and extract ~400 µL into a labeled syringe (*see Note 54*).
5. Dilute Strep + DNA beads ~100× into T50 buffer, and extract ~400 µL into a labeled syringe.

### **3.12 Sample Buffer Preparation for Oligonucleotide Hybridization Experiment**

The buffers described below should also be prepared fresh for each experiment. The final buffer should be: 100 mM Tris (pH = 8.0), 100 mM NaCl, the oxygen scavenging system (1 % glucose, 1 mg/mL glucose oxidase or 0.29 mg/mL pyranose oxidase, and 0.065 mg/mL catalase), and the triplet state quencher to prevent fluorophore blinking (1 mg/mL Trolox). One of the samples contains 1–10 nM of the fluorescently labeled oligonucleotide, while the other does not.

1. In a 1.5 mL tube, mix 789 µL of TX buffer (*see Subheading 3.8*), 43 µL of filtered 20 % (w/v) glucose, and 17 µL of filtered 5 M NaCl.
2. Split this buffer into two aliquots of 392 µL.
3. In one aliquot, add 4 µL of 1× TE buffer. This is the “blank” buffer.
4. In the other aliquot, add 4 µL of the appropriate concentration of the oligonucleotide probe (typically 1 µM, in 1× TE buffer). The final probe concentration should be 1–10 nM. This is the sample buffer. Keep in the dark.
5. Add 4 µL of GOx or POx to each tube.
6. Mix each solution well, and extract them into their respective syringes.

### 3.13 Setting Up the Instrument for an Experiment

The following steps describe the instrument startup procedure. Note that the order is important:

1. Turn on the RF amplifier. *Very important:* the RF amplifier power should always be turned on before any signal is sent to it, i.e., before the RF synthesizer power is turned on. Otherwise the amplifier may be damaged. Similarly, when shutting down the instrument, the RF synthesizer power should be turned off before turning off the RF amplifier power. The best practice is always to turn the RF amplifier power on/off as the first/last step.
2. Turn on all other power supplies, except for the APDs (*see Note 55*).
3. Run LabVIEW program. It is important that the RF synthesizer board is already on at this point since the program initializes it.

The next steps prepare the sample chamber for measurement:

4. Starting with the center channel, flow several hundred  $\mu\text{L}$  of 0.22- $\mu\text{m}$  syringe filtered 20 mM Tris buffer through, until the channel is filled and liquid comes out the outlet tubing. If using a chamber with multiple streams converging into the central channel, fill all of these simultaneously.
5. Check the outputs of the capillaries in the adjoining bead channels for fluid coming out to verify that the capillaries are not clogged (*see Note 56*).
6. Fill the outer bead channels with 0.22- $\mu\text{m}$  syringe filtered 20 mM Tris buffer.
7. Flow enough liquid through to see if there is a leak at the inlet and outlet tubing (*see Note 57*).
8. Verify by eye that there are no bubbles visible in the central channels. If there are, most can be pushed out with more buffer flow (try pulsing) or dissolved as buffer flows over them.

The following steps describe installation and alignment of the chamber in the instrument. A video monitor connected to the bright-field imaging CCD is used to check chamber alignment. It is important to adjust the chamber tilt angle for best trap performance:

9. Locate the camera CCD sensor at the focal plane of the tube lens (TL, 8"). At this position, the correctly collimated trap beam will appear focused.
10. Retract the front objective (FO) so the chamber can be placed between it and the back objectives (BO).

11. Mount the chamber on its motorized stage, a short distance ( $<1$  mm) from BO (*see Note 58*), lining up the capillaries of the chamber with the center of BO by eye. The chamber should be mounted loosely so that fine adjustments to its angle can be made later (Fig. 20).
12. Place the output tubing in a waste beaker. We recommend submerging it under some buffer, as this helps maintain flow by eliminating evaporation from the tubing ends.
13. Rotate the chamber until it looks (by eye) like the plane of the chamber is vertical.
14. Move FO toward the chamber, adding a few drops of  $0.22\text{ }\mu\text{m}$  filtered water between both objectives and the chamber when they are close enough.
15. Adjust FO until the inside surface of one of the coverslips comes into focus on the video monitor. Make sure the trap beam is in the center flow channel and does not pass through Parafilm or capillaries.
16. Flip out the IR and excitation laser filters in front of the CCD camera and flip in the ND filter to allow imaging the trapping beam.
17. Turn on one of the traps (*see Note 59*).
18. Move FO until the IR beam comes into focus on the video monitor. The trap should be collimated now. Do not adjust the FO position further. The collimation can be verified by checking that the trap beam profile remains the same size at varying distances beyond BO.
19. If the chamber is tilted relative to the beam axis, the beam image will be smeared in  $y$  (vertically), i.e., there will be a coma (Fig. 20b, beams slightly out of focus to accentuate smearing). This adversely affects trap performance, adding low frequency noise. Adjust the chamber tilt manually until the beam image on the video monitor is symmetric (Fig. 20c).
20. Flip in the IR and excitation laser filters and flip out the ND filter.
21. Scan the motorized stage and inspect each bead capillary along its length and verify that there are no bubbles. Bubbles are a common problem that will prevent the flow of beads into the main channel.

In the following steps, beads and sample buffers are flowed into the mounted chamber and the trap is checked:

22. Attach the syringe with ADig beads to the top bead channel and place it in one of the syringe pumps. Be sure to not add any air bubbles in the process.
23. Flush in ADig beads (approximately  $100\text{ }\mu\text{L}$ , at a flow rate  $100\text{ }\mu\text{L}/\text{min}$ ). It is helpful to observe the output of the bead

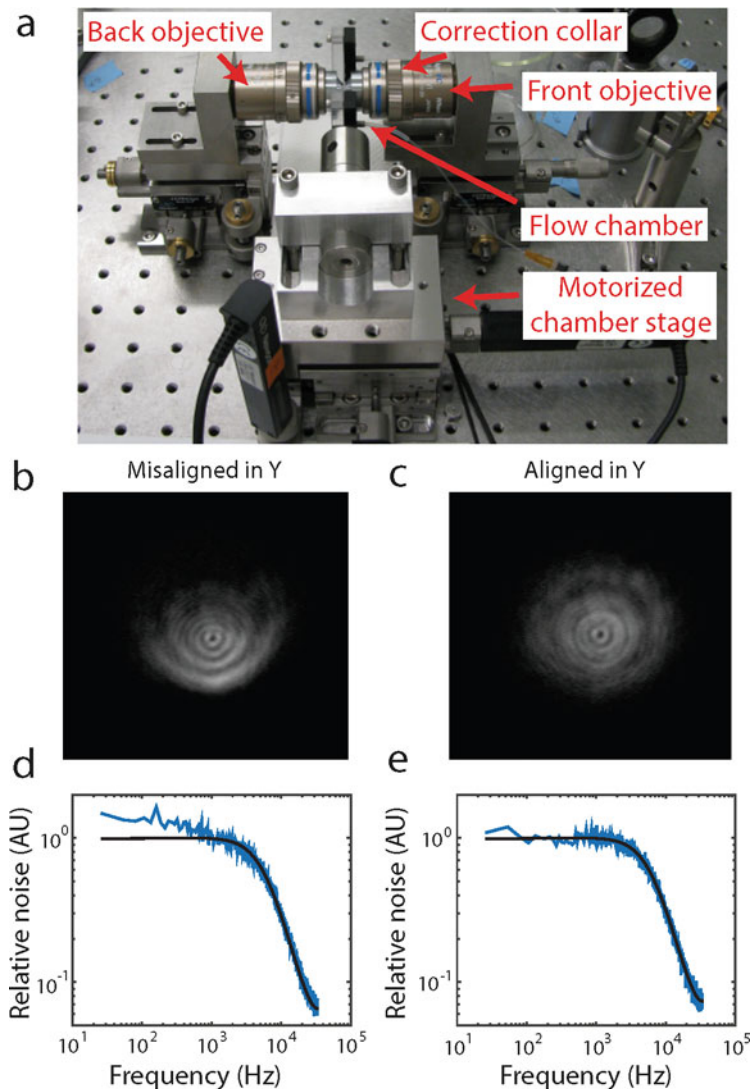


**Fig. 20** Alignment of flow chamber to front and back objectives. (a) Photograph of a mounted flow chamber resting on the motorized sample stage via a lens post, with the chamber between the front and back objectives. (b) and (c): Trapping laser beam profiles on the CCD camera when the chamber is misaligned in the *y* direction (b) and properly aligned (c). (d) and (e): Power spectra of trapped bead motion in *y* when the chamber is misaligned in the *y* direction (d) and properly aligned (e)

capillaries on the monitor when flowing in beads. Beads should be clearly seen streaming out of the capillary.

24. Capture an ADig bead with one optical trap, monitor its position using QPD2, and save the data to a file at full bandwidth (66 kHz). Make sure the trap is positioned away from either

capillary or cover glass surface as these will distort the trapping beam.

25. Determine and plot the power spectral density of the trapped bead position measured in the previous step. We use this standard approach to calibrate the optical traps [29, 46, 47], determining the conversion factors  $\alpha_x$  and  $\alpha_y$  (in nm/V) between the photodetector output signals and bead positions and the trap stiffnesses  $k_x$  and  $k_y$  (in pN/nm) along  $x$  and  $y$ . We also use the power spectra to identify alignment errors. Additional low frequency noise (<2 kHz) in the spectra can be caused by chamber tilt relative to the trapping beams (Fig. 20d). Adjust the chamber tilt angle accordingly as described in steps 19–20 above.
26. Fix the chamber post rigidly to its stage by tightening the screws.
27. *Optional:* Slightly adjust the camera position until the trapped bead is well focused on the video monitor.
28. Attach the syringe with DNA-coated Strep beads to the bottom bead channel and place it in one of the syringe pumps. Be sure to not add any air bubbles in the process.
29. Flush in DNA-coated Strep beads into the bottom bead channel (approximately 100  $\mu\text{L}$ , at a flow rate 100  $\mu\text{L}/\text{min}$ ).

The sample chamber position is controlled by a motorized 3-axis translational stage. We record several stage positions in the LabVIEW software, which allows moving rapidly to commonly used areas in the chamber (e.g., the capillaries, where beads are dispensed). This method increases throughput significantly. The following steps describe how to configure the motor controller settings:

30. Move the stage to the Strep bead capillary.
31. Choose a convenient location some short distance from the capillary, and zero the stage controller position to (0, 0, 0) (*see Note 60*).
32. Set other stage positions. We typically record five stage positions in total: by the lower capillary (*see* previous step) and the upper capillary, where beads are dispensed, within each of the flow streams in the central channel where measurements are taken (for the two-stream channels described here, in the upper and lower flow streams), and at one last position where trapped beads can be released after measurement (*see Note 61*).
33. Move to the prerecorded position in the stream where the fluorescent sample will be.

In the final experimental setup steps, the fluorescence excitation is turned on and fluorescent sample loaded:

34. Make *absolutely sure* the lights are off in the instrument room, and then turn on the APDs. Generally the instrument black out enclosures should protect the APDs if the room lights are on, but enclosure covers can be inadvertently ajar.
35. Turn on the excitation laser and adjust ND filters and AOM to produce  $\sim 3 \mu\text{W}$  of power measured before FO (averaged over interlacing, *see Note 62*).
36. Attach sample syringes to the central channel.
37. Flush 100  $\mu\text{L}$  of sample into the central channel (both center channel syringes are simultaneously injected by the syringe pump) and monitor the APD signals. The background fluorescence should increase and level off as the fluorescently labeled probe fills the channel. This is a helpful measure of the background fluorescence at the start of each experiment. For a well-passivated chamber, the background fluorescence should not drop after the buffer flow stops.
38. Switch the center channel flow to a constant rate of 100  $\mu\text{l}/\text{h}$  ( $\sim 140 \mu\text{m/s}$  linear flow speed) to maintain laminar flow and prevent the blank and fluorescent probe channels from mixing.

In the next steps, the confocal excitation is aligned laterally (in  $x$  and  $y$ ) with the optical traps and positioned where the fluorescence signal is expected. The alignment involves imaging the pair of trapped beads by scanning the fluorescence excitation beam, turned to high power, across the beads and measuring the beam's deflection using the PSD. These steps must be performed once per trapping session:

39. First, be sure the APDs are turned off.
40. Flip out the ND filter in the fluorescence excitation beam path using the motorized flip mount to increase the excitation intensity for detection beam scanning.
41. Trap a pair of beads.
42. Set the separation between the traps to where the traps are expected to be during the experiment.
43. Scan the movable mirror SM in  $x$  and  $y$  to image the pair of beads (Fig. 16).
44. Flip back in the ND filter in the fluorescence excitation beam path using the motorized flip mount to reduce the excitation intensity down for single-molecule fluorescence measurements.

45. From the image of the beads produced, find the position where the fluorophore is expected to be (centered between the beads for the DNA constructs in Fig. 1), and set the mirror voltage to this value. For the hybridization experiment, this positions the confocal spot at the binding site of the oligonucleotide probe (*see Note 63*).

### 3.14 Measuring Hybridization of Fluorescently Labeled Oligonucleotide

In the following protocol, we describe a simple proof-of-principle experiment using the optical traps and confocal microscopy. The protocol details how to capture beads with the optical traps, calibrate the traps, form a single DNA tether between the beads, take a force-extension (F-X) curve of the tethered DNA molecule, followed by data collection at constant trap separation or constant force (Fig. 21).

The conversion factors between QPD2 voltages and the positions of beads relative to the centers of their traps and the trap stiffness should be determined for each pair of beads during an

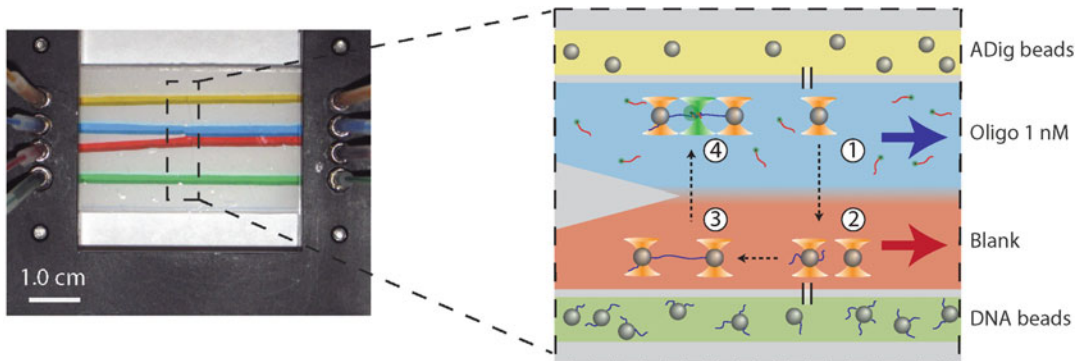


**Fig. 21** Laminar flow cell layout sequence of steps in trap + fluorescence measurement. The flow chamber consists of top (yellow) and bottom (green) channels in which anti-digoxigenin (ADig) and DNA-coated streptavidin (DNA) beads flow, and a central channel comprised of two parallel laminar flow streams containing “blank” buffer (red) and the sample (blue). (Food dye was used in the photograph to show the different channels.) Within the flow chamber, ADig beads flow through the top channel (yellow) and out of the top capillary (black vertical lines) into the sample stream (blue), where it is captured by trap 1 (position 1). The chamber stage is then translated such that the trapped bead remains in the blank buffer stream (red) and is positioned near the bottom capillary (position 2). Here, DNA-coated streptavidin beads (DNA beads) are flowed through the bottom channel (green) and out of the bottom capillary, where one of them is captured by trap 2. When both beads are trapped, the stage is translated until the trapped beads are upstream of the capillaries (position 3). Here the traps are first calibrated, then an offset curve is taken (*see Subheading 3.11*). The trapped beads are then moved close to one another to form a single DNA tether. A F-X curve is taken to verify proper elastic behavior of the tethered molecule. Finally, the stage is translated such that the trapped beads are moved into the sample stream, which contains 1 nM fluorescently labeled oligonucleotide (position 4). At this position the excitation laser (green cone) is turned ON, and the binding and unbinding of oligonucleotides is observed both by the fluorescence signal and the change in extension of the traps. Whenever possible during this sequence, solution is flowed in the two central streams in order to maintain laminar flow (photo reproduced from ref. [14] with permission from eLife Sciences Publications)

experiment. We use the standard calibration method, measuring the Brownian fluctuations of the beads in the traps and fitting the power spectral density of the bead positions to the characteristic Lorentzian shape [29, 46]. This fit is used to obtain  $\alpha$ , the conversion factor between photodetector signal and physical bead displacement in nm, and  $k$ , the stiffness of the optical trap, for each bead and in the lateral directions  $x$  and  $y$ .

The QPD voltages  $V$  are related to the physical bead displacements by  $x = \alpha(V - V_{off})/S$ , where  $V_{off}$  is a voltage offset from the photodetector, and  $S$  is the total intensity incident on the photodetector. Importantly, the offset voltage  $V_{off}$  is not constant across trap positions. There are a few sources contributing to this effect, including the imperfect deflection axis of the AOM (which causes the trapping beam to move across the QPD when scanned), AOM interference effects, cross talk between the two traps, etc. This effect is most pronounced when the traps are close together. In order to measure the correct bead displacement (and force), an “offset curve” must be taken prior to forming a tether to obtain  $V_{off}$  as a function of trap separation (Fig. 22a). The necessity of this procedure is illustrated by comparing F-X curves calculated using  $V_{off}$  values determined at a single trap position (e.g., where the traps are calibrated) vs. one calculated using the separation-dependent  $V_{off}$  values from the “offset curve” (Fig. 22b). Only when  $V_{off}$  values from an offset curve have been subtracted from the QPD voltages are accurate values for the extension and force obtained. We have found that the conversion factors  $\alpha$  and trap stiffnesses  $k$  do not change significantly with trap separation.

The following steps describe how to capture ADig and Strep beads, calibrate the trap, take an offset curve, form a tether, and take a F-X curve:

1. Move to the top ADig bead capillary.
2. Turn off the central channel flow. This ensures that beads will not be swept away by the flow before they can be trapped.
3. Turn on the ADig bead syringe pump at a low flow rate (~100  $\mu\text{l}/\text{h}$  is typical).
4. Turn on one trap.
5. Trap an ADig bead when it comes out of the capillary.
6. Turn off the ADig bead pump, and turn the center pump back on (*see Note 64*).
7. Move to the bottom Strep bead capillary.
8. Turn off the central channel pump, and turn on the Strep bead pump.
9. Turn on the second trap and set the trap separation to ~18 MHz, corresponding to ~2  $\mu\text{m}$  (*see Note 65*).

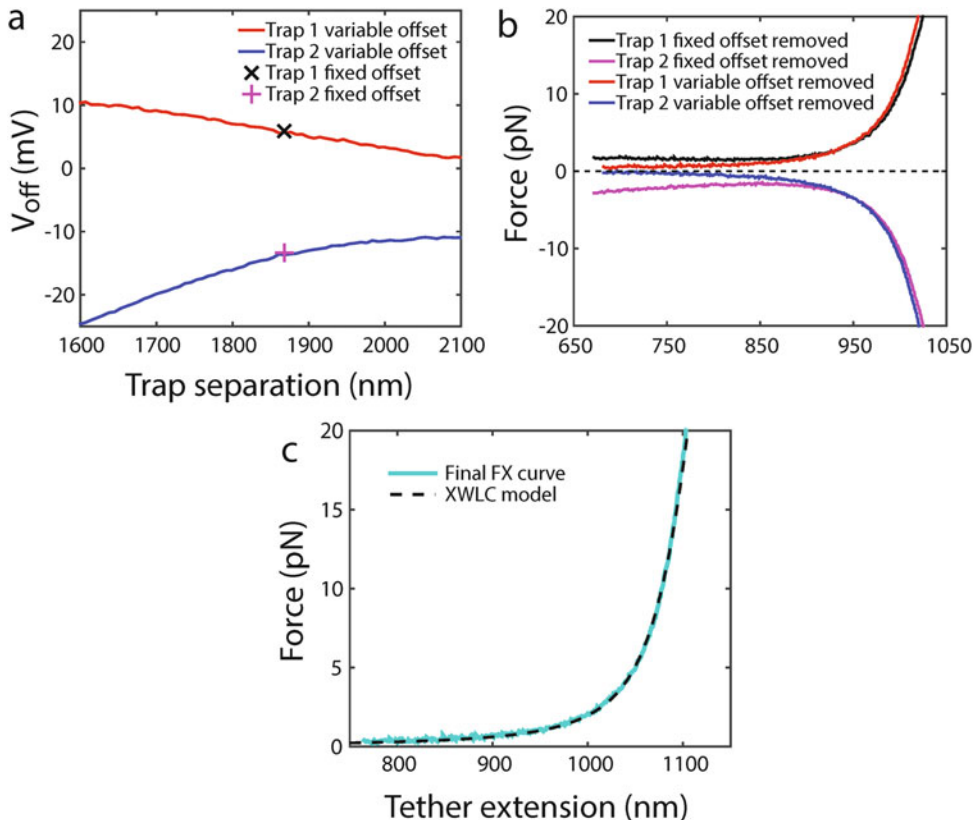


**Fig. 22** Obtaining a force-extension (F-X) curve of a DNA tether. (a) Recorded voltage from the bead position QPD as one trapped bead (in trap 1) is moved relative to the other trapped bead (in trap 2) (i.e., a blank F-X curve). The voltage offset  $V_{off}$  in the QPD output signal for trap 1 (red) and 2 (blue) depends on the separation between the two traps. Offset values obtained at the fixed positions where the traps are calibrated are also shown ( $\times$  and  $+$ ). (b) F-X curves of the DNA construct (Fig. 19) with either the “fixed” offset value (black and magenta) or the variable (separation-dependent) offset removed (red and blue). The data recorded from each trap are plotted separately for clarity. Only the F-X curves with a separation-dependent offset removed display the correct behavior. (c) The final F-X curve is plotted with the extensible wormlike chain (XWLC) model [49, 50]. The final F-X curve (cyan) is obtained by averaging the force from traps 1 and 2, where each has its variable offset removed individually. This averaged F-X curve is overlaid on the XWLC model (black dotted line) by shifting the curve along the extension axis by a small, fixed value resulting from uncertainty in the diameters of the trapped beads. The parameters used for the XWLC model for dsDNA and ssDNA are: persistence lengths  $P_{ds} = 50$  nm,  $P_{ss} = 1$  nm, helix rises  $h_{ds} = 0.34$  nm/bp,  $h_{ss} = 0.59$  nm/bp, and stretch moduli  $S_{ds} = S_{ss} = 1100$  pN [51–53]

10. Trap a Strep bead in the opposite trap, being careful not to let it fall into the trap holding the ADig bead.
11. Turn off the Strep bead pump and turn the central channel pump back on to reestablish laminar flow and wash away any excess beads (see Note 66).
12. Move to a position in the blank channel to calibrate the traps. It is a best practice always to use the same position in the chamber.

13. Turn off the central channel pump and acquire trap calibration (*see Note 67*).
14. It is useful at this point to analyze the calibration power spectra (e.g., in Matlab) to obtain  $\alpha$ ,  $k$ , and  $V_{off}$  for each bead and for both lateral directions,  $x$  and  $y$ . In this way, the calibration parameters can be input in LabVIEW to view displacements and forces in real-time (*see Note 68*).
15. Acquire an offset curve by displacing one of the traps relative to the other while recording the bead positions. Scan over a large range in separation to ensure that it covers the range over which data may be taken subsequently (Fig. 22b). In this way, the position-dependent offset can always be subtracted even if subsequent F-X curves have variable ranges.
16. Form a tether by moving the beads close together and then apart repeatedly. A tether is detected by an increase in the force on the beads when they are moved apart (*see Note 69*).
17. Take a F-X curve of the tethered DNA.
18. Assess the tether quality by comparing the F-X curve to the theoretically predicted polymer model (*see Note 70*). It is best practice to reject the bead pair and a new pair of beads captured if a “bad” tether is formed.

Option 1: Collecting a time trace using constant trap separation:

19. Move the traps to fixed positions corresponding to the desired tether tension.
20. Start saving data.
21. Move the tether into the channel containing the fluorescently labeled DNA probe, and turn on (i.e., interlace) the excitation laser and APDs.
22. Observe the binding and unbinding of oligonucleotide probes by simultaneous trap detection of changes in tether extension and by fluorescence as in Fig. 1a. The trap signal recorded in this case is the displacement of the beads from the centers of their respective traps (*see Note 71*). For the 3  $\mu$ W average fluorescence excitation power, expect to detect ~2 kHz photon rate from a single Cy3 fluorophore.

Option 2: Collecting a time trace using constant force:

Using the force-feedback system, displacements of the beads from their set-point values are compensated by a change in trap position. The displacement of the beads from their trap centers remains constant, and the data of interest are the instantaneous trap separations. Force feedback is achieved through an FPGA-programmed PID controller similar to the intensity feedback (*see Subheading 2.1*). Differential bead position signals are monitored

(i.e., bead 1 position–bead 2 position) and one trap is moved to keep this signal constant. Monitoring the differential bead position increases stability and reduces noise compared to monitoring one bead [9]. Finally, the same trap AOM simultaneously controls both the trapping beam intensity by feedback as well as the trap positions during force feedback. For these two feedback loops not to interfere with each other, we run the intensity feedback as usual at the full 66 kHz interlacing rate while running the trap position feedback 100× slower at 666 Hz.

23. Move the traps apart to exert the desired force on the tether.
24. Set the bead displacement difference as the feedback set-point value.
25. Activate the force-feedback system.
26. Move the tether into the channel containing the fluorescently labeled DNA probe, and turn on (i.e., interlace) the excitation laser and APDs.
27. Observe the binding and unbinding of the oligonucleotide probe to the tethered DNA construct by simultaneous detection of changes in tether extension and fluorescence as in Fig. 1a. The trap signal recorded in this case is the trap separation (*see Note 72*).

---

#### 4 Notes

1. These can be replaced with detectors that do not measure beam position (e.g., Thorlabs PDA36A).
2. In practice it is impossible to do this perfectly as there is no single pivot plane about which the beams are rotated inside the AOM.
3. As discussed above, we choose the 1.5 mm collimation option. To minimize noise and heat production in the instrument isolation room, we locate the laser power supply outside the room and route the fiber into the room. Since the optical fiber is the laser cavity, there are limits on the length of the fiber. We have found that a 4 m long fiber works well. We also choose the red guide laser option, which produces a red beam co-aligned with the 1064 nm trap beam. This is a very helpful alignment feature for initial coarse alignment of the laser with the isolator, power modulation stage and the AOM since it avoids the potential of damaging components with misalignment of the high power 1064 nm beam. Note that the red guide beam is not useful after the AOM since it does not diffract with the 1064 trap beam.

4. This exact mirror is no longer available. It seems that the manufacturer, CVI, will no longer make a mirror with sufficient visible transmission efficiency. As alternates, we have also successfully used similar mirrors from Semrock (NFD01-1064) and Chroma (T970dcspxr). We requested the mirrors be custom cut round with a 25 mm diameter. These two mirrors are not offered on preferable, thick substrates (4–8 mm) so care must be taken to mount the mirror without bending it. We find it best to epoxy these mirrors into the mirror mounts, although alternatives to epoxy are available (see Note 25 in ref. [47]).
5. It can be challenging to co-align the fluorescence excitation beam with the trapping beam without asymmetrically clipping the fluorescence beam. Making the fluorescence beam waist slightly smaller than the objective aperture makes this procedure easier, with the cost of a slightly larger confocal spot.
6. Given the fluorescence beam waist and the focal length of the lens imaging the fluorescence onto the pinhole (given above), we commonly use a 100  $\mu\text{m}$  diameter pinhole which achieves a modest amount of background rejection without blocking any fluorescence signal. For many typical applications we have found this to be sufficient. For stronger background rejection with modest signal loss for use in higher fluorescence background, we have found a 20  $\mu\text{m}$  diameter pinhole to be optimal.
7. This exact laser has been discontinued. However, the exact choice of 532 nm excitation laser is not critical. Any laser with the best beam quality offering 10–50 mW output power should do. The high power is not necessary for fluorescence excitation but rather for use of the laser as a detection beam for alignment purposes. We have successfully used 532 nm lasers from LASOS, CrystaLaser, Spectra among others.
8. Alternately, we use the Newport 9066-COM-E for the fine positioning stage, which integrates an encoder to read the stage position, and we move the stage with a Newport 8301NF Picomotor. This allows us to scan the confocal depth precisely and remotely, without touching and disturbing the instrument.
9. This dichroic mirror may no longer be available. We also use Semrock FF875-Di01-25.
10. This specific filter has been discontinued. One possible replacement is Chroma ZT532rdc.
11. This specific filter has been discontinued. One possible replacement is Chroma ET590/50 m.
12. This specific filter has been discontinued. One possible replacement is Chroma ET690/50 m.

13. Many LEDs have a poor illumination uniformity. This can easily be corrected by placing with a diffuser such as Thorlabs DG10-220-MD in front of the LED.
14. The exact frequency of the TCXO chip is not critical: we recommend choosing a chip with a frequency between 20 and 80 MHz. Use the RF synthesizer board clock multiplier capability to multiply the clock to a final value around 300 MHz. If the final value is lower, it may be imperfectly filtered and leak into the RF output. We note that it is becoming increasingly difficult to find high stability 14-pin DIP TCXO stocked by electronics suppliers. We have had to special-order them directly from the manufacturers. Finally, these chips are especially sensitive to damage from static electricity. Follow the usual anti-static safety protocols including grounding yourself with an anti-static strap and working with the board only on an anti-static mat.
15. The RF power amplifier gets very hot to the touch, and the best practice is to cool the amplifier with a small fan aimed at the heat sink that comes mounted to it.
16. This RF power meter converts an input RF signal into an analog voltage output corresponding to the input RF power. The power meter output can be viewed on an oscilloscope to show the RF interlacing operation directly. This can be very helpful for verifying correct operation or for debugging. The RF signal can also be viewed directly on the oscilloscope. In all cases care must be taken not to exceed the maximum input power of the test devices.
17. The fully amplified RF signal is often too large to view with test devices (e.g., RF power meter, oscilloscope) without damage. We insert RF attenuators as needed after the RF synthesizer but before the RF amplifier to scale down amplified RF signals to a safe measurement range.
18. This innovative oscilloscope design integrates a high quality RF spectrum analyzer, which can be used to verify RF signal stability. The oscilloscope can also plot the RF amplitude and frequency versus time along with traditional analog voltage inputs, which can be another useful method of verifying and debugging interlacing and timesharing operation.
19. Bead position measurements are made continuously at high speed (66 kHz, one sample per each trap ON interval). The high continuous data rate necessitates transferring data from the FPGA to the host computer using a buffered transfer method. The FPGA connects to the PC via high speed PCIe bus directly to the PC memory using a process known as Direct Memory Access (DMA). The FPGA is able to transfer data continuously via DMA to the PC. Periodically, the host

retrieves data from the RAM buffer, and then deletes them from the buffer. The host LabVIEW code then processes the data, displaying it for the user and saving it to the hard drive. The host PC must retrieve the data from the buffer in a timely way so that there is always room for the FPGA to transfer data into it. If the host falls behind, the buffer will overflow and data will be lost. If this occurs, the data streaming from the FPGA must be resynchronized by stopping data transfer, erasing the buffers, and restarting data transfer. Buffer overflow can happen if the host computer is performing too many other tasks at the same time, so measures should be taken to prevent it from diverting resources to these tasks while data is being collected. One additional method for increasing host performance is to use two separate storage drives: a solid-state drive (SSD) for running the operating system (including LabVIEW), and a larger high performance hard drive disk (HDD) onto which data files are saved directly (e.g., Western Digital 2 TB “Black” drives).

20. Note that the FPGA DAQ card must be given an “alias” in NIMAX. This alias must match the name in the host LabVIEW code where the FPGA target is initialized, or the code will not run.
21. We recommend avoiding “green” energy efficient hard disk drives, as they seem to enter a low energy consumption “sleep” mode at times, which disrupts data streaming. Western Digital Black SATA drives have worked well.
22. Avoid soldering the TCXO as they are highly susceptible to damage.
23. The parallel communication option updates all 8 bits simultaneously, whereas the serial option updates 1 bit at a time. For this reason it is best to use the parallel option.
24. The output of the RF synthesizer and amplifier should always be terminated with a  $50\ \Omega$  load to prevent reflected RF power and likely damage to components. The AOM is a  $50\ \Omega$  load and is the usual termination of the RF amplifier. When observing RF signals on an oscilloscope, set the oscilloscope to a  $50\ \Omega$  input impedance OR split the signal between the scope at high input impedance ( $1-10\ M\Omega$ ) and a  $50\ \Omega$  terminator.
25. How much the bead is displaced during the interlacing cycle will depend on whether it is tethered to the other bead and how much tension is applied in the tether.
26. The RF power driving the AOM controls the amount of incident light transmitted into the first-order diffracted beam, so a higher power will ultimately produce stiffer traps. However, while the RF amplifier is capable of producing 5 W of output power, special care must be taken when sending an amplified

signal to the AOM, since AOMs are susceptible to damage from high input power. We have found that ~2.5 W is close to the maximum that can safely be used with our AOM, which corresponds to ~40 % transmission efficiency (Fig. 9).

27. Translating the stage requires two of the five fine-adjustments to be moved simultaneously; otherwise the stage will also rotate. An easy way to do this is to use two L-shaped hex keys, so the stage can be translated smoothly by ensuring that the hex keys rotate together by the same amount while turning the fine-adjustment screws. Additionally, the region of the AOM where the intensity drops off will occur before the edge of the aperture. The AOM has an active area that is actually smaller than the aperture itself.
28. When the traps are turned off (e.g., intermittently during interlacing or completely during experiment manipulations) the entire trap laser power returns to the zeroth order beam. Depending on beam collimation and power, we have generally found that this beam is intense enough to burn a hole through a standard stainless steel iris, so rather than simply blocking it we deflect this beam to a beam dump.
29. Use the signal from the detector (e.g., QPD) to perform any synchronizations, not the output control signal of the DAQ card. There will be a delay between the time that the output signal is sent from the DAQ card to when the AOM switches the beam. This delay can be on the order of microseconds, which is similar to the interlacing cycle timing. It will therefore prevent precise synchronization.
30. Be careful to note the rise times of the QPD and PSD on the oscilloscope: the detectors do not send a signal to the oscilloscope instantaneously; there is a short lag period. This lag is longer for the PSD than the QPD. The trap is fully ON nearly as soon as the signal begins to increase, *not* when it reaches a plateau (Fig. 5). Likewise, the trap is OFF as soon as the signal begins to decrease, *not* when it reaches zero. Additionally, keep in mind that the QPD detection occurs at the *rising edge* of the square pulse timing output from the DAQ card, not the center. This edge must be aligned to the center of the trap/fluorescence interval.
31. The phase shift is robust. Thus, this synchronization procedure only needs to be performed when the instrument is set up. However, the phase will change if the alignment of the trap laser with the AOM is changed. There is a delay between the RF input switching time and the trap laser diffraction switching time determined by the speed of sound in the AOM crystal and the distance between the beam and the piezoelectric element at the edge of the crystal.

32. Note also that as the signal intensity rises and approaches the APD input limit, the recorded signal will saturate and then actually begin to drop! This can cause confusion because an increase in excitation laser intensity will cause a decrease in APD signal out. It is best to stay well away from the 1 MHz input limit for these alignments. We recommend adjusting to a robust 100 kHz signal.
33. It may be helpful to use a separate set of fluorescent beads for each APD. For APD 1 (Cy3 channel) we use beads with an excitation maximum of 540 nm and emission maximum of 560 nm. For APD 2 (Cy5 channel) we use beads with an excitation maximum of 535 nm and emission maximum of 575 nm.
34. When adjusting the phase of the APD measurement ON time, keep in mind that the fluorescent beads tend to phosphoresce. Because of this, the measured fluorescence signal will not decay instantly when the excitation laser is turned OFF. Thus, the time at which the fluorescence signal *turns ON* is the most reliable way to set this phase.
35. The beads, while not manufactured to be fluorescent, will usually produce enough fluorescence to be imaged. We have found that the material of the beads is a significant factor in this background fluorescence; polystyrene beads tend to appear bright in the fluorescence channel, while silica beads tend to be nearly invisible. For applications where the fluorophores are to be placed near a bead surface, silica beads are the better choice.
36. It is expected that the lateral focus is sharper than the axial focus (i.e., z, along the light path).
37. For a more direct comparison, it is best to measure the fluorescence intensity and trap stiffnesses for the same bead as the correction collar is changed (the bead will remain trapped if the correction collar is adjusted carefully). However, fluorescent beads photobleach over time, and so the fluorescence intensity may drop during this procedure, giving a false maximum. Thus, after scanning over some range of collar values, it is prudent to reverse direction and scan in the opposite direction as well.
38. Alternately, we avoid ethidium bromide and image GelGreen gels with a blue LED transilluminator.
39. LH and RH are designed such that the restriction sites are located within 20 bp of one end of the handle. As a result, the unwanted digestion products are short enough to be removed using a PCR cleanup kit instead of gel purification. In general, this strategy may not be possible for all DNA construct designs.

40. Avoid using agarose gels with ethidium bromide for imaging the DNA products that will later become part of the final construct. Not only is ethidium bromide an intercalating agent that may not entirely be removed later in purification steps, but it is excited by UV light, which will damage the DNA. GelGreen requires blue light (~500 nm) excitation and as a result generates less damage to DNA than ethidium bromide.
41. Since the insert used is small (19 nt), it can be removed from the reaction mix just like a primer after PCR. After the second ligation, there will be unligated RH DNA in the solution, but it is not essential to remove it by gel purification. Purification is unnecessary because the DNA will later be incubated with streptavidin beads only. Since the RH has digoxigenin on its end and not biotin, it will not bind to the beads.
42. The mass of dsDNA/bp is ~660 g/mol. LH is  $\sim 9.9 \times 10^5$  g/mol and RH is  $\sim 1.1 \times 10^6$  g/mol. Divide the LH concentration in ng/ $\mu$ L by 0.99 and the RH concentration by 1.1 to obtain the concentrations in nM.
43. Both GOx and POx will work as an oxygen scavenging system, but POx has a few benefits: first, it will not cause a decrease in pH during experiments, while GOx will. This means that experiments can be done with a lower concentration of buffering compounds like Tris. Secondly, we have found that POx has a longer shelf life. It will remain functional for 1 or 2 months if stored at 4 °C, while GOx remains functional for only 1 or 2 weeks.
44. Unless otherwise noted, use Type 1 deionized water.
45. We add this small concentration of Tween 20 to prevent the beads from sticking together and forming large aggregates. We have found that this makes the bead preparation simpler (the beads form a tighter pellet) and also reduces the frequency of aggregated beads during experiments.
46. It is preferable to print multiple copies at low laser power to avoid overheating the glass coverslips and warping the chambers, which will deform the trapping beams.
47. When cutting them, we recommend holding the end of the capillary with a pair of tweezers while cutting with the other hand to ensure that it remains in place. The capillaries should protrude past the Parafilm on either side. When melted, the Parafilm will spread and can clog the capillaries if they are too short.
48. The capillaries tend to stick electrostatically, so it is fairly difficult to actually place them in the right positions. Try rolling them along the Parafilm, but avoid rolling them on the coverslips themselves, since they tend to scratch up the surface.

49. It is important not to overheat, as the Parafilm may melt over the capillary ends and clog them. Conversely, heating too slowly may cause bubbles to form in the chamber and a poor seal.
50. It is easy to break the coverslips by over-tightening the screws. It is best to finger-tighten the mounts.
51. A common cause of leaking chambers is poorly cut Tygon tubing. If the razor blade used to cut is dull or if the tubing is cut in more than one stroke the tubing end will be frayed or chipped. Also, not making a straight cut results in a beveled edge, out of which solution can leak.
52. Do not over-tighten the tubing; this is a very common way to break chambers. When making a new chamber, however, the set screws tend to push back out a bit on their own. Keep this in mind if you see leaks. You may need to re-tighten the screws.
53. Be careful not to stab yourself with the needles as you thread them into the tubing! It is very painful. The best way to do this step is to bend the tubing away from the sharp point of the needle, such that the needle does not get caught on an inner edge of the tubing.
54. Gas-tight Hamilton syringes should be used to prevent oxygen diffusion into buffers and to enable smooth syringe motion when using syringe pumps. Be sure to remove any air bubbles from solutions drawn into the syringes.
55. APDs are highly sensitive detectors and can be permanently damaged if exposed to moderately high light intensities. They should only be turned on once the room lights are off.
56. If nothing is flowing through the capillaries, it could be a small clog. Try to release it by applying more pressure to the channel, pinching the end of the outlet tubing and pushing the input syringe moderately hard. Do not push too hard or the chamber can crack.
57. Some small chamber leaks may not be noticeable at first. Flushing a large volume of liquid through (~1 mL) should reveal any leaks. Common causes of leaks are the inlet or outlet set screws being too loose, the chamber holes not lined up with the tubing, and beveled or frayed tubing.
58. To maintain proper alignment, the back objective should always remain fixed in position and the chamber should be adjusted relative to it.
59. It is helpful to lower the intensity of the trapping beam for the initial alignment so that the beam profile is easier to see on the CCD camera.
60. This reference allows us to return approximately to the same chamber positions after uninstalling and reinstalling the chamber.

61. The measurement area should be upstream of the sample flow, so that beads dispensed from the capillaries do not flow into the traps during a measurement. Conversely, beads should be released after measurement downstream of the capillaries.
62. Be careful not to bump the pellicle mirror next to the filter mount when screwing off/on new filters; it is extremely fragile.
63. The position does not need to be extremely accurate, since the diffraction-limited spot itself is several hundred nanometers in diameter.
64. It is best to leave the central pump on whenever possible to keep the “sample” and “blank” channels separate. When the pump is off, the two streams will slowly diffuse together. The central pump must be turned off at a few points, including when beads need to be trapped.
65. Trap positioning is most accurate and reproducible if the separation between the two traps is specified by the difference in trap 1 and 2 RF frequency. For our instrument, the conversion is 123 nm/MHz.
66. In our LabVIEW code, many of these steps are automated. Such automation both makes the experiments more user-friendly and reduces the chance of user error. One of the few parts of the experimental procedure that is not automated is the actual trapping of the beads.
67. Prior to saving this file, it is prudent to move the two traps apart to the approximate position in which the experiment will be done, since the offset of the centroid from the detector is not constant from position to position. This will be corrected later in data processing, but our LabVIEW software will use this fixed value to calculate distances and forces to display to the user during the experiment, so it is most useful to have an accurate number.
68. This process can be automated as follows: a number in the header of the saved file identifies this file as a calibration. Matlab is running concurrently with LabVIEW, and periodically checks the directory in which data files are saved for any new files. When a new file appears, Matlab opens the file and checks the number in the header to identify its type. Noting that it is a calibration file, Matlab will then run a code to plot the bead power spectra and save a file into this same directory containing the values calculated from the calibration: offset, the conversion factor  $\alpha$ , and the trap stiffness  $k$ . LabVIEW will then read this file and update its parameters such that detector voltages can be displayed as bead displacements and forces in real-time for the user to see.

69. Note that moving the beads too close may result in the formation of more than one tether, so it is best to begin with a moderately large closest approach and adjust closer if no tethers are forming.
70. A F-X curve should be taken for each tether formed to ensure the quality of the DNA molecule used. This is necessary because no population of DNA molecules is perfectly homogeneous: some of them will possess defects such as nicks or other types of damage. Thus, obtaining the F-X curve of each molecule surveyed acts as a quality-control mechanism, whereby inadequate DNA molecules can be rejected.
71. This displacement corresponds to both a change in tether extension and a change in force exerted on the tether. To obtain the change in extension without the added effect of force, the trap stiffnesses and DNA tether compliance must be taken into account.
72. In some cases it is helpful to collect data only in the blank channel, where there are no diffusing fluorescent molecules. These experiments are done by first incubating the DNA tether in the channel with the fluorescent molecules, then “dipping” it into the blank channel before turning on the interlacing of the excitation laser and collecting data. In doing so, there is no background fluorescence signal from the freely diffusing fluorescently labeled molecules. This “dipping” method can therefore significantly increase signal-to-noise, and even allow for high concentrations of labeled molecules to be used with no effect on the background signal.

## Acknowledgments

We thank members of the Chemla, Ha, and Comstock laboratories for scientific discussion. Funding was provided by NSF grants MCB-0952442 (CAREER to Y.R.C.), PHY-1430124 (Center for the Physics of Living Cells to Y.R.C.), RC-105094 (to M.J.C.), and NIH grant R21 RR025341 (to Y.R.C.).

## References

1. Ashkin A (1986) Observation of a single-beam gradient force optical trap for dielectric particles. *Opt Lett* 11:288–290
2. Woodside MT, Block SM (2014) Reconstructing folding energy landscapes by single-molecule force spectroscopy. *Annu Rev Biophys* 43:19–39
3. Ritchie DB, Woodside MT (2015) Probing the structural dynamics of proteins and nucleic acids with optical tweezers. *Curr Opin Struct Biol* 34:43–51
4. Hilario J, Kowalczykowski SC (2010) Visualizing protein–DNA interactions at the single-molecule level. *Curr Opin Chem Biol* 14:15–22
5. Heller I, Hoekstra TP, King GA et al (2014) Optical Tweezers Analysis of DNA–Protein Complexes. *Chem Rev* 1:3087–3119

6. Mehta AD, Rief M, Spudich JA et al (1999) Single-molecule biomechanics with optical methods. *Science* 283:1689–1695
7. Bustamante C, Cheng W, Mejia YX (2011) Revisiting the central dogma one molecule at a time. *Cell* 144:480–497
8. Abbondanzieri EA, Greenleaf WJ, Shaevitz JW et al (2005) Direct observation of base-pair stepping by RNA polymerase. *Nature* 438:460–465
9. Moffitt JR, Chemla YR, Izhaky D et al (2006) Differential detection of dual traps improves the spatial resolution of optical tweezers. *Proc Natl Acad Sci U S A* 103:9006–9011
10. Chemla YR (2010) Revealing the base pair stepping dynamics of nucleic acid motor proteins with optical traps. *Phys Chem Chem Phys* 12:3080–3095
11. Larson MH, Landick R, Block SM (2011) Single-molecule studies of RNA polymerase: one singular sensation, every little step it takes. *Mol Cell* 41:249–262
12. Wen J, Lancaster L, Hodges C et al (2008) Following translation by single ribosomes one codon at a time. *Nature* 452:598–603
13. Cheng W, Arunajadai SG, Moffitt JR et al (2011) Single-base pair unwinding and asynchronous RNA release by the hepatitis C virus NS3 helicase. *Science* 333:1746–1749
14. Qi Z, Pugh RA, Spies M et al (2013) Sequence-dependent base pair stepping dynamics in XPD helicase unwinding. *Elife* 2:1–23
15. Moffitt JR, Chemla YR, Aathavan K et al (2009) Intersubunit coordination in a homomeric ring ATPase. *Nature* 457:446–450
16. Comstock MJ, Ha T, Chemla YR (2011) Ultrahigh-resolution optical trap with single-fluorophore sensitivity. *Nat Methods* 8:335–340
17. La Porta A, Wang MD (2004) Optical torque wrench: angular trapping, rotation, and torque detection of quartz microparticles. *Phys Rev Lett* 92(190801):190801–190804
18. Lang MJ, Fordyce PM, Engh AM et al (2004) Simultaneous, coincident optical trapping and single-molecule fluorescence. *Nat Methods* 1:1–7
19. Hohng S, Zhou R, Nahas MK et al (2007) Fluorescence-force spectroscopy maps two-dimensional reaction landscape of the holliday junction. *Science* 318:279–283
20. Van mameren J, Peterman EJ, Wuite GJ (2008) See me, feel me: methods to concurrently visualize and manipulate single DNA molecules and associated proteins. *Nucleic Acids Res* 36:4381–4389
21. Lee KS, Balci H, Jia H et al (2013) Direct imaging of single UvrD helicase dynamics on long single-stranded DNA. *Nat Commun* 4:1–9
22. Suksombat S, Khafizov R, Kozlov AG et al (2015) Structural dynamics of *E. coli* single-stranded DNA binding protein reveal DNA wrapping and unwrapping pathways. *Elife* 4:1–23
23. Comstock MJ, Whitley KD, Jia H et al (2015) Direct observation of structure-function relationship in a nucleic acid – processing enzyme. *Science* 348:352–354
24. van Dijk MA, Kapitein LC, Mameren J et al (2004) Combining optical trapping and single-molecule fluorescence spectroscopy: enhanced photobleaching of fluorophores. *J Phys Chem B* 108:6479–6484
25. Brau RR, Tarsa PB, Ferrer JM et al (2006) Interlaced optical force-fluorescence measurements for single molecule biophysics. *Biophys J* 91:1069–1077
26. Bustamante C, Chemla YR, Moffitt JR (2008) In: Selvin P, Ha TJ (eds) *Single-molecule techniques: a laboratory manual*. Cold Spring Harbor Laboratory Press, Woodbury, New York
27. Block SM (1998) In: Spector D, Goldman R, Leinward L (eds) *Cells: a laboratory manual*. Cold Spring Harbor Press, New York
28. Van mameren J, Wuite GJ, Heller I (2011) Introduction to optical tweezers: background, system designs, and commercial solutions. *Methods Mol Biol* 783:1–20
29. Neuman KC, Block SM (2004) Optical trapping. *Rev Sci Instrum* 75:2787–2809
30. Visscher K, Brakenhoff GJ, Krol JJ (1993) Micromanipulation by multiple optical traps created by a single fast scanning trap integrated with the bilateral confocal scanning laser microscope. *Cytometry* 14:105–114
31. Visscher K, Gross SP, Block SM (1996) Construction of multiple-beam optical traps with nanometer-resolution position sensing. *IEEE JSTQE* 2:1066–1076
32. Wuite GJ, Davenport RJ, Rappaport A et al (2000) An integrated laser trap/flow control video microscope for the study of single biomolecules. *Biophys J* 79:1155–1167
33. Gittes F, Schmidt CF (1998) Interference model for back-focal-plane displacement detection in optical tweezers. *Opt Lett* 23:7–9
34. Pralle A, Prummer M, Florin E et al (1999) Three-dimensional high-resolution particle

- tracking for optical tweezers by forward scattered light. *Microsc Res Tech* 44:378–386
- 35. Huisstede JHG, van Rooijen BD, van der Werf KO et al (2006) Dependence of silicon position-detector bandwidth on wavelength, power, and bias. *Opt Lett* 31:610–612
  - 36. Analog Devices (2007) User's Manual for CMOS 300 MSPS Complete DDS: AD9852, Rev. E. p. 1–52
  - 37. Ha T (2001) Single-molecule fluorescence resonance energy transfer. *Methods* 25:78–86
  - 38. Landry MP, McCall PM, Qi Z et al (2008) Characterization of photoactivated singlet oxygen damage in single-molecule optical trap experiments. *Biophys J* 97:2128–2136
  - 39. Rasnik I, McKinney SA, Ha T (2006) Non-blinking and long-lasting single-molecule fluorescence imaging. *Nat Methods* 3:891–893
  - 40. Joo C, Ha T (2008) In: Selvin PR, Ha T (eds) Single-molecule techniques: a laboratory manual. Cold Spring Harbor Laboratory Press, Woodbury, New York
  - 41. Swoboda M, Cheng H, Brugger D et al (2012) Enzymatic oxygen scavenging for photostability without pH drop in single-molecule experiments. *ACS Nano* 6:6364–6369
  - 42. Brewer LR, Bianco PR (2008) Laminar flow cells for single-molecule studies of DNA-protein interactions. *Nat Methods* 5:517–525
  - 43. Min TL, Mears PJ, Golding I et al (2012) Chemotactic adaptation kinetics of individual *Escherichia coli* cells. *Proc Natl Acad Sci U S A* 109:9869–9874
  - 44. Landry MP, Zou X, Wang L et al (2013) DNA target sequence identification mechanism for dimer-active protein complexes. *Nucleic Acids Res* 41:2416–2427
  - 45. Ha T, Rasnik I, Cheng W et al (2002) Initiation and re-initiation of DNA unwinding by the *Escherichia coli* Rep helicase. *Nature* 419:638–641
  - 46. Berg-Sørensen K, Flyvbjerg H (2004) Power spectrum analysis for optical tweezers. *Rev Sci Instrum* 75:594–612
  - 47. Nicholas MP, Rao L, Gennerich A (2014) An improved optical tweezers assay for measuring the force generation of single kinesin molecules. *Methods Mol Biol* 1136:171–246
  - 48. Humphrey W, Dalke A, Schulten K (1996) VMD: visual molecular dynamics. *J Mol Graph* 14(33–38):27–28
  - 49. Marko JF, Siggia ED (1995) Stretching DNA. *Macromolecules* 28:8759–8770
  - 50. Odijk T (1995) Stiff chains and filaments under tension. *Macromolecules* 28:7016–7018
  - 51. Bustamante C, Marko JF, Siggia E et al (1994) Entropic elasticity of lambda-phage DNA. *Science* 265:1599–1600
  - 52. Wang MD, Yin H, Landick R et al (1997) Stretching DNA with optical tweezers. *Biophys J* 72:1335–1346
  - 53. Woodside MT, Behnke-Parks WM, Larizadeh K et al (2006) Nanomechanical measurements of the sequence-dependent folding landscapes of single nucleic acid hairpins. *Proc Natl Acad Sci U S A* 103:6190–6195

# Chapter 9

## Versatile Quadruple-Trap Optical Tweezers for Dual DNA Experiments

Iddo Heller, Niels Laurens, Daan Vorselen, Onno D. Broekmans, Andreas S. Biebricher, Graeme A. King, Ineke Brouwer, Gijs J.L. Wuite, and Erwin J.G. Peterman

### Abstract

Optical manipulation techniques provide researchers the powerful ability to directly move, probe and interrogate molecular complexes. Quadruple optical trapping is an emerging method for optical manipulation and force spectroscopy that has found its primary use in studying dual DNA interactions, but is certainly not limited to DNA investigations. The key benefit of quadruple optical trapping is that two molecular strands can be manipulated independently and simultaneously. The molecular geometries of the strands can thus be controlled and their interactions can be quantified by force measurements. Accurate control of molecular geometry is of critical importance for the analysis of, for example, protein-mediated DNA-bridging, which plays an important role in DNA compaction. Here, we describe the design of a dedicated and robust quadruple optical trapping-instrument. This instrument can be switched straightforwardly to a high-resolution dual trap and it is integrated with microfluidics and single-molecule fluorescence microscopy, making it a highly versatile tool for correlative single-molecule analysis of a wide range of biomolecular systems.

**Key words** Quadruple-trap optical tweezers, Single-molecule force spectroscopy, Optical trapping, Dual DNA manipulation, Microfluidics, Fluorescence, Force detection

---

### 1 Introduction

Optical trapping is a single-molecule manipulation and force-spectroscopy method that has been applied to investigate a wide range of biomolecular systems, including molecular motors and DNA–protein interactions [1]. In such investigations, the biomolecular system of interest is typically tethered between an optically trapped microsphere (bead) and either a rigid surface or a second trapped bead [1, 2]. Through analysis of the relative extension of the biomolecular system, and/or the force on the beads, the mechanical response and structural or conformational changes of the system can be elucidated. This enables the study of kinetics and

thermodynamics of for example biopolymer mechanics, protein unfolding, and stepping of molecular motors [3–7]. Characteristic for this type of study is that the system under scrutiny is reduced to a line between its two tether points on the optically trapped beads. When studying other biomolecular phenomena, however, it can be beneficial or even essential to go beyond a simple one-dimensional system and to manipulate and study the interaction of more than one biomolecular complex concurrently. An exquisite example is the study of protein-mediated interactions between two or more remote DNA segments, i.e., protein-mediated DNA–DNA bridging, which plays a central role in DNA compaction [8–10]. For mere observation of DNA compaction, quadruple optical trapping is not strictly needed: in a dual trap assay, DNA compaction manifests itself as a readily observable shortening of the DNA tether between two beads [9]. In such a dual-trap experiment, however, intramolecular bridges can only be formed if enough slack is given to the DNA such that remote DNA segments stochastically collide to form bridges at random locations and orientations. The key advantage of quadruple optical trapping is that the molecular architecture of the intermolecular bridged structure can be defined well enough to allow quantitative analysis in either a shearing geometry, exerting force over many bridges in parallel (Fig. 1b), or in an unzipping geometry, exerting force only on the outermost bridge of the bridged region (Fig. 1c). Such level of control is not possible in dual optical trapping. Also, the study of other processes such as DNA repair through homologous recombination or nonhomologous end joining could benefit from having more than two DNA-attachment points [11–13]. In this chapter, we focus on the instrumentation required for quadruple optical trapping experiments such as have been described in Ref. 9. Chapter 10 focuses on the biophysical assays and experiments of quadruple-trap optical tweezers.

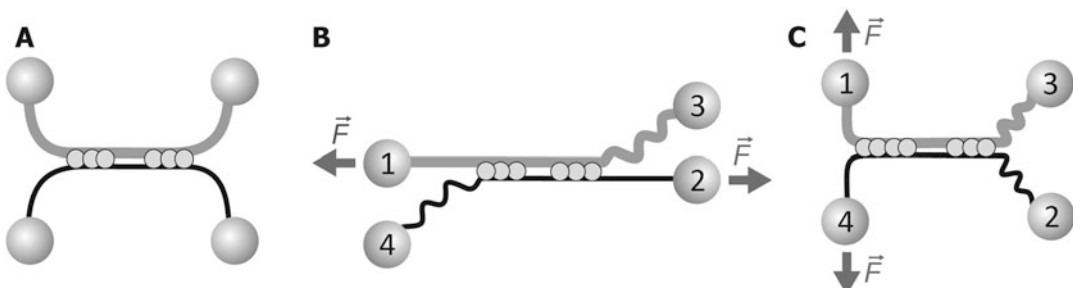


**Fig. 1** Quadruple optical trapping assays. (a) Controlled DNA-bridging assay in which parallel sections of two optically manipulated DNA molecules are bridged by DNA-binding proteins. (b) Shearing assay. A shearing force is exerted over all protein bridges along a well-defined bridged region; here, pulling on bead 2 allows the measurement of the shear force on bead 1. (c) Unzipping assay. By increasing the separation between the two beads on the same side of the bridged region (here, bead 1 and 4), an unzipping force is exerted that acts only on the terminal protein(s) of the bridged region

### 1.1 Quadruple Optical Trapping Instrumentation

In quadruple-trap optical tweezers, two DNA molecules can be manipulated independently in three dimensions [8, 14]. This has been exploited to configure two DNA molecules in wrapped, crossed, or parallel conformations to precisely control and study protein-mediated bridging between these two molecules [8, 9]. In a different application of quadruple-trap optical tweezers, one DNA molecule was wrapped around a second DNA molecule such that it functions as a scanning probe to localize and manipulate DNA-bound proteins [14]. Here, we focus on the design choices and operating principles of the quadruple-trap optical tweezers we developed and use in our laboratory (*see*, e.g., Ref. 9). In order to meet the requirements of a wide range of single-molecule experiments, the instrument is also equipped with single-molecule fluorescence imaging and microfluidics [1, 15]. Single-molecule fluorescence imaging can be performed concurrently with quadruple optical trapping experiments to be able to correlate the global mechanical control and analysis of the optical tweezers with local and specific information on the positions and dynamics of labeled components of the biomolecular system. Furthermore, a multi-channel microfluidic system has been added to allow rapid and complete buffer transfers. This enables swift *in situ* assembly of bead–DNA–bead dumbbell constructs and it allows stepping through the different phases of multistep biomolecular processes.

### 1.2 Requirements

Our quadruple-trap optical tweezers instrument has been designed to satisfy a number of specific requirements, which we list in Table 1 and discuss and motivate below.

First, it is critical for setting up quadruple optical trapping experiments that the relative position of each of the optical traps is controllable in three dimensions (Table 1, *requirement 1*): even though the actual experiment is often conducted within one plane, setting up a quadruple optical trapping experiment typically relies on a three-dimensional wrapping procedure to intertwine, cross, and/or force the interaction between two DNA molecules (*see* Chapter 10) [8]. To accomplish this in a convenient and controlled way, it should be possible to independently move the beads in both lateral and axial dimensions. The use of relatively long DNA is preferred for such quadruple optical trapping experiments: a popular choice is to use 48-kb bacteriophage lambda DNA [16]: The contour length of lambda DNA of 16  $\mu\text{m}$  facilitates wrapping, manipulating, and organizing two DNA molecules in every configuration without steric hindrance of the micrometer-sized beads. To physically enable stretching and manipulating DNA of this length, a sufficiently large lateral trap positioning range is needed (Table 1, *requirement 2*). In the case of lambda DNA, at least 30  $\mu\text{m}$  trap motion is required to change conformation of one lambda phage DNA from a relaxed random coil to its contour length and beyond, to an overstretched conformation [17]. Additionally, quadruple

**Table 1**  
**Design requirements of the quadruple-trap optical tweezers. For each requirement, the specific technical implementation is given. See Subheadings 2 and 3 as well as Subheading 4 for further explanation**

Requirement	Implementation
1 Adjust relative position of traps in three dimensions	Control of collimation and angle of the trapping beams entering the back aperture of the objective
2 Stretch and overstretch 16 $\mu\text{m}$ long lambda DNA	Trap motion $>30 \mu\text{m}$
3 Measure forces exerted on at least two out of four beads	Distinguish traps for displacement and force detection by polarization and wavelength
4 Trapping deep in solution, decoupled from surface	Use water immersion objective
5 Compatible with microfluidic system	Multichannel laminar flow cell
6 Qtrap with high trap stiffness and escape force	Laser power per trap $>1.5 \text{ W}$
7 Continuous trapping, no time-shared traps	See beam splitting scheme (Subheading 3.1)
8 Easy switching to dual trapping mode	Switch by flip-in waveplate
9 Dual trap with high resolution	Use differential force detection
10 Sub-base pair trap positioning	Trap positioning precision $<0.1 \text{ nm}$
11 Compatible with fluorescence microscopy	Wide-field epi-illuminated fluorescence

optical trapping also requires that the tension of both molecules can be monitored. To this end, it should be possible to measure the forces that are exerted on at least two of the four beads (Table 1, *requirement 3*): one bead of each DNA-dumbbell. This not only enables mechanical analysis of the DNA prior to wrapping (e.g., to check whether a single or multiple DNA molecules span a bead pair), but it also facilitates essential controls and diagnostics of tension on both molecules in a shearing or unzipping experiment [8, 9]. Such three-dimensional control of trap positioning greatly benefits from use of a water immersion objective in which trap stiffness and escape force are in principle independent of the trapping depth in solution (Table 1, *requirement 4*, and see Note 1). Working far away from a surface allows unrestricted 3D manipulation. Furthermore, deep in solution, the experiment will be optimally

decoupled from noise and drift associated with the sample stage [18]. Another advantage of having the biomolecular complex suspended in solution and free of surface tethers is that the manipulated complex can be moved freely throughout the sample cell. This is particularly advantageous when using a multichannel laminar flow cell: rapid and complete buffer transfers can be accomplished by simply moving the traps from one laminar flow lane to a parallel flow lane containing a different buffer (Table 1, *requirement 5*). This scheme enables rapid *in situ* formation of DNA-dumbbells by sequentially trapping beads, tethering DNA, probing DNA, and introducing proteins, while moving the traps between parallel laminar flow lanes with beads, DNA, buffer and proteins (*see also Chapter 10, Subheadings 3.5–3.8*) [19]. Setting up the assay in buffer flow, however, can induce considerable drag forces of tens to hundreds of piconewtons on beads and DNA. To withstand such drag forces, it is necessary to have traps with high escape forces (Table 1, *requirement 6*). Moreover, in particular in quadruple optical trapping experiments, which are more prone to stochastic attachment of multiple DNA molecules while waiting for both bead pairs to be tethered, a high escape force allows “breaking” unwanted additional DNA molecules by ramping up the tension (*see Note 2*). An average power per trap of 1–2 W, in combination with polystyrene beads larger than 2 µm, will yield an escape force of several hundreds of piconewton up to almost a nanonewton.

Previous quadruple-trap optical tweezers implementations have made use of time-shared optical traps in which the position of one trapping beam is rapidly alternated between multiple positions to create multiple optical traps [8, 14]. In the current implementation, however, we prefer the use of multiple continuously formed optical traps, rather than time-shared optical traps (Table 1, *requirement 7*). The rationale behind this choice is that the use of continuous optical trapping yields traps that are intrinsically stable over all timescales (*see Note 3*) and that have a trap stiffness that is independent of the trap position (*see Note 4*). Furthermore, continuous trapping allows for a robust and simple optical and electronic implementation when compared to time-sharing [20].

Single-molecule studies often require investigations based on a range of different assays and methods. To expand the capabilities of the discussed instrument beyond only quadruple optical trapping, the instrument should therefore also be able to function as a high-resolution dual optical trap (Table 1, *requirement 8*). Such a dual trapping scheme, in which one DNA molecule is tethered between two optically trapped beads, has proven to be successful in largely decoupling the biomolecular complex from drift and mechanical noise associated with the sample chamber and its holding stage [18]. When free of environmental noise, the resolution of an optical trapping experiment is limited by Brownian fluctuations of the bead–DNA–bead construct. Further enhancement of the spatial

resolution and force resolution can be accomplished through differential force detection (Table 1, *requirement 9*) [21]. In differential force detection, measurement of the position fluctuations of both beads enables cancelation of correlated motions to improve the overall signal-to-noise ratio. One of the most demanding experiments involves direct observation of the discrete steps of molecular motor enzymes. In the case of polymerase enzymes, the ultimate step size is one base pair of DNA: 0.34 nm [7]. In order to observe these steps in a force-clamp assay, with active feedback on trap position, it is necessary that the trap positioning accuracy is well below 0.34 nm (Table 1, *requirement 10*).

To further enhance the capabilities of the quadruple-trap optical tweezers, the instrument should be compatible with concurrent fluorescence microscopy: whereas optical tweezers probe the mechanical and structural properties and architecture of the biomolecular complex as a whole, fluorescence microscopy can give additional information about the dynamics and position of specific components on or within the biomolecular complex: the location, mobility, conformation states, affinity, and the on- and off-rates of specifically labeled components can be determined as the tethered complex is conveniently located in the focal plane. This allows synergistic experiments where the combination of optical trapping and fluorescence microscopy provides information that is not accessible with the individual techniques. For this quadruple optical trapping instrument, we chose to incorporate epi-illuminated wide-field fluorescence microscopy (Table 1, *requirement 11*): implementation of wide-field fluorescence is relatively straightforward and it allows rapid imaging of a large field of view well beyond the typical area in which quadruple optical trapping takes place ( $\sim 25 \mu\text{m} \times 25 \mu\text{m}$ ) [22, 23].

---

## 2 Materials

### 2.1 Microscope

1. Microscope body (Nikon, model TE2000-u).
2. 60 $\times$  water immersion objective (Nikon, Plan apo VC NA1.2).

### 2.2 Bright-Field Imaging

1. Pointsource LED (IMM Photonics, LED-1115-ELC-645-29-5).
2. Condensor top lens (Leica, P 1.40 OIL S1 11551004).
3. CMOS camera (Thorlabs, DCC1545M).

### 2.3 Optical Trapping

1. 1064 nm 20 W CW trapping laser (IPG Photonics, YLR-20-LP).
2. 980 nm 140 mW CW tracking laser (IQ2C140/6018 Power Technology Inc.).
3. Polarizing and non-polarizing beam-splitter cubes (Newport).
4. Closed loop piezo mirror (MadCityLabs, NanoMTA2X).

## 2.4 Force Detection

1. Position sensitive detectors (Silicon Sensor International AG, DL100-7PCBA3).

## 2.5 Fluorescence Microscopy

1. 532 nm 20 mW excitation laser (Coherent, COMPASS 2015M-20).
2. EMCCD Camera (Roper Scientific, Photometrics, Cascade 512B).

## 2.6 Microfluidics

1. Microfluidic Flow system (LUMICKS B.V., uflux).

## 3 Methods

The list of requirements as described in Table 1 guides the choice of core components of our quadruple-trap optical tweezers. Below we describe the components and how they relate to the requirements of Table 1.

### 3.1 Beam-Splitting Scheme

We create four optical traps from a single linearly polarized 1064 nm laser source. To accomplish this, one single laser beam is split first into two beams by one beam-splitter cube (PB1, Fig. 2) and subsequently by two other cubes (PB2, NB1, Fig. 2) into four beams. After each beam is reflected using a dedicated steering mirror (MM1-4, Fig. 2, *see* Subheading 3.3), the four paths are recombined again with beam-splitter cubes (PB3, NB2-3, Fig. 2). A combination of polarizing cubes (PB1-3, Fig. 2) and non-polarizing beam-splitter cubes (NB1-3, Fig. 2) ensures that one beam path (trap 1, MM1) has a unique linear polarization that is orthogonal to that of the other three traps (trap 2–4, MM2–4). Force detection of a second trap is not possible based on polarization alone. Instead, we use a low-power 980 nm detection laser that is co-aligned with one of the traps (trap 4, Fig. 2), which can be isolated from the other beams in the force detection paths based on its distinct wavelength. *See* Subheading 3.4 below for information on force detection.

### 3.2 Trapping Laser

As a result of using non-polarizing cubes in the beam-combining scheme, part of the laser power is lost after the beams are combined in the trap steering unit (*see also* Fig. 2). In fact, if the final power in each trap is equal, two-thirds of the initial laser power is lost as a result of the splitting and recombining of the beams. With the increasing availability of more cost-effective, high-power fiber lasers, however, we found this apparent disadvantage of generating four continuously illuminated optical traps to be acceptable. We are using a 20 W 1064 nm fiber laser (YB-20-LP, IPG) to create four traps with a maximum power up to 1.7 W per trap.

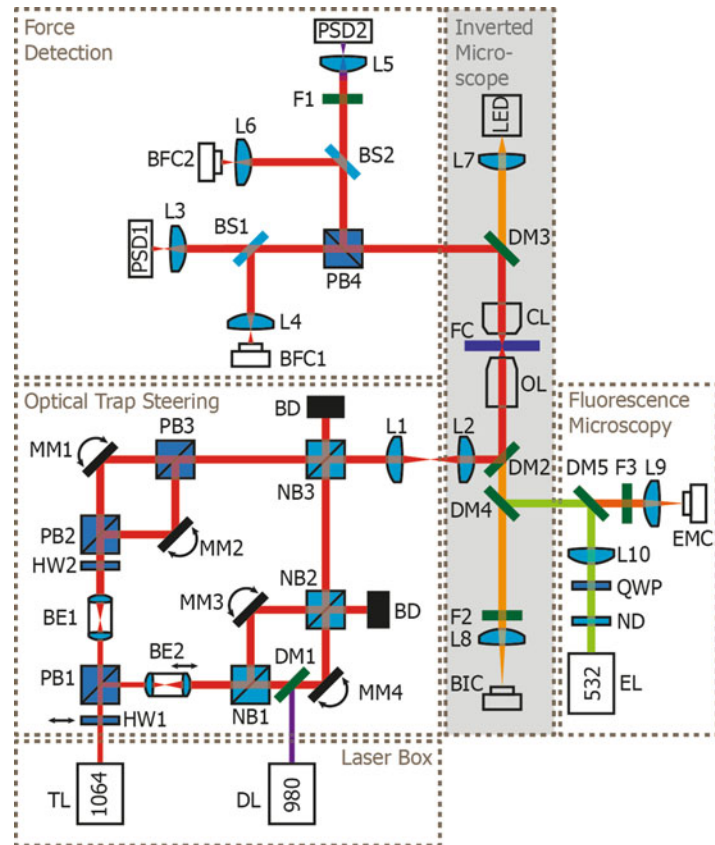


**Fig. 2** Schematic depiction of a quadruple-trap optical tweezers and fluorescence instrument. The optics are divided into five functional units: in the Trapping Laser Box, a high power 1064 nm trapping laser (TL) and a low power 980 nm detection laser (DL) are coupled into the Optical Trap Steering Unit. Here, four continuously illuminated optical traps are created using polarizing beamsplitter cubes (PB1–3) and non-polarizing beamsplitter cubes (NB1–3). Each trap (numbered 1–4) is steered using a dedicated motorized mirror (MM1–4) located in planes conjugate to the back-focal plane of the objective lens (OL). Beam expander BE2 is motorized to allow changing the collimation of traps 3 and 4 and change their axial position. A detection laser (DL) is co-aligned with trap 4. In the Force Detection Unit, two position sensitive detectors (PSD1–2) monitor the force and displacement of two traps: PSD1 monitors the 1064 nm light of trap 1, which has a unique polarization compared to the other traps, while PSD2 monitors the 980 nm light co-aligned with trap 4. The Inverted Microscope Unit is based on a commercial microscope body and uses a point-source LED to illuminate the sample plane that is imaged on a bead imaging camera (BIC). The Fluorescence Microscopy Unit consists of a simple wide-field layout where an excitation laser (EL) illuminates the sample while the fluorescence signal is imaged onto an EMCCD (EMC). Diagnostic tools added include the two cameras that image the condenser's back-focal plane (BFC1,2). Half-wave plate HWP1 can be flipped out of the beam path to guide all the trapping light to traps 1 and 2 to enter dual trapping mode. To permit differential force detection, filter F1 needs to be removed to image the 1064-nm light of trap 2 on PSD2. BD beam dump, BS beamsplitter, CL condenser lens, L lens, ND neutral density filter, QWP quarter-wave plate

### 3.3 Trap Positioning

Several computer-controlled components enable the relative positioning of the traps in three dimensions. First, each trapping path has one dedicated tip-tilt mirror (MM1–4, Fig. 2) that allows lateral

trap positioning. These automated tip-tilt mirrors are imaged onto the back-focal plane of the objective lens using a 1:1 telescope in a 4f configuration. With use of a  $60 \times 1.2\text{NA}$  water immersion objective with effective focal length of 3.3 mm, a 10 mrad change in optical path angle at the automated tip/tilt mirror is transformed into a 33  $\mu\text{m}$  change in the lateral trap position. In addition, the relative axial positioning of each pair of traps can be adjusted by altering the collimation of the trapping laser beams. In our implementation this is accomplished by changing the distance between the two lenses that are used for beam expansion (in BE2, Fig. 2), using an automated linear translation stage.

### **3.4 Force Detection**

To enable dual-molecule manipulation as well as accurate force measurements on each molecule, we employ a force-detection scheme that relies on the polarization and wavelengths of the laser beams. After passing through the objective lens and flow cell, the trapping and detection laser beams are collimated by a condenser lens and then split according to their polarizations by a polarizing beam-splitter cube. The light of trap 1 is detected on a position-sensitive detector (PSD) (PSD1, Fig. 2). A second PSD detects the filtered 980-nm light from the detection laser (PSD2, Fig. 2). This force-detection scheme relies on back-focal plane interferometry: non-scattered light from the trapping laser or detection laser interferes with light that is scattered by the trapped particle, which causes a shift in the laser's intensity distribution that directly reflects the displacement of the bead from the center of the trap and thus the external force on the trapped bead (*see Note 5*) [24]. To quantify the shift in the laser's intensity distribution, the back-focal plane of the condenser lens is imaged onto PSDs. In dual-trapping mode (*see Subheading 3.9*), the second PSD can be used to measure the force exerted on the second bead. This enables the use of differential force detection in which correlated fluctuations of the optically trapped beads can be eliminated to enhance the spatial resolution and force resolution [21, 25].

### **3.5 Calibration**

The PSDs in the force-detection unit output voltages that reflect the external force on the beads and the displacement of the beads that result from the exerted forces. For quantitative analysis of tethered biomolecular complexes, a calibration is required to translate the output voltage of the PSD to displacement and force. Among the various calibration methods that exist, we chose to acquire the power spectrum of the thermal fluctuations of the trap and then fit an equation that describes the Lorentzian power spectrum to retrieve the pN/V and trap stiffness values [26].

### **3.6 Alignment and Diagnostics**

To monitor the alignment, status, and functioning of the instrument, our quadruple-trap optical tweezers has back-focal plane camera's built into the force detection unit.

Force detection through back-focal plane interferometry relies on analyzing the intensity distribution of the trapping or detection laser light at the back-focal plane of the condenser lens using QPDs or PSDs (see Subheading 3.4). However, much more information of diagnostic value can be obtained by additionally imaging the back-focal plane of the condenser lens onto a camera (BFC1-2, Fig. 2). Figure 3 shows a number of images obtained from the back-focal plane camera to illustrate this. Figure 3a shows back-focal plane images for well-aligned traps with 0, 1, 2, and more than two trapped beads. Figure 3b–e show back-focal plane images (and bright-field images) for nonideal situations, including trapping too close to the Parafilm edge of a flow cell, air bubbles in the condenser lens immersion oil, trap–trap interference effects, and impurities on the flow cell surfaces (see caption of Fig. 3). Numerous other sources of potential experimental error can be diagnosed as well.

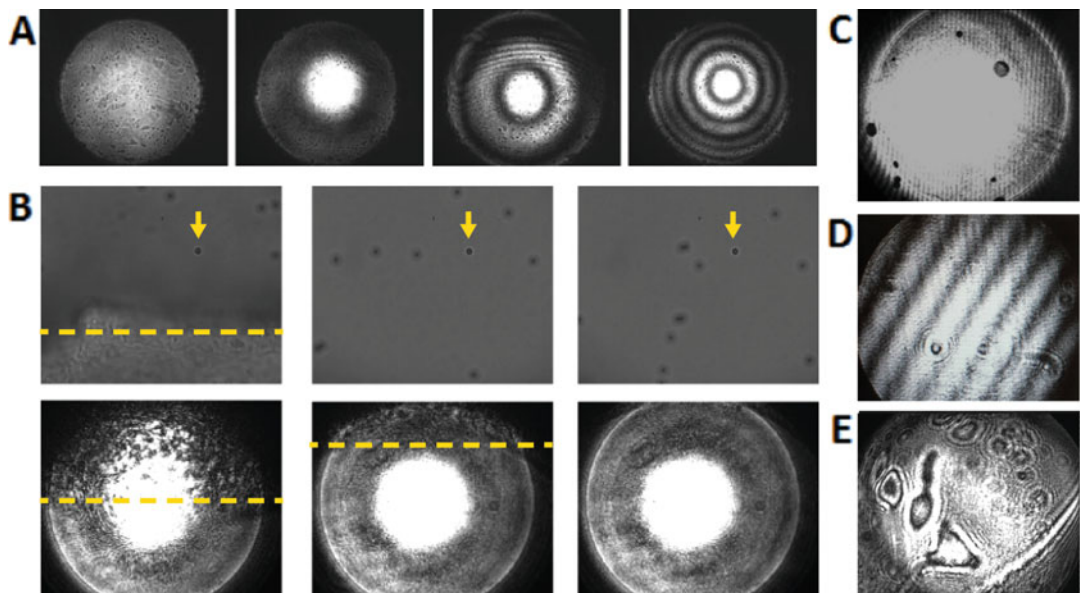


**Fig. 3** Back-focal plane camera diagnostics. Images acquired from the back-focal plane of the condenser lens (see also Fig. 2, BFC1-2 in the Force Detection Unit) can serve numerous diagnostic purposes. Several examples are given. (a) Back-focal plane images acquired for 0, 1, 2, and more than 2 beads trapped in the laser focus. (b) Images of the edge of a Parafilm of the flow cell (see also Ref. 16). The upper row shows images of the sample plane acquired through the bright-field imaging camera (see also Fig. 2, BIC in Bright Field Imaging unit) and the lower row shows the corresponding images of the back-focal plane of the condenser. In the first (left) image of the sample plane the Parafilm edge is visible at the bottom of the image. In the back-focal plane image, the Parafilm edge can indeed be observed to distort the image and therefore negatively affect the force detection. Although the Parafilm edge is moved away from the field of view in the second and third top row images, the Parafilm edge can still be observed distorting the upper part of the second back-focal plane image (bottom row). Only in the third column of images, the Parafilm no longer perturbs the optical trap. The yellow arrow indicates the position of the trapped bead, while the dashed line indicates the edge of the Parafilm. (c) Bubbles in the condenser oil appear as *black dots* in the image. (d) Trap–trap interference appears as periodic stripe pattern over the back-focal plane image. (e) Impurities on the flow-cell surfaces, for example due to salt or oil residues, are clearly visible in the back focal plane image

### 3.7 Automation and Control

Two major considerations in single-molecule experimentation are data throughput and reproducibility. In particular for quadruple optical trapping, these are points of attention, because the experimental complexity of catching two DNA molecules, manipulating them, and studying their interaction is significantly higher than, for example, studying a single DNA molecule. Automation is essential to enhance throughput, but also to minimize user input and error that can interfere with multistep experiments and reproducibility. The elements that should be considered for automation include all degrees of freedom of the trap and its immediate surroundings, such as three-dimensional trap motion, stage motion through the flow cell, and microfluidics. We control our instrument using home-built software, programmed in LabVIEW (National Instruments). Figure 4 shows the graphical user interface that controls the quadruple-trap optical tweezers. The selected parts show how the user interfaces with (1) Measurement signals (i.e., bead imaging (1a), real-time force and distance signal monitors (1b), and



**Fig. 4** Graphical user interface to control a quadruple optical trap. In *panel 1*, the user is presented with the bright-field image of the sample plane (1a). Bead positions (acquired through a template matching algorithm) and their tethers are overlaid on the image. Instantaneous force and bead separation (distance) signals are reported in real time in *panel 1b*, while *panel 1c* displays force–distance information or time traces as they are being acquired. *Panel 2* displays shutter control (2a) and trap-position control (2b). In *panel 3*, controlling a micro-positioning stage allows navigating through the flow cell (3a), and *panel 3b* allows monitoring and controlling buffer flow. *Panel 4* allows custom plugins to be displayed for dedicated experiments (4a, e.g., force–distance curve acquisition or force clamp routines), and *panel 4b* allows interaction with (meta)data storage as well as program status display. Several controls can be custom interfaced with a user-configurable joystick (not displayed)

force–distance curves and time traces (1c)); (2) Shutters (2a) and trap motion (2b); (3) Positioning (3a) and flow (3b) in flow cell; and (4) Measurement routines (4a) and data storage (4b). To further facilitate user interaction, the instrument is controlled through a user-configurable joystick. Finally, users can call on and add plugins that add new functions and automate numerous elements, such as force clamping and acquiring force distance curves.

### 3.8 Other Functionalities: Microfluidics and Fluorescence Microscopy

In our setup, quadruple optical trapping is performed in a multi-channel laminar flow cell. The use of such a flow cell in combination with a micro-positioning stage allows swiftly moving the optical traps between adjacent laminar flow channels. Figure 5a shows the workflow for *in situ* generation and analysis of two bead–DNA–bead dumbbells by trapping beads, tethering two DNA molecules in buffer flow and transfer into a protein free buffer and buffer with protein (*see Chapter 10*). In the protein-free buffer, the two DNA molecules are analyzed mechanically and manipulated in any desired configuration. Subsequent immersion into the protein channel then allows studying protein-mediated DNA–DNA interactions. The ability to build up and step through the different stages of the assay provides a great deal of experimental flexibility

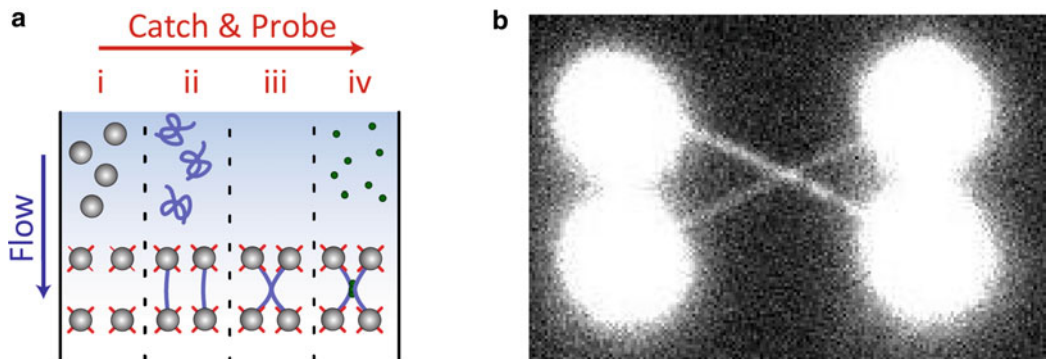


**Fig. 5** Microfluidics and fluorescence microscopy are complementary and compatible with quadruple optical trapping. (a) Schematic of quadruple optical trapping with microfluidics workflow. A single trapping laser is used to form four steerable optical traps inside a microfluidic flow cell. The flow cell is placed on a movable stage between the objective and the condenser of the microscope. Within this flow cell, four laminar buffer flows are present, allowing fast buffer exchange and easy tethering of DNA–protein complexes to beads. Steps *i*–*iv* illustrate the typical experimental workflow in the flow cell: in the bead-containing channel (*i*) beads are held in the optical traps and then moved to channel (*ii*), which contains DNA. Here, individual DNA molecules are tethered between bead pairs. Next, the DNA-bead assemblies are moved to the buffer channel (*iii*) where mechanical probing ensures that only one DNA molecule is tethered between each bead pair and the DNA is brought into the desired configuration (wrapped/crossed). Finally, the DNA-bead assemblies are moved to the protein channel (*iv*) where the DNA construct is exposed to the protein of interest. Adapted from Ref. 9. (b) Image of the fluorescence signal emitted by two 48.5-kb dsDNA molecules in half-wrapped configuration (see text) stained by 2–5 nM Sytox Orange (Invitrogen), showing the capability of the instrument to independently manipulate and intertwine two DNA molecules

and control. For example, one can choose to first intertwine the two DNA molecules before entering the protein-containing buffer or intertwine after entering the protein-containing channel. Entering the protein channel with pre-wrapped DNA can be essential to prevent saturation of all DNA-binding sites by proteins that exhibit a stable non-bridging DNA-binding mode [9]. For dynamically rearranging proteins [8], on the other hand, it may be interesting to study the transition from a non-bridging to a bridging binding mode. The ability to readily switch between protein-containing and protein-free buffers is also important to facilitate fluorescence microscopy: at high concentrations of fluorescently labeled proteins, the signal of DNA-bound proteins can easily be swamped. To circumvent this problem, a protein-coated DNA molecule can be rapidly moved to a protein-free buffer, in order to make background-free snapshots of the biomolecular complex using fluorescence microscopy [13]. Consideration of background fluorescence is particularly relevant for wide-field fluorescence microscopy as opposed to confocal microscopy [22, 25]. For its simplicity, we have chosen to implement wide-field fluorescence microscopy. Figure 5b shows an illustrative example of the combination of fluorescence microscopy and quadruple optical trapping. Here, an intercalating dye is used to reveal the presence and locations of two crossed DNA molecules. In this combination of optical techniques, care should be taken to correctly align the foci of the optical trapping beams and the focal plane of wide-field imaging: for the highest resolution and best signal-to-noise ratio, the depth at which the optical traps hold the DNA must coincide with the plane of fluorescence imaging. Here, it is important to note that the scattering force can push beads slightly beyond the laser foci, such that the DNA is shifted with respect to these foci. The shift depends on laser power, the focal intensity distribution, and the bead size and material. Although multiple alignment procedures can be conceived, the most direct alignment method is to continuously image a simple system such as intercalating dye on an optically stretched DNA molecule, while changing the axial position of the optical traps by displacing the lenses in beam expander BE1-2, or the tube lens (L9) in front of the EMCCD camera (Fig. 2). An optimal imaging position coincides with the highest local fluorescence intensity, the best signal-to-noise ratio, and the highest lateral resolution.

### 3.9 Select Trapping Mode

The instrument can be readily switched between quadruple optical trapping and dual trapping modes. To switch trapping mode, waveplate HW2 (Fig. 2) can be flipped in/out of the trapping beam path to select whether beamsplitter PB1 transmits all the trapping light to form traps 1 and 2, or whether a part of the trapping light is reflected by PB1 to additionally form traps 3 and 4. In the force-detection path, a concurrent choice needs to be made whether PSD2 detects the 980-nm light or the 1064-nm

light with a polarization orthogonal to that of trap 1. This is accomplished by changing the filtering scheme in front of PSD2. In dual optical trapping mode, differential force detection can be used to enhance the signal-to-noise ratio [21].

---

## 4 Notes

1. In contrast to using water-immersion objectives, the use of oil-immersion objectives restricts effective trapping to the first micrometers away from the substrate. At distances further away, spherical aberrations have detrimental effects on trap stiffness and escape force.
2. When ramping up the tension, DNA molecules can “break” due to several causes: the DNA might break near the overstretching force of  $\sim 65$  pN due to ligation errors or nicks in the DNA or the bead–DNA attachment might fail at the DNA–biotin–streptavidin–bead interface. The latter failure can occur at tensions much higher than the overstretching force and it can depend on the number of biotins introduced on the DNA and their spacings (as rule of thumb we use about three biotins on both ends). Note that the breaking tension will also depend on the number of parallel tethers: the actual tension on one DNA molecule in a dumbbell that consists of  $N$  DNA molecules tethered in parallel will be approximately the total force measured on the bead divided by  $N$ .
3. In time sharing, the position of one beam is rapidly alternated between  $N_{\text{trap}}$  trapping positions. This implies that, to obtain the same trap stiffness as for a continuously illuminated equivalent, the instantaneous trapping power is  $N_{\text{trap}}$  times higher, and the “on”-time of the trap is only  $1/N_{\text{trap}}$ -th of the time. In the “off” time, the beads will relax due to the force exerted by the DNA, causing an oscillatory motion.
4. The position of an optical trap is determined by the angle at which the trapping light enters the back-focal plane of the objective. This angle will change the lateral position of the diffraction limited spot that forms the optical trap in the field of view. When a continuously illuminated trap is properly aligned, this intensity distribution in the back-focal plane of the objective is independent of the incoming angle of the trapping light, yielding a trap with position-independent trap stiffness. For time sharing, on the other hand, rapidly modulated diffractive elements such as AODs, AOMs, or EODs are used. These devices typically suffer from an angle-dependent diffraction efficiency. In such time-sharing applications, additional detectors and feedback electronics are required to compensate for potential position-dependent intensity fluctuations in order to maintain a constant trap stiffness over the field of view.

5. In the so-called linear regime of an optical trap, Hooke's law  $F = -kx$ , with  $k$  the trap stiffness, applies such that the output voltage of the PSD directly reflects the force on the beads.

---

## Competing Interest Statement

The described technology is licensed to LUMICKS B.V., in which IH, GJLW, and EJGP declare a financial interest. NL, DV, ODB, ASB, GAK, and IB declare no competing financial interest.

## References

1. Heller I, Hoekstra TP, King GA, Peterman EJG, Wuite GJL (2014) Optical tweezers analysis of DNA-protein complexes. *Chem Rev* 114:3087–3119
2. Herbert KM, Greenleaf WJ, Block SM (2008) Single-molecule studies of RNA polymerase: motoring along. *Annu Rev Biochem* 77:149–176
3. Hegner M, Smith SB, Bustamante C (1999) Polymerization and mechanical properties of single RecA-DNA filaments. *Proc Natl Acad Sci U S A* 96:10109–10114
4. Block SM, Goldstein LSB, Schnapp BJ (1990) Bead movement by single kinesin molecules studied with optical tweezers. *Nature* 348:348–352
5. Gross P et al (2011) Quantifying how DNA stretches, melts and changes twist under tension. *Nat Phys* 7:731–736
6. Kellermayer, M.S. Folding-Unfolding Transitions in Single Titin Molecules Characterized with Laser Tweezers. *Science* (80). 1997;276:1112–1116.
7. Abbondanzieri EA, Greenleaf WJ, Shaevitz JW, Landick R, Block SM (2005) Direct observation of base-pair stepping by RNA polymerase. *Nature* 438:460–465
8. Dame RT, Noom MC, Wuite GJL (2006) Bacterial chromatin organization by H-NS protein unravelled using dual DNA manipulation. *Nature* 444:387–390
9. Laurens N et al (2012) Alba shapes the archaeal genome using a delicate balance of bridging and stiffening the DNA. *Nat Commun* 3:1328
10. Wiggins PA, Dame RT, Noom MC, Wuite GJL (2009) Protein-mediated molecular bridging: a key mechanism in biopolymer organization. *Biophys J* 97:1997–2003
11. Forget AL, Kowalczykowski SC (2012) Single-molecule imaging of DNA pairing by RecA reveals a three-dimensional homology search. *Nature* 482:423–427
12. De Vlaminck I et al (2012) Mechanism of homology recognition in DNA recombination from dual-molecule experiments. *Mol Cell* 46:616–624
13. van Mameren J et al (2009) Counting RAD51 proteins disassembling from nucleoprotein filaments under tension. *Nature* 457:745–748
14. Noom MC, van den Broek B, van Mameren J, Wuite GJL (2007) Visualizing single DNA-bound proteins using DNA as a scanning probe. *Nat Methods* 4:1031–1036
15. van Mameren J, Peterman EJG, Wuite GJL (2008) See me, feel me: methods to concurrently visualize and manipulate single DNA molecules and associated proteins. *Nucleic Acids Res* 36:4381–4389
16. Gross P, Farge G, Peterman EJG, Wuite GJL (2010) Combining optical tweezers, single-molecule fluorescence microscopy, and microfluidics for studies of DNA-protein interactions. *Methods Enzymol* 475:427–453
17. Smith SB, Cui Y, Bustamante C (1996) Over-stretching B-DNA: the elastic response of individual double-stranded and single-stranded DNA molecules. *Science* 271:795–799
18. Shaevitz JW, Abbondanzieri EA, Landick R, Block SM (2003) Backtracking by single RNA polymerase molecules observed at near-base-pair resolution. *Nature* 426:684–687
19. van den Broek B, Noom MC, Wuite GJL (2005) DNA-tension dependence of restriction enzyme activity reveals mechanochemical properties of the reaction pathway. *Nucleic Acids Res* 33:2676–2684
20. Comstock MJ, Ha T, Chemla YR (2011) Ultrahigh-resolution optical trap with single-fluorophore sensitivity. *Nat Methods* 8:335–340

21. Moffitt JR, Chemla YR, Izhaky D, Bustamante C (2006) Differential detection of dual traps improves the spatial resolution of optical tweezers. *Proc Natl Acad Sci U S A* 103:9006–9011
22. Heller I et al (2014) Mobility analysis of super-resolved proteins on optically stretched DNA: comparing imaging techniques and parameters. *Chemphyschem* 15:727–733
23. Candelli A, Wuite GJL, Peterman EJG (2011) Combining optical trapping, fluorescence microscopy and microfluidics for single molecule studies of DNA-protein interactions. *Phys Chem Chem Phys* 13:7263–7272
24. Gittes F, Schmidt CF (1998) Interference model for back-focal-plane displacement detection in optical tweezers. *Opt Lett* 23:7–9
25. Heller I et al (2013) STED nanoscopy combined with optical tweezers reveals protein dynamics on densely covered DNA. *Nat Methods* 10:910–916
26. Neuman KC, Nagy A (2008) Single-molecule force spectroscopy: optical tweezers, magnetic tweezers and atomic force microscopy. *Nat Methods* 5:491–505

## **Part II**

**Optical Tweezers-Based Manipulation and Analysis of  
DNA-DNA Interactions, Protein Unfolding/Refolding, and  
Motion/Force-Generation by Mechanoenzymes In Vitro**

# Chapter 10

## Probing DNA–DNA Interactions with a Combination of Quadruple-Trap Optical Tweezers and Microfluidics

Ineke Brouwer, Graeme A. King, Iddo Heller, Andreas S. Biebricher,  
Erwin J.G. Peterman, and Gijs J.L. Wuite

### Abstract

DNA metabolism and DNA compaction *in vivo* involve frequent interactions of remote DNA segments, mediated by proteins. In order to gain insight into such interactions, quadruple-trap optical tweezers have been developed. This technique provides an unprecedented degree of control through the ability to independently manipulate two DNA molecules in three dimensions. In this way, discrete regions of different DNA molecules can be brought into contact with one another, with a well-defined spatial configuration. At the same time, the tension and extension of the DNA molecules can be monitored. Furthermore, combining quadruple-trap optical tweezers with microfluidics makes fast buffer exchange possible, which is important for *in situ* generation of the dual DNA–protein constructs needed for these kinds of experiments. In this way, processes such as protein-mediated inter-DNA bridging can be studied with unprecedented control. This chapter provides a step-by-step description of how to perform a dual DNA manipulation experiment using combined quadruple-trap optical tweezers and microfluidics.

**Key words** Quadruple-trap optical tweezers, Microfluidics, Force detection, Single molecule, Protein-mediated inter-DNA bridging

---

### 1 Introduction

Over the past two decades, optical tweezers have been used extensively to elucidate the mechanics of individual DNA molecules and their interactions with proteins [1–4]. It has, however, remained a challenge to perform well-defined investigations of biological processes involving multiple DNA domains, such as protein-mediated DNA–DNA bridging. While such processes can, to some extent, be probed on an individual double-stranded DNA (dsDNA) molecule using dual-trap optical tweezers, the exact spatial configuration of the interacting DNA segments cannot be resolved or controlled.

To overcome these limitations, quadruple-trap optical tweezers have been introduced [5], which allow independent manipulation of two individual DNA molecules in three dimensions. The optical

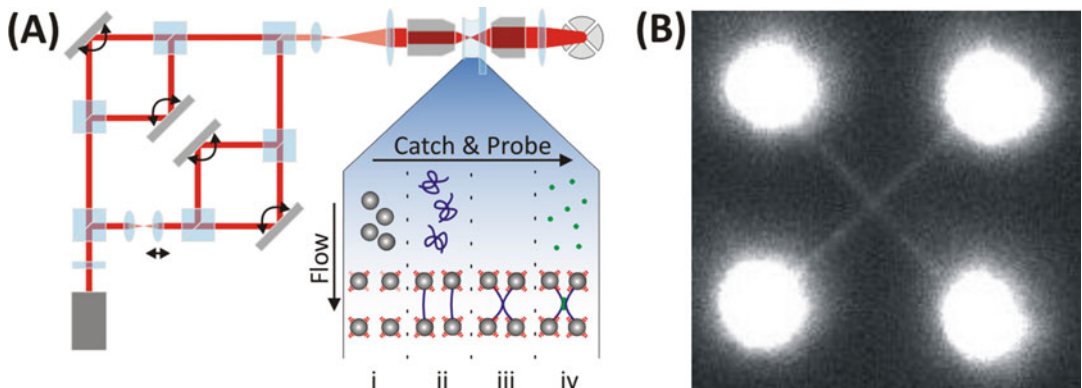


**Fig. 1** Quadruple-trap optical trapping can be used for dual DNA experiments. **(a)** Schematic of the setup. A single 1064 nm laser is used for generation of all four traps, and each trap is movable by rotation of a steerable mirror. The flow cell is placed on a movable stage between the objective and the condenser of the microscope. Within this flow cell, four laminar buffer flows are present, allowing fast buffer exchange and easy tethering of DNA–protein complexes to beads. Steps i–iv illustrate the typical experimental workflow in the flow cell: in the bead-containing channel (i) beads are held in the optical traps and then moved to channel (ii), which contains DNA. Here, individual DNA molecules are tethered between bead pairs. Next, the DNA–bead assemblies are moved to the buffer channel (iii) where mechanical probing ensures that only 1 DNA molecule is tethered between each bead pair and the DNA is brought into the desired configuration (wrapped/crossed). Finally, the DNA–bead assemblies are moved to the protein channel (iv) where the DNA construct is exposed to the protein of interest. Adapted from ref. [6]. **(b)** Image of the fluorescence signal emitted by 2 48.5 kb dsDNA molecules in half-wrapped configuration (see text) stained with 2–5 nM Sytox Orange, showing the capability of the instrument to independently manipulate two DNA molecules in three dimensions

setup used for these experiments (Fig. 1a) has been described previously [5–7] and is described in detail in Chapter 9. Concomitant fluorescence imaging can be used to confirm the presence of two DNA molecules and their configurations (Fig. 1b). In brief, the setup consists of four optical traps that are capable of trapping four micrometer-sized polystyrene beads. The four trapped beads are arranged in two pairs, after which each pair is coupled to the ends of a DNA molecule in a dumbbell configuration, typically using biotin–streptavidin linkages. The other important functionality needed for dual DNA experiments is a laminar flow cell that facilitates fast exchange between multiple buffers solutions, containing beads, DNA, protein, and buffer only [4] (Fig. 2). Fast exchange allows for efficient and effective assembly of two DNA dumbbells and then cycling through the subsequent steps of the biochemical/biophysical process of interest. Typically, we use a microfluidic flow cell with six laminar flow channels [5].

Three previous studies [5–7] have applied this technique to successfully unravel interactions between two DNA molecules. In the first case [5], one DNA molecule was held taut between two trapped beads, while another DNA molecule was wrapped around the first molecule. This second DNA construct was then slid along

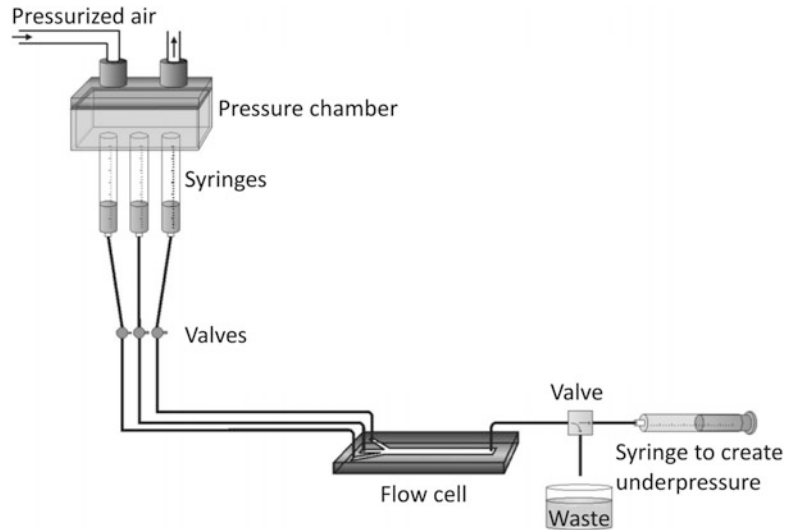


**Fig. 2** Schematic representation of the flow system. Beads, DNA, protein and buffer solutions are stored in individual syringes. By using pressurized air, a constant flow can be created through the flow cell, creating multiple laminar flows as shown in Fig. 1. Valves are used to switch the flow on or off in the individual channels. Adapted from [15]

the first DNA molecule and used as a mechanical probe to detect “roadblocks” such as proteins bound to the other DNA molecule. The mechanical force required for removal of these roadblocks could then be measured directly. In the second study [7], bridging between two DNA molecules by the bacterial nucleoid-associated H-NS protein was studied using dual DNA manipulation. Here, quadruple-trap optical tweezers enabled full control over the distinct molecular configurations in which either a shearing force is exerted over multiple H-NS bridges, or an unzipping force is exerted over a single H-NS bridge, by which the nature of DNA bridging by H-NS could be unraveled. In the third study [6], quadruple-trap optical tweezers were used in a similar way to study the DNA-organizing activity of two Archaeal proteins, Alba1 and Alba2. A combination of dual optical trapping and quadruple optical trapping was used to show that the Alba proteins can switch between DNA stiffening and bridging modes in a concentration-dependent manner. In all three studies, quadruple optical trapping was essential to control and probe the molecular architectures in order to uncover information that is otherwise not directly available. In addition, the integration of microfluidics enabled the fast generation of the protein–DNA complexes of interest. Together, these studies highlight that the combination of quadruple-trap optical tweezers and microfluidics provides a powerful means to study biological processes involving multiple DNA molecules. In addition, it is possible to further improve this

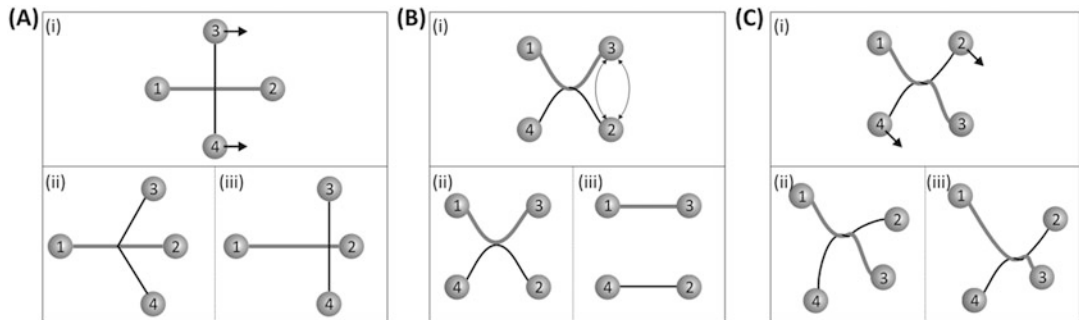


**Fig. 3** Schematic representation of different configurations for quadruple-trap experiments. **(a)** Crossed configuration (i) of the DNA molecules as suitable for friction experiments. Possible observations are the build-up of tension if there is sufficient local friction between the molecules (ii) or a lack of tension build-up if the DNA can slide over the other molecule (iii). **(b)** Half-wrapped configuration (i) suitable for probing protein-mediated inter-DNA bridging. Possible observations are DNA molecules linked together by bridges (ii), or, a lack of bridging between the DNA molecules (iii). **(c)** Fully wrapped configuration (i) suitable for scanning probe experiments [7]. Possible observations are that the wrap is immobile causing tension build up (ii), or a mobile wrap that lacks tension build-up (iii)

methodology by combining quadruple optical trapping with fluorescence microscopy, as previously has been shown for dual optical tweezers [1, 8], in order to concurrently acquire spatially resolved dynamic information on the molecular architecture of the DNA–protein complex (Fig. 1b). This improvement can further enhance the capabilities to unravel protein dynamics on DNA at the single-molecule level.

In this chapter, we provide a step-by-step guide on how to operate a quadruple-trap optical tweezers system to investigate the (protein-mediated) interactions between two DNA molecules. The optical system is shown schematically in Fig. 1a. Although quadruple-trap optical tweezers allow the user to perform experiments at any desired DNA–DNA configuration, here we focus on three particular configurations (Fig. 3): crossed, wrapped, and half-wrapped configurations. These three configurations can be used to address a range of biological questions involving multiple DNA molecules or domains. The first DNA–DNA configuration of interest is crossed DNA (Fig. 3a, top panel). This configuration is especially suitable for studying the friction between two DNA molecules and how this friction is affected by proteins. When the upper DNA molecule (between beads 3 and 4) is lowered to push down on the lower DNA molecule, the force between the two molecules increases. Having established a contact between the two DNA molecules, two beads are then moved simultaneously such that one DNA molecule is slid over the other DNA molecule. If the local interactions are sufficiently strong (due to a bound protein, for instance), the upper DNA can stick to the lower DNA molecule and tension will build up (Fig. 3a, bottom left

panel). If the molecule can slide without hindrance, no buildup of tension will occur (Fig. 3a, bottom right panel). The two molecules are shown in Fig. 3a with a perpendicular orientation, but in principle any desired angle between the DNA molecules can be achieved by moving bead 3 to the left or right.

The second DNA–DNA configuration that can be used is the half-wrapped configuration (Fig. 3b, top panel). This is particularly suitable for studying protein-mediated inter-DNA bridging, as it ensures a single point where the two DNA molecules touch and provides a potential bridging site. In a typical experiment, the DNA molecules are brought into a half-wrapped configuration, and then incubated in the protein-containing channel of the flow cell. Once they are brought back to the (protein-free) buffer channel, the DNA molecules are unwrapped. If bridging has occurred successfully, the DNA molecules will be held together by the bridge (Fig. 3b, bottom left panel). If no bridge has formed, unwrapping results in two separate DNA molecules (Fig. 3b, bottom right panel). When a bridge is detected, the mechanical properties of this bridge can be probed by applying either a shearing or an unzipping force (Fig. 4). In a shearing geometry (Fig. 4a) a uniform force is applied along all DNA–protein bridges. In a typical experiment, a bead tethered to one DNA molecule is moved parallel to the bridged region, away from the bridge, while a force is measured on the bead that tethers to the other DNA molecule on the opposite side of the bridged region. The results of such an experiment on Alba1-mediated bridges (Fig. 4c) show clear rupture events corresponding to the rupture of protein bridges. The unzipping force, on the other hand, represents the force required to open up or unzip the bridged region from one side (Fig. 4b). This can be measured by moving one of the beads to which one DNA molecule is tethered perpendicular to the bridge, while measuring the force on the bead tethered to the other DNA molecule, but on the same side of the bridged region. As such, the bridged region can be unzipped one protein at a time. An example of the results of such an experiment (Fig. 4d) on Alba1-mediated bridges shows a step-wise release of DNA stretches due to the unzipping of the bridges.

The final DNA configuration of interest is the fully wrapped configuration (Fig. 3c, top panel), which is suitable for scanning-probe experiments [5]. In this case the DNA molecules are fully wrapped around each other and one DNA molecule is used as a scanning probe by sliding along the other DNA molecule. If a roadblock is encountered, tension builds up and the sliding is blocked (Fig. 3c, bottom left panel) until the roadblock dissociates from the DNA and the tension is relieved. If no roadblock is encountered, the wrap will slide along the other DNA molecule (Fig. 3c, bottom right panel). Below we explain in detail how to perform these kinds of dual DNA experiments.

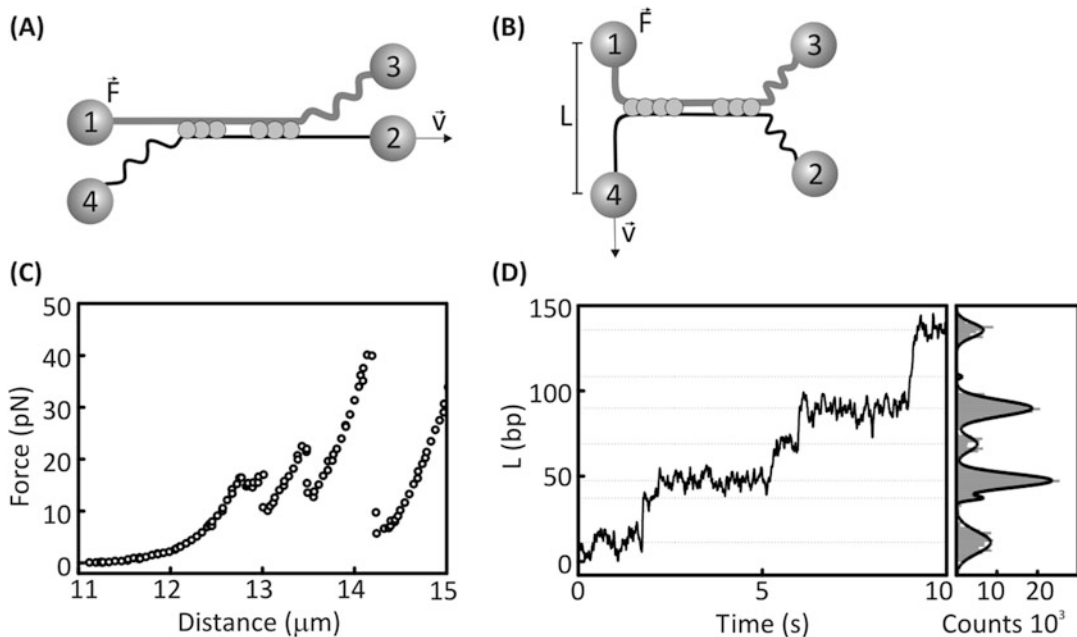


**Fig. 4** Mechanical probing of bridges can be performed by applying either a shearing force (a) or an unzipping force (b). (a) To measure the shearing force, bead 2 is moved with constant velocity in the direction of the DNA (indicated with  $v$ ). This exerts a uniform force along all DNA–protein bridges, which can be measured on bead 1 (indicated with  $F$ ). (b) The unzipping force is the force required in the direction perpendicular to the DNA to unzip the bridges. In this case, bead 4 is moved with constant velocity (indicated with  $v$ ) perpendicular to the DNA and the distance  $L$  and the force on bead 1 (indicated with  $F$ ) are monitored. (c) Measurement of shearing force generated uniformly over Alba1 bridges. The force is measured on bead 1 and rises and relaxes as protein-mediated bridges ruptured. (d) Unzipping experiment where a force up to 50 pN is built up over the first bridge. As bead 4 is moved, the length  $L$  increases in discrete steps. Adapted from [6]

## 2 Materials

### 2.1 Experimental Setup

1. The quadruple-trap optical tweezers setup (see Chapter 9 and Fig. 1a) is based on the following design. A trapping laser (a YLR-20-LP laser with a power of 20 W and a wavelength of 1070 nm, available from IPG laser GmbH) is used to generate four continuous optical traps, while the  $x$ - and  $y$ -positions of each trap within the focal plane are controlled using steerable mirrors (one piezo mirror available from MadCityLabs (MCL) and three stepper-motor mirrors from the Agilis series available from Newport). Force can be detected in two of the four traps: back-focal-plane interferometry of the trapping laser is used to detect the force of one trap that has a polarization orthogonal to the other three traps (trap 1), while interferometry of a spectrally distinct detection laser (with a power of 140 mW and a wavelength of 980 nm, available from Power Technology Inc.), co-aligned with one of the other traps, is used to detect

the force on a second trap (trap 4). Two of the traps (traps 2 and 3) can also be moved in the  $z$ -direction, perpendicular to the focal plane, by “misaligning” a telescope along its optical axis (*see Note 1*). Each of the four traps can be switched on and off by independent shutters.

2. Microfluidic flow cell containing up to six inlet channels (available from LUMICKS B.V.) (*see Note 2*). The flow cell is cleaned with bleach before use (*see Subheading 3.1*) and, depending on the proteins used for the experiments, is passivated (*see Subheadings 3.2–3.4*) to minimize interaction of the proteins interacting with the surfaces of the microfluidic system (*see Note 3*).
3. A flow system (schematically shown in Fig. 2, available from LUMICKS B.V.) based on pressurized air is used to regulate the buffer flow from individual syringes containing buffer solutions. Valves are used to switch the individual flows on and off. Tubing connecting the different components is made of Teflon or silica. The flow cell is mounted on a movable stage: this enables rapid (1–10 s) buffer exchange by moving the optical traps from one buffer flow to the other (Fig. 1).
4. Custom-written LabVIEW software is used to:
  - Create a template of an imaged bead (imaged via an LED with a wide-field camera) in order determine the bead positions and distances through a template-matching algorithm.
  - Perform force calibration using the power spectrum of the measured bead displacements (in our case corresponding to the beads in trap 1 and 4).
  - Perform real-time data acquisition of the bead displacements in the optical traps at a frequency of 50 kHz (force data) and 150 Hz (distance data).
  - Control the  $x$ ,  $y$ , and  $z$ -positions of the traps interfacing with a joystick.

## 2.2 Buffer Solutions

### 2.2.1 Buffer Solutions for Bleach Cleaning Protocol (*see Subheading 3.1*)

- MilliQ water.
- Bleach solution: 0.7 M NaClO (*see Note 4*).
- Sodium thiosulfate solution: 10 mM Na<sub>2</sub>S<sub>2</sub>O<sub>3</sub> (*see Note 5*).

### 2.2.2 Buffer Solutions for Passivation of the Flow Cell Using Casein (*see Subheading 3.2*)

- Blocking Reagent (available from Roche).
- Phosphate buffered Saline (PBS): 10 mM phosphate, 150 mM sodium chloride, pH 7.3–7.5 (available in tablet form from Invitrogen) (*see Note 6*).
- Casein storage buffer: PBS buffer with 10 mM NaN<sub>3</sub> and 1 mM EDTA.

**2.2.3 Buffer Solutions for Passivation of the Flow Cell Using a Lipid Bilayer (see Subheading 3.3)**

- POPC stock solution: 2.5 % solution of 1-Palmitoyl-2-oleoyl-phosphatidylcholine (POPC, available from Avanti Polar Lipids) in methanol.
- POPC buffer: 20 mM Tris (Tris(hydroxymethyl)aminomethane) pH 7.5 and 100 mM NaCl.
- PBS.

**2.2.4 Buffer Solutions for Passivation of the Flow Cell Using BSA with Pluronic® F127 (BASF) (see Subheading 3.4)**

- PBS.
- BSA stock solution: 0.1 % w/v BSA (available from Sigma-Aldrich) in PBS.
- Pluronic® stock solution: 0.5 % w/v Pluronic® F127 (available from Sigma-Aldrich) in PBS.
- MilliQ water.

**2.2.5 Buffer Solutions for Trapping Experiments (see Subheadings 3.5–3.8)**

- PBS.
- Solution containing beads: Typically, streptavidin-coated (see Note 7) polystyrene beads with a diameter in the range of 1–5 µm (available from Spherotech) (see Note 8) are diluted in PBS solution (see Notes 9 and 10).
- DNA solution: A DNA construct is prepared with multiple biotinylated nucleotides on each end of the molecule and diluted to the tens of picomolar range in PBS (see Note 9). Different designs of DNA constructs are possible, depending on the particular experiment (see Notes 11–14) [9].
- Protein solution: The purified proteins of interest are diluted to the desired concentration in an appropriate buffer (see Notes 15 and 16).

### 3 Methods

**3.1 Bleach Cleaning Protocol**

1. Rinse all syringes with milliQ water: fill the syringes with milliQ and subsequently remove the milliQ to leave only 1 mL in each syringe. With the residual water, flush at least 0.5 mL per channel.
2. Remove any residual water and add ~ 0.7 mL of bleach solution to each syringe. Flush this through all channels slowly for 30–60 min until the syringes are nearly empty.
3. Remove any residual solution from the channels and rinse all syringes with milliQ water: fill the syringes with milliQ and subsequently remove the milliQ to leave only 1 mL in each syringe. With the residual water, flush at least 0.5 mL per channel.

4. Remove any residual solution from the syringes, add 1.5 mL of sodium thiosulfate solution, and flush through all channels over a period of 5–10 min.

5. Remove any residual solution from the channels and rinse all syringes with milliQ water: fill the syringes with milliQ and subsequently remove the milliQ to leave only 1 mL in each syringe. With the residual water, flush at least 0.5 mL per channel.

### **3.2 Passivation of the Flow Cell Using Casein**

1. Prepare a casein solution by dissolving the Blocking Reagent at 1 % w/v in casein storage buffer. To sufficiently dissolve the casein, initially mix gently and then sonicate for 30–60 min (*see Note 17*) followed by 5 min of centrifugation at  $16,000 \times g$  (*see Note 18*). After centrifugation, keep only the supernatant and discard the precipitate in the pellet. Store the casein solution at room temperature (*see Note 19*).
2. Dilute the casein solution 5× in PBS.
3. Flush through all channels of the flow cell that are to be passivated (*see Note 20*), switch off the flow (by closing the valves) and leave to stand for at least 30 min.
4. Flush all channels of the flow cell with 0.5 mL of the buffer to be used for the experiments.

### **3.3 Passivation of the Flow Cell Using a Lipid Bilayer**

1. Take 40 μL of POPC stock solution, put it in a 1.5 mL Eppendorf tube and evaporate the methanol in a strong flow of pressurized air (*see Note 21*).
2. Add 250 μL of POPC buffer to the dried POPC and flick strongly in order to resuspend the lipids (*see Note 22*).
3. Sonicate the tube for at least 30 min until the solution is clear again (*see Note 23*).
4. Flush the flow cell with PBS buffer.
5. Make sure there are no bubbles in the flow cell.
6. Introduce 80 μL of the POPC solution into the flow cell through one of the channels, and incubate for 10 min.
7. Repeat **step 6** two times.
8. Flush all channels of the flow cell with 0.5 mL of the buffer to be used for the experiments.

### **3.4 Passivation of the Flow Cell Using BSA with Pluronic®**

1. Flush all channels of the flow cell with 0.5 mL PBS.
2. Remove any residual solution from all syringes.
3. Flush 0.5 mL of the BSA solution through each channel of the flow cell. Then apply a gentle flow for 30 min (*see Note 24*).
4. Remove any residual solution from all syringes.

5. Flush 0.5 mL of the Pluronic® solution through each channel of the flow cell. Then, apply a very slow flow for 30 min.
6. Remove residual solution from the syringes.
7. Fill all syringes with milliQ water. Remove any residual solution, leaving only 0.5 mL in each syringe. Flush this through the flow cell.
8. Flush all channels of the flow cell with 0.5 mL of the buffer to be used for the experiments.

### **3.5 Starting up Experiments**

1. Make sure all shutters (for the four traps and the detection laser) are blocking the laser beams.
2. Flush ~0.5 mL buffer through each channel of the flow cell (*see Note 25*).
3. Place immersion water/oil on the objective and condenser of the microscope as required (*see Note 26*). Using the back-focal plane camera, ensure that there are no air bubbles in the oil/water.
4. Adjust the objective height in order to focus in the middle of the flow cell (*see Note 27*).
5. Open the shutters of all four traps and the detection laser.
6. Insert beads solution into channel (i), DNA solution into channel (ii) and protein solution into channel (iv) (and if required, also in channels (v) and (vi) if using a 6-channel flow cell) (Fig. 1a). The remaining channels (usually channel (iii)) are filled with a buffer solution in which the experiment is to be performed (*see Notes 9 and 16*).
7. Open the valves (Fig. 2) and apply pressure to generate fluid flows in the channels with the beads, proteins and buffer.
8. Move the traps to the channel with the beads, catch four beads (*see Note 28*) and then move to the buffer channel.
9. Switch off all flow and calibrate the traps by fitting the power spectrum of the Brownian motion of the beads in trap 1 and 4 (*see Notes 29 and 30*).
10. Set the horizontal distance between bead pairs to at least 20 µm (*see Note 31*).
11. Reset the forces in both traps to 0 pN.
12. Check that the flow that can be generated in each channel is equal (*see Note 32*).
13. Move the traps to the channel with the DNA, open the flow and catch two DNA molecules. To catch the first DNA molecule, slowly approach bead 2 to a bead-to-bead distance of approximately 5 µm and then increase the bead-to-bead distance again to the initial position. As soon as a force is detected

on the corresponding bead (bead 1 or 4) upon bead separation (*see Note 33*), set the distance to 16  $\mu\text{m}$  and repeat this procedure for bead 3. Now, DNA has been tethered between both bead pairs.

14. Move the DNA-bead assemblies to the buffer channel and switch off all flows.
15. Test whether there is a single DNA molecule tethered between each bead pair. To do so, record for each bead pair the force-extension curves of the DNA molecule by setting the bead-to-bead distance 5  $\mu\text{m}$  and then slowly extending the DNA molecule while recording the force. The force-extension curve should look similar to force-extension curves previously described [3], with a steep force increase at the DNA contour length (16  $\mu\text{m}$  for  $\lambda$  DNA) and an overstretching plateau at 65 pN (*see Note 34*).

### **3.6 Performing a Quadruple-trap dual DNA Experiment in Crossed Configuration**

1. Catch four beads as explained in Subheading 3.5, steps 5–7.
2. Position the beads at the desired positions in the flow cell as shown in Fig. 5a (*see Note 35*).
3. Calibrate and reset the forces as described in Subheading 3.5, steps 8 and 10.
4. Switch the flow on and move to the DNA channel.
5. Catch two single DNA molecules as described in Subheading 3.5, steps 12–14.
6. Configure the DNA as shown in Fig. 6a by moving traps 3 and 4 upwards (or downwards) in the  $z$ -direction, moving bead 3 to a crossed configuration and lowering beads 3 and 4 back to the original position (*see Notes 36 and 37*).
7. If a friction study in the presence of protein is to be performed (*see Note 38*), move the DNA construct to the channel with protein. If desired, the construct can be moved back to the buffer channel after a given incubation time.
8. Slide one DNA molecule along the other in the direction indicated in Fig. 3a. Use the force on bead 1 as readout for the friction.

### **3.7 Performing a Quadruple-Trap Dual DNA Experiment in Half-Wrapped Configuration**

1. Catch four beads as explained in Subheading 3.5, steps 5–7.
2. Position the beads at the desired positions in the flow cell as shown in Fig. 5b (*see Note 35*).
3. Calibrate the beads and catch DNA as described in Subheading 3.6, steps 3–5.
4. Configure the DNA as shown in Fig. 6b (*see Notes 39 and 40*) by moving trap 3 and 4 downwards in the  $z$ -direction and moving bead 2 over the other DNA molecule. Next, move beads 3 and 4 upwards in the  $z$ -direction until they are well

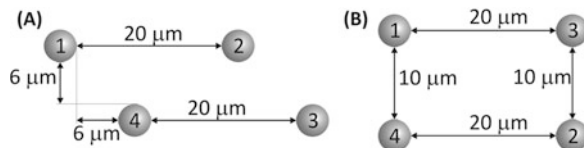


**Fig. 5** Schematic (to scale) showing optimal bead positions during DNA catching for experiments in (a) crossed and (b) wrapped configuration. The force-detection beads (bead 1 and bead 4) should ideally not be moved after force calibration is done because the force calibration and force offsets may vary when these are moved. Therefore, these beads are directly positioned in their final locations. Furthermore, the bead-to-bead distance initially should be large enough to prevent unwanted tethering of DNA to the beads. Therefore, a distance above the contour length of the DNA molecule is advised. For lambda DNA, for instance, a bead-to-bead distance around 20 μm is typically used. For half-wrapped and fully wrapped DNA configurations the initial bead positions are identical. Indicated distances are measured from the bead edge to the other bead edge (so they are independent of bead diameter)

above the other 2 beads. Then move bead 2 back to its original position and consequently move beads 3 and 4 upwards to their original  $z$ -position (see Notes 37, 41 and 42).

5. Move the DNA constructs to the protein channel. If desired, the constructs can be moved back to the buffer channel after a given incubation time.
6. Detect possible bridging by moving bead 3 slightly to the right. If a force increase is detected on bead 1 and bead 4, a bridge has been formed. If a force change is only detected on bead 4, no bridge is present.
7. If a bridge has formed, measure the shearing and/or unzipping forces by moving bead 2 and/or bead 4 in the directions indicated in Fig. 4 (see Notes 43 and 44).

### 3.8 Performing a Quadruple-Trap Dual DNA Experiment in Fully Wrapped Configuration

1. Repeat steps 1–6 as described in Subheading 3.7 to obtain a half-wrapped DNA configuration.
2. Wrap the DNA further to a fully wrapped configuration as shown in Fig. 6c by moving bead 3 and 4 upwards (in the  $z$ -direction) and moving bead 2 below the other DNA molecule. Then lower beads 3 and 4 to their original positions (see Note 37) and position beads 3 and 4 to their final positions, 10 μm to the right of beads 1 and 4 as indicated in panel (vii) of Fig. 6c (see Note 45).
3. To perform a scanning-probe experiment, move beads 2 and 4 as indicated in Fig. 3c. Use the force as readout; a sudden increase in force shows that a roadblock is encountered (Fig. 3c, bottom left panel). If no roadblock is detected, the wrap will slide along the DNA (Fig. 3c, bottom right panel).

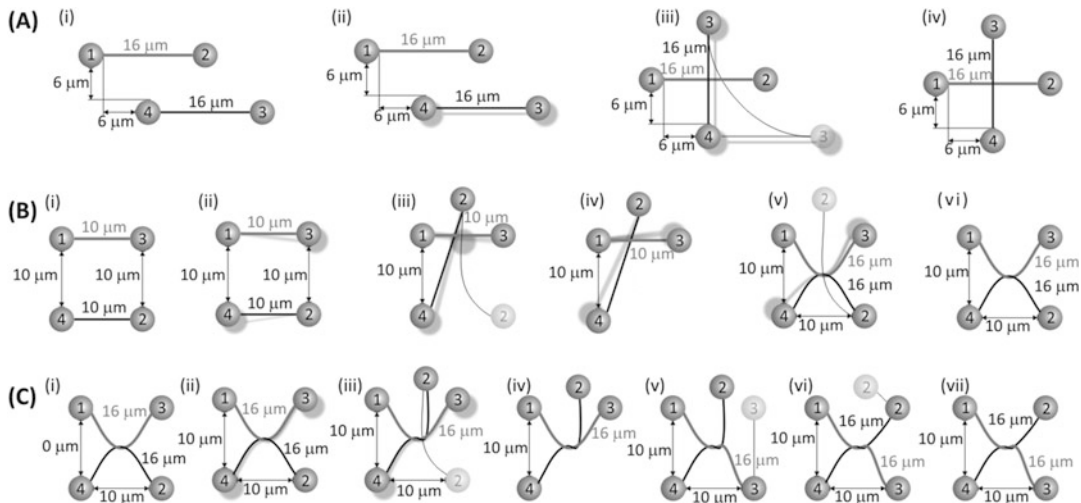


**Fig. 6** Schematics (to scale) showing how (a) crossed and (b) wrapped DNA configurations are generated. (a) To obtain a crossed DNA configuration with the DNA stretched to its contour length (16 μm for  $\lambda$  DNA) the following steps are taken: (i) Both DNA molecules are stretched to their contour lengths and (ii) the molecule between traps 3 and 4 is moved upwards (in the z-direction) to allow (iii) bead 3 to pass over the other DNA molecule. Finally, (iv) the DNA molecule between traps 3 and 4 is lowered again to its original height. (b) To achieve a half-wrapped DNA configuration with DNA stretched to its contour length (16 μm for  $\lambda$  DNA), take the following steps: (i) Position the beads in a square with 10 μm length of each side. (ii) move beads 3 and 4 upwards (in the z-direction) and (iii) move bead 2 such that it passes over the grey DNA molecule. (iv) Then lower beads 3 and 4 until they are well below the focal plane, and (v) move bead 2 back to its original position. Finally, (vi) move beads 3 and 4 back to their original z-positions. (c) To achieve a fully wrapped DNA configuration, (i) start with the half-wrapped configuration as described in (b). (ii) Move beads 3 and 4 upwards (in the z-direction) to allow (iii) bead 2 to pass below the black DNA molecule. Then (iv) lower beads 3 and 4 (in the z-direction) until all four beads are in the focal plane. Then move (v) bead 3 and (vi) bead 4 to their final positions

#### 4 Notes

1. In our particular implementation, trap 2 is controlled using a piezo mirror, which supports absolute positioning of this trap. Traps 1, 3, and 4 are controlled using stepper-motor mirrors which do not support absolute positioning but have a very large range over which the traps can be moved.
2. Other (noncommercial) options could include a flow cell design consisting of a glass slide, a Parafilm layer and a coverslip [5].
3. Many proteins have the tendency to bind to the glass flow cell or the tubing connecting this to the syringes. Equilibration of a protein solution with the microfluidic surfaces can take up to 24 h [10], which means that protein concentration depletion or leakage of previously used proteins into solution can occur on a

timescale greatly exceeding a typical experiment. To reduce this effect, surface passivation can be used. Typical passivation agents include casein, BSA or lipid bilayers (*see* Subheadings 3.2–3.4). Typically, trial and error is used to determine which surface passivation gives the best results for each protein of interest. Keep in mind that the lipid bilayer only works for glass and silica surfaces. If the tubing used is made of a plastic, this should then be passivated separately by casein or BSA-Pluronic passivation.

4. Bleach will efficiently degrade biological materials with hydrophilic degraded products, facilitating cleaning of the syringes, tubing and flow cell.
5. Sodium thiosulfate effectively destroys any residual bleach.
6. For long-term storage of either PBS solution or protein buffer, it is advised to add 1 mM of EDTA and 10 mM NaN<sub>3</sub> to prevent bacterial growths in the buffer solutions.
7. In principle, other DNA-bead attachment schemes such as anti-digoxigenin-coated beads in combination with digoxigenin-labeled DNA constructs are also possible.
8. When choosing the appropriate bead diameter, one important consideration is that smaller beads afford a higher force resolution after filtering [11]. On the other hand lower laser power is required to trap larger beads [12], reducing possible DNA damage caused by the trapping laser. In addition, larger beads ensure a spatial separation between the (diffraction-limited) focus of the trapping laser beam and the DNA–protein complex of interest.
9. In principle, any buffer with a pH of 7.0–8.0 and a monovalent salt (NaCl or KCl) at a concentration of 25–200 mM is suitable. Typically, a good buffer to use for the DNA and beads dilutions is PBS. At higher salt concentrations, the efficiency of tethering a DNA molecule is higher. The DNA concentration has to be adjusted accordingly.
10. The exact concentration of beads needs to be determined experimentally. As a rough guideline: for particles with a diameter of 2 µm a 1000× dilution of a stock solution of 1 % w/v of polystyrene is used (i.e., a concentration of 0.4 fM) and for particles with a diameter of 4.5 µm a 100× dilution of a stock solution of 0.5 % w/v is used (i.e., a concentration of 2 fM). In the rest of the methods and schematics a bead diameter of 4.5 µm is assumed.
11. The main disadvantage of using biotins on both ends of the DNA molecule to link it to the beads is that the orientation of the tethered DNA molecule remains unknown. This problem is especially apparent when studying sequence-dependent DNA–protein interactions. Possible ways to overcome this

issue would be to use different labels on each end of the DNA molecule: for instance, one end of the DNA could be attached to the bead via biotin-streptavidin linkages while the other end could be linked via digoxigenin-anti-digoxigenin interactions.

12. If the biotin labels on each end of the DNA molecule are on the same strand, the other strand can be melted off *in situ* using force-induced melting [9], thus generating single-stranded DNA.
13. Most constructs we use are based on the 48.5 kb  $\lambda$ -phage DNA or the 8.5 kb pKYB-I DNA because these are commercially available and are sufficiently long to efficiently catch the molecules by flow stretching. In the rest of the methods and schematics it is assumed that a 48.5 kb  $\lambda$ -DNA construct is used.
14. Besides DNA constructs that consist of either torsionally unconstrained double- or single-stranded DNA, other constructs are also possible, such as molecules that are partially single- and partially double stranded or constructs that are torsionally constrained [9].
15. The minimum volume of protein solution needed for a typical experiment is around 500  $\mu$ L.
16. Often, the buffer in which the experiments are performed will be the same as in which the protein is diluted but in principle, a different buffer can be used.
17. The casein solution will appear opaque because it contains micelles.
18. Centrifugation is necessary to remove larger particles and aggregates. This cannot be done by filtering, because the blocking agent casein will efficiently clog the filter pores.
19. Casein can be stored for months at room temperature if stored in the presence of 1 mM of EDTA and 10 mM  $\text{NaN}_3$ . The quality is most easily checked by the smell. If it starts to smell like cheese, discard the solution.
20. Because air bubbles tend to stick to the casein on the surface of the flow cell, it is advantageous to passivate only the channels of the flow cell which are exposed to proteins.
21. It should take several minutes to evaporate the methanol.
22. After resuspension, the mixture should be opaque.
23. Make sure to place the tube in the sonicator in a place where the water level is strongly agitated.
24. Make sure there are no bubbles in the flow cell during the passivation steps.
25. Use the appropriate buffer for each channel. For the beads channel, use the buffer that the beads are diluted in, for the DNA channel, use the buffer that the DNA is diluted in, etc.

26. In our system, we use a water-immersion objective and an oil-immersion condenser, so water is used for the objective–flow cell interface and oil for the condenser–flow cell interface.
27. This is most easily done by focusing first on the edge of the lower fluid–glass interface and then moving the objective up by 50 µm (the height of the fluid layer in our flow cell is 100 µm).
28. The four trapped beads should look very similar. If one or more beads do not appear homogeneous, there is most likely a piece of dirt from one of the buffer solutions stuck on the bead. If one or more look significantly bigger, there might be multiple beads in that particular trap. Also, some of the beads in the bead sample might be of a different size. In all of these cases, discard those beads and catch new beads, until four homogeneous beads with similar diameters are in the traps.
29. Here, the power spectrum of the Brownian motion of a trapped bead is used for force calibration. Recently, a method has been developed to calibrate the forces using momentum transfer [13]. In principle, this method could be implemented in the current system. This would be advantageous because it does not require *a priori* knowledge of the size and shape of the trapped particle. In addition, it would allow for force detection in three dimensions while the power spectrum motion method only allows for calibration of the forces in *x*, and *y*-directions.
30. Before starting the power spectrum calibration, make sure that both the trapping laser and the detection laser have been switched on sufficiently long to have stable power outputs.
31. This large distance prevents unintentional and uncontrolled tethering of DNA between the bead pairs.
32. If the force increases are not approximately equal for all channels, there is either a blockage in one of the channels or an air bubble in the tubing or the flow cell. By visual inspection of the flow cell, one can determine if or where such bubbles exist. If this is the case, they can be removed either by flushing the buffer solution briefly at a high pressure or by sucking the bubbles out from the exit channel with a syringe while all inlet channels are open. If no bubbles are visible but one of the channels is still not flowing as much as the others, there is most likely a blockage in one of the tubes. Here, it is advisable to disconnect the tubing, trim its end (where blockages are most likely to occur) and reconnect.
33. The rationale behind these “approach and retraction” cycles is that DNA will spontaneously attach to the beads and, with the buffer flow, extend in the direction of the flow. By approaching and retracting the second bead, one can “fish” the other end of the flow-stretched DNA and form a stable tether.

34. If the force rises at a distance below the contour length of the DNA molecule and the overstretching plateau is at forces much higher than 65 pN, there are most likely multiple DNA molecules tethered, in which case the options are either to wait (at a relatively high tension) for the additional molecules to break or to discard the bead pair and start the catching procedure again.
35. These configurations are designed based on the following considerations: (1) only traps 3 and 4 can move in the *z*-direction; (2) the *x*- and *y*-positions of the force detection beads (traps 1 and 4) do not change during wrapping or crossing because that would require a new force calibration.
36. The distances indicated in Fig. 6 are chosen such, that at the final configuration (Fig. 6a (iv), 6b (vi) and 6c (vii)) the DNA molecules are at their contour length. In principle, these configurations can be achieved at other DNA extensions as well. One has to keep in mind that, at end-to-end lengths well below the DNA contour length, the DNA will be quite floppy and thus the exact molecular configuration might be less well defined. At much larger end-to-end lengths, there is the risk that during wrapping or crossing, when beads 3 and 4 are moved in the *z*-dimension, the absolute force on the DNA (including the *z*-component of the force) might be so large, that the DNA structure changes due to the overstretching transition. In this case, it can no longer be assumed that an interaction between two purely double-stranded DNA molecules is studied.
37. To determine whether the beads are in the same plane, look closely at their diffraction rings. These should be identical to those of the other traps (traps 1 and 2) when the *z*-positions are the same. Alternatively, one could use the template matching score provided by the bead tracking algorithm to determine the correct *z*-position of these beads.
38. In principle, the crossed configuration is also suitable for studying DNA–protein bridging. The reason why the half-wrapped configuration is suggested for bridging experiments, is that in the crossed configuration it is difficult to directly control whether the DNA molecules are in contact in the *z*-direction, as there is no bead tracking in this dimension. In a wrapped configuration, it is certain that the DNA molecules are in contact at the wrapping point. If the crossed configuration is to be used for a bridging assay, the easiest way to see whether the DNA is in contact is, after crossing, to keep moving bead 3 and 4 down until a force increase is detected on bead 1. Then the DNA molecules are definitely in contact.

39. These steps will generate a right-handed DNA wrap. If a left-handed wrap is desired, reverse the direction of motion of beads 3 and 4 in the *z*-dimension.
40. A possible improvement to the current system could be to automate the wrapping process. When DNA wraps consisting of multiple turns are desired, this can significantly speed up the experiments.
41. Another possible improvement of the system could be to implement both force detection [13] and bead tracking [14] in the *z*-direction. Currently, only force detection and bead tracking in *x*- and *y*-directions are possible.
42. After wrapping one DNA around the other, check whether the DNA molecules are successfully wrapped by slightly moving bead 2 to the right. A resulting force change should be detectable in both traps 1 and 4.
43. Keep in mind that moving beads 1 and 4 will change their respective force calibrations or force offsets.
44. In principle, the most accurate way of measuring both the shearing and unzipping forces is by moving bead 2 (because that trap supports absolute positioning) and detecting the force on bead 1 (that trap has a unique polarization for force detection giving the highest force resolution). In that case, the positions of bead 2 and 4 have to be exchanged (with respect to the positions shown in Fig. 4b) after DNA catching.
45. For DNA wraps consisting of n turns, repeat these steps n times.

## References

1. Heller I, Hoekstra TP, King GA et al (2014) Optical tweezers analysis of DNA–protein complexes. *Chem Rev* 114:3087–3119
2. Chu S (1991) Laser manipulation of atoms and particles. *Science* 253:861–866
3. Smith SB, Cui Y, Bustamante C (1996) B-DNA : the elastic response of overstretching individual double-stranded and single-stranded. *Science* 271:795–799
4. Candelli A, Wuite GJL, Peterman EJG (2011) Combining optical trapping, fluorescence microscopy and micro-fluidics for single molecule studies of DNA-protein interactions. *Phys Chem Chem Phys* 13:7263–7272
5. Noom MC, van den Broek B, van Mameren J et al (2007) Visualizing single DNA-bound proteins using DNA as a scanning probe. *Nat Methods* 4:1031–1036
6. Laurens N, Driessens RPC, Heller I et al (2012) Alba shapes the archaeal genome using a delicate balance of bridging and stiffening the DNA. *Nat Commun* 3:1328
7. Dame RT, Noom MC, Wuite GJL (2006) Bacterial chromatin organization by H-NS protein unravelled using dual DNA manipulation. *Nature* 444:387–390
8. Ishijima A, Kojima H, Funatsu T et al (1998) Simultaneous observation of individual ATPase and mechanical events by a single myosin molecule during interaction with actin. *Cell* 92:161–171
9. Candelli A, Hoekstra TP, Farge G et al (2013) A toolbox for generating single-stranded DNA in optical tweezers experiments. *Biopolymers* 99:611–620
10. Biebricher AS, Heller I, Roijmans RFH et al (2015) The impact of DNA intercalators on DNA and DNA-processing enzymes elucidated through force-dependent binding kinetics. *Nat Commun* 6:7304

11. Moffitt JR, Chemla YR, Smith SB et al (2008) Recent advances in optical tweezers. *Annu Rev Biochem* 77:205–228
12. Gittes F, Schmidt CF (1998) Signals and noise in micromechanical measurements. *Methods Cell Biol* 55:129–156
13. Thalhammer G, Obmascher L, Ritsch-Marte M (2015) Direct measurement of axial optical forces. *Opt Express* 23:6112
14. Gosse C, Croquette V (2002) Magnetic tweezers: micromanipulation and force measurement at the molecular level. *Biophys J* 82:3314–3329
15. Gross P (2011) The DNA double helix challenged by force, PhD dissertation

# Chapter 11

## Probing Single Helicase Dynamics on Long Nucleic Acids Through Fluorescence-Force Measurement

Chang-Ting Lin and Taekjip Ha

### Abstract

Helicases are nucleic acid-dependent ATPases which can bind and remodel nucleic acids, protein–nucleic acid complexes, or both. They are involved in almost every step in cells related to nucleic acid metabolisms, including DNA replication and repair, transcription, RNA maturation and splicing, and nuclear export processes. Using single-molecule fluorescence-force spectroscopy, we have previously directly observed helicase translocation on long single-stranded DNA and revealed that two monomers of UvrD helicase are required for the initiation of unwinding function. Here, we present the details of fluorescence-force spectroscopy instrumentation, calibration, and activity assays in detail for observing the biochemical activities of helicases in real time and revealing how mechanical forces are involved in protein–nucleic acid interaction. These single-molecule approaches are generally applicable to many other protein–nucleic acid systems.

**Key words** Single-molecule, TIRF, Optical tweezers, Fluorescence localization, Helicase, UvrD, NS3, Translocation, Unwinding

---

### 1 Introduction

In the past decade, many techniques were developed in the single-molecule field that enable us to directly observe the dynamics of nucleic acids and protein and interactions in real time [1–3]. In particular, single-molecule fluorescence and optical tweezers are the two approaches that have been most widely used [4–10]. In contrast to conventional ensemble methods, single-molecule methods provide an opportunity to explore the heterogeneity among molecules, revealing transitions and different modes of molecular dynamics which are otherwise hidden in ensemble measurements [11–13].

Helicases bind to either single-stranded or double-stranded nucleic acids or both, and remodel their substrates with or without other bound proteins [14–16], thereby contributing to essentially every nucleic acid metabolism process [17, 18]. The two major activities of helicases that are powered by ATPase activity are

translocation and unwinding, which were generally studied at biochemical, structural and genetic levels [14, 19–23]. But more recently, single-molecule measurement tools have become powerful enough to reveal such activities. However, limitations of experimental approaches restricted full characterization of helicase activities. Here, we have applied a hybrid platform of single-molecule fluorescence localization combined with optical tweezers under total internal reflection fluorescence (TIRF) configuration to reveal helicase translocation and unwinding in real time [24, 25]. This approach allowed us to directly image single helicase translocation on ssDNA [24], show that a UvrD monomer is stalled at ss/dsDNA junctions until the arrival of a second monomer activates unwinding [24], and image a new mode of translocation for NS3 helicase [25].

In this chapter, we describe detailed procedures for the building and calibration of instrumentation and experimental assays mentioned above, including the materials and steps for sample preparation, data acquisition and analysis [26]. This instrument can also be applied to detect nucleic acid-protein interactions of proteins other than helicases, such as simple diffusion, target searching, and complex formation [27].

## 2 Materials

### 2.1 Single/Double-Stranded DNA Preparation

1. ssDNA template (5'-AGG AGA AAA AGA AAA AAA GAA AAG AAG G-3').
2. Primer (5'-Biotin-TCT CCT CCT TCT-3').
3. T4 DNA ligase (NEB).
4. 25 μM dTTP.
5. 25 μM dCTP.
6. 2 % BSA (NEB).
7. Phi29 DNA polymerase (NEB).
8. Digoxigenin-11-ddUTP (Roche).
9. Antidigoxigenin-coated beads (*see* Subheading 3.2).
10. 4957 bp double-stranded DNA (*see* Subheading 3.1).
11. Bacteriophage λ DNA (NEB).
12. Terminal transferase (NEB).
13. T7 exonuclease (NEB).

### 2.2 Coating Polystyrene Bead with Anti-digoxigenin Antibodies

1. Protein G-coated polystyrene beads (Spherotech, 880 nm in diameter).
2. MES (2-(*N*-morpholino) ethanesulfonic acid, Sigma-Aldrich).
3. EDC (*N*-(3-Dimethylaminopropyl)-*N'*-ethylcarbodiimide hydrochloride, Sigma-Aldrich).

4. NHS (*N*-Hydroxysuccinimide, Sigma-Aldrich).
5. Anti-digoxigenin (Roche).
6. MES buffer (100 mM MES. Adjust pH to 6.5 with 5 M NaOH, *see Note 1*).
7. Reconstitution buffer (0.019 M NaH<sub>2</sub>PO<sub>4</sub>, 0.081 M Na<sub>2</sub>HPO<sub>4</sub>, 0.14 M NaCl, 2.7 mM KCl).
8. Bead storage buffer (0.039 M NaH<sub>2</sub>PO<sub>4</sub>, 0.061 M Na<sub>2</sub>HPO<sub>4</sub>, 0.14 M NaCl, 2.7 mM KCl, 0.1 mg/mL BSA, 0.1 % (v/v) Tween 20, 0.02 % (w/v) sodium azide).
9. Termination buffer (1 M Tris-HCl, pH 6.8).

### **2.3 Polymer-Passivated Surface Preparation**

1. Cover glass (white borosilicate, VWR).
2. Glass slide (Erie Scientific).
3. Aminosilane (*N*-(2-Aminoethyl)-3-Aminopropyltrimethoxysilane, United Chemical).
4. 10 % Alconox.
5. Acetone ( $\geq$ 99.7 %, VWR).
6. 1 M/3 M/5 M KOH.
7. MeOH ( $\geq$ 99.7 %, VWR).
8. Biotin-PEG-Succinimidyl Valerate (Laysan Bio).
9. mPEG-Succinimidyl Valerate (Laysan Bio).
10. Acetic acid ( $\geq$ 99.7 %, Fisher Chemical).
11. 0.1 M sodium bicarbonate buffer (*see Note 2*).
12. Polypropylene (PP, Bel-Art, Scienceware<sup>®</sup>) slide holder.
13. Hexane (Fisher Chemical).
14. Dichlorodimethylsilane (DDS, >99.5 %, Aldrich).

### **2.4 Imaging Buffer Preparation**

1. T50 buffer (10 mM Tris-HCl, 50 mM NaCl, pH 8.0).
2. 0.8 % (w/v) D-glucose.
3. 1 mg/mL (165 U/mL) glucose oxidase (*see Subheading 3.4*).
4. 0.04 mg/mL (2170 U/mL) catalase (*see Subheading 3.4*).
5. 3 mM Trolox ( $\pm$ -6-Hydroxy-2,5,7,8-tetramethylchromane-2-carboxylic acid, adjust to pH 8.0) (*see Subheading 3.4*).
6. 5 mM MgCl<sub>2</sub>.
7. 1 M DTT.
8. 100 mM ATP.
9. 10× BSA.
10. 20 mM Tris-HCl (pH 8.0).
11. 2 % (v/v) glycerol.

**2.5 TIRF-Optical****Tweezers****Instrumentation,  
Alignment, and  
Calibration**

1. Inverted Microscope (IX71, Olympus).
2. XYZ piezo-nanostage (Mad City Labs).
3. Manual stage with 2  $\mu\text{m}$  for the  $XY$  axis (KM3, Sermprex).
4. 1064 nm Nd-YAG laser (Spectra Physics).
5. 532 nm diode-pumped solid-state laser (Spectra Physics).
6. Objective (UPlanSApo100 $\times$ , Olympus).
7. EMCCD camera (iXon, Andor).
8. QPD (Pacific Sensors).
9. Immersion oil Type F (Olympus).
10. Slide chambers (*see* Subheading 3.6).
11. Protein G coated polystyrene beads (Spherotech).
12. 10 $\times$  BSA (NEB).
13. FluoSpheres<sup>®</sup> carboxylate modified microsphere (200 nm in diameter, fluorescent (625/645), Invitrogen).
14. 20 pM Cy3 labeled DNA oligo.

**2.6 Sample Preparation for TIRF-Optical Tweezers Assay**

1. PEG passivated slides (cover glass and glass slide).
2. Double-sided tape (3 M).
3. Epoxy (All-spec).
4. T50 buffer (10 mM Tris-HCl, 50 mM NaCl, pH 8.0).
5. 10 $\times$  BSA (NEB).
6. 0.2 mg/mL neutravidin (Thermo Fisher Scientific).
7. DNA construct.
8. Large orifice tip (VWR).
9. Coated anti-digoxigenin bead.
10. Imaging buffer (*see* Subheading 3.4).

**2.7 Data Acquisition and Analysis**

- TIRF-Optical tweezers control and data analysis software (programmed in-house using Microsoft Visual C++ and MathWorks MATLAB).

**3 Methods****3.1 Single/Double-Stranded DNA Preparation**

*The following steps refine the synthesis and purification of secondary-structure free single-stranded DNA*

Long single-stranded DNA (ssDNA) molecules without secondary structures are synthesized following the method reported previously [27, 28].

1. 0.2  $\mu$ M ssDNA template is annealed to 0.2  $\mu$ M primer at 70 °C for 2.5 min and then slowly cooled to room temperature (*see Note 3*).
2. 600 U of T4 DNA ligase are then added to ligate the nick at 16 °C for 5 h to form covalently closed circular ssDNA templates.
3. Incubate 50 nM closed circular ssDNA template, 25  $\mu$ M each of dTTP and dCTP, 2 % BSA, and 5 U phi29 DNA polymerase together with 1× phi29 DNA polymerase buffer for 12 min (*see Note 4*).
4. After the replication process, 2.5  $\mu$ M digoxigenin-11-ddUTP (Roche) is added to quench the reaction and label the 3'-end of the ssDNA product with digoxigenin.

*The following steps refine the synthesis of partial duplex DNA substrate*

5. 4957 bp dsDNA constructs are synthesized from the sequence (19,360, 24,316) of bacteriophage  $\lambda$  DNA by PCR reaction with one biotinylated primer and one regular primer [[24](#)].
6. Terminal transferase and digoxigenin-11-ddUTP are added with purified PCR products to attach digoxigenin at 3'-end.
7. Immobilize the 5-kbp dsDNA (4957 bp + 1 nt) onto the cover glass via neutravidin and biotin interaction, 10 min.
8. T7 exonuclease is incubated with dsDNA constructs in the chamber (*see Note 5*).
9. A partial duplex with long 3'-ssDNA tail constructs are generated when the reaction has been quenched (*see Note 6*).

### **3.2 Coating Polystyrene Bead with Anti-digoxigenin Antibodies**

Here, 880 nm diameter (Spherotech) protein G coated polystyrene beads are chosen and are coated with anti-digoxigenin in our experiments (*see Note 7*). The following protocol describes the coating of protein G polystyrene beads with anti-digoxigenin [[29](#)].

1. Resuspend the solution of protein G coated beads.
2. Transfer 250  $\mu$ L of beads into a fresh made MES buffer. Rinse beads with centrifugation and resuspend in MES buffer for three times. Final volume of the bead solution resuspended in MES buffer should be 175  $\mu$ L.
3. Dissolve 50 mg EDC in 1 mL MES buffer. Add 50  $\mu$ L of EDC solution to the bead solution.
4. Dissolve 50 mg NHS in 1 mL MES buffer. Add 25  $\mu$ L of NHS solution to the bead solution.
5. Sonicate briefly for several seconds, and tumble the tube for 30 min at RT.
6. Dissolve 200  $\mu$ g of anti-digoxigenin in 200  $\mu$ L of the reconstitution buffer. Add 30  $\mu$ L of the anti-digoxigenin solution into the tube.

7. Tumble the tube for 2 h at RT.
8. Add 15  $\mu$ L of the termination buffer to stop the crosslinking reaction.
9. Tumble for 30 min.
10. Transfer beads into the bead storage buffer three times with centrifugation.
11. Store at 4 °C.

### 3.3 Polymer-Passivated Surface Preparation

To prevent nonspecific adsorption of proteins, a layer of polyethyleneglycol (PEG) coats the cover glass and glass slide. The following is the general protocol of PEGylation [30] (*see Note 8*).

1. Two holes are manually drilled per sample channel (inlet and outlet), and the numbers of holes will depend on one's application (*see Note 9*).
2. Pre-warm the aminosilane solution from -20 °C freezer by keeping it in the dark for a few hours at room temperature (RT).
3. Scrub the slides with 10 % Alconox and rinse with distilled water. Make sure that there is no visible residue on the slides.
4. Microwave slides in water for 10 min.
5. Put the slides and new coverslips in separate containers.
6. Pour acetone in the containers and sonicate for 30 min.
7. In the meantime, sonicate a separate flask with 1 M KOH for 10 min. Then rinse with water, pour in MeOH, and sonicate for 20 min.
8. Rinse the containers with the slides and coverslips with water.
9. In the meantime, rinse the flask with MeOH three times when the sonication is done. The flask should be air-dried with nitrogen and sealed with Parafilm.
10. Burn the slides and coverslips with a propane torch and put them back into dried containers (*see Note 10*).
11. Pour 3 M KOH in the slide and coverslip containers and sonicate for 20 min.
12. Rinse with water three times.
13. Rinse with MeOH twice and sonicate the containers with MeOH for 5 min.
14. Pre-warm biotin-PEG and mPEG powders from -20 °C freezer, and keep it in the dark at RT before use.
15. Remove the seal from the flask. Then pour 150 mL MeOH, 7.5 mL acetic acid and 1.5 mL aminosilane into the flask. Quickly mix well.
16. Remove MeOH from the containers and pour the solution from the flask into the containers.

17. Incubate for 10 min on bench top. Sonicate for 1 min, and incubate for another 10 min. In the meantime, dehydrate and seal the aminosilane bottle, and store it back at  $-20^{\circ}\text{C}$  freezer.
18. Remove the solution in the containers and rinse with clean MeOH at least twice or until there is no acetic acid smell.
19. Air-dry coverslips, glass slides and the containers with nitrogen and cover the lids of the containers.
20. Prepare sodium bicarbonate buffer (84 mg of sodium bicarbonate in 10 mL of water).
21. Dissolve 2 mg biotin-PEG and 100 mg mPEG into 400  $\mu\text{L}$  of sodium bicarbonate buffer. The total amount of PEG solution can be scaled up while the ratio is maintained, 80  $\mu\text{L}$  of PEG solution is required per slide.
22. Mix it gently by pipetting, and then centrifuge 2 min at  $10,000 \times g$ .
23. Prepare moisture boxes in which slide can be incubated. Place slides in the box, put 80  $\mu\text{L}$  of the PEG solution on top of the slide, and then sandwich the solution with a coverslip.
24. In the meantime, dehydrate and seal the PEG bottles, then store them back at  $-20^{\circ}\text{C}$ . Clean the containers and the flask.
25. Incubate for at least 5 h and no longer than 12 h to avoid drying out PEG solution.
26. After incubation with PEG solution, clean the PEGylated coverslips and slides with water and air-dry them. Store sets of sample chambers individually in 50 mL tube with a hole at the end; a single set of sample chamber includes one coverslip and one slide.
27. Vacuum seal tubes in food saver bags and store them at  $-20^{\circ}\text{C}$  freezer.

*The following is the new surface passivation protocol*

Recently, our lab developed a new single-molecule surface passivation protocol, dichlorodimethylsilane (DDS) coated surface, which provides better ability of reducing nonspecific protein binding to the passivate surface [31]. Basically, the cleaning steps are the same as the previous method.

1. Sonicate the coverslips and slides with 1 M KOH for an hour. Then burn the coverslips and slides briefly.
2. Rinse the slides and coverslips with acetone once. Then sonicate in acetone for 20 min.
3. Rinse the slides and coverslips with methanol once. Then sonicate in methanol for 20 min.
4. Sonicate the slides and coverslips in 5 M KOH for an hour. Then air-dry coverslips and slides with nitrogen.

5. Clean a polypropylene slide holder by rinsing and sonicating with hexane three times. Keep the PP slide holder away from contamination.
6. Air-dry the PP slide holder and place coverslips and slides in the holder.
7. Rinse coverslips and slides with hexane twice.
8. Add 75 mL hexane and ~50  $\mu$ L DDS through 1 mL syringe with needle (*see Note 11*).
9. Seal the holder tight immediately. Gently shake the holder at RT for one and half hours.
10. After the incubation, rinse and sonicate the coverslips and slides with hexane for one min. Repeat this step three times.
11. Air-dry coverslips and slides with nitrogen and store as sets within tubes.
12. Vacuum seal the tube in food saver bags and store at  $-20^{\circ}\text{C}$  freezer.

### **3.4 Imaging Buffer Preparation**

To enhance the photostability of fluorophores, an enzymatic oxygen scavenging system is applied [30]. Prepare the following solution separately: 3 mM Trolox (*see Note 12*) and 0.8 % (w/w) dextrose monohydrate.

#### *Glucose oxidase solution*

1. Weigh 10.3 mg glucose oxidase into a low binding affinity 0.6-mL Eppendorf tube.
2. Add 80  $\mu$ L T50 buffer and 20  $\mu$ L catalase.
3. Spin down 30 s and mix with pipette (avoid bubbles).
4. Then spin for 2 min at 10,000  $\times g$ .
5. Move the supernatant to a new Eppendorf tube.

Imaging Buffer is composed of the following components: 10 mM Tris–HCl (pH 8.0), 5 mM MgCl<sub>2</sub>, 100 mM NaCl, 2 % (v/v) glycerol, 0.8 % (w/w) dextrose monohydrate, 3 mM Trolox, 2 mM ATP, 1 mM DTT, 1 % BSA, and 1 % (v/v) glucose oxidase solution (*see Note 13*).

### **3.5 TIRF-Optical Tweezers Instrumentation, Alignment, and Calibration**

The instrument is an objective-type TIRF microscope combined with a single optical trap (*see Notes 14 and 15*). A schematic representation of the assay is shown in Fig. 1 [24].

*The following steps refine the instrumentation of TIRF-Optical Tweezers*

The optical layout of the experimental setup from our previous publication is shown in Fig. 2 [24].

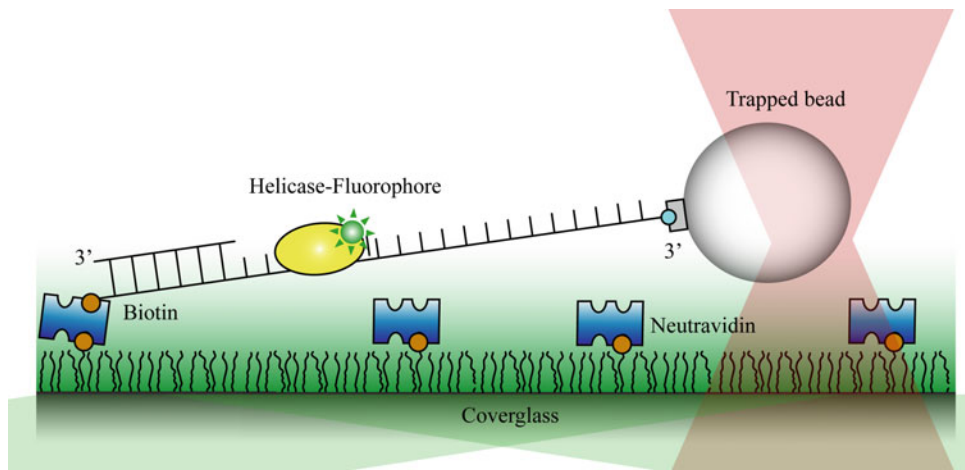


**Fig. 1** Schematic of the experimental assay, figure reproduced from Lee et al. [24]. One end of a nucleic acid construct is immobilized on the PEG-passivated surface, and the other end is attached to a polystyrene bead confined in the optical trap (pink). Green excitation laser selectively illuminates molecules within a few hundred nanometers from the cover glass surface by TIRF

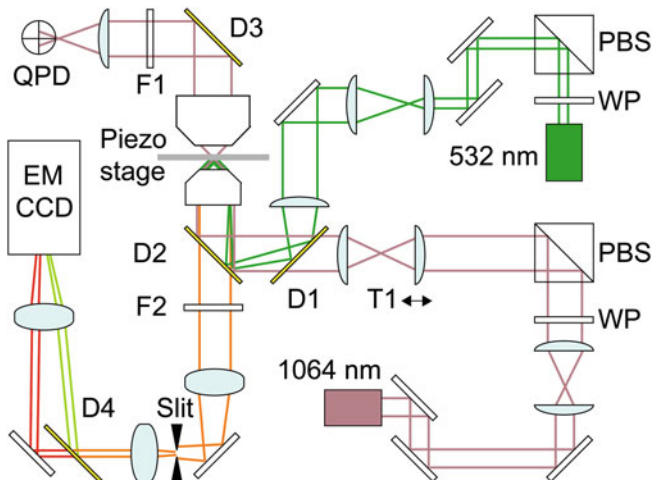


**Fig. 2** Instrument layout, figure adapted from Lee et al. [24]. The light paths of the 1,064 nm trapping laser (red), 532 nm fluorescence excitation laser (green) and fluorescence emission (orange) are depicted. Both the fluorescence excitation laser and trapping laser are tuned by half-wave plates (WP) and polarizing beam splitters (PBS). Two beams are coupled through the dichroic mirror (D1) and guided into the microscope side port. QPD reports the position of trapped bead by measuring the interference of the scattered and non-scattered light from trapped bead. The objective-type TIRF microscope illuminates the sample, which is mounted on piezo stage; the fluorescence emission signal collected by the objective lens is imagined by an EMCCD camera; D1-3, dichroic mirrors; F1-F2, filters; T1, telescope

1. A slight modification is made to mount a condenser and a dichroic mirror more stably with microscope.
2. A program controlled XYZ piezo-nanostage is mounted on a manual stage with  $2 \mu\text{m}$  for the XYaxis, which is fixed on top of the microscope.

3. A dichroic mirror is used to couple the IR laser (1,064 nm Nd-YAG) and green excitation laser (532 nm diode-pumped solid-state laser) into the side port TIRF microscope.
4. An oil immersion objective lens is used for objective-type TIRF microscopy and optical trapping. The emission of fluorescence of labeled molecules is backward collected through the objective and viewed by an EMCCD at a frame rate of 20 Hz.
5. The optical trapping position is centered at the fluorescence imaging area (*see Note 16*).
6. A quadrant photodiode (QPD) is used to collect the interference of the non-scattered and scattered laser light from a trapped bead and reports the position of trapped bead [32].

*The following steps refine the calibration of QPD and trap stiffness determination*

A QPD is composed of a two by two array of photodiodes, and is used for detecting the position of trapped bead in optical tweezers [32]. The non-scattered and scattered light from a trapped bead hits the QPD and returns readouts of total intensity,  $V_{\text{sum}}$ ; intensity difference in the horizontal direction,  $V_x$ ; and intensity difference in the vertical direction,  $V_y$ . When the position of a bead moves during trapping, the pattern of light scattered on the QPD changes as well, and as a result, the readouts give a new set of  $V_{\text{sum}}$ ,  $V_x$ , and  $V_y$ . Hence, mapping between the position of a trapped bead and voltage signals from a QPD is the first step in calibration (*see Note 17*).

Here, the power spectrum method is used for calibration [33, 34] (*see Note 18*). Approximating an optical trap as a harmonic potential, the Langevin equation describes the motion of bead in the trap, according to the Einstein–Ornstein–Uhlenbeck theory of Brownian motion [35].

$$m\ddot{x}(t) + \gamma\dot{x}(t) + \kappa x(t) = (2k_B T \gamma)x^{\frac{1}{2}}\eta(t), \quad (1)$$

where  $m$  is the mass of the bead,  $x$  is the position of the bead,  $\gamma$  is the friction coefficient,  $\kappa$  is the trap stiffness, and the right hand side of the equation is the random Brownian force at the absolute temperature  $T$  ( $k_B$ , the Boltzmann constant);  $\eta$  is the viscosity of the medium.

We can only detect motion through the change of voltage by QPD; therefore, coupling voltage into Langevin equation,  $x$  can be rewritten as:

$$x(t) = \beta V(t), \quad (2)$$

where  $V$  is the normalized voltage signal from the position detector ( $V_x/V_{\text{sum}}$  or  $V_y/V_{\text{sum}}$ ) and  $\beta$  is the conversion factor for the QPD (*see Note 19*).

The remaining unknowns are the friction coefficient  $\gamma$ , the trap stiffness  $\kappa$ , and the conversion factor  $\beta$ . Inertial terms are dropped out following Einstein and rewriting the Langevin equation in  $V$  instead of  $x$  yields [33],

$$\dot{V}(t) + 2\pi f_c V(t) = (2D^V)^{1/2} \eta(t), \quad (3)$$

where the corner frequency  $f_c$  and the diffusion constant  $D^V$  are

$$f_c = \frac{\kappa}{2\pi\gamma} \quad (4)$$

$$D^V = \frac{k_B}{\gamma\beta^2}. \quad (5)$$

The power spectrum derived from (Eq. 3) is,

$$P_k \equiv \langle P_k^{\text{exp}} \rangle = \frac{D^V}{2\pi^2 (f_c^2 + k^2)}, \quad (6)$$

and fitting (Eq. 6) to the experimentally measured power spectral distribution returns the corner frequency  $f_c$  and the diffusion constant  $D^V$ .

Therefore, if the friction coefficient  $\gamma$  is determined, both the trap stiffness and the conversion factor of QPD are resolved:

$$\kappa = 2\pi\gamma f_c \quad (7)$$

$$\beta = (k_B T / \gamma D^V)^{1/2}. \quad (8)$$

In our system, because the position of the trapped bead is placed very close to the passivated surface, the friction coefficient would be affected. In our system, the modified friction coefficient ( $\gamma$ ) can be estimated by Faxen's law [36] (Eq. 9), since the height of the bead from the surface ( $h$ ) can be determined (described in later paragraph) and the diameter of the bead ( $r$ ) is known:

$$\gamma = \frac{6\pi\eta r}{\left[1 - \frac{9}{16}\left(\frac{r}{h}\right) + \frac{1}{8}\left(\frac{r}{h}\right)^3 - \frac{45}{256}\left(\frac{r}{h}\right)^4 - \frac{1}{16}\left(\frac{r}{h}\right)^5\right]}. \quad (9)$$

1. Inject proper diluted trapping beads into assembled chamber.
2. Trap a bead with IR laser and record the thermal motion of the bead.
3. Apply the power spectrum fitting procedure mentioned above, to received  $f_c$  and  $D^V$  from recorded data. With the

determination of the trap height (see paragraph below), the trap stiffness  $\kappa$  and the conversion factor  $\beta$  are resolved.

*The following steps describe the mapping of EMCCD camera to the piezo-electric stage*

To analyze the dynamics of observed molecules in real time with physical units, a coordinated calibration between the camera screen and the piezo-electric stage has to be performed.

1. To create the mapping file, fluorescent beads are immobilized on the passivated coverslip surface and fluorescence images are recorded via EMCCD while scanning the piezo-electric stage in  $X$  and  $Y$  axis.
2. Applying a 2D, fifth order polynomial fitting to the scanned file, the pixel-to-nanometer conversion factor can be determined.

*The following steps describe the determination of the trapping height*

The previous approaches merely calibrate the lateral directions, while the calibration of the axial height remains to be performed.

1. To verify the trapping focus height, Cy3-labeled nucleic acids and beads are immobilized on the surface. Under TIRF excitation, maximize the fluorescence intensity of Cy3-labeled nucleic acids. Then set the axial position as origin.
2. Image immobilized beads with bright-field microscopy at various axial positions, which are positioned through a computer-controlled piezoelectric stage and data are recorded [37].
3. Axial scanning as described in previous step is performed with trapped beads as well.
4. A series of radii of defocussed immobilized beads and trapped beads are recorded through bright-field images. Radii are determined by fitting series of bright-field images to a 2D defocused-Gaussian function (MATLAB).
5. Plot radii as a function of axial distance.
6. The shift of the axial positions of the immobilized bead and trapped bead, at which the radii coincide, corresponds to the axial distance from the passivated surface to the trapping center (see Note 20).

### **3.6 Sample Preparation for TIRF-Optical Tweezers Assay**

*The following steps describe the assembly of the flow chamber*

1. Take one 50-mL tube containing a sample chamber set from the  $-20^{\circ}\text{C}$  freezer and keep it in the dark until it warms up to RT.
2. Attach two pieces of double-sided tape to the PEG-passivated glass slide in such a way that a  $\sim 8$  mm gap is formed between the two tapes perpendicular to the slide's long axis.

3. Put a coverslip over the double-sided tapes to form a ~20  $\mu\text{L}$  volume sample channel. Make sure the PEG passivated side of the coverslip is facing inside the channel.
4. Seal the gaps, which are parallel to the slide's long axis, between coverslip and glass slide with epoxy and let sit for 5 min. Leave drilled holes (inlet and outlet) open on glass slide for further buffer flow.

*The following steps describe the loading of the flow chamber*

1. Wash the sample channel twice with 100  $\mu\text{L}$  T50 buffer.
2. Inject 1 % BSA solution and incubate for 10 min (*see Note 21*).
3. Wash out the excess BSA with 100  $\mu\text{L}$  T50 buffer twice.
4. Inject 0.2 mg/mL neutravidin solution into the channel. Incubate for 5 min. Then wash out as in **step 3**.
5. Depending on the purpose of experiments, such as translocation, unwinding, or diffusion studies, different constructs of nucleic acids are incubated in this step. Generally speaking, 100  $\mu\text{L}$  of 250 pM nucleic acid constructs are incubated for 30 min in the channel.
6. After incubation with the nucleic acid constructs, wash out the unbound constructs with two rinses of 100  $\mu\text{L}$  T50 buffer (*see Note 22*).
7. Take 3  $\mu\text{L}$  of the anti-digoxigenin beads solution and mix with 397  $\mu\text{L}$  T50 buffer.
8. Centrifuge at 18,000  $\times g$  for 5 min at 4 °C.
9. Remove the supernatant and resuspend the pellet, diluting 25–100 $\times$ . Repeat the dilution step once and then sonicate for 10 s (*see Note 23*).
10. Inject solution with diluted anti-digoxigenin beads into sample channel and incubate for 45 min.
11. Wash out the excess nucleic acid constructs with two rinses of 100  $\mu\text{L}$  T50 buffer.
12. Depending on the purpose of experiments, different protein solutions can be added into channel. In general, protein solution is mixed with imaging buffer to 100  $\mu\text{L}$ . The final concentration of protein solution is 2 nM. Here, Cy3-labeled UvrD is the protein we are interested in. When mixing protein solution with imaging buffer, Glucose oxidase solution has to be added into the imaging buffer immediately before injecting the imaging buffer into the sample channel to avoid acidification of solution (*see Subheading 3.4* for image buffer and Glucose oxidase solution).

13. To prevent the evaporation of solution inside the channel, cover the in-let and out-let of the sample channel with immersion oil droplet.

### **3.7 Data Acquisition and Analysis**

*The following steps describe data acquisition*

1. Mount the sealed sample chamber on the microscope, using immersion oil to engage the condenser lens with the slide and the objective lens with the coverslip (*see Note 24*).
2. Trap one free bead, and then align the position of the position detector by adjusting the manual stages on which the position detector is mounted.
3. Next, find and trap a tethered bead whose radius of tethered diffusion corresponds to the length of the DNA constructs.
4. To determine the origin of trapped tether on surface and apply external force accurately, record force-extension curves through the stretching of the nucleic acid-tether in *x*- and *y*-direction using a computer-controlled stage movement at 20 pN constant force (*see Note 25*).
5. Apply a desirable force to the tether by moving the piezo stage, generally the applied force can be in the range of 1–30 pN. Use TRIF-based fluorescence excitation to image the movement of fluorescent labeled protein, Cy3-labeled UvrD under desirable external force. The time trajectories of applied force and the time series of the fluorescence images of the DNA-tether and Cy3-labeled UvrD are monitored and recorded at the same time.

*The following steps describe the analysis of the force-extension relation of the ssDNA substrate*

In order to get the extension per single nucleotide as a function of the applied force, we fit the obtained force-extension curves, which are used to identify the origin of the DNA constructs on surface, with the extensible worm-like chain (XWLC) model with a stretch modulus [38]. One thing to keep in mind is that the applied stretch modulus depends on the nucleic acid and the ionic strength. This parameter should therefore be chosen properly for the given experimental condition and the type of nucleic acid constructs being used. Figure 3 shows a comparison between different polymer models and the determination of extensions per single nucleotides [27].

*The following steps describe the generation of a kymograph and two-dimensional Gaussian fitting of fluorescence traces on the kymograph*

Generating a kymograph (*see Fig. 4*) for each movie provides a useful means for a quick screening for interesting motility events, which significantly reduces the time spent defining the rectangular

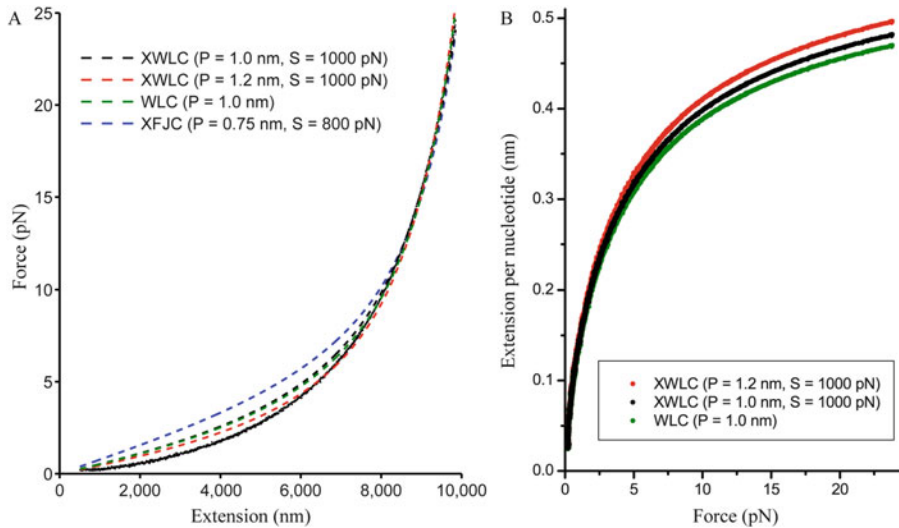


**Fig. 3** Force-extension relation of the ssDNA construct, figure reproduced from Lee et al. [27]. (a) Force-extension data for the ssDNA construct (*black dots*) are shown along with theoretical curves based on standard polymer models (*dashed lines*). The *black* and *green dashed lines* are the fitting results based on an extensible worm-like chain (XWLC) model with a stretch modulus of 1000 pN and (inextensible) WLC model, respectively. In both cases, the persistence length and the contour length of one nucleotide are fixed at 1.0 and 0.6 nm. However, neither curve fits well at forces below 10 pN. The *red dashed line* is the fitting result when the persistence length is also varied: the fitting results in a persistence length of 1.2 nm. With the increased persistence length, the *red dashed line* fits better to the experimental data. For comparison, an extensible freely jointed chain (XFJC) model with a contour length of 0.59 nm, a persistence length of 0.75 nm, and a stretch modulus of 800 pN is shown in blue. It is clear that a WLC model provides a better fit than a FJC model. (b) Extension per one nucleotide as a function of the force applied to the ssDNA construct. As standard polymer models fail to describe the force-extension data for the ssDNA construct, the experimentally obtained force-extension data was used to convert the number of nucleotides in 1 nm. To do so, the extension is divided by the number of nucleotides as determined by the fitting in the *left panel*

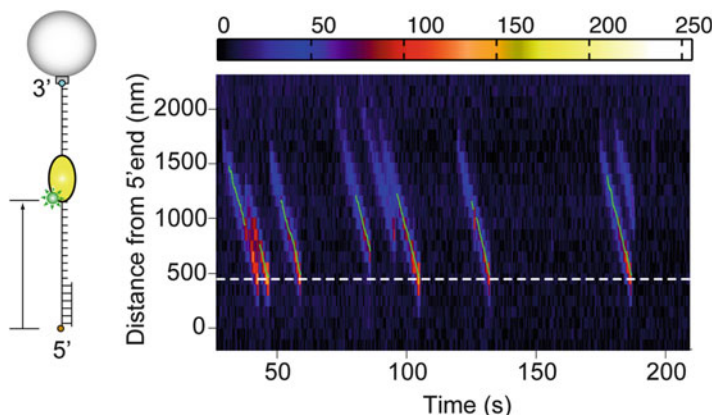


**Fig. 4** A kymograph showing multiple translocation events of monomeric Cy3-labeled UvrD. The position trajectory (*light green*) obtained from 2D Gaussian fitting of fluorescence images is overlaid on *top*. Adapted from Lee et al. [24]

subregions for 2D Gaussian fitting in each frame. Moreover, the trajectories obtained from the Gaussian fitting algorithm can be compared with the trajectories in the kymographs, which is useful for discarding outliers.

To generate a kymograph, we smoothed a movie by applying a moving average of 10 frames. For each frame of the ‘smoothed’ movie, the intensities of the pixels nearest to a line segment where the DNA construct lies are analyzed. For each pixel on the line, the mean of the intensity of the pixel and the 2 neighboring pixels across the line are taken to generate a strip with a 1-pixel width for the frame, representing the location and orientation of the DNA. This is repeated for all frames and the strip generated for each frame is put together to generate an image as wide as the number of frames.

Then we apply a 2D Gaussian fitting algorithm to obtain a sub-pixel localization precision of the fluorescent molecules [37, 39] in the recorded images. Rectangular subregions containing only the molecule of interest are manually defined (the fitting algorithm will return inaccurate center-of-mass positions if the subregion contains multiple fluorescence spots). The fitting result of individual trace is overlaid with the raw data on kymograph.

*The following steps describe an example of helicase translocation*

Figure 5b shows an example trace of UvrD translocation on a partial duplex DNA construct with a long 3'-ssDNA tail. The top graph shows the non-smoothed (20 Hz frame rate, thin solid line) and smoothed (10 frame sliding average) positions of Cy3-labeled UvrD along the *x*- and *y*-axis. Binding and dissociation of a fluorescently tagged protein can be monitored by the sudden jump and drop in the fluorescence intensity (magenta dashed line). The translocation rate of the protein can be determined by fitting a straight line to the position trajectory, while the number of photo-bleaching steps can be analyzed to obtain information about the stoichiometry of the protein. The fluorescence intensity gradually increases as the protein approaches the glass surface as the TIRF excitation field decreases exponentially with the distance for the coverslip surface. There is a wiggle in the fluorescence intensity because the illumination is not perfectly uniform throughout the entire imaging area due to interference effects of the coherent light used.

In biochemical and mechanistic studies of helicases, the determination of biochemical properties such as translocation rate, unwinding rate, and processivity with different nucleic acids constructs is important to quantitatively understand the detailed dynamics of target helicases. In the last paragraph, we have briefly described how to determine the translocation rate in our system. However, the same method of analysis can also be applied to determine unwinding rates. To measure the processivity of helicases, individual translocation events (‘run lengths’) are plotted in a

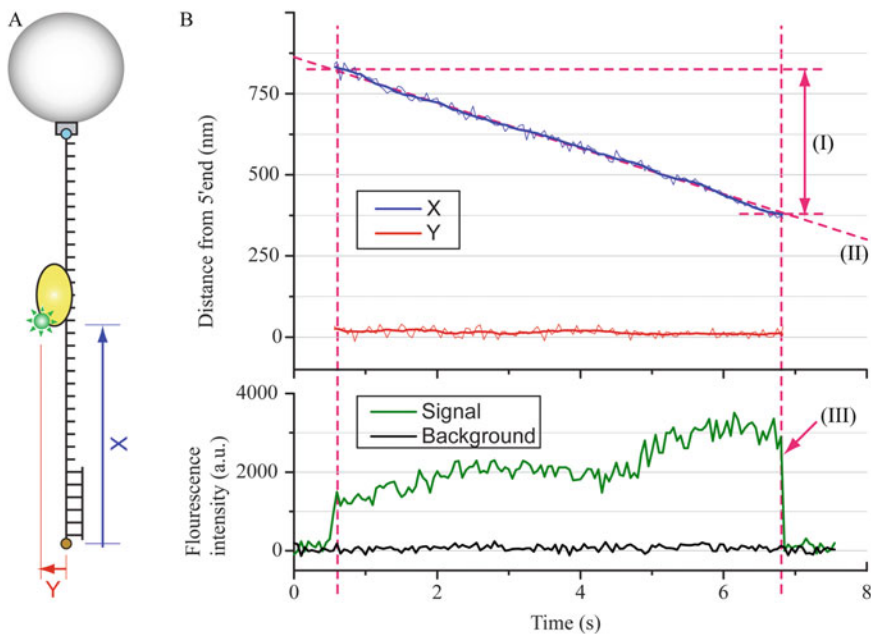


**Fig. 5** An analyzed sample trace showing the translocation trajectories of a monomeric Cy3-labeled UvrD. **(a)** the 5'-end of the DNA substrate (brown circle) is chosen as the origin. X axis (blue line) is along the DNA toward 3'-end (light blue circle), while the Yaxis (red) is in the perpendicular direction to the Xaxis. **(b)** The top and bottom graphs are position and fluorescence intensity trajectories of Cy3-labeled UvrD obtained from 2D Gaussian fitting of the fluorescence images. The bottom graph shows the trajectories of the DNA-bound Cy3-labeled UvrD (green) and background (black). Reproduced from [24]

histogram and fit to an exponential decay curve. The inverse of the decay constant represents the processivity. It can be either the processivity of translocation or the processivity of unwinding, depending on the type of experiment.

#### 4 Notes

1. The MES buffer should be freshly prepared and kept on ice.
2. The sodium bicarbonate buffer should be freshly prepared.
3. The product ssDNA polymers are only composed of pyrimidine nucleobases (thymine and cytosine), which prevents intramolecular base-pairing interactions.
4. The replication process of DNA polymerase can generate single-stranded DNA of up to tens of thousands nucleotides. Based on our experiences, these reaction conditions generally yield an average size of ~20,000 nucleotide (nt) ssDNA substrates.
5. As the 5'-end in one strand is protected as a result of surface immobilization through biotin-neutravidin coupling,

the 5'-end of the complementary strand is exposed and therefore selectively digested by T7 exonuclease.

6. The length of the ssDNA strand can be adjusted depending on the experimental purpose by changing the incubation time of the exonuclease reaction.
7. There are various reasons for choosing different sizes of dielectric beads in experiments. Generally speaking, larger beads provide more stable optical trapping and are easier to work with. However, considering the assay geometry, observation of fluorescent biomolecule dynamics on a nucleic acid stretched between the passivated surface and a trapped bead, beads with smaller diameter will be a better option. Since we acquired the real movement of fluorescently labeled protein along nucleic acid construct through multiply the observed movement at  $x$ -direction with the arctangent of the height of a trapped bead to the lateral displacement of the trap center from the 5'-end of nucleic acid construct. By minimizing the distance between trapped bead and passivated surface; therefore, one can record subtler changes.
8. The PEGylation buffer needs to be prepared fresh each time before use.
9. When recycling previously used slide chambers, incubate chamber in beaker filled with water and heat for 10 min in microwave. Then, remove the coverslips from the slides and clean up the remaining epoxy and tape residue using a razor blade.
10. The burning step removes the fluorescent organic dirt remaining on the slides or coverslips. In our fluorescence-force spectroscopy experiments, we image only the coverslip surface so only coverslips require the burning step.
11. Place the needle tip under hexane to avoid air contact and inject DDS quickly since it is extremely reactive with moisture.
12. After dissolving Trolox powder into proper concentration with ddH<sub>2</sub>O, wrap the tube with aluminum foil and slowly rotate it on a rotor at least 6 h. Then filter the solution with a 0.22  $\mu$ m filter and vacuum the tube.
13. The salt, glycerol and ATP concentrations depend on the purpose of the experiment and the system one works with. RNase inhibitor needs to be added when a RNA substrate is used. The pH value is extremely important when an oxygen scavenging system is used in the imaging buffer; always add the glucose oxidase solution at the last step of imaging buffer preparation. Due to the fast dropping of pH, imaging buffer is only good for 2 h after addition of glucose oxidase. If longer observation times are desired, adding fresh imaging buffer is required or

alternatively, to use an oxygen scavenging system that does not effect the pH (e.g., pyranose oxidase/catalase) [40].

14. There are two types of configurations of TIRF microscopes depending on whether the TIRF field is achieved by directing a laser beam through either the cover glass (objective-type TIRF) or the microscope slide (prism-type TIRF). Because the optical trap should be positioned close to the coverslip surface (less than 1  $\mu\text{m}$ ), we chose the objective-type TIRF microscope.
15. Several adjustments have been made to combine these two single-molecule techniques (TIRF and Optical tweezers) without impairing either. One of the challenges is that the photo-bleaching lifetime of fluorophores is greatly reduced due to the massive photon flux of the trapping laser [41]. Another challenge is that a section of the DNA adjacent to the trap remains outside the evanescent field of fluorescence illumination. To maximize the imageable portion of the DNA tether, we adjust the height of the trap to so that it is close to the surface. Moreover, using a longer DNA substrate can reduce trap-induced photobleaching by physically separating a large portion of the DNA from the trap center. However, a compromise has to be made since the resolution for detecting changes in tether extension decreases with increasing tether length [26], and the entire DNA substrate needs to be imaged on the EMCCD camera, i.e., lie within the imageable field of view.
16. To ensure that the majority of the DNA substrate stretched by the trap is placed within the evanescence field, the axial position of the trapped bead is placed close to the passivated surface of the sample chamber (less than 250 nm from the coverslip).
17. Near the center of a trap, bead displacements result in a linear response in  $V_x/V_{\text{sum}}$  and  $V_y/V_{\text{sum}}$  in the respective axes, which facilitates determining the conversion factor between the relative voltage and the real displacement of the trapped bead. However, when needed, the maximum radius of the calibrated positions can be extended past the linear region by using a 2D, fifth order polynomial fit to cover larger bead-displacements [42].
18. One great advantage of the power spectrum approach is that both the conversion factor of QPD and the trap stiffness can be obtained at the same time.
19. Since the manufacturer provides the density and the size of the beads with high precision, one can calculate the mass of the bead,  $m$ , assuming an ideal sphere.
20. The radius of a trapped bead shows a constant value while the radii of immobilized beads increase when the axial position approaches the axial position of the trapping laser focus. The

*z*-position of a trapped bead does initially not change when the piezo-stage approaches the trapped bead but starts to follow the movement of immobilized beads when the glass surface touches the bottom of the trapped bead.

21. BSA is used as a blocking reagent to prevent nonspecific binding to the channel surface. In some cases, tRNA is also used to prevent the nonspecific binding of single-stranded nucleic acids to the surface.
22. After the DNA constructs are attached to the surface in sample channel, all injections have to be performed with extreme care and gentleness. Alternatively, an automated pump (PHD 22/2000 series syringe pump; Harvard Apparatus) together with a syringe/tubing system for solution injections at a speed of 20  $\mu\text{L}/\text{min}$  can be used.
23. The sonication is a very critical step; if injected without sonication, beads will aggregate together, which prevents the formation of a one-bead, one-tether configurations.
24. The axial position of the condenser lens should be adjusted before the experiment by establishing Köhler illumination [43]. Make sure that the immersion oil between the objective lens and the coverslip and between the condenser lens and the glass slide does not contain any air bubbles since air bubbles can interfere with the position detection.
25. The coordinate of the symmetrical center from the force-extension curves at both *x*- and *y*-direction represents the position of biotin-end of the trapped nucleic acid tether. Then, the program overlays the coordinate of the biotin-end of the trapped nucleic acid construct with the position of the center of the optical trapped bead in *x*- and *y*-axis. By doing so, the origin of the tether is reset and shares the same coordinate as the trapping center.

## Acknowledgements

T. H. is an Investigator of the Howard Hughes Medical Institute. This work is supported by NIH grant GM065367 and NSF grants PHY-1430124 to T. H. We would like to thank Olivia Yang for proofreading the manuscript and Dr. Kyung Suk Lee for constructing the original instrument and training.

## References

1. Lu HP, Xun L, Xie XS (1998) Single-molecule enzymatic dynamics. *Science* 282 (5395):1877–1882. doi:[10.1126/science.282.5395.1877](https://doi.org/10.1126/science.282.5395.1877)
2. Robison AD, Finkelstein IJ (2014) High-throughput single-molecule studies of protein-DNA interactions. *FEBS Lett* 588

- (19):3539–3546. doi:[10.1016/j.febslet.2014.05.021](https://doi.org/10.1016/j.febslet.2014.05.021)
3. Ilya JF, Eric CG (2013) Molecular traffic jams on DNA. *Annu Rev Biophys* 42(1):241–263. doi:[10.1146/annurev-biophys-083012-130304](https://doi.org/10.1146/annurev-biophys-083012-130304)
  4. Ha T, Enderle T, Ogletree DF et al (1996) Probing the interaction between two single molecules: fluorescence resonance energy transfer between a single donor and a single acceptor. *Proc Natl Acad Sci U S A* 93(13):6264–6268
  5. Roy R, Hohng S, Ha T (2008) A practical guide to single molecule FRET. *Nat Methods* 5(6):507–516. doi:[10.1038/nmeth.1208](https://doi.org/10.1038/nmeth.1208)
  6. Visscher K, Gross SP, Block SM (1996) Construction of multiple-beam optical traps with nanometer-resolution position sensing. *IEEE J Sel Top Quantum Electron* 2(4):1066–1076. doi:[10.1109/2944.577338](https://doi.org/10.1109/2944.577338)
  7. Comstock MJ, Whitley KD, Jia H et al (2015) Direct observation of structure-function relationship in a nucleic acid-processing enzyme. *Science* 348(6232):352–354. doi:[10.1126/science.aaa0130](https://doi.org/10.1126/science.aaa0130)
  8. Moffitt JR, Chemla YR, Izhaky D et al (2006) Differential detection of dual traps improves the spatial resolution of optical tweezers. *Proc Natl Acad Sci U S A* 103(24):9006–9011. doi:[10.1073/pnas.0603342103](https://doi.org/10.1073/pnas.0603342103)
  9. Woodside MT, Anthony PC, Behnke-Parks WM et al (2006) Direct measurement of the full, sequence-dependent folding landscape of a nucleic acid. *Science* 314(5801):1001–1004. doi:[10.1126/science.1133601](https://doi.org/10.1126/science.1133601)
  10. Weiss S (2000) Measuring conformational dynamics of biomolecules by single molecule fluorescence spectroscopy. *Nat Struct Mol Biol* 7(9):724–729
  11. Greenleaf WJ, Woodside MT, Block SM (2007) High-resolution, single-molecule measurements of biomolecular motion. *Annu Rev Biophys Biomol Struct* 36:171
  12. Joo C, Balci H, Ishitsuka Y et al (2008) Advances in single-molecule fluorescence methods for molecular biology. *Annu Rev Biochem* 77:51
  13. Walter NG, Huang CY, Manzo AJ et al (2008) Do-it-yourself guide: how to use the modern single-molecule toolkit. *Nat Methods* 5:475
  14. Matson SW, Bean DW, George JW (1994) DNA helicases: enzymes with essential roles in all aspects of DNA metabolism. *Bioessays* 16(1):13–22. doi:[10.1002/bies.950160103](https://doi.org/10.1002/bies.950160103)
  15. Schmid SR, Linder P (1992) D-E-A-D protein family of putative RNA helicases. *Mol Microbiol* 6(3):283–292. doi:[10.1111/j.1365-2958.1992.tb01470.x](https://doi.org/10.1111/j.1365-2958.1992.tb01470.x)
  16. Jankowsky E, Gross CH, Shuman S et al (2001) Active disruption of an RNA-protein interaction by a DExH/D RNA helicase. *Science* 291(5501):121–125. doi:[10.1126/science.291.5501.121](https://doi.org/10.1126/science.291.5501.121)
  17. Lohman TM, Bjornson KP (1996) Mechanisms of helicase-catalyzed DNA unwinding. *Annu Rev Biochem* 65(1):169–214. doi:[10.1146/annurev.bi.65.070196.001125](https://doi.org/10.1146/annurev.bi.65.070196.001125)
  18. Tuteja N, Tuteja R (2004) Prokaryotic and eukaryotic DNA helicases. Essential molecular motor proteins for cellular machinery. *Eur J Biochem* 271(10):1835–1848. doi:[10.1111/j.1432-1033.2004.04093.x](https://doi.org/10.1111/j.1432-1033.2004.04093.x)
  19. Singleton MR, Dillingham MS, Wigley DB (2007) Structure and mechanism of helicases and nucleic acid translocases. *Annu Rev Biochem* 76:23–50
  20. Mackintosh SG, Raney KD (2006) DNA unwinding and protein displacement by superfamily 1 and superfamily 2 helicases. *Nucleic Acids Res* 34(15):4154–4159. doi:[10.1093/nar/gkl501](https://doi.org/10.1093/nar/gkl501)
  21. Donmez I, Patel SS (2006) Mechanisms of a ring shaped helicase. *Nucleic Acids Res* 34(15):4216–4224. doi:[10.1093/nar/gkl508](https://doi.org/10.1093/nar/gkl508)
  22. Jankowsky E, Fairman ME (2007) RNA helicases—one fold for many functions. *Curr Opin Struct Biol* 17(3):316–324. doi:[10.1016/j.sbi.2007.05.007](https://doi.org/10.1016/j.sbi.2007.05.007)
  23. Vindigni A (2007) Biochemical, biophysical, and proteomic approaches to study DNA helicases. *Mol Biosyst* 3(4):266–274. doi:[10.1039/B616145F](https://doi.org/10.1039/B616145F)
  24. Lee KS, Balci H, Jia H et al (2013) Direct imaging of single UvrD helicase dynamics on long single-stranded DNA. *Nat Commun* 4:1878. doi:[10.1038/ncomms2882](https://doi.org/10.1038/ncomms2882)
  25. Lin C-T, Tritschler F, Suk Lee K et al (2014) Single-molecule imaging reveals the translocation dynamics of hepatitis C virus NS3 helicase. *Biophys J* 106(2):72a. doi:[10.1016/j.bpj.2013.11.474](https://doi.org/10.1016/j.bpj.2013.11.474)
  26. Lee KS (2013) Fluorescence imaging of single molecule dynamics on long single stranded DNA. (Doctor of Philosophy Doctoral dissertation), University of Illinois at Urbana-Champaign. <http://hdl.handle.net/2142/42452>
  27. Lee KS, Marciel AB, Kozlov AG et al (2014) Ultrafast redistribution of *E. coli* SSB along long single-stranded DNA via intersegment transfer. *J Mol Biol* 426(13):2413–2421. doi:[10.1016/j.jmb.2014.04.023](https://doi.org/10.1016/j.jmb.2014.04.023)
  28. Brockman C, Kim SJ, Schroeder CM (2011) Direct observation of single flexible polymers

- using single stranded DNA. *Soft Matter* 7 (18):8005–8012. doi:[10.1039/C1SM05297G](https://doi.org/10.1039/C1SM05297G)
29. Zhou R, Schlierf M, Ha T (2010) Chapter Sixteen - Force-fluorescence spectroscopy at the single-molecule level. In: Nils GW (ed) *Methods in enzymology*, vol 475. Academic, New York, NY, pp 405–426. doi:[10.1016/S0076-6879\(10\)75016-3](https://doi.org/10.1016/S0076-6879(10)75016-3)
  30. Selvin PR, Ha T (2008) Single-molecule techniques: a laboratory manual. Cold Spring Harbor Laboratory Press, Cold Spring Harbor, NY
  31. Hua B, Han KY, Zhou R et al (2014) An improved surface passivation method for single-molecule studies. *Nat Methods* 11 (12):1233–1236. doi:[10.1038/nmeth.3143](https://doi.org/10.1038/nmeth.3143), <http://www.nature.com/nmeth/journal/v11/n12/abs/nmeth.3143.html> - supplementary-information
  32. Rice SE, Purcell TJ, Spudich JA (2003) [6] Building and using optical traps to study properties of molecular motors. In: Nils GW (ed) *Methods in enzymology*, vol 361. Academic, New York, NY, pp 112–133. doi:[10.1016/S0076-6879\(03\)61008-6](https://doi.org/10.1016/S0076-6879(03)61008-6)
  33. Berg-Sørensen K, Flyvbjerg H (2004) Power spectrum analysis for optical tweezers. *Rev Sci Instrum* 75(3):594–612. doi:[10.1063/1.1645654](https://doi.org/10.1063/1.1645654)
  34. Berg-Sørensen K, Peterman EJG, Weber T et al (2006) Power spectrum analysis for optical tweezers. II: laser wavelength dependence of parasitic filtering, and how to achieve high bandwidth. *Rev Sci Instrum* 77(6):063106. doi:[10.1063/1.2204589](https://doi.org/10.1063/1.2204589)
  35. Kubo R, Toda M, Hashitsume N (1991) Statistical physics II: nonequilibrium statistical mechanics. Springer, Berlin
  36. Neuman KC, Block SM (2004) Optical trapping. *Rev Sci Instrum* 75(9):2787–2809. doi:[10.1063/1.1785844](https://doi.org/10.1063/1.1785844)
  37. Toprak E, Balci H, Blehm BH et al (2007) Three-dimensional particle tracking via bifocal imaging. *Nano Lett* 7(7):2043–2045. doi:[10.1021/nl0709120](https://doi.org/10.1021/nl0709120)
  38. Baumann CG, Smith SB, Bloomfield VA et al (1997) Ionic effects on the elasticity of single DNA molecules. *Proc Natl Acad Sci U S A* 94 (12):6185–6190
  39. Yildiz A, Forkey JN, McKinney SA et al (2003) Myosin V Walks hand-over-hand: single fluorophore imaging with 1.5-nm localization. *Science* 300(5628):2061–2065. doi:[10.1126/science.1084398](https://doi.org/10.1126/science.1084398)
  40. Swoboda M, Henig J, Cheng H-M et al (2012) Enzymatic oxygen scavenging for photostability without pH drop in single-molecule experiments. *ACS Nano* 6(7):6364–6369. doi:[10.1021/nn301895c](https://doi.org/10.1021/nn301895c)
  41. van Dijk MA, Kapitein LC, van Mameren J et al (2004) Combining optical trapping and single-molecule fluorescence spectroscopy: enhanced photobleaching of fluorophores. *J Phys Chem B* 108(20):6479–6484. doi:[10.1021/jp049805+](https://doi.org/10.1021/jp049805+)
  42. Lang MJ, Asbury CL, Shaevitz JW et al (2002) An automated two-dimensional optical force clamp for single molecule studies. *Biophys J* 83(1):491–501. doi:[10.1016/S0006-3495\(02\)75185-0](https://doi.org/10.1016/S0006-3495(02)75185-0)
  43. Köhler A (1984) New method of illumination for photomicrographical purposes. *J R Microsc Soc* 14:261–262

# Chapter 12

## Mechanically Watching the ClpXP Proteolytic Machinery

Juan Carlos Cordova, Adrian O. Olivares, and Matthew J. Lang

### Abstract

Energy-dependent protein degradation is studied through the dual bead ClpXP motility assay. Processing of folded proteins involves recognition, unfolding, translocation, and degradation stages. A dual optical trap, in a passive force-clamp geometry, exhibits bead-to-bead displacements that directly follow subprocesses underlying protein degradation. Discrete nanometer-scale displacements of the bead position reveal steps, dwells and pauses during the unfolding and translocation substeps. With a few structural modifications to the protease machinery and an engineered substrate, the assay represents a “chassis” for the measurement of a wide range of substrates and related machinery. The methods described faithfully record our assay as implemented, including substrate design, wet assay preparation, and the motility assay experiment protocol. The strategies herein permit adaptation of the ClpXP mechanical assay to a wide range of protein degradation systems.

**Key words** ClpXP, Optical tweezers, Proteasome, Dual trap, Unfolding, Translocation, Single molecule degradation, Passive force clamp, ATPase, AAA+ protease

---

### 1 Introduction

ClpXP is a member of the AAA+ (ATPase associated with various cellular activities) protease family in *Escherichia coli* and model for understanding how energy-dependent protein degradation machinery, such as the eukaryotic proteasome, work in all cells. The ClpXP system processes proteins tagged for destruction by performing many tasks including recognition, unfolding, translocation and degradation. ClpXP consists of the ClpX and ClpP multimeric rings stacked in a barrel like geometry with rings encompassing a central axis of symmetry. The system also contains mirror like symmetry with two back-to-back seven member ClpP rings, forming a central degradation chamber, capped by two 6 member ClpX rings where proteins enter. The ATP processing ClpX rings perform recognition, unfolding and translocation tasks that control access to ClpP by feeding an unfolded polypeptide through a small opening to the inner chamber of ClpP where catalytic degradation of the peptide backbone occurs [1].

The broader AAA+ superfamily of molecular machines, which function in diverse cellular processes, contains a massive number of members, over 30,000, found in all forms of life [2–5]. Some of the best-known examples used for single molecule studies are cytoplasmic dynein [6, 7], which is a processive microtubule minus end-directed motor, and the Φ29 DNA-packaging motor, which transports and packages the phage genome [8–10]. AAA+ member activities are diverse [11], and include circadian clock oscillators [12], microtubule-severing enzymes such as Katanin and Spastin [13], and Hsp104 and ClpB, which disassemble protein aggregates [14].

From a geometrical and design perspective, the diverse family of AAA+ motors retains ring hierarchy where sub-tasks are organized within or adjacent to ring elements [15]. From a protein sequence perspective these systems may assemble from separate AAA+ ATPase subunits (as in ClpX and ClpP), be concatenated into a single large polypeptide (as in dynein) or linked sequentially vertically from one ring function to the next such as in FtsH [16].

The assay detailed in this chapter overcame a number of challenges. Fortunately, a substantial foundation of work detailing the biochemical requirements for the initiation of ClpXP's processing of a wide range of proteins helped us to establish a reliable single-molecule assay. The assay includes inherently fluorescent substrates such as GFP and CFP, recognition sequences, and details relating to the nucleotide identity and/or concentration and underlying requirements for executing recognition, unfolding and translocation tasks [17]. Effectively, ClpXP travels on a protein-based track, navigating along both folded and unfolded elements of the polypeptide chain. While a foundation of single molecule literature/work detailed methods for motility experiments using actin, microtubules, DNA, and RNA as substrates, adaptation to a polypeptide track was required. Unlike these other tracks, the only regular periodicity of the ClpXP track is the peptide bond. ClpXP must therefore denature diverse structures of folded proteins as well as process strands of varied amino acid sequences.

Motility is initiated through a peptide based signal (the ssrA tag) that when covalently linked to a protein, facilitates recognition by ClpXP. Still a number of challenges were present when adapting these well-established bulk assay protocols to the single molecule arena. Disassembly of the ClpXP system at very low concentrations utilized in single-molecule studies proved to be fatal as the ClpX ring equilibrium would shift to monomers. A single chain hexamer was developed to link the ring together using a variant of ClpX lacking its N-terminal domain [18]. A biotin molecule was also engineered within the ring to permit physical immobilization to a coverslip surface or bead.

The first robust single-molecule assay for ClpXP immobilized ClpXP to a streptavidin-coated surface and utilized GFP as well as Cy3-tagged substrates [19]. Here, many ClpXP motors could be

watched simultaneously in a single field of view by following degradation of the fluorescent substrates. A strategy was developed to stall and synchronize ClpXP activity. To do this, a substrate was engineered with a recognition tag followed by a weakened titin domain followed by the more mechanically stable GFP and a terminal handle that was functionalized with a Cy3 fluorescent dye. The titin domain contains the V15P single point mutation, which can be degraded by ClpXP using ATP $\gamma$ S as a fuel substitute for ATP. Unlike V15P, GFP degradation stalls in the presence of ATP $\gamma$ S and requires ATP for successful processing [20]. Synchronization of the motors through exchange of ATP for ATP $\gamma$ S utilized a strategy to load ATP into the ClpX nucleotide binding pockets but prevent hydrolysis by chelating and starving the system of magnesium, which is required for hydrolysis. The fluorescence-based assay permitted direct observation of the degradation kinetics of ClpXP and featured many of the assay elements needed for adapting to a mechanical based optical tweezers measurement.

Adapting the single molecule fluorescence assay to optical tweezers was first attempted by attaching ClpXP to the coverslip surface followed by introducing substrates tethered to beads, but given the nanometer-scale displacements and the low motor velocity (~3 nm/s), motility records suffered from large sample drift. Furthermore, all pre-assembled tethers in the flow cell initiate motility at the start of the experiment, creating a problem in experimental throughput for optical trapping measurements, which typically observe a single molecule at a time. These problems could be partially solved using the dual-bead system (Fig. 1), which

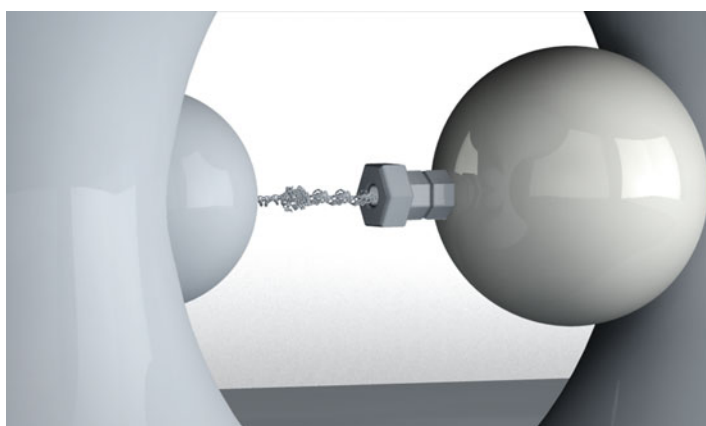


**Fig. 1** Rendering of the dual bead optical trap assay for mechanically visualizing ClpXP machinery. ClpXP recognizes, unfolds, translocates, and degrades protein substrates tagged for destruction. Two beads of slightly different sizes are held using two optical traps originating from the same laser source. A protein multimer containing a recognition sequence, four titin<sup>127</sup> domains and a HaloTag is linked to the smaller bead using a DNA tether as in Cordova et al. [24]. The slightly larger bead is functionalized with ClpXP. The hexameric ClpX recognizes, unfolds, and translocates the polypeptide into ClpP, which catalytically degrades the polypeptide. By measuring precise bead-to-bead separation, displacements due to unfolding and translocation steps along the polypeptide can be recorded

offers a number of advantages to the tethered-bead assay. First, due to the use of a common mode differential strategy for the detection of the distance between two beads held by a dual-beam optical trap but synthesized by the same laser source, it is not subject to stage drift and therefore exhibits lower noise. Second, each substrate-motor tether can be assembled individually, in real time, permitting multiple experiments per slide. Third, much of the physical linkages could be more easily controlled on bead surfaces rather than cover glass surfaces, which can be finicky.

In addition to the dual-bead geometry, use of a multi-domain substrate was advantageous for two reasons. The presence of several folded domains in a single substrate allows for multiple unfolding and translocation events to be measured from a single tether thereby achieving “more bang for your buck” during an experiment. Additionally, this substrate design ensures that we catch unfolding and translocation events that might be missed in a single domain substrate due to the time it takes to begin data collection once an active tether is formed in the presence of ATP.

Early work establishing the dual-bead assay to investigate ClpXP motility used a filamin polyprotein [21], and single or double GFP substrates [22]. These assays revealed sequential unfolding and translocation as well as the force velocity relation and direct observation of stepping. More recent studies include the work by Sen et al. [23], who investigated translocation and unfolding of GFP and unfolded substrates under varied nucleotide concentrations, and the work by Cordova et al. [24], which demonstrated unfolding and stepping through a series of weakened titin domains and ClpX mutants that lacked the ability to hydrolyze ATP. Olivares et al. [25] adapted the assay to investigate ClpAP motility, which features a double ring ATPase structure and a biotin labeled ClpP construct for bead attachment. More recently, Iosefson et al. [26] probed motility of ClpX constructs bearing pore-loop mutations. Throughout these studies a foundation of solution-based biochemical work has been integral to the development of assays and the interpretation of motor function. The ability to directly watch mechanical sub-processes and manipulate motor performance using these single-molecule assays has revealed much about ClpXP and proteasome-related machinery.

---

## 2 Materials

### 2.1 Motor System

Two strategies are used to link the AAA+ protease to a polystyrene trapping bead. One involves biotinylation of a single chain variant of ClpX missing its N-terminal domain (<sup>SC</sup>ClpX $\Delta$ N), which is dispensable for the degradation of ssrA-tagged substrates [18]. Complexes of ClpXP are assembled on bead surfaces by adding excess ClpP in the flow chamber during an experiment. A second strategy

uses a biotinylated ClpP variant that can bind a AAA+ unfoldase on one face of the heptameric ring ( $\text{ClpP}^{\text{platform}}$ ) [25]. The advantage of this method of attaching a AAA+ protease to a bead is that single chain variants of the ATPase ring are not required and use of full-length enzymes is possible.  $\text{ClpP}^{\text{platform}}$  is bound to a streptavidin-coated bead and the ATPase ClpX or ClpA are added in solution. Free ATPase can optionally be removed by centrifugation of the resulting ClpXP or ClpAP beads followed by washing the beads with a solution containing ATP before use in an experiment. Components of the motor system include:

1. ClpX: In its native state, ClpX forms a hexamer by association of individual ClpX ATPase domains. The dilute enzyme concentrations typical in single-molecule studies (~pM) did not permit stable ring formation from ClpX monomers and required using a ClpX variant where the individual domains (residues 61–423) were linked in a “single chain hexamer”,  $^{SC}\text{ClpX}\Delta\text{N}$ . This construct is produced using an *E. coli* expression system and also includes a biotin tag on the C terminus. In order to investigate the roles of individual ATPase subunits, a ClpX system has been generated linking two trimers through sortase-based coupling [27].
2. ClpP: The ClpP-His<sub>6</sub> unit is a seven membered ring. Two rings associate symmetrically to form a 14-member chamber where catalytic degradation occurs. This double ring system naturally binds to the ClpX hexamer. The ring system is stable at single-molecule concentrations.
3. Biotin linker: A biotin molecule is used to tether ClpXP to a bead. Typically, the biotin is located on the ClpX ring as part of the single-chain expression. Biotin molecules can also be incorporated within ClpP.

## **2.2 Buffers for Protein Expression, Purification, Modification, Filtration, and Storage**

1. Lysis Buffer (LB1): 20 mM Hepes pH 7.6, 10 mM imidazole, 400 mM NaCl, 100 mM KCl, 10 % glycerol, 10 mM  $\beta$ -mercaptoethanol.
2. S-Buffer: 50 mM sodium phosphate pH 8.0, 1 M NaCl, 10 % glycerol, 5 mM imidazole.
3. Elution Buffer (EB1): 20 mM Hepes pH 7.6, 250 mM imidazole, 400 mM NaCl, 100 mM KCl, 10 % glycerol, 10 mM  $\beta$ -mercaptoethanol.
4. W20 Buffer: 50 mM sodium phosphate pH 8.0, 1 M NaCl, 10 % glycerol, 20 mM imidazole.
5. W500 Buffer: 50 mM sodium phosphate pH 8.0, 1 M NaCl, 10 % glycerol, 500 mM imidazole.
6. ResBuffer: 50 mM Hepes pH 7.6, 150 mM KCl, 0.5 mM EDTA, 10 % glycerol.

7. Biotinylation Buffer (BB1): 20 mM Hepes pH 7.6, 300 mM KCl, 10 % glycerol, 0.5 mM TCEP.
8. S300 Buffer (SB1): 20 mM Hepes pH 7.6, 300 mM KCl, 5 mM MgCl<sub>2</sub>, 0.1 mM EDTA, 10 % glycerol, 0.5 mM TCEP.
9. Ring Separation Buffer: 50 mM Hepes pH 7.6, 0.7 M KCl.
10. W-20B Buffer: 50 mM Hepes pH 7.6, 150 mM KCl, 0.5 mM EDTA, 20 mM imidazole, 10 % glycerol.
11. W-500B Buffer: 50 mM Hepes pH 7.6, 150 mM KCl, 0.5 mM EDTA, 500 mM imidazole, 10 % glycerol.
12. ClpP Storage Buffer: 50 mM Hepes pH 7.6, 150 mM KCl, 0.5 mM EDTA, 10 % glycerol.

### **2.3 Multidomain Substrate System**

The multidomain substrate contains an N-terminal HaloTag® domain fused to four repeats of the ~100 amino acid I27 domain of the human muscle protein titin (titin<sup>127</sup>) and ends with the *E. coli* ssrA degradation tag, which allows for efficient targeting to the ClpXP and ClpAP ATP-dependent proteases. HaloTag is a modified haloalkane dehalogenase that is used to covalently link our substrate to a 3500 bp DNA linker [24, 25]. This long ~1 μm linker allows for sufficient separation of the two beads used in the experiment, ensuring that beads remain trapped by the appropriate laser. Similar strategies have been used to covalently link substrate to DNA using a SNAP-tag®, which is the modified DNA repair protein O<sup>6</sup>-alkylguanine-DNA alkyltransferase [22, 23]. Titin<sup>127</sup> possesses a β-sheet-rich, Ig-like fold and is used here as a model substrate for examining how protein stability affects the kinetics of unfolding. The mutation of valines to prolines near the C-terminus of titin<sup>127</sup> (V13P and V15P) affect the thermodynamic, kinetic and mechanical stabilities such that the wild-type protein (WT) is the most resistant to unfolding with increasing weakening of the structure as one disrupts the C-terminal strand where the AAA+ protease is pulling on (i.e., WT > V15P > V13P) [28]. Additionally, carboxymethylation of buried cysteines within titin<sup>127</sup> yields an unfolded protein for the study of polypeptide translocation [28]. The very C-terminus of the substrate contains a hexahistidine (His<sub>6</sub>) tag for purification and the ssrA tag, which is a small peptide sequence that is cotranslationally appended to incomplete proteins that arise due to ribosomal stalling and efficiently targets these proteins to ATP-dependent proteases like ClpXP in bacteria [29]. Substrates used in published work are found in Table 1.

#### **2.3.1 Specific Components of the Multidomain Substrate**

1. Recognition domain: a C-terminal AANDENYALAA ssrA tag.
2. His<sub>6</sub> tag.
3. Multi-domain protein substrate: These typically consist of sequential polyprotein elements that form the motility substrate of ClpXP. Elements include immunoglobulin repeats 1–8 of filamin A (accession CAI43198; residues 279–1066),

**Table 1**  
**lists various substrate elements, residue length, typical unfolding distance and unfolding time from dual bead ClpXP mechanical degradation assays**

Substrate	Residue length (aa)	Unfolding distance (nm)	Unfolding time (s)	References
Filamin A (Ig 1–8)	98	15	5–25	[21]
Titin I27 (wt)	89	12	>55	[24]
Titin I27 (V13P)	89	12	5.9	[24–26]
Titin I27 (V15P)	89	12	17	[24]
GFP	238 <sup>a</sup>	50	9.1	[22, 23, 25, 26]
Halo Tag	294 <sup>b</sup>	25	8.7	[21, 24–26]

<sup>a</sup>Truncated version [20]

<sup>b</sup>150–170 amino acids are degraded by ClpXP

residues 5303–5341 of human titin (accession CAA62188; corresponding to the C-terminal half of the I27 domain), mutant I27 domains and GFP domains.

### 2.3.2 DNA Tethers for Substrate and Aptamer

- Linker: a linker of 47 residues containing two TEV protease sites.
- HaloTag: haloalkane dehalogenase, a protein used as a covalent linker to 3500 bp DNA.
- Forward primer (25 μL, 20 μM): 5'-Biotin-AAT CCG CTT TGC TTC TGA CT-3' diluted from 100 μM with ddH<sub>2</sub>O (IDT custom oligo).
- Reverse primer (25 μL, 20 μM): 5'-Amino-TTG AAA TAC CGA CCG TGT GA-3' diluted from 100 μM with ddH<sub>2</sub>O (IDT custom oligo).
- dNTPs (8 μL, 25 μM) (New England Biolabs cat#N04475).
- M13mp18 plasmid (5 μL, 50 ng/μL) (Bayou Biolabs cat#P-105).
- TE buffer (Ambion cat#AM9849).
- UltraPure water (727 μL) (Invitrogen cat#10977-015).
- Phusion DNA Polymerase (10 μL) (New England Biolabs cat#M0530S).
- QIAquick PCR purification kit (Qiagen cat#28106).
- UV-Vis spectrophotometer (Thermo Scientific NanoDrop 2000).

### 2.3.3 DNA-Amine to Thiol-HaloTag Ligand Conjugation

- NH<sub>2</sub>-DNA (200 ng/μL in PBS).
- UltraPure distilled water (Invitrogen cat#10977-015).

3. Sulfo-SMCC (Pierce cat#22622 in 2 mg sealed tubes).
4. PBS buffer at pH 7.4.
5. For HaloTag conjugation: HaloTag Thiol Ligand (Promega cat#P6761).
6. For aptamer conjugation: glass binding peptide with cysteine and two glycine residues added at the N-terminus (CGGRSGRRSHHRL).
7. Bio-Rad Micro Bio-Spin 30 columns (MBS30) (BioRad cat#732-6223).
8. Bio-Rad Micro Bio-Spin 6 columns (MBS6) (BioRad cat#732-6221).
9. UV-Vis spectrophotometer (Thermo Scientific NanoDrop 2000).

**2.4 Protein Degradation Buffer (PD buffer)**

1. 0.59575 g HEPES (25 mM).
2. 0.7455 g KCl (100 mM).
3. 0.2033 g MgCl<sub>2</sub> (10 mM).
4. 90 mL ddH<sub>2</sub>O.
5. 10 mL glycerol (10 %).
6. 100 µL Tween 20 (0.1 %).
7. 0.2 µm filter.
8. Mix everything. Adjust pH to 7.6 with KOH. Pass through a 0.2 µm filter.

**2.5 ATP Regenerating System (Prepared at 20×)**

1. Creatine phosphokinase (Calbiochem 238395).
2. Creatine phosphate (Calbiochem 2380).
3. Adenosine triphosphate (Sigma A7699).
4. Potassium hydroxide (Sigma 221473).
5. PD buffer.

**2.6 Oxygen Scavenging System (Prepared at 100×)**

1. 16,500 U/mL glucose oxidase (Sigma, G2133).
2. 217,000 U/mL catalase (Sigma, C100) in PD.
3. 500 mg/mL D-Glucose (Sigma, G8270) in PD.

**2.7 Flow Chambers**

1. Scotch Permanent Double Sided Tape (3 M cat#137DM-2).
2. Potassium hydroxide (Sigma 221473).
3. Glass coverslips (24 × 40, thickness 1.5) (Fisher cat#12-544-C).
4. Glass microscopy slides (VWR cat# 48312-068) chemically etched in ethanolic base as below.

## 2.8 ClpXP Dumbbell Assay

1. ClpX (biotinylated) 3  $\mu$ L, ~5–6  $\mu$ M.
2. ClpP (with his tag) 11  $\mu$ L, 20  $\mu$ M.
3. ATP, 20 $\times$  with regeneration system.
4. HaloTag terminated substrate, 3  $\mu$ L, 20  $\mu$ M.
5. HaloTag–3500 bp DNA–biotin in PBS, 15  $\mu$ L, ~150 ng/ $\mu$ L.
6. A08–3500 bp DNA–biotin, 50  $\mu$ L of 0.5 ng/ $\mu$ L.
7. 1  $\mu$ m streptavidin coated polystyrene beads (Polysciences Inc 24162-1).
8. 1.26  $\mu$ m streptavidin coated polystyrene beads (Spherotech SVP-10-5).
9. Oxygen scavenging system at 100 $\times$ .
10. Dithiothreitol (100 mM, Thermo 20290).
11. Casein (Sigma C7078).
12. Bovine serum albumin (Calbiochem 2905-OP).
13. PD buffer.
14. PBS.
15. 0.2  $\mu$ M syringe filters (Fisher SLMP025SS).
16. Microcentrifuge tubes (1.5 and 0.7 mL, Fisher 02-682-556 and 05-408-120).
17. Flow cells.
18. Vacuum grease (VWR 59323-011).

## 2.9 Dual-Beam Trapping Instrument

The optical trapping microscope is a high-end custom-built instrument featuring separate trap and position sensing systems and a high degree of automation. The design contains many of the features described by Lang et al. [30]. The dual trap is achieved by incorporating a pair of polarizers as detailed by Visscher et al. [31]. When designing a system one must consider stability throughout the system ranging from choosing high quality components to housing the instrument in an acoustically quiet, tight temperature controlled environment. The system is only as stable as the noisiest component. Herein we list some of the specific choices in components as a guide.

1. Microscope, Nikon TE 2000-U, mechanically stabilized through direct bolting to the optical table and custom machined sample stage, objective holder, trap injecting mirror holder and condenser side detector branch. Our objective is a Nikon Oil IR, 1.40 NA and the condenser is a wide lens Oil 1.4 NA.
2. Trapping laser: IPG Photonics model YLD-10-1064. This laser is fiber coupled, reasonably stable with a reasonable mode. Fiber coupling permits locating the laser outside of the

trapping instrument room such that heat dissipation and acoustical noise do not interfere with the microscope. Fiber coupling also helps to reduce pointing instabilities and other noise sources related to laser cavities.

3. Detection laser and subsystem: Avanex A1998 PLM, a 14-pin butterfly laser mounted in a Thor labs housing and driven by a Thor Labs Controller (ITC 510). The laser outputs 975 nm light through a single-mode fiber that can be output-coupled to produce a beam of the desired width. The optical fiber launch helps to reduce noise associated with pointing. The laser also features a fiber Bragg grating which stabilizes the lasing mode. The laser is isolated along the detection branch with an Andover 970FS10-50 band pass filter. A number of wavelengths and laser sources are appropriate for the detection laser. The primary requirement should be stability and wavelength cross-section with the position sensing detectors. Our instrument utilizes dual lateral position sensing devices, PSD's, from Pacific Silicon Sensor (model 10-018) with an approximately 1 cm<sup>2</sup> active area for Silicon based detection. Signals from the PSD's are amplified approximately 10× using low noise voltage-regulated amplifier chips and fed into an "anti-alias filter" (Kron-Hite Model 3384, 8 pole LP/HP Butterworth Bessel).
4. Some of the automated features include: computerized ability to move the optical trap through acoustic optic deflectors or AOD's (IntraAction DTD-276HD6); movement of the sample through a piezo stage (Physik Instrumente P-527.3CD stage and E-710.3CD controller); shutters for turning on and off beams (Uniblitz); and picomotor actuators for fine positioning of trap and detection lasers (NewFocus).

### 3 Methods

#### 3.1 Expression of Proteins in *E. coli*

1. Use freshly transformed *E. coli* expression strains harboring plasmids for expression of multidomain ssrA-tagged substrate, <sup>SC</sup>ClpXΔN, ClpP-His<sub>6</sub>, or ClpP<sup>platform</sup> variants ClpP-TEV-His<sub>6</sub> and ClpP<sup>M15A</sup>-bioAP-His<sub>6</sub> described below.
2. Grow overnight at 37 °C on LB-agar with the appropriate antibiotic.
3. Multidomain substrate and <sup>SC</sup>ClpXΔN are overexpressed in an *E. coli* ER2566 lysis strain described in Shin et al. [19], which is available upon request or the commercially available BLR (DE3), *recA*<sup>-</sup>, which prevents the unwanted recombination of repeat sequences. ClpP variants are expressed in JK10 cells (clpP::cat, Δlon, slyD::kan, λDE3) described in Kenniston et al. [32].

4. Pick colony from overnight plate and grow 50 mL overnight culture in LB antibiotic at 37 °C.
5. Transfer 10 mL overnight culture into 1 L LB-antibiotic and grow, shaking at 37 °C. When OD<sub>600</sub> reaches ~0.6, cool at 4 °C for 15 min and lower shaker temperature to 25 °C. Induce cultures with 0.5 mM IPTG and grow for 3–4 h. Harvest cells at 4000 × g for 15 min at 4 °C. Resuspend cells in 10 mL Lysis Buffer per each gram of cell paste. For ClpP variants, resuspend cells in 20 mL S-buffer per 1 L cells.
6. Flash-freeze in liquid nitrogen and store pellets at –80 °C.

### **3.2 Ni-NTA Purification of Multidomain Substrate and ClpX Proteins**

The following steps are performed at 4 °C unless stated otherwise.

1. Thaw cells in ice water bath for 15–20 min. Make sure that cells are well suspended and then pass through a French press at 25 kpsi. If you do not have a French press, sonication or freeze-thaw cycles with lysozyme can be done to break open the cells. Add 1 mM PMSF to lysate. If lysate is viscous, incubate with 500 U benzonase and 2 mM MgCl<sub>2</sub> for 20 min. Clarify lysate at 30,000 × g for 30 min.
2. Equilibrate NiNTA resin (Qiagen) with LB1 (use 1 mL resin per 2 L culture). Add supernatant to resin and bind in batch for 1 h. Collect resin at 1000 × g, discard supernatant and wash in batch with 30 mL LB1 per mL resin. Transfer resin to empty column and wash with more LB1 (40 mL per mL resin). Elute with 10–15 mL Elution Buffer, taking 1 mL fractions and check purification by SDS-PAGE.
3. Pool fractions and concentrate using a centrifugal concentration device (such as Millipore Centriprep Ultracel YM-30 Cat No 4306) according to the manufacturer's instructions.

### **3.3 Ni-NTA Purification of ClpP Variant Proteins**

The following steps are performed at 4 °C unless stated otherwise.

1. Thaw cells in ice water bath for 15–20 min. Make sure that cells are well suspended and then pass through a French press at 25 kpsi. If you do not have a French press, sonication or freeze-thaw cycles with lysozyme can be done to break open the cells. If lysate is viscous, incubate with 500 U benzonase and 2 mM MgCl<sub>2</sub> for 20 min. Clarify lysate at 30,000 × g for 30 min.
2. Equilibrate NiNTA resin (Qiagen) with S-buffer (use 1 mL resin per 1 L culture). Add supernatant to resin and bind in batch for 1 h. Collect resin at 1000 × g and discard supernatant. Transfer resin to empty column and wash with 50 mL S-buffer per mL resin. Wash with W20 buffer. Elute with 15 mL W500 buffer per mL resin, taking 1.5 mL fractions and check purification by SDS-PAGE.

3. Pool fractions, concentrate and buffer exchange into ResBuffer using a centrifugal concentration device according to the manufacturer's instructions. Briefly, for buffer exchange, concentrated protein (1–2 mL for a 15 mL concentration device) is diluted with ResBuffer to the maximum volume of the concentration device and centrifuged following the manufacturer's instructions. Concentration and dilution is repeated for a total of three times.

### **3.4 Exogenous Biotinylation of Proteins with Biotin Ligase, BirA**

For <sup>35</sup>ClpXΔN or ClpP-biotin acceptor peptide-His<sub>6</sub>, concentrated proteins purified by Ni-NTA are buffer exchanged into Biotinylation Buffer by dialysis or using PD-10 Desalting Columns (GE Healthcare Life Sciences).

Add 50 mM bicine, pH 8.3, 4 mM ATP, 5 mM Mg-acetate, 1 mM d-biotin, and 1 μM BirA to the buffer exchanged protein. A BirA-His<sub>6</sub> plasmid is available through Addgene (#20857) with subsequent purification described by Howarth et al. [33]. Incubate reaction for 1–1.5 h at room temperature.

### **3.5 Gel Filtration of Proteins**

Multidomain substrate and <sup>35</sup>ClpXΔN are further purified on a Sephadryl S-300 HR size exclusion column in S300 Buffer. No more than 5 % of the total column volume is loaded on the column to ensure proper separation of proteins from the contaminants. Fractions are collected, checked by SDS-PAGE and pooled. If required, pooled fractions are concentrated using a centrifugal concentration device, apportioned into small aliquots, flash-frozen in liquid nitrogen and stored at –80 °C.

### **3.6 ClpP<sup>platform</sup> Ring Assembly**

ClpP<sup>platform</sup> consists of a ClpP variant with abrogated AAA+ unfoldase binding activity (M5A; Bewley et al. [34]) containing a biotin acceptor peptide (sequence GLNDIFEAQKIEWHE), C-terminal hexahistidine tag (ClpP<sup>M5A</sup>-bioAP-His<sub>6</sub>) and WT ClpP (expressed as ClpP-TEV-His<sub>6</sub>). ClpP tetradecamers are first disassembled into heptameric rings at high salt and no glycerol. Variants are then mixed and reassembled into 14-mers by lowering salt concentration and adding glycerol.

1. For M5A variant, exchange into BB1 and follow protocol for exogenous biotinylation of protein described above.
2. Add TEV (20 μM) to ClpP-TEV-His<sub>6</sub> and rock overnight at 4 °C. A His<sub>6</sub>-TEV-polyArg plasmid is available through Addgene (#8827) with subsequent purification described by Kapust et al. [35].
3. Pass overnight ClpP/TEV reaction over Ni-NTA column and wash with ResBuffer. Collect flow-through.
4. Mix excess of tagless WT ClpP variant with biotinylated M5A variant (5:1 tagless:M5A) and dialyze against Ring Separation Buffer for 3 h at room temperature.

5. Dilute ring separated mixture in 50 mM Hepes pH 7.6 and glycerol to give a final concentration of 0.3 M KCl and 15 % glycerol. Incubate at 4 °C overnight.
6. Pass ClpP<sup>platform</sup> mix over Ni-NTA column. Wash with 40 mL W-20B buffer per 1 mL Ni-NTA resin. Elute with W-500B buffer. Concentrate on centrifugal concentration device. Exchange into ClpP storage buffer.
7. Check by SDS-PAGE, apportion into small aliquots, flash-freeze in liquid nitrogen and store at –80 °C.

**3.7 PCR Amplification of 3500 bp DNA Tether Formation for Substrate and Aptamer**

1. PCR reaction mixture. Mix the following items: 715 µL Ultra-Pure water, 25 µL of 20 µM biotin primer in TE buffer, 25 µL of 20 µM amino primer in TE buffer, 20 µL of 10 mM dNTPs mixture, 5 µL of 50 ng/µL m13mp18 plasmid in TE buffer, 200 µL of 5× GC buffer, and 10 µL Phusion polymerase.
2. Mix thoroughly by gently pipetting the solution up and down.
3. Add 100 µL of PCR reaction mixture to 10 flat-cap PCR tubes.
4. Immediately transfer tubes to PCR machine and run the following program/cycles: (1) 98 °C during 30 s, (2) 98 °C during 10 s, (3) 49 °C during 30 s, (4) 72 °C during 90 s, (5) repeat steps 2–4 for a total of 35×, (6) 72 °C during 10 min, (7) keep at 4 °C.
5. Purify DNA fragments using the Qiagen PCR purification kit. In the last step, resuspend DNA using 30 µL of 1× PBS instead of the elution buffer included in the kit.
6. Measure nucleic acid concentration of the purified DNA using the NanoDrop. Normal yields are ~200 ng/µL (100 nM for 3500 bp dsDNA) (see Note 1).

**3.8 SMCC Based Coupling of 3500 bp DNA-Amine to Thiol-HaloTag or Thiol-Aptamer Ligand Conjugation**

1. Remove a 2 mg Sulfo-SMCC tube from the freezer and equilibrate to room temperature for 30 min.
2. Dissolve 2 mg Sulfo-SMCC in 200 µL UltraPure water by perforating the tube with a pipette tip only delivering the water. Mix for ~15 min.
3. Immediately combine 60 µL of Sulfo-SMCC solution with 60 µL NH<sub>2</sub>-DNA-Biotin at ~200 ng/µL.
4. Incubate for 2 h at room temperature on a rotator.
5. Remove unreacted Sulfo-SMCC with gel chromatography columns: Exchange buffer in six MBS6 tubes (see Note 2). Place 60 µL of DNA-SMCC solution in two columns. Spin column at 100 × g for 4 min and collect flow-through. Clean a total of three times.
6. Combine cleaned DNA-Maleimide with 2 µL of 100 mM Thiol-HaloTag Ligand (or 2 µL of Thiol-aptamer ligand), wrap in aluminum foil and rotate overnight at 4 °C.

7. Remove unreacted HaloTag Ligand using gel chromatography columns: Prepare 10 MBS6 columns by exchanging the buffer to PBS as described above in **step 5**. Place a maximum of 70  $\mu$ L DNA-HaloTag Ligand (or DNA-aptamer) on each column. Spin at  $1000 \times g$  for 4 min and retain flow-through. Clean a total of three times.
8. Measure nucleic acid concentration of the biotin-DNA-HaloTag Ligand (or biotin-DNA-aptamer) using the NanoDrop. The NanoDrop nucleic acid setting estimates the DNA concentration by measuring the ratio of absorption by nucleic acids at 260/280 nm. Normal yields produce ~100 ng/ $\mu$ L.

### **3.9 HaloTag-Based Coupling of 3500 bp DNA to Multi-domain Substrate**

Mix 3  $\mu$ L of 20  $\mu$ M substrate with 15  $\mu$ L of ~150 ng/ $\mu$ L (~0.1  $\mu$ M) HaloTag–3500 bp DNA–biotin in PBS (*see Note 3*). Wrap in aluminum foil to maintain in the dark. Incubate rotating overnight in a cold room or cold environment.

### **3.10 ATP Regeneration Solution at 20 $\times$**

1. Prepare the following stock solutions in PD buffer and keep on ice: 300 mM ATP (pH to 7.6 with KOH), 3 mg/mL creatine phosphokinase, 1 M creatine phosphate.
2. Mix the following on ice: 633.4  $\mu$ L PD, 200  $\mu$ L creatine phosphokinase stock, 100  $\mu$ L creatine phosphate stock, and 66.6  $\mu$ L ATP stock.
3. Vortex and aliquot 40  $\mu$ L volumes per tube.
4. Flash-freeze with liquid nitrogen and store at –80 °C. Aliquots are used within 3 months.

### **3.11 Chemical Etching of Glass Coverslips**

This procedure was adapted from a protocol originally used in the Block Lab.

1. Dissolve ~100 g of KOH pellets in ~300 mL ethanol in a large 1 L beaker. This takes about 30 min.
2. Load teflon coverslip racks with glass coverslips.
3. Fill 2 or more beakers with ~300 mL ddH<sub>2</sub>O and degas in a bath sonicator for 5 min.
4. Fill a beaker with ~300 mL ethanol and degas for 5 min.
5. Submerge one coverslip rack in the KOH/ethanol solution and sonicate for 5 min.
6. Wash the coverslips by dipping the rack up and down and spinning it in the ethanol beaker.
7. Wash the coverslips similarly in the ddH<sub>2</sub>O beaker.
8. Submerge the coverslip rack in the second ddH<sub>2</sub>O beaker and sonicate for 5 min.
9. Remove the coverslip rack and spritz each coverslip with a ddH<sub>2</sub>O spray bottle, use lots of water.

10. Spritz the coverslips with an ethanol filled spray bottle. Spritz until the ethanol smoothly flows off the coverslip surface.
11. Repeat the steps with other racks of coverslips.
12. Place coverslips in an oven for ~15 min.
13. Store the racks in sealed plastic Nalgene containers.

### **3.12 Flow Cell Construction**

1. Place two double sticky tape across the short axis of the glass slides with an approximately 5 mm space between them. This gap creates a volume between 10 and 15  $\mu\text{L}$ .
2. Place an etched coverslip on top of the two pieces of tape. Align so that the long axis of the coverslip is perpendicular to the long axis of the slide.
3. Use a wooden Q-tip, the bottom of an Eppendorf tube, or a large pipette tip to gently press the cover slip and slide together to seal the tape. Start at one edge of the tape and work systematically in one direction to push bubbles out of the tape/glass interface. The cloudy interface will become clearer when done properly.

### **3.13 Motility Assay and Wet Preparation**

1. Prepare surface blocking buffer: make a 1 mg/mL casein solution in PBS, filter with 0.2  $\mu\text{M}$  syringe filter and keep in a microtube on ice (*see Note 4*).
2. Prepare anti-clumping buffer: make a 5 mg/mL BSA solution in PD (typically 3–6 mL is made at this stage by weighing 15–30 mg of BSA), vortex to dissolve, filter with 0.2  $\mu\text{M}$  syringe filter, transfer 1.5 mL of buffer to a 1.5 mL microtube and add 15  $\mu\text{L}$  of DDT at 100 mM and keep on ice (*see Note 5*).
3. Introduce 0.5 ng/ $\mu\text{L}$  A08–3500 bp DNA–biotin into flow chamber and incubate for 30 min in a humidity chamber at room temperature (*see Note 6*). When adding solution to the flow cell for the first time, introduce adjacent to the cover glass centered on the opening of the channel and allow capillary action to fill the flow cell (*see Note 7*) (see also illustrations in Fig. 2).
4. Casein incubation: wash out unbound A08–DNA–biotin and coat the coverslip surface by flowing 100  $\mu\text{L}$  of casein solution through the chamber. Incubate for 20 min at room temperature (*see Note 8*).
5. Bead solution preparation: bead solutions are prepared during the casein incubation. In two separate tubes, mix 180  $\mu\text{L}$  PD with 3  $\mu\text{L}$  of 1  $\mu\text{m}$  and 1.26  $\mu\text{m}$  streptavidin bead stock solution, respectively. Wash beads by spinning down at  $8000 \times g$  for 3 min. Remove supernatant and resuspend

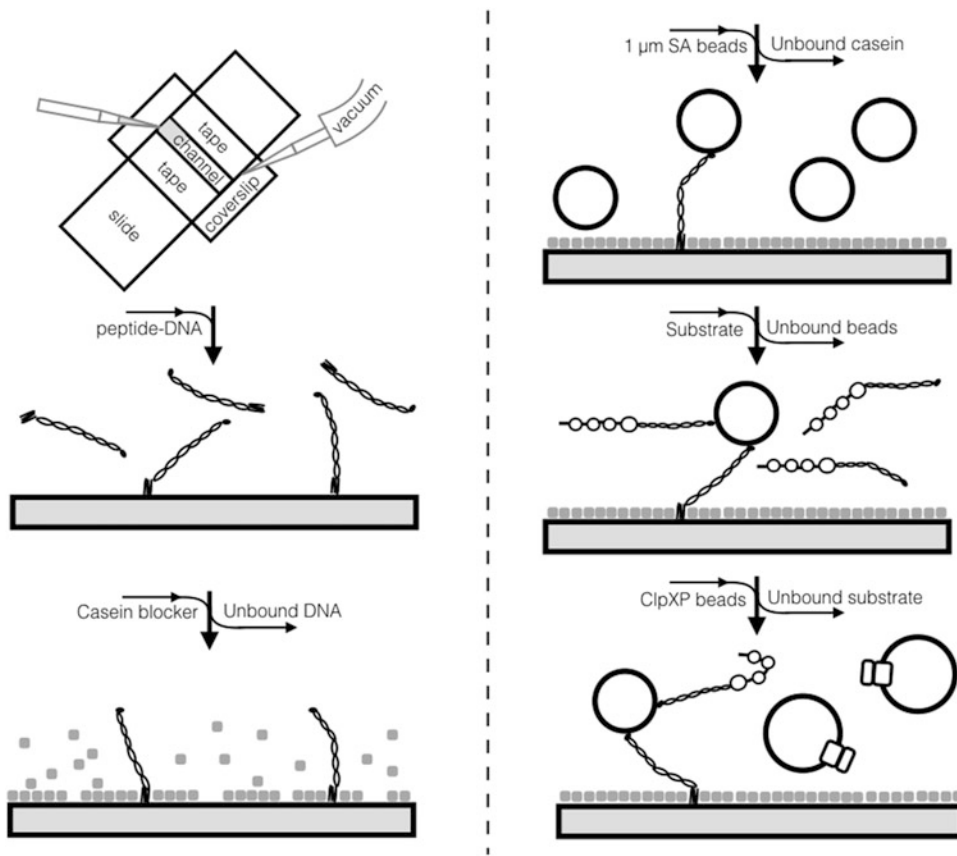


**Fig. 2** Cartoon outlining ClpXP flow cell preparation. A solution (~10  $\mu$ L) containing A08 peptide-DNA is added into a flow cell (*panel 1*) directly at the channel entry. The peptide-DNA is allowed to bind the glass coverslip (*panel 2*) by incubating in a humidity chamber. Casein blocking buffer is then introduced to coat the coverslip surface around the pre-bound peptide-DNA tethers (*panel 3*) to prevent nonspecific binding of assay components during upcoming steps. This step also removes unbound peptide-DNA. Streptavidin-coated beads (1  $\mu$ m in diameter) are then flowed in and allowed to bind the biotinylated surface-tethered DNA strands (*panel 4*). Unbound beads are removed using a buffer wash, after which substrate–DNA–biotin constructs are flowed into the slide chamber (*panel 5*) to bind the surface tethered beads. Excess substrate–DNA is then washed out, and a final reaction mixture that includes ClpXP beads (1.26  $\mu$ m in diameter) and ATP is flowed in (*panel 6*). At this point, the slide is sealed with vacuum grease and loaded onto the optical tweezers instrument for dumbbell assembly and measurement

thoroughly in 180  $\mu$ L PD. After centrifugation a white pellet of beads will be clearly visible near the bottom of the microtube. Use a pipette to remove the supernatant without disturbing the pellet. Repeat for a total of three washes. The final resuspension is in 60  $\mu$ L of BSA solution. Sonicate both bead solutions for 2 min at 40 % in a cup sonicator. Fill the cup sonicator with cold water, but not ice. After sonication, keep beads on ice.

6. Flow 20  $\mu\text{L}$  of cleaned 1  $\mu\text{m}$  streptavidin beads into flow chamber and incubate for 10 min. This chamber is cloudy like slightly diluted milk.
7. During the bead incubation, functionalize 1.26  $\mu\text{m}$  beads with ClpXP. Mix 14  $\mu\text{L}$  of 1.26  $\mu\text{m}$  streptavidin beads solution, 5  $\mu\text{L}$  of  $\sim$ 5–6  $\mu\text{M}$  ClpX, 2.3  $\mu\text{L}$  of 44.4  $\mu\text{M}$  ClpP, and 6  $\mu\text{L}$  of 10 $\times$  ATP with regeneration system and 60  $\mu\text{L}$  BSA solution. Allow protein to bind beads by incubating for 30 min at room temperature. To remove unbound ClpXP, spin down at  $6000 \times g$  for 1 min. Carefully remove supernatant as the pellet is very small/almost invisible. Look closely to make sure that pellet is not removed along with the supernatant and resuspend gently in 51  $\mu\text{L}$  BSA solution, 6  $\mu\text{L}$  of 20 $\times$  ATP regeneration system, and 3  $\mu\text{L}$  of 44.4  $\mu\text{M}$  ClpP. Keep on ice.
8. Wash the flow cell with 100  $\mu\text{L}$  of BSA solution to remove unbound beads. After this wash the flow cell is clear, not milky.
9. Mix 6  $\mu\text{L}$  of substrate-DNA-biotin with 12  $\mu\text{L}$  of BSA solution, flow in channel and incubate for 20 min at room temperature.
10. Wash channel with 100  $\mu\text{L}$  BSA solution to remove unbound substrate-DNA-biotin.
11. Mix the following immediately before flowing into flow cell: 15  $\mu\text{L}$  of 1.26  $\mu\text{m}$  ClpXP functionalized beads, 8.1  $\mu\text{L}$  of BSA solution, 6  $\mu\text{L}$  of 20 $\times$  ATP with regeneration system, 0.3  $\mu\text{L}$  of 100 $\times$  catalase, 0.3  $\mu\text{L}$  of 100 $\times$  glucose oxidase, and 0.3  $\mu\text{L}$  of 100 $\times$  glucose.
12. Flow into channel and seal chamber with vacuum grease. Start a timer for 1 h after which ATP regeneration system is no longer effective.

### **3.14 Motility Assay Measurement**

1. Warm up instrument by turning lasers and other equipment on prior to the wet assay preparation. Load a dummy flow cell filled with water and adjust the power of the lasers to achieve the desired trap stiffnesses. Trap 2 is typically 3–5 $\times$  stiffer than trap 1. Typically, powers are measured prior to the laser being reflected into the objective. For a force clamp of  $\sim$ 10 pN, our instrument requires  $\sim$ 220 mW for Trap 2 and 75 mW for Trap 1 measured before the microscope objective.
2. Load slide on microscope. Typically only the fine focus is adjusted as the day-to-day height is very consistent given the tight tolerances on coverslip and tape dimensions. A single drop of DF oil (Cargille) is used between the objective and cover glass. Between the microscope slide and condenser, the laser beams can be quite wide and thus generous  $\sim$ 3–4 drops of Type A (Nikon) oil is recommended.

3. Start LabVIEW programs including Trap 1 and Trap 2 calibration routines, voltage recording routines and a program to move the AOD controlled trap. Voltages are typically recorded at 3000 scans/s. Filtering is typically set to 1.5 kHz. Have these programs ready to go as open windows on the recording computer so that routines can be easily initiated.
4. Focus near the surface and survey fields of view to identify suitable locations with 1  $\mu\text{m}$  substrate- and A08-DNA-tethered beads where performing the assay would be unimpeded by neighboring beads (see illustrations in Fig. 3).
5. Turn on Trap 1 and capture a 1.26  $\mu\text{m}$  ClpXP coated bead and bring near the surface bound substrate beads.
6. Fish along the diagonal to achieve a connection by mechanically moving or tapping the stage position micrometers to see if there is inter-bead tension. When you see inter-bead tension, turn on Trap 2 to capture the 1  $\mu\text{m}$  substrate-bound bead and displace the stage horizontally away from Trap 1 to break the connection between the 1  $\mu\text{m}$  bead and surface. Defocus to drop the cover glass slightly below the suspended dumbbell so that the beads are clear of interacting with the surface.
7. Check the voltage recording for Trap 1 to verify that a single tether is connected between the beads. Single tethers will provide consistent voltages at these stages. Start recording Trap 1 and Trap 2 position voltages.
8. Adjust the MHz values of Trap 1 to move to the passive force clamp location along the diagonal. This is typically done in two or more stages so that the bead is not lost and kicked out of the trap by too drastic of a move. The passive force clamp region MHz values are 25.93/25.93 for our instrument, with conversions of approximately 3400 nm/MHz on each axis. Both vertical and horizontal AOD's are moved to maintain the dumbbell oriented along the diagonal.
9. Record the experiment as illustrated in Figs. 4 and 5. Be as quiet as possible and keep the room dark as light signals may be detected by the position sensing subsystem. By zooming the voltage window one may be able to directly watch small displacements, typically unfolding events, although usually data processing after the experiment is required to ensure the presence or lack of successful degradation activity for a specific dumbbell. Tether connections can break spontaneously or at the end of the motility record indicating the experiment is finished.
10. Calibrate beads at the end of each dumbbell. First move Trap 1 back to the 26.00/26.00 MHz location and calibrate Trap 1 by running the fifth order calibration routine for the

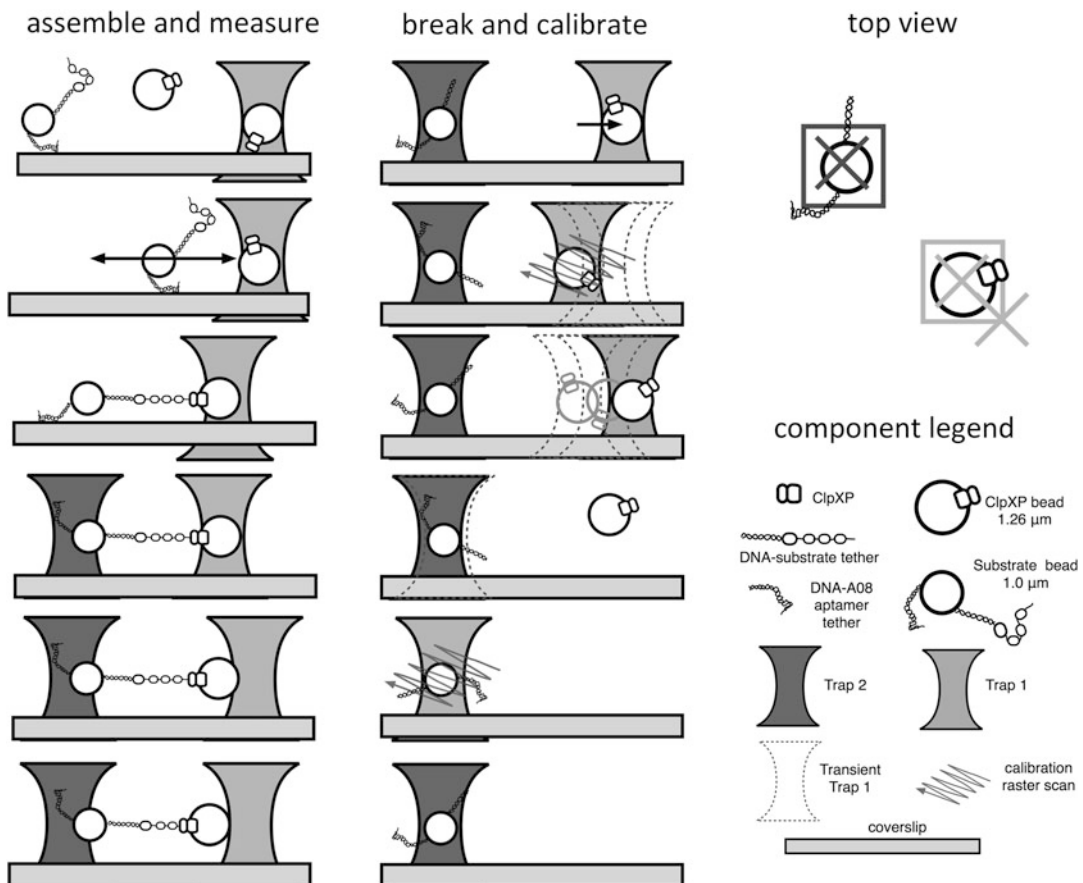


**Fig. 3** Scenes depicting a 12-step process for active assembly, measurement and calibration of the ClpXP mechanical assay. Scenes are read from *top* to *bottom*. *Assemble and measure.* *Scene 1:* substrate tethered beads are attached to the cover glass surface through a DNA-aptamer tether. Slightly larger ClpXP labeled beads are free in solution, trapped with Trap 1 and brought in the vicinity of the substrate bead. *Scenes 2 and 3:* a fishing procedure is initiated by gently moving the ClpXP bead near the substrate bead until correlated motion is observed indicating recognition and attachment of the substrate. *Scene 4:* Trap 2 is then turned on and the sample translated away, diagonally in the XY plane, from the ClpXP bead as well as dropped in Z so that the aptamer-surface interaction breaks and a suspended dual bead assay is achieved. *Scene 5:* Trap 1 is then moved away from Trap 2 to achieve the passive force clamp location. This motion is performed in two or three moves so that the bead can be maintained stably in Trap 1 during the sudden trap displacements. *Scene 6:* the system is held in the passive force clamp geometry while recording bead position to observe motility until break. *Break and calibrate.* Upon break in *Scene 7*, Trap 1 is moved back to the measurement zone (*Scene 8*) and calibrated through a raster scan displacement to map position to voltage signals. Again, Trap 1 is moved in stages so that the bead can be held without release. *Scene 9:* Trap 1 moves the ClpXP bead away, near the passive force clamp location, so that it can be released at a location where Trap 2 will not capture it. *Scene 10:* Trap 1 is then moved, while off, to overlap with the Trap 2 location. *Scene 11:* Trap 1 is turned on and Trap 2 is turned off. Trap 1 then raster scans the substrate bead to map the position calibration for the Trap 2 location. *Scene 12:* at the end of the raster scan, Trap 2 is then turned on and Trap 1 is turned off, so that the stiffness of Trap 2 with the substrate bead can be determined.

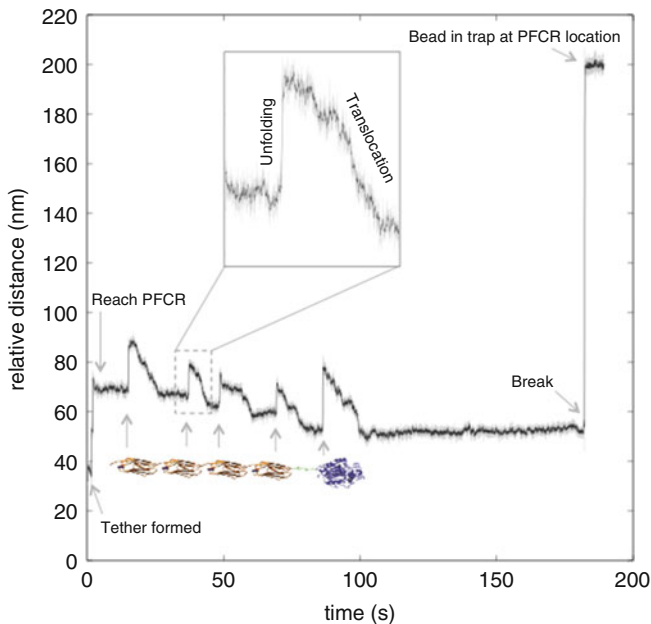


**Fig. 4** Representative trace showing global bead position and motility record. Initially, position recording is started within ~5 s of dumbbell formation. Then, the position of Trap 1 is moved away to place the bead in Trap 1 at the passive force clamp region (PFCR). Usually, 2–3 AOD steps are used to reach this trap location. Upon reaching the PFCR, position data is recorded until dumbbell rupture/break, which is evident by a large change in bead position as both beads return to the center of their respective trap positions. Before tether rupture, successful unfolding and translocation events (*inset*) results in small bead movements, which are often difficult to observe during acquisition, but are evident after data processing. Upon dumbbell rupture, continuous position recording is stopped and saved, and position/force calibration procedures are carried out

“Trap 1 location.” After the Trap 1 calibration, move Trap 1 away from Trap 2 (such as by stepping past the force clamp region) and release the 1.26  $\mu\text{m}$  bead about 1  $\mu\text{m}$  farther away so that it does not fall into Trap 2. Turn off Trap 1 and move to overlap with Trap 2 (at 26.50/26.50 MHz). Turn on Trap 1 and turn off Trap 2, which should be holding the 1.0  $\mu\text{m}$  substrate bead at the same location. Run the fifth order calibration routine for the “Trap 2 location.” After the position scanning portion of the program, but before the stiffness determination, turn on Trap 2 and turn off Trap 1. This trick allows for mapping the position space for the “Trap 2 location” using the AOD controlled trap, while recording the stiffness of Trap 2 used in the experiment.

11. Two file sets of fifth order parameters, one for the Trap 1 location and one for the Trap 2 location are recorded along with two stiffness files and data streams for the position voltages for each trap.

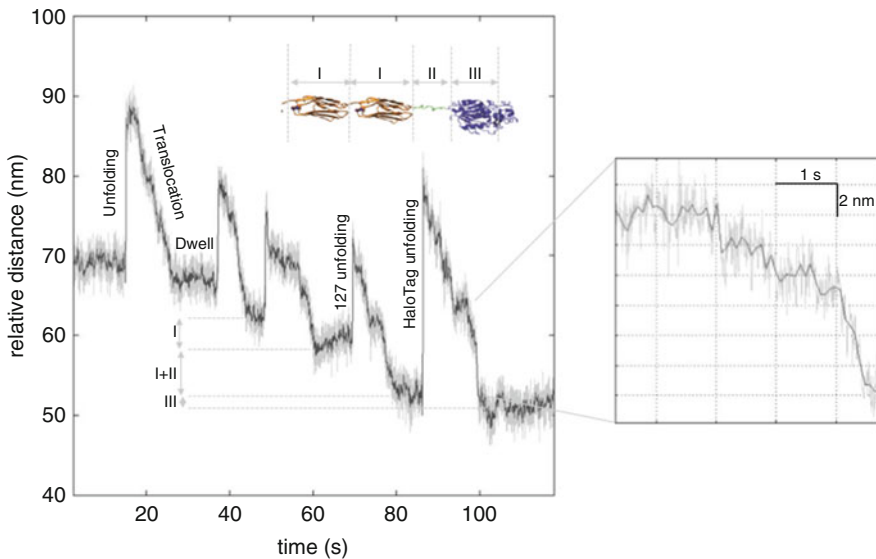


**Fig. 5** Signature features of a single molecule degradation trace. For ClpXP mediated degradation of multidomain substrates, such as the Halo-V13P( $\times 4$ )-ssA substrate in this trace, tracking changes in inter-bead distances with time shows abrupt displacements in bead position directly followed by continuous slower decreases in distance. The abrupt increases in relative distance correspond to the unfolding of single domains. Depending on the domain being unfolded the magnitude of the distance change varies. For example, the first four unfolding events ( $\sim 15$  nm) in this trace correspond to V13P domains, while the fifth larger unfolding event ( $\sim 25$  nm) corresponds to the terminal HaloTag domain. Translocation of each domain directly follows unfolding and is evident by a stepwise decrease in distance. The steps during translocation range in size from  $\sim 1\text{--}4$  nm (inset). Following translocation of a domain, there are periods of constant inter-bead distance, which correspond to unfolding dwells (the time necessary for ClpXP to achieve successful unfolding of the abutting domain). Consecutive dwell periods are spaced by the distance of a folded domain (I), the folded domain plus a linker (I + II), or the portion of HaloTag successfully unfolded (III)

### 3.15 Passive Force Clamp Determination

The passive force clamp makes use of the nonlinear stiffness at the extreme edge of an optical trap. Typically, linear ranges where “Hookean” type behavior is observed lie within  $\sim 100\text{--}150$  nm of the trap center. At the edge of the trap, the force becomes weaker and the transition region represents a “constant force zone” as described by Greenleaf et al. [36]. Determining the passive force clamp location can be performed using a DNA tether or with a ClpX tether as shown in Fig. 6.

---

## 4 Notes

1. DNA gel electrophoresis is performed to ensure the PCR amplification reaction and purification yields the desired length and quality of DNA. Here, standard DNA gel electrophoresis methods are employed (Owl EasyCast B1 Mini Gel

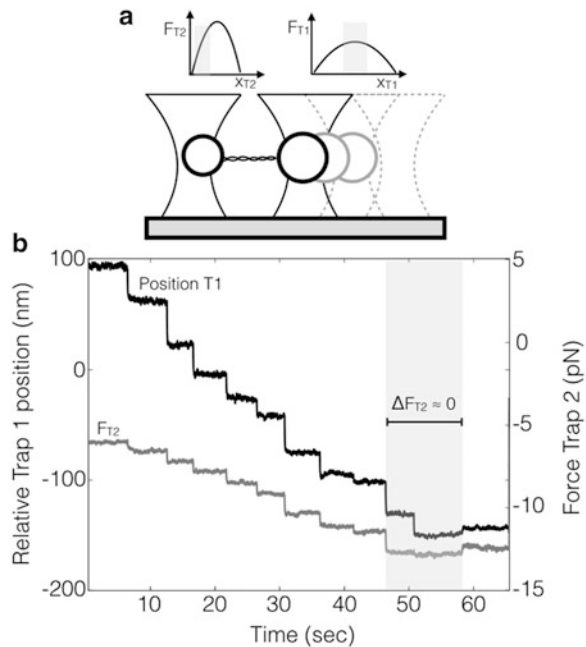


**Fig. 6** Passive force clamp (PFC) tutorial. To determine the location of the PFCR, we use the same procedure described in this chapter to form dumbbells, except the Biotin–DNA–HaloTag–Substrate construct is replaced with a strand of Biotin–DNA–Digoxigenin and an Anti-digoxigenin-coated bead is used instead of the ClpXP-coated bead. Upon formation of the DNA dumbbell, Trap 1 is stepped away from Trap 2 (Panel a) using AOD movements. Since Trap 2 is three times stiffer than Trap 1, as Trap 1 is moved away, the bead in Trap 1 is in turn pulled out from the center of the trap. The Trap 1 position is continually stepped until the dumbbell connection breaks, or the bead in Trap 1 pulls out far enough so that Trap 2 swallows it. The position of the PFC is evident when viewing the position and forces plot for the test. The trace in Panel (b) shows that the force in Trap 2 changes with every AOD step taken in Trap 1, except at ~50 s where the force in Trap 2 remains nearly constant when an AOD step is taken in Trap 1. We note the number of AOD steps required to place the bead in Trap 1 in this region, and use this position during the ClpXP experiments

Electrophoresis System). An agarose gel is used (VWR EM-2120) with a dsDNA ladder mixture (Bayou biolabs L-201) and a SybrGreen at 10,000 $\times$  (Molecular Probes S7563) to indicate the DNA bands. If the band is not nicely resolved, for example squiggly or smeared, it is possible the concentration of DNA in the well is too high. Titrate the concentration for better band resolution.

2. During the SMCC conjugation, primary amines must not be present. Samples in Tris buffer (TE) must undergo a buffer exchange: Invert/mix the MBS6 or MBS30 column, snap tip, and drain for 2 min in a 2 mL tube. Empty flow-through, spin at 1000  $\times$   $g$  for 2 min, and discard flow-through. Load 500  $\mu$ L PBS, spin 1000  $\times$   $g$  for 1 min and discard flow-through. Repeat the PBS load and spin a total of three times.

3. Excess substrate is needed for sufficient labeling of the long DNA spacer. Excess substrate is removed during the dumbbell assembly process steps.
4. This solution is made fresh every day and used within 6 h.
5. This solution is made fresh everyday and used within 6 h, and BSA must always be stored at 4 °C.
6. Humidity chambers are formed using an empty pipette tip box. The bottom is filled with water. Flow cells are stored on the lid of the empty pipette tip holding manifold with the lid closed. The humidity chamber is vital in preventing evaporation of the flow cell contents during incubation periods in this assay. All incubations are at room temperature.
7. Normally 3–5 tethers per field of view are desired, so the A08–DNA concentration can be tuned to achieve the appropriate density.
8. A vacuum linked pipette tip is used to establish flow through the channel. Flow rates can be controlled more readily through such application of vacuum on the opposite side of a channel. Although liquid is initially introduced into an empty channel directly near the cover glass slide inlet, subsequent washes are introduced by dripping solution farther away from the inlet to help control flow rates. Flow rates are slow (typically 100 µL over 3 min) to avoid unbinding and shearing of surface bound flow cell contents such as A08-tethered beads.

## Acknowledgements

We are grateful to Bob Sauer, Tania Baker and members of the Sauer, Baker and Lang Labs who over the years developed and refined the protocols and methods detailed herein. This work was supported by grants from the National Science Foundation (MCB-1330792) and the NIH (GM-101988). J.C.C was supported in part by a GAANN fellowship from the US Department of Education under grant no. P200A090323.

## References

1. Olivares AO, Baker TA, Sauer RT (2016) Mechanistic insights into bacterial AAA+ proteases and protein-remodelling machines. *Nat Rev Microbiol* 14:33–44
2. Sauer RT, Baker TA (2011) AAA+ proteases: ATP-fueled machines of protein destruction. *Annu Rev Biochem* 80:587–612
3. Striebel F, Kress W, Weber-Ban E (2009) Controlled destruction: AAA+ ATPases in protein degradation from bacteria to eukaryotes. *Curr Opin Struct Biol* 19:209–217
4. Wendler P, Ciniawsky S, Kock M, Kube S (2012) Structure and function of the AAA+ nucleotide binding pocket. *Biochim Biophys Acta* 1823:2–14
5. Erdmann R (2012) AAA ATPases: structure and function. *Biochim Biophys Acta* 1823:1
6. Gennerich A, Carter AP, Reck-Peterson SL, Vale RD (2007) Force-induced bidirectional stepping of cytoplasmic dynein. *Cell* 131: 952–965

7. Mallik R, Carter BC, Lex SA, King SJ, Gross SP (2004) Cytoplasmic dynein functions as a gear in response to load. *Nature* 427:649–652
8. Smith DE, Tans SJ, Smith SB, Grimes S, Anderson DL, Bustamante C (2001) The bacteriophage straight phi29 portal motor can package DNA against a large internal force. *Nature* 413:748–752
9. Moffitt JR, Chemla YR, Aathavan K, Grimes S, Jardine PJ, Anderson DL, Bustamante C (2009) Intersubunit coordination in a homomeric ring ATPase. *Nature* 457:446–450
10. Rao VB, Feiss M (2008) The bacteriophage DNA packaging motor. *Annu Rev Genet* 42: 647–681
11. Ogura T, Wilkinson AJ (2001) AAA+ superfamily ATPases: common structure–diverse function. *Genes Cells* 6:575–597
12. Egli M, Johnson CH (2013) A circadian clock nanomachine that runs without transcription or translation. *Curr Opin Neurobiol* 23: 732–740
13. Diaz-Valencia JD, Morelli MM, Bailey M, Zhang D, Sharp DJ, Ross JL (2011) Drosophila katanin-60 depolymerizes and severs at microtubule defects. *Biophys J* 100:2440–2449
14. Desantis ME, Shorter J (2012) The elusive middle domain of Hsp104 and ClpB: location and function. *Biochim Biophys Acta* 1823: 29–39
15. Hwang W, Lang MJ (2013) Nucleotide-dependent control of internal strains in ring-shaped AAA+ motors. *Cell Mol Bioeng* 6: 65–73
16. Erzberger JP, Berger JM (2006) Evolutionary relationships and structural mechanisms of AAA+ proteins. *Annu Rev Biophys Biomol Struct* 35:93–114
17. Baker TA, Sauer RT (2012) ClpXP, an ATP-powered unfolding and protein-degradation machine. *Biochim Biophys Acta* 1823:15–28
18. Martin A, Baker TA, Sauer RT (2005) Rebuilt AAA + motors reveal operating principles for ATP-fuelled machines. *Nature* 437:1115–1120
19. Shin Y, Davis JH, Brau RR, Martin A, Kenniston JA, Baker TA, Sauer RT, Lang MJ (2009) Single-molecule denaturation and degradation of proteins by the AAA+ ClpXP protease. *Proc Natl Acad Sci U S A* 106:19340–19345
20. Martin A, Baker TA, Sauer RT (2008) Protein unfolding by a AAA+ protease is dependent on ATP-hydrolysis rates and substrate energy landscapes. *Nat Struct Mol Biol* 15:139–145
21. Aubin-Tam ME, Olivares AO, Sauer RT, Baker TA, Lang MJ (2011) Single-molecule protein unfolding and translocation by an ATP-fueled proteolytic machine. *Cell* 145:257–267
22. Maillard RA, Chistol G, Sen M, Righini M, Tan J, Kaiser CM, Hodges C, Martin A, Bustamante C (2011) ClpX(P) generates mechanical force to unfold and translocate its protein substrates. *Cell* 145:459–469
23. Sen M, Maillard RA, Nyquist K, Rodriguez-Aliaga P, Presse S, Martin A, Bustamante C (2013) The ClpXP protease unfolds substrates using a constant rate of pulling but different gears. *Cell* 155:636–646
24. Cordova JC, Olivares AO, Shin Y, Stinson BM, Calmat S, Schmitz KR, Aubin-Tam ME, Baker TA, Lang MJ, Sauer RT (2014) Stochastic but highly coordinated protein unfolding and translocation by the ClpXP proteolytic machine. *Cell* 158:647–658
25. Olivares AO, Nager AR, Iosefson O, Sauer RT, Baker TA (2014) Mechanochemical basis of protein degradation by a double-ring AAA+ machine. *Nat Struct Mol Biol* 21:871–875
26. Iosefson O, Olivares AO, Baker TA, Sauer RT (2015) Dissection of axial-pore loop function during unfolding and translocation by a AAA+ proteolytic machine. *Cell Rep* 12:1032–1041
27. Stinson BM, Baytshtok V, Schmitz KR, Baker TA, Sauer RT (2015) Subunit asymmetry and roles of conformational switching in the hexameric AAA+ ring of ClpX. *Nat Struct Mol Biol* 22:411–416
28. Kenniston JA, Baker TA, Fernandez JM, Sauer RT (2003) Linkage between ATP consumption and mechanical unfolding during the protein processing reactions of an AAA+ degradation machine. *Cell* 114:511–520
29. Karzai AW, Roche ED, Sauer RT (2000) The SsrA-SmpB system for protein tagging, directed degradation and ribosome rescue. *Nat Struct Biol* 7:449–455
30. Lang MJ, Asbury CL, Shaevitz JW, Block SM (2002) An automated two-dimensional optical force clamp for single molecule studies. *Biophys J* 83:491–501
31. Visscher K, Gross SP, Block SM (1996) Construction of multiple-beam optical traps with nanometer-resolution position sensing. *IEEE J Sel Top Quantum Electron* 2:1066–1076
32. Kenniston JA, Baker TA, Sauer RT (2005) Partitioning between unfolding and release of native domains during ClpXP degradation determines substrate selectivity and partial processing. *Proc Natl Acad Sci U S A* 102: 1390–1395
33. Howarth M, Takao K, Hayashi Y, Ting AY (2005) Targeting quantum dots to surface proteins in living cells with biotin ligase. *Proc Natl Acad Sci U S A* 102:7583–7588

34. Bewley MC, Graziano V, Griffin K, Flanagan JM (2006) The asymmetry in the mature amino-terminus of ClpP facilitates a local symmetry match in ClpAP and ClpXP complexes. *J Struct Biol* 153:113–128
35. Kapust RB, Tozser J, Fox JD, Anderson DE, Cherry S, Copeland TD, Waugh DS (2001) Tobacco etch virus protease: mechanism of autolysis and rational design of stable mutants with wild-type catalytic proficiency. *Protein Eng* 14:993–1000
36. Greenleaf WJ, Woodside MT, Abbondanzieri EA, Block SM (2005) Passive all-optical force clamp for high-resolution laser trapping. *Phys Rev Lett* 95:208102

# Chapter 13

## Deciphering the Molecular Mechanism of the Bacteriophage φ29 DNA Packaging Motor

Shixin Liu, Sara Tafoya, and Carlos Bustamante

### Abstract

The past decade has seen an explosion in the use of single-molecule approaches to study complex biological processes. One such approach—optical trapping—is particularly well suited for investigating molecular motors, a diverse group of macromolecular complexes that convert chemical energy into mechanical work, thus playing key roles in virtually every aspect of cellular life. Here we describe how to use high-resolution optical tweezers to investigate the mechanism of the bacteriophage φ29 DNA packaging motor, a ring-shaped ATPase responsible for genome packing during viral assembly. This system illustrates how to use single-molecule techniques to uncover novel, often unexpected, principles of motor operation.

**Key words** Single-molecule manipulation, Optical tweezers, Viral DNA packaging, Molecular motor, Ring ATPase

---

### 1 Introduction

Many essential cellular processes are driven by nanometer-scale machine-like devices, known as molecular motors, which harness energy from chemical reactions to perform mechanical tasks. Single-molecule manipulation instruments, such as optical tweezers, are ideally suited for studying molecular motors, because the characteristic mechanical parameters of the motor—force, step size, cycle time, etc.—are variables that can be directly measured using these instruments.

One fascinating example of nanomachines is the packaging motor found in double-stranded DNA viruses, including tailed bacteriophages and human pathogens such as herpesviruses [1]. The packaging motor contains multiple ATPase subunits, which form a ring structure and thread viral DNA through the central pore into a preformed protein capsid. The packaging motor of bacteriophage φ29, a small virus that infects *Bacillus subtilis*, is a model system for studying the mechanism of viral packaging and, more generally, the operation of the ubiquitous ring NTPases [2].

These studies have been made possible by the existence of a robust *in vitro* reconstituted system and extensive biochemical, structural, and single-molecule results. In particular, a series of optical-tweezers-based assays enabled us to tackle fundamental and sophisticated questions regarding the force generation and intersubunit coordination of the  $\varphi$ 29 motor [3–8]. The complete mechanochemical model derived from these studies, which precisely describes the coordinated actions of all ATPase subunits (Fig. 1), showcases the power of optical tweezers in elucidating the mechanism and regulation of molecular motors.

In this chapter, we describe protocols for the single-molecule DNA packaging assay with the  $\varphi$ 29 motor, which includes bulk activity assessment, microfluidic chamber construction, sample preparation, instrument operation, data acquisition, and data analysis. It is worth noting that the protocols for the  $\varphi$ 29 system have been adapted to study other viral packaging motors and ring ATPases, yielding many interesting features of motor dynamics and providing a broad panorama of the diversity of operation of these important cellular machines [9].

## 2 Materials

### 2.1 Bulk DNA Packaging Assay

1. Viral components:  $\varphi$ 29 proheads and ATPase gp16 (store in small aliquots at  $-80^{\circ}\text{C}$ ),  $\varphi$ 29 genomic DNA with terminal gp3 protein (DNA-gp3, store at  $4^{\circ}\text{C}$ ). Purified as described in [10]. *See Note 1.*
2. 0.025- $\mu\text{m}$  membrane filter (Millipore).
3. 1 M Tris-HCl (pH 7.8).
4. 0.5 $\times$  TMS buffer: 25 mM Tris-HCl (pH 7.8), 50 mM NaCl, and 5 mM MgCl<sub>2</sub>.
5. 100 mM ATP. Store at  $-20^{\circ}\text{C}$ .
6. DNase I (Calbiochem).
7. 0.5 M EDTA.
8. Proteinase K (New England Biolabs).

### 2.2 DNA Preparation for Single-Molecule Packaging Assay

1. DNA-gp3 (see above).
2. 1 M Tris-HCl (pH 7.8).
3. Selected restriction enzyme ClaI, XbaI, BstEII, or NcoI with its respective 10 $\times$  buffer (New England Biolabs).
4. Klenow fragment exo<sup>-</sup> (New England Biolabs).
5. Biotinylated deoxyribonucleotides (Invitrogen).
6. T4 DNA ligase and 10 $\times$  T4 ligase buffer (New England Biolabs).
7. 100 mM ATP.
8. PCR thermocycler.

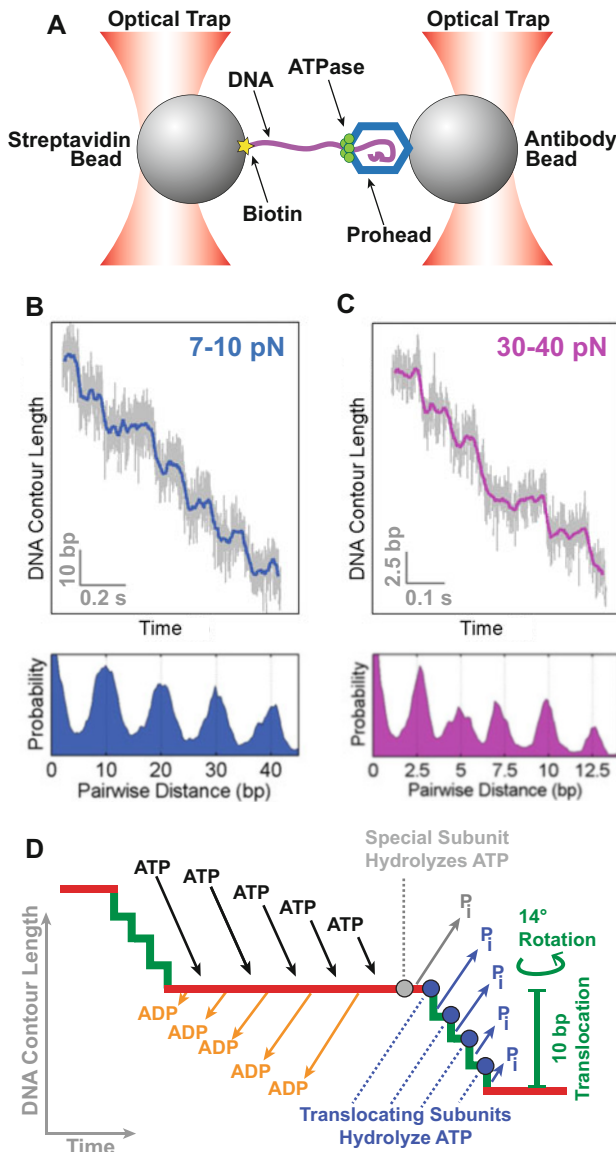


**Fig. 1** Single-molecule DNA packaging assay with the  $\varphi 29$  motor. **(a)** Geometry of the dual-trap optical tweezers experiment. **(b)** (Top) A sample packaging trace collected at an external force of 7–10 pN. (Bottom) The corresponding pairwise distance distribution (PWD) demonstrates that DNA is translocated in 10-bp bursts in this force regime. 2500-Hz raw data are shown in gray and 250-Hz filtered data in blue. **(c)** A sample packaging trace collected at an external force of 30–40 pN (Top) and its corresponding PWD (Bottom). In this force regime the 10-bp bursts break up into four 2.5-bp steps. **(d)** Mechanicochemical model of the  $\varphi 29$ -packaging motor. ADP release and ATP binding events in the five ATPase subunits occur in an interlaced fashion during the dwell phase (red). One of the five subunits is “special” in that its hydrolysis and inorganic phosphate release do not result in DNA translocation, but rather signal the other four subunits to hydrolyze ATP, release  $P_i$ , and each translocate 2.5 bp of DNA during the burst phase (green). In each cycle, 10-bp DNA translocation is accompanied by a 14° DNA rotation relative to the motor. This rotation ensures that the DNA makes specific contacts with the same special subunit in the next cycle. Adapted from refs. [7] and [8] with permission from Elsevier

**2.3 Bead Preparation**

1. 1× phosphate buffered saline (PBS buffer).
2. 0.5× TMS buffer (see above).
3. Polystyrene beads stock solution: 1 % (w/v) 0.88-μm Protein G-coated beads, 1 % (w/v) 0.90-μm streptavidin-coated beads (Spherotech). Store at 4 °C.
4. Vortexer.
5. Rotator.
6. Anti-phage antibodies stock solution (1 mg/mL) (produced by the Jardine and Grimes Lab, University of Minnesota). Store in 20 μL aliquots at –80 °C.

**2.4 Microfluidic Chamber Construction**

1. Cover glass (VWR, size #1, 24 × 60 mm).
2. Nescofilm (Karlann).
3. Laser cutter (Universal Laser Systems).
4. Glass dispenser tube (King Precision Glass, 0.1-mm diameter).
5. Heat block (100 °C).
6. PE20 polyethylene tubing (BD Intramedic).

**2.5 Single-Molecule Packaging Assay**

1. 10× TMS buffer: 500 mM Tris–HCl (pH 7.8), 1 M NaCl, and 100 mM MgCl<sub>2</sub>.
2. BSA (20 mg/mL) (New England Biolabs).
3. RNaseOUT (40 units/μL) (Invitrogen).
4. 100 mM ATP.
5. 100 mM ATPγS (Sigma-Aldrich).
6. Oxygen-scavenging system: 100 μg/mL glucose oxidase, 20 μg/mL catalase, and 5 mg/mL dextrose (Sigma-Aldrich).
7. ApaLI (10 units/μL) (New England Biolabs).
8. 1-mL syringes (BD).
9. Needles (BD PrecisionGlide, 26 G × ½ in.).
10. High-resolution dual-trap optical tweezers. *See Note 2.*

**2.6 Data Analysis**

1. Custom LabView software.
2. Custom MATLAB software.

**3 Methods****3.1 Bulk DNA Packaging Assay**

The in vitro DNA packaging activity of the motor is evaluated by measuring the amount of packaged DNA inside the phage capsid that is resistant to DNase digestion [10].

1. DNA-gp3, isolated from phage-infected *B. subtilis* cells or purified phages, is dialyzed on a 0.025-μm membrane filter against 10 mM Tris–HCl (pH 7.8) for 45 min.

2.  $\varphi29$  proheads ( $1 \times 10^{11}$  copies) are mixed with DNA-gp3 ( $5 \times 10^{10}$  copies) and gp16 [ $(1.2\text{--}1.5) \times 10^{12}$  copies] in  $0.5\times$  TMS buffer in a total volume of 18  $\mu\text{L}$ . The mixture is incubated for 5 min at room temperature.
3. Add 2  $\mu\text{L}$  of 5 mM ATP and incubate the mixture for 15 min at room temperature.
4. Unpackaged DNA is digested by adding DNase I to 1  $\mu\text{g}/\text{mL}$ . Incubate for 10 min at room temperature.
5. To deactivate DNase I and release the packaged DNA from viral capsids, the mixture is treated with 25 mM EDTA (final concentration) and 500  $\mu\text{g}/\text{mL}$  Proteinase K (final concentration) for 30 min at 65 °C.
6. DNA packaging efficiency is evaluated by running a 1 % agarose gel.

### **3.2 DNA Preparation for Single-Molecule Packaging Assay**

The  $\varphi29$  genomic DNA is 19.3-kbp in length, with one copy of the terminal protein gp3 covalently bound to each 5' terminus. To systematically investigate the effect of capsid filling level on the motor's packaging behavior, we use DNA substrates of various lengths in the single-molecule packaging assay (Table 1) [8].

1. After dialysis in 10 mM Tris-HCl, DNA-gp3 is digested with one selected restriction enzyme (Table 1). Use 1 unit of enzyme to digest 1  $\mu\text{g}$  of DNA-gp3 for 1 h. Choose the optimal buffer and temperature according to the manufacturer's protocol.
2. The 5' overhang from the restriction cut is filled in with biotinylated nucleotides using the Klenow fragment of DNA polymerase I (exo<sup>-</sup> mutant). Use 1 unit of Klenow fragment and 100 pmol of nucleotides for every 1  $\mu\text{g}$  of DNA-gp3. Set the reaction at 37 °C for 30 min, then 75 °C for 15 min to deactivate the enzyme.
3. Dialyze the solution on a 0.025- $\mu\text{m}$  membrane filter against 10 mM Tris-HCl (pH 7.8) for 45 min. Store the DNA substrate at 4 °C. See Note 3.

**Table 1**  
**Summary of the different DNA lengths used in the single-molecule packaging experiments**

Capsid filling level (%)	DNA length (bp)	Restriction enzyme used	Remaining overhang
32	6147	ClaI	5' CG
46	8929	XbaI	5' CTAG
65	12,466	BstEII	5' GTCAC
78	15,023	NcoI	5' CATG

4. To generate DNA substrates longer than the  $\varphi$ 29 genome length, a biotinylated DNA piece is ligated to the enzyme-digested DNA-gp3. For example, to create a 21-kbp DNA substrate, first generate a 6-kbp DNA piece that is PCR amplified from lambda DNA using a biotinylated primer and cut with NcoI; then ligate it to NcoI-cut DNA-gp3. Use 5× molar excess of 6-kbp DNA to DNA-gp3. Use New England Biolabs' standard T4 DNA ligase protocol.
5. After the ligation reaction, dialyze the mixture in 10 mM Tris-HCl (pH 7.8) for 45 min. Store the product at 4 °C.

### **3.3 Bead Preparation**

In the single-molecule experiment, a prohead-ATPase-DNA complex is tethered between two beads held in two laser traps (Fig. 1a). The viral capsid is attached to a bead coated with antibodies against the major capsid protein gp8. The biotinylated distal end of the DNA substrate is attached to a streptavidin-coated bead.

#### *3.3.1 Preparing Antibody-Coated Beads*

1. Pipette 40 µL of 1 % (w/v) 0.88-µm Protein G-coated beads in a 1.5-mL microcentrifuge tube.
2. Add 1× PBS buffer to a total volume of 200 µL.
3. Resuspend the beads by vortexing the solution on high speed for 30 s. Spin the beads down at 10,000  $\times \text{g}$  for 2 min in a benchtop centrifuge.
4. Remove the supernatant.
5. Repeat steps 2–4 twice.
6. Resuspend the pellet in 30 µL of 1× PBS buffer.
7. Add 20 µL of anti-phage antibodies (1 mg/mL; purified from rabbit antisera prepared against  $\varphi$ 29 proheads). Gently tumble the mixture for 4 h in a tube rotator at room temperature.
8. Wash the beads by repeating steps 2–4 three times.
9. Resuspend the beads in 60 µL of 1× PBS buffer. Store at 4 °C.

#### *3.3.2 Preparing Streptavidin-Coated Beads*

1. Pipette 30 µL of 1 % (w/v) 0.90-µm streptavidin-coated beads in a 1.5-mL microcentrifuge tube.
2. Add 0.5× TMS buffer to a total volume of 200 µL.
3. Resuspend the beads by vortexing the solution on high speed for 30 s. Spin the beads down at 10,000  $\times \text{g}$  for 2 min in a benchtop centrifuge.
4. Remove the supernatant.
5. Repeat steps 2–4 twice.
6. Resuspend the pellet in 60 µL of 0.5× TMS buffer. Store at 4 °C.

### 3.4 Microfluidic Chamber Construction

The design of the microfluidic chamber is shown in Fig. 2.

1. Drill six holes on a cover glass using a laser cutter.
2. Make a three-channel pattern on a piece of Nescofilm using a laser cutter.
3. Lay the patterned Nescofilm on a second cover glass. Use two glass dispenser tubes to connect the channels. Then put the drilled cover glass on top of the Necofilm.
4. Put the chamber on a 100 °C heat block for 30 s. Gently press the chamber to seal the two cover glasses. Inspect for any air bubbles.
5. Mount the chamber onto a metal frame. Assemble the inlet/outlet tubings. Then place the chamber between the two objectives of the optical tweezers instrument.
6. Wash the channels with 1 mL of water and then 1 mL of 0.5× TMS buffer before each experiment.

### 3.5 Single-Molecule Packaging Assay

DNA packaging is initiated in a 1.5-mL microcentrifuge tube by feeding DNA substrates to reconstituted prohead/ATPase complexes in the presence of ATP. Packaging is then stalled by adding the non-hydrolyzable analog ATPγS. The stalled packaging complexes are delivered to the microfluidic chamber and restarted in an ATP-containing solution. *See Note 4.*

#### 3.5.1 Bead Passivation

1. Add 2 µL of stock streptavidin-coated or antibody-coated beads and 1 µL of 20 mg/mL BSA to 20 µL of 0.5× TMS buffer.
2. Vortex at high speed for 45 min at room temperature. Then put the beads on ice.
3. Unused passivated beads are stored at 4 °C. Vortex again before using them the next day.

#### 3.5.2 Assembling Stalled Packaging Complexes

1. Add in order: 4.5 µL of H<sub>2</sub>O, 1 µL of 10× TMS buffer, 0.5 µL of RNaseOUT, 2 µL of biotinylated DNA-gp3 ( $2.5 \times 10^{10}$  copies), and 4 µL of proheads ( $1 \times 10^{11}$  copies). Mix gently.
2. Add 4 µL of gp16 ( $2.5 \times 10^{12}$  copies). Mix gently. Incubate the mixture for 5 min at room temperature.
3. Packaging is initiated by adding 2 µL of 5 mM ATP. Mix well and incubate for 30 s.
4. Packaging is stalled by adding 2 µL of 5 mM ATPγS. Mix well.
5. The stalled complexes are stored on ice and must be used within the same day. *See Note 5.*

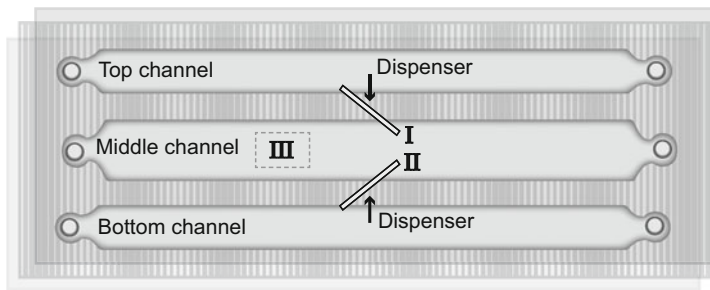


**Fig. 2** Microfluidic chamber design. The solutions flow from *left* to *right*

### 3.5.3 Making Solutions for the Three Channels of the Microfluidic Chamber (Fig. 2)

1. Top channel solution. 4  $\mu$ L of passivated streptavidin-coated beads are diluted in 1 mL of 0.5 $\times$  TMS buffer.
2. Middle channel solution. 1 mL of 0.5 $\times$  TMS buffer supplemented with the oxygen scavenger system (to prevent the formation of reactive singlet oxygen that would damage the tether) and ATP. A typical saturating ATP concentration is 250  $\mu$ M.
3. Bottom channel solution. Mix in order: 10  $\mu$ L of 0.5 $\times$  TMS buffer, 2  $\mu$ L of 5 mM ATP, 2  $\mu$ L of 5 mM ATP $\gamma$ S, 0.5  $\mu$ L of RNaseOUT, 0.5  $\mu$ L of ApaLI, 4  $\mu$ L of passivated antibody-coated beads, and 1  $\mu$ L of stalled complexes. Incubate for 20 min at room temperature. Then dilute the mixture in 1 mL of 0.5 $\times$  TMS buffer containing 100  $\mu$ M ATP and 100  $\mu$ M ATP $\gamma$ S. *See Note 6.*

### 3.5.4 Forming Tethers and Recording Packaging Trajectories

1. Transfer the solutions above from 1.5-mL microcentrifuge tubes to 1-mL syringes. Connect the syringes to the inlet tubings of the microfluidic chamber via 26G $\frac{1}{2}$  needles.
2. Push ~50  $\mu$ L of the top channel solution into the top channel. Streptavidin-coated beads are delivered to Position I of the middle channel through the dispenser tube (Fig. 2). Catch a single bead in Trap A (Fig. 1a, left).
3. Push ~50  $\mu$ L of the bottom channel solution into the bottom channel. Antibody-coated beads, which are conjugated to stalled complexes, are delivered to Position II of the middle channel through the dispenser tube. Catch a single bead in Trap B (Fig. 1a, right).
4. Bring Trap A and Trap B close to each other, while quickly moving them to Position III (within 10 s). *See Note 7.*
5. Move the two traps apart. If the force reading increases as the traps are being separated, it is an indication that a tether has formed. *See Note 8.*

6. Start recording the positions of the two beads and the trap separation at 2.5-kHz bandwidth. *See Note 9.*
7. The packaging experiment is typically conducted in a semi-passive mode, in which the distance between the two optical traps is adjusted periodically so that the force applied to the motor is kept within a small range (e.g., 7–10 pN). *See Note 10.*

### 3.6 Data Analysis

1. Trap stiffness and detector response are calibrated by fitting a modified Lorentzian to the fluctuation power spectrum of a trapped bead [11, 12].
2. The optical force  $F$  is determined by  $F = kd$ , where  $k$  is the trap stiffness, and  $d$  is the displacement of the bead from the trap center achieved by back focal plane interferometry at the position-sensitive photodetectors.
3. The extension of the tether is calculated by subtracting the bead displacements and the bead radii from the trap separation.
4. The DNA tether's contour length is calculated from the measured force and tether extension using the worm-like chain model of double-stranded DNA elasticity [13], using a persistence length of 53 nm and a stretch modulus of 1200 pN. Length in nm is then converted to base pairs (bp) using an average B-form DNA rise of 0.34 nm/bp.
5. Raw 2.5-kHz data are filtered to 100–250 Hz for further analysis. A modified Schwarz Information Criterion (SIC) algorithm is used to find steps in the packaging traces (Fig. 3). *See Notes 11 and 12.*

## 4 Notes

1.  $\varphi29$ -like phages have a unique and essential RNA component, known as the prohead RNA (pRNA), in their packaging motor complexes. Some experiments involve the usage of truncated or mutated versions of pRNA. In these cases, purified proheads are first treated with RNase to remove the wild-type pRNA. These RNA-free proheads are then incubated with fresh pRNA molecules prior to use.
2. The single-molecule packaging experiments are conducted on a home-built high-resolution dual-trap optical tweezers instrument. Detailed information on the concept, design, and use of this instrument can be found in [14].
3. Despite the fact that two biotinylated DNA-gp3 species are generated by this procedure, it was shown that the left end of the  $\varphi29$  genome is preferentially packaged into the prohead

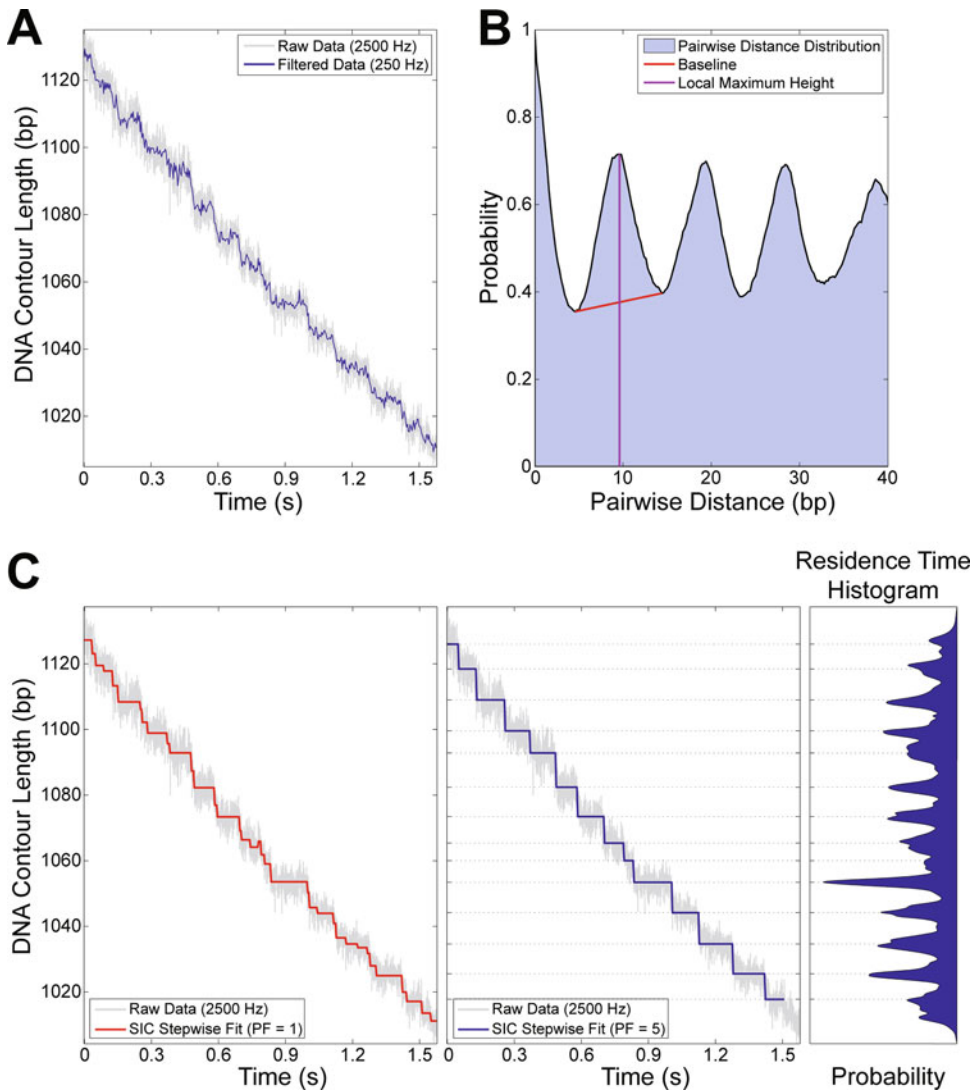


**Fig. 3** Step finding in single-molecule packaging traces. **(a)** A sample packaging trace shown in the 2500-Hz raw form (gray) and the 250-Hz filtered form (blue). **(b)** PWD for the trace shown in Panel **(a)**. The PWD plot contains peaks at integer multiples of 10 bp. We define PWD contrast as the height of the local maximum divided by the baseline, which is determined by the two nearest local minima. Traces with a PWD contrast larger than 1.2 typically exhibit clear stepping and are used for further dwell-time analysis. **(c)** *(Left)* The SIC step-finding algorithm in its original form [17] over-fits the trace from Panel **(a)**. *(Middle)* A modified SIC algorithm with a penalty factor of 5 yields a more reasonable stepwise fit (see Note 11). 250-Hz filtered data are used for step finding. *(Right)* To construct a residence-time histogram, each filtered point is represented as a Gaussian function centered at the mean of the data, with a width equal to the local standard error of the unfiltered data. The residence-time histogram is the sum of the Gaussian functions of all filtered data points. The local maxima in the residence-time histogram coincide with the dwells identified by the modified SIC algorithm, thus validating this method. Reproduced from ref. [7] with permission from Elsevier

(pRNA likely plays a key role in such selection) [15]. Therefore, it is not necessary to separate these two species before mixing them with the proheads in a single-molecule packaging experiment.

4. Packaging can also be initiated *in situ* without prepackaging and stalling in the tube [6, 16]. In this case, the biotinylated DNA is bound to a streptavidin-coated bead, and the prohead/ATPase complex is attached to an antibody-coated bead. Packaging is then initiated by bringing the two beads into close contact in the presence of ATP. This procedure allows for the detection of very early stages of packaging.
5. The quality of the stalled complexes is essential for the outcome of the single-molecule packaging experiment. Once prepared, the stalled complexes can be used for the entire day. However, we notice that the efficiency of forming active tethers slowly drops with time, perhaps due to residual packaging and/or disassembly of the stalled complexes in the tube. Thus it is advised to prepare a fresh stalled complex sample every 4–5 h.
6. The ApaLI cutting site is located near the left end of the φ29 genome (214 bp from the left terminus). DNA is protected from ApaLI cleavage if packaging is properly initiated. Therefore we add ApaLI to the mixture in order to avoid tethering with inactive prohead/ATPase/DNA complexes that did not initiate packaging.
7. Recording of DNA packaging activity is performed at Position III, away from the dispenser tubes opposite to the direction of flow. This is to avoid accidentally capturing additional beads into the traps during data collection. This region also has reduced buffer turbulence, which helps lower data noise.
8. The likelihood of forming a tether is dependent on the density of stalled complexes on the bead. Too high a density causes multiple tethers between the bead pair, whereas too low a density makes experiments time-consuming. We empirically adjust the ratio of bead concentration to stalled complex concentration, such that on average one tether forms every three to four bead pairs. Under this condition most tethers are single tethers, which is desired.
9. During data recording, we sample the voltages proportional to the position of the light centroid in *x* and *y* directions at the two position-sensitive photodetectors, and the voltage proportional to the total amount of light at each detector. We also record the voltages proportional to the horizontal and vertical angle of the piezo mirror that controls the position of the steerable trap. These eight voltage signals are acquired at a rate of 500 kHz, or 62.5 kHz per channel. They are then averaged to 2.5-kHz bandwidth before saving.

10. After the packaging process has completed, the tether is intentionally broken by applying a high force (~30 pN). Two additional calibration files are collected with the same bead pair. First, the positions of the two beads are recorded at 62.5 kHz to determine their fluctuation power spectra. Second, the two beads (untethered) are slowly brought together and the voltage signal as a function of trap separation is recorded. Residual force calculated from this baseline signal is subtracted from the force measured during packaging to correct for the interference pattern between the two traps.
11. The SIC algorithm is an iterative procedure that fits a series of steps to the data and assesses the fit quality for every round of fitting. In the original algorithm [17], the quality of the fit is determined via the formula  $SIC(j_1, \dots, j_k) = (k+2) \log(n) + n \log(\hat{\sigma}_{j_1, \dots, j_k}^2)$ , where  $n$  is the number of data points,  $k$  is the number of steps, and  $\hat{\sigma}_{j_1, \dots, j_k}^2$  is the maximum likelihood estimator of variance when  $k$  steps are fitted to the data. We find that the original SIC algorithm over-fits experimental data containing colored noise (Fig. 3). We therefore introduce an additional penalty factor (PF):  $SIC(j_1, \dots, j_k) = PF(k+2) \log(n) + n \log(\hat{\sigma}_{j_1, \dots, j_k}^2)$  [7]. Optimal stepwise fits can usually be achieved using PF values of 3–5. Steps assigned by this method are validated using a residence time histogram analysis (Fig. 3).
12. Optimal resolution of an optical tweezers measurement is achieved when the DNA tether length is less than 2 kbp, since longer tethers are intrinsically noisier. Thus, in order to probe the stepping behavior of the motor at different capsid filling levels, DNA substrates of various lengths are used (Table 1).

## Acknowledgments

We thank Shelley Grimes, Paul Jardine, and Dwight Anderson for developing the *in vitro* packaging system and critically reading the manuscript. We thank Gheorghe Chistol, Craig Hetherington, Jeffrey Moffitt, Yann Chemla, Aathavan Karunakaran, Douglas Smith, Sander Tans, Adam Politzer, Ariel Kaplan, Thorsten Hugel, Jens Michaelis, and Steven Smith for their contributions to the development of the single-molecule packaging assay, optical tweezers instrumentation, and data analysis tools. The authors are supported by NIH grants R01GM071552 (to C.B.) and K99GM107365 (to S.L.) and a UC MEXUS-CONACYT doctoral fellowship (to S.T.). C.B. is a Howard Hughes Medical Institute investigator.

## References

1. Hetherington CL, Moffitt JR, Jardine PJ et al (2012) Viral DNA packaging motors. In: Goldman YE, Ostap EM (eds) Molecular motors and motility. Elsevier, Oxford, pp 420–446
2. Morais MC (2012) The dsDNA packaging motor in bacteriophage  $\varphi$ 29. In: Rossmann MG, Rao VB (eds) Viral molecular machines. Springer, New York, NY, pp 511–547
3. Smith DE, Tans SJ, Smith SB et al (2001) The bacteriophage  $\varphi$ 29 portal motor can package DNA against a large internal force. *Nature* 413:748–752
4. Chemla YR, Aathavan K, Michaelis J et al (2005) Mechanism of force generation of a viral DNA packaging motor. *Cell* 122:683–692
5. Moffitt JR, Chemla YR, Aathavan K et al (2009) Intersubunit coordination in a homomeric ring ATPase. *Nature* 457:446–450
6. Aathavan K, Politzer AT, Kaplan A et al (2009) Substrate interactions and promiscuity in a viral DNA packaging motor. *Nature* 461:669–673
7. Chistol G, Liu S, Hetherington CL et al (2012) High degree of coordination and division of labor among subunits in a homomeric ring ATPase. *Cell* 151:1017–1028
8. Liu S, Chistol G, Hetherington CL et al (2014) A viral packaging motor varies its DNA rotation and step size to preserve subunit coordination as the capsid fills. *Cell* 157:702–713
9. Liu S, Chistol G, Bustamante C (2014) Mechanical operation and intersubunit coordination of ring-shaped molecular motors: insights from single-molecule studies. *Biophys J* 106:1844–1858
10. Zhao W, Morais MC, Anderson DL et al (2008) Role of the CCA bulge of prohead RNA of bacteriophage  $\varphi$ 29 in DNA packaging. *J Mol Biol* 383:520–528
11. Neuman KC, Block SM (2004) Optical trapping. *Rev Sci Instrum* 75:2787–2809
12. Berg-Sørensen K, Flyvbjerg H (2004) Power spectrum analysis for optical tweezers. *Rev Sci Instrum* 75:594–612
13. Bustamante C, Marko JF, Siggia ED et al (1994) Entropic elasticity of lambda-phage DNA. *Science* 265:1599–1600
14. Bustamante C, Chemla YR, Moffitt JR (2008) High-resolution dual-trap optical tweezers with differential detection. In: Selvin PR, Ha T (eds) Single-molecule techniques: a laboratory manual. Cold Spring Harbor Laboratory Press, Cold Spring Harbor, NY, pp 297–324
15. Grimes S, Jardine PJ, Anderson D (2002) Bacteriophage  $\varphi$ 29 DNA packaging. *Adv Virus Res* 58:255–294
16. Rickgauer JP, Fuller DN, Grimes S et al (2008) Portal motor velocity and internal force resisting viral DNA packaging in bacteriophage  $\varphi$ 29. *Biophys J* 94:159–167
17. Kalafut B, Visscher K (2008) An objective, model-independent method for detection of non-uniform steps in noisy signals. *Comput Phys Commun* 179:716–723

# Chapter 14

## Single-Molecule Protein Folding Experiments Using High-Precision Optical Tweezers

Junyi Jiao\*, Aleksander A. Rebane\*, Lu Ma, and Yongli Zhang

### Abstract

How proteins fold from linear chains of amino acids to delicate three-dimensional structures remains a fundamental biological problem. Single-molecule manipulation based on high-resolution optical tweezers (OT) provides a powerful approach to study protein folding with unprecedented spatiotemporal resolution. In this method, a single protein or protein complex is tethered between two beads confined in optical traps and pulled. Protein unfolding induced by the mechanical force is counteracted by the spontaneous folding of the protein, reaching a dynamic equilibrium at a characteristic force and rate. The transition is monitored by the accompanying extension change of the protein and used to derive conformations and energies of folding intermediates and their associated transition kinetics. Here, we provide general strategies and detailed protocols to study folding of proteins and protein complexes using optical tweezers, including sample preparation, DNA-protein conjugation and methods of data analysis to extract folding energies and rates from the single-molecule measurements.

**Keywords** Optical tweezers, Single-molecule manipulation, Protein folding, gp41, SNARE proteins, SNARE assembly, Hidden Markov modeling, Energy landscape

---

### 1 Introduction

As one of life's building blocks, proteins play essential roles in almost all cellular activities. Their functions rely on their structures, stabilities, and dynamics [1]. Misfolding of proteins contributes to numerous human diseases [2, 3]. Accessing folding stability and kinetics of proteins is crucial for understanding their working mechanisms, functions, and dysfunctions. Various experimental approaches have been developed to study protein folding [4–6]. They differ in the proteins of interest and ways to induce protein unfolding and to detect subsequent folding. Despite great efforts, measuring membrane protein folding and stabilities remains

---

\*Author contributed equally with all other contributors.

challenging [6]. Thus, we focus on soluble proteins here. One of the first and main challenges for protein folding studies is to unfold proteins. Some proteins or protein domains are marginally stable in solution, whose folding and stabilities can directly be probed by NMR and/or hydrogen–deuterium exchange [5, 7]. However, most proteins are very stable and rarely unfold spontaneously due to thermal fluctuations, making it difficult to observe protein folding. In addition, when proteins do unfold this way, many of them refold so rapidly (within 1 ms) that it is difficult to accurately follow their folding kinetics. To overcome these difficulties, proteins are often destabilized by chemical denaturants such as urea and guanidinium chloride [8], temperature jumps [9], or pressure and pH changes [10]. These methods also slow down protein folding, facilitating its detection. Once proteins are unfolded, their synchronized folding kinetics can be monitored by various spectroscopic techniques [4], such as circular dichroism [8], fluorescence [11], absorbance, and Raman scattering [12]. While these ensemble-based approaches have greatly contributed to our understanding of protein folding, they share several weaknesses. They require synchronization of proteins in the unfolded states and often lack sufficient resolution to resolve multiple folding intermediates. Moreover, the denaturing environment makes it impossible to study protein folding regulated by other proteins, an important aspect of protein folding *in vivo* [13, 14].

Optical tweezers force microscopy is a unique tool to study protein folding [15–17]. OT use optical traps to confine micron-sized beads in harmonic potentials as a force and displacement sensor [18–20]. A protein is attached to the surface of a trapped bead at one end and to a second surface at another end [15]. The latter surface can be provided by a microscope glass slide or by another bead in a different optical trap or sucked into or attached to the tip of a micropipette. The protein is pulled by separating the two surfaces or protein attachment sites. The pulling force and the extension of the protein accompanying its folding and unfolding transition are derived from displacements of the beads in the optical traps. The displacement is typically measured by an optical interference method called back-focal plane interferometry [21]. The method can achieve sub-angstrom spatial resolution and better than  $\sim 10 \mu\text{s}$  temporal resolution [22, 23]. However, the resolution of optical tweezers is limited by Brownian motion of the beads in the optical traps, leading to typically 0.2–0.4 nm spatial resolution [22, 24–26]. To achieve such high resolution, two optical traps are used to completely suspend the dumbbell formed by two beads connected by a single protein, which maximally decouples force and extension measurements from environmental noise sources, such as stage drift, and laser pointing fluctuations [22, 24]. In addition, a protein molecule can be held at constant force to observe its folding and unfolding transitions for more than

an hour [15, 19, 27]. The extremely large dynamic range of measurements makes it possible to pinpoint multi-scale protein folding in real time among many distinct intermediate states with large energy differences.

The application of optical tweezers to folding studies of macromolecules was pioneered by Bustamante and coworkers [15, 16, 28]. Since 1997, optical tweezers have been used to measure folding energies and kinetics of numerous proteins or protein complexes, including RNase H [15], von Willebrand factor [29], T4 lysozyme [30], GCN4 leucine zipper [31, 32], calmodulin [33, 34], and prion proteins [35]. In this work, we will describe the basic strategies and protocols to study protein folding using two membrane fusion protein complexes, the human immunodeficiency virus type 1 (HIV-1) glycoprotein 41 (gp41) complex [36] and the synaptic soluble *N*-ethylmaleimide-sensitive-factor attachment protein receptor (SNARE) complex [13, 27, 37] as examples. Both complexes thermodynamically couple their concurrent folding and assembly to membrane fusion [38, 39]. In this process, the fusion proteins generate large forces to draw two membranes into proximity to merge. In particular, the synaptic SNARE complex mediates fusion of neurotransmitter-containing synaptic vesicles to presynaptic plasma membranes at nerve endings, leading to neurotransmitter release [38]. The released neurotransmitters can elicit action potentials in the postsynaptic neurons at synaptic junctions or lead to contraction of muscles at neuromuscular junctions. The gp41 complex mediates fusion between viral and host cell membranes, the first step leading to HIV infection [39, 40]. Both fusion protein complexes assemble in a step-wise manner, generating many intermediates [13, 27, 36, 40]. The SNARE folding intermediates can serve as targets for other regulatory proteins to control membrane fusion, for example, calcium-triggered synaptic vesicle fusion [38]. In contrast, gp41 folding intermediates can be targeted by various fusion-inhibitors to inhibit gp41 folding, thereby blocking HIV infection [36]. Therefore, optical tweezers is an ideal tool to measure the force and energy generated by fusion proteins and their folding intermediates and kinetics.

In the following, we first describe our experimental setup and the protein and DNA constructs required to pull single proteins. We then provide protocols to prepare the protein and DNA samples, to perform DNA-protein conjugation, and to conduct single-molecule experiments using optical tweezers. Finally, we outline our methods of data analysis.

## 2 Materials

### 2.1 Protein Expression and Purification

1. BL21 Gold (DE3) competent cells (Agilent Technologies).
2. LB medium: Dissolve 25 g LB broth (Miller) into 1 L ddH<sub>2</sub>O, autoclave for 30 min.

3. SOC medium (Sigma): 20 g/L tryptone, 5 g/L yeast extract, 4.8 g/L MgSO<sub>4</sub>, 3.603 g/L dextrose, 0.5 g/L NaCl, 0.186 g/L KCl.
4. IPTG stock solution (1000 ×): Dissolve 2.38 g IPTG powder in 10 mL ddH<sub>2</sub>O to make 1 M stock solution. Filter the solution with 0.22 μm syringe filter.
5. Kanamycin stock solution (1000 ×): Dissolve 1.5 g kanamycin powder into 30 mL ddH<sub>2</sub>O to make 50 mg/mL solution and filter with 0.22 μm syringe filter.
6. Selective LB plate: Dissolve 25 g LB broth (Miller) and 15 g Agar into 1 L ddH<sub>2</sub>O. Autoclave for 30 min. After autoclaving, cool to approximately 55 °C and add 1 mL kanamycin stock solution (50 mg/mL) to final concentration of 50 μg/mL, and pour into petri dishes.
7. Lysis buffer: 25 mM HEPES (pH 7.7), 400 mM KCl, 0.5 mM TCEP, 10 % glycerol, 10 mM imidazole.
8. Needles: 18 G × 1 needle (1.2 mm × 25 mm) and 23 G × 1 needle (0.6 mm × 25 mm) (BD precision gliding needle).
9. Protease inhibitor cocktail tablet, EDTA free (cOmplete™, Roche).
10. Nickel nitriloacetic acid (Ni-NTA) beads: Ni Sepharose 6 Fast Flow (GE Healthcare Lifesciences).
11. Wash buffer I: 25 mM HEPES, pH 7.7, 400 mM KCl, 0.5 mM TCEP, 10 % glycerol, 30 mM imidazole.
12. Wash buffer II: 25 mM HEPES, pH 7.7, 400 mM KCl, 0.5 mM TCEP, 10 % glycerol, 50 mM imidazole.
13. Elution buffer: 25 mM HEPES, 200 mM potassium glutamate, 300 mM imidazole.
14. Amicon (or Centricon, EMD Millipore).

## **2.2 Protein Biotinylation In Vitro**

1. BirA biotin ligase (3 mg/mL, Avidity).
2. Biomix-A (10 × concentration: 0.5 M bicine buffer, pH 8.3, Avidity).
3. Biomix-B (10 × concentration: 100 mM ATP, 100 mM MgOAc, 500 μM D-biotin, Avidity).
4. Additional D-biotin (10 × concentration: 500 μM, Avidity).
5. NuPAGE Novex 4–12 % Bis-Tris precast protein gels (Thermo Fisher).
6. 4 × SDS loading buffer (Thermo Fisher).
7. Streptavidin (1 mg/1 mL): Add 1 mL ddH<sub>2</sub>O to 1 mg streptavidin powder (Promega).

8. SDS-PAGE Coomassie staining solution: 0.1–0.2 g Coomassie G-250, 225 mL methanol, 225 mL H<sub>2</sub>O, 50 mL glacial acetic acid.
9. SDS-PAGE Coomassie destaining solution: 150 mL methanol, 300 mL ddH<sub>2</sub>O, 50 mL glacial acetic acid.

### **2.3 DNA Handle**

1. Taq DNA polymerase with ThermoPol buffer (NEB).
2. dNTP mix (10 mM, Invitrogen).
3. PCR purification kit (Qiagen).
4. PureLink PCR Purification Kit (Invitrogen).
5. Lambda DNA (NEB).

### **2.4 Chemical Cross-Linking**

1. Buffer A: 0.1 M sodium phosphate buffer, pH 5.8, 400 mM NaCl.
2. Buffer C: 0.1 M sodium phosphate buffer, pH 8.5, 400 mM NaCl.
3. 10 mM 2,2'-dithiodipyridine disulfide (DTDP) stock solution: Dissolve 11 mg DTDP powder into 1 mL acetonitrile and then add 4 mL ddH<sub>2</sub>O to dilute to 10 mM.
4. Bio-spin columns (Bio-Rad, Micro Bio-spin 6 columns).

### **2.5 Single-Molecule Experiments with Optical Tweezers**

1. Phosphate-buffered saline (PBS): 137 mM NaCl, 2.7 mM KCl, 8.1 mM Na<sub>2</sub>HPO<sub>4</sub>, 1.8 mM KH<sub>2</sub>PO<sub>4</sub>, pH 7.4.
2. Catalase from bovine liver: aqueous suspension, 10,000–40,000 units/mL (Sigma-Aldrich).
3. Glucose oxidase from *Aspergillus niger*: 50 mg/mL, ≥100 units/mg (Sigma-Aldrich).
4. Glucose stock solution: 400 mg/mL.
5. PBS buffer with oxygen scavenging system: Add 75 µL glucose, 6 µL glucose oxidase (final concentration ≥10 units/mL), and 4.7 µL catalase (final concentration 15.7–62.7 units/mL) to 3 mL PBS.
6. Polystyrene beads: 1 % w/v anti-digoxigenin antibody coated polystyrene particles (2.1 µm, called DIG beads), streptavidin-coated polystyrene particles (1.8 µm), both from Spherotech, IL.
7. Customized glass tubing (King Precision Glass, Inc., CA): Bead dispenser tubes with 100 µm outer diameter (OD) and 25 µm inner diameter (ID); protein injection tube with 80 µm OD and 40 µm ID.
8. Slides: Microscope cover glass (60 × 24 × 0.17 mm) (Fisherbrand).

9. Plastic tubing: Polyethylene tubing PE10, PE50 (Becton Dickinson).
10. Nescofilm (Karlan research).
11. Sodium azide: Make 0.02 % sodium azide solution and filter with 0.22  $\mu$ m syringe filter.

## **2.6 Dual-Trap High-Resolution Optical Tweezers**

Our dual-trap optical tweezers setup is home-built and calibrated as previously described [24, 26, 27]. Briefly, a 1064 nm laser beam is expanded, collimated, and split into two orthogonally polarized beams. One beam is reflected by a mirror attached to a nano-positioning stage that can tip/tilt in two axes (Mad City Labs, WI). The two beams are then combined, further expanded, and focused by a 60 $\times$  water-immersion objective (NA = 1.2, Olympus, PA) to form two optical traps (Fig. 1a). One trap can be moved by adjusting the mirror and the other trap is stationary. The outgoing laser beams are collimated by a second objective, split again by polarization, and projected onto two position-sensitive detectors (Pacific Silicon Sensor, CA) to detect bead positions using back-focal-plane interferometry. Before every experiment, the spring constant of each optical trap is determined by measuring the power-spectrum density distribution of the Brownian displacements of the trapped bead at 80 kHz [41]. The power-spectrum is fitted with the Lorentz distribution and the spring constant of the trap is calculated from the best-fit corner frequency. During the experiment, bead displacements, and other measurements are acquired at 20 kHz, filtered online to 10 kHz, and stored on hard disk. The force acting on the beads at each time point is determined from the measured displacements by using Hooke's law and the spring constants determined from trap calibration.

## **2.7 Laser Engraver**

Epilog Zing laser engraving and cutting system. Used to cut holes in coverslips and to cut Nescofilms into patterns to form the microfluidic chamber.

## **3 Methods**

### **3.1 Basic Experimental Setup to Pull a Single Protein**

We use high-resolution dual-trap optical tweezers to exert force on a single protein complex (Fig. 2). The protein is attached to two polystyrene beads via one or two DNA handles that are covalently bound to the protein by disulfide bonds [15]. DNA handles are necessary to provide sufficient spatial separation of the two optical traps: the size of a typical protein is only a few nanometers and direct attachment of a single protein to both beads would be technically difficult, if not impossible, and impede accurate measurement of bead displacements. For this purpose, the total handle length typically ranges from 500 base pairs to a few thousand base

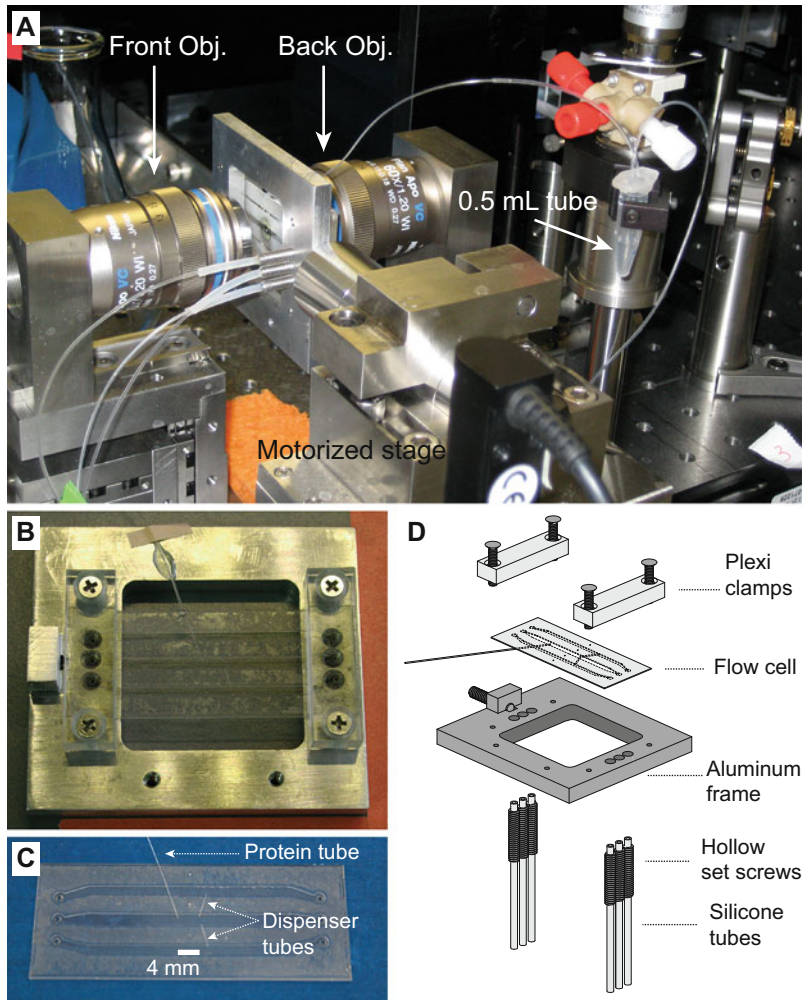


**Fig. 1** Microfluidic chamber used in optical trapping experiments. **(a)** Microfluidic chamber installed on a motorized translational stage and positioned between two objectives. The PE tubing connected to the three channels and to the protein tube can be seen. **(b)** Microfluidic chamber installed on the chamber frame. **(c)** Microfluidic chamber showing three channels, two dispenser tubes, and the protein tube. The thickness of channels between two coverslips is around 180  $\mu\text{m}$ . **(d)** Diagram illustrating how the microfluidic channel is assembled onto the frame. The figure is reproduced from our earlier work with permission [41].

pairs. However, longer DNA handles reduce the signal-to-noise ratio of the detected protein transitions due to their increased compliance [42]. In addition, long handles are difficult to make in the molar amounts that are needed to efficiently cross-link the handles to proteins. To facilitate a specific attachment, two different beads are used, one coated with streptavidin and the other coated with anti-digoxigenin antibody. Correspondingly, the DNA handles and/or the protein are labeled with biotin and digoxigenin moieties. For simplicity, we typically use one 2260 bp DNA handle in our pulling experiments [27, 32, 36, 43]. The DNA handle is

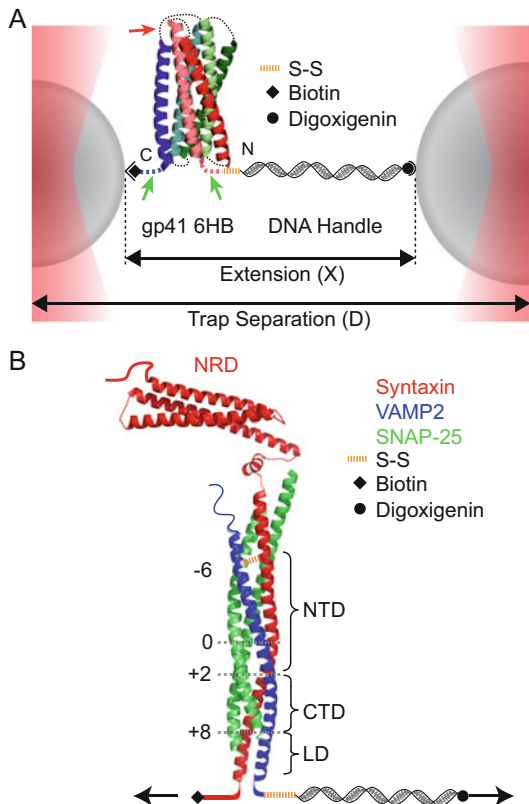


**Fig. 2** Experimental setup to pull a single protein complex using dual-trap high-resolution optical tweezers. **(a)** A single gp41 complex in a fully folded six-helix bundle conformation is tethered between two polystyrene beads via a 2260 bp DNA handle and pulled by increasing the trap separation [36]. The extension and tension of the protein–DNA tether are detected. **(b)** SNARE construct used to measure the energetics and kinetics of SNARE assembly using optical tweezers [13]. A fully assembled cytoplasmic synaptic SNARE complex is pulled from the C-termini of syntaxin and VAMP2 while cross-linked at the N-termini near the  $-6$  layer. The SNARE complex consists of the N-terminal domain (NTD), the C-terminal domain (CTD), the linker domain (LD), and the N-terminal regulatory domain (NRD) in syntaxin. The positions of different layers are indicated by *black numbers*

labeled with two digoxigenin moieties at one end and a thiol group at another end. The handle is cross-linked to a unique cysteine residue on the surface of the protein. The protein contains a biotin moiety that is used to directly immobilize the protein to the streptavidin-coated bead. Tethering the protein to the two bead surfaces by these methods, we do not find significant nonspecific interactions between the proteins and the bead surfaces [43]. Thus, folding energy and dynamics of the protein are not affected by its immobilization to the bead surface. The force load on the tethered

protein is controlled by specifying the trap separation. The load can be increased by moving one trap away from the other at a constant speed (typically 10 nm/s), or kept at a constant average value by holding the trap separation constant.

### 3.2 Protein Constructs

We use two fusion proteins to demonstrate two complementary methods to study coupled folding and assembly of multi-protein complexes. Once a multi-protein complex unfolds, its different protein subunits will dissociate, making the folding process irreversible. To facilitate reversible folding measurements of multi-protein complexes, we covalently link the different subunits in a complex. The linkage has to be designed to allow functional folding of the complex and may vary between protein complexes. For this reason, we fuse three gp41 proteins into a single polypeptide and use a disulfide bond to cross-link two SNARE proteins in a SNARE complex [13, 36, 37].

#### 3.2.1 Gp41 Protein

The gp41 complex is a homotrimer that forms a six-helix bundle [44] (Fig. 2a). Each gp41 monomer contains an N-terminal heptad repeat (NHR), a loop, and a C-terminal heptad repeat (CHR), which form a helical hairpin. In the six-helix bundle, the three NHRs associate into a central three-helix bundle, while the three CHRs bind their grooves in an anti-parallel fashion. To characterize the folding/unfolding of a single gp41 complex, we join three gp41 hairpins with six amino acid flexible linkers to a single polypeptide. In addition, a cysteine residue followed by a spacer sequence (CGGSGGSKGGGSNG) is added to the N-terminus of the tandem gp41 sequences. At the C-terminus, (GGNSGDYKDDDDKGSGGGSGNGGSGDSLEFIASKLAG) acts as a spacer sequence, followed by an AviTag sequence (GLNDIFEAQ**KIEWHE**). The AviTag sequence can be recognized by the biotin-ligase BirA and specifically labeled by biotin on the lysine residue. The spacer sequence before the AviTag is used to facilitate the enzymatic biotinylation by minimizing possible steric hindrance of the gp41 six-helix bundle to BirA binding to the AviTag. In addition, the spacer allows the gp41 protein to stay away from the bead surface in the presence of force, preventing nonspecific interactions between the gp41 protein and the bead surface. Finally, the natural cysteine residues in the loop of the gp41 monomer are mutated to serine, because they would compete against the N-terminal cysteine for cross-linking to the DNA handle, and thereby change the pulling site on the protein. However, other proteins may contain functionally important cysteine residues on their surfaces. Thus, these cysteine residues cannot be removed. In this case, alternative protein labeling methods such as the CoA-based method and click chemistry [45, 46] can be employed to conjugate the protein to the DNA handle.

### 3.2.2 SNARE Protein Complex

The fully assembled synaptic SNARE complex comprises three proteins: syntaxin, SNAP-25, and VAMP2 (also called synaptobrevin) [47] (Fig. 2b). They form a parallel four-helix bundle, with SNAP-25 contributing two helices. Along the spine of the bundle are 15 layers (numbered from -7 to -1 at the N-terminus and from +1 to +8 at the C-terminus) of hydrophobic amino acids and one layer (“0” layer) of hydrophilic amino acids consisting of three glutamines and one arginine [48]. The helices of syntaxin and VAMP2 further extend into the linker domain (LD) and the transmembrane domain to form a two-stranded coiled coil at their C-termini [49]. Before membrane fusion, syntaxin and SNAP-25 are located on the target plasma membrane and partially fold into a binary t-SNARE complex, while VAMP2 is anchored on the vesicle membrane (thus called v-SNARE) and is mainly disordered. During membrane fusion, the t- and v-SNAREs first pair at their membrane-distal N-termini and then zipper toward their membrane-proximal C-termini to drive membrane fusion. To facilitate reversible folding/unfolding of the SNARE complex, we cross-link the N termini of syntaxin and VAMP2 by a disulfide bridge at the -6 layer and pull the complex from their C-termini [13]. The SNAP-25 molecule is not covalently joined to other SNARE proteins and can therefore dissociate when the SNARE complex is completely unfolded [27].

After individual SNARE proteins are purified (please find the detailed protocol in Subheading 3.3 Protein expression and purification), the ternary SNARE complexes are formed by following the protocol listed below:

1. Mix syntaxin, SNAP-25 and VAMP2 proteins in a molar ratio of 0.8:1:1.2 in buffer containing 25 mM HEPES (pH 7.7), 400 mM KCl, and 5 mM TCEP.
2. Incubate the mixture at 4 °C overnight [27].
3. Purify the SNARE complex using the His-Tag on SNAP-25 by incubating the protein mixture with washed Ni-NTA beads while rotating at 4 °C for 2 h. The beads volume is determined by the amount of His-tagged protein in the solution (*see Note 1*).
4. Wash the beads solution with buffer C three times to remove TCEP and prepare for future cross-linking. For each wash, add buffer C to resuspend the beads and then centrifuge at  $344 \times g$  for 2 min. Then remove the supernatant. The volume of buffer C should be three to fivefold of the volume of Ni-NTA beads.
5. Elute the SNARE complex using 0.1 M phosphate buffer containing 0.2 M NaCl and 0.3 M imidazole at pH 8.5.
6. Confirm the formation of the ternary complex by SDS polyacrylamide gel electrophoresis. The band corresponding to the SDS-resistant ternary SNARE complex disappears if the sample is boiled prior to loading the gel.

### 3.3 Protein Expression and Purification

Once the amino acid sequences of the protein constructs have been designed, their corresponding gene sequences can be optimized for expression in bacteria, chemically synthesized, and inserted into an expression vector. We typically insert the gene into a pET SUMO expression vector (Invitrogen, CA). The vector will add a His-tag followed by a small ubiquitin-like modifier (SUMO) protein domain to the N-terminus of the protein of interest. After purification, this N-terminal addition can be cleaved by SUMO protease.

In this section, we will describe how the recombinant gp41 construct is purified from *E. coli*. The gp41 gene has been cloned into the pet SUMO plasmid vector. The SNARE proteins are purified in similar fashion.

#### 3.3.1 Transformation

We transform the above plasmid into the BL21 Gold (DE3) competent cells for gp41 expression.

1. Mix 30  $\mu$ L of BL21 Gold (DE3) competent *E. coli* with 10–50 ng plasmid by gently tapping the tube. Avoid pipetting up and down.
2. Incubate on ice for 30 min.
3. Heat-shock the cells at 42 °C for 30 s.
4. Immediately place the tube with the competent cells on ice and wait for 2 min.
5. Add 200  $\mu$ L of the S.O.C. medium at room temperature and shake at 37 °C for 1 h.
6. Spread 100  $\mu$ L of the competent cells evenly on a selective LB plate containing 50  $\mu$ g/mL kanamycin pre-warmed to 37 °C.
7. Incubate at 37 °C overnight.

#### 3.3.2 Protein Expression

We usually grow 1 L bacterial culture for protein purification. Depending on the expression level of the protein, one may need to adjust the culture volume.

1. Pick a single colony from the plate and resuspend it in 100 mL LB with 50  $\mu$ g/mL kanamycin. Grow overnight at 37 °C while shaking. This is the preculture sample.
2. Decant the precultured bacterial sample into 1 L LB with 50  $\mu$ g/mL kanamycin and grow the culture until mid-logarithmic phase ( $OD_{600} = 0.6\text{--}0.8$ ).
3. Induce expression of the gp41 protein by adding IPTG to a final concentration of 1 mM.
4. Grow the cells by shaking the culture in the presence of IPTG for 3–5 h at 37 °C. Too short or too long culture time may reduce the amount of protein expression.

5. Harvest the cells by centrifuging the culture at  $6056 \times g$  for 15 min at 4 °C. Discard the supernatant and collect the pellet. The cells can be stored at –20 °C.

### 3.3.3 Protein Purification

The purification is carried out on ice or in the cold room (4 °C) unless stated otherwise.

1. Thaw the cell pellet for 15 min on ice. Resuspend cells in 30 mL lysis buffer in which one tablet of protease inhibitor cocktail has been dissolved. Pipette up and down (*see Note 2*).
2. Homogenize cells. Using a 30 mL syringe, pass the cell suspension first through a 18 G × 1 needle and then through a 23 G × 1 needle. This breaks cell aggregates that may block the cell disruptor used in the next step.
3. Disrupt cells using a French press (or another suitable lysis system). Pass the cell suspension through the cell disruptor 4–5 times until the suspension becomes clear.
4. Centrifuge the cell suspension at 186,000 × g for 1 h at 4 °C to precipitate the cellular debris. Save the clarified supernatant and store on ice.
5. Wash Ni-NTA beads. For 1 L *E. coli* culture, take 600 µL of Ni-NTA beads from the stock solution and add to 8 mL lysis buffer. Centrifuge at  $344 \times g$  for 3 min. Discard the supernatant and repeat the washing step three times. After the last spin, suspend the washed beads in 1 mL lysis buffer.
6. Add the Ni-NTA beads to the supernatant from **step 4** and rotate the bead solution at 4 °C for 2 h to allow gp41 to bind to the Ni-NTA beads.
7. Centrifuge the Ni-NTA beads at  $344 \times g$  for 5 min at 4 °C. Collect the protein-bound Ni-NTA beads at the bottom.
8. Wash the beads with wash buffer I (WBI) three times. For each wash, resuspend the Ni-NTA beads with 10 mL WBI by pipetting up and down. Rotate the bead solution at 4 °C for 10–15 min. Centrifuge to collect the Ni-NTA beads (*see Note 2*).
9. Wash the Ni-NTA beads with wash buffer II (WBII) three times as in **step 8**.
10. Add 1 mL elution buffer to the Ni-NTA beads and rotate the beads at 4 °C for over 30 min to dissociate gp41 from the beads (*see Note 3*).
11. Centrifuge the bead solution and save the supernatant. Run SDS-PAGE to check the protein quality and concentration. Use Amicon to concentrate the protein to a final concentration of 4 mg/mL.

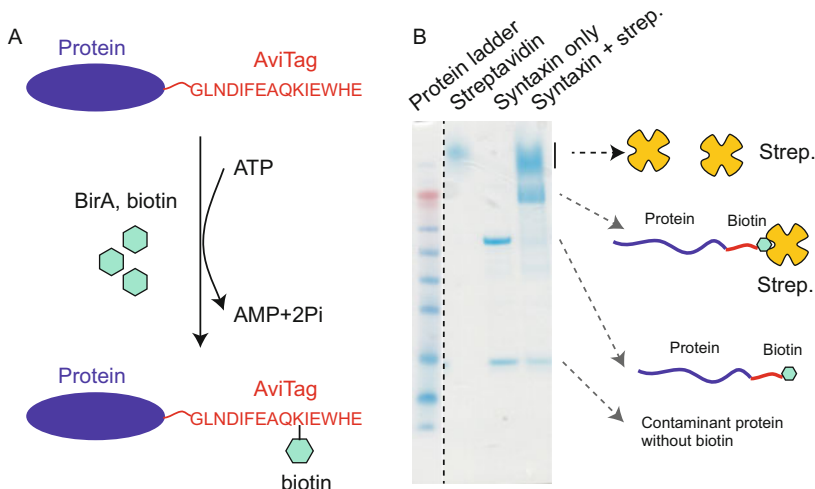


**Fig. 3** Enzymatic protein biotinylation. (a) Diagram showing the biotinylation reaction catalyzed by BirA biotin ligase. It recognizes the 15 amino acid AviTag (red) and conjugates biotin to the lysine residue in the presence of ATP. (b) SDS gel electrophoresis to test the yield of protein biotinylation

### 3.4 Protein Biotinylation

#### 3.4.1 Biotinylation, SUMO Cleavage, and Purification

The following protocol is slightly modified from the biotinylation kit provided by Avidity [50] (Fig. 3a).

- To prepare biotinylation reaction, pipette together 420  $\mu$ L AviTag containing 1.6 mg gp41 in elution buffer, 60  $\mu$ L Biomix-A (10 $\times$ ), 60  $\mu$ L Biomix-B (10 $\times$ ), 60  $\mu$ L D-biotin (10 $\times$ ) and 4  $\mu$ L (12  $\mu$ g) BirA enzyme (see Note 4).
- Perform the biotinylation at 4 °C overnight (see Note 4). After the biotinylation reaction is complete, the free biotin will be removed from the biotinylated protein by performing the following steps.
- Dilute the biotinylated protein solution from step 2 (604  $\mu$ L) with 3.4 mL lysis buffer to reduce the imidazole concentration to <50 mM. Incubate the diluted protein solution with 500  $\mu$ L washed Ni-NTA beads by rotating at 4 °C for 2 h to bind the biotinylated gp41 protein back to the Ni-NTA beads.
- Wash the Ni-NTA beads with lysis buffer three times to remove free biotin. At this step, one may save 10–20  $\mu$ L beads and elute gp41 from the beads using 10–20  $\mu$ L elution buffer to test the biotinylation efficiency with SDS-PAGE (see the following step).
- Resuspend the Ni-NTA beads in 500  $\mu$ L lysis buffer and add 20  $\mu$ L 3 mg/mL SUMO protease to cleave the SUMO tag. Rotate at 4 °C overnight. Note that imidazole at high concentration inhibits the cleavage reaction, thus ensure that imidazole concentration is <50 mM, as in step 3 (see Note 2).

6. Precipitate the beads by centrifuging the bead solution at  $344 \times g$  for 3 min. Save the supernatant containing the final biotinylated and purified gp41. The purified protein can be stored at  $-80^{\circ}\text{C}$  after adding glycerol to 10 %.

### *3.4.2 Determination of the Biotinylation Level*

We test the purity, yield, and biotinylation level of the purified protein using SDS polyacrylamide gel electrophoresis (PAGE) (Fig. 3b). To distinguish the biotin-labeled and unlabeled protein molecules, we bind all the biotinylated protein molecules to streptavidin and then run the SDS gel. Streptavidin is SDS resistant and tightly binds biotin on the protein gel even in the presence of SDS. Thus, the biotinylated protein molecules migrate differently from unlabeled protein molecules. The detailed protocol is listed below.

1. Prepare three 20  $\mu\text{L}$  protein samples (a, b, c) in the SDS loading buffer containing 2 mM TCEP and the follow proteins: (a) 6  $\mu\text{g}$  streptavidin, (b) 6  $\mu\text{g}$  streptavidin and 2  $\mu\text{g}$  biotinylated protein, and (c) 2  $\mu\text{g}$  biotinylated protein. Incubate the samples at room temperature for 5–10 min.
2. Load the sample to a protein SDS gel and run the gel at 200 V for 35 min.
3. Stain the protein gel with Coomassie blue by microwaving the gel immersed in the Coomassie blue staining solution for 2 min.
4. De-stain the gel by shaking the gel in fresh de-staining solution at room temperature for 2 h.

Figure 3b shows the gel used to test the biotinylation level of syntaxin. Comparing the two syntaxin lanes with and without streptavidin, one finds that the band corresponding to free syntaxin nearly disappears in the presence of streptavidin, while a new band with higher molecular weight appears. This new band results from streptavidin-bound syntaxin. The gel analysis reveals that the syntaxin molecules are ~100 % biotinylated, which is the typical biotinylation yield for soluble proteins. In general, a protein with a biotinylation yield over 50 % can efficiently be tethered between two beads in our single-molecule experiments. The protein molecules that are not biotinylated cannot form tethers between two beads, and thus cannot be pulled.

### **3.5 DNA Handle Preparation**

Two types of DNA handles are used to pull on proteins. One type of DNA handle has two blunt ends (Fig. 2a), one end with a thiol group and the other with digoxigenin or biotin moieties. The DNA handle is directly cross-linked to the cysteine residue on the protein through the thiol group. The other type of DNA handle contains a 20–30 nucleotide overhang at one end so that it can hybridize with its complementary oligonucleotide [23, 33, 51] (Fig. 4a). The other end of the DNA handle is again blunt and labeled with

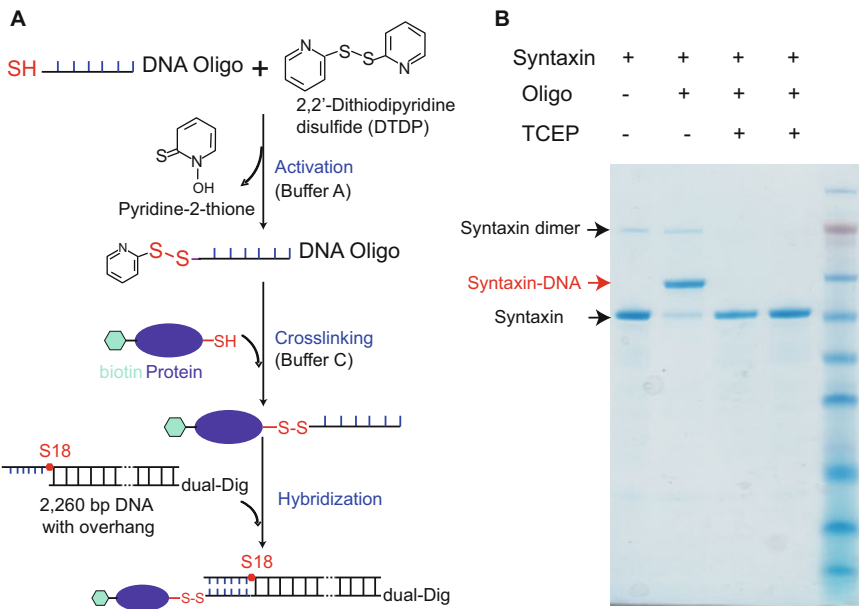


**Fig. 4** Protein–DNA cross-linking. **(a)** Reaction schemes to cross-link a DNA oligonucleotide to the protein and attach the protein to a long DNA handle by hybridization. **(b)** SDS gel electrophoresis to test the yield of protein–oligonucleotide cross-linking

digoxygenin or biotin moieties. In this case, the protein is first cross-linked to the oligonucleotide and then the DNA handle is hybridized to the oligonucleotide through the overhang. The DNA duplex formed between the oligonucleotide and the overhang is strong enough to hold more than 30 pN for extended time periods required for protein folding studies ( $>20$  min). The yield of the cross-linking reaction depends on the molar concentrations of both protein and DNA molecules. The concentration of the long DNA handle generally does not exceed 80 nM, leading to relatively low cross-linking efficiency if the handle is directly cross-linked to the protein. We partially overcome the issue by increasing the protein concentration, typically with over 50:1 protein to DNA molar ratio in the cross-linking reaction. The excess of protein can be removed by first binding the DNA molecule to the bead. In contrast, the oligonucleotide can be synthesized in high concentrations ( $>100$   $\mu$ M). As a result, nearly 100 % of the protein molecules can be cross-linked to the oligonucleotides (Fig. 4b).

### 3.5.1 DNA Handle with Blunt Ends

The dsDNA handle typically used in our single-molecule experiments is 2260 bp in length and contains a thiol (-SH) group at one end and two digoxigenin moieties at the other end. Both labels are added to the 5' ends of the PCR primers during synthesis. We found that two digoxigenin moieties are required to strongly attach the DNA handle to anti-digoxigenin antibody coated polystyrene beads.

### 3.5.2 DNA Handle with an Overhang

The DNA handle contains a 30-nucleotide overhang at one end and either two digoxigenin moieties or one biotin moiety at the other end. The overhang is again introduced through the PCR primer. To prevent polymerase extension to the overhang region, the overhang is attached to the 5'-end of the primer through an 18-atom hexa-ethyleneglycol spacer (S18 from IDT) (Fig. 4a).

Forward primer containing overhang (61 nt):

C GCC TGC GTA GGA TAT CGC AGA TAC CGC ATC AGT  
CCA S18 TCT AAG TGA CGG CTG CAT ACT AAC (The overhang sequence is underlined)

Reverse primer:

Dual-Dig-ATC CAG TAA TGA CCT CAG AAC TCC

Oligonucleotide complementary to the overhang (40 nt):

TGG ACT GAT GCG GTA TCT GCG ATA TCC TAC GCA  
 GGC GTT T-Thiol

### 3.5.3 Preparation of DNA Template

1. In a PCR microcentrifuge tube, prepare a 50 µL reaction mixture containing 5 µL ThermoPol buffer (10×), 1 µL 10 mM dNTP mix, 0.5 µL 100 µM forward primer, 0.5 µL 100 µM reverse primer, 20 ng DNA template, 0.5 µL Taq DNA Polymerase. Add H<sub>2</sub>O to a final volume of 50 µL (*see Note 5*).
2. Perform PCR amplification using an initial denaturation at 95 °C for 3 min and 32 cycles of denaturation at 95 °C for 30 s, annealing at 55 °C for 40 s, and extension at 65 °C for 2 min, followed by a final extension for 5 min at 72 °C.
3. Use the PureLink PCR Purification Kit to purify the PCR product (*see Note 6*).

## 3.6 Protein and DNA Handle Cross-Linking

Here we provide the protocol that we use to directly cross-link the DNA handle or the oligonucleotide (called DNA below) to proteins (adapted from Cecconi and coworkers [15, 52, 53]).

1. Reduce the DNA and protein by treating them with 2 mM TCEP at room temperature for 1 h. For each cross-linking reaction, 8–10 µg DNA is used and the protein amount is derived based on a protein to DNA molar ratio of 50:1 in the final cross-linking reaction. For oligo, we usually use protein to oligo molar ratio of 1:10.
2. Remove TCEP from the DNA by changing to buffer A using the Bio-spin column.
3. Add DTDP to the DNA sample to a final concentration of 1 mM. Incubate at room temperature for 1 h.
4. Remove DTDP from DNA by changing buffer A to buffer C using a PCR purification spin column. For oligo, we usually use a nucleotide removal kit to purify it.

5. Remove TCEP from the protein sample by changing lysis buffer to buffer C. Pass the sample through the Bio-spin columns twice.
6. Mix the protein and DNA samples immediately following steps 4 and 5. Incubate the reaction overnight at room temperature.
7. The cross-linked sample can be tested directly using optical tweezers, or stored in the freezer ( $-20^{\circ}\text{C}$ ) for more than 3 months after adding glycerol to 10 % v/v.

### **3.7 Microfluidic Chamber**

We use a home-made microfluidic chamber in our single-molecule experiments [41] (Fig. 1d). The chamber is formed by sandwiching two microscopic coverslips with Nescofilms cut into specific shapes to form three channels: the top and bottom channels for bead injection and the central channel for optical trapping and single-molecule manipulation (Fig. 1d). The top and bottom channels are connected to the central channel through dispenser glass tubing (Fig. 1c). The chamber is affixed to a customized chamber frame (Fig. 1b), connected to plastic tubing (Fig. 1a), and installed on a motorized stage that can move in three axes and positioned between two objectives in a vertical direction.

### **3.8 Single Protein Folding Studies Using Optical Tweezers**

#### *3.8.1 Measure the Force-Extension Curves*

Here, we demonstrate how to pull the gp41 protein using optical tweezers [36]. The biotinylated gp41 protein is cross-linked to a 2260 bp DNA handle that contains two digoxigenin moieties at the protein-distal end. The following protocols describe acquisition of the force-extension curves (FECs) of the gp41 protein and the time-dependent trajectories at constant trap separation.

1. Thoroughly wash the three channels in the microfluidic chamber and the connection PE tubing with 3–4 mL PBS using syringes.
2. Bind cross-linked protein–DNA to DIG beads. Mix an aliquot of the cross-linked protein–DNA mixture containing 10–100 ng DNA with 20  $\mu\text{L}$  DIG beads and incubate at room temperature for 15 min. Dilute the beads into 1 mL PBS buffer and transfer the beads to a 1 mL syringe.
3. Dilute 2  $\mu\text{L}$  of streptavidin coated beads into 1 mL PBS. Transfer the beads to a 1 mL syringe.
4. Prepare 3 mL PBS containing the oxygen scavenging system and transfer the PBS to a 10 mL syringe. The oxygen scavenging system consumes free oxygen from the solution by enzymatically catalyzing the oxidation of glucose. The reaction results in a decrease in pH over time. Therefore, the oxygen scavenging solution must be replaced every 2–3 h.
5. Connect the syringes to the three channels in the microfluidic chamber through the washed PE tubing and minimize the flow in all three channels.

6. Catch beads. Slowly inject the two types of beads to the top and bottom channels until the beads diffuse from the tips of the dispenser tubes into the central channel. Separate the two optical traps to maximum distance. Move the chamber stage to position one trap near the tip of glass tubing connected to the top channel and catch a single DNA-bound DIG bead. Similarly catch a single streptavidin-coated bead from the bottom channel.
7. Calibrate optical traps. First, clear stray beads from the trap surroundings by gently flowing PBS through the central channel, then move the two trapped beads upstream of the two bead fountains. Stop the flow and measure the time-dependent displacements of both beads due to their Brownian motion in the optical traps. Determine the trap stiffness of each trap and the voltage-to-displacement conversion constants by fitting the measured power-spectrum density distributions to the Lorentz distribution. The typical trap stiffness for our experiments is 0.1–0.2 pN/nm. If the trap stiffness falls out of this range, adjust the laser intensity entering the objective.
8. Form a protein–DNA tether. Move the two beads close to each other to allow the biotinylated protein to bind streptavidin on the bead surface and then slowly separate the two beads to check if the force between two the beads increases upon their separation. If the force increases, a tether is formed between the two beads. Otherwise, repeat the above approach-separation cycle until a tether is formed. Alternatively, test a different pair of beads.
9. Once a tether is formed, adjust the trap separation speed to 10 nm/s and pull the protein to maximum force until the protein is completely unfolded. Measure the corresponding force–extension curve (FEC). The maximum force is generally limited by digoxigenin–antibody binding strength. With two digoxigenin moieties, the protein–DNA tether typically breaks between 30 and 60 pN.
10. Pull more single gp41 protein molecules by repeating the steps 6–9 to confirm the measured FECs.
11. Pull to completely unfold the gp41 protein and then relax the gp41 protein to detect protein refolding (Fig. 5a). Repeat the pulling and relaxation cycle for several rounds to obtain consistent FECs. Finally pull to high force to break the tether. A one-step force drop to zero generally indicates a single protein–DNA tether is studied. A representative FEC is shown in Fig. 5.
12. At the end of the experiment, flush all three channels using 0.02 % sodium azide and then seal the channels in this solution to prevent bacterial growth in the microfluidic chamber.

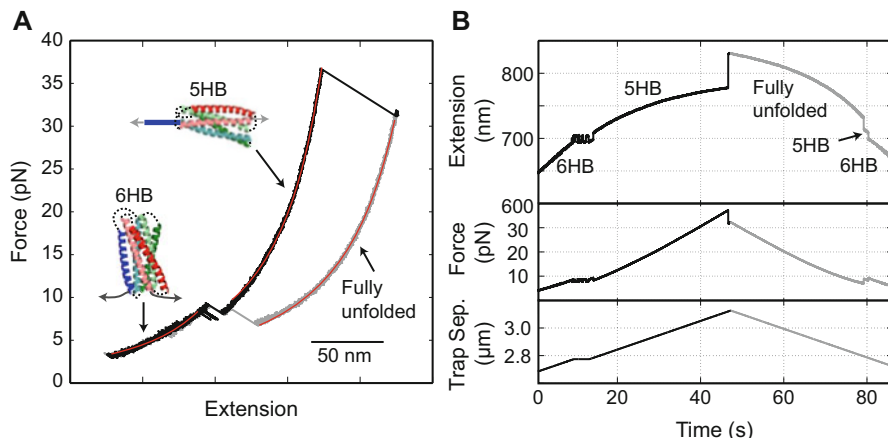


**Fig. 5** Stage-wise unfolding and refolding a single gp41 complex [36]. (a) Force–extension curves (FECs) obtained by pulling (black) and relaxing (gray) the gp41 complex. The continuous regions of the FECs are fit with a worm-like chain model (red lines), revealing different gp41 folding states (6HB, 5HB, and the fully unfolded state). (b) Time-dependent extension, force, and trap separation corresponding to the force and extension shown in (a)

### 3.8.2 Measure the Time-Dependent Trajectories at Constant Trap Separation

The time-dependent trajectories at different constant trap separations allow us to determine protein folding energy and kinetics under equilibrium conditions in much greater detail (Fig. 6a). At a fixed trap separation, the force applied on the protein–DNA tether varies in response to protein folding and unfolding. Consequently, the average force applied on a protein in its folded state is slightly higher than that in its unfolded state. We define the mean of the average forces applied on all states and simplified call it as force throughout the text if not otherwise specified [32]. The mean force is approximately proportional to the trap separation. Although data interpretation may be more straightforward for experiments conducted under constant force, experiments at fixed trap separation offer simpler instrumentation and higher spatiotemporal resolution [26]. In the approach described here, an increasing constant mean force is applied to unfold the protein in a step-wise manner at different reversible transitions. At each trap separation, the protein transition is typically detected for 5–500 s, depending on the transition rate. To acquire protein unfolding/refolding trajectories at different constant trap separations, perform the following steps:

1. Choose the transition to be investigated based on the measured FEC and pull the protein with a force corresponding the lower bound of the force range of the transition.
2. Measure the time-dependent extension and trap separation for a time period such that every state in the transition is visited at least ten times.

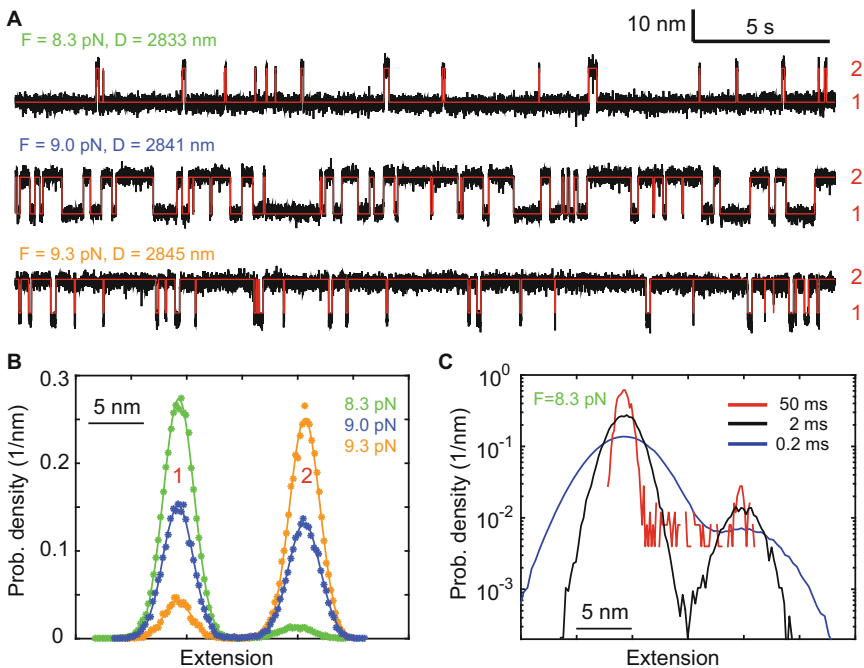


**Fig. 6** Two-state gp41 hairpin folding and unfolding transition. (a) Extension–time trajectories (*black*) at three constant mean forces (*F*) or trap separations (*D*). The *red lines* are the idealized extension trajectories derived from hidden Markov modeling. (b) Probability density distributions of the extensions shown in (a). (c) Probability density distributions of the extension at 8.3 pN calculated after mean-filtering the trajectory using three time windows (0.2, 2, and 50 ms)

3. Increase the trap separation by 2–5 nm.
4. Measure the single-molecule trajectories at incrementally higher forces by repeating steps 2 and 3 until the force reaches the upper bound of the transition’s force range.
5. Measure the FEC of the protein by pulling and relaxing the molecule to confirm whether it exhibits a typical FEC.

### 3.9 Data Analysis

The goal of data analysis is to (1) identify possible intermediates involved in protein folding, (2) measure conformations, lifetimes, populations, and energies of the states involved in the folding processes and their associated transition kinetics as a function of force, and (3) infer the corresponding parameters in the absence of force. Complementary information on protein folding can be obtained from the FECs and the time-dependent trajectories at constant trap separation. The former is measured under essentially nonequilibrium conditions, although fast transitions can reach equilibrium when the protein is being slowly pulled. As a result, the protein transition patterns in the measured FECs often depend on the pulling speed. In contrast, the latter is acquired under equilibrium. In addition, protein unfolding and refolding

transitions involved in hysteresis and seen in the FECs may reach equilibrium under constant mean force if given sufficient time. In the following, we will describe our methods to analyze the results from the two types of experiments.

### 3.9.1 Force–Extension Curves (FECs)

The FECs provide a complete phase diagram of protein folding and unfolding transitions over a large force range. Figure 5a shows an exemplary FEC for the gp41 6-helix bundle. The corresponding time-dependent extension, force, and trap separation are shown in Fig. 5b. At the beginning of the pulling phase (*black*) in the force range below 7 pN, both force and extension continuously increase with trap separation. This is due to the stretching of the elastic DNA handle and any unfolded polypeptide linkers directly attached to the handle or beads (Fig. 2a, *green arrows*) while the protein remains in the approximately folded 6HB state. The elastic response in such continuous stretches can be quantified using the worm-like chain model (WLC) [54, 55], as shown by the red fitted curves in Fig. 5a. At around 7 pN, the extension starts to flicker as a result of reversible folding–unfolding transitions of the protein between the fully folded state and an intermediate state (Fig. 5b). The unfolding transition increases the tether extension by about 10 nm, suggesting that the intermediate state is a five-helix bundle (5HB) in which the CHR is unfolded. The conformation is confirmed by more quantitative analysis as described below. This extension increase allows the beads to slightly retract towards the trap center, thereby reducing the force by approximately 1 pN. Similarly, refolding is accompanied by extension decrease and force increase. When pulled to higher force beyond 10 pN, the flickering stops at a greater extension, indicating that the gp41 protein is stabilized in the intermediate state. At around 41 pN, the FEC shows an irreversible rip, due to further cooperative unfolding of the protein (Fig. 5a). Pulling the protein to higher force does not reveal any additional unfolding, indicating that the protein is fully unfolded. Then we start to relax the protein to low force to observe its possible refolding (*gray*). The gp41 protein remains in the fully unfolded state until the force drops to ~7 pN, leading to a distinct FEC that is shifted to higher extension compared to the FEC in the pulling phase. Such FEC hysteresis and the irreversibility of the second unfolding transition indicate a large energy barrier for refolding of the fully unfolded gp41 protein construct, at least in the presence of forces above ~7 pN. However, upon further relaxation, the gp41 protein first irreversibly folds into the intermediate state and then reversibly folds to the fully folded state, resulting in a FEC that overlaps with the FEC of the pulling phase in the force range below 7 pN. Therefore, the FECs show different protein folding states, protein folding and unfolding pathways, and approximate stabilities of the different states and their associated transition kinetics.

### 3.9.2 Time-Dependent Trajectories Obtained at Constant Trap Separation

We measured gp41 transitions in the force region of 8–10 pN (trap separations 2831–2853 nm) in a total of seven steps, with approximately 90 s at each step. Figure 6a (*black*) shows excerpts of the measured time-extension trajectories for three steps, mean-filtered to 500 Hz bandwidth. Flickering occurs between the 6HB state and the 5HB state, labeled as states 1 and 2, respectively (Fig. 6a, *red*). The flickering is overlain with Gaussian noise due to the Brownian motion of the beads in the trap. These single-molecule trajectories contain information on both thermodynamics and kinetics of protein folding, which are the major subject of data analysis. In the following, we will use two approaches, the histogram analysis and the hidden Markov modeling (HMM) to analyze the trajectories. The histogram analysis is easy to understand and to use. It can be utilized to determine the number of states involved in the transition and the extension, population, and force of each state. The HMM involves more sophisticated computer algorithms and is more computationally intensive than the Gaussian fitting. However, HMM can additionally reveal the kinetics of protein transitions with high spatiotemporal resolution.

### 3.9.3 Histogram Analysis

In this method, the histogram or the probability density distribution of the extension at a given mean force is calculated from the corresponding measured trajectory. We will fit the distribution with a sum of multiple Gaussian functions to determine the number of distinct states involved in the protein transition and their associated average extensions, forces, and probabilities. The fitting with Gaussian functions is justified, because the major measurement noise in OT comes from Brownian motion of the beads in harmonic potentials imposed by the optical traps [24]. The histogram analysis can be similarly performed on both the extension–time and the force–time trajectories for each trap separation. For simplicity, we use the extension trajectory as an example to demonstrate the histogram analysis:

1. Choose the time region of interest in the whole extension–time trajectory and parse the trajectory into segments corresponding to different trap separations. Mean-filter the trajectories using a proper time window to reduce the noise without blurring the protein transitions.
2. Calculate the probability density distribution of the extension,  $\rho(X)$ . The probability density is calculated as the number of extension data points,  $N_i$ , falling into the  $i$ -th bin with an average extension of  $X_i$ , i.e.,  $\rho_i = N_i / (N_T dX)$ , where  $N_T$  is the total number of data points in all bins and  $dX$  the size of each bin. The bin number should be chosen to reveal a smooth distribution with a maximum number of distinct peaks, which typically ranges from 20 to 100. If a peak is not clear, choose a

different mean-filtering time window and repeat **steps 1–2** (*see Note 7* and Figs. 6c and 8). Based on the probability density distribution, one can estimate the number of states  $N_{\text{st}}$  as the number of distinct peaks in the distribution.

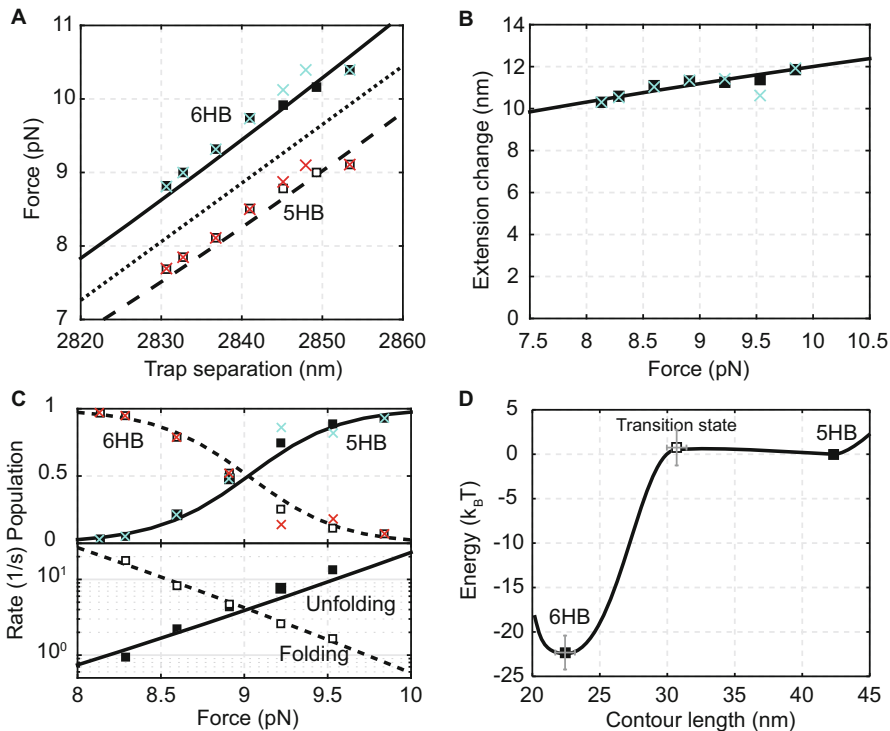
3. Fit the probability density distribution with a sum of  $N_{\text{st}}$  Gaussian functions. Good fitting confirms the number of states identified.
4. Calculate the average extension, fluctuation, and probability of each state from the best-fit parameters.

Figure 6b shows the extension histograms corresponding to the trajectories shown in Fig. 6a. Two distinct peaks in the histogram distributions (*symbols*) are accurately fitted with double-Gaussians (*solid curves*), indicating a two-state transition. Prominence of the peaks strongly depends on the time window used in data filtering and becomes optimal with a time window of 2 ms (Fig. 6c, *black*). The histogram analysis reveals the state positions, populations, forces, and position difference between the two states (Fig. 7a–c, *red* and *cyan*).

The gp41 trajectories have a high signal-to-noise ratio, because the state transition is relatively slow and involves a large extension change. Figure 8a shows a trajectory with a low signal-to-noise ratio that is mean-filtered with a 0.2 ms time window (*blue*). The extension trajectory barely exhibits folding and unfolding transition of the SNARE linker domain at a constant mean force of 14.1 pN, as suggested by the approximately unimodal extension histogram distribution (Fig. 8b, *blue*). However, when the same trajectory is mean-filtered using a 1 ms time window (*black*), a distinct two-state transition is seen from both the extension trajectory and the corresponding probability density distribution. In contrast, the two-state transition becomes indiscernible when further smoothing the trajectory using a 10 ms time window (*red*). This comparison demonstrates that proper filtering of the time-dependent trajectory is important to reliably extract information from the trajectories and histogram distributions.

### 3.9.4 Hidden Markov Modeling (HMM)

HMM models the state transitions underlying the observed trajectory using a Markov model and the associated measurement noise using a Gaussian model [32, 56, 57]. HMM assumes that the noise is uncorrelated. This assumption holds true as long as HMM is performed on the extension trajectory filtered to a bandwidth below the corner frequency of bead Brownian motion. We typically mean-filter the time series to 5 or 1 kHz and then carry out HMM [27]. Given a hidden Markov model, the likelihood to observe a single-molecule trajectory can be computed using the forward–backward algorithm [56]. In addition, the corresponding state transitions (or a Markov chain) can be calculated by the Viterbi



**Fig. 7** Comparison of properties of the gp41 hairpin transition derived from the histogram analysis (crosses), the HMM analysis (squares) and best model fitting (dashed and solid curves). **(a)** Average forces of the folded state (solid square or cyan cross) and the unfolded state (hollow square or red cross) as a function of trap separation. The mean force is shown as the dotted line. **(b)** Extension difference between the folded and unfolded states as a function of the mean force. **(c)** State populations (top) and transition rates (bottom) as a function of the mean force. **(d)** Simplified energy landscape of gp41 hairpin folding at zero force determined by the model fitting in **(a)–(c)**

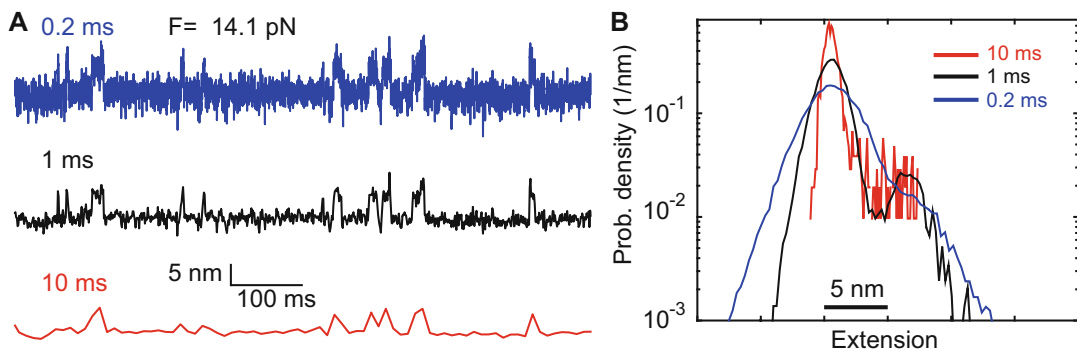


**Fig. 8** Extension–time trajectories mean-filtered using different time windows **(a)** and their corresponding probability density distributions **(b)**. The three trajectories are filtered from the same trajectory exhibiting two-state folding and unfolding transition of the SNARE linker domain [13]

algorithm [58]. More importantly, HMM can optimize the model parameters by maximizing the likelihood of observing the trajectory based on the model, which is efficiently implemented by Baum's algorithm [59]. The algorithm iteratively optimizes model parameters. The hidden Markov model used for the extension–time trajectory includes the number of states ( $N_{\text{st}}$ ), the transition probabilities ( $P_{ij}$  from states  $i$  to  $j$ ,  $i, j = 1, \dots, N_{\text{st}}$ ) during each time step ( $dt$ ), the average extensions, and the state fluctuations. The optimized model parameters are then used to calculate the state properties. In particular, the transition rate between states  $i$  and  $j$  is calculated as  $k_{ij} = p_{ij}/dt$  and the state probability  $p_i$ ,  $i = 1, \dots, N_{\text{st}}$  is computed as the eigenvector  $\mathbf{p}$  of the transpose of the transition probability matrix  $\mathbf{P}$ . Finally, the lifetime of state  $i$  is calculated as  $\tau_i = 1/\sum_{j \neq i} k_{ij}$ . The typical protocol to perform HMM is described below.

Baum's algorithm requires inputs of initial tentative model parameters. Although the final optimized parameters are independent of the initial parameters, the inputs affect the computation time required for the iterative algorithm to reach convergence, especially for the trajectories with low signal-to-noise ratios. We typically use outputs from the histogram analysis as the input for the HMM analysis.

1. For each segment of the trajectory corresponding to a constant trap separation, record the trap separation, the beginning and ending time points, and the state extensions determined from the histogram analysis. List all these parameters in a text file, with one row for each trap separation, to be read by the MATLAB program that carries out the HMM analysis [27].
2. Set the initial model parameters for HMM analysis. We choose the values loaded from the text file prepared in **step 1** as initial state positions. Set the parameters that are independent of states and trap separations as constants. In particular, the state fluctuation is chosen as 3 nm and the transition probability matrix is set to values corresponding to a lifetime of 10 ms for each state.
3. Run the MATLAB program to compute the optimized model parameters that maximize the likelihood.
4. Calculate the idealized sequence of state transitions using the optimized model parameters. Verify the HMM fitting by comparing the idealized and measured trajectories.
5. Calculate the average state forces based on the idealized state transitions for the extension trajectory.
6. Plot the state extensions, forces, populations, lifetimes, and transition rates as a function of trap separation.

Using a two-state hidden Markov model, we fit the gp41 extension trajectory at each trap separation (Fig. 6a, *red*) and determine average populations, extensions, forces, lifetimes, and fluctuations of all states and their associated transition rates (Fig. 7a–c). This analysis reveals that in the narrow force range of the reversible gp41 transition, the average forces of both folded and unfolded states increases approximately linearly with trap separation (Fig. 7a). We therefore use the mean of the state forces to represent the force applied to the molecule (Fig. 7a, *dotted*), which is done throughout the text if not otherwise specified. Similarly, the extension slightly changes upon the state transition and linearly increases with the force, due to stretching of the unfolded polypeptide (Fig. 7b). The state populations show a sigmoidal shape, consistent with a two-state transition (Fig. 7c). The two states equilibrate at a force of  $9.0 \pm 0.1$  pN, characterized by equal folding/unfolding rates and populations. Finally, the state forces, extensions, and populations obtained from the HMM analysis match the corresponding calculations from the histogram analysis, demonstrating the consistency between both methods of data analysis.

### 3.9.5 Calculating Conformations and Energies of Protein Folding States Under Unloaded Conditions

We fit the HMM-derived observables with a nonlinear model to derive the conformations and energies of all states involved in the transition in the absence of force [60]. The model assumes an unfolding pathway based on the crystal structure of the protein in its native state. Protein conformations along the pathway are parameterized using the contour length of the unfolded and stretchable polypeptide *l* (Fig. 9). In the inferred gp41 unfolding pathway, amino acids in the CHR (*blue*) are successively peeled, from its C-terminus to N-terminus, off the remaining five-helix bundle (5HB). Folding of gp41 exactly reverses this process. Each unfolded amino acid contributes 0.365 nm to the contour length. For instance, the folded state of gp41 shown in Fig. 2a has a total of 59 unstructured and stretched amino acids stemming from the polypeptide linkers indicated by the green arrows. Accordingly, the contour length of the folded state is  $59 \times 0.365$  nm = 21.535 nm. Fully unfolding the blue CHR, including the linker indicated by the red arrow, contributes an additional 57 amino acids to the contour length (37 from the helix and 20 from the linker). The resulting contour length of this state is  $(59 + 57) \times 0.365$  nm = 42.340 nm. Importantly, the remaining structured portion of the protein is assumed to remain in its native conformation. As a result, the contour length unambiguously specifies conformations along the inferred folding/unfolding pathway.

The full energy landscapes of protein folding can be obtained from high-resolution measurements of protein folding trajectories from optical tweezers [51, 61], which requires sophisticated

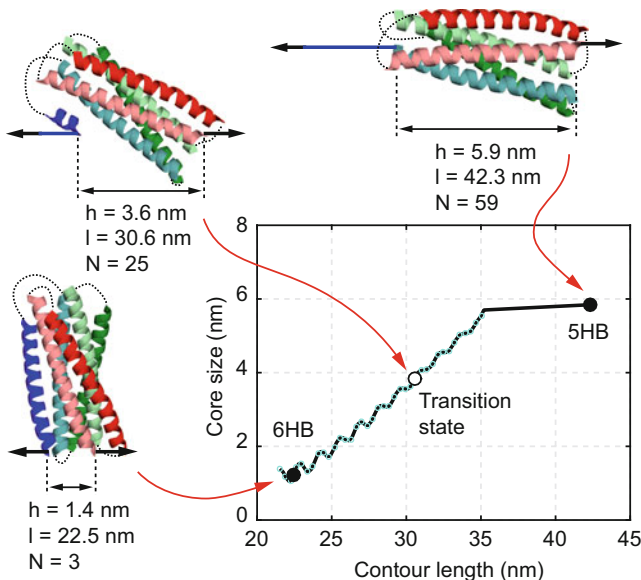


**Fig. 9** The size of the folded gp41 portion as a function of the contour length of the unfolded polypeptide calculated from the crystal structure of the gp41 six-helix bundle [60]. The gp41 conformations and their associated core sizes ( $h$ ), contour length positions ( $l$ ), and numbers of amino acids unfolded ( $N$ ) are shown as *insets*

deconvolution methods. Here we characterize protein folding–unfolding transitions in terms of the simplified energy landscape ( $l_i$ ,  $V_i$ ), where  $l_i$  is the contour length of the unfolded peptide in the  $i$ -th stable state or transition state, and  $V_i$  is the associated free energy at zero force. Model fitting for gp41 involves two stable states, i.e., the folded 6HB state and the unfolded 5HB state, and one transition state. For a given set of parameters ( $l_i, V_i$ ) and trap separation  $D$  the model computes the tether extensions  $X_i$ , state forces  $F_i$ , and the total energies  $G_i$  of the protein–DNA tether and trapped beads. The energies  $G_i$  directly yield state populations and transition rates via the Boltzmann distribution and the Kramers’ equation, respectively. Consequently, we can determine ( $l_i, V_i$ ) by simultaneously fitting the model-based calculations to all the experimental measurements obtained at different trap separations (Fig. 10). Note that for the unfolded gp41 5HB state, the contour length of the unfolded polypeptide is known and its free energy is chosen as zero. Thus, the parameters ( $l_i, V_i$ ) associated with the folded state and the transition state, but not the unfolded state, are chosen as fitting parameters.

Specifically, the tether extension in the  $i$ -th state is expressed as

$$X_i = x^{(m)}(F_i, l_i) + H(F_i, l_i) + x^{(\text{DNA})}(F_i), \quad (1)$$

where  $x^{(m)}$  and  $H$  are the extensions of the unfolded and stretched polypeptide and the folded protein portion, respectively, and

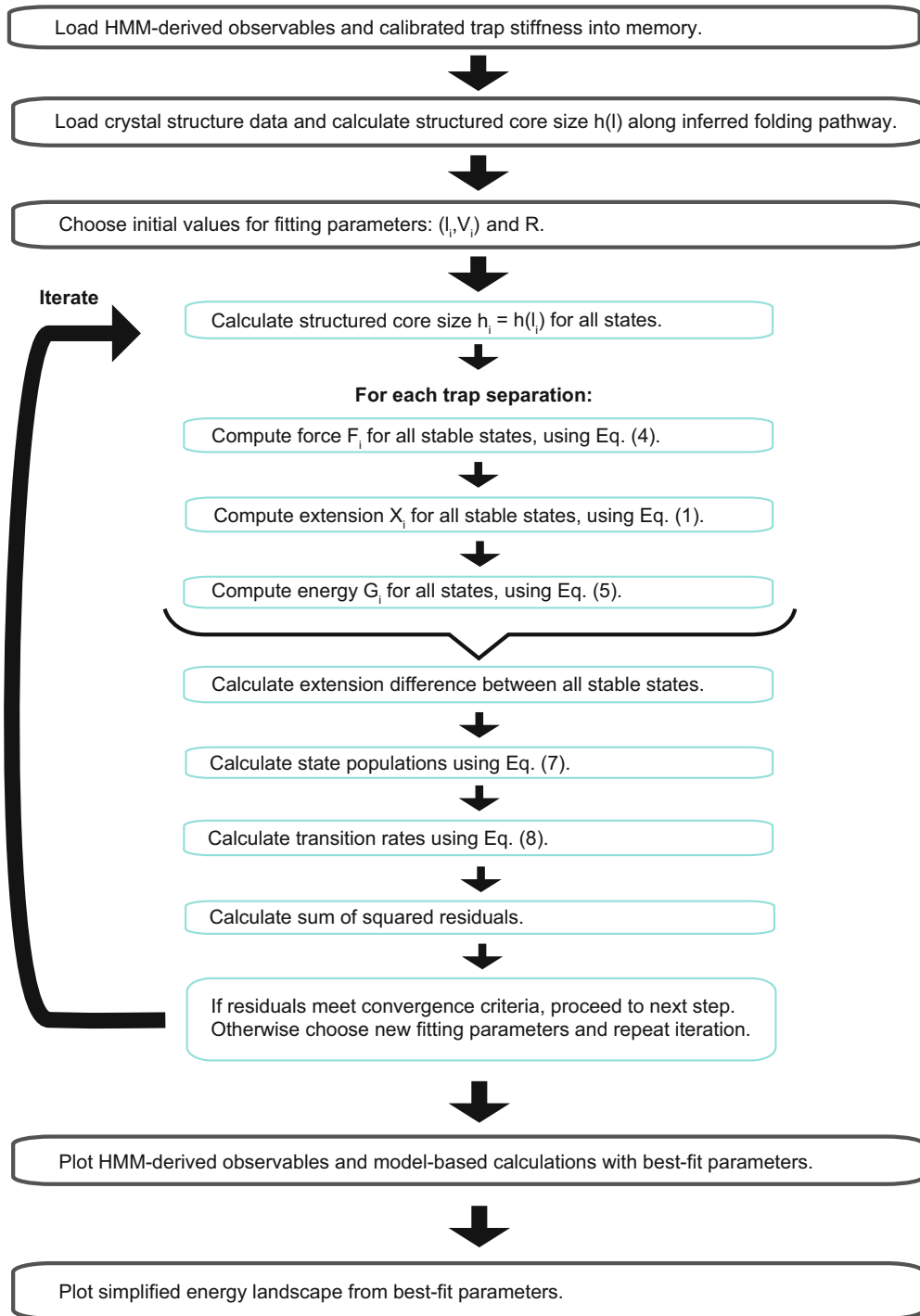


**Fig. 10** Flowchart to optimize model parameters by fitting model calculations to the experimental measurements

$x^{(\text{DNA})}$  is the extension of the DNA handle. The extensions  $x^{(\text{DNA})}$  and  $x^{(\text{m})}$  at state force  $F_i$  are implicitly given by the Marko–Siggia formula for a semi-flexible worm-like chain (WLC) [55]:

$$F_i = \frac{k_{\text{B}} T}{P} \left[ \frac{1}{4(1 - \frac{x}{L})^2} + \frac{x}{L} - \frac{1}{4} \right], \quad (2)$$

where  $P$  is the persistence length and  $L$  the contour length of the polymer. For DNA, we adopt  $P_{\text{DNA}} = 40$  nm and  $L_{\text{DNA}} = 0.34 \times N_{\text{bp}}$  nm, where  $N_{\text{bp}}$  is the number of base pairs in the DNA handle. For polypeptide, we adopt  $P_{\text{m}} = 0.6$  nm and  $L_{\text{m}} = l_i$ . The extension of the folded protein portion  $H$  is calculated based on a freely jointed chain model, i.e.,

$$H_i = -\frac{k_{\text{B}} T}{F_i} + b_i \coth\left(\frac{F_i b_i}{k_{\text{B}} T}\right), \quad (3)$$

where  $b_i$  is the size of the folded protein portion along the pulling direction, which is determined from the crystal structure and expressed as a function of the contour length  $l$  (Fig. 9). Furthermore, the tether extension  $X_i$  is related to the trap separation  $D$  by

$$D = X_i + \frac{F_i}{k_{\text{traps}}} + R, \quad (4)$$

where  $F_i/k_{\text{traps}}$  is the total bead displacement with  $k_{\text{traps}} = k_1 k_2 / (k_1 + k_2)$  the effective trap stiffness of the two traps, and  $R$  is the sum of the bead radii (Fig. 2a). Substituting Eqs. 1–3 into Eq. 4 and solving for  $F_i$  yields the state force.

The total energy of the protein, the DNA handle, and trapped beads is expressed as

$$G_i = G^{(\text{m})}(F_i, l_i) + V_i + G^{(\text{DNA})}(F_i) + \frac{F_i^2}{2k_{\text{traps}}}, \quad (5)$$

where  $G^{(\text{m})}$ ,  $G^{(\text{DNA})}$ , and  $F_i/k_{\text{traps}}$  are the energies of the unfolded polypeptide, the DNA handle, and the beads in optical traps, respectively.  $G^{(\text{m})}$ ,  $G^{(\text{DNA})}$  result from the entropy change of the worm-like chain due to stretching and are calculated as

$$G_i^{(\text{m or DNA})} = \frac{k_{\text{B}} T}{P} \frac{L}{4(1 - \frac{x}{L})} \left[ 3\left(\frac{x}{L}\right)^2 - 2\left(\frac{x}{L}\right)^3 \right]. \quad (6)$$

The state populations  $P_i$  are related to the system energies  $G_i$  of stable states by the Boltzmann distribution, i.e.,

$$P_i = \frac{e^{-\frac{G_{ij}}{k_B T}}}{\sum_{j=1}^N e^{-\frac{G_j}{k_B T}}}, \quad (7)$$

where  $N$  is the total number of stable states involved in the protein transition. In addition, the transition rate  $k_{ij}$  from state  $i$  to state  $j$  is calculated using the Kramers' equation

$$k_{ij} = k_m e^{-\frac{G_{ij}-G_i}{k_B T}}, \quad (8)$$

where  $G_{ij}$  is the free energy of the transition state between stable states  $i$  and  $j$ , and the pre-factor  $k_m$  is the diffusion-limited rate constant in the absence of any energy barrier. Independent of the measurement method and the protein investigated, no consistent pre-factor has been obtained with a wide range of values reported in literature ( $10^5$ – $10^9$  s $^{-1}$ ) [31, 62, 63]. For coiled-coil proteins such as gp41 and SNARE complex, we therefore use  $k_m = 10^6$  s $^{-1}$ , consistent with the maximum folding speed observed for short helical proteins.

Finally, we use the nonlinear least-squares method to fit the model-based calculations at all trap separations to the corresponding experimental measurements. The target function is the sum of the squared residuals of state forces, populations, logarithms of the transition rates, and extension differences between folded and unfolded states. The fitting yields the best-fit parameters for the simplified energy landscape at zero force. The flowchart for the model fitting is shown in Fig. 10.

The fitting results obtained for the two-state transition of gp41 are shown in Fig. 7a–c as curves. The experimental data are well fit by the model, corroborating our model. Figure 7d exhibits the optimized energy landscape parameters ( $l_i, V_i$ ). Thus, the folding energy of a single gp41 hairpin in the gp41 complex is  $22 k_B T$ . The best-fit contour lengths  $l_i$  reveals an approximately 6HB conformation in the folded state, with three amino acids unfolded at the C-terminal end. The frayed end may be due to marginal instability of the C-terminal end under tension or due to an experimental error. In addition, the folding proceeds over a small energy barrier of  $1 k_B T$ , whose position lies close to the 6HB state (Fig. 7d).

Similarly, we analyze the extension–time trajectory of a single SNARE complex pulled to a force of 17.4 pN [13]. Smoothed to 1 kHz, the trajectory shows a three-state folding–unfolding transition of the SNARE four-helix bundle (Fig. 11a), as is demonstrated by the three distinct peaks in the corresponding probability density distribution that can be fit by a sum of three Gaussian functions (Fig. 11b). Accordingly, the extension can be

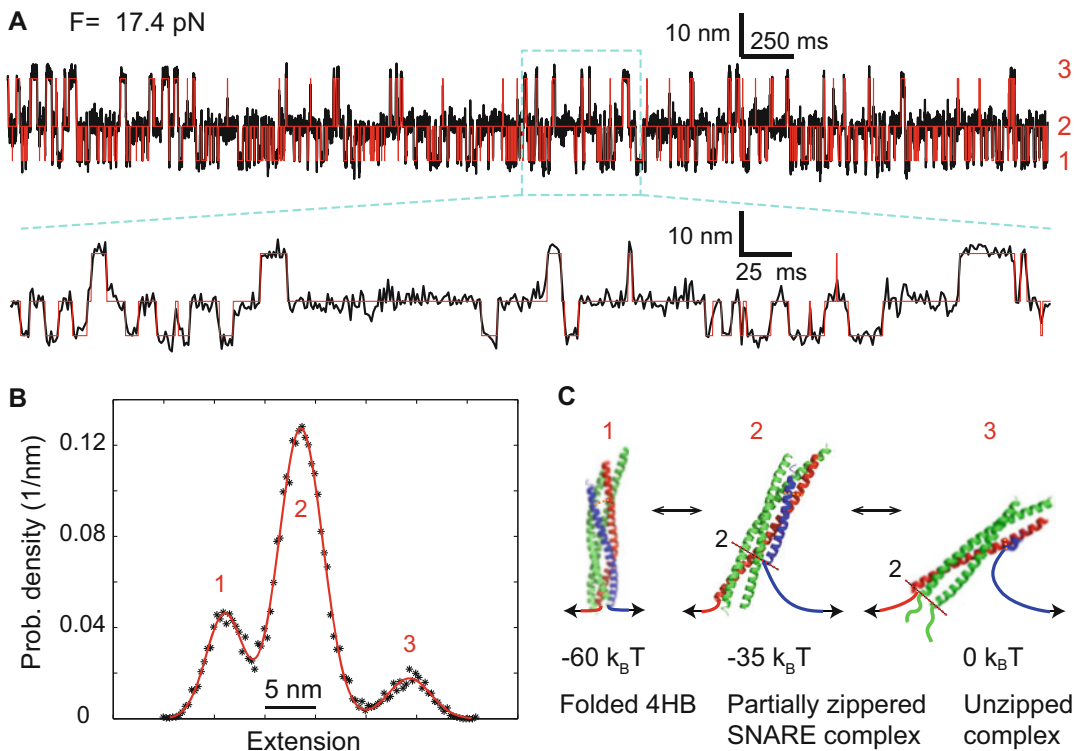


**Fig. 11** Three-state folding and unfolding transitions of the SNARE complex [13]. **(a)** Extension–time trajectory at a constant mean force of 17.4 pN. The red line shows the idealized extension trajectories derived from a three-state hidden Markov model. A close-up view of the region marked by a cyan box is shown. Data were mean-filtered to 1 kHz and plotted. **(b)** Probability density distribution of the extension shown in **(a)**. **(c)** Derived conformations of the three SNARE folding states and their energies

well simulated by a three-state hidden Markov model (Fig. 11a, red). Detailed model fitting reveals that the three states are the folded 4HB state (state 1), the partially zippered SNARE complex (state 2), and the unzipped state (state 3), as well as their associated folding energies (Fig. 11c). These results showcase the applicability of the single-molecule manipulation approach to more complex protein folding transitions with multiple intermediates.

#### 4 Notes

1. The Nickel beads binding capacity is about 40 mg histidine-tagged protein/mL. Please adjust the beads volume accordingly.
2. The imidazole concentration in the lysis buffer can be adjusted to a lower concentration (e.g., 1 mM) if the target protein

binds poorly to the Ni-NTA column or to a higher concentration (e.g., 20 mM) if too many proteins nonspecifically bind the column. The same principle can be applied to adjust the imidazole concentration in wash buffer or any other buffer that aims to rebind proteins to Nickle-NTA beads.

3. Treating the beads with the elution buffer once often fails to completely elute the protein. To improve the protein yield, one may elute the protein from the beads twice (600  $\mu$ L for each elution) or increase the imidazole concentration up to 500 mM.
4. Our experience suggests that many commonly used reagents such as glycerol and NaCl can inhibit the BirA activity (e.g., 5 % glycerol and 100 mM NaCl). Thus, the concentration of these reagents should be minimized in the biotinylation reaction. In addition, a high substrate concentration leads to higher yield of biotinylation. Finally, the biotinylation reaction may be carried out at a higher temperature (e.g., 30 °C) for a higher rate and yield of protein biotinylation.
5. To prepare greater amount of the DNA handle, we usually scale up the PCR mixture to 1 mL and then aliquot the mixture to 50  $\mu$ L per PCR tube.
6. This purification step is required to remove the primer with a long overhang from the PCR product.
7. In general, an increase in the time window leads to a decrease in the amplitude of fluctuation around each peak, which may distinguish two peaks that are otherwise overlapping in the distribution that is obtained using a smaller time window (Figs. 6c and 8). In principle, the time window should be at least twofold smaller than the smallest lifetime of the state involved in the transition.

## References

1. Bukau B, Weissman J, Horwich A (2006) Molecular chaperones and protein quality control. *Cell* 125:443–451
2. Knowles TP, Vendruscolo M, Dobson CM (2014) The amyloid state and its association with protein misfolding diseases. *Nat Rev Mol Cell Biol* 15:384–396
3. Selkoe DJ (2012) Preventing Alzheimer’s disease. *Science* 337:1488–1492
4. Morris ER, Searle MS (2012) In Current protocol protein science, vol Chapter 28, pp. Unit 28 22 21–22.
5. Englander SW, Mayne L (2014) The nature of protein folding pathways. *Proc Natl Acad Sci U S A* 111:15873–15880
6. Fleming KG (2014) Energetics of membrane protein folding. *Annu Rev Biophys* 43:233–255
7. Wand AJ (2001) Dynamic activation of protein function: a view emerging from NMR spectroscopy. *Nat Struct Biol* 8:926–931
8. Fasshauer D, Antonin W, Subramaniam V, Jahn R (2002) SNARE assembly and disassembly exhibit a pronounced hysteresis. *Nat Struct Biol* 9:144–151
9. Huang CY et al (2002) Helix formation via conformation diffusion search. *Proc Natl Acad Sci U S A* 99:2788–2793
10. Dumont C, Emilsson T, Gruebele M (2009) Reaching the protein folding speed limit with

- large, sub-microsecond pressure jumps. *Nat Methods* 6:515–519
11. Pobbatli AV, Stein A, Fasshauer D (2006) N- to C-terminal SNARE complex assembly promotes rapid membrane fusion. *Science* 313:673–676
  12. Yeh SR, Takahashi S, Fan BC, Rousseau DL (1997) Ligand exchange during cytochrome c folding. *Nat Struct Biol* 4:51–56
  13. Ma L et al (2016) Munc18-1-regulated stage-wise SNARE assembly underlying synaptic exocytosis. *eLIFE* 4:e09580
  14. Mashaghi A et al (2013) Reshaping of the conformational search of a protein by the chaperone trigger factor. *Nature* 500:98–U125
  15. Cecconi C, Shank EA, Bustamante C, Marqusee S (2005) Direct observation of the three-state folding of a single protein molecule. *Science* 309:2057–2060
  16. Kellermayer MSZ, Smith SB, Granzier HL, Bustamante C (1997) Folding-unfolding transitions in single titin molecules characterized with laser tweezers. *Science* 276:1112–1116
  17. Zoldak G, Rief M (2013) Force as a single molecule probe of multidimensional protein energy landscapes. *Curr Opin Struct Biol* 23:48–57
  18. Neuman KC, Block SM (2004) Optical trapping. *Rev Sci Instrum* 75:2787–2809
  19. Zhang XM, Ma L, Zhang YL (2013) High-resolution optical tweezers for single-molecule manipulation. *Yale J Biol Med* 86:367–383
  20. Moffitt JR, Chemla YR, Smith SB, Bustamante C (2008) Recent advances in optical tweezers. *Annu Rev Biochem* 77:205–228
  21. Gittes F, Schmidt CF (1998) Interference model for back-focal-plane displacement detection in optical tweezers. *Opt Lett* 23:7–9
  22. Abbondanzieri EA, Greenleaf WJ, Shaevitz JW, Landick R, Block SM (2005) Direct observation of base-pair stepping by RNA polymerase. *Nature* 438:460–465
  23. Zoldak G, Stigler J, Pelz B, Li HB, Rief M (2013) Ultrafast folding kinetics and cooperativity of villin headpiece in single-molecule force spectroscopy. *Proc Natl Acad Sci U S A* 110:18156–18161
  24. Moffitt JR, Chemla YR, Izhaky D, Bustamante C (2006) Differential detection of dual traps improves the spatial resolution of optical tweezers. *Proc Natl Acad Sci U S A* 103:9006–9011
  25. Comstock MJ, Ha T, Chemla YR (2011) Ultrahigh-resolution optical trap with single-fluorophore sensitivity. *Nat Methods* 8:335–340
  26. Sirinakis G, Ren YX, Gao Y, Xi ZQ, Zhang YL (2012) Combined and versatile high-resolution optical tweezers and single-molecule fluorescence microscopy. *Rev Sci Instrum* 83:093708
  27. Gao Y et al (2012) Single reconstituted neuronal SNARE complexes zipper in three distinct stages. *Science* 337:1340–1343
  28. Liphardt J, Onoa B, Smith SB, Tinoco I, Bustamante C (2001) Reversible unfolding of single RNA molecules by mechanical force. *Science* 292:733–737
  29. Zhang XH, Halvorsen K, Zhang CZ, Wong WP, Springer TA (2009) Mechanoenzymatic cleavage of the ultralarge vascular protein von Willebrand factor. *Science* 324:1330–1334
  30. Shank EA, Cecconi C, Dill JW, Marqusee S, Bustamante C (2010) The folding cooperativity of a protein is controlled by its chain topology. *Nature* 465:637–U134
  31. Gebhardt JCM, Bornschlogl T, Rief M (2010) Full distance-resolved folding energy landscape of one single protein molecule. *Proc Natl Acad Sci U S A* 107:2013–2018
  32. Gao Y, Sirinakis G, Zhang YL (2011) Highly anisotropic stability and folding kinetics of a single coiled coil protein under mechanical tension. *J Am Chem Soc* 133:12749–12757
  33. Stigler J, Ziegler F, Gieseke A, Gebhardt JCM, Rief M (2011) The complex folding network of single calmodulin molecules. *Science* 334:512–516
  34. Stigler J, Rief M (2012) Calcium-dependent folding of single calmodulin molecules. *Proc Natl Acad Sci U S A* 109:17814–17819
  35. Yu H et al (2012) Direct observation of multiple misfolding pathways in a single prion protein molecule. *Proc Natl Acad Sci U S A* 109:5283–5288
  36. Jiao JY, Rebane AA, Ma L, Gao Y, Zhang YL (2015) Kinetically coupled folding of a single HIV-1 glycoprotein 41 complex in viral membrane fusion and inhibition. *Proc Natl Acad Sci U S A* 112:E2855–E2864
  37. Zorman S et al (2014) Common intermediates and kinetics, but different energetics, in the assembly of SNARE proteins. *eLIFE* 3:e03348
  38. Sudhof TC, Rothman JE (2009) Membrane fusion: grappling with SNARE and SM proteins. *Science* 323:474–477
  39. Pancera M et al (2014) Structure and immune recognition of trimeric pre-fusion HIV-1 Env. *Nature* 514:455–461
  40. Munro JB et al (2014) Conformational dynamics of single HIV-1 envelope trimers on the surface of native virions. *Science* 346:759–763
  41. Zhang YL, Sirinakis G, Gundersen G, Xi ZQ, Gao Y (2012) DNA translocation of ATP-

- dependent chromatin remodelling factors revealed by high-resolution optical tweezers. *Methods Enzymol* 513:3–28
42. Wen JD et al (2007) Force unfolding kinetics of RNA using optical tweezers. I. Effects of experimental variables on measured results. *Biophys J* 92:2996–3009
  43. Xi ZQ, Gao Y, Sirinakis G, Guo HL, Zhang YL (2012) Direct observation of helix staggering, sliding, and coiled coil misfolding. *Proc Natl Acad Sci U S A* 109:5711–5716
  44. Chan DC, Fass D, Berger JM, Kim PS (1997) Core structure of gp41 from the HIV envelope glycoprotein. *Cell* 89:263–273
  45. Maillard RA et al (2011) ClpX(P) generates mechanical force to unfold and translocate its protein substrates. *Cell* 145:459–469
  46. Yu ZB et al (2012) Click chemistry assisted single-molecule fingerprinting reveals a 3D biomolecular folding funnel. *J Am Chem Soc* 134:12338–12341
  47. Sollner T et al (1993) SNAP receptors implicated in vesicle targeting and fusion. *Nature* 362:318–324
  48. Sutton RB, Fasshauer D, Jahn R, Brunger AT (1998) Crystal structure of a SNARE complex involved in synaptic exocytosis at 2.4 angstrom resolution. *Nature* 395:347–353
  49. Stein A, Weber G, Wahl MC, Jahn R (2009) Helical extension of the neuronal SNARE complex into the membrane. *Nature* 460:525–528
  50. Chattopadhyaya S, Tan LP, Yao SQ (2006) Strategies for site-specific protein biotinylation using in vitro, in vivo and cell-free systems: toward functional protein arrays. *Nat Protoc* 1:2386–2398
  51. Woodside MT et al (2006) Direct measurement of the full, sequence-dependent folding landscape of a nucleic acid. *Science* 314:1001–1004
  52. Cecconi C, Shank EA, Dahlquist FW, Marqusee S, Bustamante C (2008) Protein-DNA chimeras for single molecule mechanical folding studies with the optical tweezers. *Eur Biophys J* 37:729–738
  53. Cecconi C, Shank EA, Marqusee S, Bustamante C (2011) DNA molecular handles for single-molecule protein-folding studies by optical tweezers. *DNA Nanotechnol* 749:255–271
  54. Bustamante C, Marko JF, Siggia ED, Smith S (1994) Entropic elasticity of lambda-phage DNA. *Science* 265:1599–1600
  55. Marko JF, Siggia ED (1995) Stretching DNA. *Macromolecules* 28:8759–8770
  56. Rabiner LR (1989) A tutorial on hidden Markov-models and selected applications in speech recognition. *Proc IEEE* 77:257–286
  57. McKinney SA, Joo C, Ha T (2006) Analysis of single-molecule FRET trajectories using hidden Markov modeling. *Biophys J* 91: 1941–1951
  58. Viterbi AJ (1967) Error bounds for convolutional codes and an asymptotically optimum decoding algorithm. *IEEE Trans Inf Theory* 13:260–269
  59. Baum LE, Petrie T, Soules G, Weiss N (1970) A maximization technique occurring in statistical analysis of probabilistic functions of Markov chains. *Ann Math Stat* 41:164
  60. Rebane AA, Ma L, Zhang YL (2016) Structure-based derivation of protein folding intermediates and energies from optical tweezers. *Biophys J* 110:441–454
  61. Woodside MT, Block SM (2014) Reconstructing folding energy landscapes by single-molecule force spectroscopy. *Annu Rev Biophys* 43:19–39
  62. Yu H et al (2012) Energy landscape analysis of native folding of the prion protein yields the diffusion constant, transition path time, and rates. *Proc Natl Acad Sci U S A* 109: 14452–14457
  63. Popa I, Fernandez JM, Garcia-Manyes S (2011) Direct quantification of the attempt frequency determining the mechanical unfolding of ubiquitin protein. *J Biol Chem* 286:31072–31079

# Chapter 15

## Observing Single RNA Polymerase Molecules Down to Base-Pair Resolution

Anirban Chakraborty\*, Cong A. Meng\*, and Steven M. Block

### Abstract

During transcriptional elongation, RNA polymerases (RNAP) employ a stepping mechanism to translocate along the DNA template while synthesizing RNA. Optical trapping assays permit the progress of single molecules of RNA polymerase to be monitored in real time, at resolutions down to the level of individual base pairs. Additionally, optical trapping assays permit the application of exquisitely controlled, external forces on RNAP. Responses to such forces can reveal details of the load-dependent kinetics of transcriptional elongation and pausing. Traditionally, the bacterial form of RNAP from *E. coli* has served as a model for the study of transcriptional elongation using optical traps. However, it is now feasible to perform optical trapping experiments using the eukaryotic polymerase, RNAPII, as well. In this report, we describe the methods to perform optical trapping transcriptional elongation assays with both prokaryotic RNAP and eukaryotic RNAPII. We provide detailed instructions on how to reconstitute transcription elongation complexes, derivatize beads used in the assays, and perform optical trapping measurements.

**Key words** Single-molecule, Optical trapping, RNA polymerase, RNA polymerase II, Transcription

---

### 1 Introduction

Transcription is the first and the most highly regulated step in gene expression. The molecular motor responsible for transcription, RNA polymerase is the direct or indirect target of all forms of transcriptional regulation. The multi-subunit RNA polymerases are structurally and functionally conserved across all three domains of life: bacteria, archaea, and eukaryotes [1]. Prokaryotic RNAP is the best-studied of the multi-subunit RNA polymerases, and has traditionally served as a model to analyze transcription. However,

---

\*Author contributed equally with all other contributors.

**Electronic supplementary material** The online version of this chapter (doi:[10.1007/978-1-4939-6421-5\\_15](https://doi.org/10.1007/978-1-4939-6421-5_15)) contains supplementary material, which is available to authorized users.

driven by improvements in biochemical methodologies and in vitro transcription assays over the past few years, it is now possible to study messenger RNA (mRNA) production by eukaryotic RNA polymerase II (RNAPII), as well [2–6].

The process of transcription may be subdivided, broadly, into three distinct phases: initiation, elongation, and termination. Transcription elongation complexes (TEC) are typically stable and processive, transcribing up to several thousands of base pairs before releasing from the DNA template [5, 7]. However, the processive motion is irregular, because it is frequently interrupted by transcriptional pausing, as RNA polymerase enters into one or more off-pathway states. In both prokaryotes and eukaryotes, transcriptional pausing can serve, among other things, as an important gene regulatory mechanism, by controlling the overall speed of elongation, and thereby the rate of production of cellular mRNA [8–11].

The motion of RNAP during its elongation phase is a process ideally suited for optical trapping studies [12–16]. Translocation not only involves significant displacement of RNAP but also the generation of force, and both these quantities can be measured directly with optical traps. Using an optical trapping assay, an external force can be applied between the transcription elongation complex (TEC) and the template DNA in a direction that either assists or hinders transcription. The directionality and magnitude of the applied load can also affect the elongation kinetics, and particularly the propensity to enter into, or exit from, transcriptional pause states [6, 8–11].

In the original single-molecule assay for TEC motion, a transcriptionally stalled RNAP from *E. coli* was attached directly to the cover glass surface in a flow cell, while the downstream end of its associated DNA template (typically, a few kb in length) was attached to a gold particle, to produce a “tethered particle assay,” where the Brownian motion of the bead was constrained by the length of its tether to the surface [17]. Subsequent transcription, which could be reactivated triggered by introducing the four ribonucleotides (NTPs) into the flow cell, would shorten the tether, and thereby reduce the extent of the Brownian motion, which could be monitored by video analysis. In a subsequent adaptation of this assay that considerably improved upon its temporal and spatial resolution, an optical trap was used to capture the diffusing, tethered bead (now made of polystyrene), and subsequently used to stretch out the DNA tether under constant tension, thereby allowing elongation to be scored in real-time by simply measuring the trapped bead displacement [13, 14]. The main limitation of the surface-tethered assay is mechanical stability of the cover glass surface, which can be subject to significant drift and vibrational noise.

The advent of the “dumbbell assay” circumvented the limitations of the surface-tethered assay, by optically levitating the assay

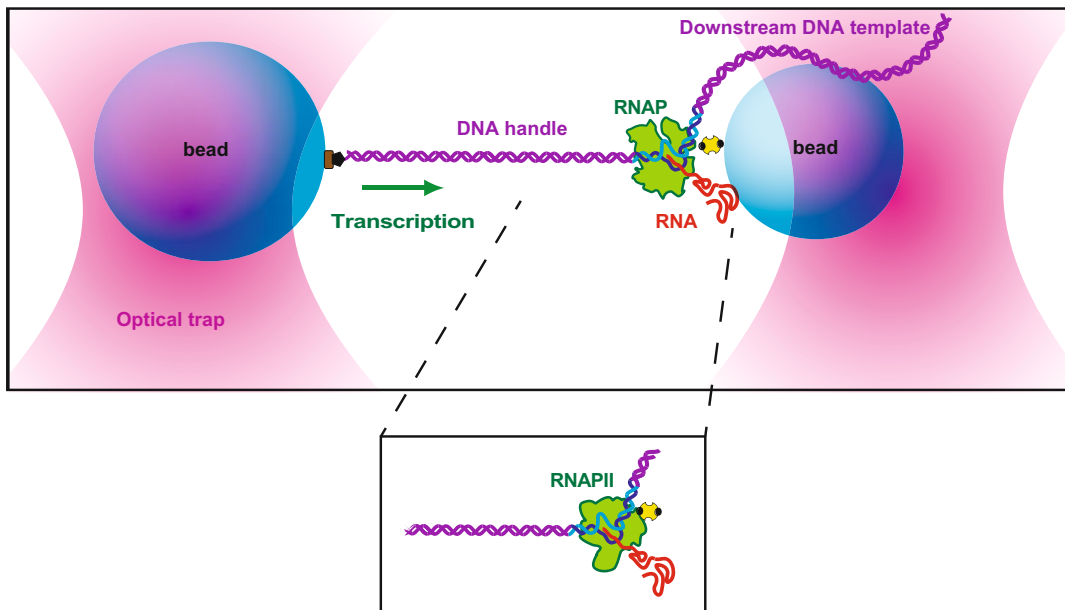


**Fig. 1** “Dumbbell” tether (not to scale) is formed between two beads (blue) held in separate optical traps (pink), with one bead attached to RNAP (green) via an avidin–biotin linkage (yellow, black), and the other bead attached to a upstream DNA handle (purple) via a digoxigenin–anitdigoxigenin linkage (brown, black). As transcription proceeds (green arrow indicates direction), the tether extension (inter-bead distance) increases. The same “dumbbell” geometry can be applied to study RNAPII TEC (see *inset*)

components above the cover glass surface. Owing to its enhanced mechanical stability, the dumbbell assay has achieved, with appropriate instrumentation, angstrom-level resolution (over a bandwidth of ~100 Hz), which is more than adequate to detect transcriptional motion down to the level of individual base pairs. The dumbbell assay has therefore become the method of choice for analyzing transcriptional elongation and pausing [11, 12]. In the assay (shown in Fig. 1), a molecule of biotin-labeled RNAP (transcriptionally stalled on its DNA template) is attached to a small polystyrene bead via a biotin–avidin linkage, while the upstream end of the digoxigenin-labeled DNA template is attached to a slightly larger bead, via a digoxigenin–antidigoxigenin linkage. The entire bead-RNAP-DNA-bead assembly is levitated above the cover glass surface by dual optical traps, and held under constant tension by the use of a force clamp (this clamp may be active or passive; see [18, 19]). Upon the addition of four NTPs, the transcriptionally stalled RNAP actively elongates, and its subsequent motion is monitored by measuring extensional changes in the DNA, which drive displacement of the trapped beads.

In this chapter, we describe protocols for performing two variants of the optical trapping dumbbell assay. The first is an assay designed to measure transcriptional elongation and pausing

by *E. coli* RNAP under assisting loads [9]. The second is an assay designed to measure transcriptional elongation and pausing by *Saccharomyces cerevisiae* RNAPII under assisting loads [4]. Although both the prokaryotic and eukaryotic versions of these assays exploit nearly identical experimental geometries, the procedures for assembling the enzyme complexes differ significantly. Transcriptionally stalled *E. coli* TECs can be reconstituted by the incubation of RNAP with a DNA template containing an appropriate promoter sequence, and the subsequent addition of a subset of the four NTPs, to walk it out to a known location near the promoter (Fig. 2a) [11]. An analogous strategy to prepare *S. cerevisiae* TEC is not feasible [5]: under single-molecule conditions, RNAPII molecules only rarely bind the promoter region and ultimately enter into a state of elongation. Instead, RNAPII typically requires the presence of at least five general transcription factors in order to bind the promoter and transition to a functional TEC [20]. General transcription factors may be omitted from RNAPII assays, however, by using a promoter-less approach: one that involves assembling an artificial transcription bubble that mimics the transcriptional complex configuration of the elongation phase, consisting of a DNA “scaffold” and a short RNA oligomer, to function as a nascent transcript (Fig. 2b) [4, 21–23]. When appropriately produced, both RNAP and RNAPII elongation complexes produce reasonable density of tethers that can be optically trapped in the dumbbell assay. However, the RNAPII assay for *S. cerevisiae* is less efficient: Upon the addition of all four NTPs, the fraction of active TECs is much lower than for RNAP from *E. coli*.

## 2 Materials

### 2.1 Optical Trapping

#### Assay for *E. coli* RNA

##### *Polymerase* *Transcription* *Elongation*

###### 2.1.1 Preparation of DNA Template

1. Microcentrifuge tube.
2. Plasmid pALB3 (*see Note 1*).
3. Forward primer: 5'-GCCCGACCGCTGCGCCTTATCC-3' (*see Note 2*).
4. Reverse primer: 5'-CGCCAATACGCAAACCGCCTCT-3' with a 5'-digoxigenin modification (*see Note 2*).
5. Deoxynucleotide mix: 2.5 mM dATP, 2.5 mM dGTP, 2.5 mM dCTP, 2.5 mM dTTP.
6. Deionized water.
7. OneTaq polymerase kit (New England Biolabs).
8. Thermal cycler.
9. Qiaquick PCR purification kit (Qiagen).

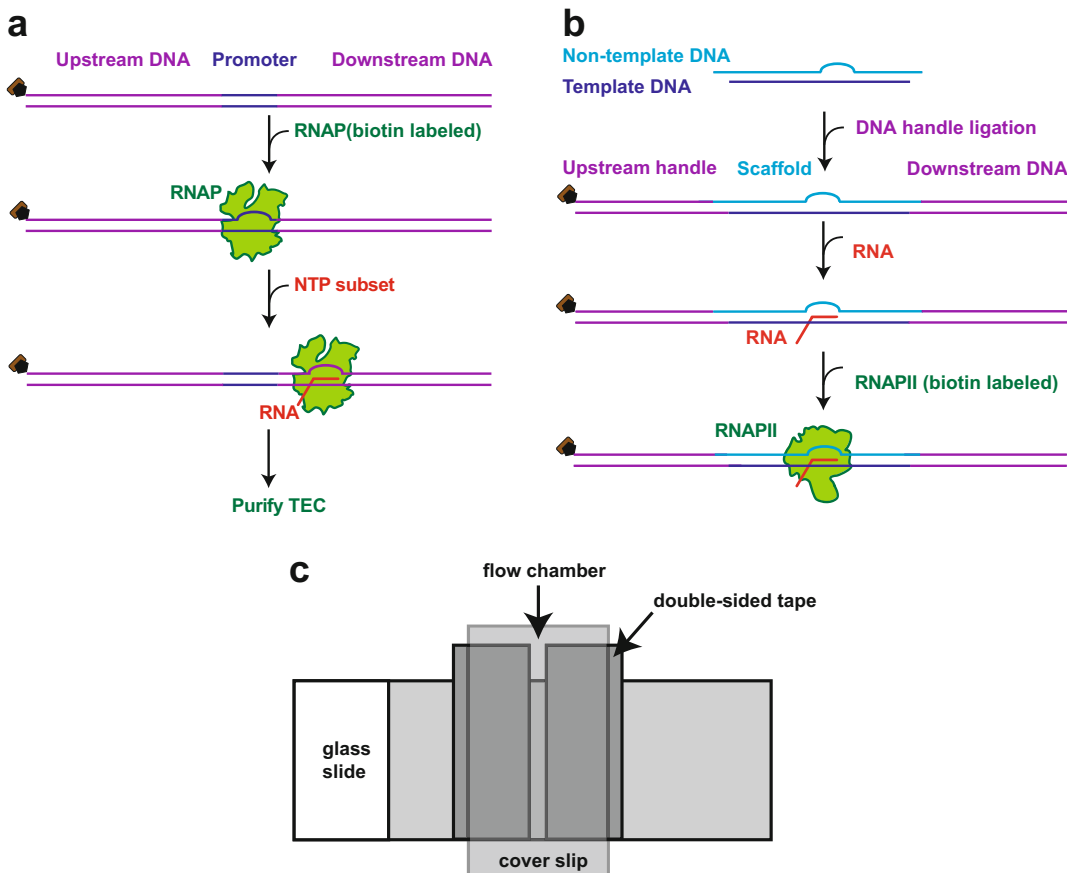


**Fig. 2** (a) Schematic representation of steps to assemble *E. coli* TEC. A DNA template (purple) containing a promoter sequence (dark blue) is incubated with a RNAP and a subset of NTPs. RNAP is stalled at the nucleotide deficient site and forms a TEC, which can then be purified and used for optical trapping. (b) Schematic representation of steps for reconstituting RNAPII TEC. Non-template DNA (light blue) containing an 11 nt noncomplementary sequence anneals to a template DNA (dark blue) and forms a scaffold containing an artificial transcription bubble. The scaffold is ligated to an upstream DNA handle and a downstream DNA template (both in purple), and annealed to a 14 nt RNA fragment (red). Biotin labeled RNAPII (green) is incubated with the scaffold to form the TEC. (c) Schematic diagram of a typical flow cell assembly. Two strips of double-sided tape, separated by 1.5–2 mm, are applied to a glass slide. A plasma-cleaned cover glass is then applied to the double-sided tape, allowing a flow chamber to be formed between glass slide and cover glass. The assembly is then pressed to seal the flow chamber

### 2.1.2 Preparation of RNA Polymerase Transcription Elongation Complex

1. ACG ribonucleotide mix: 25 μM ATP, 25 μM CTP, 25 μM GTP.
2. 31.5 mM initiating dinucleotide: ApU.
3. 1 mg/ml nuclease-free acetylated BSA.
4. 50 % glycerol.
5. Biotin-labeled *E. coli* RNAP.
6. T7A1 buffer: 20 mM Tris-HCl, pH 8.0, 14 mM MgCl<sub>2</sub>, 20 mM NaCl, 14 mM 2-mercaptoethanol, 0.1 mM EDTA pH 8.0.

7. PHC column buffer: 50 mM HEPES, pH 8.0, 130 mM KCl, 4 mM MgCl<sub>2</sub>, 0.1 mM EDTA, pH 8.0, 20 µg/ml acetylated BSA, 4 % glycerol.
8. CL-6B sepharose (Sigma-Aldrich).
9. Geiger counter.

**2.1.3 Coupling Anti-digoxigenin to Carboxyl-Polystyrene Beads**

1. Carboxyl-polystyrene beads, 0.92 µm average diameter (Bangs Laboratories).
2. Anti-digoxigenin antibody (Roche).
3. 1-ethyl-3-(3-dimethylaminopropyl)carbodiimide · HCl (EDC).
4. N-hydroxysulfosuccinimide (Sulfo-NHS).
5. 1 M glycine.
6. Tween 20.
7. MES buffer: 100 mM MES, pH 5, 0.5 % Tween.
8. Phosphate buffer: 100 mM NaH<sub>2</sub>PO<sub>4</sub>, pH 7.5, 0.5 % Tween.
9. 2-mercaptoethanol.
10. Microcentrifuge.
11. Tube rotator.
12. Sonicator.

**2.1.4 Coupling Avidin to Carboxyl-Polystyrene Beads**

1. Carboxyl-polystyrene beads, 0.6 µm average diameter (PolyMicrospheres).
2. 5 bottles of 1 mg/ml Avidin-DN (Vector Laboratories).
3. 1-ethyl-3-(3-dimethylaminopropyl)carbodiimide · HCl (EDC).
4. N-hydroxysulfosuccinimide (Sulfo-NHS).
5. 10 mg/ml biotin-X-cadaverin (Life Technologies; *see Note 3*).
6. 1 M glycine.
7. Tween 20.
8. MES buffer: 100 mM MES, pH 5, 0.1 % Tween.
9. Phosphate buffer: 100 mM NaH<sub>2</sub>PO<sub>4</sub>, pH 7.5, 0.1 % Tween.
10. Microcentrifuge.
11. Tube rotator.
12. Sonicator.

**2.1.5 Flow Cells Preparation**

1. Microscope cover glass (22 mm × 40 mm × 0.15 mm; Fisherbrand).
2. Plasma cleaner (Harrick Plasma PDC-001).
3. Ceramic rack for cover glass.
4. Double-sided tape (0.5 in. width).

5. Microscope slides (1 mm thick, 25 × 75 mm; Thermo Scientific).
6. 100 % ethanol.

#### *2.1.6 Single-Molecule Optical Tweezers Assay*

1. Anti-digoxigenin-coated polystyrene beads, 0.915 μm average diameter.
2. Avidin-coated polystyrene beads, 0.6 μm average diameter.
3. *E. coli* transcription buffer: 50 mM HEPES pH 8.0, 130 mM KCl, 4 mM MgCl<sub>2</sub>, 0.1 mM EDTA, 1 mM DTT.
4. Nuclease-free acetylated BSA.
5. *E. coli* transcription buffer supplemented with 3 mg/ml BSA (*see Note 4*).
6. Trapping buffer: *E. coli* transcription buffer supplemented with 8.3 mg/ml glucose (Sigma), 46 units/ml glucose oxidase (Calbiochem), 94 units/ml catalase (Sigma Aldrich) (*see Note 5*).
7. 1 mM ribonucleotide triphosphate solution (NTP): 1 mM ATP, 1 mM GTP, 1 mM CTP, and 1 mM UTP.
8. 3 μM biotin-labeled *E. coli* RNAP.
9. Home-built high-resolution dual-beam optical trap: the core components include 1064 nm ND:YVO<sub>4</sub> laser (Spectra-Physics, T-Series), inverted microscope (Nikon), Nikon oil immersion objective (1.4 NA, APO, PLAN), eight-pole low-pass Bessel filter (Krohn-Hite), position-sensitive detector (Pacific Silicon Sensors), and acousto-optical deflectors (IntraAction) [15, 16]. Refer to Fig. 3 for other optical components.

## **2.2 Optical Trapping Assay for *S. cerevisiae* RNAPII Transcription Elongation**

### *2.2.1 Preparation of DNA Template*

1. Microcentrifuge tube.
2. Plasmid pPM172 (*see Note 6*).
3. Forward primer: 5'-CACAGGCGCGCCACGGGGTGAG-CAGTCACG-3' (*see Note 7*).
4. Reverse primer: 5'-TGCAGGCGGGAACACAACCTGG-3' (*see Note 7*).
5. Deoxynucleotide mix: 2.5 mM dATP, 2.5 mM dGTP, 2.5 mM dCTP, 2.5 mM dTTP.
6. Deionized water.
7. OneTaq polymerase kit (New England Biolabs).
8. Thermal Cycler.
9. Qiaquick PCR purification kit (Qiagen).
10. Restriction enzyme: DraIII (*see Note 8*).
11. UV spectrophotometer.

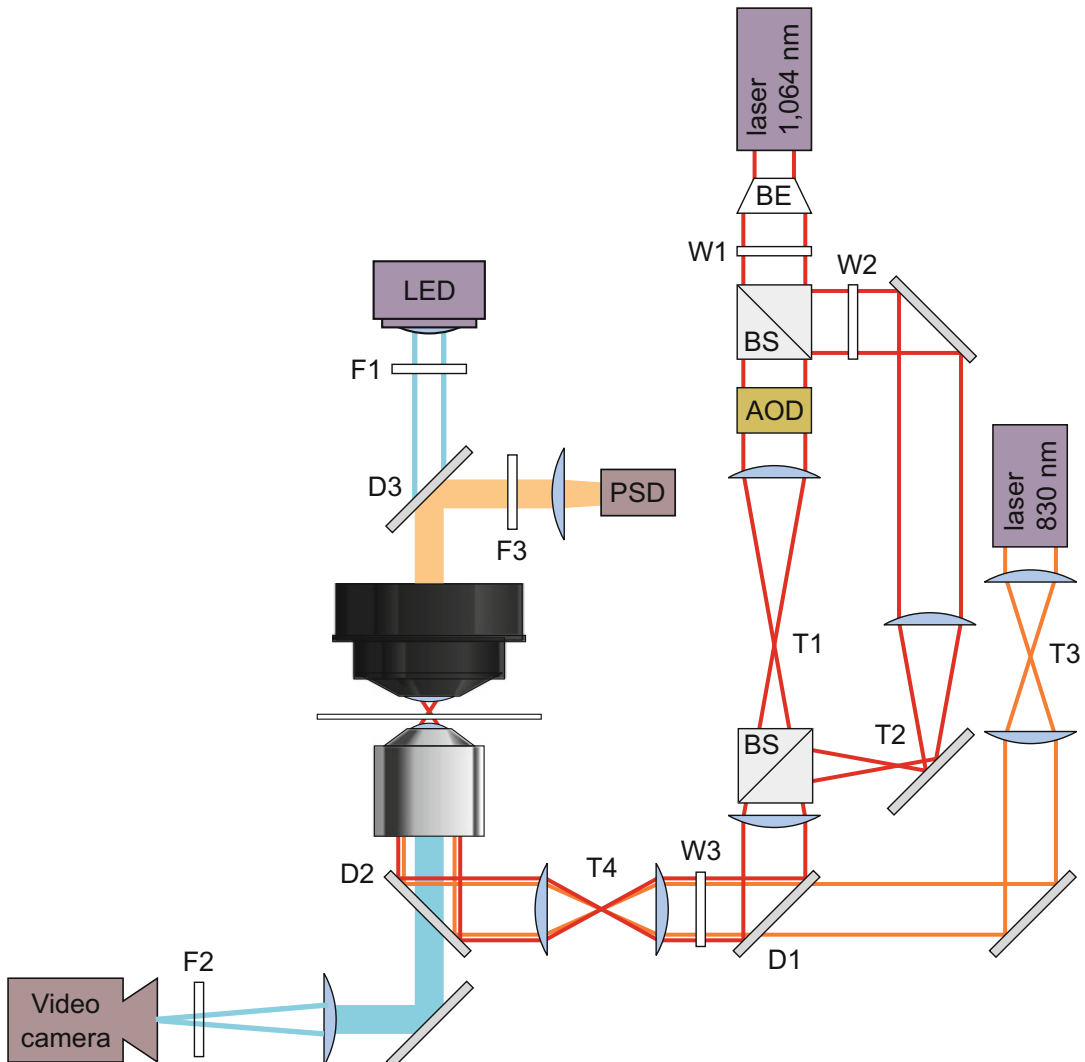


**Fig. 3** Trapping optics: Schematic optical layout of the dual-beam optical traps. *Solid lines* indicate lasers and light sources: 830 nm detection laser (orange), 1064 nm trapping laser (red), and illuminating LED (blue). Filled bars are emissions received by detectors: position sensitive detector (PSD), and a video camera. Trapping laser is expanded using a beam expander (BE), and then split by a polarizing beam splitting cube (BS). The strong trapping beam is then steered in position by acousto-optical deflectors (AOD), thus making it movable. A telescope T3, is used for manually steering and aligning detection beam position in the specimen plane. Similarly, telescope T4 is used for crude aligning both trapping and detection lasers in specimen plane. Filters (F), Wollaston prisms (W), pinholes (P), dichroic mirrors (D), mirrors (M), and telescopes (T) are labeled. In brief, F1 is used to adjust brightness of microscope illumination. F2 and F3 are IR filters (1064 nm) to shield video camera and PSD from the trapping laser

#### 2.2.2 Preparation of DNA Handle

1. Microcentrifuge tube.
2. Plasmid pRL702.
3. Forward primer: 5'-CAGCGGTAATTCCGAGCTGCA-3' (*see Note 9*).

4. Reverse primer: 5'-CGATTCCAGCGCACGTTGTC-3' with a 5'-digoxigenin modification (*see Note 9*).
5. 10 mM deoxynucleotide (dNTP) mix: 2.5 mM dATP, 2.5 mM dGTP, 2.5 mM dCTP, 2.5 mM dTTP.
6. Deionized water.
7. OneTaq polymerase kit (New England Biolabs).
8. Thermal cycler.
9. Qiaquick PCR purification kit (Qiagen).
10. Restriction enzyme: StyI (*see Note 10*).
11. UV spectrophotometer.

#### *2.2.3 DNA Scaffold Assembly*

1. Microcentrifuge tube.
2. Template oligo: 5'-GCTTTTCGCCTTGTCTGGCTGCGCGT CGGTGGGTGTTCTGATGGCTGTTGTTCTATAG C-3' (*see Note 11*).
3. Non template oligo: 5'-CAAGGCTATAAGGAAACAATGTC GGTAGACGAAACACCCACCGACGCGCAGCCGACAAGG CGAAAAGCGGG-3' (*see Note 11*).
4. Reconstitution Buffer (RB): 10 mM Tris-HCl, pH 7.9, 40 mM KCl.
5. Deionized water.
6. Thermal cycler.
7. T4 DNA ligase.
8. T4 DNA ligase buffer.
9. Agarose.
10. TAE buffer: Tris-acetate-EDTA.
11. 1 kb plus DNA ladder (Life Technologies).
12. SYBR Gold stain (ThermoFisher Scientific).

#### *2.2.4 Reconstitution of RNAPII Transcription Elongation Complex*

1. Yeast elongation buffer (YEB): 25 mM HEPES, pH 8.0, 130 mM KCl, 5 mM MgCl<sub>2</sub>, 0.15 mM EDTA, 1 mM DTT, 5 % glycerol, 0.125 mg/ml BSA.
2. 2 μM RNA: 5'-UUUUUACAGCCAUC-3'.
3. 300 μM *S. cerevisiae* RNAPII.
4. ACG ribonucleotide mix: 4 mM ATP, 4 mM CTP, 4 mM GTP.
5. Liquid nitrogen.

#### *2.2.5 Single-Molecule Optical Trapping Assay*

1. Anti-digoxigenin-coated polystyrene beads, 0.92 μm average diameter (*see Subheading 2.1.3*).
2. Avidin-coated polystyrene beads, 0.6 μm average diameter (*see Subheading 2.1.4*).

3. *S. cerevisiae* transcription buffer: 20 mM HEPES (pH 8.0), 80 mM potassium acetate, 5 mM magnesium acetate, 0.1 mM EDTA, and 0.1 mM DTT.
4. Nuclease-free BSA.
5. *S. cerevisiae* transcription buffer supplemented with 3 mg/ml BSA.
6. Trapping buffer: *S. cerevisiae* transcription buffer supplemented with 8.3 mg/ml glucose (Sigma), 46 units/ml glucose oxidase (Calbiochem), 94 units/ml catalase (Sigma) (see Note 5).
7. 1 mM ribonucleotide triphosphate solution (NTP): 1 mM ATP, 1 mM GTP, 1 mM CTP, and 1 mM UTP.
8. 300 nM biotin-labeled *S. cerevisiae* RNAPII.
9. Home-built high-resolution dual-beam optical trap (see Subheading 2.1.6, item 9).

### 3 Methods

#### 3.1 Optical Trapping Assay for *E. coli* RNA Polymerase Transcription Elongation

##### 3.1.1 Preparation of DNA Template

1. In a PCR microcentrifuge tube, prepare a 50  $\mu$ l reaction mixture containing 0.2 ng/ml plasmid pALB3, 0.2  $\mu$ M forward primer, 0.2  $\mu$ M reverse primer, 0.8 mM dNTP mix, 10 units of OneTaq DNA polymerase in 1 $\times$  standard *Taq* buffer (see Notes 1 and 2).
2. Perform PCR amplification using an initial denaturation at 94 °C for 5 min and 34 cycles of denaturation at 94 °C for 1 min, annealing at 55 °C for 1 min, and extension at 72 °C for 6 s, followed by a final extension for 10 min at 72 °C.
3. Purify the 4750 bp DNA fragment using Qiaquick PCR purification kit. Determine the concentration of the DNA fragment by measuring UV absorbance using a spectrophotometer.

##### 3.1.2 Reconstitution of RNA Polymerase Transcription Elongation Complex

1. Prepare a 200  $\mu$ l transcription reaction mixture containing 2.5  $\mu$ M ATP, 2.5  $\mu$ M GTP, 2.5  $\mu$ M CTP, 250  $\mu$ M ApU, 10 nM DNA template, 20  $\mu$ g/ml BSA, 1.5 % glycerol, 30  $\mu$ Ci [ $\alpha^{32}$ P]-GTP, and 50 nM biotin-labeled *E. coli* RNAP, in T7A1 buffer.
2. Incubate the transcription reaction mixture at 37 °C for 20 min.
3. Apply 200  $\mu$ l reaction mixture from step 1, to a 12 ml CL-6B sepharose column (pre-equilibrated with 100 ml PHC column buffer).
4. Elute the column with 4 ml PHC column buffer. Collect 300  $\mu$ l fractions in microcentrifuge tubes.
5. Identify fractions containing TEC by measuring the radioactivity signal in each tube with a Geiger counter.

### 3.1.3 Coupling Anti-digoxigenin to Carboxyl-Polystyrene Bead

1. Remove polystyrene beads container from fridge, and vortex the container for 30 s. Sonicate the container in ice water for 3 min.
2. In a 1.5 ml microcentrifuge tube, add 150  $\mu$ l polystyrene beads, and 150  $\mu$ l MES buffer. Mix well by inverting the tube.
3. Centrifuge the beads at  $8500 \times g$  for 3 min. Remove the supernatant and resuspend the beads in 200  $\mu$ l MES buffer. Repeat this step twice.
4. In a separate 1.5 ml microcentrifuge tube, add 900  $\mu$ l MES buffer and 2.1 mg sulpho-NHS. Vortex the solution and add to the beads in **step 3**.
5. Add 5 mg EDC to the bead mixture. Vortex the tube to mix the contents, and then rotate the tube at room temperature for 30 min. (This reaction couples an amine-reactive group to the beads).
6. Quench the reaction by adding 1  $\mu$ l 2-mercaptoethanol to the bead mixture. Vortex and rotate the tube at room temperature for 10 min.
7. Centrifuge the beads at  $8500 \times g$  for 5 min. Remove the supernatant and resuspend beads in 200  $\mu$ l phosphate buffer. Repeat this step twice. After the last centrifugation, resuspend the beads in 500  $\mu$ l phosphate buffer.
8. Separately, add 1 ml phosphate buffer to a microcentrifuge tube containing 200  $\mu$ g anti-digoxigenin antibody. Dissolve the anti-digoxigenin antibody by rotating the tube at room temperature for 20 min.
9. Add the anti-digoxigenin antibody to the beads from **step 7**. Rotate the tube for 2 h at room temperature.
10. Quench the reaction by adding 30  $\mu$ l 1 M glycine. Rotate the tube for 10 min at room temperature.
11. Centrifuge the bead mixture at  $8500 \times g$  for 6 min. Remove the supernatant and resuspend the beads in 200  $\mu$ l phosphate buffer. Repeat this step four times.
12. Label and store the solution from **step 11** on a rotator at 4 °C (*see Note 12*).
13. Transfer 50  $\mu$ l beads to a new microcentrifuge tube.
14. Centrifuge the beads at  $8500 \times g$  for 6 min. Remove supernatant and resuspend the beads in 600  $\mu$ l phosphate buffer. Repeat this step four times. After the centrifugation, resuspend the beads in 50  $\mu$ l phosphate buffer.
15. Sonicate the beads in ice water for 3 min (*see Note 13*).

### 3.1.4 Coupling Avidin to Carboxyl-Polystyrene Beads

1. Remove polystyrene beads container from fridge, and vortex the container for 30 s. Sonicate the container in ice water for 3 min.
2. In a 15 ml tube, combine 200  $\mu$ l beads, 200  $\mu$ l 10 mg/ml biotin-X-cadaverin solution, 20 mg Sulfo-NHS, and 1.6 ml MES buffer. Mix by inverting the tube. Add 50 mg EDC. Vortex the falcon tube to mix the contents.
3. Rotate the tube for 16 h at room temperature.
4. Quench the reaction by adding 500  $\mu$ l 1 M glycine. Rotate the tube for 15 min at room temperature.
5. Prepare five 500  $\mu$ l aliquots of the beads in 1.5 ml microcentrifuge tubes.
6. Centrifuge the bead aliquots at  $8500 \times g$  for 5 min. Remove the supernatants and resuspend each pellet in 200  $\mu$ l phosphate buffer. Repeat this step four times. After the last centrifugation, resuspend each bead pellet in 500  $\mu$ l phosphate buffer. Sonicate the tube in ice water for 2 min.
7. Add each of the bead suspensions to a corresponding tube of 1 ml 1 mg/ml Avidin-DN. Mix quickly with a pipette and transfer each mixture to a 1.5 ml microcentrifuge tube (see Note 14). Label and store the tubes on a rotator at 4 °C. Incubate, at least overnight, before the next step (see Note 15).
8. Take one tube from step 7.
9. Centrifuge the beads at  $8500 \times g$  for 6 min. Remove supernatant and resuspend the beads in 600  $\mu$ l phosphate buffer. Repeat the step four times. After the last centrifugation, resuspend the beads in 40  $\mu$ l phosphate buffer. Sonicate the tube in ice water for 3 min (see Note 13).

### 3.1.5 Flow Cell Preparation

1. Place a microscope cover glass in a ceramic cover glass rack.
2. Place the rack in the plasma cleaning chamber.
3. Start the vacuum pump. Adjust the air intake until pressure inside the chamber drops to 1 Torr. Expose the cover glass to plasma discharge for 5 min.
4. Use the cleaned cover glass immediately, or alternatively, store them in a closed container.
5. Use 100 % ethanol to clean a designated bench surface.
6. Place a glass slide on the cleaned bench surface. On the glass slide, apply two parallel strips of double-sided tape separated by 1–2 mm.
7. Place a plasma-cleaned cover glass on the tape strips and press down to form seal. A chamber thus formed, can retain of 5–7  $\mu$ l sample. See Fig. 2c for schematic diagram of a flow cell.
8. The assembled cover glass can be readily used or stored in closed container for future usage.

### 3.1.6 Single-Molecule Optical Trapping Assay

1. Add 2  $\mu$ l anti-digoxigenin-coated polystyrene beads and 2  $\mu$ l avidin-coated polystyrene beads in two separate 0.5 ml microcentrifuge tubes. Resuspend the beads in each tube in 60  $\mu$ l *E. coli* transcription buffer supplemented with 3 mg/ml BSA (*see Note 16*).
2. Centrifuge the beads at  $8500 \times g$ . Remove the supernatant and resuspend each bead pellet in 2  $\mu$ l transcription buffer. Sonicate on ice water for 5 min at 50 % intensity. After sonication, place the beads on ice.
3. In a microcentrifuge tube, mix, anti-digoxigenin-coated polystyrene beads, avidin-coated polystyrene beads and 2  $\mu$ l TEC (from Subheading 3.1.2). Incubate at room temperature for 40 min (*see Note 17*). At this stage, the “dumbbell” (bead-RNAPII-DNA-bead complex) is formed (Fig. 1) and is ready for optical trapping.
4. In a 0.5 ml microcentrifuge tube, add 1  $\mu$ l of the bead-RNA-PII-DNA-bead complex and 30  $\mu$ l *E. coli* trapping buffer. Mix gently with a pipette and keep on ice.
5. Fill a flow cell channel with 7  $\mu$ l suspension from step 4.
6. Prepare 30  $\mu$ l 1 mM NTP solution in *E. coli* trapping buffer. Place on ice (*see Note 18*).
7. Mount the flow cell on the microscope stage. Adjust the objective and condenser to bring the surface of the cover glass into focus.
8. Use a customized LabView program to maneuver the optical trap to pick up a free-floating 0.6  $\mu$ m bead, and perform position calibration (*see Note 19*).
9. Flow 7  $\mu$ l 1 mM NTP solution into the sample chamber.
10. Identify a candidate tether (a typical candidate tether is represented by a 0.6  $\mu$ m bead floating in the vicinity of a surface-adhered 0.92  $\mu$ m bead.).
11. First, maneuver static optical trap to capture the floating 0.6  $\mu$ m bead in the candidate tether, then maneuver the steerable optical trap to capture the surface-adhered 0.92  $\mu$ m bead. Monitor the increase in tether extension while ramping up the force (up to a maximum force of 15 pN). Plot force parameterized by extension to generate a force extension curve (FEC). Fit the curve to a worm-like chain (WLC) model of DNA elasticity and determine the persistence length of the DNA (the WLC model provides a relation between force, extension, and persistence length of DNA) [24]. For a single tether, the appropriate persistence length is >20 nm and the tether extension is within 50 nm of expectation.

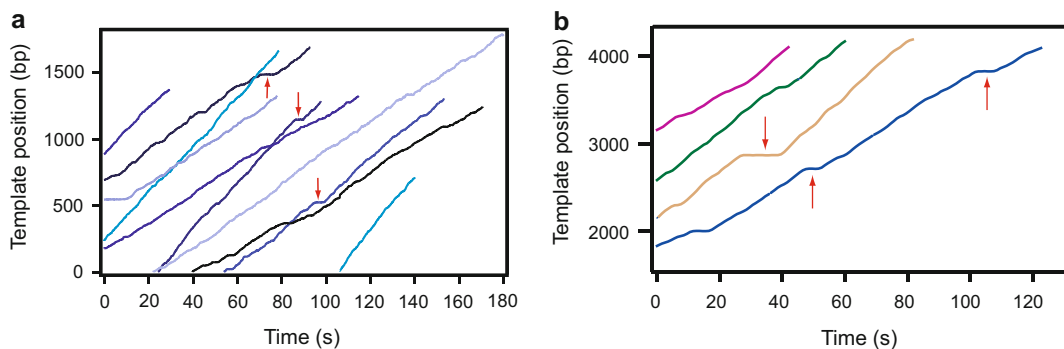


**Fig. 4** Representative traces of transcription elongation are shown in panel (a) (RNAP) and (b) (RNAPII). Tether length is converted to RNAP's position along the DNA template and plotted as a function of time. The change in translocational position of RNAP with time shows transcription elongation which is occasionally interrupted by ubiquitous pauses (red arrows)

### 3.2 Optical Trapping Assay for *S. cerevisiae* RNAPII Transcription Elongation

#### 3.2.1 Preparation of DNA Template

12. Upon finding an appropriate tether, turn on active force clamp program at the desired force (5–30 pN) (*see Note 20*).
  13. Analyze the data using established methods using a customized program (*see Note 21*) [4, 9, 11, 12]. *See Fig. 4a* for representative traces.
1. In a PCR microcentrifuge tube, prepare a 50  $\mu$ l reaction mixture containing 8  $\mu$ l 10 ng/ $\mu$ l plasmid pPM172, 2.5  $\mu$ l 10  $\mu$ M forward primer, 2.5  $\mu$ l 10  $\mu$ M reverse primer, 1  $\mu$ l 10 mM dNTP mix (10 mM each of dATP, dCTP, dTTP, and dGTP), 5  $\mu$ l 10 $\times$  standard *Taq* reaction buffer, and 10 units of One *Taq* DNA polymerase (*see Notes 6 and 7*).
  2. Perform PCR amplification using an initial denaturation at 94 °C for 30 s and 30 cycles of denaturation at 94 °C for 30 s, annealing at 65 °C for 30 s, and extension at 65 °C for 5 min, followed by a final extension at 65 °C for 9 min.
  3. Purify the 4750 bp DNA fragment using Qiaquick PCR purification kit.
  4. Digest the purified DNA fragment with DraIII, following manufacturer's protocol for 3 h at 37 °C (*see Note 8*).
  5. Purify the digested DNA fragment using Qiaquick PCR purification kit. Determine the concentration of the DNA fragment by measuring UV absorbance using spectrophotometer.

#### 3.2.2 Preparation of DNA Handle

1. In a PCR microcentrifuge tube, prepare a 50  $\mu$ l reaction mixture containing 8  $\mu$ l of 10 ng plasmid pPM172, 2.5  $\mu$ l 10  $\mu$ M forward primer, 2.5  $\mu$ l 10  $\mu$ M reverse primer, 1  $\mu$ l 10 mM dNTP mix, 5  $\mu$ l 10 $\times$  standard *Taq* reaction buffer and 10 units of One *Taq* DNA polymerase (*see Note 9*).

2. Perform PCR amplification using an initial denaturation at 94 °C for 30 s and 30 cycles of denaturation at 94 °C for 30 s, annealing at 65 °C for 30 s, and extension at 65 °C for 3 min, followed by a final extension at 65 °C for 5 min.
3. Purify the 2700 bp DNA fragment using Qiaquick PCR purification kit.
4. Digest the purified DNA fragment with StyI for 3 h at 37 °C following manufacturer's protocol (*see Note 10*).
5. Purify the digested DNA fragment using Qiaquick PCR purification kit. Determine the concentration of the DNA fragment by measuring UV absorbance using a spectrophotometer.

### *3.2.3 DNA Scaffold Assembly*

1. In a PCR microcentrifuge tube, mix 1 µl 5 µM template oligo, 1 µl 5 µM non-template oligo, 2 µl 5× RB, and 6 µl water (*see Note 11*).
2. Anneal the oligos in a thermal cycler by incubating the mixture at 45 °C for 5 min and then cooling down to 25 °C at the rate of 1 °C/min. This produces 5 µM scaffold.
3. In a microcentrifuge tube, mix 0.4 µM scaffold, 0.4 µM DNA handle, 0.4 µM DNA template, 400 units T4 DNA ligase in T4 DNA ligase buffer to a total reaction volume of 50 µl. Incubate the mixture for 16 h at 4 °C.
4. Prepare a 0.8 % agarose gel in TAE buffer. In consecutive wells, load (1) 1 Kb plus DNA ladder, (2) 5 µl ligation product (from **step 3**), (3) 22.5 µl ligation product (from **step 3**), (4) 22.5 µl ligation product (from **step 3**). Run the gel at 100 V for 1.5 h.
5. Excise lanes (1) and (2). Stain the excised lanes in SYBR Gold solution (following manufacturer's staining protocol), and identify the 7500 bp DNA band. Use this stained gel fragment as a reference to excise the 7500 bp bands from the unstained gel fragment.
6. Extract the 7500 bp band from the agarose gel using the Qiaquick Gel Extraction Kit. Elute the band in 30 µl EB following manufacturer's protocol.

### *3.2.4 Reconstitution of Transcription Elongation Complex*

1. In a microcentrifuge tube, mix 30 µl gel extracted ligated product (from Subheading **3.2.3**), 8 µl 5× YEB, and 1 µl of 2 µM RNA. Incubate for 45 min at 30 °C.
2. Add 1 µl 300 nM RNAPII. Mix well and incubate for 15 min at 30 °C.
3. Add 1 µl ACG mix and incubate for 30 min at 30 °C.
4. Prepare 2 µl aliquots of the RNAPII TEC and freeze the aliquots in liquid nitrogen. Store at –80 °C.

### 3.2.5 Single-Molecule Optical Trapping Assay

1. Prepare anti-digoxigenin-coated polystyrene beads and avidin-coated polystyrene beads as described in Subheadings 3.1.3 and 3.1.4.
2. Prepare flow cells as described in Subheading 3.1.5.
3. Add 2.0  $\mu\text{l}$  anti-digoxigenin-coated polystyrene beads and 2.0  $\mu\text{l}$  avidin-coated polystyrene beads in two separate 0.5 ml microcentrifuge tubes. Resuspend the beads in each tube in 60  $\mu\text{l}$  *S. cerevisiae* transcription buffer supplemented with 3 mg/ml BSA (see Note 4).
4. Centrifuge the beads at  $8500 \times g$ . Remove the supernatant and resuspend each bead pellet in 2  $\mu\text{l}$  *S. cerevisiae* transcription buffer. Sonicate on ice water for 5 min at 50 % intensity. After sonication, place the beads on ice.
5. Add 2  $\mu\text{l}$  RNAPII TEC (from Subheading 3.2.4) to the avidin-coated beads. Gently mix with a pipette, and incubate at room temperature for 40 min (see Note 14).
6. Centrifuge the RNAPII-bead mixture at  $8500 \times g$  for 30 s. Remove the supernatant and resuspend the beads in 1  $\mu\text{l}$  *S. cerevisiae* transcription buffer. Sonicate the tube on ice water for 2 min at 50 % intensity.
7. Add the anti-digoxigenin-coated beads from step 2. Mix gently with a pipette. Incubate at room temperature for 30 min and then place the tube on ice. At this stage, the “dumbbell” (bead-RNAPII-DNA-bead complex) is formed (see Fig. 2b) and is ready for optical trapping.
8. In a 0.5 ml microcentrifuge tube, add 1  $\mu\text{l}$  of the bead-RNAPII-DNA-bead complex and 30  $\mu\text{l}$  oxygen-scavenging system. Mix gently with a pipette and keep on ice.
9. Fill a flow cell channel with 7  $\mu\text{l}$  suspension from step 7.
10. Prepare 30  $\mu\text{l}$  1 mM NTP solution in *S. cerevisiae* transcription buffer. Place on ice (see Note 18).
11. Mount the flow cell on the microscope stage. Adjust the objective and condenser to bring the surface of the cover glass into focus.
12. Use a customized LabView program to maneuver the optical trap to pick up a free-floating 0.6  $\mu\text{m}$  bead, and perform position calibration. In brief, a second, low-power detection laser is deployed to perform laser-based position detection (see Note 19).
13. Flow 7  $\mu\text{l}$  1 mM NTP solution into the sample chamber.
14. Perform steps 10–13 in Subheading 3.1.6.

---

**4 Notes**

1. The plasmid pALB3 encodes a bacterial template DNA containing the following modules in succession: (1) a 2640 bp upstream DNA sequence, (2) a T7A1 promoter DNA, (3) a 1693 bp downstream DNA sequence from the *E. coli* rpoB gene.
2. The forward primer and the reverse primer are used to amplify a 4408 bp DNA fragment.
3. Biotin-X-cadaverine is reconstituted in DMSO.
4. BSA concentration in this buffer is critical for achieving optimal stickiness between the bead and the surface. With too high BSA concentration, most of the beads would not adhere to the surface. Conversely, with low BSA concentration, beads may adhere too strongly to the surface, making it very difficult to levitate the beads off of the surface using optical traps. If optical trapping is performed in the presence of other proteins and/or other buffer conditions, the optimal BSA concentration at this step may have to be reassessed.
5. Optical trapping can produce free radicals. This buffer contains a glucose/glucose oxidase/catalase mediated oxygen scavenging system to prevent the oxidative damage. Typically the oxygen scavenging components can last for 1.5 h on ice, after which the pH of the solution may decrease. Thus, the buffer needs to be made fresh every 1.5 h.
6. Plasmid pPM172 contains a 4750 bp transcription template which consists of a fragment from the human POLR2A gene encoding the UTR and several exons and introns.
7. The forward primer and the reverse primer are used to amplify a 4750 bp DNA fragment.
8. Restriction digestion with DraIII creates a 5' sticky end, capable of ligating to the DNA scaffold.
9. The forward primer and the reverse primer are used amplify a 2700 bp DNA fragment
10. Restriction digestion with StyI creates a 3' sticky end, capable of ligating to the DNA scaffold.
11. Annealing of the template oligo produces a 70 bp scaffold which contains: (1) a 5' DraIII sticky end, (2) an artificial transcription bubble, (3) a 3' StyI sticky end.
12. At this stage, the beads can stay on the rotator at 4 °C for at least 6 months.
13. At this stage, the beads are ready for use and can last for at least 1 month on rotator at 4 °C.

14. When mixing, avoid introducing bubbles to the solution.
15. At this stage, the beads can stay on the rotator and last for at least 6 months.
16. In preparation for assembling the “dumbbell” tether complex, home-made polystyrene beads derivatized with avidin or anti-digoxigenin linkages need to be washed. This step requires suspending the beads in transcription buffer, and coating the beads with BSA.
17. This step allows RNAP to form biotin-avidin linkage with the beads.
18. The solution should be used within 1.5 h. After 1.5 h on ice, the oxygen scavenging system is exhausted.
19. In brief, a low-power detection laser is deployed to perform position calibration, which is achieved by performing back focal plane detection of the signal, based on interference patterns in the detection laser beam [15]. This interference is generated between the forward-scattered detection laser light from the bead and unscattered light. To capture the signal, position sensitive detectors (PSD) are mounted at a plane that is conjugate to the back focal plane of the condenser. The main advantage of back focal plane detection scheme is that it is sensitive to the bead displacement from laser beam axis and insensitive to absolute bead position.
20. In brief, the customized LabView force clamp program actively measures tether extension, adjusts the steerable trap’s position through a feedback loop to maintain a constant tension on the “dumbbell” tether. The program records the change in tether extension in real time. This permits the monitoring of RNAP translocation as a continuous increase in DNA extension.
21. In order to identify the sequence-dependent kinetics of transcriptional elongation, it is necessary to convert the change in tether extension in nanometers to translocational position of RNAP in base pairs. This conversion requires the fitting of a DNA to a WLC model and subsequent estimation of the rise per base pair corresponding to the assisting load (i.e., the force used in the force clamp program).

---

## Electronic Supplementary Material

Below is the link to the electronic supplementary material. Capturing and testing a dumbbell with optical tweezers (WMV 14,606 kB).

## References

1. Decker KB, Hinton DM (2013) Transcription regulation at the core: similarities among bacterial, archaeal, and eukaryotic RNA polymerases. *Annu Rev Microbiol* 67:113–139. doi:[10.1146/annurev-micro-092412-155756](https://doi.org/10.1146/annurev-micro-092412-155756)
2. Hodges C, Bintu L, Lubkowska L, Kashlev M, Bustamante C (2009) Nucleosomal fluctuations govern the transcription dynamics of RNA polymerase II. *Science* 325(5940):626–628. doi:[10.1126/science.1172926](https://doi.org/10.1126/science.1172926)
3. Horn AE, Goodrich JA, Kugel JF (2014) Single molecule studies of RNA polymerase II transcription in vitro. *Transcription* 5(1):e27608
4. Larson MH, Zhou J, Kaplan CD, Palangat M, Kornberg RD, Landick R, Block SM (2012) Trigger loop dynamics mediate the balance between the transcriptional fidelity and speed of RNA polymerase II. *Proc Natl Acad Sci U S A* 109(17):6555–6560. doi:[10.1073/pnas.1200939109](https://doi.org/10.1073/pnas.1200939109)
5. Zhou J, Schweikhard V, Block SM (2013) Single-molecule studies of RNAPII elongation. *Biochim Biophys Acta* 1829(1):29–38. doi:[10.1016/j.bbagen.2012.08.006](https://doi.org/10.1016/j.bbagen.2012.08.006)
6. Galburt EA, Grill SW, Wiedmann A, Lubkowska L, Choy J, Nogales E, Kashlev M, Bustamante C (2007) Backtracking determines the force sensitivity of RNAP II in a factor-dependent manner. *Nature* 446(7137):820–823. doi:[10.1038/nature05701](https://doi.org/10.1038/nature05701)
7. Galburt EA, Grill SW, Bustamante C (2009) Single molecule transcription elongation. *Methods* 48(4):323–332. doi:[10.1016/j.jymeth.2009.04.021](https://doi.org/10.1016/jymeth.2009.04.021)
8. Herbert KM, Greenleaf WJ, Block SM (2008) Single-molecule studies of RNA polymerase: motorizing along. *Annu Rev Biochem* 77:149–176. doi:[10.1146/annurev.biochem.77.073106.100741](https://doi.org/10.1146/annurev.biochem.77.073106.100741)
9. Herbert KM, La Porta A, Wong BJ, Mooney RA, Neuman KC, Landick R, Block SM (2006) Sequence-resolved detection of pausing by single RNA polymerase molecules. *Cell* 125(6):1083–1094. doi:[10.1016/j.cell.2006.04.032](https://doi.org/10.1016/j.cell.2006.04.032)
10. Neuman KC, Abbondanzieri EA, Landick R, Gelles J, Block SM (2003) Ubiquitous transcriptional pausing is independent of RNA polymerase backtracking. *Cell* 115(4):437–447
11. Shaevitz JW, Abbondanzieri EA, Landick R, Block SM (2003) Backtracking by single RNA polymerase molecules observed at near-basepair resolution. *Nature* 426(6967):684–687. doi:[10.1038/nature02191](https://doi.org/10.1038/nature02191)
12. Abbondanzieri EA, Greenleaf WJ, Shaevitz JW, Landick R, Block SM (2005) Direct observation of base-pair stepping by RNA polymerase. *Nature* 438(7067):460–465. doi:[10.1038/nature04268](https://doi.org/10.1038/nature04268)
13. Wang MD, Schnitzer MJ, Yin H, Landick R, Gelles J, Block SM (1998) Force and velocity measured for single molecules of RNA polymerase. *Science* 282(5390):902–907
14. Yin H, Wang MD, Svoboda K, Landick R, Block SM, Gelles J (1995) Transcription against an applied force. *Science* 270(5242):1653–1657
15. Neuman KC, Block SM (2004) Optical trapping. *Rev Sci Instrum* 75(9):2787–2809. doi:[10.1063/1.1785844](https://doi.org/10.1063/1.1785844)
16. Perkins TT (2014) Angstrom-precision optical traps and applications. *Annu Rev Biophys* 43:279–302. doi:[10.1146/annurev-biophys-042910-155223](https://doi.org/10.1146/annurev-biophys-042910-155223)
17. Schafer DA, Gelles J, Sheetz MP, Landick R (1991) Transcription by single molecules of RNA polymerase observed by light microscopy. *Nature* 352(6334):444–448. doi:[10.1038/352444a0](https://doi.org/10.1038/352444a0)
18. Greenleaf WJ, Woodside MT, Abbondanzieri EA, Block SM (2005) Passive all-optical force clamp for high-resolution laser trapping. *Phys Rev Lett* 95(20):208102
19. Visscher K, Gross SP, Block SM (1996) Construction of multiple-beam optical traps with nanometer-resolution position sensing. *IEEE J Sel Top Quantum Electron* 2(4):1066–1076. doi:[10.1109/2944.577338](https://doi.org/10.1109/2944.577338)
20. Fazal FM, Meng CA, Murakami K, Kornberg RD, Block SM (2015) Real-time observation of the initiation of RNA polymerase II transcription. *Nature* 525(7568):274–277. doi:[10.1038/nature14882](https://doi.org/10.1038/nature14882)
21. Palangat M, Larson MH, Hu X, Gnatt A, Block SM, Landick R (2012) Efficient reconstitution of transcription elongation complexes for single-molecule studies of eukaryotic RNA polymerase II. *Transcription* 3(3):146–153. doi:[10.4161/trns.20269](https://doi.org/10.4161/trns.20269)
22. Komissarova N, Kireeva ML, Becker J, Sidorenkov I, Kashlev M (2003) Engineering of elongation complexes of bacterial and yeast RNA polymerases. *Methods Enzymol* 371:233–251. doi:[10.1016/S0076-6879\(03\)71017-9](https://doi.org/10.1016/S0076-6879(03)71017-9)
23. Kettenberger H, Armache KJ, Cramer P (2004) Complete RNA polymerase II elongation complex structure and its interactions with NTP and TFIIS. *Mol Cell* 16(6):955–965. doi:[10.1016/j.molcel.2004.11.040](https://doi.org/10.1016/j.molcel.2004.11.040)
24. Bustamante C, Marko JF, Siggia ED, Smith S (1994) Entropic elasticity of lambda-phage DNA. *Science* 265(5178):1599–1600

# Chapter 16

## Optical Tweezers-Based Measurements of Forces and Dynamics at Microtubule Ends

Marian Baclayon, Svenja-Marei Kalisch, Ed Hendel, Liedewij Laan, Julien Husson, E. Laura Munteanu, and Marileen Dogterom

### Abstract

Microtubules are dynamic cytoskeletal polymers that polymerize and depolymerize while interacting with different proteins and structures within the cell. The highly regulated dynamic properties as well as the pushing and pulling forces generated by dynamic microtubule ends play important roles in processes such as in cell division. For instance, microtubule end-binding proteins are known to affect dramatically the dynamic properties of microtubules, and cortical dyneins are known to mediate pulling forces on microtubule ends. We discuss in this chapter our efforts to reconstitute these systems *in vitro* and mimic their interactions with structures within the cell using micro-fabricated barriers. Using an optical tweezers setup, we investigate the dynamics and forces of microtubules growing against functionalized barriers in the absence and presence of end-binding proteins and barrier-attached motor proteins. This setup allows high-speed as well as nanometer and piconewton resolution measurements on dynamic microtubules.

**Key words** Cytoskeleton, Microtubules, Microtubule ends, Micro-fabrication, SU8 barriers, Gold-coated barriers, Optical trapping, Force generation

---

### 1 Introduction

Microtubules (MTs) are cytoskeletal structures that constantly switch between periods of polymerization and depolymerization in a process called dynamic instability [1]. Dynamic MTs play an important role in essential biological processes such as cell division. Specifically, they interact in a concerted fashion with different MT-associated proteins and cytoskeletal motors to generate forces at the different stages of cell division [2]. In mammalian cells, MTs grow out radially from centrosomes and interact with the cell cortex, the kinetochores, and each other to generate pushing as well as pulling forces during spindle positioning, chromosome organization and chromosome separation. In many cases, these forces are generated via direct end-on contacts of dynamic microtubules with different cellular structures [3]. For instance, MT growth against the cell

periphery generates pushing forces that may help position the centrosomes, while dynein-mediated depolymerization at the cortex generates pulling forces during spindle positioning [4–6]. The evidence of forces generated by MTs in cells is abundant, but the nano-scale details of how dynamic MT ends generate forces and interact with dynein and other proteins remain largely unknown.

To better understand MT force generation and its role in aster positioning processes, we designed various *in vitro* experiments where MT growth, with or without microtubule-associated proteins (MAPs) and cytoskeletal motors such as dynein, is reconstituted in micro-fabricated devices and emulsion droplets [7–11]. In addition, we developed optical tweezers-based techniques to investigate MT dynamics and the forces that MTs exert as they grow against micro-fabricated walls at the nano-scale [10, 12, 13]. Figure 1 shows the general schematic of such experiments: MTs are growing from an axoneme, which is attached to a bead held by an optical trap in front of a micro-fabricated barrier. With this setup, the growth dynamics and forces generated by MTs in the presence and absence of MAPs and motors can be followed with nanometer and piconewton resolution. In this chapter, we describe the methods used for these experiments: the fabrication and functionalization of the barriers, the preparation and purification of the proteins used, and the work flow in performing the optical tweezers experiments.

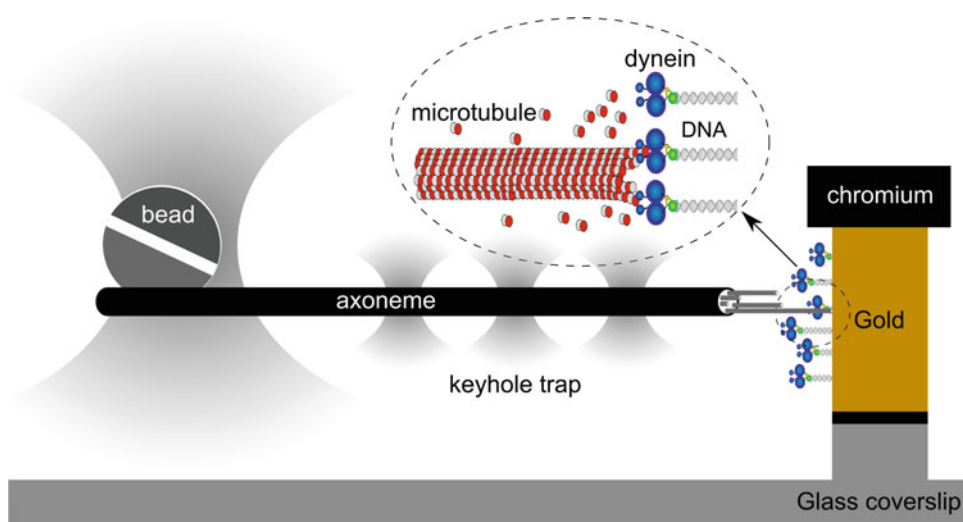


**Fig. 1** Optical-tweezers based measurement of MT dynamics and forces. Microtubules nucleate from an axoneme, which is attached to a bead and held by a “keyhole” optical trap, and grow against a micro-fabricated barrier. In this experimental assay, the interaction of MTs with microtubule-associated proteins (MAPs) and motor proteins like dynein can be investigated by adding proteins in solution and/or by chemically functionalizing the barriers to attach proteins/motors specifically

Micro-fabricated walls or barriers are made using the photolithography of SU8 photoresist, or gold so that they may be functionalized using gold-thiol chemistry [14–16]. The gold barriers are functionalized with thiol-biotin, and spacers are made using a series of biotin–streptavidin links or DNA, to which dynein can be specifically attached. GFP-tagged dynein is purified from budding yeast *Saccharomyces cerevisiae*, and conjugated with biotin, DNA-thiol spacer, or DNA-biotin spacer [17, 18]. Axonemes, which are used as nucleation sites for growing microtubules, are purified from the cilia of *Tetrahymena thermophila* [19–21]. To follow MT growth, a bead–axoneme construct is held by a keyhole trap, which is made of multiple time-shared optical traps that includes a main trap to hold the bead and multiple weaker traps to hold and align the axoneme towards the barrier [10, 12, 13]. The growth dynamics of microtubules can optionally be monitored at constant force by implementing a force-feedback system on the optical trap. We present example results for microtubules growing in the presence of the slowly hydrolyzable analog of GTP, GMPCPP, and MT tip-binding protein Mal3 in solution, and in the presence of dynein motors attached to a SU8 barrier.

---

## 2 Materials

### 2.1 Barrier Micro-fabrication

#### 2.1.1 SU-8 Barriers

1. Glass coverslips.
2. SU-8 2005 (Microchem, negative photoresist).
3. MRDEV600 (Shipley, developer for SU-8).
4. 2-propanol.
5. Spin coater with Schott BG12 filter (Karl Suss Delta 10).
6. Optical lithography system (Karl Suss MJB3).
7. Hotplates.

#### 2.1.2 Gold-Coated Barriers

1. Chromosulfuric acid.
2. Chromium and gold pellets for vapor deposition.
3. Hexamethyldisilazane, HMDS.
4. S1813 (Microchem, positive photoresist).
5. MF319 (Microchem, developer for S1813).
6. Chromium etchant (standard etchant for chromium and chromium oxide films, and compatible with both positive and negative photoresists).
7. Gold etchant (selectively dissolves gold and compatible with both positive and negative photoresists).
8. 20 % KOH

### 2.1.3 Functionalizing the Gold Barriers with Biotin

1. 200 mM 11-mercaptopropanoic acid in ethanol.
2. Pentafluorophenol (PFP) in ethanol.
3. 100 mM 1-ethyl-3-(3-dimethylaminopropyl)carbodiimide (EDAC) in ethanol (Molecular Probes): store at -20 °C.
4. 0.1 mM biotin-PEO-LC-amine (Pierce Inc.): store at -20 °C.
5. 0.1 % Tween (Calbiochem) in ddH<sub>2</sub>O.
6. 0.01 % Triton X-100 (Plus One) in ddH<sub>2</sub>O.
7. 2 M NaCl in ddH<sub>2</sub>O.
8. Ethanol, 2-propanol, acetone.

## 2.2 Axoneme Purification

1. *Tetrahymena thermophila* (SB715 strain) [22].
2. NEFF medium = 0.25 % proteose peptone, 0.25 % yeast extract, 0.5 % glucose, 33.3 µM FeCl<sub>3</sub>.
3. Antibiotic/antimycotic (ABAM, 100×): contains 10,000 units/mL of penicillin, 10,000 µg/mL of streptomycin, 25 µg/mL of amphotericin B (Sigma-Aldrich).
4. 2 mg/mL Dibucaine-HCl in Neff medium.
5. 0.25 % Igepal CA-630.
6. Hepes buffer (pH 7.4): 10 mM Hepes, 100 mM NaCl, 4 mM MgCl<sub>2</sub>, 0.1 mM EGTA.
7. High-salt Hepes buffer with DTT: hepes buffer, 600 mM NaCl, 1 mM DTT.
8. 100 % glycerol.
9. Optional: 20 mM EGS, DMSO, 1 M Trizma HCl, pH 8.
10. Culture tubes/flasks and shaker.
11. Ultrahigh speed centrifuge.

## 2.3 Dynein Purification

### 2.3.1 Growing the Yeast Cells

1. *Saccharomyces cerevisiae* yeast strains with cargo-domain truncated dynein [17].
2. Growth media: YP = 2.2 % Bacto peptone and 1.1 % yeast extract,  
YPD = YP medium and 2 % dextrose (glucose),  
YPRaf = YP medium and 2 % raffinose,  
YPGal = YP medium and 2 % galactose,  
YES = 0.5 % yeast extract, 3 % glucose, 0.0225 % each of adenine, histidine, leucine, uracil, and lysine hydrochloride.  
Autoclave the YP medium and sterile-filter the sugars before combining.
3. YPD agar plate medium = 2.2 % Bacto agar, 2.2 % Bacto peptone, 1.1 % yeast extract, 2.0 % dextrose. Autoclave, cool down to 50 °C and pour 10 mL into sterile petri dishes, avoiding bubble formation. Dry the plates at 37 °C, upside down and open the lid a little.

### 2.3.2 Purifying Dynein

1. 5× Lysis stock buffer: 150 mM Hepes (pH 7.4), 250 mM potassium acetate, 10 mM magnesium acetate, 5 mM EGTA (ethylene glycol tetraacetic acid), and 50 % glycerol. Filter sterilize.
2. 5× TEV stock buffer: 50 mM Tris-HCl (pH 8.0), 750 mM KCl, and 50 % glycerol. Filter-sterilize.
3. 100 mM PMSF: dissolve 17.4 mg PMSF (phenylmethanesulfonyl fluoride) in 1 mL of 100 % ethanol. Make 2 mL on the day of purification.
4. 1 M dithiothreitol DTT solution, kept at -20 °C.
5. 100 mM MgATP solution, kept at -20 °C.
6. 20 % Triton X-100.
7. IgG bead Sepharose fast flow (GE Healthcare).
8. (Ac)TEV protease (Thermo Fisher Scientific).
9. SNAP-biotin (New England BioLabs).
10. Fluorescent tags: HaloTag TMR, HaloTag Alexa 660 (Promega).
11. Coffee grinder.
12. Ultrahigh speed centrifuge at 4 °C (Beckmann), rotor (Beckman 70.1 Ti) and 10-mL tubes (Beckman).
13. Poly Prep chromatography column (Bio-Rad 731 1550).
14. Incubator at 16 °C with shaker.
15. 0.1-μm filter spin column (Millipore Ultrafree-MC with Durapore membrane).
16. Tabletop low speed centrifuge at 4 °C (Eppendorf 5415R).
17. 4× Lysis buffer with no detergent: 4× Lysis stock buffer, 4 mM DTT, 0.4 mM MgATP, 2 mM PMSF.
18. 4× Lysis buffer: 4× Lysis buffer with no detergent, 0.2 % Triton X-100.
19. Wash buffer: 1× Lysis buffer with no detergent, 250 mM KCl, 0.1 % Triton X-100.
20. TEV buffer: 1× TEV stock buffer, 1 mM DTT, 0.1 mM MgATP, 0.5 mM PMSF, 0.1 % Triton X-100.

### 2.3.3 Labeling with DNA Oligos

1. 2 mg BG-GLA-NHS (New England BioLabs).
2. 6.9 nmol NH<sub>2</sub>-oligos (5'-amine) (Bioneer).
3. 6.7 nmol complementary Thiol-oligos (5'-thiol) or biotin-oligos (5'-biotin) (Bioneer).
4. Dimethyl sulfoxide (DMSO).
5. 400 mM hepes buffer pH 8.5.
6. 1× TE buffer.

7. 3 M sodium acetate pH 5.2.
8. 95 % ethanol.
9. Gravity-driven column for DNA (GE Illustra NAP-5 column Sephadex G-25 DNA Grade).
10. 20 % TBE gel electrophoresis for DNA: pre-cast gel, SYBR Gold stain, 10-bp DNA ladder (Thermo Fisher Scientific).

## **2.4 Optical Tweezers Experiment**

### *2.4.1 Optical Tweezers Setup*

1. Trapping laser (Nd:YVO4, 1064 nm, Spectra Physics).
2. Detection laser (HeNe, 633 nm, Uniphase 1125P).
3. Acousto-Optic Deflector, AOD (2-axis deflection system, Intraaction DTD-274HA6).
4. Quadrant Photo-Detector, QPD (First Sensor).
5. Nano-positioning stage (PI P730.4C).
6. Inverted microscope with Differential Interference Contrast (DIC) imaging (Leica DMIRB).
7. 100×, 1.3 NA oil-immersion objective and condenser lenses (Leica).
8. CCD camera (Kappa CF8/4).
9. Anti-reflection coated achromatic lenses.
10. Dichroic mirrors (Chroma Technology and Semrock).
11. In-house developed software with force-feedback.

### *2.4.2 Building the Flow Channel*

1. Microscope glass slide with holes for tubes connecting to the syringe pump.
2. Syringe pump (ProSense BV).
3. Syringe and needle.
4. Parafilm.
5. 1 % Hellmanex.
6. 70 % ethanol.
7. 100 mM KOH.
8. Sonicator.

### *2.4.3 Passivating the Surface*

1. MRB80 buffer: 80 mM Pipes, 4 mM MgCl<sub>2</sub>, 1 mM EGTA, pH 6.8 with KOH.
2. 1 % Triton X-100 in ddH<sub>2</sub>O.
3. 10 % Pluronic F127 in DMSO.
4. 2 mg/mL PLL-PEG (Surface Solutions). Store at -80 °C.
5. 5 mg/mL k-casein. Store at -80 °C.

#### 2.4.4 Optical Trapping Assay for MT Growth

##### Dynamics and Force Generation With and Without MAPs

1. 100  $\mu$ M unlabeled tubulin (Cytoskeleton, Tebu-Bio). Store at  $-80^{\circ}\text{C}$ .
2. 50  $\mu$ M labeled tubulin: Biotin, Rhodamine, HiLyte 488, HiLyte 635 (Cytoskeleton, Tebu-Bio). Store at  $-80^{\circ}\text{C}$ .
3. 50 mM guanosine-5'-triphosphate (GTP). Store at  $-80^{\circ}\text{C}$ .
4. 50 mM adenosine triphosphate (ATP). Store at  $-80^{\circ}\text{C}$ .
5. 10 mM guanosine monophosphate (GMPCPP, Jena Biosciences). Store at  $-80^{\circ}\text{C}$ .
6. 1 M glucose.
7. 10 mg catalase.
8. 20 mg glucose oxidase.
9. 1 M DTT.
10. 5 mg/mL streptavidin. Store at  $-80^{\circ}\text{C}$ .
11. 25 mg/mL (biotin)-BSA. Store at  $-80^{\circ}\text{C}$ .
12. 25 mg/mL BSA. Store at  $-80^{\circ}\text{C}$ .
13. 1 M KCl.
14. 1 % (w/v) methyl cellulose.
15. 2- $\mu$ m polystyrene beads (Spherotech).
16. Airfuge (Beckman-Coulter).
17. Oxygen scavenger system, 50 $\times$ : 10 mg/mL catalase, 20 mg/mL glucose oxidase, 200 mM DTT. Store at  $-80^{\circ}\text{C}$ .
18. Tubulin mix: 10–25  $\mu$ M unlabeled or (fluorescent)-labeled tubulin, 1 mM GTP (or 1 mM GMPCPP), 1 mM ATP, 0.5 mg/mL k-casein, 50 mM KCl, 0.1 % methyl cellulose, 1 $\times$  oxygen scavenger system, in MRB80 buffer. Airfuge the mix at 30 psi (200,000  $\times$   $g$ ) for 5 min to get rid of aggregates.
19. Streptavidin mix: 0.5 mg/mL streptavidin, 1 mg/mL k-casein, 5 mg/mL BSA.
20. Biotin mix: 1.5 mg/mL (biotin)-BSA, 1 mg/mL k-casein, 5 mg/mL BSA.
21. Dynein mix: 20 nM Biotinylated dynein, 1 mg/mL k-casein, 5 mg/mL BSA.

## 3 Methods

### 3.1 Barrier Micro-fabrication

Figure 2 illustrates the procedures for making chambers or barriers made from SU8 photoresist or chromium/gold on glass coverslips. SU8 barriers are made for experiments where the forces generated by growing microtubules against a rigid wall are measured, with and without the presence of MAPs in solution, and with or without

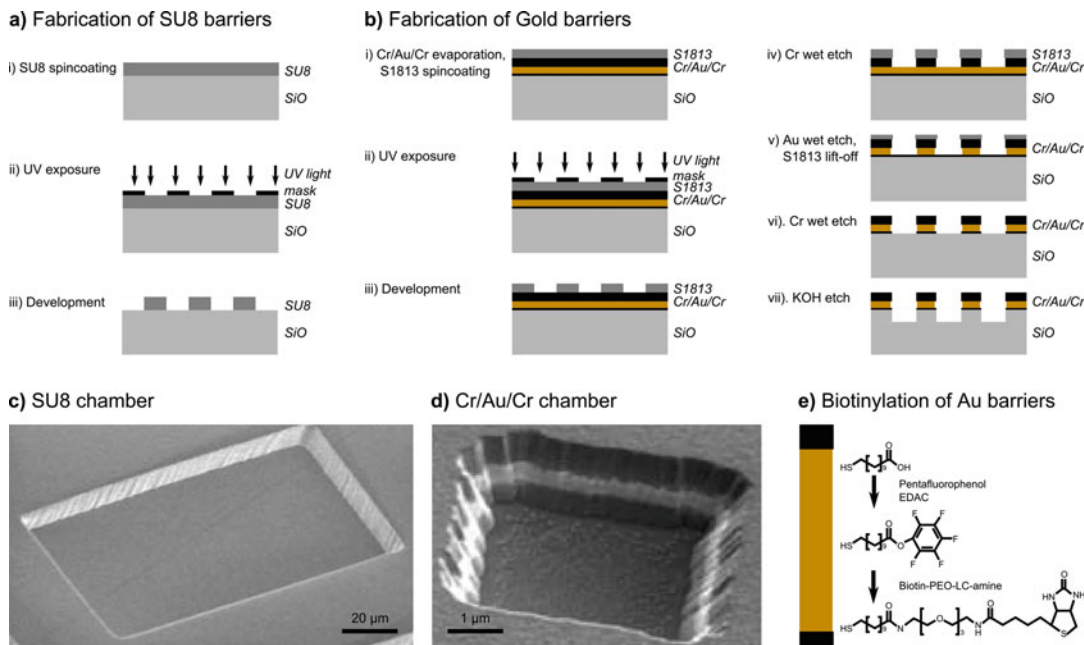


**Fig. 2** Fabrication of artificial chambers and barriers. Procedures for making (a) SU8 and (b) Gold barriers. Scanning Electron Microscopy (SEM) images of a (c) SU8 and (d) Gold barrier. (e) Chemical functionalization of gold barriers using thiol-chemistry. SEM images are reproduced from ref. [14]

proteins nonspecifically attached to the wall. Gold barriers can be made for experiments where proteins need to be specifically bound to the barrier. In this case, the gold surface is functionalized using thiol-chemistry, to which proteins such as dynein motors can then be specifically attached.

### 3.1.1 *SU-8 Barriers*

1. Spin-coat clean glass coverslips with SU-8 photoresist at 1000 rpm for 25 s to produce a 7- $\mu\text{m}$ -thick layer. Soft-bake on a hot plate at 65 °C for 2 min and then another 2 min at 95 °C.
  2. Expose the coverslips to UV light for 32 s through a mask (*see Note 1*).
  3. Bake the exposed coverslips on a hot plate at 65 °C for 1 min and then another 2 min at 95 °C.
  4. Develop the coverslips by immersing them in a beaker filled with the developer (MRDEV600) for 90 s, then rinse in a beaker with 2-propanol for 20 s.
  5. Blow-dry with N<sub>2</sub> gas and hard-bake on a hot plate at 160 °C for 10 min.

### *3.1.2 Gold-Coated Barriers*

1. Clean the coverslips in chromosulfuric acid for a few hours, and rinse with ddH<sub>2</sub>O water 3× and blow-dry with N<sub>2</sub> gas.
  2. Coat the coverslip with a 5-nm thin layer of chromium, a 750-nm layer of gold and a 250-nm thick layer of chromium.

using vapor deposition. Coat the upper chromium surface by evaporation with HMDS by placing the coverslips and a beaker with 5 mL HMDS inside a desiccator for 1 h.

3. Spin-coat the coverslips with S1813 photoresist at 1000 rpm for 40 s. Soft bake on a hot plate at 115 °C for 90 s.
4. Expose the coverslips to UV light for 12 s through a chromium mask. Bake the exposed coverslips on a hot plate at 130 °C for 30 min (*see Note 2*).
5. Develop the coverslips by immersing them in a beaker filled with the developer (MF319) for 60 s, then rinse in a beaker with ddH<sub>2</sub>O and blow-dry with N<sub>2</sub> gas. Remove the remaining photoresist by sonication in acetone for 5 min.
6. Excavate the barriers by consecutively immersing the coverslips in beakers filled with chromium etchant, acetone, gold etchant, and chromium etchant again for about 30 s in each step. Repeat the process until the desired barriers are obtained by imaging under a microscope in between each wet etching step. Rinse thoroughly with ddH<sub>2</sub>O and blow-dry with N<sub>2</sub> gas.
7. To make higher walls for optical tweezers experiments, incubate the gold barriers in 20 % KOH at 80 °C for 30 min to etch about 2 μm into the glass. Rinse thoroughly with ddH<sub>2</sub>O and blow-dry with N<sub>2</sub> gas.

### **3.1.3 Functionalizing the Gold Barriers with Biotin [23, 24]**

1. Clean the gold barriers by sonicating in ethanol for 20 min (*see Note 3*).
2. Immerse the gold barriers consecutively in 200 mM 11-mercapto-1-undecanoic acid in ethanol for 3 h, 100 mM EDAC and 200 mM PFP in ethanol for 20 min, and 0.1 mM biotin-PEO-LC-amine for 20 min.
3. To remove unspecific interactions of the thiol groups, immerse the barriers consecutively in beakers containing 2 M NaCl for 7 min, 0.1 % Tween in ddH<sub>2</sub>O for 15 min, 0.01 % Triton X-100 for 7 min, and rinse with ddH<sub>2</sub>O. Store the barriers in ethanol. They can be used for several weeks.

## **3.2 Axoneme Purification**

Tetrahymena thermophila is a water-borne protozoa, which uses the numerous cilia surrounding its body to propel itself. It is one of the standard model organisms in molecular biology [22]. Tetrahymena thermophila can be easily grown in large volumes and each individual has hundreds of cilia. It can be deciliated with an anaesthetic like dibucaine and the organism survives and regrows its cilia after a few hours [25]. Each cilium contains a cytoskeletal structure called an axoneme which is composed of a ring of nine microtubule doublets and a central doublet, coupled to each other by dynein motors. The dynein motors can be removed from the axoneme and

purified separately if desired [26]. The axonemes are stable structures that can be used as nucleating sites for growing microtubules. In addition, it is (weakly) trappable and easily sticks nonspecifically to a polystyrene bead, which makes it easy to manipulate using optical tweezers.

### 3.2.1 Growing *Tetrahymena thermophila*

1. Thaw a 1-mL frozen stock directly in a 42 °C water bath. After 15 s, add 1 mL of Neff medium (pre-warmed at 42 °C). When the pellet is fully dissolved, pipette the contents into a plate/tube containing 10 mL of Neff medium + 100 µL of 100 × ABAM. Culture the cells at 30 °C (see Note 4).
2. In a 250-mL culture flask, fill with 24 mL of Neff medium and 1 mL of the cell culture. Grow the cells shaken at room temperature and out of direct sunlight.
3. After 1–2 days, this 25 mL culture is used to inoculate 1 L Neff medium in a 2.8-L flask. The culture is then grown on a shaker at room temperature for another 1–2 days. The culture conditions can be slightly modified such as temperature (to 30 °C) to increase the growth rate (see Note 5).

### 3.2.2 Purifying the Axonemes

1. Pellet the cells by spinning down at 500 ×  $\text{g}$  for 6 min at room temperature. Discard the supernatant and combine all the sloppy pellets into a 50-mL tube and re-spin at 500 ×  $\text{g}$  for 5 min.
2. Resuspend the pellet in filtered Neff medium. Add 2 mL of medium for every gram of pellet. About 5–6 g pellet is retrieved per liter of culture.
3. Dissolve dibucaine with filtered Neff medium with the same volume as in the resuspended tetrahymena with a concentration of 2 mg/mL. Add dibucaine to the resuspended tetrahymena cells. Final dibucaine concentration must be 1 mg/mL (2.6 mM).
4. Flow a small amount (10–20 µL) of the sample into the flow cell and observe under a microscope. See when they stop moving, which means they have shed most of their cilia (see Note 6).
5. Immediately after they have shed their cilia, dilute the cells 10× with filtered Neff medium. For larger volumes, separate them into two tubes.
6. Pellet the shedded cells at 500 ×  $\text{g}$  for 6 min at RT. Keep the supernatant (contains the cilia) and discard the pellet (or add to a new culture to regenerate cilia).
7. Re-spin the supernatant at 1000 ×  $\text{g}$  for 10 min at 4 °C to remove residual tetrahymena cells. Keep the supernatant and discard the pellet. Repeat twice. From now on, keep everything on ice and work at 4 °C by cooling the centrifuge before using.

8. Collect the cilia by centrifugation at  $13,700 \times g$  for 25 min at 4 °C. Keep the pellet.
9. Exchange the buffer to Hepes by resuspending the pellet in 1 mL of Hepes buffer (see Note 7). Combine the resuspended pellets and dilute to a final volume of 50 mL Hepes buffer. Spin at  $250 \times g$  for 1 min, discard the pellet and keep the supernatant.
10. Wash the cilia 3× by spinning at  $12,500 \times g$  for 15 min at 4 °C. Keep the pellet and resuspend in 50 mL Hepes buffer (except for the third wash).
11. Solubilize the membrane of the cilia by resuspending in 40 mL Hepes buffer with 0.25 % Igepal. Incubate for 30 min on ice.
12. Pellet the axonemes at  $12,500 \times g$  for 10 min at 4 °C. Resuspend the axonemes in 1 mL Hepes buffer (without detergent) and dilute to a final volume of 45 mL Hepes buffer. If not crosslinking, dilute up to 50 mL and spin at  $250 \times g$  for 1 min, discard the pellet and keep the supernatant.
13. To stiffen the axonemes, they can be chemically cross-linked with EGS [27]. Prepare a 20 mM EGS stock by adding 46 mg in 5 mL DMSO. Add 5 mL EGS stock to the resuspended axonemes and incubate for 15 min at RT. Neutralize the EGS by adding 0.5 mL of 1 M Trizma HCl pH 8 and let react for 3 min. Spin at  $250 \times g$  for 1 min, discard the pellet and keep the supernatant.
14. Wash the axonemes 3× in Hepes buffer (without detergent). Spin at  $12,500 \times g$  for 15 min at 4 °C. Keep the pellet and resuspend in 50 mL Hepes buffer (except for the third wash).
15. Remove dynein by resuspending the axonemes in 50 mL high salt Hepes buffer with DTT, incubate on ice for 30 min. *Note:* Add DTT just before using!
16. Collect the axonemes by spinning at  $12,500 \times g$  for 15 min at 4 °C. Keep the pellet and resuspend in a small volume of Hepes buffer (200–500 µL) and observe under the microscope. The image should contain many axonemes. If clean enough, add glycerol to a 30 % final concentration, otherwise, repeat step 15. Aliquot in 5 or 10 µL and flash-freeze. Store at –80 °C.

### 3.3 Dynein Purification

Dynein is purified from the budding yeast *Saccharomyces cerevisiae* [17]. Each monomeric unit of the motor is labeled with GFP and has a ZZ tag (IgG-binding domain of protein A) for purification. In addition, it has Halo- and SNAP-tags to which fluorophores and chemical moieties can be attached to. For example, Rhodamine-TMR fluorophores are attached to the Halo tags and BG-conjugated oligos to the SNAP tags [18]. The end of the complementary DNA oligos is labeled with biotin or a thiol group such that dynein can be specifically attached to streptavidin or gold-coated surfaces later in the experiment.

### 3.3.1 Growing the Yeast Cells

1. Grow cells in 0.8 mL YES medium at 25–32 °C for 2 days, until OD > 1.5.
2. Mix with 0.8 mL 50 % glycerol in YES buffer in a cryo-tube. Place the cultures at –70 °C. No flash-freezing! (see Note 8).
3. Streak out a minute amount of cells from the frozen stock and draw on the plate using sterile sticks or heated metal wire. Incubate at 30 °C for 2 days. From the plated culture, pick a single colony (pinkish-colored colonies contain the strain GFP-conjugated dynein) and draw on another plate a rectangular plot, fully covered with yeast cells. Incubate at 30 °C for 2 days.
4. From the rectangular plot of yeast, take out one or two length-wise streaks using a sterile stick, and grow in 10 mL YP-D medium. Incubate at 30 °C, shaken at 250 rpm overnight. The following day, measure the concentration (OD<sub>600</sub> > 3.0) and transfer the culture to a 250-mL flask with 50 mL YP-Raf medium. Grow at 30 °C, shaken at 250 rpm. In the afternoon (after 8 h), check under the microscope for contamination and measure the concentration (OD<sub>600</sub> > 2.0). Dilute the culture in 2 L of YP-Gal medium. Grow at 30 °C and shaken at 170–200 rpm overnight in a sterile 6 L Erlenmeyer flask (see Note 9).
5. Check the concentration of the culture such that the OD<sub>600</sub> > 2.0 (see Note 10). Spin the culture in 1 L centrifuge tubes at 9000 × g for 6 min at 4 °C. Remove the supernatant directly after spinning. The pellet should be pinkish if the expression went well.
6. Resuspend the cells in a bit of distilled H<sub>2</sub>O and gently mix by rotating the tube. Collect all cells into one bottle and fill with distilled H<sub>2</sub>O. Spin the resuspended cells. Collect the pellet (tooth paste consistency) with a spatula and fill into a 50-mL syringe. Flash-freeze the cells by dropping the yeast suspension from the syringe into a plastic beaker containing liquid nitrogen, mixing to break them into small pellet sizes. The cells can be stored at –80 °C for later use; otherwise, lyse right away by grinding the frozen pellets with a coffee grinder until a very fine powder is formed.

### 3.3.2 Purifying Dynein

1. Make the following buffers on the day of purification. For each yeast strain to purify, prepare: 15 mL of 4× Lysis buffer with no detergent, 10 mL of 4× Lysis buffer, 15 mL Wash buffer and 20 mL TEV buffer. Keep the buffers at 4 °C.
2. Precool an empty 100 mL beaker at 4 °C (on ice) to which ground yeast cells can be transferred to later. Precool coffee grinder by filling with liquid nitrogen for 30 s. Take out yeast cells from –80 °C and powderize using the coffee grinder for 30 s, repeat 4× or until the pellets are well-powderized. Quickly transfer the powder to the precooled beaker.

3. Add 4× Lysis buffer to the lysate, equivalent to 1/3 of the yeast volume (assume 1 mg yeast powder = 1 mL) resulting to a concentration of 1× Lysis buffer. Quickly thaw the lysate by immersing the beaker above a 37 °C water bath (1–2 min). Mix with spatula until dissolved and put the lysate at 4 °C. Transfer the lysate to the centrifuge tubes and spin at 300,000 ×  $\text{g}$  for 35 min.
4. Meanwhile, prepare the IgG beads. Use 10  $\mu\text{L}$  beads per 1 mL of lysate and vortex well. Wash the IgG beads by diluting with 1 mL of 1× Lysis buffer and centrifuging at 600 ×  $\text{g}$  for 1 min at 4 °C. Remove the supernatant. Wash three times.
5. Take the supernatant from the spun lysate and transfer into a 50-mL tube (*see Note 11*). Add the IgG beads and nutate the solution slowly (130 rpm) in the cold room for 1 h.
6. Add the protein-bead solution to the Bio-Rad columns (may be pre-washed with 200–500  $\mu\text{L}$  of 1× Lysis buffer). Wash the protein-beads twice with 5 mL of Wash buffer (*see Note 12*). Wash the protein-beads twice with 3 mL of TEV buffer. Seal with the cap leaving about 200  $\mu\text{L}$  of liquid inside.
7. Label the dynein with Snap-biotin, Halo-TMR/660 dyes and DNA-oligos at 10  $\mu\text{M}$  (*see Subheading 3.3.3*). Add the labeling solution to the protein-beads in the column and make sure a cap seals the column. Do the reaction at room temperature and in dark condition (cover with aluminum foil) for 20 min, and then put the sample back to 4 °C.
8. Remove the affinity binding between dynein (protein A) and beads (IgG) by TEV cleavage. First wash the protein beads once with 5 mL of wash buffer. Then wash twice with 3 mL of TEV buffer. Seal with the cap. Add about 200  $\mu\text{L}$  TEV buffer and mix.
9. Transfer the protein beads to 2 mL round-bottom Eppendorf tubes. Remove buffer and make the final volume to 200–300  $\mu\text{L}$  depending on desired concentration (*see Note 13*).
10. Add 2  $\mu\text{L}$  of TEV protease (concentration about 2–4 mg/mL) per 100  $\mu\text{L}$  of TEV buffer and incubate at 16 °C for 1 h, slowly rotating (30 rpm). If using AcTEV protease: add 1  $\mu\text{L}$  per 100  $\mu\text{L}$  of TEV buffer.
11. Transfer the beads first to a spin column with 0.1–0.2  $\mu\text{m}$  size cutoff and spin at 16,000 ×  $\text{g}$  at 4 °C for 1 min to collect the cleaved dynein using a tabletop centrifuge. Keep the supernatant. Aliquot into desired volume, flash-freeze and store at –80 °C or preferably at –150 °C freezer (or liquid nitrogen tank).

### 3.3.3 Labeling with DNA Oligos

1. Add nonaqueous DMSO to the vial containing the dry BG-NHS using a needle to a final concentration of 20 mM: 207 µL DMSO to 2 mg BG-NHS (*see Note 14*).
2. Resuspend the NH<sub>2</sub>-oligos in H<sub>2</sub>O (5'Amine) to a final concentration of 1–2 mM (*see Note 15*).
3. Let the dissolved BG-NHS and NH<sub>2</sub>-oligos react in 100 mM Hepes (*see Note 16*). Incubate at room temperature for 30 min. It is normal to see white precipitate in the reaction mix.
4. Add 76 µL of 1× TE buffer to the reaction mix, transfer to a 0.1 µm filter and spin at 12,000 × *g* for 4 min to remove any precipitate. Take out 0.5 µL for gel electrophoresis.
5. Remove the unreacted BG by column purification, using GE Illustra NAP-5 column Sephadex G-25 DNA Grade at 4 °C. Place appropriate tubes for collecting the eluted sample (*see Note 17*).
6. Make the sample concentrated using ethanol precipitation (*see Note 18*).
7. Resuspend the complementary oligos (5'-thiol or 5'-biotin) to a concentration of 1 mM (*see Note 19*).
8. Mix the BG-oligo-labeled protein and the complementary oligo, and let anneal at 4 °C for 30 min (*see Note 20*).
9. The BG-oligo sample is now ready to bind to SNAP-tagged dynein. If not using right away, store at –20 °C.

## 3.4 Optical Tweezers Experiment

The experiment uses an optical tweezers system to (1) manipulate the position of the MTs in solution such that it grows against the barrier end-on, and (2) to measure the growth length and the forces generated by or acting on MTs with nanometer and piconewton resolutions. It has a keyhole configuration, in which a main optical trap manipulates the bead where one end of the axoneme is attached to, and multiple time-shared low-power optical traps to hold the rest of the length of the axoneme. Optionally, a feedback loop between the force detection part and the nano-positioning stage can be implemented to apply a constant force on the microtubule as it grows against the barrier.

### 3.4.1 Optical Tweezers Setup

1. Turn on the interlock system for the lasers. Pre-warm the trapping laser for at least 30 min before starting the actual experiment. Turn on all the other equipment (AOD, QPD, nano-positioning stage, and camera) before the computer to establish the hardware–software communication well. Turn on the computer and open the software. Figure 3a shows a schematic of the optical tweezers setup.
2. Adjust the condenser lens to attain uniform illumination (Kohler illumination) and adjust the Wollaston prisms and polarizers to optimize the DIC imaging.

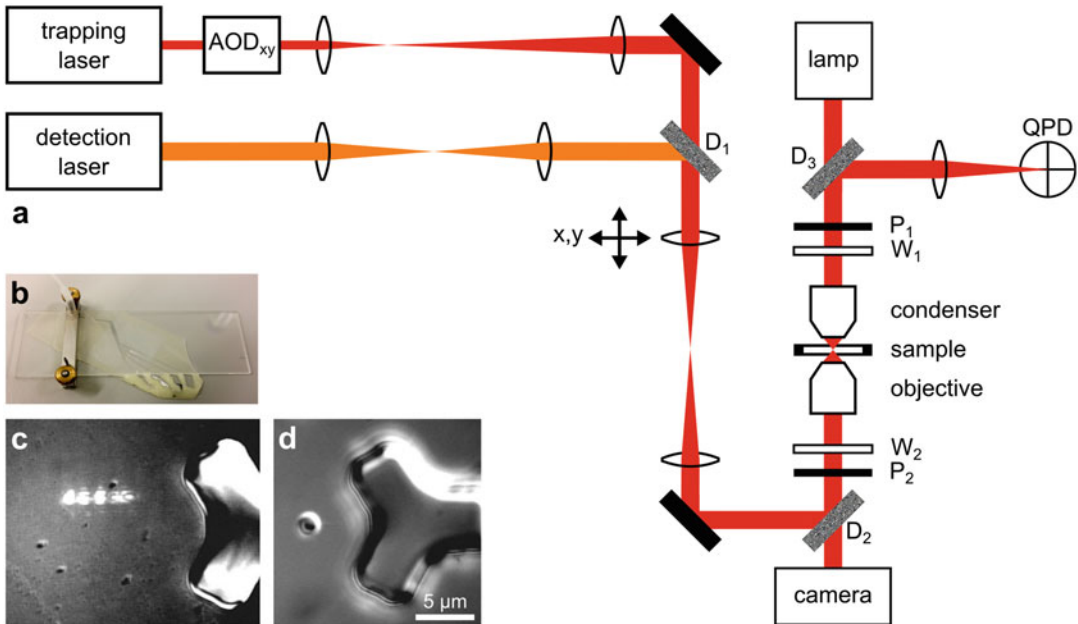


**Fig. 3** Optical tweezers setup. (a) The trapping laser ( $\text{Nd}:YVO_4$ , 1064 nm) is divided into multiple time-shared traps using two acousto-optic deflectors (AOD), the detection laser (HeNe, 633 nm) measures the force with back-focal plane interferometry using a quadrant photodiode (QPD). The bead–axoneme construct is imaged using differential interference contrast (DIC) microscopy using coupled polarizers ( $P_{1,2}$ ) and Wollaston prisms ( $W_{1,2}$ ). The laser beams are combined using a dichroic mirror ( $D_1$ ), while short-pass dichroic mirrors  $D_2$  and  $D_3$  (cutoff at 600 nm) reflect the beams to the objective and QPD, and transmit light from the lamp for DIC imaging and also partially the back-reflected beams from the sample to the camera for rough alignment of the lasers. (b) Picture of the flow channel. The coverslip at the bottom contains the SU8 barriers, and the extended part is used as reservoirs for the buffer, bead and growth solutions. The outlet goes through a tubing to the syringe pump drawing liquid at a rate of 1.0  $\mu\text{L}/\text{min}$ . DIC images of a SU8 barrier with (c) back-reflection of the trapping laser in the keyhole trap configuration and (d) a trapped bead–axoneme construct with microtubules (not visible) growing against the wall

3. Turn on the trapping and detection lasers and open the shutters. Check the alignment of the lasers from the back-reflected image as captured by the camera. The two beams must overlap each other.
4. Check the alignment of the detection laser onto the QPD. Adjust the position such that the recorded sum signal is optimum and centered on the QPD.
5. Deflect the laser along the  $x$  and  $y$  axes using the AOD. Check if the deflection is properly calibrated and the beam intensity is fairly uniform within the deflection range ( $\pm 10 \mu\text{m}$ ). Make a time-shared line trap (keyhole configuration) with one trap and check the intensities and beam profiles [28]. Figure 3c shows a sample image of the back-reflected light from the keyhole trap and SU8 barrier very close to the sample’s bottom surface.

### 3.4.2 Building the Flow Channel

1. Place the glass slides with holes in an appropriate rack for sonication and storage. Sonicate in 1 % Hellmanex for 10 min, rinse with deionized H<sub>2</sub>O and sonicate for 5 min. Sonicate in 70 % ethanol for 10 min, rinse with deionized H<sub>2</sub>O and sonicate for 5 min. Store in 100 mM KOH (cover with Parafilm). Before use, rinse with deionized H<sub>2</sub>O and sonicate for 5 min, and blow dry with N<sub>2</sub> gas.
2. Clean the coverslip with SU8 barriers by immersing in isopropanol for 10 min. Do not sonicate. Rinse with deionized H<sub>2</sub>O and blow dry with N<sub>2</sub> gas.
3. Make a flow channel by sandwiching a piece of Parafilm in between the glass slide and coverslip with SU8 barriers. Cut out a channel pattern in a piece of Parafilm, slightly longer than the short side of the glass slide. One end of the channel leads to the outlet that goes to a syringe pump and the other end leads to the reservoir. Place the Parafilm flat on the glass slide.
4. Take a coverslip with SU8 or gold barriers, align it on a 30° angle with respect to the glass slide and place on top of the Parafilm. The extended part will serve as the reservoir. Flip the flow channel upside down (the barrier is on the bottom).
5. Place the sandwich on a hotplate and press together to make a tight and leak-free channel. Build the reservoir by making a well with candle wax or Valap.
6. Attach the metal rods and tubing to the syringe. Figure 3b shows an example of the actual flow channel.

### 3.4.3 Passivating the Surface

1. Passivate the channels and tubing with 0.01 % Triton X-100. Fill the syringe with approximately 200 µL of Triton, and using a needle inject into the channel through the outlet tube. Fill the channel until the liquid fills the reservoir. Incubate for 10 min. From now on, the flow will be in the reverse direction (*see Note 21*).
2. Turn on the syringe pump and first set the flow rate to 1.0 µL/min. Fill the reservoir with MRB80 buffer and slowly increase the flow rate. Rinse the channel with 40 µL MRB80 buffer and then passivate with 20 µL 0.3 % Pluronic. Stop the flow after filling the channel fully with Pluronic and incubate for 10 min. Rinse the channel with 40 µL MRB80 buffer.
3. Passivate further with 0.2 mg/mL of PLL-PEG and 0.1 mg/mL of k-casein, incubate for 10 min and in between passivation, rinse the channel with 40 µL MRB80 buffer (*see Note 22*).

### 3.4.4 Optical Trapping Assay for MT Growth Dynamics and Force Generation With and Without MAPs

In this section, we discuss the workflow in using the optical tweezers to investigate microtubule growth dynamics and force generation in the absence and presence of MAPs and motor proteins [13]. We show sample results on (1) nano-scale details of MT growth in the presence of the slowly hydrolyzable GTP-analog GMPCPP, (2) details around catastrophes in the presence of GTP and the end-binding protein Mal3, and (3) generation of pulling forces in the presence of dynein motors which are nonspecifically attached to SU8 walls.

#### *Position and force calibration of the trap*

1. Vortex the stock of polystyrene beads and dilute 500× with MRB80. Turn on the flow at 1.0  $\mu\text{L}/\text{min}$  and after about 2 min, fill the reservoir with 10  $\mu\text{L}$  beads. Wait for a few min until the beads are seen flowing into the channel. Make sure not to empty the reservoir.
2. Measure the spring constant of the trapped bead using the spectral analysis method (*see Note 23*) [29].

#### *Optical trapping with force feedback (optional)*

3. With force feedback, the force on the trapped bead is constantly monitored [30]. As a growing MT pushes against the wall, the bead is pushed out of the trap. The restoring force of the trap pulls the bead back, resulting in a force on the microtubule that depends on the bead displacement from the center of the trap. To maintain a constant force on the MT, a feedback algorithm is set up such that as the bead is moved away from the trap, this is returned back to a desired position relative to the trap center by translating the sample through a nano-positioning stage (piezo-controlled), as shown in Fig. 4. There are two ways of monitoring the force on the bead: via the QPD signal or using the online video bead tracker.

#### *Making the bead–axoneme construct*

4. Mix together an appropriate concentration of beads and axonemes in a tube. The goal is to be able to attach nonspecifically at least one axoneme per bead. Using the trap, a bead–axoneme construct can also be made by placing a trapped bead close to a free-floating axoneme and trying to attach it to the bead (*see Note 24*).
5. Trap a bead–axoneme construct and move it around such that the axoneme can be seen pointing away from the bead. Make a line trap where the axoneme is positioned and trap the axoneme (Fig. 3d). To see if the axoneme is attached well to the bead, push it against a barrier slowly by moving the sample using the nano-positioning stage in 100-nm steps and monitor the force on the bead. Alternatively, using video microscopy, monitor the relative displacement of the barrier and the bead

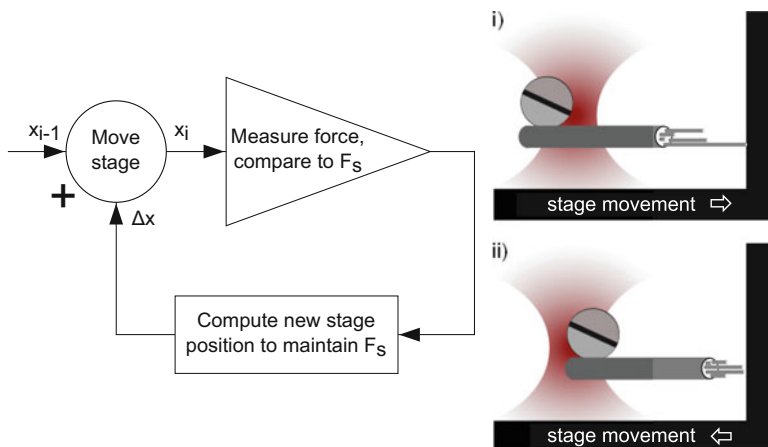


**Fig. 4** Schematic of the force-feedback scheme. The force as measured by the QPD is monitored and used as feedback to adjust the sample using the nano-positioning stage (piezo controlled) such that the force on the bead is clamped at  $F_s$ . When microtubules are growing against the wall, a pushing force acts on the bead (bead pushed to the left from the trap center). To maintain a force clamp at 0 pN, the stage moves to the right to position the bead back to the center of the trap (i). Likewise, when microtubules undergo shrinkage and catastrophe, the stage moves to the left to counteract the pulling force on the bead (ii)

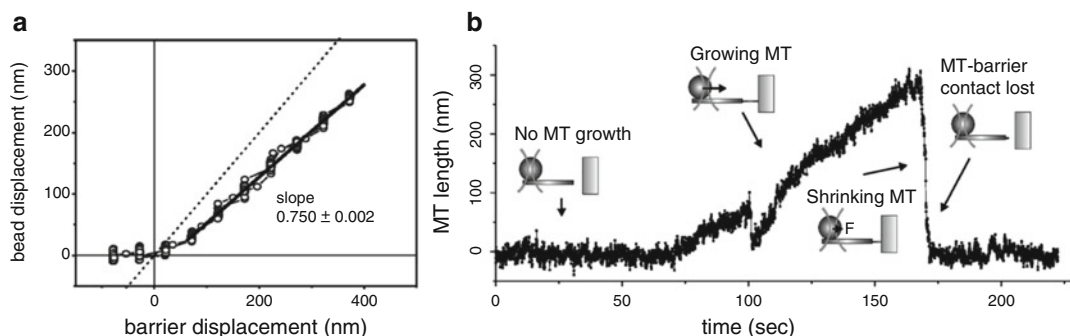


**Fig. 5** Experiment using optical tweezers. (a) Stiffness calibration of the bead–axoneme construct as it is pushed against the barrier. This is used to correct for the actual growth length of the microtubule. (b) Graphical illustration and the high-resolution plot of a microtubule growing against the wall, showing different phases such as no growth, steady growth, shrinkage, rescue and catastrophe (reproduced from refs. [14] and [15])

(online bead tracker at 1 Hz). A linear relationship will show how stiff the bead–axoneme connection is, and this plot will serve as a calibration factor that will be used to be able to use the bead displacement as a measure for the length increase of microtubules growing against the wall (Fig. 5a).

#### *Growing microtubules against a SU8 barrier with/without MAPs*

6. Once a good bead–axoneme construct is found, rinse the flow chamber with MRB80 to remove the free-floating beads and axonemes (*see Note 25*).

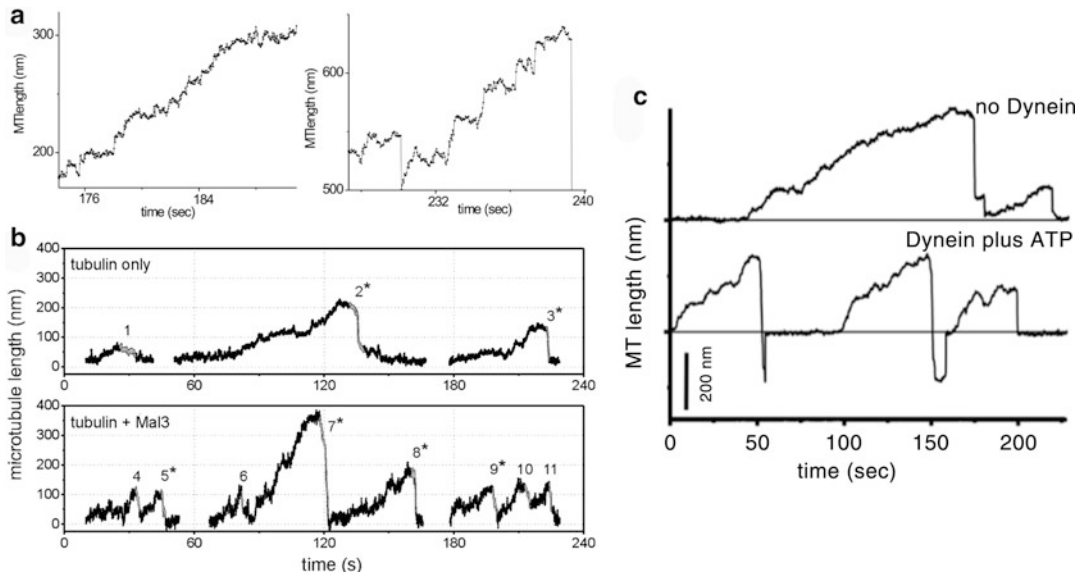


**Fig. 6** High-resolution MT growth in the presence of MAPs. (a) Growth of microtubules in the presence of the slowly hydrolyzing GTP analog, GMPCPP showing more rescue events and less catastrophe. (b) In the presence of end-binding protein Mal3, microtubules grow faster, the average growth length is longer and the frequency of rescue after catastrophe increases. (c) MT growth with and without dynein, showing pulling forces (negative force) acted on the microtubule by dynein (reproduced from ref. [10])

7. Position the tip of the axoneme approximately 100 nm from the barrier and flow in the tubulin mix at 1.1  $\mu\text{L}/\text{min}$  (added using a pipette to the reservoir). After 3–5 min, slow down to 0.1  $\mu\text{L}/\text{min}$  or stop the flow.

8. Start observing if there is MT growth by turning on the bead tracker. Figure 5b shows a plot of growing MTs from the axoneme tip against a SU8 barrier. Initially, there is no MT growth and thus the relative distance between the trap and bead is zero. As the microtubule starts to grow, it pushes the bead out of the trap, which can be determined from either the force on the bead (via the QPD signal) or the increasing distance between the bead and barrier. As the microtubule undergoes catastrophe or shrinkage, the force goes back to zero and the distance between the bead and barrier returns to the initial distance ( $t = 170$  s). Intermediate catastrophe and rescue can also occur as shown at  $t = 100$  s.

Figure 6a shows nano-scale details of microtubule growth in the presence of the slowly hydrolyzable analog of GTP, GMPCPP. These high-resolution data show that with GMPCPP, microtubules may experience gradual growth (left plot) or high-speed growth bursts followed by a long stall period that cannot be attributed to the hydrolysis of GTP [31]. Catastrophes are however never observed [32, 33].

Figure 6b shows the growth dynamics of MTs in the absence and presence of GTP and the fission yeast end-binding protein Mal3 [34, 35]. These data confirm that in the presence of Mal3, both the growth speed and catastrophe rate increase. Interestingly, catastrophes often appear to consist of a first slow shrinking phase, followed by a fast complete depolymerization of the MT (starred numbers).

9. After the experiment, turn on the flow faster to remove free tubulin. Test again the attachment of the bead–axoneme construct and compare with the pre-experiment calibration measurement.

#### *Growing microtubules against a barrier with dynein*

10. To investigate the end-on interaction of MT ends with proteins found at the cell cortex or the kinetochore, proteins or motors can be nonspecifically attached to SU8 barrier, or alternatively, specifically adhered to gold barriers functionalized with biotin using thiol-chemistry (not shown).
11. First the surfaces are blocked by incubating the flow chamber with 0.2 mg/mL PLL-PEG for 5 min and subsequently 0.1 mg/mL k-casein in MRB80.
12. For the biotinylated dynein: a series of biotin-streptavidin linkage is established by sequentially incubating the barriers in the streptavidin mix and biotin mix solutions for 5 min while rinsing with MRB80 in between [23].
13. Incubate with the dynein mix for 5 min. Rinse with MRB80 and use right away to optimize measurement time wherein dynein motors are still active.
14. Repeat the procedure starting from making bead–axoneme constructs (*see steps 4–9*).

Figure 6c shows a plot of MT dynamics in the absence and presence of dynein which are nonspecifically attached to a barrier. The plot shows that in the presence of dynein, the microtubule often experiences a pulling force as exhibited by a negative force. That is, as the microtubule shrinks, the bead is pulled away from the trap center towards the barrier. This indicates that the shrinking MT is still in contact with the barrier, and dynein can hold on to the shrinking MT against forces of up to several piconewtons [10].

## 4 Notes

1. Make sure to maintain tight contact between the photoresist and mask to make even and sharp walls. Note that with SU-8 as a negative photoresist, the area exposed to light becomes insoluble to the developer.

2. Note that with S1813 as a positive photoresist, the area exposed to light becomes soluble to the developer.
3. The gold barriers can be pretreated with UV/ozone radiation or exposure to plasma/glow discharge for 10 min before sonicating in ethanol [36].
4. Live cells can often be observed within 30–60 min and should be visible within 24 h. Once the culture is established, it can be transferred to a culture flask for large volume production or diluted further for long-term storage by serial transfer [19]. It is important to make sure no detergent remains on the glassware—Tetrahymena are more sensitive than *E. coli*.
5. The goal is to simply get enough Tetrahymena (but not too many dead ones) to make a high-yield axoneme purification.
6. Motility generally stops within 2–3 min. Make sure that they are not dead and lysed. Note that for a large volume it can take a while. For instance for a 12 g pellet (~50 mL volume), it may take about 30 min. It is important that the cells are intact (not lysed) so that no other proteins except the cilia are purified.
7. The pellet can be hard and stuck at the bottom of the tube. Dissolve well by pipetting in/out (cut the tip to enlarge).
8. The frozen cells can be stored at –70 °C and remain viable for several years.
9. Autoclave in advance the YP medium inside the flask to minimize contamination. Check growth rate by measuring the concentration every 2–3 h using a spectrophotometer. Image the sample under the microscope to check for contamination (especially bacterial contamination). If contamination is already detected in the YP-D or YP-Raf media, it is better to start the growth over again because bacteria proliferate very quickly than yeasts.
10. The OD must be >2.0 to have enough yeast cells. For example, for strain Y753 an OD<sub>600</sub> ~ 2.2 harvested an amount of 15 g of yeast pellet.
11. The supernatant looks golden-yellow and there is a greasy top layer (membrane). Do not take the membrane! Use a long needle and 10 mL syringe to take the supernatant.
12. Avoid bubbles and running the column dry during the washing steps.
13. Add more TEV buffer (200 µL each time) to the column to get most of the beads out. Let the solution sit for a while on the tube until the beads have settled down to the bottom (2–3 min). Remove bubbles and excess buffer to make the final volume needed (200–300 µL).

14. Do this at room temperature to reduce condensation. Ideally, BG-NHS in DMSO must be used up the day it is dissolved because of degradation due to hydrolysis, or store at  $-20^{\circ}\text{C}$  (maximum of 4 months).
15. For Bioneer 61-nucleotide oligo (5'Amine): add 6.86  $\mu\text{L}$  to make 1 mM. Take out 0.5  $\mu\text{L}$  for gel electrophoresis to check the concentration.
16. For the Bioneer 61-nucleotide oligo: add 12  $\mu\text{L}$  of 20 mM BG-NHS in DMSO, 6  $\mu\text{L}$  of 1 mM NH<sub>2</sub>-oligos, 6  $\mu\text{L}$  of 400 mM Hepes pH 8.5.
17. This gravity-driven column will trap the free BG molecules and let the oligos flow through. Mount the column on a vertical holder and put a catch beaker at the bottom. Perform the purification at  $4^{\circ}\text{C}$  or in the cold room. Remove the top and bottom caps and let the storage buffer flow through completely. Equilibrate the column with 10 mL of 1  $\times$  TE buffer. Flow through completely (~45 min). Add the 100  $\mu\text{L}$  sample to the column and let it flow through the bead column completely. Add 400  $\mu\text{L}$  of 1  $\times$  TE buffer. Flow through the bead completely (does not contain the sample yet). Save it just to be sure (500  $\mu\text{L}$ ). Take out 1  $\mu\text{L}$  for gel electrophoresis. Place an appropriate collection tube under the column (2 mL tube) and elute by flowing through 500  $\mu\text{L}$  of 1  $\times$  TE buffer. Collect the 500  $\mu\text{L}$  elution, which now contains the purified BG-oligos.
18. Add 50  $\mu\text{L}$  of 3 M sodium acetate pH 5.2 to the sample (1/10 volume of the sample). Add 2.5–3.0  $\times$  volume (calculated after addition of sodium acetate) of at least 95 % ethanol (1.0–1.5 mL). Incubate on ice or at  $-80^{\circ}\text{C}$  for 30 min. Centrifuge at 16,000  $\times g$  for 30 min at  $4^{\circ}\text{C}$ . Discard supernatant carefully (DNA pellet may not be visible). Add 1 mL of 70 % ethanol and centrifuge again at 16,000  $\times g$  for 15 min. Discard supernatant and leave open to let ethanol evaporate for 5 min. Dissolve pellet in 55  $\mu\text{L}$  of TE buffer (100  $\mu\text{M}$  or desired concentration). Make sure the buffer comes into contact with the whole surface of the tube since a significant portion of DNA may be deposited on the walls instead of in the pellet. Take out 1  $\mu\text{L}$  for gel electrophoresis.
19. For Bioneer 61-nucleotide (5'-thiol) or (5'-biotin). Add 6  $\mu\text{L}$  H<sub>2</sub>O (or TE buffer) + 1  $\mu\text{L}$  of 1 M DTT. Take out 0.5  $\mu\text{L}$  for gel electrophoresis.
20. It is advised to take less of the complementary oligo, so no extra purification is needed for removing the un-combined oligos. Or purify with a filter that lets through the oligos and retain the proteins. Take out 0.5  $\mu\text{L}$  for gel electrophoresis. Check the fraction of BG-labeled oligos by gel electrophoresis.

21. Avoid introducing air bubbles into the channel and the tubing because it will create a blockage and make it difficult to draw liquid during the experiment. Mount the syringe to the pump machine carefully such that you are not drawing out liquid from the flow channel, otherwise inject the liquid back to the channel until the reservoir is filled again.
22. Keep a close eye on the reservoir. Never let it go empty as this will introduce air bubble into the channel.
23. The software measures bead motion using the QPD and computes the power spectral density which is fitted by a Lorentzian function. The spring constant is computed from the corner frequency,  $f_c$  and is given by the expression,  $k = 2\pi\gamma f_c$  where the drag coefficient  $\gamma = 3\pi d\eta$  is dependent on the bead diameter,  $d$  and viscosity of the solution  $\eta$ . The force on the bead is computed as  $f_x = k_x \Delta x$ , where  $\Delta x$  is the displacement of the bead relative to the trap center.
24. The first method can be optimized by mixing 1:1 ratio of beads and axonemes and incubate for at least an hour before the experiment (e.g., while making the flow channel). This way, the probability of having 2 or more axonemes in one bead is minimized. The second method can be implemented by trapping a bead first and then flow out the axonemes. Once a good bead–axoneme construct is found, the rest of the beads and axonemes are flowed out. Try not to lose the construct by hiding it against high flow in between the barriers. However, if the construct is lost, then the process is repeated from the beginning. To prevent this, multiple mini inlets can be made (as shown in Fig. 3b) where one channel only contains buffer. Once a construct is found, it is brought to this channel using the trap to measure its properties if it is good enough without flowing out the beads and axonemes. Otherwise go back to the channel where the beads and axonemes are.
25. Make sure not to lose the construct by keeping it close to a barrier and away from the direct flow. Check that there is enough MRB80 left on the reservoir.

---

## Acknowledgments

We thank Matthew Footer for the help in setting up the axoneme purification from *Tetrahymena thermophila* and Samara Reck-Peterson and her lab for the training and assistance in setting up the dynein purification from *Saccharomyces cerevisiae*.

## References

1. Mitchison T, Kirschner M (1984) Dynamic instability of microtubule growth. *Nature* 312:237–242. doi:[10.1038/312237a0](https://doi.org/10.1038/312237a0)
2. Scholey J, Brust-Mascher I, Mogilner A (2003) Cell division. *Nature* 422:746–752. doi:[10.1038/nature01599](https://doi.org/10.1038/nature01599)
3. Howard J, Hyman AA (2003) Dynamics and mechanics of the microtubule plus end. *Nature* 422:753–758. doi:[10.1038/nature01600](https://doi.org/10.1038/nature01600)
4. Grill S, Hyman AA (2005) Spindle positioning by cortical pulling forces. *Dev Cell* 8:461–465. doi:[10.1016/j.devcel.2005.03.014](https://doi.org/10.1016/j.devcel.2005.03.014)
5. Tran PT, Marsh L, Doye V, Inoue S, Chang F (2001) A mechanism for nuclear positioning in fission yeast based on microtubule pushing. *J Cell Biol* 153:397–411. doi:[10.1083/jcb.153.2.397](https://doi.org/10.1083/jcb.153.2.397)
6. Kimura A, Onami S (2007) Local cortical pulling-force repression switches centrosomal centration and posterior displacement in *C. elegans*. *J Cell Biol* 179:1347–1354. doi:[10.1083/jcb.200706005](https://doi.org/10.1083/jcb.200706005)
7. Dogterom M, Surrey T (2013) Microtubule organization in vitro. *Curr Opin Cell Biol* 25:23–29. doi:[10.1016/j.ceb.2012.12.002](https://doi.org/10.1016/j.ceb.2012.12.002)
8. Dogterom M, Yurke B (1997) Measurement of the force-velocity relation for growing microtubules. *Science* 278:856–860. doi:[10.1126/science.278.5339.856](https://doi.org/10.1126/science.278.5339.856)
9. Janson M, de Dood M, Dogterom M (2003) Dynamic instability of microtubules is regulated by force. *J Cell Biol* 161:1029–1034. doi:[10.1083/jcb.200301147](https://doi.org/10.1083/jcb.200301147)
10. Laan L, Pavin N, Husson J, Romet-Lemonne G, van Duijn M, Preciado-Lopez M, Vale RD, Jülicher F, Reck-Peterson SL, Dogterom M (2012) Cortical dynein controls microtubule dynamics to generate pulling forces that position microtubule asters. *Cell* 148:502–514. doi:[10.1016/j.cell.2012.01.007](https://doi.org/10.1016/j.cell.2012.01.007)
11. Roth S, Laan L, Dogterom M (2014) Reconstitution of cortical dynein function. In: Vale RD (ed) Reconstituting the cytoskeleton, vol 540, Methods in enzymology. Academic, New York, NY, pp 205–230. doi:[10.1016/B978-0-12-397924-7.00012-1](https://doi.org/10.1016/B978-0-12-397924-7.00012-1)
12. Kerssemakers JWJ, Munteanu EL, Laan L, Noetzel TL, Janson ME, Dogterom M (2006) Assembly dynamics of microtubules at molecular resolution. *Nature* 442:709–712. doi:[10.1038/nature04928](https://doi.org/10.1038/nature04928)
13. Kerssemakers JWJ, Janson ME, van der Horst A, Dogterom M (2003) Optical trap setup for measuring microtubule pushing forces. *Appl Phys Lett* 83:4441–4443. doi:[10.1063/1.1629796](https://doi.org/10.1063/1.1629796)
14. Laan L, Dogterom M (2010) In vitro assays to study force generation at dynamic microtubule ends. In: Wilson L, Correia JJ (eds) Microtubules, in vitro, vol 95, Methods in cell biology. Springer, Berlin, pp 617–639. doi:[10.1016/S0091-679X\(10\)95031-0](https://doi.org/10.1016/S0091-679X(10)95031-0)
15. Kalisch S-M, Laan L, Dogterom M (2011) Force generation by dynamic microtubules in vitro. *Methods Cell Biol* 777:147–165. doi:[10.1007/978-1-61779-252-6\\_11](https://doi.org/10.1007/978-1-61779-252-6_11)
16. Love J, Estroff L, Kriebel J, Nuzzo R, Whitesides G (2005) Self-assembled monolayers of thiophanes on metals as a form of nanotechnology. *Chem Rev* 105:1103–1169. doi:[10.1021/cr0300789](https://doi.org/10.1021/cr0300789)
17. Reck-Peterson SL, Yildiz A, Carter AP, Gennerich A, Zhang N, Vale RD (2006) Single-molecule analysis of dynein processivity and stepping behavior. *Cell* 126:335–348. doi:[10.1016/j.cell.2006.05.046](https://doi.org/10.1016/j.cell.2006.05.046)
18. Goodman BS, Reck-Peterson SL (2014) Engineering defined motor ensembles with DNA origami. In: Vale RD (ed) Reconstituting the cytoskeleton, vol 540, Methods in enzymology. Academic, New York, NY, pp 169–188. doi:[10.1016/B978-0-12-397924-7.00010-8](https://doi.org/10.1016/B978-0-12-397924-7.00010-8)
19. Cassidy-Hanley DM (2012) Tetrahymena in the laboratory: strain resources, methods for culture, maintenance, and storage. *Methods Cell Biol* 109:237–276. doi:[10.1016/B978-0-12-385967-9.00008-6](https://doi.org/10.1016/B978-0-12-385967-9.00008-6)
20. Gutierrez JC, Orias E (1992) Genetic characterization of *Tetrahymena thermophila* mutants unable to secrete capsules. *Dev Genet* 13:160–166. doi:[10.1002/dvg.1020130210](https://doi.org/10.1002/dvg.1020130210)
21. Thompson GA, Baugh LC, Walker LF (1974) Nonlethal deciliation of *Tetrahymena* by a local anesthetic and its utility as a tool for studying cilia regeneration. *J Cell Biol* 61:253–257. doi:[10.1083/jcb.61.1.253](https://doi.org/10.1083/jcb.61.1.253)
22. Mucus minus tetrahymena strain: SB715, Cornell Tetrahymena Stock Center, ID: SD01508 *exoA1/exoA1; chx1-1/CHX1-1 (exoA1; CHX1; exo minus; cy-s, II)*, (<http://tetrahymena.vet.cornell.edu/>).
23. Romet-Lemonne G, van Duijn M, Dogterom M (2005) Three-dimensional control of protein patterning in microfabricated devices. *Nano Lett* 5:2350–2354. doi:[10.1021/nl0507111](https://doi.org/10.1021/nl0507111)
24. Dogterom M, Kerssemakers JWJ, Romet-Lemonne G, Janson ME (2005) Force generation by dynamic microtubules. *Curr Opin Cell Biol* 17:67–74. doi:[10.1016/j.ceb.2004.12.011](https://doi.org/10.1016/j.ceb.2004.12.011)

25. Satir B, Sale WS, Satir P (1976) Membrane renewal after dibucaine deciliation of Tetrahymena – freeze-fracture technique, cilia, membrane structure. *Exp Cell Res* 97:83–91. doi:[10.1016/0014-4827\(76\)90657-1](https://doi.org/10.1016/0014-4827(76)90657-1)
26. Johnson KA (1986) Preparation and properties of dynein from Tetrahymena cilia. *Methods Enzymol* 134:306–317
27. Boal AK, Tellez H, Rivera SB, Miller NE, Bachand GD, Bunker BC (2006) The stability and functionality of chemically crosslinked microtubules. *Small* 2:793–803. doi:[10.1002/smll.200500381](https://doi.org/10.1002/smll.200500381)
28. Visscher K, Gross SP, Block SM (1996) Construction of multiple-beam optical traps with nanometer-resolution position sensing. *IEEE J Sel Top Quantum Electron* 2:1066–1076. doi:[10.1109/2944.577338](https://doi.org/10.1109/2944.577338)
29. Gittes F, Schmidt CF (1998) Signals and noise in micromechanical measurements. *Methods Cell Biol* 55:129–156
30. Visscher K, Schnitzer MJ, Block SM (1999) Single kinesin molecules studied with a molecular force clamp. *Nature* 400:184–189. doi:[10.1038/22146](https://doi.org/10.1038/22146)
31. Laan L, Husson J, Munteanu EL, Kerssemakers JWJ, Dogterom M (2008) Force-generation and dynamic instability of microtubule bundles. *Proc Natl Acad Sci U S A* 105:8920–8925. doi:[10.1073/pnas.0710311105](https://doi.org/10.1073/pnas.0710311105)
32. Muller-Reichert T, Chretien D, Severin F, Hyman AA (1998) Structural changes at microtubule ends accompanying GTP hydrolysis: information from a slowly hydrolyzable analogue of GTP, guanylyl (alpha, beta)methylene-diphosphonate. *Proc Natl Acad Sci U S A* 95:3661–3666. doi:[10.1073/pnas.95.7.3661](https://doi.org/10.1073/pnas.95.7.3661)
33. Gardner MK, Zanic M, Howard J (2013) Microtubule catastrophe and rescue. *Curr Opin Cell Biol* 25:14–22. doi:[10.1016/j.ceb.2012.09.006](https://doi.org/10.1016/j.ceb.2012.09.006)
34. Bieling P, Laan L, Schek H, Munteanu EL, Sandblad L, Dogterom M, Brunner D, Surrey T (2007) Reconstitution of a microtubule plus-end tracking system in vitro. *Nature* 450:1100–1105. doi:[10.1038/nature06386](https://doi.org/10.1038/nature06386)
35. Akhmanova A, Steinmetz MO (2008) Tracking the ends: a dynamic protein network controls the fate of microtubule tips. *Nat Rev Mol Cell Biol* 9:309–322. doi:[10.1038/nrm2369](https://doi.org/10.1038/nrm2369)
36. Ron H, Matlis S, Rubinstein I (1998) Self-assembled monolayers on oxidized metals. 2. Gold surface oxidative pre-treatment, monolayer properties, and depression formation. *Langmuir* 14:1116–1121. doi:[10.1021/la970785v](https://doi.org/10.1021/la970785v)

# **Chapter 17**

## **Simultaneous Manipulation and Super-Resolution Fluorescence Imaging of Individual Kinetochores Coupled to Microtubule Tips**

**Yi Deng and Charles L. Asbury**

### **Abstract**

Kinetochores are large multiprotein complexes that drive mitotic chromosome movements by mechanically coupling them to the growing and shortening tips of spindle microtubules. Kinetochores are also regulatory hubs, somehow sensing when they are erroneously attached and, in response, releasing their incorrect attachments and generating diffusible wait signals to delay anaphase until proper attachments can form. The remarkable ability of a kinetochore to sense and respond to its attachment status might stem from attachment- or tension-dependent changes in the structural arrangement of its core subcomplexes. However, direct tests of the relationship between attachment, tension, and core kinetochore structure have not previously been possible because of the difficulties of applying well-controlled forces and determining unambiguously the attachment status of individual kinetochores *in vivo*. The recent purification of native yeast kinetochores has enabled *in vitro* optical trapping-based assays of kinetochore tip-coupling and, in separate experiments, fluorescence imaging of single kinetochore particles. Here we introduce a dual instrument, combining optical trapping with multicolor total internal reflection fluorescence (TIRF) imaging, to allow kinetochore structure to be monitored directly with nanometer precision while mechanical tension is simultaneously applied. Our instrument incorporates differential interference contrast (DIC) imaging as well, to minimize the photo-bleaching of fluorescent tags during preparative bead and microtubule manipulations. A simple modification also allows the trapping laser to be easily converted into a real-time focus detection and correction system. Using this combined instrument, the distance between specific subcomplexes within a single kinetochore particle can be measured with 2-nm precision after 50 s observation time, or with 11-nm precision at 1 s temporal resolution. While our instrument was constructed specifically for studying kinetochores, it should also be useful for studying other filament-binding protein complexes, such as spindle poles, cortical microtubule attachments, focal adhesions, or other motor–cytoskeletal junctions.

**Key words** Total Internal Reflection Fluorescence (TIRF) Microscopy, Super-resolution, Centroid tracking, Differential Interference Contrast (DIC), Optical tweezers, Focus correction, Surface passivation, Kinetochore, Microtubule, Intramolecular distance

---

## 1 Introduction

Optical tweezers are ideal tools for manipulating sub-micrometer objects such as colloidal particles or bacterial cells, and for generating and quantifying forces in the pico-Newton range [1–3]. They have become popular instruments for biophysical studies at the single molecule level in vitro, such as of motor proteins or protein complexes that are processive on linear cellular structures, including kinesin and dynein motors on microtubules [4–8], myosin on F-actin [9–11], and polymerases on DNA and RNA [12–16]. Typically, the optical tweezers are combined with wide-field microscopy or differential interference contrast (DIC) microscopy [17], which provides visual cues for the experimentalist to manipulate trapped particles into the desired spatial configuration. DIC microscopy is a popular choice, because the appearance of micrometer scale colloidal particles under DIC imaging is clearly distinctive from protein aggregates or bead clumps that, if trapped, would lead to errors in estimating the force generated by the optical tweezers. DIC imaging can also allow objects ten times smaller than the illumination wavelength to be viewed. As an example, microtubules, which are 25 nm in diameter, are visible under DIC microscopy with video enhancements [18, 19]. This has made DIC imaging especially useful in single molecule tweezers studies of microtubule-associated motor proteins such as kinesins and cytoplasmic dynein. Another combination of optical tweezers that has become increasingly common is with fluorescence microscopy [5, 20, 21]. Simultaneously recording single-molecule fluorescence while also applying controlled mechanical perturbations can provide correlated information that is very valuable for uncovering how complex molecular machines function [22–24].

Most previous combined single-molecule fluorescence/optical tweezers instruments were designed for studying nucleic acid-interacting proteins rather than microtubule-interacting complexes. Studying protein machines that interact with microtubules, particularly dynamic microtubules, poses extra challenges. Microtubules are assembled in vitro and are never monodisperse in length, whereas DNAs can be made or purchased in highly monodisperse form. In experiments that must accommodate microtubule filaments of variable length, it is important to image the microtubules, whereas in DNA assays it is often feasible to leave the DNAs invisible. Video-enhanced differential interference contrast (VE-DIC) microscopy allows the use of unstained microtubules, avoiding possible interference from dye-labeled tubulin subunits, and enabling long-term imaging over hours without photobleaching [25–27].

In this chapter we introduce a combined instrument of optical tweezers, DIC and TIRF microscopy, each method working independently and simultaneously. To demonstrate its use,

intra-kinetochore stretch distance is measured in vitro. Kinetochores are complex multi-protein machines that serve not only as mechanical couplers between mitotic chromosomes and dynamic microtubule tips [28, 29], but also as signaling hubs. Mechanical forces on kinetochores are widely believed to control the generation of wait signals (Spindle Assembly Checkpoint signals), which help to ensure the accuracy of mitosis by delaying anaphase chromosome separation until all kinetochores are properly tip-attached and under tension [30, 31]. Kinetochore tension is also believed to control an error avoidance mechanism that triggers detachment of erroneously attached kinetochores that lack tension, while selectively stabilizing proper kinetochore–microtubule attachments that bear tension [32–34]. Presumably, therefore, tension must affect kinetochore structure in such a way as to control the localization or activity of signal-generating and error-correcting factors. Recent work confirms the structural plasticity of kinetochores *in vivo* [35–38]. However, it remains unclear whether the rearrangements observed *in vivo* are direct responses to mechanical force, or whether they result indirectly from other signaling events or from differences in the attachment status of the kinetochores, which can be difficult to determine unambiguously *in vivo*. Our approach of observing the fluorescence from single kinetochore particles bound to individual microtubules *in vitro* (Fig. 1) provides a new and more direct means to uncover how mechanical force affects kinetochore architecture. Our combined fluorescence and trapping-based methods will also be useful for directly examining how attachment status affects the affinity of the kinetochore for key checkpoint signaling and error correction factors. Ultimately, the approach might also be useful for studying protein assemblies from other cytoskeletal junctions, such as spindle poles, cortical attachment sites, or focal adhesions.

This chapter describes the design of the three major optical components of our instrument, the surface preparation we use for single kinetochore imaging, and a novel kinetochore-stretching assay. We also describe the design of an extension to the instrument that converts the optical tweezers into a focus detection and correction system. Optical trap calibration and kinetochore purification are covered only very briefly, since more detailed information can be found in the cited references (and in the other chapters of this volume).

---

## 2 Materials

### 2.1 Instrument Design and Optical Alignment

Many optical tweezers instruments are built by modifying commercial bright-field or DIC microscopes [39]. Whereas DIC and fluorescence imaging can be naturally combined with optical tweezers, the two imaging methods are not readily compatible by many

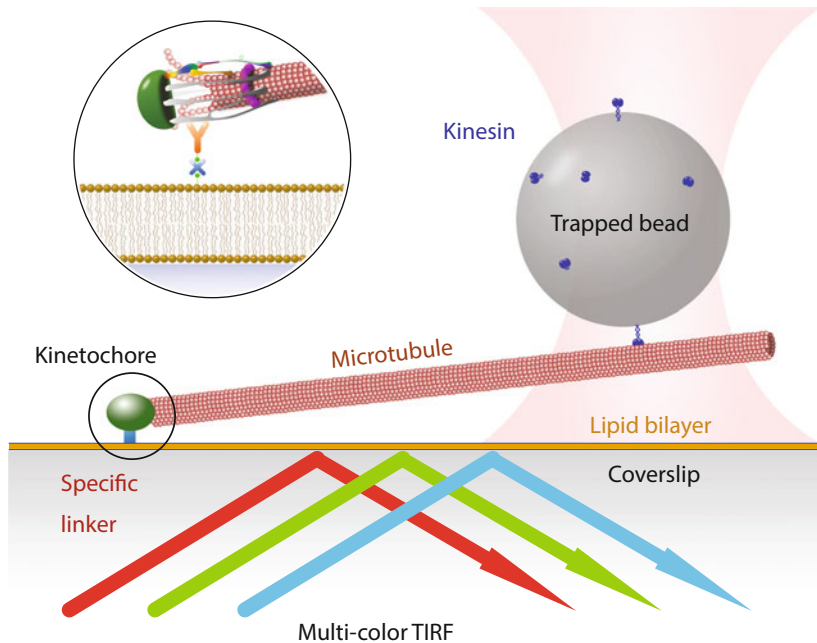


**Fig. 1** Schematic of the kinetochore stretching experiment. The glass surface is passivated by a supported lipid bilayer to provide specific binding of kinetochores. A small portion of the lipid is biotinylated, which allows avidin to bind, followed by biotinylated anti-His antibody. The kinetochores are His-tagged and are therefore diffusively anchored on the surface. Microtubules spontaneously form end-on attachments to the kinetochores, and a polystyrene bead that is functionalized by kinesin is trapped optically and then bound to the free end of the microtubule. The kinetochore is dragged along the lipid bilayer by the trapped bead, and time-lapse fluorescence images of the differentially labeled kinetochore are recorded

standard microscope designs. The reason lies in the optical train of DIC, which has a pair of Wollaston or Nomarski prisms conjugated to the back-focal planes of the objective and condenser lenses. The prism on the objective side will split the emitted light based on its polarization, giving rise to two spatially displaced images corresponding to the two polarization directions. This artifact is undesirable in most applications, especially in single-molecule imaging, unless emission polarization is studied specifically. Wollaston or Nomarski prisms also affect the trapping laser in similar manner. For a circularly polarized incident trapping beam, the Nomarski prism will generate two slightly displaced traps, which can be approximated as one elliptically shaped trap. For a linearly polarized incident beam with polarization direction parallel with one of the axes of the prism, the beam will not be split, but the trap will still be anisotropic due to the polarization [40]. While anisotropy of the laser trap can be measured and accounted for [39], the artifact in fluorescence is not acceptable when imaging resolution is close to the diffraction limit. Here we overcome this limitation by relaying the back-focal plane of the objective lens via a  $4f$  lens system (as detailed below, in Subheading 2.1.3). The trapping,

fluorescence, and DIC imaging beam paths are then well separated, so that the Nomarski prism does not affect the other two optical paths. By implementing this modification, we show that DIC is perfectly compatible with fluorescence imaging and optical tweezers. In our combined system, we can manipulate an optically trapped object according to DIC images, and acquire fluorescence signals only when necessary to minimize photobleaching.

In addition to the incorporation of TIRF and DIC microscopy capability into optical tweezers, we also describe a practical modification that converts the optical tweezers setup into a real-time focus detection and correction system, or a focus lock, which compensates sample stage drift due to temperature fluctuations or slide creep. The principle is similar to many setups that use total internal reflection to convert sample movement into a translating optical signal [41]. Instead of using a separate light source, however, the trapping beam is converted from focusing at the imaging plane into a total-internal-reflection configuration by a few extra inexpensive optical elements, and is reflected back to a position-sensitive photodetector. This addition allows us to correct focal drift at video frequency, independent of DIC and TIRF functionalities.

Our instrument is built on a standard Nikon TE inverted microscope base, on which TIRF, optical tweezers, DIC, and focus lock are built sequentially. Three diode lasers at 488, 561, and 647 nm with a maximum power of 100 mW are used as excitation light sources that provide a good coverage of a wide range of fluorophore choices. Commercial DIC microscopes usually use green illumination, around 530 nm wavelength, which conflicts with one of the fluorescence channels. For this reason, we replaced the green DIC source with a 780-nm wavelength near-infrared LED (Thorlabs [M780L3](#)).

### *2.1.1 TIRF Microscopy and Image Channel Position Registration*

The laser beams from three solid-state lasers at 488 nm (Coherent Sapphire), 561 nm (Coherent Sapphire), and 641 nm (Coherent Cube) pass three half-wave plates, three polarized cube beam splitters, and three mechanical shutters (Uniblitz VS 25S2ZMO). Then they are expanded individually each by a pair of telescope lenses L1 ( $f = 12$  mm) and L2 ( $f = 500$  mm), as shown in Fig. 2. The expanded beams then pass a 1:1 telescope with the first lens L3 ( $f = 100$  mm) on a translational stage so that the incident angle on the image plane is adjustable. Therefore, users can easily switch between TIR, epi, and oblique illumination. Three laser beams are combined by two dichroic mirrors, DM1 and DM2, placed between L3 and L4 ( $f = 100$  mm). The combined and steered beams that pass through lens L4 are focused by the tube lens L5 ( $f = 150$  mm) to the back-focal plane of the objective lens. A multi-band dichroic mirror DM3 between L5 and the objective lens reflects the incident excitation lasers while passing the emitted fluorescence and the bright-field (DIC) illumination. The focal

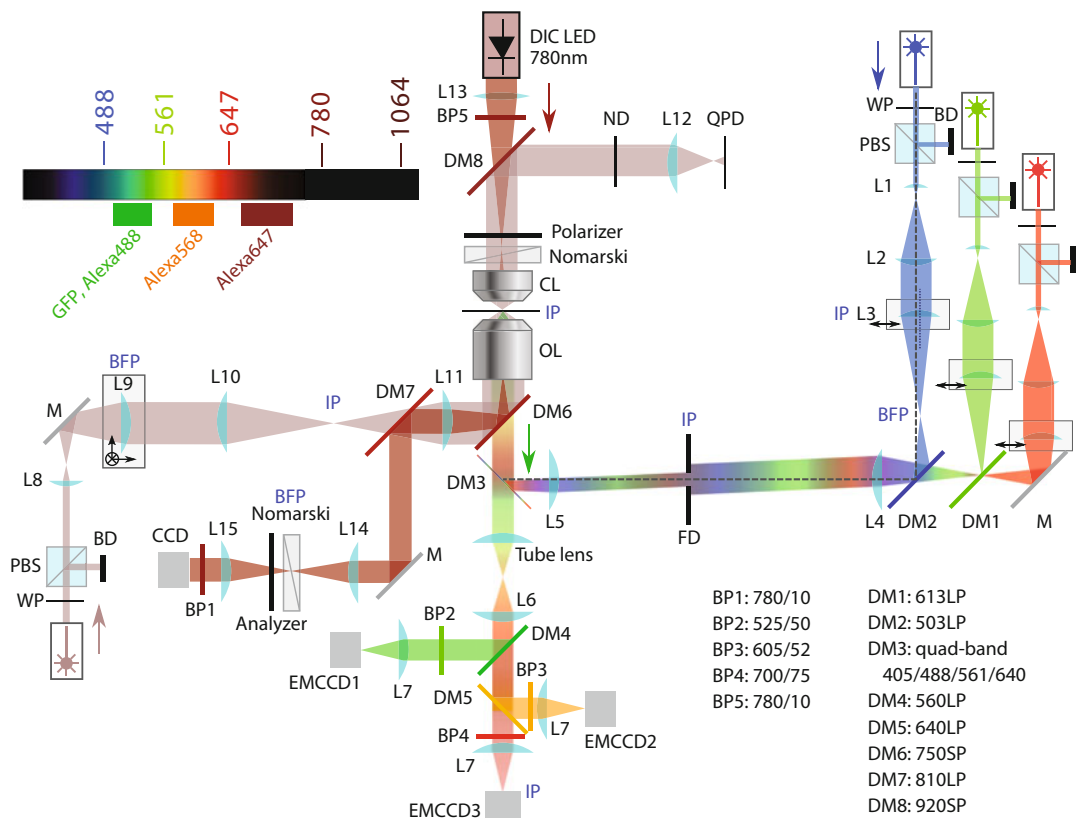


**Fig. 2** Diagram of the optical layout of the TIRF-Trap-DIC setup. *BD* beam dump, *BFP* back-focal plane, *BP* band-pass filter, *CCD* charge-coupled device (for bright-field detection), *CL* condenser/collection lens, *DM* dichroic mirror, *EMCCD* electron-multiplying CCD (for fluorescence detection), *FD* field diaphragm, *IP* image plane, *L* lens, *LED* light-emitting diode, *M* mirror, *OL* objective lens, *PBS* polarizing beam splitter, *QPD* quadrant photodiode, *S* shutter, *WP* half-wave plate

points of lens pairs L1/L2, L3/L4, and L5/objective coincide. An illumination field diaphragm (FD) is placed downstream of L4 at a distance of  $2f$ , and upstream of lens L5 at a distance of  $1f$ , so that both the field iris and the translating lens L3 are conjugated to the image plane. The iris allows adjustment of the illuminated area to prevent unnecessary photobleaching outside the imaging field of view (FOV). With this design, when L3 moves, it only translates the focused beam at the back-focal plane of the objective, and thus changes the incident angle at the image plane without changing the illuminated area. The emission signals are collected by the objective lens, sent through dichroic mirror DM3, and imaged by the built-in tube lens of the microscope base, followed by L6 ( $f = 60$  mm) and L7 ( $f = 125$  mm) onto three EMCCD cameras (Andor iXon897+). The fluorescence is split by DM4 and DM5 and cleaned by emission filters BP2-4. The sample is mounted on a piezo-driven nano-positioning stage (Physik Instrumente

P-571.3CL) that provides programmable movement and focusing correction in software.

To align the TIRF setup, a regular CCD camera is mounted at one of the view ports and aligned according to the images from the eyepiece. The camera is then used as a position indicator for laser beam alignment. First, the lasers are mounted and adjusted by several beam-folding mirrors. Beams of three colors are combined in this step by dichroic mirrors (DM1 and DM2). Then, the telescope assembly L4-iris-L5 is mounted to the backport of the microscope base and adjusted in position according to the beam pattern on the camera. Finally, lens L3 is installed, followed by the expansion telescope L2/L1 for each one of the three colors.

In applications where multiple fluorescence color channels are involved, accurate position registration across color channels is essential, especially when distances between components labeled in different colors need to be quantified. In the demonstration in this chapter, kinetochores are dragged along the lipid surface over micrometer-scale distances, while the nanometer-scale distance between two kinetochore components is measured by precisely tracking their locations in two different color channels. Accurate position registration is absolutely crucial. If, for example, the images in one channel were enlarged by just 1 % relative to the other channel, then a 50 nm artificial displacement would arise from a 5  $\mu\text{m}$  movement across the FOV.

There are many standard procedures that address the position registration problem. Typically, a fluorescent object, usually a bead that is visible in multiple color channels, is raster-scanned across the FOV [42, 43]. The bead positions are used to obtain the registration correction. Here, we describe a highly automated and quick procedure that takes advantage of the features of the instrument and the nature of the imaging data. Our kinetochore images contain sparsely distributed diffraction-limited spots at tunable density. The instrument also works in a “focus lock” mode (which will be introduced in Subheading 2.1.4), where the sample slide remains in focus while the slide is moved by the nano-positioner to explore other fields of view for imaging. A customized LabVIEW program automatically coordinates the stage movements, focus stabilization, and fluorescence imaging. This program adjusts the sample  $z$ -position into focus, sequentially takes fluorescence images in selected color channels, moves the stage lateral position to the next field, and repeats the cycle to fully explore the area accessible to the piezo stage. With this automated instrument and software, we can acquire hundreds of fields that contain  $10^5$  kinetochores within several minutes. Kinetochores in these images are randomly localized, and a fraction (typically between 10 and 50 %) of the particles are dual-colored, containing fluorescent components in two color channels.

The transformation between corresponding coordinates in two channels is assumed to be linear. That is, if one location at coordinate  $\mathbf{x} = (x, y)^T$  in channel 1 corresponds to a location at  $\mathbf{x}' = (x', y')^T$  in channel 2, the two coordinates are related by  $\mathbf{x}' = \mathbf{Ax} + \mathbf{b}$  for all  $\mathbf{x}$  and  $\mathbf{x}'$ , where  $\mathbf{A}$  is a  $2 \times 2$  matrix and  $\mathbf{b} = (x_0, y_0)^T$  is a translation. This linear model covers rotation, scaling and shearing as four degrees of freedom in  $\mathbf{A}$ . We find that this simple model is adequate for better than 5 nm precision. If more precision is needed, a more sophisticated, location-dependent nonlinear registration correction could also be obtained as described in [43].

To extract registration information  $\mathbf{A}$  and  $\mathbf{b}$  from the images of kinetochores, we implemented an unsupervised machine-learning algorithm that identifies the dual-colored particles. First, a spot detection routine finds the coordinates of bright spots in the two color channels separately. Then the pairwise relative positions of the detected bright spots are calculated within each FOV, and the relative positions are collected from all FOVs. The distribution of the pairwise relative position is shown in Fig. 3. If the detected spots in the two channels are not co-localized at all and randomly distributed, the pairwise relative position is uniformly distributed (not considering boundary effects). The co-localized spots, on the other hand, will generate a peaked distribution near the origin. The localization error and intrinsic physical distance between fluorophores broaden the distribution, while the registration error causes scaling, rotation, shearing, and nonlinear distortion of the distribution. Nevertheless, relative positions of separated particles and co-localized particles have very distinctive features. The two clusters of spots are modeled by a mixture of two 2D normal distributions (*see Note 1*), one of which has a very broad and isotropic spread centered at the origin, the other with a sharper but undetermined covariance matrix and center location. Because the widths of the two peaks are typically different by two orders of magnitude, they can be effectively separated following the standard expectation–maximization algorithm (*see Note 2*). The coordinates  $\mathbf{x}$  and  $\mathbf{x}'$  of the co-localized pairs in both channels are then used to estimate  $\mathbf{A}$  and  $\mathbf{b}$  through a linear regression  $\mathbf{x}' = \mathbf{Ax} + \mathbf{b}$ . The registration information is immediately used to obtain the corrected coordinates, and a new pairwise relative position is calculated, and the process iterates until  $\mathbf{A}$  and  $\mathbf{b}$  converge (Fig. 4).

The convergence is usually reached within a few iterations when the co-localization fraction is above 10 %, so that the central co-localization peak is distinctive from the background. Figure 3 compares the pairwise relative position before and after the linear registration correction. The distribution indicates that the distance of co-localized pairs after correction is tightly and isotropically centered around the origin. The cause of the residual spread is possibly due to residual localization inaccuracy, field-dependent image distortion, and intrinsic intramolecular distance between the fluorescent markers.

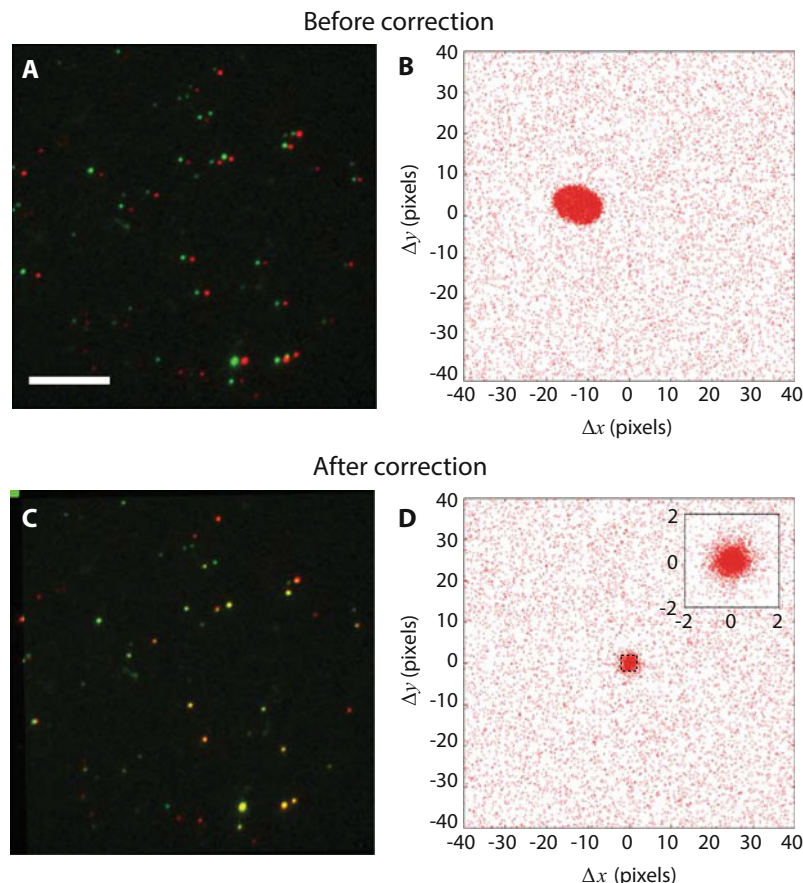


**Fig. 3** Color channel position registration can be obtained directly from kinetochore imaging data without need for a separate registration step. **(a)** Raw images of fluorescently labeled kinetochores with Alexa Fluor 546 (false-colored in green) and Alexa Fluor 647 (false-colored in red) on two kinetochore components. Scale bar, 5  $\mu\text{m}$ . **(b)** Pairwise distances between all detected spots in two color channels before registration correction. A distinctive cluster is formed near the origin. **(c)** Kinetochores after registration correction appear overlapping. **(d)** Pairwise relative distances form a tighter cluster at the origin after correction. The *inset* shows the zoomed-in distribution

#### 2.1.2 Optical Tweezers

A 3 W Nd:YAG laser at 1064 nm wavelength (Spectra-Physics J20-BL10-106C) is used for trapping. The beam passes a half-wave plate and a polarized cube beam splitter for manual power adjustment (*see Note 3*). The beam is then expanded by a pair of telescope lenses, L8 ( $f = 25 \text{ mm}$ ) and L9 ( $f = 200 \text{ mm}$ ), as shown in Fig. 2, with L9 mounted on a three-dimensional translation stage, and passes through a mechanical shutter (Uniblitz VS 25S2ZMO). The expanded trapping beam passes a pair of 1:1 telescope lenses, L10 and L11 ( $f = 175 \text{ mm}$ ), and is directed to the objective lens by a dichroic mirror, DM6, mounted between the multi-band dichroic

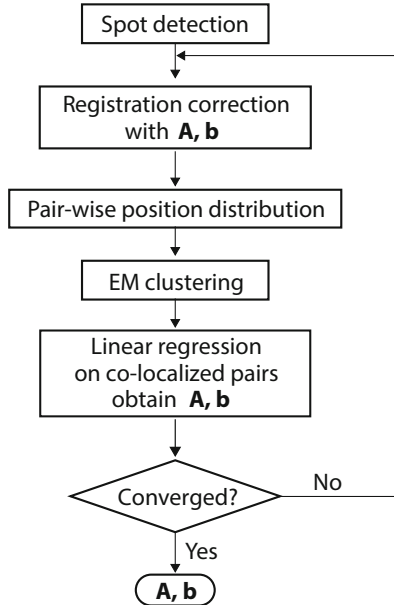


**Fig. 4** Flowchart for the image registration algorithm. A spot detection procedure is first applied on the images in both channels. The coordinates are corrected using an initial guess of  $\mathbf{A}$  and  $\mathbf{b}$ , then the pairwise relative position is calculated in each frame. An expectation–maximization routine identifies the co-localized pairs (distinguishing them from single-color spots lacking signal in the other channel), and the coordinates of these co-localized pairs are used to obtain registration correction through linear regression. The procedure is repeated until  $\mathbf{A}$  and  $\mathbf{b}$  converge

mirror for TIRF and the objective lens. The focal points of lens pairs L8/L9, L10/L11, and L11/objective coincide, and L9 is on the upstream focal plane of L10, so that telescope pair L10/L11 images L9 near the back aperture of the objective lens (*see Note 4*). When L9 is moved to adjust the optical trap position, the beam intensity at the specimen does not change significantly. The transmitted light is collected by the condenser lens CL, collimated, and redirected by a dichroic mirror mounted inside the condenser turret through a cut hole. The transmitted beam is focused by lens L12 ( $f = 80$  mm) and sent to a quadrant photodiode (QPD). Lens L12 images the condenser back-focal plane onto the QPD, so that the position signal is insensitive to the specific location of the trap when L9 is moved (although it is not necessary to move the trap position in the application of this chapter, and L9 in practice is rarely moved). The QPD signal is low-passed filtered, amplified, and digitized by an A/D converter (National Instruments USB-6212), and recorded by a computer. The alignment process is similar to that used for the TIRF microscope. The fine alignment and calibration of the optical tweezers follows standard procedures as described in [7, 39, 44–46].

### 2.1.3 DIC Microscopy

Because visible bands are occupied by fluorescence channels, a 780 nm LED (Thorlabs M780L3) is used as the light source for the DIC imaging, fed in at the backport of the condenser turret, in place of the regular green illumination. The slightly longer wavelength compared to the usual green illumination makes it more challenging to image microtubules. Our Nikon microscope base offers DIC imaging by allowing users to insert two Wollaston prisms near the back apertures of the objective lens and the condenser lens. However, this setup would significantly degrade TIRF imaging, as the randomly polarized or un-polarized emission light will be split by the objective Wollaston prism so that the point-spread functions for different polarizations are displaced. For this reason, the plane for placing the Wollaston prism under the objective lens is relayed downstream of the DIC beam path by a  $4f$  lens pair.

The dichroic beam splitter DM6 for sending the trapping laser to the objective lens has a cutoff wavelength of 750 nm, and so the DIC illumination (780 nm) is also reflected along the trapping path, and goes through lens L11, the last telescope lens for the trapping beam. Past L11, the DIC beam is separated from the trapping beam by a NIR long-pass dichroic mirror DM7 with 810-nm cutoff wavelength. L11 and another lens with identical focal length, L14 ( $f = 175$  mm), form the  $4f$  system that recreates the back aperture where the Wollaston prism is placed. The Wollaston prism is mounted on a stage with 3D-translational and rotational degrees of freedom. Finally, the DIC image is obtained by an imaging lens L15 ( $f = 125$  mm) and a CCD camera (Point Grey FL3-GE-03S1M-C). It is worth noting that in the Nikon DIC configuration, the direction of Wollaston prism axes are  $45^\circ$  from the  $x$ - and  $y$ -axes of the image, or the directions of the side ports and backport. The dichroic mirror that reflects both the trapping and DIC beams has a coating that complicates the phase relation between  $s$ -polarized and  $p$ -polarized waves at 780 nm. For this reason, the Wollaston prism axes are rotated to be parallel to the  $s$ - and  $p$ -directions of the dichroic mirror. The condenser turret is rotated  $45^\circ$  to achieve this configuration.

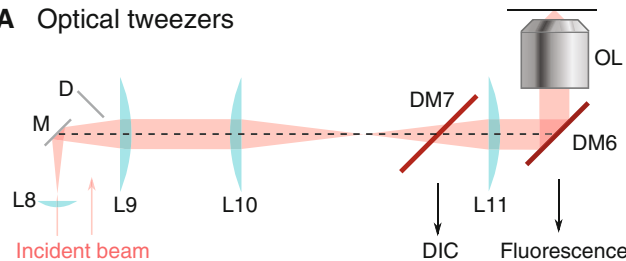
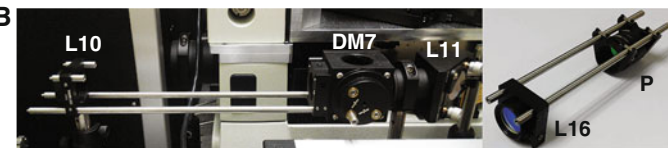
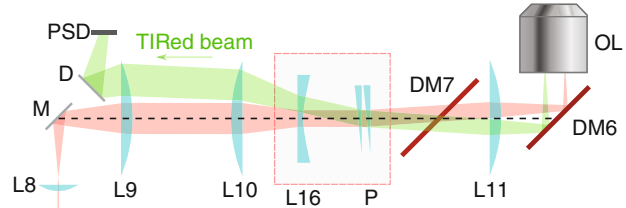
The optical tweezers should be aligned prior to setting up the DIC path. Lens L11 is shared by the tweezers and the DIC, so it should remain fixed in space. Using the auxiliary camera for TIRF alignment and the image of the field iris in the condenser turret, the condenser lens is aligned, so is the DIC illumination path. The second telescope lens L14 and the imaging lens L15 can be aligned similarly by centering the image on the DIC camera. Finally, the Wollaston prism is placed at the focal plane of L14 between L14 and L15. To adjust the  $x$ - $y$  location of the Wollaston prism on the imaging side, move the prism until the image is the dimmest, and then move away from the dimmest position until the image is near

saturation for the best contrast. To adjust the axial location of the Wollaston prism along the beam propagation direction, move the prism on both axial and perpendicular directions, so that the image changes in brightness uniformly, instead of having a wide dark stripe across the image.

Microtubules imaged by DIC have low contrast, and therefore the DIC images need to be processed for better visibility. Commercially available video enhancement devices can be found for analog video signals (e.g., the Hamamatsu Argus). The same real-time image/video processing task can now be carried out by computers, with the advantage of better coordination with nano-positioner control, optical trapping laser control, and fluorescence cameras. To maximize microtubule contrast, the DIC camera works at near saturation so that its dynamic range is fully exploited. The images typically have an uneven illumination, and likely contain several dust particles in the field, both of which can have higher brightness variation than microtubule images. Fortunately, these static background contributions can be recorded at a clean field or by focusing inside the coverslip, and can be subtracted from the images with beads and microtubules. In case the background illumination is still uneven, a high-pass filter is applicable. For our particular setup, we use LabVIEW for image acquisition and processing. Filtering the images with a large kernel is slow and not suitable for real-time processing. Instead, we resize the images 32 times smaller, median filter them, and then resize them back to the original size using interpolation, which is significantly faster than filtering. The smoothed background is subtracted to approximate high-pass filtering.

#### *2.1.4 Focus Detection*

The 1064-nm trapping laser can be used for focal detection with simple modifications to the trapping beam path. The design is similar to the commercially available focus locks provided with most microscopes, but at far lower cost. In a TIR configuration, the incident beam is reflected by the glass-water interface and sent back to the objective. An axial shift in the position of the sample results in a translational movement of the reflected beam. This movement can be picked up by a position-sensitive detector (PSD; Pacific Silicon Sensors DL100-7PCBA3) as an indication of the sample axial location. Different from the trap configuration, the laser beam in TIR configuration is collimated on the imaging plane instead of focused. To convert the trapping beam to a TIR beam, a concave lens L16 ( $f = -150$  mm) is added between the 1:1 telescope L10-L11 (Fig. 5). With the concave lens, the laser beam will be collimated, centered and parallel to the objective axis. To create an incident angle greater than the critical angle, a pair of wedge prisms P, each having  $2^\circ$  beam deviation, is also inserted so that the incident angles can be adjusted to any value between  $0^\circ$  and

**A Optical tweezers****B****C Focus detection****D**

**Fig. 5** Focus lock design. **(a)** Diagram of the optical tweezers configuration. The incident 1064 nm beam is collimated at the back-focal point of the objective lens and focused on the image plane. **(b)** Photograph of the actual optical elements. The extra elements for converting to a focus lock are removed, and pictured separately at right. **(c)** Optical diagram of the focus detection configuration. An added convex lens L16 converts the beam collimation so that the laser is focused at the back-focal plane. A wedge glass pair P steers the incident angle beyond the critical angle. **(d)** Photograph showing the actual parts with focus detection components inserted

4° from any direction. The TIR beam is spatially separated from the incident beam, and is redirected onto the PSD by a D-shaped mirror (D) between L8 and L9 so that the incident beam is not blocked (Fig. 5).

For easy installation and removal of the three additional optical elements (one convex lens and two wedge prisms), lens L10 and L11 in the optical tweezers setup are mounted on a cage system with an open top, and the additions of the concave lens L16 and prism pair are mounted on complementary cage rails (Fig. 5). To adjust the prism pair, set the wedge of the prisms pointing in opposite directions initially, so that the beam out of the objective

has zero incident angle about the axis. With a sample slide on the microscope stage, rotating the prisms in opposite directions will change the incident angle (the elevation angle), while rotating in the same direction rotates the collimated beam about the axis (the azimuthal angle). Adjust the prisms so that the incident beam reaches TIR condition. A bright reflection should be detectable along the beam path and on the PSD. The PSD signal is low-pass filtered, digitized by the acquisition board, and then monitored and controlled if needed by custom software written in LabVIEW.

## **2.2 Single Kinetochore Imaging and Manipulation Assay**

### **2.2.1 Kinetochore, Tubulin, and Kinesin Purification**

### **2.2.2 Microbeads Functionalized with a Strong MT-Binding Protein**

### **2.2.3 Microtubules**

### **2.2.4 Small Unilamellar Vesicles (SUVs) for Lipid-Based Surface Passivation**

For in vitro experiments on kinetochores, we follow the protocol in ref. [47] to purify kinetochores from a yeast strain that carries genes encoding labeled kinetochore components. Tubulin is purified from calf brains following [48]. In order for the beads to attach to microtubules, we purify a His-tagged and biotinylated recombinant kinesin motor domain from *E. coli* cells [49, 50]. The biotinylation is achieved by an enzymatic ligation [51]. The materials can be found in the corresponding references.

1. Streptavidin coated polystyrene beads, 440 nm in diameter, 1 % weight/volume.
2. Biotinylated kinesin (*see Note 5*), 100 µg/ml.
3. Assay buffer, containing 25 mM HEPES-KOH at pH 7.6, 50 mM potassium glutamate, 1 mM magnesium acetate, 10 % glycerol, 0.1 mM EDTA, 0.5 mM EGTA, 0.1 % tergitol-type NP-40.
4. Oxygen-scavenging system for reducing photobleaching and photo-damage: mix glucose oxidase at 20 mg/ml, catalase at 4 mg/ml in BRB80 with 20 % glycerol (100× stock), and 2 M glucose in water in a separate tube (100× stock).
5. 5 mg/ml *k*-casein in assay buffer.
1. BRB80 buffer: 80 mM PIPES, 1 mM MgCl<sub>2</sub>, 0.5 mM EGTA (*see Note 6*).
2. Microtubule polymerization buffer: 5 % v/v DMSO, 1 mM GTP, 4 µM additional MgCl<sub>2</sub> in BRB80 1×.
3. 10 mM taxol stock solution in DMSO.
4. Purified bovine tubulin at approximately 1 mg/ml.
5. Fluorescently labeled bovine tubulin (optional).
6. Ultracentrifuge.
1. 1-palmitoyl-2-oleoyl-*sn*-glycero-3-phosphocholine (POPC), 25 mg/ml in chloroform.
2. 1,2-dioleoyl-*sn*-glycero-3-phosphoethanolamine-*N*-(cap biotinyl) sodium salt (bio-cap-PE), 10 mg/ml.

3. Compressed nitrogen gas.
4. Lipid buffer: 25 mM HEPES-KOH and 150 mM NaCl at pH 7.6.
5. Tip sonifier.
6. Pasteur pipette, glass test tubes, desiccator and vacuum pump.

#### **2.2.5 Disposable Channel-Slides**

1. 24 × 40 glass coverslips, glass slides, and double-sided tape.
2. Bench top plasma cleaner with vacuum pump.
3. Hot plate or oven.
4. Nail polish.

#### **2.2.6 Preparing Slides for the Single Kinetochore Imaging and Manipulation Assay**

1. Assay buffer.
2. 0.1 mg/ml avidin-DN in assay buffer.
3. 20 nM penta-His antibody in assay buffer.
4. Vacuum source such as water aspirator with water trap.
5. Purified His-tagged kinetochore particles in assay buffer.
6. Functionalized beads prepared in Subheading 3.1.2.
7. 5 mg/ml *k*-casein in assay buffer.

### **3 Methods**

#### **3.1 Single Kinetochore Imaging and Manipulation Assay**

To demonstrate the application of our combined instrument, we use it to measure inter-molecular distances within a single kinetochore particle. Kinetochores are protein complexes that assemble on centromeric DNA during mitosis and meiosis and act as load-bearing linkers to the growing and shrinking tips of spindle microtubules in order to segregate chromosomes [52, 53]. Beyond their role as mechanical “tip-couplers,” kinetochores also facilitate crucial regulatory functions including modulation of microtubule tip dynamics [34, 47, 54] and monitoring the spindle–chromosome attachment configuration [30, 31]. The core kinetochore components are largely conserved in eukaryotes from yeast to human. The total molecular weight of a kinetochore is roughly in the megadalton range, but the total weight and the copy number of each component varies across species [55]. Kinetochores are organized into a layered structure, with inner kinetochore components bound to centromeric DNA and outer components forming attachments to spindle microtubules. Their architecture has been mapped with nanometer accuracy by fluorescently tagging particular pairs of kinetochore components and measuring their separation (the “delta measurement”) in fixed or live cells of both yeast and humans [35, 36, 38, 56, 57]. Electron microscopy has also provided high-resolution views of kinetochores. However, due to

the difficulty of associating component identity with specific structures, only limited success has been achieved in resolving particular kinetochore proteins within electron micrographs [58–60].

Because of the mechanical role of kinetochores in spindle-chromosome attachment, optical tweezers have proven useful for probing the nature of these attachments [47, 54, 61–64]. Similar to optical tweezers experiments on motor proteins, purified kinetochores (or kinetochore subcomplexes) were immobilized on dielectric beads, and were allowed to bind on surface-anchored microtubules. Mechanical measurements alone have revealed many interesting properties of kinetochores. For example, kinetochore–microtubule tip attachments exhibit catch bond-like behavior, where the lifetime of the attachment increases with increasing tension, until an optimal tension is reached, where the lifetime is maximal [47]. Optical tweezers experiments have also shown that meiotic kinetochores attach microtubule tips more strongly than mitotic kinetochores, suggesting that sister kinetochores in meiosis are mechanically fused together [64]. In the same work, TIRF microscopy was used, in addition to and separately from tweezers experiments, to show that the meiotic kinetochores contained more copies of the components than the mitotic ones, giving rise to brighter particles under fluorescence imaging. Thus, optical tweezers and quantitative TIRF microscopy have both provided independent means to quantify the differences between meiotic and mitotic kinetochores.

The structural arrangement of core kinetochore components changes dynamically *in vivo* depending on the cell cycle stage or after treatment with microtubule poisons. Because the separation distance between certain inner and outer kinetochore components increases at metaphase, when the kinetochores are likely to be supporting relatively high levels of tension, these rearrangements have sometimes been referred to as “intra-kinetochore stretch” [35, 37, 57]. In principle, such attachment- or tension-dependent changes in core kinetochore structure could control the key signalling events at kinetochores, including the generation of checkpoint wait signals and the selective destabilization of erroneous attachments [65]. However, whether the observed structural changes are caused directly by attachment or tension remains unproven and whether they play any role in modulating kinetochore function is also unclear [66, 67]. Resolving these issues will require observing nanometer-scale deformations under controlled forces *in vitro*. Optical tweezers can generate forces to recapitulate physiological levels of spindle tension while the movement of various kinetochore components is measured using TIRF microscopy and centroid tracking in real time. DIC imaging is particularly useful in this experiment as well, because the 25 nm thick microtubules are visible under DIC, so that fluorescence imaging is not required during the initial preparative manipulations before recording.

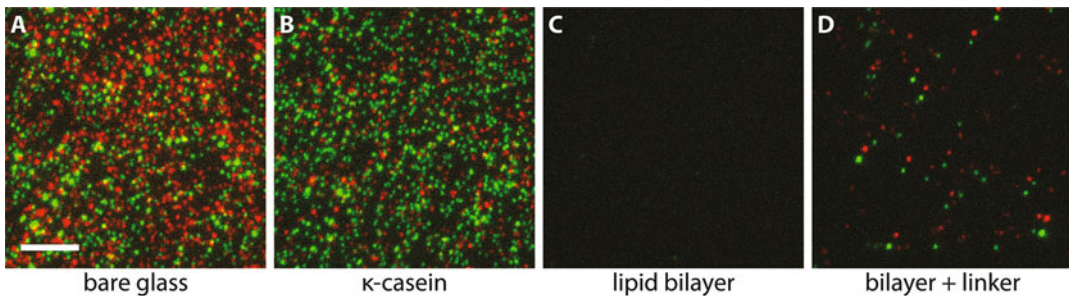


**Fig. 6** Lipid bilayer blocks nonspecific interactions while allowing kinetochores to be specifically anchored to the coverslip. **(a)** Kinetochores nonspecifically adsorbed on a clean glass surface at high density. Kinetochore components Mtw1 and Nuf2 that are fluorescently labeled are shown in red and green false colors, respectively. Image color channel registration is not corrected, so that the co-localized particles appear as *red-green doublets*. **(b)** The addition of 0.5 mg/ml  $\kappa$ -casein does not block nonspecific interaction to a workable level for single-molecule experiments. **(c)** A POPC lipid bilayer in coordination with 0.1 mg/ml  $\kappa$ -casein effectively blocks nonspecific adsorption of kinetochores onto the surface. **(d)** After specific linkers were provided to the same surface in **(c)**, kinetochores were able to anchor specifically via their His-tags. Scale bar, 5  $\mu$ m

Single molecule TIRF experiments typically require surface engineering to achieve specificity for the molecules of interest and to passivate against all other components in the assay. This is often achieved by introducing nonspecifically absorbed proteins (e.g., BSA or casein), or by chemical surface treatments that cover the glass surface. In less demanding situations, bovine serum albumin (BSA) or casein is sufficient to provide a layer of blocking protein to prevent nonspecific binding (*see Note 7*). When higher specificity is required, the glass surface can be silanized and polyethylene glycol (PEG) can be covalently attached at high density [68, 69]. In the third type of passivation strategy, a supported lipid bilayer self-assembles on the glass surface via vesicle fusion. Under this treatment, the ratio of specifically vs. nonspecifically immobilized molecules can be extremely high (Fig. 6). In these methods, a portion of the passivating molecules carry specific linkers, commonly biotin, so that molecules of interest can be immobilized via these linker molecules. Here, we use a lipid bilayer as our surface passivation. We find that supported lipid bilayers provide far superior blocking than simple protein passivation, and they are more reproducible in our hands than silanization followed by PEGylation.

A unique property of supported lipid bilayers is their fluidity. Unlike linkers on a silanized surface that are covalently attached to the glass substrate, lipid molecules are diffusive within the bilayer, and thus the linked molecules are mobile. This property allows novel experimental designs such as DNA curtains [70], which are dense arrays of DNA molecules each with one end attached to the lipid head groups. Here we introduce a novel method to utilize the fluid nature of the lipid bilayer to study kinetochore structure.

In our experimental setup, a kinetochore is dragged on the bilayer surface, thus remaining close to the surface and oriented in the direction of tension applied via an attached microtubule (Fig. 1). Under TIRF microscopy, the locations of multiple kinetochore components are tracked and the intra-kinetochore stretch is quantified (similarly to the “delta measurement”). To accommodate the finite movement range of our piezo-controlled specimen stage, each kinetochore is dragged in a circle instead of linearly. Following this routine, the intra-kinetochore stretch of an individual kinetochore is identified with better than 10 nm accuracy at a temporal resolution of seconds.

### 3.1.1 Kinetochore and Tubulin Purification

In brief, *Saccharomyces cerevisiae* (budding yeast) kinetochores are genetically tagged by 6 × His and 3 × Flag tags on the C-terminus of the kinetochore protein, Dsn1. In addition, SNAP and CLIP tags [71, 72] are fused onto selected kinetochore components. Yeast cells are grown, harvested, and lysed by either a blender or bead-beating or a freezer mill. Flag tags on Dsn1 are used to purify the kinetochores using anti-Flag antibody coated magnetic beads. During the purification procedure, the fluorescently labeled SNAP- and CLIP-tag ligands are added to label the kinetochores. The kinetochores are then eluted by Flag peptides and stored at –80 °C. Details of the purification procedure can be found in [47, 64].

Bovine tubulin can be obtained from commercial sources or purified from cow brains. We followed the protocol in [48] with minor modification to purify bovine tubulin. Calf brains were extracted, cleaned and homogenized at 4 °C so that microtubules were forced to depolymerized, followed by ultracentrifugation to clarify the lysate. Then microtubule polymerization was promoted by the addition of glycerol and GTP at 37 °C, and the filaments were then pelleted by ultracentrifugation. The resuspended microtubules were cold-treated again and ultracentrifuged. This cycle of polymerization–depolymerization was repeated one more time, and the harvested tubulin was aliquoted and stored at –80 °C.

### 3.1.2 Microbeads Functionalized with a Strong MT-binding Protein

Optically trapped beads are used to apply force to a microtubule that has one end attached to a kinetochore. The beads are functionalized with kinesin so that they bind to the microtubule lattice when brought to the vicinity of the microtubule by the optical tweezers. To conjugate kinesin to the bead surface, we purchased streptavidin-functionalized polystyrene beads (Spherotech SVP-05-10), which were further functionalized by biotinylated kinesin. The kinesin was constructed based on the N-terminal 401-amino-acid motor domain (K401) of *Drosophila* kinesin [49, 50], and the biotinylation is achieved by an enzymatic ligation [51]. A 15-amino-acid AviTag recognized by biotin ligase BirA and a Flag-tag used for immunopurification are both fused to the K401 gene and transformed into *E. coli* BL21 (DE3) competent cells

(New England BioLabs). A plasmid carrying the ligase gene, pBirA, was transformed into a different strain. Both strains were harvested separately, mixed and lysed with the addition of biotin so that the recombinant kinesin was biotinylated in vitro and purified to 100 mg/ml in BRB80. Note that the kinesin used in this chapter is purified via Flag-tag instead of the more common choice of His-tag because the kinetochores are immobilized on the surface via His-tags and surface bound anti-his antibody. Kinesin should not interact with the surface engineered this way. The following procedure describes how to make 100  $\mu$ l functionalized beads, enough for approximately ten tunnel slides.

1. Dilute 1 % w/v streptavidin coated polystyrene beads in 25 mM HEPES buffer to 0.1 %. Prepare at least 50  $\mu$ l and sonicate (across the tube wall) by placing the tube near a flat-tip sonicator or in a bath sonicator immersed in a cold-water bath for 2 min at medium power setting. This step breaks most of the bead clumps into individual beads.
2. Take 2  $\mu$ l of the sonicated beads, mix with 2  $\mu$ l 100  $\mu$ g/ml biotinylated kinesin. Place on rotor at 4 °C for 1 h.
3. Add 86  $\mu$ l assay buffer with 10  $\mu$ M taxol to the 4  $\mu$ l bead-kinesin mix. Prior to use, briefly sonicate the diluted mixture for 5–10 s at medium to low power setting to break bead clumps. The diluted mixture can be kept on ice and remain active for a day. Sonicate when significant clumping occurs.
4. Dilute scavenger mix and glucose fivefold in assay buffer separately. Take 8.8  $\mu$ l diluted bead mix, add 0.2  $\mu$ l 5 mg/ml *k*-casein, 0.5  $\mu$ l diluted glucose solution and 0.5  $\mu$ l diluted scavenger mix. Avoid mixing scavenger and glucose much earlier before the slide is ready.

### 3.1.3 Microtubules

In live cells, kinetochores attach to dynamic spindle microtubules during mitosis and meiosis. In this in vitro experiment, microtubules are polymerized and stabilized by taxol before introduction into the flow chamber, where kinetochores have previously been anchored to the surface. Fluorescent tubulin is helpful to visualize attachment between a kinetochore and a microtubule, in addition to the DIC images.

1. Mix thawed 6.4  $\mu$ l 1 mg/ml tubulin with 24.4  $\mu$ l microtubule polymerization buffer. If fluorescence image is needed, mix 2 % fluorescently labeled tubulin.
2. Incubate at 37 °C for 45 min.
3. Add 200  $\mu$ l warm BRB80 with 10  $\mu$ M taxol.
4. Spin the grown microtubule at 37 °C at 100,000  $\times g$  for 10 min in an ultracentrifuge.
5. Discard the supernatant, and resuspend the pelleted microtubule in BRB80 with 10  $\mu$ M taxol by vigorous pipetting.

### 3.1.4 Small Unilamellar Vesicles (SUVs) for Lipid-Based Surface Passivation

Phospholipid small unilamellar vesicles (SUVs) can spontaneously form supported bilayers on clean glass substrates by vesicle fusion onto the surface. A supported bilayer very effectively blocks soluble proteins and small molecules from adhering to the surface. A small fraction of the phospholipid can carry biotinylated head groups, so that molecules of interest can be specifically anchored to the surface via biotin–streptavidin interactions at controlled density. To prepare lipid SUVs, a lipid mixture dissolved in chloroform is thoroughly dried to form a lipid cake, followed by rehydration in lipid buffer. The suspension is sonicated with a micro-tip that is immersed directly into 300  $\mu$ l of fluid to form SUVs. The following procedure describes how to make 300  $\mu$ l lipid SUVs, enough for approximately 30 tunnel slides.

1. Add 12  $\mu$ l 25 mg/ml POPC and 4  $\mu$ l 0.1 mg/ml biotin-cap-PE to 84  $\mu$ l chloroform in a glass test tube. The volume of the chloroform does not need to be exact. Mix well by brief vortexing. The mixture contains 0.1 % biotinylated lipid. Never use plastic pipettes or syringes to transfer chloroform. Wash syringes ten times with clean chloroform before and after each use.
2. Dry the lipid mixture in chloroform by blowing nitrogen over the mixture for 5–10 min. Rotate the test tube while drying the mixture until the lipid forms a thin semi-transparent film at the bottom of the tube.
3. Further dry the lipid cake in a vacuum desiccator without desiccant overnight (*see Note 8*). POPC lipid cake can be stored in a desiccator for weeks before passivation ability is compromised.
4. After the lipid cake is thoroughly dried, take the tube out of the desiccator. Add 300  $\mu$ l lipid buffer, and rehydrate by rigorous vortexing. The lipid suspension should turn cloudy white.
5. Transfer the rehydrated lipid to a 1.5 ml tube, and mount the tube in a container filled with cooling water. Place the tube under the sonication tip so that the tip is immersed but not touching the tube wall.
6. Sonicate the lipid suspension for 5 min at 50 % duty cycle and a low power setting, depending on the specific sonifier. The duty cycle setting prevents constant formation of cavitation bubbles, and helps heat dissipation. The lipid suspension should turn clear after sonication, which suggests that the vesicle size is well below the wavelength of visible light.
7. Keep the SUVs on ice and they are ready to use. SUVs can be stored at 4 °C for days. A 5-min sonication is recommended before use each day.

### 3.1.5 Disposable Channel-Slides

The channel slides used in this experiment are the common slides made of coverslips and double-sided tape as spacers. In order for the lipid SUVs to fuse on the surface, the coverslip needs to be

cleaned thoroughly. A bench top plasma cleaner is a quick and convenient tool to provide sufficiently clean glass without additional washing.

1. Clean coverslip and glass slides on glass rack in plasma cleaner for 3 min.
2. Lay rows of double-sided tape perpendicular to the long edge of the cleaned glass slide with approximately 3 mm separation. Place the coverslip on top and briefly press. The volume of the tunnel at this width is approximately 5  $\mu$ l.
3. Bake the tunnel slide on 60 °C hot plate or oven for 5 min. Press to form tight seal between glass and coverslip. The baking step greatly reduces the chance that the coverslip lifts during the following steps.
4. If multiple tunnels are prepared on one slide, carefully brush a drop of nail polish between tunnels to prevent overflowing to adjacent tunnels in the following steps. Put the slide away until nail polish dries.

### *3.1.6 Preparing Slides for the Single Kinetochore Imaging and Manipulation Assay*

In this step, the SUVs, linker molecules, kinetochores, microtubules and beads prepared above are flowed into the tunnel slide in turn to establish the designed experimental configuration illustrated in Fig. 1. The preparation steps are summarized in Fig. 7.

1. Feed 5  $\mu$ l of lipid buffer into the tunnel slide.
2. Feed 10  $\mu$ l SUVs into the tunnel slide with vacuum suction on the other opening of the tunnel. Incubate at room temperature for 5 min.
3. Wash the chamber with 35  $\mu$ l lipid buffer. 5–10 times the volume of the chamber is sufficient to wash away the majority of the solution in the chamber.
4. Feed 10  $\mu$ l 0.1 mg/ml avidin DN (*see Note 9*) into the tunnel slide. Incubate for 5 min.
5. Wash with 35  $\mu$ l lipid buffer.
6. Feed 10  $\mu$ l 20 nM anti-his antibody into the tunnel slide. Incubate for 10 min.
7. Wash with 35  $\mu$ l lipid buffer.
8. Flow in tagged kinetochores in assay buffer at proper concentration. Incubate for 10 min. We found that 0.3 nM of kinetochore provides a good density of kinetochores on the surface. Incubate for 5 min.
9. Wash with 35  $\mu$ l assay buffer.
10. Flow in taxol-stabilized microtubules in assay buffer with 10  $\mu$ M taxol and 0.1 mg/ml *k*-casein. Incubate for 5 min. To obtain ideal microtubule lengths, microtubules can be briefly vortexed for 5 s.

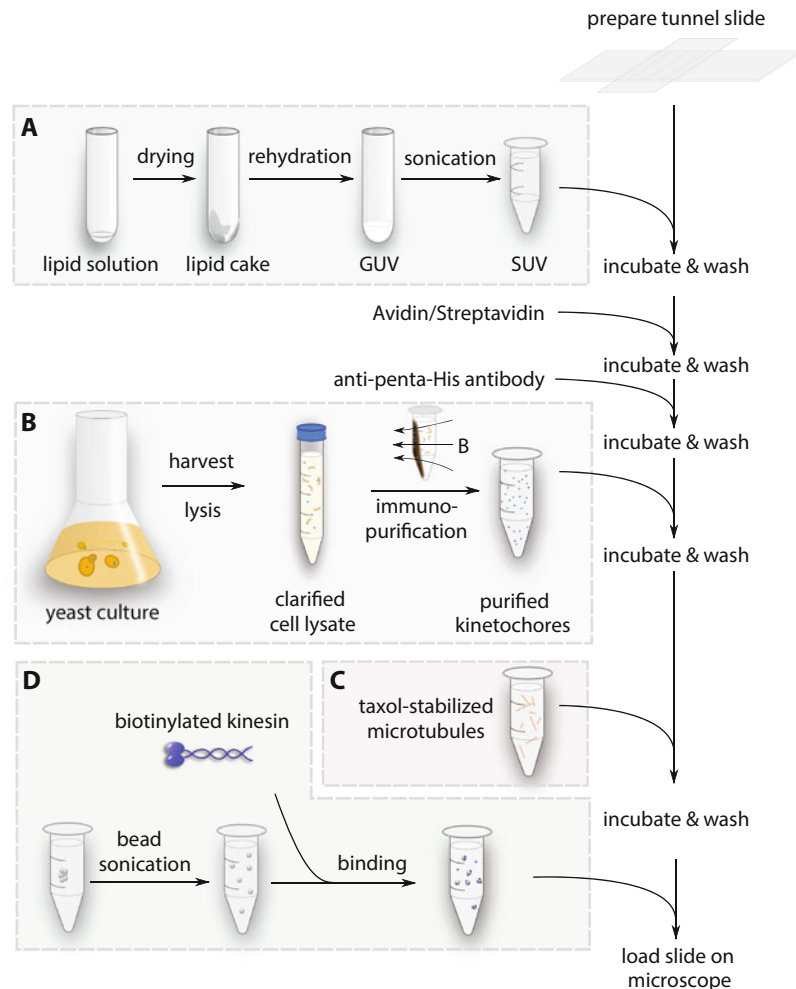


**Fig. 7** Procedure for sample slide preparation. The boxes summarize four separate procedures that prepare intermediate reagents used sequentially during slide preparation. (a) The lipid solution is dried, rehydrated, and sonicated into SUVs that will create a supported bilayer on a glass substrate. (b) Yeast cells are grown, harvested, and lysed. Kinetochore particles are labeled and immunopurified from the cell lysate. (c) Microtubules are grown from purified tubulin, and stored in buffer with taxol. (d) Streptavidin coated polystyrene beads are briefly sonicated, and incubated with purified biotinylated kinesin. The functionalized beads are diluted in assay buffer. After the tunnel slides are prepared, lipid SUVs, avidin, anti-penta-His antibody, kinetochores, microtubules, and beads are flowed in sequentially with washes and incubations between each step

- Without washing away the excess microtubules, very slowly feed in the kinesin-functionalized beads prepared in Subheading 3.1.2. The flow speed should be slow because end-on attached microtubules can be washed away by the shear force. Seal the ends of the chamber with nail polish and mount on the microscope for tweezers manipulation and TIRF imaging.

### 3.1.7 Performing the Single Kinetochore Imaging and Manipulation Assay

Following the procedure described in the previous sections, kinetochores are anchored on the lipid bilayer via specific linkages. Microtubules are then flowed in and allowed to bind to the lipid-anchored kinetochores. The kinesin-functionalized beads are slowly introduced. The slide is mounted on the microscope. The slide is searched to find an end-on attached microtubule on a kinetochore that has fluorescent tags on both Mtw1 and Dam1 in two different color channels. Then the optical trap is switched on to trap a kinesin-functionalized bead nearby. The bead is brought close to the free end of the microtubule until a kinesin-microtubule attachment is established. During the bead manipulation, the fluorescence excitation is turned off and DIC is used to provide visual guidance. Because the transition temperature of the lipid mixture is below room temperature, the kinetochores anchored to the lipid heads remain diffusive on the surface. After the attachments on both ends of the microtubule are established, a customized Lab-VIEW program moves the piezo stage in a circle with radius larger than the distance between the kinetochore and the bead. The movement speed is set between 0.1 and 0.5  $\mu\text{m}/\text{s}$ , which allows several revolutions of motion before photobleaching. Fluorescence images of the kinetochore components are recorded as it moves over the lipid surface. Because the lipid molecules to which the kinetochore is anchored are dragged through the bilayer, a tensile drag force is transmitted to the kinetochore.

In the laboratory frame of reference, the trapped bead remains nearly stationary, and the lipid surface moves in a circle driven by the piezo stage. The force balance and geometric relations are simpler to understand in the frame attached to the slide, in which the bead moves along a circle, and the kinetochore is dragged behind by the microtubule along a smaller circle (Fig. 8a). The bead velocity  $v'_{\text{bead}}$  is along the tangential direction of the bead trajectory, but has an angle  $\alpha$  with respect to the microtubule. The velocity component parallel to the microtubule  $v'_{||}$  is equal to the kinetochore velocity  $v'_{\text{KT}}$ , because the microtubule length  $l$  does not change.  $l$  and the radii of the two circular trajectories  $R$  and  $r$  form the three sides of a right triangle, with  $R^2 = l^2 + r^2$ . The circular movement of the kinetochore has a phase lag  $\alpha$ , behind the bead movement, that is determined by  $\sin(\alpha) = l/R$ . In the lab frame, the bead remains trapped, and all velocities in the slide frame are transformed by subtracting the instantaneous velocity of the bead in the slide frame  $v'_{\text{bead}} = -v_{\text{stage}}$  (Fig. 8b). The kinetochore velocity  $v_{\text{KT}}$  equals the tangential component of the stage velocity  $v_{\text{stage}}$ , whereas the normal component of  $v_{\text{stage}}$  creates an outward drag along the microtubule. Note that in the lab frame, the kinetochore moves with a phase lead  $\pi/2 - \alpha$ , ahead of the stage movement. Figure 9a shows a snapshot of the bead, kinetochore and microtubule positions, overlaid by the trajectory of the kinetochore and the stage.

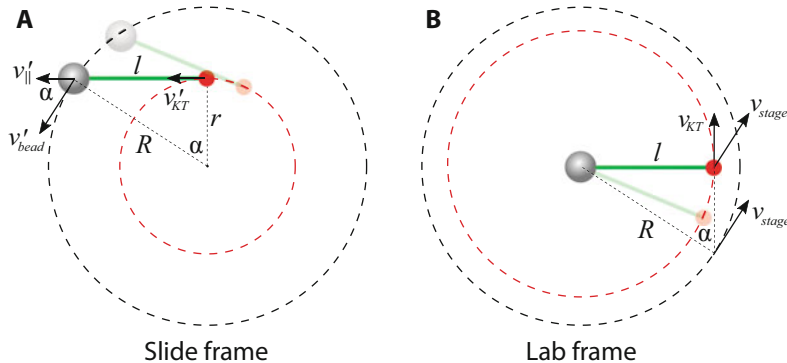


**Fig. 8** Velocity diagrams of the trapped bead (gray sphere) and the dragged kinetochore (red dot) in the slide frame and the laboratory frame. **(a)** In the slide frame where the slide remains stationary, both the bead and the kinetochore move in circles with different radii  $R$  and  $r$ . The parallel component of the bead velocity  $v_{||}'$  is identical to the kinetochore velocity  $v_{KT}$ . **(b)** In the lab frame, the bead is trapped and stationary. The stage moves in a circle of radius  $R$  and drives the kinetochore with it. The tangential component of the instantaneous stage velocity  $v_{stage}$  is equal to the kinetochore velocity  $v_{KT}$ , i.e.,  $|v_{KT}| = |v_{stage}| \cos(\pi/2 - \alpha)$ . The microtubule is depicted as a *thick green line*, and the bead-microtubule-kinetochore shown semi-transparently represents the configuration at an earlier time point

The centroids of the labeled kinetochore components are obtained from the time-lapse movies of both the Mtw1 and Dam1 channels. The coordinates are corrected according to the registration transformation. Figure 9b shows the kinetochore coordinates as functions of time. Because the kinetochores move along a circle, the coordinates are simple sinusoidal functions. The positions of Dam1 relative to Mtw1, which we chose as a fiducial marker, are calculated from the corrected coordinates, and plotted in Fig. 9c. The relative distance between Dam1 and Mtw1 also appears sinusoidal, and the phase follows the movement of the kinetochore shown in Fig. 9b. In rotating polar coordinates centered at the location of Mtw1 and following the direction of the microtubule, the radial and tangential coordinates of Dam1 are shown in Fig. 9d, with average values of  $44 \pm 33$  nm and  $-7.5 \pm 33$  nm (mean  $\pm$  SD), respectively. If smoothed by a 1 s moving window-average (as indicated by the solid lines), the standard deviation of the estimated mean location of the smoothed trace is 11 nm. Overall, the averaged separation in 45 s of data is  $44.6 \pm 1.8$  nm. Force was measured by the bead displacement in the trap. Intra-kinetochore tension generated by the viscous lipid is  $0.076 \pm 0.003$  pN along the radial direction and  $0.008 \pm 0.003$  pN along the tangential direction (Fig. 9e). Note that at the typical speed of the bead moving in buffer, the viscous drag on the bead is below 10 fN (assuming a sphere of  $0.5 \mu\text{m}$  diameter moving at  $1 \mu\text{m}/\text{s}$  in water). Thus the major contribution to the tension measured by the optical trap is viscous drag associated with moving the kinetochore-lipid anchor through the bilayer. Figure 9f

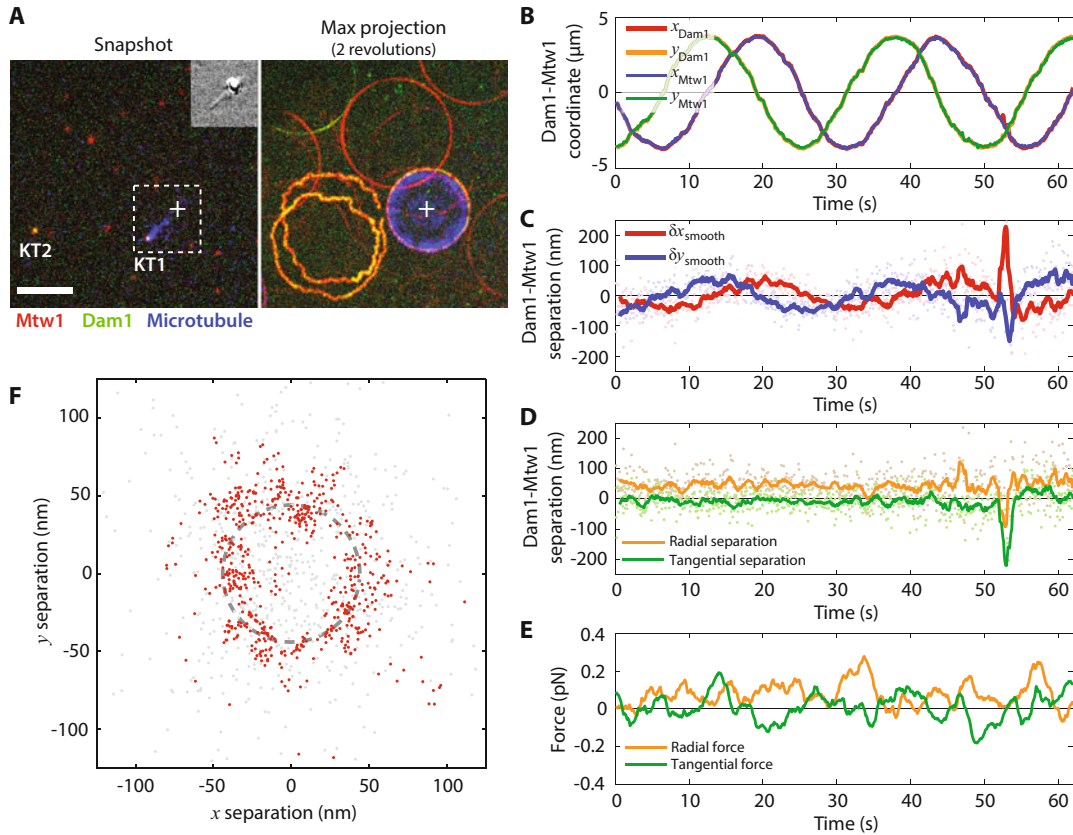


**Fig. 9** Intra-kinetochore stretch measured by tracking the centroids of kinetochore components as the kinetochore is dragged on the lipid bilayer. **(a)** One frame of the three-color fluorescence movie (left). Kinetochore components Mtw1, Dam1, and microtubules are pseudo-colored red, green, and blue, respectively. The cross marks the position of the trapped bead. *Inset* shows the simultaneous DIC image. The maximum projection of two revolutions is shown on the right. KT1 and KT2 mark a dragged kinetochore and a non-dragged kinetochore, respectively. Note that the circular path of the dragged kinetochore is smaller than the circular path followed by the piezo, as indicated in Fig. 8. Scale bar, 5  $\mu\text{m}$ . **(b)** The Cartesian coordinates of kinetochore 1 (KT1) Mtw1 and Dam1 indicate circular trajectories. **(c)** The position of Dam1 relative to Mtw1 also varies sinusoidally, in-phase with the orientation of the microtubule. **(d)** The parallel (radial) and perpendicular (tangential) components indicate that Dam1 and Mtw1 are separated by  $44 \pm 33$  nm (mean  $\pm$  standard deviation). **(e)** The parallel (radial) and perpendicular (tangential) components of the microtubule tension measured by the trapped bead. **(f)** The positions of Dam1 relative to Mtw1 follow a circle of radius  $44 \pm 33$  nm. Gray points show raw positions and red points show the same data after smoothing with a 1-s window average. Dashed line marks a circle of 44 nm radius

indicates the time projection of the position of Dam1 relative to Mtw1. Raw data (gray points), moving-window smoothed data (red points), and a circle of 44 nm radius are plotted together for comparison.

As a control, the position of Dam1 relative to Mtw1 on an unattached kinetochore is shown in Fig. 10. Because this kinetochore is not oriented to any particular direction, the separation is

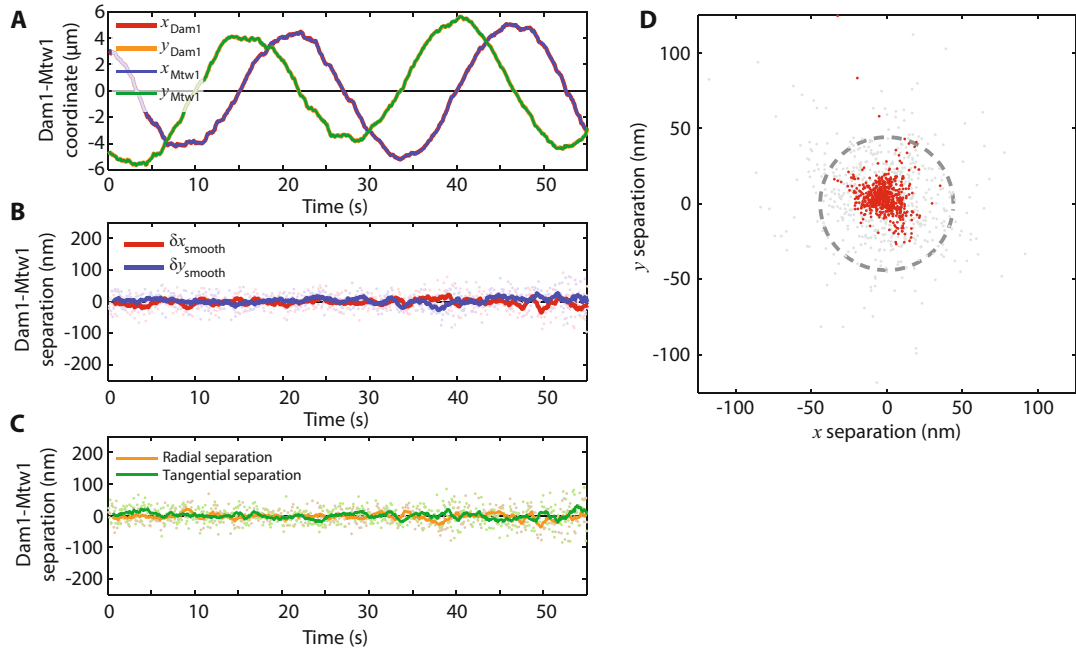


**Fig. 10** Unstretched kinetochores showed no separation between components. **(a)** The Cartesian coordinates of Mtw1 and Dam1 of kinetochore 2 (KT2 in Fig. 9a). **(b, c)** The positions of Dam1 relative to Mtw1 in Cartesian (**b**) and polar (**c**) coordinates. **(d)** The positions of Dam1 relative to Mtw1 form a cluster. *Gray points* show raw positions and *red points* show the same data after smoothing with a 1-s window average. *Dashed line* marks a circle of 44 nm radius, as in Fig. 9f

small and unbiased towards any direction. This negative control also proves that the position registration is accurate. The radial and tangential components of separation are  $-1.6 \pm 1.1$  nm and  $-0.4 \pm 1.1$  nm (mean  $\pm$  SD of the mean).

In summary, we demonstrate the construction and application of a combined instrument of optical tweezers with TIRF and DIC microscopy. With this instrument, the distance between two protein components within a single kinetochore particle can be measured with 10 nm precision over 1 s of observation time, or with better than 2 nm precision over 50 s, internally controlled and bias-free. Fluorescence microscopy allowed us to observe the brightness and location of specifically tagged components, while the protein complex was simultaneously manipulated by optical tweezers at controllable and known force. DIC microscopy was used to avoid photobleaching when fluorescence images were not recorded, providing visual guidance to establish the correct experimental configuration and to monitor the progress of the dragging experiment.

The surface treatment selectively immobilized our protein complex of interest, while blocking all other components of the experiment such as microtubules, beads, and incomplete

kinetochore assemblies. We adopted supported lipid bilayers as the surface passivation treatment, a less common method than silanization followed by PEGylation. Compared to PEGylation, we find that a lipid bilayer is considerably easier to prepare, and in our hands it provides a more reliable and cost-effective passivation. It also offers flexibility through the incorporation of different functionalized lipids. In the demonstration of this chapter, we utilized the fluidity property of the bilayer to mitigate possible errors due to color channel mis-registration. In principle, the viscosity of the lipid could be tuned by introducing various species of lipids to generate different forces. Alternatively, a lipid with transition temperature above room temperature could be used to create a gel-phase bilayer to more firmly immobilize the anchored molecules.

We have also introduced an addition to the combined instrument that incorporates focus detection into the existing setup. The addition shares the detection beam with the trapping laser, but converts it to a total-internal reflection configuration with a few extra, simple optical components. Axial position is converted to translational beam position, collected by a position-sensitive photodetector, and digitized. This position signal can be used to compensate focal drift during long-term imaging, or to execute a programmed axial scan for optical sectioning. Because a laser source, a data acquisition device, and a nano-positioning stage are usually standard components of an optical tweezers setup, the addition of focus detection is inexpensive and easy to implement.

The experimental platform we describe above is suitable for studying nanometer-scale structural changes in filament-binding complexes under tension. Our instrument was constructed with the goal of studying kinetochores, but we envision that it could also be useful for studying other cytoskeletal junctions as well. Kinetochores undergo conformational changes that are suspected to play important roles in spindle-assembly checkpoint signaling. It is not yet clear whether the changes in intra-kinetochore distance observed *in vivo* are caused by changes in kinetochore tension, by changes in kinetochore–microtubule attachment status, or by more complex signaling events [73]. Our single kinetochore imaging and manipulation assay represents a new, direct way of testing whether tension alone can induce structural changes in kinetochores, and whether the spindle assembly checkpoint system responds to such changes. The approach might also be generally useful for studying other protein complexes that associate with cytoskeletal filaments, such as the centrosomes and yeast spindle pole bodies that anchor spindle microtubules, the desmosomes that provide cell-to-cell adhesions, the LINC complexes that connect cytoskeletal to nucleoskeletal filaments, or the focal adhesion complexes that underlie cellular mechanosensation.

---

**4 Notes**

1. Strictly speaking, the distribution for the random relative position is the convolution of two uniform distributions with a boundary of the size of the FOV. In practice, it is approximated well by a two-dimensional normal distribution with a covariance matrix equal to the identity matrix multiplied by a constant proportional to the square of the FOV size.
2. Expectation–maximization is a powerful machine learning algorithm that performs clustering in this case. The association of each pair of spots with the two clusters is unknown, and the shape and location of the clusters are also unknown. In the expectation–maximization algorithm, initial guesses of the cluster shape and location are given, followed by the clustering of pairs according to these guesses. The cluster shape and location are then updated using the clustering results. This process iterates until convergence is achieved.
3. Ideally, a Faraday optical isolator should be installed first to prevent back reflection from the surfaces.
4. In our setup, L9 is conjugated with the back-focal plane of the objective lens. But the back aperture is very close to the back-focal plane (in fact, the focal point is inside the objective lens), and the back aperture is slightly overfilled. The difference in beam profiles between the back aperture and the back-focal point is insignificant.
5. We used the K401 construct of drosophila kinesin, which will exhibit motility in the presence of ATP or GTP. This is not a concern in the demonstration, but one can implement the rigor mutation on kinesin when ATP or GTP will be present.
6. Microtubules are grown in PIPES based BRB80 buffer. The final dragging assay is performed in a different buffer based on HEPES. We found that PIPES buffer greatly reduced the interaction between the microtubules and kinetochores, as well as the kinetochore-associated motor protein, Cin8. The exact mechanism of this inhibition has not been further investigated. Microtubules cannot be stored stably in HEPES-based buffer over the time scale of hours, even in the presence of taxol. Therefore, prior to each experiment, microtubules were either freshly grown or stored in BRB80 with taxol (where they can remain stably assembled), pelleted and resuspended in the assay buffer.
7. The role of casein in surface treatment is largely unclear. While casein is widely used as a passivation protein, whole casein is also frequently used in kinesin–microtubule gliding assays, and different casein components provide variable support. In our

study, we found that *k*-casein, a component of whole casein, provided the best passivation result. However, the presence of *k*-casein severely impaired or even completely abolished the kinesin–microtubule interaction. While it is tempting to supplement the final assay buffer with a high amount of casein to prevent bead clumping, the bead-microtubule attachment tolerates the presence of only a small amount of *k*-casein.

8. The vacuum pump used for the plasma cleaner can also be used for drying lipid cake.
9. We find that streptavidin and avidin DN work indistinguishably. However, neutral avidin has a nonspecific interaction with microtubules and should therefore be avoided.

## References

1. Neuman KC, Nagy A (2008) Single-molecule force spectroscopy: optical tweezers, magnetic tweezers and atomic force microscopy. *Nat Methods* 5:491–505
2. Moffitt JR, Chemla YR, Smith SB et al (2008) Recent advances in optical tweezers. *Annu Rev Biochem* 77:205–228
3. Kapanidis AN, Strick T (2009) Biology, one molecule at a time. *Trends Biochem Sci* 34:234–243
4. Lang MJ, Asbury CL, Shaevitz JW et al (2002) An automated two-dimensional optical force clamp for single molecule studies. *Biophys J* 83:491–501
5. Blehm BH, Selvin PR (2014) Single-molecule fluorescence and *in vivo* optical traps: how multiple dyneins and kinesins interact. *Chem Rev* 114:3335–3352
6. Korten T, Nitzsche B, Gell C et al (2011) Fluorescence imaging of single kinesin motors on immobilized microtubules. *Methods Mol Biol* 783:121–137
7. Nicholas MP, Rao L, Gennrich A (2014) An improved optical tweezers assay for measuring the force generation of single kinesin molecules. *Methods Mol Biol* 1136:171–246
8. Gennrich A, Reck-Peterson SL (2011) Probing the force generation and stepping behavior of cytoplasmic dynein. *Methods Mol Biol* 783:63–80
9. Vanzi F, Capitanio M, Sacconi L et al (2006) New techniques in linear and non-linear laser optics in muscle research. *J Muscle Res Cell Motil* 27:469–479
10. Ketelaar T, van der Honing HS, Emons AM (2010) Probing cytoplasmic organization and the actin cytoskeleton of plant cells with optical tweezers. *Biochem Soc Trans* 38:823–828
11. Sommese RF, Sung J, Nag S et al (2013) Molecular consequences of the R453C hypertrophic cardiomyopathy mutation on human  $\beta$ -cardiac myosin motor function. *Proc Natl Acad Sci U S A* 110:12607–12612
12. Mehta AD, Rief M, Spudich JA et al (1999) Single-molecule biomechanics with optical methods. *Science* 283:1689–1695
13. Abbondanzieri EA, Greenleaf WJ, Shaevitz JW et al (2005) Direct observation of base-pair stepping by RNA polymerase. *Nature* 438:460–465
14. Herbert KM, Greenleaf WJ, Block SM (2008) Single-molecule studies of RNA polymerase: motoring along. *Annu Rev Biochem* 77:149–176
15. Perkins TT (2014) Ångström-precision optical traps and applications. *Annu Rev Biophys* 43:279–302
16. Heller I, Hoekstra TP, King GA et al (2014) Optical tweezers analysis of DNA–protein complexes. *Chem Rev* 114:3087–3119
17. Padawer J (1968) The Nomarski interference-contrast microscope: an experimental basis for image interpretation. *J R Microsc Soc* 88:305–349
18. Allen RD, Allen NS, Travis JL (1981) Video-enhanced contrast, differential interference contrast (AVEC-DIC) microscopy: a new method capable of analyzing microtubule-related motility in the reticulopodial network of *Allogromia laticollaris*. *Cell Motil* 1:291–302
19. Walker RA, O’Brien ET, Pryer NK et al (1988) Dynamic instability of individual microtubules analyzed by video light microscopy: rate constants and transition frequencies. *J Cell Biol* 107:1437–1448

20. Elting MW, Spudich JA (2012) Future challenges in single-molecule fluorescence and laser trap approaches to studies of molecular motors. *Dev Cell* 23:1084–1091
21. Joo C, Balci H, Ishitsuka Y et al (2008) Advances in single-molecule fluorescence methods for molecular biology. *Annu Rev Biochem* 77:51–76
22. Swoboda M, Grieb MS, Hahn S et al (2014) Measuring two at the same time: combining magnetic tweezers with single-molecule FRET. *EXS* 105:253–276
23. Savinov A, Perez CF, Block SM (2014) Single-molecule studies of riboswitch folding. *Biochim Biophys Acta* 1839:1030–1045
24. Hohng S, Lee S, Lee J et al (2014) Maximizing information content of single-molecule FRET experiments: multi-color FRET and FRET combined with force or torque. *Chem Soc Rev* 43:1007–1013
25. Salmon E, Tran P (1998) High-resolution video-enhanced differential interference contrast (VE-DIC) light microscopy. *Methods Cell Biol* 56:153–185
26. Grishchuk EL, Molodtsov MI, Ataullakhanov FI et al (2005) Force production by disassembling microtubules. *Nature* 438:384–388
27. Driver JW, Powers AF, Sarangapani KK et al (2014) Measuring kinetochore-microtubule interaction in vitro. *Methods Enzymol* 540:321–337
28. Yamagishi Y, Sakuno T, Goto Y et al (2014) Kinetochore composition and its function: lessons from yeasts. *FEMS Microbiol Rev* 38:185–200
29. Cheerambathur DK, Desai A (2014) Linked formation and regulation of microtubule attachments during chromosome segregation. *Curr Opin Cell Biol* 26:113–122
30. London N, Biggins S (2014) Signalling dynamics in the spindle checkpoint response. *Nat Rev Mol Cell Biol* 15:736–748
31. Gorbsky GJ (2015) The spindle checkpoint and chromosome segregation in meiosis. *FEBS J* 282:2471–2487
32. Nicklas RB (1997) How cells get the right chromosomes. *Science* 275:632–637
33. Pinsky BA, Biggins S (2005) The spindle checkpoint: tension versus attachment. *Trends Cell Biol* 15:486–493
34. Joglekar AP, Bloom KS, Salmon E (2010) Mechanisms of force generation by end-on kinetochore-microtubule attachments. *Curr Opin Cell Biol* 22:57–67
35. Wan X, O’Quinn RP, Pierce HL et al (2009) Protein architecture of the human kinetochore microtubule attachment site. *Cell* 137:672–684
36. Joglekar AP, Bloom K, Salmon ED (2009) In vivo protein architecture of the eukaryotic kinetochore with nanometer scale accuracy. *Curr Biol* 19:694–699
37. Maresca TJ, Salmon ED (2009) Intrakineto-chore stretch is associated with changes in kinetochore phosphorylation and spindle assembly checkpoint activity. *J Cell Biol* 184:373–381
38. Dumont S, Salmon ED, Mitchison TJ (2012) Deformations within moving kinetochores reveal different sites of active and passive force generation. *Science* 337:355–358
39. Neuman KC, Block SM (2004) Optical trapping. *Rev Sci Instrum* 75:2787–2809
40. Rohrbach A (2005) Stiffness of optical traps: quantitative agreement between experiment and electromagnetic theory. *Phys Rev Lett* 95:168102
41. Dempsey GT, Wang W, Zhuang X (2009) Fluorescence imaging at sub-diffraction-limit resolution with stochastic optical reconstruction microscopy. In: *Handbook of single-molecule biophysics*. Springer, New York, NY, pp 95–127
42. Churchman LS, Okten Z, Rock RS et al (2005) Single molecule high-resolution colocalization of Cy3 and Cy5 attached to macromolecules measures intramolecular distances through time. *Proc Natl Acad Sci U S A* 102:1419–1423
43. Pertisnidis A, Zhang Y, Chu S (2010) Subnanometre single-molecule localization, registration and distance measurements. *Nature* 466:647–651
44. Berg-Sørensen K, Flyvbjerg H (2004) Power spectrum analysis for optical tweezers. *Rev Sci Instrum* 75:594–612
45. Shaevitz JW (2006) A practical guide to optical trapping. [http://genomics.princeton.edu/shaevitzlab/OT\\_Practice\\_Guide.pdf](http://genomics.princeton.edu/shaevitzlab/OT_Practice_Guide.pdf). Accessed 11 January 2016
46. Tolić-Nørrelykke SF, Schäffer E, Howard J et al (2006) Calibration of optical tweezers with positional detection in the back focal plane. *Rev Sci Instrum* 77:103101
47. Akiyoshi B, Sarangapani KK, Powers AF et al (2010) Tension directly stabilizes reconstituted kinetochore-microtubule attachments. *Nature* 468:576–579
48. Castoldi M, Popov AV (2003) Purification of brain tubulin through two cycles of polymerization–depolymerization in a high-molarity buffer. *Protein Expr Purif* 32:83–88

49. Gilbert SP, Johnson KA (1993) Expression, purification, and characterization of the *Drosophila* kinesin motor domain produced in *Escherichia coli*. *Biochemistry (Mosc)* 32:4677–4684
50. Young EC, Berliner E, Mahtani HK et al (1995) Subunit interactions in dimeric kinesin heavy chain derivatives that lack the kinesin rod. *J Biol Chem* 270:3926–3931
51. de Boer E, Rodriguez P, Bonte E et al (2003) Efficient biotinylation and single-step purification of tagged transcription factors in mammalian cells and transgenic mice. *Proc Natl Acad Sci U S A* 100:7480–7485
52. Cheeseman IM, Drubin DG, Barnes G (2002) Simple centromere, complex kinetochore: linking spindle microtubules and centromeric DNA in budding yeast. *J Cell Biol* 157:199–203
53. Cheeseman IM (2014) The kinetochore. *Cold Spring Harb Perspect Biol* 6:a015826
54. Franck AD, Powers AF, Gestaut DR et al (2007) Tension applied through the Dam1 complex promotes microtubule elongation providing a direct mechanism for length control in mitosis. *Nat Cell Biol* 9:832–837
55. Joglekar AP, Salmon ED, Bloom KS (2008) Counting kinetochore protein numbers in budding yeast using genetically encoded fluorescent proteins. *Methods Cell Biol* 85:127–151
56. Aravamudhan P, Felzer-Kim I, Gurunathan K et al (2014) Assembling the protein architecture of the budding yeast kinetochore-microtubule attachment using FRET. *Curr Biol* 24:1437–1446
57. Suzuki A, Badger BL, Wan X et al (2014) The architecture of CCAN proteins creates a structural integrity to resist spindle forces and achieve proper intrakinetochore stretch. *Dev Cell* 30:717–730
58. Brinkley B, Stubblefield E (1966) The fine structure of the kinetochore of a mammalian cell in vitro. *Chromosoma* 19:28–43
59. DeLuca JG, Dong Y, Hergert P et al (2005) Hec1 and Nuf2 are core components of the kinetochore outer plate essential for organizing microtubule attachment sites. *Mol Biol Cell* 16:519–531
60. Gonen S, Akiyoshi B, Iadanza MG et al (2012) The structure of purified kinetochores reveals multiple microtubule-attachment sites. *Nat Struct Mol Biol* 19:925–929
61. Asbury CL, Gestaut DR, Powers AF et al (2006) The Dam1 kinetochore complex harnesses microtubule dynamics to produce force and movement. *Proc Natl Acad Sci U S A* 103:9873–9878
62. Powers AF, Franck AD, Gestaut DR et al (2009) The Ndc80 kinetochore complex forms load-bearing attachments to dynamic microtubule tips via biased diffusion. *Cell* 136:865–875
63. Sarangapani KK, Akiyoshi B, Duggan NM et al (2013) Phosphoregulation promotes release of kinetochores from dynamic microtubules via multiple mechanisms. *Proc Natl Acad Sci U S A* 110:7282–7287
64. Sarangapani KK, Duro E, Deng Y et al (2014) Sister kinetochores are mechanically fused during meiosis I in yeast. *Science* 346:248–251
65. Musacchio A (2015) The molecular biology of spindle assembly checkpoint signaling dynamics. *Curr Biol* 25:R1002–R1018
66. Maresca TJ, Salmon E (2010) Welcome to a new kind of tension: translating kinetochore mechanics into a wait-anaphase signal. *J Cell Sci* 123:825–835
67. Wang Y, Jin F, Higgins R et al (2014) The current view for the silencing of the spindle assembly checkpoint. *Cell Cycle* 13:1694–1701
68. Sofia SJ, Premnath V, Merrill EW (1998) Poly (ethylene oxide) grafted to silicon surfaces: grafting density and protein adsorption. *Macromolecules* 31:5059–5070
69. Roy R, Hohng S, Ha T (2008) A practical guide to single-molecule FRET. *Nat Methods* 5:507–516
70. Collins BE, Ye LF, Duzdevich D et al (2013) DNA curtains: novel tools for imaging protein-nucleic acid interactions at the single-molecule level. *Methods Cell Biol* 123:217–234
71. Kepler A, Gendreizig S, Gronemeyer T et al (2003) A general method for the covalent labeling of fusion proteins with small molecules *in vivo*. *Nat Biotechnol* 21:86–89
72. Gautier A, Juillerat A, Heinis C et al (2008) An engineered protein tag for multiprotein labeling in living cells. *Chem Biol* 15:128–136
73. McEwen BF, Dong Y (2009) Releasing the spindle assembly checkpoint without tension. *J Cell Biol* 184:355–356

# Chapter 18

## Measurement of Force-Dependent Release Rates of Cytoskeletal Motors

Sinan Can and Ahmet Yildiz

### Abstract

Optical tweezers permit measuring motor–filament rupture forces with piconewton sensitivity. For deeper structural and mechanistic understanding of motors, different structural constraints can be induced by pulling motor proteins at various positions and manipulating the direction of the exerted force. Here, we present an optical-trapping approach to investigate the effect of the magnitude and direction of tension applied to the linker element of cytoskeletal motors on motor–filament interactions. Using this approach, force-dependent microtubule release rates of monomeric kinesins can be directly measured by pulling on kinesin’s “neck linker” with a constant force.

**Key words** Molecular motors, Kinesin, Interhead coordination, Gating, Rupture forces, DNA tether, Optical trapping

---

### 1 Introduction

Motor proteins play crucial roles in cargo transport, organelle positioning, and cell division by generating force and motility along cytoskeletal tracks [1–3]. A comprehensive understanding of these major cellular functions requires a detailed understanding of the molecular mechanisms of individual motors’ motility and force generation *in vitro*. Optical trapping studies have had a tremendous impact in the cytoskeletal motor field by determining the piconewton forces and nanometer-scale displacements that molecular motors generate along their associated filaments. Optical tweezers have the capability to apply calibrated forces to specific domains of a motor and put different geometrical constraints on a motor’s conformation for a deeper understanding of its mode of action.

One of the pressing questions in the motor field is how a dimeric motor can walk processively without dissociating from its track [4, 5]. Recent studies have shown that the mechanochemical cycles of the motor domains (heads) of kinesin-1 are highly

coordinated through 14-amino acid long “neck linkers” (NL) that interconnect the two heads [6–8]. The NL of the front and rear heads create the required asymmetry to coordinate the movement of the two heads in a two-head-bound state [9, 10]. In this state, the NL of the front head is pointed backward and the NL of the rear head is pointed toward the motor’s natural direction of motion (Fig. 1a). In addition, the NL has been proposed to function as a tension sensor for communication between the heads [11].

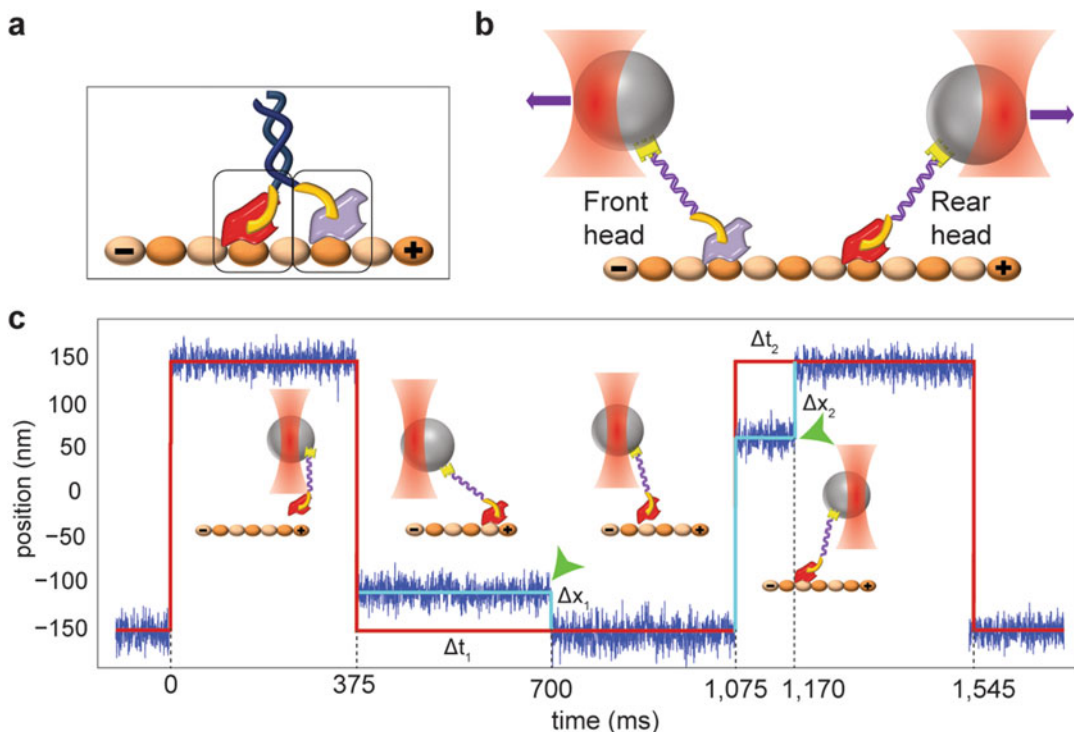


**Fig. 1** Force-dependent release of kinesin from MTs. (a) Kinesin dimer in a two-heads-bound state. The NL of the front head (*purple*) is oriented backward and that of the rear head (*red*) is oriented forward. (b) The NL (*yellow*) orientation of the front and rear heads can be mimicked by pulling a kinesin monomer on its NL via a short DNA tether using an optical trap (not to scale). (c) Example trace of a trapped bead (*blue*) oscillating  $\pm 150$  nm along the MT long axis. The trap position and step fitting are shown with *red* and *cyan* lines, respectively. When kinesin is not attached to the MT, the bead follows the trap. Kinesin binding to the MT restricts the movement of the bead. In this case, when the trap is moved to its next trap position at  $t = 0.375$  s, it exerts a constant force toward the MT minus end as a function of bead-trap separation ( $\Delta x_1$ ) on the motor until it releases from the MT ( $\Delta t_1$ ). At  $t = 0.700$  s (*green arrow*), kinesin releases from the MT and the bead resumes following the trap. Kinesin rebinds to the MT and the movement of the bead is restricted when the trap is moved to its next position at  $t = 1.075$  s. In this state, the trap exerts a constant force towards the MT plus-end as a function of bead-trap separation ( $\Delta x_2$ ) until the motor releases from the MT ( $\Delta t_2$ ). Kinesin releases from the MT at  $t = 1.170$  s (*green arrow*) and the bead resumes following the trap

To investigate the NL's role in the coordination of motor movement, it is essential to mimic the NL orientation of a head in front and rear positions of the dimer. Here we discuss an optical trapping approach that points NL in a particular direction and exert different amounts of force on NL of a single head [12, 13] (Fig. 1b). Kinesin monomers are attached to micron-sized polystyrene beads via a DNA handle connected to the C-terminal end of NL [14]. The beads are then moved  $\pm 150$  nm between two positions above the microtubule track in a square wave pattern (Fig. 1c). When a monomer binds to the MT, the bead is unable to follow the trap to the next position. In this state the trap exerts a constant force on the motor, the magnitude of which depends only on the bead-trap separation, until the motor releases from the MT. The assay directly measures the release rate of a head over a large range of forces (0.5–12 pN) exerted toward either the plus or minus end of the MT. MT residence times as short as 1 ms can be reliably detected.

Previously, several approaches have been developed to measure motor rupture forces. These assays apply linearly increasing forces to the motor and measure loading rate-dependent unbinding forces. These rupture force measurements can be transformed into force-dependent release rates by using theoretical models [15]. Our constant-load assay allows direct measurement of motor–filament unbinding rates as a function of force. Because a motor can, in principle, bind any available tubulin binding site when the bead is moved back and forth between the two user-defined positions, release rate of a motor can be measured for the entire force range in a single experiment without adjusting the parameters of the assay. This “constant load” assay also represents the situation in a walking dimeric motor where the heads are likely to experience a constant force before releasing from the MT.

Using our square wave unbinding experiment, we measured the force-dependent release rates of kinesin monomers from MTs under different nucleotide conditions and pulling geometries to decipher the underlying principles of how NL facilitates the motor's coordinated motility. We found that pulling NL in the backward direction inhibits nucleotide binding and subsequent release from the MT. This inhibition was independent from the magnitude of tension (2–8 pN) exerted on NL. Our results provide evidence that the front head of a kinesin dimer is gated by the backward orientation of its NL until the rear head releases from the microtubule [12]. Similar approaches have also been used to study force-dependent release properties of myosin [16] and dynein motors [13, 17].

---

## 2 Materials

### 2.1 DNA Tethering of Proteins

1. BRB80 buffer: 80 mM PIPES, 1 mM MgCl<sub>2</sub>, 1 mM EGTA, pH 6.8.
2. DNA hybridization buffer: 80 mM NaHCO<sub>3</sub>, 200 mM KCl, 5 mM MgCl<sub>2</sub>, pH 8.4.
3. 5'-biotin labeled short oligo—74 base pairs (100 µM).
4. 5'-amine labeled short oligo—74 base pairs (100 µM).
5. Alkyl chloride-NHS (AC-NHS) (40 mM).
6. Sulfosuccinimidyl 4-(*N*-maleimidomethyl)cyclohexane-1-carboxylate Sulfo-SMCC (2 mg, lyophilized powder).
7. Illustra MicroSpin™-25 (GE Healthcare) spin columns with elution containers.

### 2.2 Optical Trapping Assay Sample Preparation

#### Preparation

1. Polarity-marked MTs (1 mg/mL) [18].
2. Polystyrene beads, streptavidin coated—1 µm diameter.
3. Biotinylated-BSA (1 mg/mL).
4. Streptavidin (1 mg/mL).
5. Mg<sup>2+</sup>-adenosine 5'-triphosphate (Mg-ATP) (100 mM, pH 7).
6. Protocatechuate-3,4-dioxygenase—PCD (2 µM).
7. Protocatechuic Acid—PCA (250 mM).
8. Dithiothreitol—DTT (1 M).
9. Casein (pre-blocking agent) (40 mg/mL) (*see Note 1*).
10. Apyrase (1000 units/mg protein, lyophilized powder).
11. Hexokinase (130 units/mg, lyophilized powder).
12. Creatine phosphate (100 mM).
13. Creatine kinase (150 units/mg, lyophilized powder).
14. Dimethyl sulfoxide (DMSO) (anhydrous, ≥99.9 %).
15. Glucose (10 %).

---

## 3 Methods

This section explains a detailed methodology for performing the constant load motor-unbinding assay using kinesin-1. Specifically, we describe preparation of kinesin constructs with different labeling geometries, coupling of kinesin motors to polystyrene beads using functionalized DNA tethers, sample preparation, optical trapping and data analysis (Fig. 2). To specifically pull kinesin from its NL and head, two different labeling procedures are described.

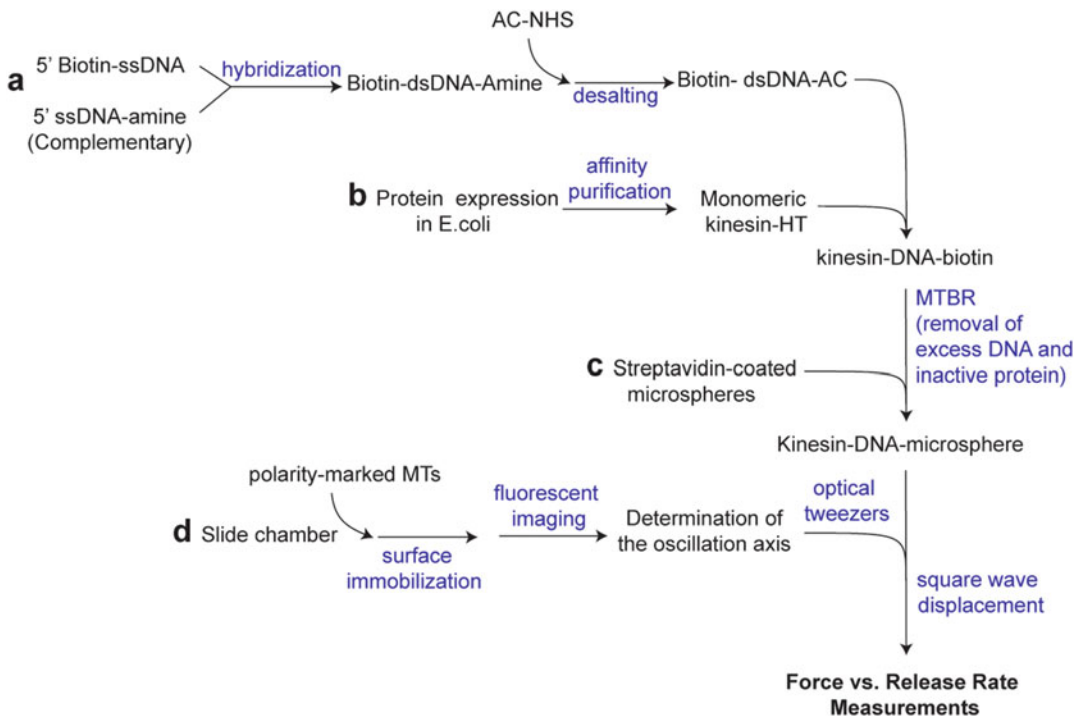


**Fig. 2** Protocol summary. Each pathway (a–d) summarizes the major steps in preparing reagents and experimental procedures. (a) DNA-tether preparation for motor-bead attachment. (b, c) Kinesin purification and bead attachment with DNA tether prepared in step (a). Procedure for DNA tethering of kinesin to beads from its NL is shown. A similar approach has been used to tether kinesin to beads from its head region (see text). (d) Experimental procedure for the optical trapping assay and data collection

### 3.1 Preparation of Kinesin Constructs

1. To specifically label kinesin at the motor domain, use a “cysteine-light” kinesin construct as a template, in which all surface exposed cysteines are changed to alanines [8, 19–21] and introduce a surface exposed cysteine located at the motor domain and distal from regions known to be critical for motility, such as the NL, nucleotide binding cleft and MT binding surface. We introduced a cysteine at the plus-end tip of kinesin’s motor domain (E215C, Fig. 3b, red sphere).
2. To label kinesin at its NL domain, insert HaloTag (HT, a 26 kDa protein tag) to the C-terminus to label kinesin at the distal end of the NL (hK349-HT).
3. Express 6×-His tagged human kinesin-1 monomers (hK349, containing the entire motor domain, NL and a short region of the neck coiled coil) in *E. coli* and purify by Ni-NTA affinity chromatography as described previously [22, 23].
4. Purify active monomers by a MT-binding and -release assay [24].

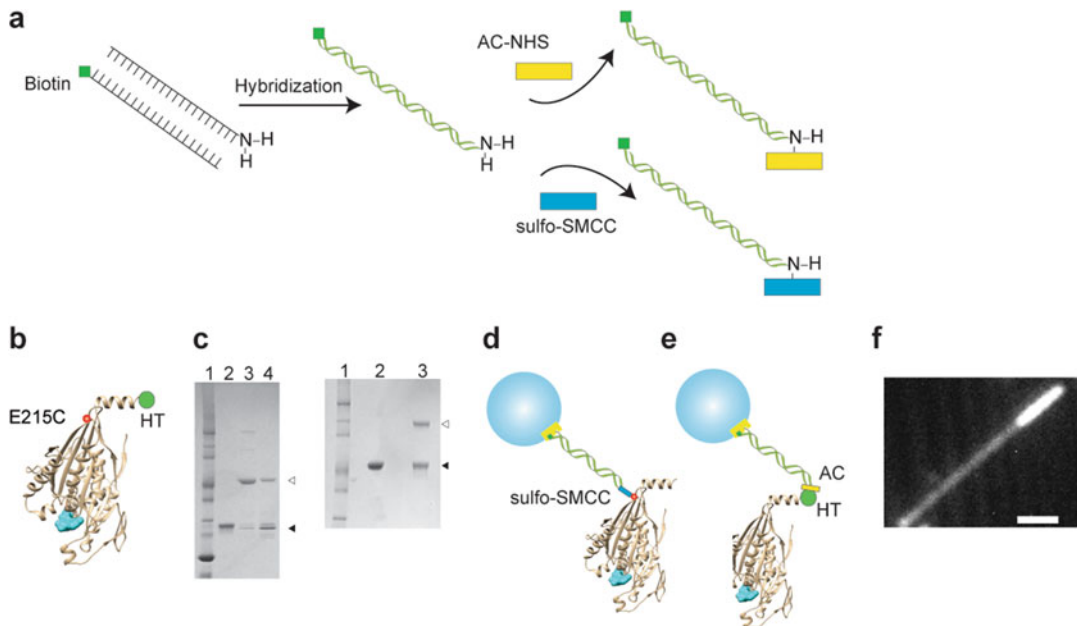


**Fig. 3** Labeling of human kinesin monomers with a DNA tether at the head and the NL. (a) Two complementary 74 nt-long ssDNA oligos with functional groups at the 5' end (biotin and amine) are hybridized. The 5' amine group reacts with either a HaloTag ligand (alkyl chloride—AC) or sulfo-SMCC using the NHS chemistry. (b) The atomic structure of rat kinesin monomer in the ADP-bound state (PDB entry 2KIN), numbered as in human kinesin. The protein is truncated at the C-terminus, containing amino acids 1–349 (hK349). A cysteine is introduced at the plus-end tip of the cysteine-light kinesin (E215C, *red sphere*) for the labeling with sulfo-SMCC. *Cyan space-fill* represents ADP. (c) (*Left*) A denaturing protein gel shows that hK349-E215C was labeled with the DNA tether. The lanes represent the molecular weight marker (1), kinesin (2), kinesin + Biotinylated DNA (3–4). (*Right*) hK349-HT was labeled with the DNA tether functionalized with AC. Lanes represent molecular weight marker (1), kinesin (2), kinesin + biotinylated DNA (3). The labeling efficiencies can be calculated from the intensity ratio of labeled (*white arrowhead*) and unlabeled (*black arrowhead*) motors. (d) hK349 E215C was labeled at the head with the DNA tether functionalized with sulfo-SMCC. (e) To label kinesin at the C-terminus of the NL, a 26 kDa HaloTag was fused to hK349 at the C-terminus (hK349-HT). The HT tag was labeled with the DNA tether functionalized with AC. (f) The MT minus end was labeled with Cy5. Polarity marked MTs are used to determine the direction of the release events (scale bar, 2  $\mu$ m)

5. Measure protein concentration by Bradford assay using BSA as standard.
6. Save the protein in 20 % sucrose, flash freeze in liquid nitrogen and store at  $-80^{\circ}\text{C}$ .

### 3.2 Construction of the DNA Tethers

Complementary 74 nucleotide (nt)-long DNA oligomers are used to form a DNA tether between the motor and the bead using orthogonal attachment chemistries. Because we use a DNA tether that is shorter than the DNA persistence length, a stiff linkage between the bead and motor can be established without introducing too much additional compliance [14].

1. Design two complementary 74 nt-long DNA strands (strand 1 and 2). Choose the nucleotide sequence accordingly to minimize potential secondary structures. Add a 2 nt overhang on each end to prevent steric hindrance [25].
2. Order strand 1 with a biotin modification at its 5'-end for bead attachment and strand 2 modified with a 12-carbon spacer terminating with an amine group at its 5'-end for kinesin attachment (Fig. 3a).
3. Dissolve the DNA strands in water to 100  $\mu\text{M}$ , mix 30  $\mu\text{L}$  of each strand and 20  $\mu\text{L}$  of DNA hybridization buffer solution in a PCR tube.
4. Place it in Peltier thermal cycler. Heat to 90 °C for 2 min. Cool to 25 °C for 40 min for hybridization.
5. Add 40× excess HaloTag Amine Ligand (AC-NHS) or sulfo-SMCC to the hybridized DNA strands based on the chosen orthogonal attachment chemistry. Mix by pipetting and incubate reaction at room temperature for 6 h.
6. Quench the reaction by incubating for 10 min with 1 mM Tris-HCl (pH 8.0).
7. Desalt DNA into the BRB80 buffer twice using G-25 size exclusion columns (see Note 2).

### **3.3 Labeling Kinesin with DNA Tethers**

1. To label kinesin with DNA at its head region, incubate the DNA-AC tether with 1  $\mu\text{M}$  hK349-HT.
2. To label kinesin with DNA at its NL region, incubate the DNA-SMCC tether with 1  $\mu\text{M}$  hK349-E215C monomers in BRB80 for 3 h at 4 °C.
3. Purify active monomers with using a MT-binding and -release assay (MTBR). This also serves to remove excess DNA from the labeling reaction (see Note 3) (Fig. 3c).

### **3.4 Coating Beads with Monomeric Kinesin**

1. Dilute the DNA-labeled kinesin monomers in BRB80 supplemented with 1 mg/mL casein (BRBC) to a working concentration (see Note 4) and incubate with 860 nm diameter streptavidin-coated polystyrene beads (1 % weight/volume) for 10 min on ice (Fig. 3d,e).
2. Remove the residual ATP present in the kinesin solution by diluting the bead/motor mix in 250  $\mu\text{L}$  BRBC and pellet the beads on tabletop centrifuge for 3 min (see Note 5). Discard the supernatant and resuspend the pellet in BRBC + 1 mM DTT to a final bead concentration of 0.1 % weight/volume.
3. Add the desired nucleotide for each experimental condition to beads:
  - (a) No nucleotide: Add 0.5 U/mL apyrase to consume leftover ATP.

- (b) ADP: Add 1 mM ADP with 2 U/mL hexokinase and 0.4 % glucose to convert leftover ATP to ADP.
  - (c) ATP: Add 1 mM (saturating) ATP. If desired, add 10 mM creatine phosphate and 2 U/mL creatine kinase to regenerate the ATP in the assay solution.
4. Add 2.5 mM PCA and 50 nM PCD to scavenge the free oxygen in assay solution, which minimizes premature bleaching of the organic dyes [26].

### **3.5 Chamber Preparation**

1. Prepare a flow chamber by using double-sided tape as a spacer between the coverslip and slide. Add solutions from one side using a pipette while using a tissue at the other side to create a flow. The flow chamber holds ~10  $\mu$ L.
2. Flow 10  $\mu$ L of 0.2 mg/mL Biotin-BSA in BRB80 buffer and incubate for 3 min. Wash with 30  $\mu$ L BRBC to remove the excess Biotin-BSA and block the surface.
3. Flow 10  $\mu$ L of 0.5 mg/mL streptavidin in BRB80 buffer and incubate for 3 min. Wash with 30  $\mu$ L BRBC to remove the unbound streptavidin.
4. Flow 10  $\mu$ L 0.1 mg/mL biotinylated, fluorescently labeled (Cy5) polarity marked MTs to the chamber and incubate for 2 min. Wash with 30  $\mu$ L BRBC to remove the unbound MTs.
5. Flow the bead-motor mixture (with the nucleotides and the oxygen scavenger system present).
6. Seal the chamber with clear nail polish, let it dry for 2 min and place it on the microscope's sample holder.

### **3.6 Optical Trapping Microscopy**

1. A single-beam optical trapping microscope is custom built with a Nikon Ti-Eclipse microscope body, 100 $\times$  1.49 NA Plan-Apo objective, 2 W 1064-nm continuous wave NdYag laser (Coherent) and M686XY piezo-motor driven microscope stage (25 mm full travel, 0.3  $\mu$ m step resolution, Physik Instrumente). A position-sensitive detector (PSD) is located at the back-focal plane to detect bead displacement [27]. The microscope is controlled using custom-written LabVIEW software [12, 25].
2. The 1064 nm trapping beam is steered by two orthogonal computer-controlled acousto-optic deflectors (AOD, AA Electronics) to capture and position floating monodisperse beads.
3. Calibrate the trap stiffness for each sample by fitting the windowed power spectrum of a bead trapped 3  $\mu$ m above the surface of the coverslip to a Lorentzian curve [28].
4. Adjust the power of the trapping beam to achieve a spring constant of ~0.05 pN nm $^{-1}$  (see Note 6).

5. Record the PSD data at 20 kHz for calibration and 5 kHz for data acquisition. Calibrate the PSD response in each sample by rapidly scanning the laser across a trapped bead in both  $x$  and  $y$  directions and fitting the resulting curve to a cubic polynomial [27]. Repeat this calibration once at the coverslip surface and once 3  $\mu\text{m}$  into the solution to avoid systematic errors in either experimental data or stiffness calibrations [29].

### 3.7 TIRF Microscopy

The optical trap microscope is combined with an objective-type, total internal reflection fluorescence (TIRF) microscope, using a 633 nm HeNe laser beam for Cy5 excitation. Fluorescence signals are collected with an electron-multiplied charge coupled device (EM-CCD) camera (Andor Ixon, 128  $\times$  128 pixels, 16  $\mu\text{m}$  pixel size) at 0.2 s exposure time under 10 mW laser exposure.

### 3.8 Microscopy Assay

1. In TIRF mode, identify a surface-immobilized MT with clear MT polarity (*see Note 7*) (Fig. 3f).
2. Move the microscope stage to place the selected MT to the center of the calibrated trapping region.
3. Trap a free bead from the solution with the trapping beam and position it over the Cy5-labeled MT.
4. Use the MT long axis as the oscillation axis (*see Note 8*).
5. Oscillate the bead  $\pm 150$  nm (*see Note 9*) along the long axis of the MT in a square wave pattern with a periodicity of 0.75 s (*see Notes 10* and *11*).

### 3.9 Data Analysis

A graphical overview of the important steps in data analysis is shown in Fig. 4a.

1. The release of each monomeric head from the MT is a single step process if there is one motor bound (*see Note 4*).
2. Use the Schwartz information criterion step-finding algorithm [30] to determine release events that occur between  $\pm 150$  nm dwell locations of the beads.
3. Visually confirm that the release of a bead from the MT is a single step process, making sure that a single motor was bound to MT. The bead rapidly snaps back to the trap center after the release of the motor from MT.
4. Discard the multiple release events in one period of oscillation, which correspond to the release of multiple motors from MT (*see Note 12*).
5. Discard events in which the bead is stalled at a position different than the trap center (*see Note 13*).
6. Discard MT dwell times shorter than 1 ms (*see Note 14*).

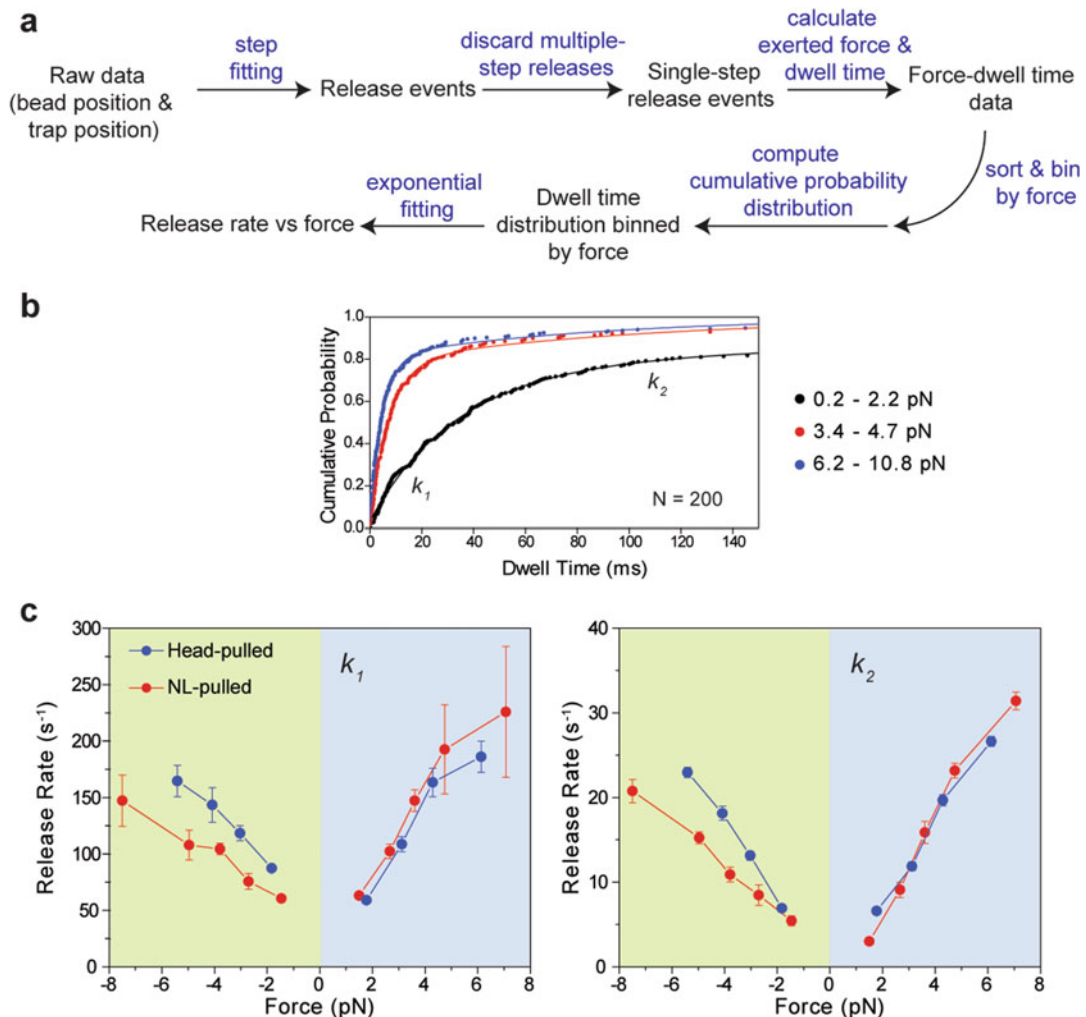


**Fig. 4** Data analysis for force-dependent release rate measurements. (a) Graphical overview of the data analysis routine for force dependent directional release of kinesin monomers. (b) Cumulative probability distributions (solid circles) represent the dwell time data for kinesin monomers pulled on the head toward the plus-end in the absence of nucleotide at different force ranges;  $n = 200$  for each histogram. The release rates ( $k_1$  and  $k_2$ ) at a given force range were calculated by a two-exponential-decay fit (solid curves). (c) MT release rates of head- and NL-pulled kinesins under 1 mM ADP. The kinesin release rate increases with increasing force in both directions. The release of NL-pulled kinesins was slower than head-pulled kinesins under backward forces. Error bars represent 95 % confidence intervals

7. Calculate the magnitude of the force exerted on a motor during binding by multiplying the trap stiffness and the bead-trap separation.
8. Determine the force direction from the bead-trap separation vector. Assign positive and negative signs for forces directed toward the MT plus and minus ends, respectively.

9. Sort the MT dwell-time data by applied force and bin under different forces for equal number of data points. Assign the average force for each bin (*see Note 15*).
10. Plot the cumulative distribution of the each binned data set (*see Note 16*) (Fig. 4b).
11. Fit the resulting cumulative distributions to an exponential decay in MATLAB. Resulting decay constants were assigned as force-dependent release rate of kinesin monomers (*see Note 17*).
12. Plot the release rate as a function of the average force in the bin (Fig. 4c).

---

## 4 Notes

1. Solution is prepared from lyophilized casein powder. Do not use dry milk because it contains massive amounts of biotin.
2. Removal of excess AC-NHS is important to get efficient labeling of kinesin with DNA-AC tether.
3. Removal of excess DNA is important to have efficient binding of kinesin-DNA to beads.
4. To record data from single monomers, motors are diluted to a level where the probability of motor binding to MTs is reduced to 5–15 % during the oscillation of the beads. Under these conditions, less than 10 % of the release events occur in multiple steps [12]. At a tenfold higher motor concentration, a significant increase in multiple release events can be observed. To rule out nonspecific interactions, confirm that no events are detectable in the absence of motor.
5. Simple benchtop centrifuge is enough to spin down 1  $\mu\text{m}$  or bigger beads at 4000 rcf.
6. For 0.9  $\mu\text{m}$  diameter polystyrene beads, we obtain a spring constant of  $\sim 0.05 \text{ pN/nm}$  at 50 mW 1064 nm laser excitation.
7. A fluorescence image reveals the MT long axis and its polarity.
8. Since every MT is randomly positioned on coverslip, the oscillation axis is manually determined for each MT by using custom written LabVIEW software.
9. This distance is selected to keep the bead within the linear range of the trap during oscillations. The trap stiffness can be adjusted to increase or decrease the range of measurable forces.
10. Depending on the binding affinity of the motor, alter the oscillation period to optimize the binding conditions.
11. To allow the measurement of very long dwells (with durations greater than the period of the square wave), we implemented

an automated latching algorithm that prevented the trap from changing positions while a motor was bound.

12. 90 % of the binding events terminated with a single release step, indicative of binding of a single kinesin monomer.
13. In these cases, release forces are overestimated because the exerted force is shared between two monomers and dwell time is not clear for each monomer.
14. Shorter dwells are discarded because the corner frequency of the bead (~700–800 Hz) limits the measurement of faster events.
15. Because the method has no bias toward detecting release events under low or high forces, the distribution of release events is nearly uniform over a wide range of forces. This enables the determination of the force-dependent release profile of a motor for each nucleotide and pulling condition in a single experiment without adjusting the parameters of the trapping assay.
16. Cumulative distribution functions are built to eliminate the bias on the rates when different bin sizes are used for making histograms.
17. It is crucial to run a F-test to verify whether addition of a second exponential is statistically justified. Two distinct release rates under the same force regime may result from strong and weak binding modes of a motor to MT.

## Acknowledgements

We thank V. Belyy, for helpful discussions. This work was supported by a grant from the NIH (GM094522) and the NSF (MCB-1055017) to AY.

## References

1. Hirokawa N, Noda Y, Tanaka Y, Niwa S (2009) Kinesin superfamily motor proteins and intracellular transport. *Nat Rev Mol Cell Biol* 10:682–696. doi:[10.1038/nrm2774](https://doi.org/10.1038/nrm2774)
2. Vallee RB, Williams JC, Varma D, Barnhart LE (2004) Dynein: an ancient motor protein involved in multiple modes of transport. *J Neurobiol* 58:189–200. doi:[10.1002/neu.10314](https://doi.org/10.1002/neu.10314)
3. Belyy V, Yildiz A (2014) Processive cytoskeletal motors studied with single-molecule fluorescence techniques. *FEBS Lett* 588:3520–3525. doi:[10.1016/j.febslet.2014.05.040](https://doi.org/10.1016/j.febslet.2014.05.040)
4. Hua W, Young EC, Fleming ML, Gelles J (1997) Coupling of kinesin steps to ATP hydrolysis. *Nature* 388:390–393. doi:[10.1038/41118](https://doi.org/10.1038/41118)
5. Schnitzer MJ, Block SM (1997) Kinesin hydrolyses one ATP per 8-nm step. *Nature* 388:386–390. doi:[10.1038/41111](https://doi.org/10.1038/41111)
6. Guydosh NR, Block SM (2006) Backsteps induced by nucleotide analogs suggest the front head of kinesin is gated by strain. *Proc Natl Acad Sci U S A* 103:8054–8059. doi:[10.1073/pnas.0600931103](https://doi.org/10.1073/pnas.0600931103)
7. Shastry S, Hancock WO (2010) Neck linker length determines the degree of processivity in kinesin-1 and kinesin-2 motors. *Curr Biol* 20:939–943. doi:[10.1016/j.cub.2010.03.065](https://doi.org/10.1016/j.cub.2010.03.065)

8. Yildiz A, Tomishige M, Gengerich A, Vale RD (2008) Intramolecular strain coordinates kinesin stepping behavior along microtubules. *Cell* 134:1030–1041. doi:[10.1016/j.cell.2008.07.018](https://doi.org/10.1016/j.cell.2008.07.018)
9. Clancy BE, Behnke-Parks WM, Andreasson JOL et al (2011) A universal pathway for kinesin stepping. *Nat Struct Mol Biol* 18:1020–1027. doi:[10.1038/nsmb.2104](https://doi.org/10.1038/nsmb.2104)
10. Rosenfeld SS, Jefferson GM, King PH (2001) ATP reorients the neck linker of kinesin in two sequential steps. *J Biol Chem* 276:40167–40174. doi:[10.1074/jbc.M103899200](https://doi.org/10.1074/jbc.M103899200)
11. Hyeon C, Onuchic JN (2007) Internal strain regulates the nucleotide binding site of the kinesin leading head. *Proc Natl Acad Sci U S A* 104:2175–2180. doi:[10.1073/pnas.0610939104](https://doi.org/10.1073/pnas.0610939104)
12. Dogan MY, Can S, Cleary FB et al (2016) Kinesin's front head is gated by the backward orientation of its neck linker. *Cell Rep* 10:1967–1973. doi:[10.1016/j.celrep.2015.02.061](https://doi.org/10.1016/j.celrep.2015.02.061)
13. Cleary FB, Dewitt MA, Bilyard T et al (2014) Tension on the linker gates the ATP-dependent release of dynein from microtubules. *Nat Commun* 5:4587. doi:[10.1038/ncomms5587](https://doi.org/10.1038/ncomms5587)
14. Guydosh NR, Block SM (2009) Direct observation of the binding state of the kinesin head to the microtubule. *Nature* 461:125–128. doi:[10.1038/nature08259](https://doi.org/10.1038/nature08259)
15. Dudko OK, Hummer G, Szabo A (2008) Theory, analysis, and interpretation of single-molecule force spectroscopy experiments. *Proc Natl Acad Sci U S A* 105:15755–15760. doi:[10.1073/pnas.0806085105](https://doi.org/10.1073/pnas.0806085105)
16. Capitanio M, Canepari M, Maffei M et al (2012) Ultrafast force-clamp spectroscopy of single molecules reveals load dependence of myosin working stroke. *Nat Methods* 9:1013–1019. doi:[10.1038/nmeth.2152](https://doi.org/10.1038/nmeth.2152)
17. Nicholas MP, Berger F, Rao L et al (2015) Cytoplasmic dynein regulates its attachment to microtubules via nucleotide state-switched mechanosensing at multiple AAA domains. *Proc Natl Acad Sci U S A* 112:6371–6376. doi:[10.1073/pnas.1417422112](https://doi.org/10.1073/pnas.1417422112)
18. Hyman AA (1991) Preparation of marked microtubules for the assay of the polarity of microtubule-based motors by fluorescence. *J Cell Sci Suppl* 14:125–127
19. Rice S, Lin AW, Safer D et al (1999) A structural change in the kinesin motor protein that drives motility. *Nature* 402:778–784. doi:[10.1038/45483](https://doi.org/10.1038/45483)
20. Mori T, Vale RD, Tomishige M (2007) How kinesin waits between steps. *Nature* 450:750–754. doi:[10.1038/nature06346](https://doi.org/10.1038/nature06346)
21. Tomishige M, Stuurman N, Vale RD (2006) Single-molecule observations of neck linker conformational changes in the kinesin motor protein. *Nat Struct Mol Biol* 13:887–894. doi:[10.1038/nsmb1151](https://doi.org/10.1038/nsmb1151)
22. Stock MF, Hackney DD (2001) Expression of kinesin in Escherichia coli. *Methods Mol Biol* 164:43–48
23. Bornhorst JA, Falke JJ (2000) Purification of proteins using polyhistidine affinity tags. *Methods Enzymol* 326:245–254
24. Tomishige M, Vale RD (2000) Controlling kinesin by reversible disulfide cross-linking. Identifying the motility-producing conformational change. *J Cell Biol* 151:1081–1092
25. Belyy V, Hendel NL, Chien A, Yildiz A (2014) Cytoplasmic dynein transports cargos via load-sharing between the heads. *Nat Commun* 5:5544. doi:[10.1038/ncomms6544](https://doi.org/10.1038/ncomms6544)
26. Aitken CE, Marshall RA, Puglisi JD (2008) An oxygen scavenging system for improvement of dye stability in single-molecule fluorescence experiments. *Biophys J* 94:1826–1835. doi:[10.1529/biophysj.107.117689](https://doi.org/10.1529/biophysj.107.117689)
27. Neuman KC, Block SM (2004) Optical trapping. *Rev Sci Instrum* 75:2787–2809. doi:[10.1063/1.1785844](https://doi.org/10.1063/1.1785844)
28. Visscher K, Block SM (1998) Versatile optical traps with feedback control. *Methods Enzymol* 298:460–489
29. Schäffer E, Nørrelykke SF, Howard J (2007) Surface forces and drag coefficients of microspheres near a plane surface measured with optical tweezers. *Langmuir* 23:3654–3665. doi:[10.1021/la0622368](https://doi.org/10.1021/la0622368)
30. Kalafut B, Visscher K (2008) An objective, model-independent method for detection of non-uniform steps in noisy signals. *Comput Phys Commun* 179:716–723. doi:[10.1016/j.cpc.2008.06.008](https://doi.org/10.1016/j.cpc.2008.06.008)

# Chapter 19

## Measuring the Kinetic and Mechanical Properties of Non-processive Myosins Using Optical Tweezers

Michael J. Greenberg, Henry Shuman, and E. Michael Ostap

### Abstract

The myosin superfamily of molecular motors utilizes energy from ATP hydrolysis to generate force and motility along actin filaments in a diverse array of cellular processes. These motors are structurally, kinetically, and mechanically tuned to their specific molecular roles in the cell. Optical trapping techniques have played a central role in elucidating the mechanisms by which myosins generate force and in exposing the remarkable diversity of myosin functions. Here, we present thorough methods for measuring and analyzing interactions between actin and non-processive myosins using optical trapping techniques.

**Key words** Actomyosin, Kinetics, Mechanochemistry, Single molecule

---

### 1 Introduction

Myosins are cytoskeletal motors that use the energy from ATP hydrolysis to generate force and movement along actin filaments. Humans express 38 myosin motor proteins [1] with diverse biochemical and mechanical properties that enable them to function in a wide array of cellular processes, including muscle contraction, cell migration, mechanosensing, intracellular transport, generating membrane dynamics, and cellular signaling [2–4]. Mutations in myosin genes can result in cardiomyopathies, hearing loss, blindness, cancer, and developmental defects [5].

Despite their diverse functions, all characterized myosins follow similar ATPase and mechanochemical cycles [4]. The rate and equilibrium constants that define the ATPase pathway vary substantially across the myosin family, resulting in differences in the steady-state populations and lifetimes of intermediates that confer diverse mechanical functions to the motors. It has been a substantial challenge to the field to determine how the biochemical intermediates on the myosin ATPase pathway are linked to structural changes that ultimately lead to force generation. Additionally, it has been a challenge to determine how divergent biochemical properties lead

to mechanical differences among different myosins isoforms, how mechanical loads affect myosin power output, and how myosin mutations affect motor function in disease.

Single-molecule techniques, in conjunction with biochemical, spectroscopic, and structural studies, have been incredibly powerful in their ability to elucidate the molecular mechanisms of molecular motors [6, 7]. Notably, optical tweezers have served as an indispensable tool for discovering the mechanisms of myosin function. Pioneering work by the laboratory of Dr. James Spudich led to the development of an assay to probe the properties of non-processive myosin motors (i.e., motors that only take a single step on actin before detaching), dubbed the three-bead assay [8]. In this assay, an actin filament is suspended between two optically trapped beads, tensed, and then lowered onto a pedestal bead that is sparsely coated with myosin (Fig. 1). The myosin motor can then bind to the actin, displacing the beads. From these displacements, it is possible to extract information about the myosin working stroke, attachment lifetime, and magnitude of force generation. The three-bead assay has also been used to probe the kinetics and mechanics of processive myosins [9, 10]. It is worth noting that other geometries have also been employed to study single non-processive motors [11–13].

To conduct the three-bead assay, one must (1) couple beads to actin, (2) prepare flow cells with pedestal beads, (3) attach myosins to the pedestal, and (4) identify single-molecule interactions between myosin and actin. In this chapter, we describe the procedures for performing this assay along with techniques for measuring myosin's force-dependent kinetics and stiffness. We also describe techniques for data analysis. Our optical trapping setup is briefly described in Subheading 3.9 below. For detailed instructions on building a dual-beam optical trap for the three-bead assay, the

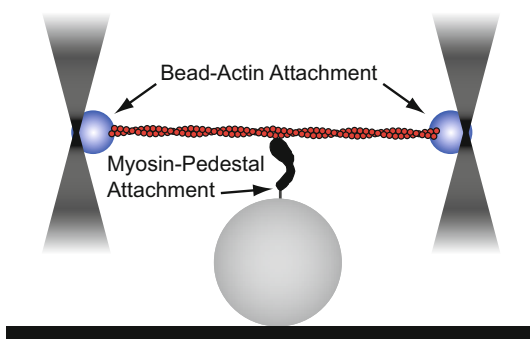


**Fig. 1** Cartoon of the three-bead geometry. A dual-beam optical trap is used to form a bead–actin–bead dumbbell. This dumbbell is then lowered over a surface-bound bead that is sparsely coated with myosin and single-molecule interactions between myosin and actin can be detected

reader is directed to an excellent chapter by the Spudich laboratory [14]. For single-bead assays, the reader is referred to experiments in Chaps. 5, 17, and 18.

## 2 Materials

### **2.1 Preparation of Acetone Powder for Actin Purification**

1. Appropriate muscle tissue (*see Note 1*).
2. Myosin extraction solution (0.5 M KCl, 0.1 M K<sub>2</sub>HPO<sub>4</sub> cooled to 4 °C).
3. Cold distilled water (chilled to 4 °C).
4. 1 M sodium carbonate.
5. Cold reagent grade acetone (chilled to 4 °C).
6. Chloroform.
7. Meat grinder.
8. Cheesecloth.
9. Blender or Omni Mixer.

### **2.2 Preparation of Actin from Acetone Powder**

1. Buffer A (2 mM Tris, pH 8.0 at 25 °C, 0.2 mM ATP, 0.5 mM DTT, 1 mM sodium azide, 0.1 mM CaCl<sub>2</sub>) (*see Note 2*).
2. 2 M KCl.
3. 1 M MgCl<sub>2</sub>.
4. Cheesecloth.
5. Dounce homogenizer (*see Note 3*).

### **2.3 Bead–Actin Linkages: Preparation of N-Ethylmaleimide Modified Myosin Beads**

1. High Salt Buffer (HSB) (500 mM KCl, 4 mM MgCl<sub>2</sub>, 1 mM EGTA, 20 mM KH<sub>2</sub>PO<sub>4</sub>, pH 7.2).
2. KMg25 buffer (25 mM KCl, 60 mM MOPS pH 7.0, 1 mM EGTA, 1 mM MgCl<sub>2</sub>, 1 mM DTT), (*see Note 4*).
3. 1 mL of 1 M Dithiothreitol (DTT), (*see Note 5*).
4. 50 mM N-ethylmaleimide (Sigma 04259-5G) in water prepared fresh (*see Note 6*).
5. Skeletal muscle myosin in glycerol (*see Note 7*).
6. Glycerol (Sigma G7893).
7. Polystyrene beads (1.1 μm diameter, 10 % solids, Sigma LB-11).
8. Bovine serum albumin (BSA, Fisher 50-230-3400).

### **2.4 Bead–Actin Linkages: Preparation of Neutravidin-Coated Beads**

1. KMg25 buffer (25 mM KCl, 60 mM MOPS pH 7.0, 1 mM EGTA, 1 mM MgCl<sub>2</sub>, 1 mM DTT), (*see Note 4*).
2. Polystyrene beads (1.1 μm diameter, 10 % solids, Sigma LB-11).

3. Neutravidin (Fisher 31000) can be diluted to 0.1 mg/mL in water and frozen at -20 °C.
4. Biotinylated actin (*see Note 8*).
5. 50 µM TRITC-labeled phalloidin (Sigma P1951) in methanol (*see Note 9*).

**2.5 Bead–Actin Linkages: Purification of HaloTagged, Actin-Binding Domain of α-Actinin (HT-ABD)**

1. Lysis buffer (25 mM Tris, pH 7.5, 20 mM Imidazole, 300 mM NaCl, 0.5 mM EGTA, 0.5 % Igepal, 1 mM beta-mercaptoethanol, 1 mM PMSF, 0.01 mg/mL aprotinin and leupeptin) (*see Note 10*).
2. Wash buffer (same as lysis buffer minus Igepal).
3. Elution buffer (12 mM imidazole, 300 mM NaCl, 25 mM Tris, pH 7.5, 1 mM EGTA, 1 mM DTT).
4. FPLC buffer A (10 mM Tris, pH 7.5, 50 mM KCl, 1 mM DTT, 1 mM EGTA).
5. FPLC buffer B (same as buffer A except 1 M KCl).
6. KMg25 buffer (25 mM KCl, 60 mM MOPS, pH 7.0, 1 mM EGTA, 1 mM MgCl<sub>2</sub>, 1 mM DTT).

**2.6 Bead–Actin Linkages: Coupling HT-ABD to Beads**

1. 1 µm diameter Polybead amino microspheres (Polysciences 17010-5).
2. Bovine serum albumin (BSA, Fisher 50-230-3400).
3. HaloTag succinimidyl-ester (O2) ligand (Promega P1691) (*see Note 11*).
4. Phosphate buffered saline (PBS; Fisher 14190-136).
5. KMg25 buffer (25 mM KCl, 60 mM MOPS, pH 7.0, 1 mM EGTA, 1 mM MgCl<sub>2</sub>, 1 mM DTT).

**2.7 Preparation of Flow Cells for Optical Trapping**

1. Amyl acetate (Electron Microscopy Sciences 10815).
2. 2 % nitrocellulose in amyl acetate (Electron Microscopy Sciences 1262030).
3. Dry silica beads, 2.5-µm diameter (Bangs Laboratories SS05N).
4. Borosilicate cover glass (Fisher 12-544B).
5. Double-sided tape (Scotch 391775).
6. Silicon vacuum grease (Fisher 146355D).
7. Razor cutting tool (single-edged razor or X-ACTO knife).

**2.8 Filling Flow Cells for Optical Trapping**

1. Myosin (*see Subheading 3*).
2. Actin (*see Subheadings 3.1 and 3.2*).
3. 10 mL KMg25 buffer (25 mM KCl, 60 mM MOPS, pH 7.0, 1 mM EGTA, 1 mM MgCl<sub>2</sub>, 1 mM DTT) (*see Note 4*).

4. 0.1 mg/mL streptavidin (Sigma S0677-5MG) in water (250  $\mu$ L stock, stored at  $-80^{\circ}\text{C}$ ) (*see Note 12*).
5. 10 mg/mL bovine serum albumin (1 mL, 10 $\times$  stock) (BSA, Fisher 50-230-3400) in KMg25 made fresh.
6. 1 mL of 1 mg/mL bovine serum albumin in KMg25 (from the 10 $\times$  stock).
7. ATP (Sigma A2383-25G) dissolved in water, pH 7.0 (*see Note 13*).
8. 250 mg/mL glucose (Sigma G8270) in water (*see Note 14*).
9. 50  $\mu$ L 192 U/mL glucose oxidase (Sigma G2133) in KMg25 prepared fresh.
10. Catalase from bovine liver (Sigma C3155).
11. 100 $\times$  GOC mixture (prepared fresh). Add 2  $\mu$ L catalase to 20  $\mu$ L glucose oxidase solutions. Centrifuge at 15,000  $\times \mathcal{g}$  for 1 min and save the supernatant.
12. 50  $\mu$ M TRITC-labeled phalloidin (Sigma P1951) in methanol (*see Note 15*).
13. 100  $\mu$ L 2  $\mu$ M TRITC-labeled phalloidin stabilized actin in KMg25. Add 1.1 M excess TRITC-labeled phalloidin to actin in KMg25. Let sit overnight on ice or 30 min at room temperature.
14. 1 M MgCl<sub>2</sub>.
15. Calmodulin (*see Note 16*).
16. 5–10 nM myosin in KMg25 (*see Note 17*).
17. Coated beads for trapping (*see Subheadings 3.3–3.6*).
18. Activation buffer (1 mg/mL BSA, 1  $\mu$ L 100 $\times$  glucose, 1  $\mu$ L GOC, 0.2 nM TRITC-labeled phalloidin stabilized actin, MgATP), (*see Notes 16 and 18*).

---

### 3 Methods

In the three-bead geometry, an actin filament is stretched between two optically trapped beads and then lowered on to a pedestal bead that is sparsely coated with myosin (Fig. 1). Therefore, before starting, one must: (1) purify actin and myosin, (2) functionalize beads so that they can stick to actin, and (3) assemble and load flow cells with the necessary components. Here, we provide protocols for each of these procedures.

Optical trapping assays require purified actin and myosin. The purification of myosin will depend on the specific myosin construct being used. Myosin can be tissue purified or produced recombinantly using an appropriate eukaryotic expression system [15–19].

### 3.1 Preparation of Acetone Powder for Actin Purification

While various systems are used to prepare myosin, actin can be prepared in large quantities from rabbit back muscle [20]. In the first part of this preparation, muscle is ground and washed with both aqueous and organic solvents to form an “acetone powder.” This powder can be stored for long periods at  $-20^{\circ}\text{C}$  and can be used for a simple actin-extraction preparation (Subheading 3.2 and Note 19). The procedure for generating acetone powder is the following:

1. If whole muscle tissue is used, cut into 1 in. pieces and grind 2 $\times$  in a meat grinder. Place on plastic wrap and weigh. A typical adult rabbit yields  $\sim$ 300 g muscle.
2. Extract the myosin for exactly 10 min using 3 mL of myosin extracting solution per gram of starting tissue while stirring in the cold room. Longer incubation times prematurely extract the actin.
3. Centrifuge for 15 min at  $4000 \times g$  and save the pellet. Discard the myosin-containing supernatant.
4. Add 3 mL of cold distilled water per gram of starting tissue. Stir in the cold room and adjust the pH to 8.2–8.5 with 1 M sodium carbonate.
5. Centrifuge at  $4000 \times g$  at  $4^{\circ}\text{C}$  and save the pellet. Mark the volume of the pellet with a pen directly on the centrifuge tube.
6. Discard the supernatant and repeat steps 4 and 5 up to four times. As soon as the pellet begins to swell, continue to the next step, regardless of the number of washes.
7. Add 2–3 volumes of cold acetone to the muscle residue and stir 20 min vigorously in a fume hood. Acetone is flammable, so take appropriate precautions.
8. Filter the muscle residue through cheesecloth and save the insoluble material.
9. Repeat steps 7 and 8. At this stage, the insoluble material should be mostly white.
10. Spread the insoluble material on a large piece of filter paper in a fume hood and allow it to dry overnight at room temperature (see Note 20).
11. The next day, wash the muscle residue twice with enough chloroform to cover the residue. Filter the muscle residue with cheesecloth and save the insoluble material.
12. When dry, very briefly disperse the acetone powder in a blender or Omni Mixer to break up chunks.
13. Store the acetone powder desiccated at  $-20^{\circ}\text{C}$ . A typical yield is 10 % of the starting muscle weight.

### **3.2 Preparation of Actin from Acetone Powder**

The procedure for purifying actin from acetone powder is the following:

1. Add 20 mL Buffer A per gram of muscle acetone powder and stir on ice for 30 min (*see Note 21*).
2. Centrifuge for 30 min at  $4000 \times g$  at  $4^\circ\text{C}$ .
3. Filter through cheesecloth and save the actin-containing supernatant.
4. Resuspend pellets in original volume of Buffer A and repeat steps 2 and 3.
5. Measure the volume of the actin-containing supernatant. Add KCl to 50 mM and  $\text{MgCl}_2$  to 2 mM to polymerize the actin. Cover and stir slowly for 1 h at room temperature. The solution will become viscous and air bubbles will remain suspended in solution due to the viscosity of the filamentous actin.
6. Add solid KCl to the solution to a final concentration of 800 mM while stirring in the cold room for 30 min to dissociate contaminating tropomyosin from the actin filaments.
7. Centrifuge the actin for 5 min at  $4000 \times g$  to remove remaining acetone powder. Save the actin-containing supernatant.
8. Ultracentrifuge the actin for 2 h at  $142,000 \times g$  to pellet the filamentous actin.
9. Discard the supernatant and gently resuspend the pellets in 3 mL of Buffer A per gram of starting material. Scrape the pellets off the side of the centrifuge tube with a stainless steel spatula. Homogenize the pellets using a Dounce homogenizer. Dialyze in Buffer A with three buffer changes over 2 days to depolymerize the actin filaments.
10. Clarify the depolymerized actin solution by ultracentrifugation at  $142,000 \times g$  for 2 h. Save the supernatant containing actin monomers on ice for up to 1 month (*see Note 22*).
11. Measure the concentration of actin by absorbance at 290 nm. The extinction coefficient is  $26,600 \text{ M}^{-1} \text{ cm}^{-1}$ .

### **3.3 Bead–Actin Linkages: Preparation of N-Ethylmaleimide (NEM) Modified Myosin Beads**

Building a stable and well-defined bead–actin–bead dumbbell is crucial for measuring single-molecule attachment events. The dumbbell consists of two optically trapped beads and a single actin filament, and the actin filament must remain stably associated with the beads (i.e., it must not dissociate or slip) in the presence of mechanical tension. Several methods have been developed to couple actin filaments to polystyrene beads. Here, we will describe three different reagents for creating actin-bead attachments: *N*-ethylmaleimide modified myosin, neutravidin-biotin, and a HaloTagged, actin-binding domain from  $\alpha$ -actinin (HT-ABD).

*N*-ethylmaleimide (NEM) modifies reactive sulfhydryl residues in myosin, resulting in a nonenzymatically active motor domain that binds strongly to actin. NEM-myosin bound to beads has been shown to be highly effective for creating stable dumbbells for experiments performed at low ATP concentrations. However, at ATP concentrations >100  $\mu$ M, we find that the linkages between the actin and the NEM-myosin slip when the dumbbell is placed under tension. Perform the following steps:

1. Dilute 0.8 mg of rabbit skeletal myosin to ~1 mg/mL in water to a final volume of 0.8 mL. Myosin will start to form filaments once the salt is lowered below 200 mM KCl [21] and the final salt concentration should be less than 25 mM after dilution in water. If the initial stock concentration of myosin is dilute, then dilute 0.8 mg of myosin into a solution that contains less than 25 mM salt, concentrate, and proceed as described below.
2. Centrifuge at 15,000  $\times g$  at 4 °C for 30 min in a benchtop centrifuge. Discard the supernatant and save the myosin pellet.
3. Resuspend the pellet in 110  $\mu$ L HSB. The high salt depolymerizes the myosin.
4. Add 12  $\mu$ L of 50 mM NEM to the myosin. Let incubate 90 min at room temperature (*see Note 23*).
5. Add 1 mL of water and DTT to 20 mM to quench the reaction and polymerize the myosin.
6. Centrifuge at 15,000  $\times g$  at 4 °C for 30 min using a benchtop centrifuge. Discard the supernatant and save the myosin pellet.
7. Resuspend the pellet in 200  $\mu$ L HSB and add 200  $\mu$ L glycerol. Add DTT to 10 mM. NEM-modified myosin can be stored up to 1 month at -20 °C.
8. Wash 2  $\mu$ L of polystyrene beads two times with 250  $\mu$ L Milli-Q H<sub>2</sub>O to remove surfactants. Centrifuge at 15,000  $\times g$  at 4 °C for 2 min using benchtop centrifuge. Remove the supernatant. If a well-formed pellet is not formed, remove some supernatant and centrifuge again.
9. Resuspend the beads in ~15  $\mu$ L Milli-Q H<sub>2</sub>O and agitate in a bath sonicator for 30 s.
10. Add 80  $\mu$ L of NEM-modified myosin to the beads and let sit for 2 h at 4 °C or overnight on ice.
11. Prepare BSA-coated 1.5 mL microcentrifuge tubes during the incubation above. Prepare two tubes with 1 mL HSB containing 1 mg/mL BSA and two tubes with 1 mL KMg25 containing 1 mg/mL BSA. Let sit at room temperature for at least 30 min (*see Note 24*).

12. After 2 h, add 1 mL of HSB to the beads and then centrifuge in the BSA coated tubes at  $10,000 \times g$  for 8 min using the benchtop centrifuge. Repeat wash.
13. Wash beads one time in 1 mL KMg25. Centrifuge in a BSA coated tube at  $10,000 \times g$  for 8 min using a benchtop centrifuge.
14. Resuspend the pellet in 200  $\mu$ L KMg25 (without BSA) and transfer to the last BSA-coated tube (after removing the BSA solution from the tube).
15. Store NEM-myosin coated beads at 4 °C for up to 10 days.

### **3.4 Bead–Actin Linkages: Preparation of Neutravidin-Coated Beads**

Biotinylated-actin binding to neutravidin (or streptavidin)-coated beads is an easily implemented, high-affinity linkage that is very stable to applied tension, tolerant of a wide-range of solution conditions, and insensitive to physiological MgATP concentrations. The disadvantages of the linkage are that it requires covalent modification of actin, and that it cannot be used if myosin is adhered to pedestals using a biotin–neutravidin/streptavidin attachment strategy. Biotinylated actin can be prepared by the experimenter or purchased from commercial sources (*see Note 8*). Perform the following steps:

1. Add 1  $\mu$ L of beads to 50  $\mu$ L of neutravidin and incubate at room temperature overnight.
2. Wash beads three times in KMg25 buffer. Centrifuge at  $10,000 \times g$  for 8 min in the benchtop centrifuge after each wash to pellet the beads.
3. When conducting the experiment, copolymerize 25 % biotinylated actin with unlabeled actin. Add 1.1-fold molar ratio excess TRITC phalloidin to actin in KMg25. Let sit overnight on ice or 30 min at room temperature. Use this stock for all trapping experiments (*see Note 25*).

### **3.5 Bead–Actin Linkages: Purification of HaloTagged, Actin-Binding Domain of $\alpha$ -Actinin (HT-ABD)**

Recently, our lab attached beads to the actin-binding domain of  $\alpha$ -actinin fused to a HaloTag [22]. This strategy generates an ATP-insensitive bead-to-actin linkage that does not interfere with other biotin-streptavidin linkages in solution. The preparation is more complicated than the methods described above, and it requires bacterial expression and purification of a recombinant protein. The sequence details of the HT-ABD construct containing a hexahistidine tag for purification is described in detail elsewhere [22]. The procedure is the following:

1. Express HT-ABD using the pLT36 plasmid available from the Ostap Lab in Rosetta2(DE3) pLysS cells using standard techniques. Expression is induced with 0.1 mM IPTG after cells

reach a density of 0.6–0.8 OD and then the cells are grown for 3 h. The cell pellet can be stored at –80 °C.

2. For each liter of cells, resuspend in 50 mL lysis buffer on ice using a homogenizer.
3. Sonicate cells five times for 15 s using a probe-tip sonicator.
4. Centrifuge at 25,000 ×  $\text{g}$  for 30 min at 4 °C. Save the supernatant.
5. Load the supernatant onto a 2 mL nickel-NTA column at 1 mL/min using a peristaltic pump.
6. Wash the column five times with 3 mL of wash buffer.
7. Add 5 mL of elution buffer to the column. Let sit for 30 min.
8. Elute the protein and then repeat step 7.
9. Dialyze the elutant versus FPLC buffer A overnight at 4 °C.
10. Use FPLC with a MonoQ column to purify the protein with a gradient of FPLC buffers A and B.
11. Concentrate protein using centrifugal filter units (Millipore UFC901024), dialyze versus 1 L KMg25 overnight, and then freeze and store in liquid nitrogen in 50  $\mu\text{L}$  aliquots.

### **3.6 Bead–Actin Linkages: Coupling of HT-ABD to Beads**

The HT-ABD construct is linked to beads to create an ATP-insensitive actin-linkage. Amino-functionalized beads are linked via a succinimidyl ester to a chloroalkane group. The chloroalkane covalently links to the HaloTag gene-product fused to the  $\alpha$ -actinin actin-binding-domain. Perform the following steps:

1. Use a bath sonicator to disperse 50  $\mu\text{L}$  of amino microspheres in 1 mL of water.
2. Wash beads three times in 1 mL water. Centrifuge at 10,000 ×  $\text{g}$  for 8 min in a benchtop centrifuge after each wash to pellet the beads.
3. Resuspend the beads in 200  $\mu\text{L}$  of phosphate buffered saline (PBS). Split this volume into 40  $\mu\text{L}$  aliquots and sonicate the beads using a bath sonicator for 20 min.
4. Add 2  $\mu\text{L}$  of 100 mM succinimidyl ester ligand to each aliquot. Sonicate beads for 30 min in a bath sonicator. Let the beads sit at room temperature for 30 min. During the incubation, the succinimidyl ester becomes covalently linked to the amino-groups on the beads.
5. Prepare BSA-coated 1.5 mL Eppendorf tubes while you wait. Prepare two tubes of 1 mL KMg25 + 1 mg/mL BSA. Let sit at room temperature for at least 30 min.
6. Combine all of the bead aliquots in a BSA-coated tube and then wash beads three times with 1 mL PBS. Centrifuge at 10,000 ×  $\text{g}$  for 8 min in the benchtop centrifuge after each wash.

7. Resuspend the beads in 200  $\mu\text{L}$  of PBS. Split this volume into 40  $\mu\text{L}$  aliquots and sonicate the beads using a bath sonicator for 20 min with added ice to prevent the temperature from rising.
8. Add 50  $\mu\text{L}$  of HT-ABD to each aliquot. Let sit in a water bath at 37 °C for 1 h.
9. Combine all of the bead aliquots in a BSA-coated tube and then wash beads three times with 1 mL PBS. Centrifuge at 10,000  $\times g$  for 8 min in the benchtop centrifuge after each wash.
10. After the final wash, resuspend the beads in 1 mL of KMg25. Store the beads in 20  $\mu\text{L}$  aliquots, snap freeze in liquid nitrogen, and store in liquid nitrogen or in a –80 °C freezer.

### **3.7 Preparation of Bead-Coated Slides**

In the three-bead geometry, silica beads are adhered to the surface of the cover glass to act as myosin-binding pedestals. Pedestal beads are coated with nitrocellulose to aid with protein binding to the flow cell surface and to adhere the beads to the cover glass. Here, we describe the assembly of flow cells for the three-bead assay (Fig. 2):

1. Suspend silica beads in amył acetate by vigorous pipetting and vortexing. The beads should be suspended at a concentration of 200 mg/mL to give a 100× solution. This solution can be stored at 4 °C (*see Note 26*).
2. Prepare a fresh solution of beads in 0.1 % nitrocellulose by adding 1  $\mu\text{L}$  of 100× bead solution to 94  $\mu\text{L}$  amył acetate and 5  $\mu\text{L}$  2 % nitrocellulose. Pipet vigorously.
3. Spread 4  $\mu\text{L}$  of the diluted bead solution across the end of the short axis of a precleaned cover glass in a straight line (Fig. 2a).
4. Use the plastic pipet tip to spread the solution evenly over the surface of the cover glass in one continuous motion (*see Note 27*).
5. Let the coated cover glass dry for at least 30 min in a covered petri dish. Cover glasses should be stored covered and used within 48 h of coating (*see Note 28*).
6. Take a clean (non-coated) cover glass and place it on a cutting mat with the long axis of the glass parallel to the cutting mat.
7. Place pieces of double stick tape perpendicular to the long axis of the cover glass on both sides of the glass (only on the face up side). Press down the tape with a razor.
8. Use a razor to cut off the extra tape so that the remaining tape is even with the long axis of the cover glass.
9. Apply vacuum grease on the glass next to the sides of the tape using a syringe. Ensure that the lines of grease are continuous.

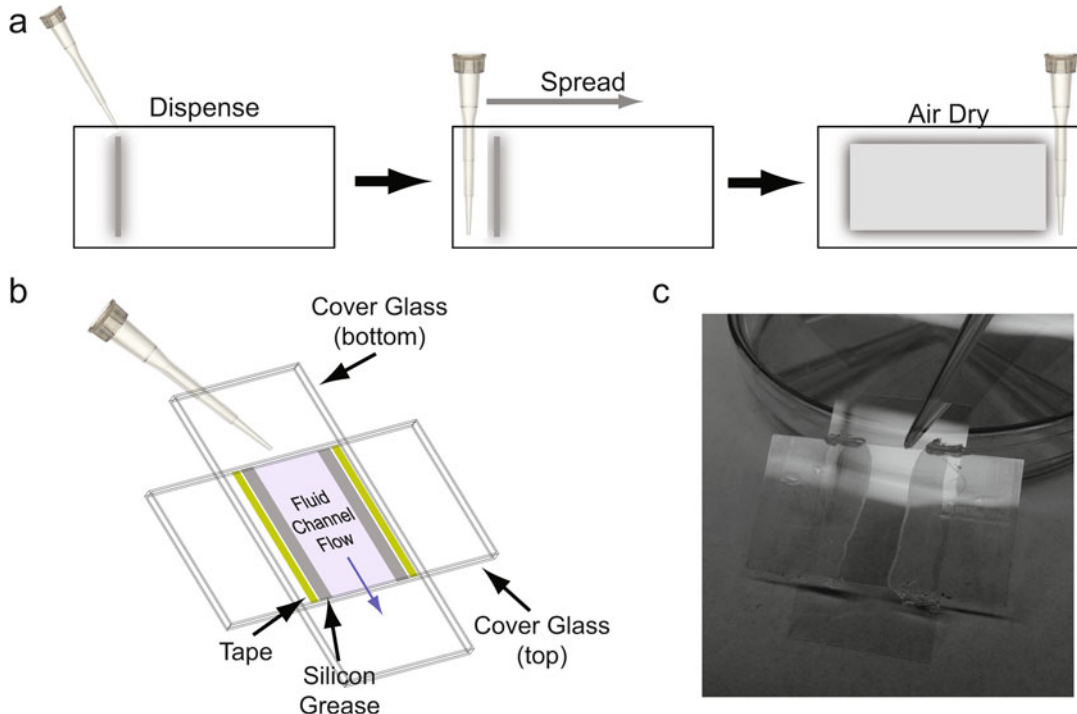


**Fig. 2** Preparation of flow chambers for optical trapping. (a) Beads in nitrocellulose are first added to one side of a clean cover glass in a straight line. A pipet tip is then used to spread the beads across the surface of the glass. Bead-coated cover glasses are dried, wet side up, in petri dishes. Pipet tips are used to elevate the cover glass (visible in 2c). (b) Fully assembled chambers are formed using double-stick tape and vacuum grease. (c) Flow chambers are filled by adding liquids to chambers that are raised on petri dishes. Liquid that has flowed through the chamber can be collected using cotton-tipped applicators or filter paper

10. Place a bead-coated cover glass orthogonal to the taped and greased glass. Ensure that the bead-coated side faces the interior of the chamber (Fig. 2b).
11. Carefully squeeze the two pieces of glass together using a razor blade.
12. Apply a thin layer of vacuum grease at the tape-glass interface so that liquids cannot go under the tape.
13. The flow chamber is now ready to be filled.

### 3.8 Filling Flow Cells for Optical Trapping

Place the flow cell at a ~30° angle by resting its the top on an elevated surface (we use the petri dish that was used for storing the cover glass after drying, Fig. 2c). Add solutions to the top of the flow cell and ensure that all liquid flows through the flow cell. If necessary, use absorbent filter paper or cotton-tipped applicators to wick the solutions at the bottom of the flow chamber while being careful not to over draw the solution through the chamber. Perform the following steps:

1. If the myosin will be attached to the surface via biotin-streptavidin linkages, add 50  $\mu\text{L}$  of the streptavidin to the flow cell surface and incubate for 5 min. If myosin will be adsorbed to the surface directly, add it now and skip steps 4 and 5.
2. Add 50  $\mu\text{L}$  1 mg/mL BSA. Let incubate 5 min. This passivates the surface and prevents nonspecific sticking of actin to the flow cell surface.
3. Repeat step 2.
4. During this incubation, prepare the myosin (with calmodulin if necessary, *see Note 16*).
5. Add 50  $\mu\text{L}$  myosin. Let incubate for 5 min.
6. During this incubation, prepare the activation buffer. Cut the tips off of the pipet tips before dispensing actin to minimize shearing of the filaments.
7. Wash the flow cell with 100  $\mu\text{L}$  KMg25.
8. Add 100  $\mu\text{L}$  activation buffer.
9. Briefly sonicate functionalized beads (<5 s) in a bath sonicator. Add ~4  $\mu\text{L}$  to the flow cell to fill ~1/3 of the flow cell (*see Note 29*).
10. Seal the flow cell with vacuum grease to prevent evaporation and flow artifacts.

### **3.9 Performance of the Three-Bead Assay**

Dumbbells are formed by stringing an actin filament between two optically trapped beads. Therefore, a dual-beam optical trap must be employed [14]. Our optical trapping instrument has been described previously [23]. In our system, a 1064 nm solid-state laser beam is split into two polarization-separated beams using a half wave plate and a polarizing beam splitter (Fig. 3). These two beams can be independently steered by acoustic optical deflectors (AODs), enabling the manipulation of the beads necessary to form bead–actin–bead dumbbells. The beams are recombined in a prism, expanded, and then relayed through the objective to the sample plane. The detection of the optically trapped beads occurs at the back-focal plane where movements of the optically trapped beads relative to the center of the optical trap are detected using polarization separated quadrant photodiodes (QPDs). Back-focal plane detection measures forces (i.e., the relative displacement of the bead from the center of the optical trap) and not the absolute position of the beads in space. To identify single-molecule interactions, perform the following steps:

1. Translate the flow chamber to the region where the beads are located. Optically trap two beads and position the traps approximately 10  $\mu\text{m}$  apart.

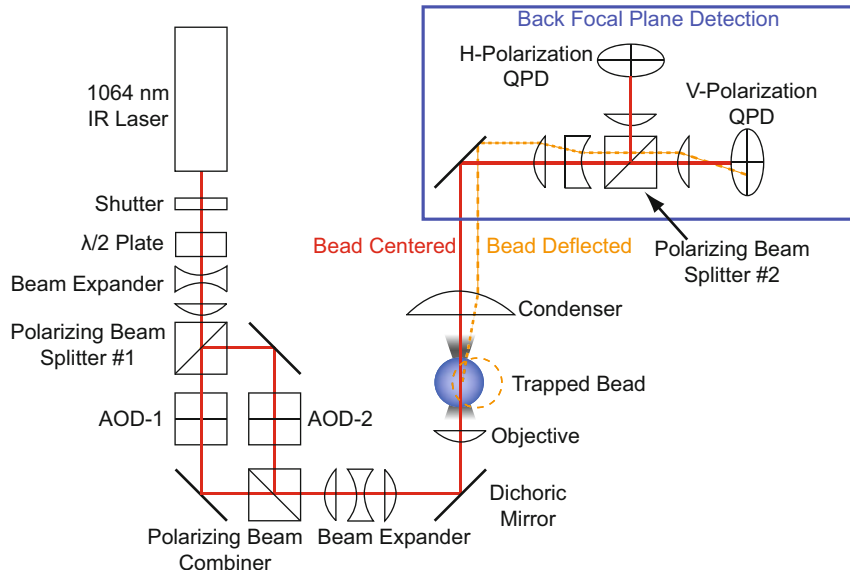


**Fig. 3** Dual-beam optical trap layout. A 1064 nm wavelength laser passes through a half-wave plate and then the beam is separated into two beam paths (i.e., two traps) by a polarizing beam splitter. The two independent beams can then be independently steered by acoustic-optical deflectors (AODs) before being recombined by a polarizing beam combiner. Diffraction-limited optical traps are formed in the focal plane by a water immersion objective lens. After interacting with the beads, the laser light is collimated by a condenser lens, and the polarized beams are collected separately on two quadrant photodiodes (QPDs). The deflection of the laser beam on the QPDs reports the magnitude of the force on the beads, which can be converted to distance by dividing by the trap stiffness. Figure is adapted from [23]

2. Translate the flow chamber to move the trapped beads away from the free beads in solution. Visualize the fluorescent actin using epifluorescence. Bring one bead into contact with the end of an actin filament that is at least 10  $\mu\text{m}$  long to attach one bead to the actin.
3. Move the stage so that the actin filament orients towards the second optically trapped bead by hydrodynamic drag. Move the unattached bead so that it just touches the end of the actin filament and becomes attached.
4. Once the actin filament is stably attached to both beads, shutter the fluorescence excitation to prevent photobleaching of the actin.
5. Move the trapped beads close to the surface of the flow cell (i.e., the surface with the pedestal beads), near the height where data will be collected. Move the trapped beads toward each other so that there is no tension applied to the actin filament.
6. Zero the position of the beams on the quadrant photodiodes.

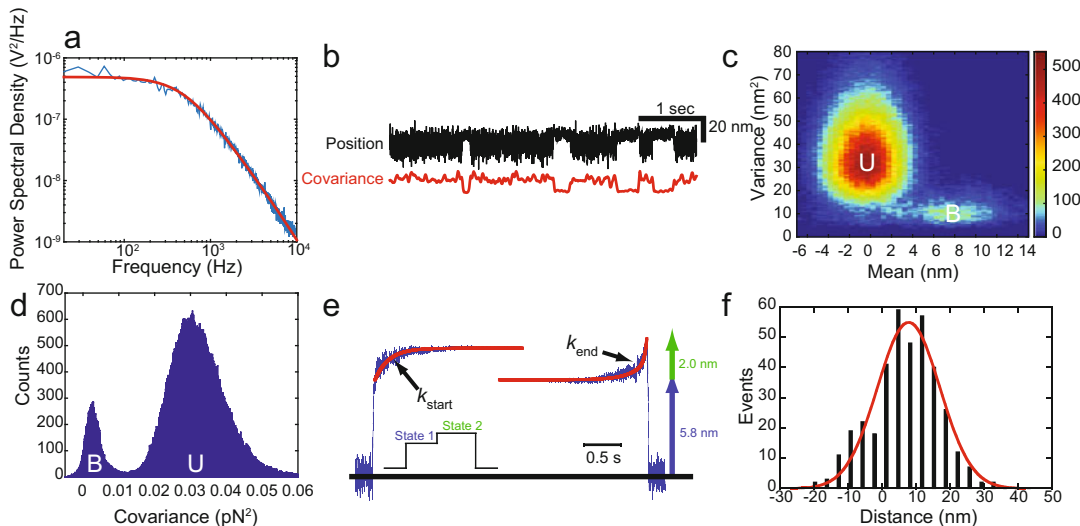


**Fig. 4** Detection and measurement of the myosin working stroke. (a) Power spectral density (PSD) of an optically trapped bead. The red line shows a fit of a Lorentzian function to the data. The corner frequency is 440 Hz and the calibration factor is 18 pN/V. (b, Upper trace) Sample data showing the position of one bead from a bead–actin–bead dumbbell as it interacts with Myo1c on an immobilized pedestal bead. (b, Lower trace) The covariance of the two optically trapped beads. Binding interactions can clearly be resolved from both the reduction in variance of the black trace and covariance of the beads (red trace) with myosin binding. (c) Mean-variance histogram of Myo1c interactions with actin was generated by calculating the mean and variance of the bead position over a sliding window. The number of events at each point is shown via a color map. There are two resolvable distributions, one with a peak of ~0 nm displacement and high variance corresponding to an unbound (U) state and a second with a peak ~8 nm with a lower variance corresponding to the actin-bound (B) state. (d) Histogram of covariance values for interactions between actin and Myo1c calculated over the entire data trace. Two peaks are clearly resolved, one with high covariance corresponding to the unbound (U) state and one with low covariance corresponding to the bound (B) state. The minimum value between the two peaks is used as a covariance threshold in selection of events. (e) Ensemble averages of the Myo1c working stroke were generated as described in Subheading 3.12. The ensemble averages reveal that the Myo1c working stroke is composed of two substeps. The rates of the increase in position in the ensemble averages can be used to measure the lifetimes of state 1 and state 2. The total working stroke measured via ensemble averaging agrees well with the value measured via mean-variance analysis. Figure is adapted from [22]. (f) Histogram of individual working stroke displacements for Myo1c selected by covariance thresholding. The data are well fit by a single Gaussian function centered at 7.8 nm, consistent with the measured values from the ensemble averages and mean-variance analysis. Figure is adapted from [22]

7. Record 5 s of data at 20 kHz, filtered at 10 kHz to measure the power spectral density (PSD) of the trapped beads (see [24], Fig. 4a). A Lorentzian function can be fit to the PSD to calculate the trap stiffness and the conversion between V and pN:

$$PSD(f) = \frac{4\gamma k_B T}{C^2 \left(1 + \frac{f^2}{f_c^2}\right)} + y_0,$$

where  $\gamma$  is the viscous drag coefficient,  $k_B$  is Boltzmann's constant,  $T$  is the temperature,  $C$  is the calibration constant for pN/V,  $f$  is the frequency,  $f_c$  is the corner frequency, and  $y_0$  is the noise floor. The viscous drag coefficient for a bead is given by  $\gamma = 6\pi\eta r$  where  $r$  is the radius of the bead and  $\eta$  is the viscosity of water. The trap stiffness,  $k$ , is related to the corner frequency by  $k = 2\pi\gamma f_c$ .

8. Move one of the optically trapped beads to put tension on the actin filament. This “pretension” is critical to ensure that the bead–actin–bead linkages are stretched and are not more compliant than the myosin–pedestal attachment. A minimum of 2–4 pN of tension should be applied to each bead (*see Note 30*).
9. Carefully bring the bead–actin–bead dumbbell over a surface-bound pedestal bead. Use the piezoelectric stage to lower the dumbbell until the force on the beads increases due to the bending of the actin filament over the pedestal bead. Move away from the surface bead using the piezoelectric stage so that the beads are no longer deflected. The actin is now properly positioned to observe myosin-binding events.
10. Scan the surface of the pedestal for myosin binding events, waiting ~30 s at each position before moving. Binding events are identified by a change in the variance of the force on both beads (Fig. 4b). If binding events are not observed, move the actin filament to a new position on the pedestal in ~20 nm increments. Repeat this scanning until actomyosin binding is identified or until the surface of the pedestal has been scanned.
11. To ensure single-molecule conditions, only 1 in 10 beads should give binding interactions. At this density, the likelihood that a given bead has more than one myosin that can interact with the actin is less than 5 % [25]. Adjust the concentration of myosin to achieve these conditions.
12. Record actomyosin interactions at 2–20 kHz depending on the length of the binding interactions and required time resolution. Data should be filtered according to the Nyquist criterion (i.e., filtered at  $1/2$  of the sampling rate).

### **3.10 Identification of Binding Interactions**

Several methods have been developed to detect actomyosin-binding interactions (Fig. 4). Most of these methods rely on changes in the Brownian motion of the optically trapped beads when myosin binds to actin (e.g., [8, 23, 26–28]). The variance in the position of the beads is reduced when myosin binds to actin. The variance can be calculated over a sliding time window and a variance threshold can be chosen to discriminate bound and unbound states [29, 30]. Alternatively, a sinusoidal waveform can be actively applied to one of the optically trapped beads and the passive response of the second bead can be measured [31, 32].

This methodology increases the temporal resolution by magnifying the difference in the variance between the bound and unbound states.

For our data analysis, we prefer using a covariance threshold since it utilizes information from both optically trapped beads [27, 33], which requires the simultaneous detection of forces on both beads (i.e., two QPDs are necessary; Fig. 3). In the absence of myosin binding, the two optically trapped beads are mechanically coupled through the actin filament. When myosin binds to actin, the coupling between the beads is reduced. The covariance, a measurement of bead motion coupling, is high in the absence of myosin binding and low when myosin binds. The covariance is calculated over a sliding time window (Fig. 4b) and a histogram of covariance values for the data trace can be calculated (Fig. 4d). The histogram should show two distributions with a peak of lower covariance corresponding to the actin-myosin bound state and a peak of higher covariance corresponding to the unbound state. The separation between the peaks will depend on the pretension of the actin filament and the stiffness of the myosin. These peaks can be used to select bound and unbound states.

To achieve good separation between the covariance distributions, there must be a measurable change in the covariance during a binding interaction over the averaging window. As such, increasing the pretension on the bead–actin–bead dumbbell will increase the separation between the peaks. Moreover, the size of the sliding window used to calculate the covariance can be increased. While increasing the size of the window will increase the separation between the covariance distributions, it will also make it very challenging to detect binding events with durations smaller than the size of the window. Therefore, when analyzing a data set, there is a tradeoff between better covariance peak separation and temporal resolution.

The selection of binding events is based on the distribution of the covariances. One could define a binding event as one in which the covariance drops below a given threshold for at a user-specified amount of time (*see Note 31*). With good separation between the bound and unbound covariance peaks, it is useful to select the minimum value between the two peaks as the covariance threshold. These selection criteria will maximize the temporal resolution, but it will result in the identification of more “false positives.” Alternatively, one could require a binding event to start when the covariance value transitions from the value of the unbound peak to the value of the bound peak and then end once the covariance transitions from the value of the bound peak to the value of the unbound peak. This methodology limits the number of detected “false positive” events, but it also reduces the temporal resolution.

### **3.11 Analysis of the Actomyosin Lifetime**

Once binding events are identified, it is possible to determine the lifetime of the bound states from the distribution of individual attachment durations. Several methods have been developed to

determine actin-attachment lifetimes, but we prefer utilizing maximum likelihood estimation (MLE) of the data [34]. MLE determines the optimum parameters of a model-dependent probability density function (PDF) from the data without the need for binning. This technique is appropriate for the analysis of single-molecule data for several reasons. Most importantly, single-molecule data are often not normally distributed, which is what is required in traditional least-squares fitting. Additionally, in experiments where the duration of short-lived binding interactions is similar to the dead time of the instrument, techniques such as averaging and fitting functions to histograms will lead to an over-estimate of the attachment lifetime. MLE does not have these limitations.

The interpretation of the data will depend on the number of processes observed. Statistical methods should be used when fitting models of increasing complexity to the data to justify model selection. When using MLE, the ratio of the log-likelihoods can be compared to a chi-squared distribution [35].

### **3.12 Measurement of the Myosin Working-Stroke Displacement**

The displacement of the bead–actin–bead dumbbell during the myosin working stroke is often of the same magnitude as the variance in bead position due to thermally driven motions of the dumbbell. Therefore, determining the magnitude of the myosin-driven displacement is not trivial. However, several methods have been utilized to measure this displacement, and some of these techniques have been successful in detecting and quantifying working-stroke sub-steps as has been seen in some myosin isoforms [10, 22, 32, 33, 36, 37]. Here, we describe three of these techniques.

1. Mean-variance analysis [26]. When myosin binds to actin and undergoes its working stroke, it causes a change in both the mean (due to the working stroke displacement) and variance (due to actin attachment) of the force/position of the optically trapped beads. To detect these changes, a sliding time window is used to calculate the mean and variance of the bead position/force over the entire data trace. Two distinct populations appear, one with no displacement and a higher variance corresponding to the unbound state and one with a finite displacement and a lower variance corresponding to the bound state (Fig. 4). By changing the width of the sliding time-window, the mean attachment duration can be calculated. This method is straightforward, since it does not require the investigator to resolve individual interactions. However, the method does not allow determination of the distribution of displacements from individual interactions.
2. Quantification of displacements of individual binding interactions. After selecting individual binding interactions, the average position of the trapped beads immediately before and

during actomyosin interactions (as determined in Subheading 3.11) can be calculated to generate a histogram of displacements (Fig. 4f). The displacement distribution can be fit to an appropriate model, which in most published studies has been a Gaussian function. Because the average displacement is reported, substeps are not considered, which can result in incorrect measurements of the final displacement. For example, if there is a substep with a large displacement within the last milliseconds of a 1 s interaction, the overall displacement will be substantially underestimated due to averaging. Finally, bias in the position at which myosin binds trapped actin filaments may alter the observed working-stroke displacement [38].

3. Post-synchronization of individual interactions (i.e., ensemble averaging) [22, 32, 33, 36, 37, 39–41]. Post-synchronized ensembles of single molecule events are created by temporally lining up many interactions at their start or end points and then averaging the data (Fig. 4e). The averaged traces reveal the lifetimes of the substates of the molecules leading up to and following the synchronized transition, allowing information hidden in the noisy single trajectories to be analyzed [39]. Post-synchronization is well suited for examining substep displacements and the kinetics of the working stroke, as shown in pioneering experiments [32, 37]. A myosin with a two-substep working stroke will show a displacement increase after the initial attachment in the averages synchronized at myosin attachment, followed by an exponential increase in force that reports the lifetime of the first, lower displacement state (State 1, Fig. 4e). For a two-step displacement, ensemble averages created by synchronizing interactions at their endpoints will show an exponential increase in displacement to the level of the final displacement, with a rate equal to the inverse of the lifetime of the state populated before detachment (State 2, Fig. 4e). This technique is very powerful since it allows one to examine both the kinetics and displacements of the myosin working stroke. However, correctly identifying the starting and ending points of interactions is crucial for the averages to be useful. The reader is directed to kinetic tools that have been developed to analyze post-synchronized traces [39].

### **3.13 Measurement of Myosin's Force-Dependent Properties**

Myosins adjust their motile properties in response to mechanical forces on the lever arm, and several optical trapping techniques using the three-bead geometry have been used to measure the effects of these loads on actomyosin attachment durations. Some techniques use active force- or position-feedback loops to apply loads to myosin by steering the trapping beam using an acousto-optic deflector (AOD; Fig. 3). Other techniques apply forces without active feedback. Selected examples of these techniques are discussed below.

Active force feedback upon engagement of actomyosin relies on detecting a change in trap motion to identify binding events (e.g., variance) [8]. Once a detection threshold is crossed for a given amount of time, the feedback is engaged. Active feedback loops can work by increasing the trap stiffness or moving the trap once a binding interaction is identified. Drawbacks of these techniques are that the feedback loops are necessarily slower since calculations must be done before engaging the feedback loop, and one must account for nonlinear series compliances in the bead–actin attachments. Techniques to speed up the feedback loops have been implemented where the bead–actin–bead dumbbell is oscillated, increasing the ability to distinguish binding interactions and activate the feedback loop [37, 42].

The isometric optical clamp is an active feedback loop developed by the Goldman and Shuman Laboratories [23, 43]. This technique uses an active feedback loop in which one of the optically trapped beads (motor bead) is actively moved to maintain the other optically trapped bead (transducer bead) at a constant position. This is achieved using an AOD to steer the motor bead. This technique has the advantage that the feedback is always engaged and thus there is not a delay time beyond the time-constant of the feedback loop itself. Also, one need not correct for system compliances since the position of the transducer bead is held constant. The procedure for collecting data using the isometric optical clamp is similar to the procedure used to collect data in the absence of feedback. Before an experiment, the time constant of the feedback loop is adjusted to the desired value by forming a bead–actin–bead dumbbell, applying a square wave to the transducer bead, and then watching the time response of the motor bead. After the feedback loop time constant is set and a single active myosin on the surface is identified, the feedback loop is engaged and data are collected. Actin filaments have polarity and thus the feedback loop direction might need to be reversed to ensure that the applied forces oppose the myosin’s working stroke. Binding interactions are identified post acquisition using the covariance thresholding described earlier, and the attachment durations and the force on the myosin (exerted by the motor bead) can be measured.

The Spudich Laboratory implemented a novel method for measuring the force dependence of myosin interactions in which the stage is oscillated during an actomyosin attachment, resulting in the force of the stage oscillations being transferred to the myosin and the optically trapped beads [44]. This technique, dubbed harmonic force spectroscopy, has the advantage that the force is applied to the myosin rapidly, no feedback loops are required, and forces are not applied by expensive and difficult-to-align optical components. This method is well suited for single force-dependent transitions that limit detachment over the range of all probed forces. However, this technique has the limitation that analysis of

complex force-dependent processes will not be straightforward. For example this technique would not have allowed for the determination of the force-dependent mechanism of Myo1c or Myo6 [22, 45].

An ultra-fast feedback system was developed by the Capitanio Laboratory to enable the detection of binding events with sub-millisecond resolution [28]. In this setup, force is applied to one of the optically trapped beads, causing it to move at a constant velocity when no myosin is bound. When myosin binds, the force that was applied to the first bead is rapidly transferred to the myosin. By observing changes in the velocity of the beads, one can determine, with sub-millisecond resolution, when binding occurs. This technique gives excellent temporal resolution [28], but it is technically challenging to implement.

### **3.14 Analysis of Force-Dependent Data**

To analyze the force-dependence of actomyosin detachment and attachment durations are measured over a range of forces. According to Arrhenius transition theory, force affects the rate of a transition by [46]:

$$k(F) = k_0 \cdot e^{-\frac{Fd}{k_B T}}, \quad (1)$$

where  $k_0$  is the rate in the absence of force,  $F$  is the force,  $k_B$  is Boltzmann's constant,  $T$  is the temperature, and  $d$  is the distance to the force-dependent transition state, also known as the distance parameter. Note that  $k(F)$  changes exponentially with the vector quantity  $d$  (i.e., it depends on the direction of the applied force). A larger  $d$  is indicative of a more force-sensitive transition. The probability density function of the attachment durations is given by:

$$\text{PDF} = k(F) \cdot e^{-k(F)t}. \quad (2)$$

As a consequence, if a single transition limits actomyosin dissociation at a given force, the distribution of attachment durations will be exponentially distributed at each force.

For data best fit by a simple exponential function, the reciprocal value of the mean attachment duration will equal the characteristic rate. Therefore, one method of analyzing the data is to plot the mean detachment rate at each force as a function of force and then fit Eq. 1 to the data using least-squares fitting to obtain the force dependence of the detachment rate. If the data are not exponentially distributed, this methodology will not work since the reciprocal value of the mean attachment duration will not equal the characteristic rate. There are two important situations where the data will not be exponentially distributed.

1. As described earlier, there will be a minimum observable attachment duration due to the instrumental dead time and as such, some short-lived binding events will be missed.

Missing short-lived binding events will make the reciprocal value of the mean attachment duration appear slower than the true rate.

2. While Eq. 1 describes how force will affect the rate of a given transition, a single transition may not limit actomyosin dissociation, leading to a more complicated behavior. For example, in Myo1c and Myo1b, one transition limits detachment at low forces and a different transition limits detachment at higher forces [22, 33]. There will exist a set of forces where the rates of these transitions are similar and the net detachment rate will not be exponentially distributed, skewing this analysis.

As described earlier (Subheading 3.11), these caveats mean that simple least-squares fitting of the mean values will not give the correct answer and MLE must be used [34, 47]. To determine the errors in the MLE fitting and the sensitivity of the data to outliers, bootstrapping simulations can be used. In this method, a data set with  $N$  points is randomly resampled to generate a new data set with  $N$  points and then MLE is used to determine the values of the fitting parameters. By conducting a large number of simulations, it is possible to determine the uncertainty in each of the fit parameters.

### **3.15 Measurement of Myosin's Stiffness**

The abilities of myosin to generate and sense forces depend on the stiffness of the myosin. Several methodologies have been developed to measure myosin's stiffness using the three-bead geometry. Here, we discuss selected methods. In one technique, a sinusoidal oscillation is applied to one bead and the passive response of the second optically trapped bead is recorded [31]. In the absence of myosin binding, the passive bead will follow the actively driven bead. When myosin binds to actin, the myosin acts as an additional elastic element in the system, damping the response of the passive bead to the active oscillations. By measuring the force on the actively driven bead and the position response of the passive bead, it is possible to measure the stiffness of the myosin. A method developed by the Sleep Laboratory uses a slow triangular wave applied to both optically trapped beads [48]. When the myosin binds to the actin, the myosin is stretched and a force–extension curve can be generated. A similar technique was applied to study muscle myosin-II filaments and the actin extension was corrected by measuring the position of a quantum dot covalently attached to the actin [49]. In another method, the passive response of the beads to Brownian motion in the presence and absence of myosin is measured [27, 48]. As described earlier, when myosin binds to actin, the covariance between the two optically trapped beads is reduced in proportion to the stiffness of the myosin. The correlation coefficient or the cross power spectral densities can be calculated to give the stiffness of the myosin.

---

## 4 Notes

1. Tissue can be obtained from fresh rabbit skeletal muscle or from commercially available cryoground tissue (Pel-Freez Biologicals) [50].
2. Buffer A can be prepared in a 100× stock and stored at –20 °C. If preparing a 100× stock, omit the calcium chloride from the stock and add the calcium chloride when preparing the 1× solution.
3. We find the glass-ball-type Dounce homogenizers to be preferable to Teflon-coated homogenizers.
4. This buffer can be prepared as a 5× stock and frozen at –20 °C.
5. This solution can be aliquoted and frozen at –20 °C.
6. NEM is highly reactive, so it should be stored desiccated, and aqueous solutions should be made immediately before use.
7. This myosin can be purified from rabbit back muscle using established protocols [51].
8. Biotinylated actin can be purchased from commercial sources (Cytoskeleton AB07) or prepared from purified actin [52].
9. This should be stored at –20 °C in an amber microcentrifuge tube.
10. PMSF should be prepared fresh in ethanol.
11. This reagent can be stored as 100 mM in DMSO at –80 °C.
12. This is only necessary if using streptavidin to attach biotinylated myosin to the coverslip surface.
13. As in any kinetic experiment, the concentration of ATP should be checked spectrophotometrically by measuring the absorbance at 259 nm. The extinction coefficient for ATP is equal to  $15,400 \text{ M}^{-1} \text{ cm}^{-1}$ . This solution can be frozen at –20 °C. ATP should not be stored with magnesium since magnesium accelerates its hydrolysis.
14. This is a 100× stock that can be frozen at –20 °C in 100 µL aliquots.
15. This should be stored at –20 °C in an amber microcentrifuge tube.
16. For some myosins, weak-binding light chains (e.g., calmodulin) will need to be included at an appropriate concentration [53].
17. Prepare this solution immediately before loading into the flow cell, since the myosin will stick to the tube and the effective concentration will change with longer incubations.

18. This buffer should be prepared right before loading the flow cell. The concentration of actin should be checked before loading the flow cell by examining the fluorescence of individual filaments. There should be approximately one filament per  $50 \times 50 \mu\text{m}$  field of view.
19. All steps of this protocol should be conducted at  $4^\circ\text{C}$  and in a cold room if possible.
20. Filter paper or cheesecloth can also be placed on top of the powder to prevent it from blowing away or becoming contaminated.
21. 0.5 g of acetone powder will produce more than enough actin for 1 month of experiments.
22. When placed under tension in the optical trapping assay, actin will sometimes break. The frequency of breakage increases with the age of the actin. If breaking is problematic, prepare fresh actin.
23. The amount of NEM added may need to be adjusted depending on the age of the myosin. Older ( $>6$  months) myosin preparations lose activity and may require less NEM to render the myosin inactive.
24. BSA-coating minimizes adsorption of beads to the tubes.
25. The percentage of biotinylated actin can be optimized by the experimenter, as 25 % is generally the upper limit.
26. It is difficult to get a homogenous suspension, and vigorous mixing is required. Over time, the amyl acetate from the stock is lost due to its low vapor pressure and additional amyl acetate can be added.
27. Always check to see whether the coating looks uniform. If there are bare patches on the glass or if the liquid is not evenly spread, the cover glass should be discarded.
28. We tape plastic pipet tips to the bottom of a petri dish and then let the bead-coated cover glass dry while resting at an angle on the tip.
29. It is best to transfer a small volume of beads to a fresh tube before sonicating to avoid sonicating the stock suspension.
30. Higher pretensions increase the temporal resolution but increase the probability of actin breakage.
31. In our experiments with myosin-I isoforms, this is usually set to 10 ms.

## Acknowledgements

The authors wish to acknowledge grants from the National Institutes of Health (R01GM057247 and P01GM087253 to E.M.O. and R00HL123623 to M.J.G.).

## References

1. Gray KA, Yates B, Seal RL, Wright MW, Bruford EA (2015) Genenames.org: the HGNC resources in 2015. *Nucleic Acids Res* 43:D1079–D1085
2. Krendel M, Mooseker MS (2005) Myosins: tails (and heads) of functional diversity. *Physiology (Bethesda)* 20:239–251
3. Hartman MA, Spudich JA (2012) The myosin superfamily at a glance. *J Cell Sci* 125:1627–1632
4. De La Cruz EM, Ostap EM (2004) Relating biochemistry and function in the myosin superfamily. *Curr Opin Cell Biol* 16:61–67
5. Redowicz MJ (2002) Myosins and pathology: genetics and biology. *Acta Biochim Pol* 49:789–804
6. Elting MW, Spudich JA (2012) Future challenges in single-molecule fluorescence and laser trap approaches to studies of molecular motors. *Dev Cell* 23:1084–1091
7. Batters C, Veigel C, Homsher E, Sellers JR (2014) To understand muscle you must take it apart. *Front Physiol* 5:90
8. Finer JT, Simmons RM, Spudich JA (1994) Single myosin molecule mechanics: piconewton forces and nanometre steps. *Nature* 368:113–119
9. Altman D, Sweeney HL, Spudich JA (2004) The mechanism of myosin VI translocation and its load-induced anchoring. *Cell* 116:737–749
10. Takagi Y, Farrow RE, Billington N, Nagy A, Batters C, Yang Y, Sellers JR, Molloy JE (2014) Myosin-10 produces its power-stroke in two phases and moves processively along a single actin filament under low load. *Proc Natl Acad Sci U S A* 111:E1833–E1842
11. Nishizaka T, Miyata H, Yoshikawa H, Ishiwata S, Kinosita K Jr (1995) Unbinding force of a single motor molecule of muscle measured using optical tweezers. *Nature* 377:251–254
12. Kishino A, Yanagida T (1988) Force measurements by micromanipulation of a single actin filament by glass needles. *Nature* 334:74–76
13. Kitamura K, Tokunaga M, Iwane AH, Yanagida T (1999) A single myosin head moves along an actin filament with regular steps of 5.3 nanometres. *Nature* 397:129–134
14. Sung J, Sivaramakrishnan S, Dunn AR, Spudich JA (2010) Single-molecule dual-beam optical trap analysis of protein structure and function. *Methods Enzymol* 475:321–375
15. Srikantham R, Winkelmann DA (1999) Myosin II folding is mediated by a molecular chaperonin. *J Biol Chem* 274:27265–27273
16. Resnick DI, Deacon JC, Warrick HM, Spudich JA, Leinwand LA (2010) Functional diversity among a family of human skeletal muscle myosin motors. *Proc Natl Acad Sci U S A* 107:1053–1058
17. Deacon JC, Bloemink MJ, Rezavandi H, Geeves MA, Leinwand LA (2012) Identification of functional differences between recombinant human alpha and beta cardiac myosin motors. *Cell Mol Life Sci* 69:2261–2277
18. Manstein DJ, Ruppel KM, Spudich JA (1989) Expression and characterization of a functional myosin head fragment in Dictyostelium discoideum. *Science* 246:656–658
19. Sweeney HL, Straceski AJ, Leinwand LA, Tikunov BA, Faust L (1994) Heterologous expression of a cardiomyopathic myosin that is defective in its actin interaction. *J Biol Chem* 269:1603–1605
20. Spudich JA, Watt S (1971) The regulation of rabbit skeletal muscle contraction. I. Biochemical studies of the interaction of the tropomyosin-troponin complex with actin and the proteolytic fragments of myosin. *J Biol Chem* 246:4866–4871
21. Kaminer B, Bell AL (1966) Myosin filamentogenesis: effects of pH and ionic concentration. *J Mol Biol* 20:391–401
22. Greenberg MJ, Lin T, Goldman YE, Shuman H, Ostap EM (2012) Myosin IC generates power over a range of loads via a new tension-sensing mechanism. *Proc Natl Acad Sci U S A* 109:E2433–E2440
23. Takagi Y, Homsher EE, Goldman YE, Shuman H (2006) Force generation in single conventional actomyosin complexes under high dynamic load. *Biophys J* 90:1295–1307

24. Svoboda K, Block SM (1994) Biological applications of optical forces. *Annu Rev Biophys Biomol Struct* 23:247–285
25. Norstrom MF, Smithback PA, Rock RS (2010) Unconventional processive mechanics of non-muscle myosin IIB. *J Biol Chem* 285:26326–26334
26. Guilford WH, Dupuis DE, Kennedy G, Wu J, Patlak JB, Warshaw DM (1997) Smooth muscle and skeletal muscle myosins produce similar unitary forces and displacements in the laser trap. *Biophys J* 72:1006–1021
27. Mehta AD, Finer JT, Spudich JA (1997) Detection of single-molecule interactions using correlated thermal diffusion. *Proc Natl Acad Sci U S A* 94:7927–7931
28. Capitanio M, Canepari M, Maffei M, Benvenuti D, Monico C, Vanzi F, Bottinelli R, Pavone FS (2012) Ultrafast force-clamp spectroscopy of single molecules reveals load dependence of myosin working stroke. *Nat Methods* 9:1013–1019
29. Molloy JE, Burns JE, Kendrick-Jones J, Tregear RT, White DC (1995) Movement and force produced by a single myosin head. *Nature* 378:209–212
30. Knight AE, Veigel C, Chambers C, Molloy JE (2001) Analysis of single-molecule mechanical recordings: application to acto-myosin interactions. *Prog Biophys Mol Biol* 77:45–72
31. Veigel C, Bartoo ML, White DC, Sparrow JC, Molloy JE (1998) The stiffness of rabbit skeletal actomyosin cross-bridges determined with an optical tweezers transducer. *Biophys J* 75:1424–1438
32. Veigel C, Coluccio LM, Jontes JD, Sparrow JC, Milligan RA, Molloy JE (1999) The motor protein myosin-I produces its working stroke in two steps. *Nature* 398:530–533
33. Laakso JM, Lewis JH, Shuman H, Ostap EM (2008) Myosin I can act as a molecular force sensor. *Science* 321:133–136
34. Press WH (1992) Numerical recipes in C: the art of scientific computing. Cambridge University Press, Cambridge
35. Wilks SS (1938) The large-sample distribution of the likelihood ratio for testing composite hypotheses. *Ann Math Stat* 9:60–62
36. Veigel C, Wang F, Bartoo ML, Sellers JR, Molloy JE (2002) The gated gait of the processive molecular motor, myosin V. *Nat Cell Biol* 4:59–65
37. Veigel C, Molloy JE, Schmitz S, Kendrick-Jones J (2003) Load-dependent kinetics of force production by smooth muscle myosin measured with optical tweezers. *Nat Cell Biol* 5:980–986
38. Sleep J, Lewalle A, Smith D (2006) Reconciling the working strokes of a single head of skeletal muscle myosin estimated from laser-trap experiments and crystal structures. *Proc Natl Acad Sci U S A* 103:1278–1282
39. Chen C, Greenberg MJ, Laakso JM, Ostap EM, Goldman YE, Shuman H (2012) Kinetic schemes for post-synchronized single molecule dynamics. *Biophys J* 102:L23–L25
40. Laakso JM, Lewis JH, Shuman H, Ostap EM (2010) Control of myosin-I force sensing by alternative splicing. *Proc Natl Acad Sci U S A* 107:698–702
41. Lewis JH, Greenberg MJ, Laakso JM, Shuman H, Ostap EM (2012) Calcium regulation of myosin-I tension sensing. *Biophys J* 102:2799–2807
42. Kad NM, Patlak JB, Fagnant PM, Trybus KM, Warshaw DM (2007) Mutation of a conserved glycine in the SH1-SH2 helix affects the load-dependent kinetics of myosin. *Biophys J* 92:1623–1631
43. Takagi Y, Shuman H, Goldman YE (2004) Coupling between phosphate release and force generation in muscle actomyosin. *Phil Trans Roy Soc Lond Ser B Biol Sci* 359:1913–1920
44. Sung J, Nag S, Mortensen KI, Vestergaard CL, Sutton S, Ruppel K, Flyvbjerg H, Spudich JA (2015) Harmonic force spectroscopy measures load-dependent kinetics of individual human beta-cardiac myosin molecules. *Nat Commun* 6:7931
45. Sweeney HL, Park H, Zong AB, Yang Z, Selvin PR, Rosenfeld SS (2007) How myosin VI coordinates its heads during processive movement. *EMBO J* 26:2682–2692
46. Bell GI (1978) Models for the specific adhesion of cells to cells. *Science* 200:618–627
47. Capitanio M, Canepari M, Cacciafesta P, Lombardi V, Cicchi R, Maffei M, Pavone FS, Bottinelli R (2006) Two independent mechanical events in the interaction cycle of skeletal muscle myosin with actin. *Proc Natl Acad Sci U S A* 103:87–92
48. Lewalle A, Steffen W, Stevenson O, Ouyang Z, Sleep J (2008) Single-molecule measurement of the stiffness of the rigor myosin head. *Biophys J* 94:2160–2169
49. Kaya M, Higuchi H (2013) Stiffness, working stroke, and force of single-myosin molecules in skeletal muscle: elucidation of these mechanical properties via nonlinear elasticity evaluation. *Cell Mol Life Sci* 70:4275–4292
50. Greenberg MJ, Shuman H, Ostap EM (2014) Inherent force-dependent properties of beta-cardiac myosin contribute to the force-velocity

- relationship of cardiac muscle. *Biophys J* 107: L41–L44
51. Kielley WW, Bradley LB (1956) The relationship between sulfhydryl groups and the activation of myosin adenosinetriphosphatase. *J Biol Chem* 218:653–659
52. Rock RS, Rief M, Mehta AD, Spudich JA (2000) In vitro assays of processive myosin motors. *Methods* 22:373–381
53. Lin T, Tang N, Ostap EM (2005) Biochemical and motile properties of Myo1b splice isoforms. *J Biol Chem* 280:41562–41567

# **Part III**

## **Quantitative Optical Tweezers Studies In Vivo**

# Chapter 20

## Quantifying Force and Viscoelasticity Inside Living Cells Using an Active–Passive Calibrated Optical Trap

Christine M. Ritter, Josep Mas, Lene Oddershede,  
and Kirstine Berg-Sørensen

### Abstract

As described in the previous chapters, optical tweezers have become a tool of precision for in vitro single-molecule investigations, where the single molecule of interest most often is studied in purified form in an experimental assay with a well-controlled fluidic environment. A well-controlled fluidic environment implies that the physical properties of the liquid, most notably the viscosity, are known and the fluidic environment can, for calibrational purposes, be treated as a simple liquid.

In vivo, however, optical tweezers have primarily been used as a tool of manipulation and not so often for precise quantitative force measurements, due to the unknown value of the spring constant of the optical trap formed within the cell’s viscoelastic cytoplasm. Here, we describe a method for utilizing optical tweezers for quantitative in vivo force measurements. The experimental protocol and the protocol for data analysis rely on two types of experiments, passive observation of the thermal motion of a trapped object inside a living cell, followed by observations of the response of the trapped object when subject to controlled oscillations of the optical trap. One advantage of this calibration method is that the size and refractive properties of the trapped object and the viscoelastic properties of its environment need not be known. We explain the protocol and demonstrate its use with experiments of trapped granules inside live *S. pombe* cells.

**Key words** Optical tweezers, Viscoelasticity, Cytoplasm, In vivo, Force measurements, Spring constant

---

### 1 Introduction

Optical tweezers have been widely used in the field of biophysics in the past decades to perform quantitative force measurements on biomolecules [1–4]. Most of these force measurements were performed in vitro, where the experimental conditions can be controlled. Sophisticated calibration procedures for in vitro experiments, where the object of interest is in a purely viscous environment, have been developed [5–8]. One standard procedure is the power spectrum analysis [5]. In this calibration procedure,

the Brownian motion of a particle trapped in the quasi-harmonic potential of optical tweezers is interpreted by its power spectrum.

In vitro measurements of single molecules have given us a better understanding of how these molecules work. To get an even better understanding of their role within the cell, measurements in the natural environment of these molecules are necessary [9–13]. Optical tweezers can be used to trap organelles or internalized handles inside living cells or even entire cells without disrupting the cell wall [14–17]. Choosing an infrared or near-infrared laser for the optical tweezers can minimize the amount of energy deposited in a cell which reduces physiological damage and the effect of heating [18–20]. Other commonly used techniques for in vivo measurements are atomic force microscopy [21] and magnetic tweezers [22]. Atomic force microscopy, however, cannot reach within the cell without penetrating the cell wall and magnetic tweezers rely on the internalization of magnetic handles whereas optical tweezers can trap endogenous objects.

The complex structure of the cell and its nontrivial diffractive properties make it difficult to perform precise force measurements with optical tweezers within living cells [14, 23]. Also, the lack of knowledge of the size and refractive index of the trapped particle renders most methods inadequate [24]. For instance, as the Brownian motion of a particle in such a viscoelastic environment is different from that within a viscous environment [25–27], the power spectrum analysis is not directly applicable inside a living cell.

One proposed way to retrieve the optical force acting on a trapped particle within a cell is by detecting light momentum changes [28–31]. However, using this method, the spring constant characterizing the strength of the optical trap, the position of the particle and the viscoelastic properties of the cytoplasm cannot be deduced. It has also been suggested to calibrate optical tweezers within a cell with resort to a model for the viscoelastic response of the cell's cytoplasm. This procedure thus relies on specific assumptions about the cytoplasm. It is described in ref. [32] and in the subsequent chapter of this book.

The active–passive calibration procedure presented here is based on the fluctuation-dissipation theorem (FDT) and the only assumption regarding the cytoplasm is that it can be treated as a viscoelastic medium. The calibration procedure assumes that the response of a system in equilibrium to small externally driven perturbations is the same as its response to internal fluctuations. In other words, the procedure is based on the assumption that the amplitude of the driving motion is at the order of magnitude of the Brownian motion occurring in the equilibrium state. For calibration purposes, perturbations can be caused by oscillating the sample with respect to the trapping laser, either by moving the sample stage or by oscillating the trapping laser itself [33–35]. A more detailed theoretical background can be found in refs. [36–38].

This calibration method was proposed in ref. [38] and demonstrated in actin networks and yeast cells in refs. [36, 37]. The method can be applied to any viscoelastic medium without any prior knowledge or assumptions about the medium's viscoelasticity and with no need for external calibration [39, 40]. In addition, no prior knowledge of the shape and size of the trapped particle is necessary. The combination of active and passive measurements for quantitative *in vivo* measurements has been proposed and applied in refs. [6, 34, 38, 41–44]. By combining active and passive measurements, the absolute value of the trap's spring constant for every trapped object in the cell's cytoplasm can be determined. Additionally, the viscoelastic properties of the medium can be inferred from this calibration procedure, as it also allows quantifying the viscoelastic moduli.

## 2 Materials

### 2.1 Experimental Setup

1. Infrared laser for trapping, here: 1064 nm Nd:YVO<sub>4</sub> laser (5 W, Spectra Physics BL-106C).
2. Optical microscope with high NA objective, here: Leica DMRB with Leica HCX PL APO 100×, NA = 1.4, OIL CS.
3. Quadrant photodiode (QPD), here: S5981, Hamamatsu.
4. CCD camera, here: A11 KODAK Pike, 60 Hz.
5. Piezo-stage for stage-oscillation, here: Physik Instrumente P-517.3CL.
6. PC with rapid data acquisition card, here: NI PCI-6040E.

### 2.2 Cell Sample

Any type of live cells with naturally occurring organelles, like lipid granules, that may be trapped by an optical trap due to a higher refractive index of the organelle than of the surrounding cytoplasm. In the case described here, SPK10 wild type *S. pombe* cells were used.

### 2.3 Cell Growth

1. YPD broth: Common liquid growth medium for yeast culture. If purchased in powder form, follow instructions to dissolve in water.
2. AA medium: Medium containing 1.7 g Bacto yeast nitrogen base without amino acids or ammonium sulfate, 5 g ammonium sulfate, 2 g drop-out mix, 450 ml H<sub>2</sub>O. Autoclave before adding 50 ml 40 % glucose. Drop-out mix: 0.4 g para-amino benzoic acid, 4 g L-leucine, 2 g each of needed amino acids (L-alanine, L-arginine, L-asparagine, L-cysteine, L-glutamine, L-glutamic acid, L-glycine, L-histidine, L-isoleucine, L-lysine, L-methionine, L-phenylalanine, L-proline, L-serine, L-threonine, L-tryptophan, L-tyrosine, L-valine, myo-inositol, adenine, uracil).

3. AA minus leucine agar plates: Add 20 g Bacto agar in 500 ml H<sub>2</sub>O to AA medium not containing L-leucine and pour into plates.

## 2.4 Sample Chamber

1. Sterile and clean slides (25 × 60 mm, thickness 1 mm) and coverslips (18 × 18 mm, thickness 0.17 mm).
2. 100 % ethanol.
3. millipore H<sub>2</sub>O.
4. Poly-L-lysine: Use high molecular weight (MW) poly-L-lysine (>300 kDa), as high MW molecules have more attachment sites.
5. Vacuum grease.
6. Double-sided scotch tape: optional.
7. Mechanical tweezers.
8. Syringe.
9. Petri dish.

## 3 Methods

### 3.1 Optical Tweezers Setup

The presented calibration procedure can be utilized by a great variety of optical tweezers setups. It is, however, necessary to be able to make fast and precise position measurements, which are most conveniently done by a photodiode, and to oscillate either the laser or the sample stage. In the experiments from which data are shown in this chapter, the optical tweezers setup was implemented by directing the infrared laser into an inverted microscope (Fig. 1); further details for this particular setup can be found in ref. [45]. Briefly, the laser is focused into a diffraction-limited spot onto the sample plane through an oil immersion objective. After passing through the sample, the laser light is captured by a condenser and projected onto a QPD placed conjugate to the condenser's back-focal plane, allowing for high-precision positional detection [46, 47]. A CCD camera, mounted on the side port of the microscope, establishes a second, bright-field based detection system to record movements of sufficiently optically dense objects in the sample plane (Fig. 1).

The sample is mounted on a piezo-electric translation stage, which can oscillate the sample. The voltage signals providing the positions of the stage and the voltage signals of the QPD, generated by the light scattered by a trapped particle, are read out simultaneously by an acquisition card (*see Note 1*). Alternatively, the particle of interest can be oscillated by using an acousto-optic deflector (AOD) instead of a Piezo-stage [34]. This can be accomplished by placing an AOD in the beam path before the laser enters the microscope at a plane conjugate telecentric to the back-focal plan of the microscope objective (Fig. 1) (*see Notes 2 and 3*).

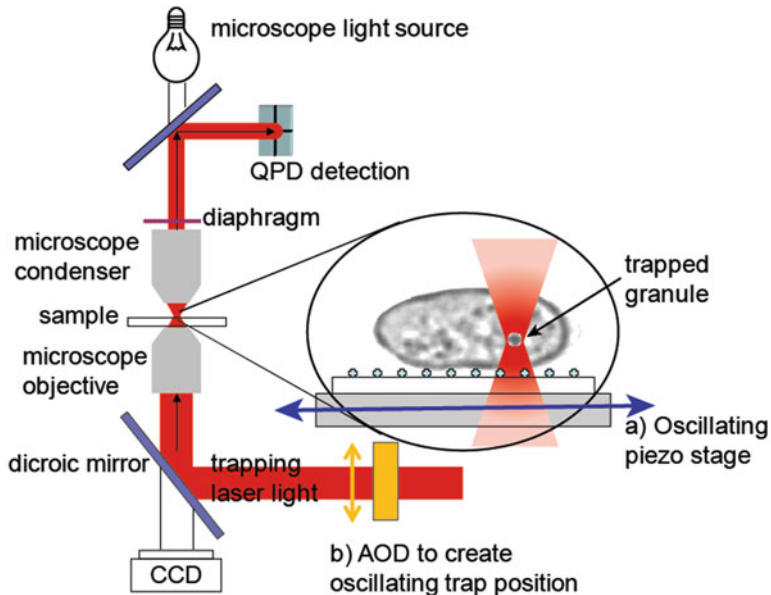


**Fig. 1** Experimental setup: a 1064 nm laser is focused through an oil immersion objective into a microscope to form the optical tweezers. The movement of a lipid granule inside a living *S. pombe* cell is recorded by a QPD placed conjugate to the back-focal plane of the condenser or by the use of a CCD camera. The sample is mounted on a piezo stage, which is used to position the cell of interest in the focus and to oscillate the sample in a controlled fashion. Alternatively, the trapped granule can be oscillated with respect to the sample chamber by placing an AOD in the beam path before the laser enters the objective lens

### 3.2 Cell Sample Preparation

1. Culture SPK10 wild type *S. pombe* cells on AA minus leucine agar plates at 30° for 18–20 h and store them afterwards at 4 °C.
2. The day before the cells are needed for experiments, transfer a fraction of the cells from the plates to liquid YPD medium and grow them in a shaking bath overnight at 30°.
3. Centrifuge cells for 5 min at 1764 ×  $\varphi$  (5000 rpm). (i.e. 0.35 g per rpm).
4. Remove the supernatant.
5. Resuspend cells in AA medium with a dilution factor of 10–100. Use AA medium instead of the YPD medium during experiments, as the YPD medium interferes with the poly-L-lysine coating.

### 3.3 Perfusion Chamber

1. Dissolve poly-L-lysine in millipore H<sub>2</sub>O (to a final concentration of 1 mg/ml).
2. Place a clean and sterile coverslip with mechanical tweezers into a petri dish and add 50  $\mu$ l of poly-L-lysine solution on top. Poly-L-lysine promotes the adhesion of the cells to the glass surface

by enhancing electrostatic interaction between its positively charged sites and the negatively charged ions of the cell membrane.

3. Rock coverslips for 30 min at room temperature.
4. Wash coverslip at least ten times with millipore H<sub>2</sub>O to remove any free polyamino acids, which can be cytotoxic.
5. Rinse a slide with absolute ethanol and let dry. Tip: Lean slide on the side of the petri dish to dry.
6. Fill syringe with vacuum grease.
7. When the slide is dry, apply two thin lines of vacuum grease or two lines of two layers of double-sided scotch tape, to create a sufficiently high chamber, in parallel along the long sides of the slide (Fig. 2).
8. Place the poly-L-lysine coated coverslip (from step 4) on top of the scotch tape/vacuum grease (poly-L-lysine side towards the slide).
9. Perfuse a suspension containing living cells into the assembled sample chamber.
10. Seal the open ends of the chamber with vacuum grease.

When working with different cell types, cells may adhere well to the coverslip without the use of poly-L-lysine or by using alternative adhesion-promoting reagents such as gelatin or collagen [48]. In this case, leave out steps 1–4 and use normal growth medium in step 9 to fill the chamber. Of course, cells can also be seeded in more complex microfluidic environments allowing for a constant flow across the cells, for buffer exchange or for perfusion with fresh media.

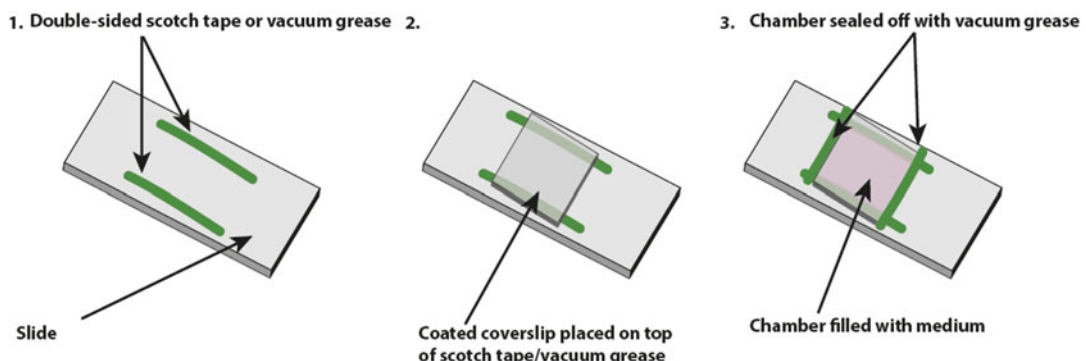


**Fig. 2** Preparation of a sample chamber: (1) Apply double-sided scotch tape or vacuum grease to the sides of a clean slide. (2) Place a coated coverslip on top of the scotch tape/vacuum grease, with the coated side facing towards the slide. (3) Fill chamber with cells or beads in medium and seal the open ends with vacuum grease

### 3.4 Introduction to the Active–Passive Calibration Procedure

The main part of this chapter describes the active–passive calibration procedure. In the following sections, we outline the protocols for the passive (Subheading 3.5) and active calibration measurements (Subheading 3.6).

Assuming that a particle trapped in an optical tweezers setup experiences a harmonic potential, the force,  $F$ , acting on the particle can be determined as:  $F = \kappa x$ , with  $x$  being the displacement of the particle from the equilibrium position and  $\kappa$  being the spring constant, which characterizes the trapping stiffness (see Note 4). By measuring  $x$  and the spring constant  $\kappa$ , the force can be extracted. Hence, in order to perform absolute force measurements inside a living cell or organism, it is crucial to accurately determine  $\kappa$ . In the following, we will demonstrate how the active–passive calibration method can be used to extract an absolute value for  $\kappa$ , which, in connection with a measurement of the particle’s position,  $x$ , is all that is needed to quantify the force of a trapped particle within a living cell. Additionally, this method allows for quantification of the cell cytoplasm’s viscoelastic properties through extraction of the viscoelastic moduli,  $G$  and  $G'$ .

### 3.5 Passive Calibration Measurements

For the passive measurements, the optical trap is focused onto a particle and the position of the particle,  $x_p(t)$ , is recorded by the QPD (Fig. 3). The thereby acquired time series is used to calculate the power spectrum  $P(\omega)$  of the positional fluctuations within the trap (Fig. 3):

$$P(\omega) = \lim_{T_{\text{Meas}} \rightarrow \infty} \frac{|\tilde{x}_p(\omega)|^2}{T_{\text{Meas}}} \quad (1)$$

Here,  $\tilde{x}_p(\omega)$  is the Fourier transformed position of the particle in the trap,  $T_{\text{Meas}}$ , the duration of the measurement and  $\omega = 2\pi f$  is the angular frequency with  $f$  being the normal frequency.

Steps for extracting the power spectrum:

1. Place sample on the sample stage, so that the coverslip faces the objective.
2. Adjust condenser height: Set up Köhler illumination for optimal contrast and precision.
3. Find laser in the sample plane and adjust the QPD position, so that the laser hits the center of the photodiode.
4. Adjust data amplification if necessary.
5. Choose a granule for data acquisition; record and store an image for later use (see example in Subheading 3.8).
6. Record the position,  $x_p(t)$ , of the trapped granule for 3 s with the QPD at a sampling rate of 22 kHz [58].

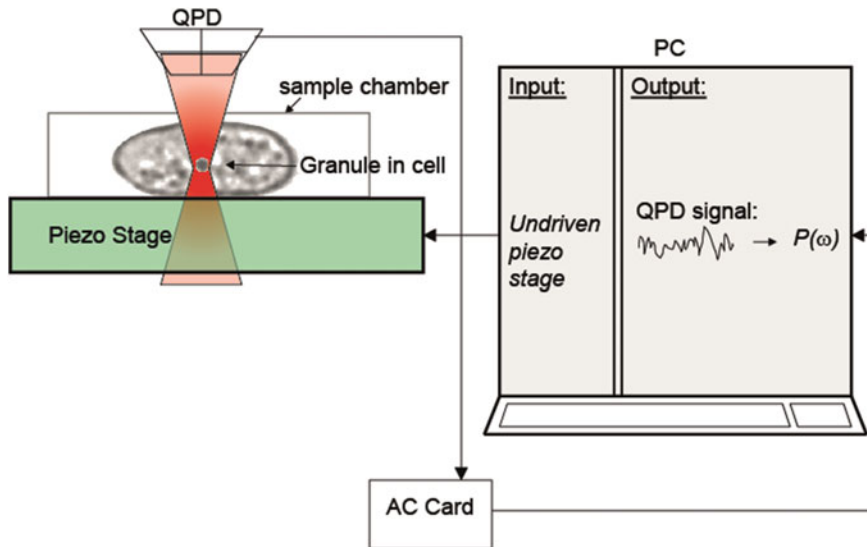


**Fig. 3** Illustration of the passive measurement: A power spectrum,  $P(\omega)$ , is obtained by tracking and recording the position of a lipid granule inside a living *S. pombe* cell using a fixed optical trap and a fixed stage

7. Repeat this measurement 30 times.
8. Calculate an average power spectrum  $|P(\omega)|$  from the 30 measurements [36].

### 3.6 Active Calibration Measurements

To calibrate an optical trap in a viscoelastic environment, not only the information from the passive measurements, but also information on how the particle moves in such a viscoelastic environment is needed. To obtain this additional information, the trapped particle is moved by oscillating the sample stage with respect to the trapping laser. The movement causes a small perturbation of the system. Using linear response theory, the linear response function of the medium,  $\chi(\omega)$ , relates the Fourier-transformed external force,  $\tilde{F}_{\text{ext}}(\omega)$ , to the average Fourier-transformed position of the particle,  $\langle \tilde{x}(\omega) \rangle$ :

$$\langle \tilde{x}(\omega) \rangle = \chi(\omega) \tilde{F}_{\text{ext}}(\omega). \quad (2)$$

The linear response function,  $\chi(\omega)$ , can therefore be regarded as an inverse spring constant.

In order to retrieve an absolute value for the spring constant,  $\kappa$ , and the viscoelastic modulus,  $G(\omega)$ , it is necessary to convert the measured quantities to SI units. Additionally, it is necessary to quantify the error in the system due to time delay between the electronic systems that record the position of the stage and the position of the trapped particle. To accomplish this, three steps are added to the calibration procedure: A direct positional calibration, a pixel calibration and a phase correction calibration, which are outlined below.

### 3.6.1 Active Force Calibration

During the active force calibration, the trapped particle is moved sinusoidally by oscillating the sample stage. This step is illustrated in Fig. 4. The position of the stage is recorded and given by  $x_S(t) = A_S \sin(\omega t + \phi_S)$ , with  $A_S$  being the amplitude,  $\phi_S$  the phase, and  $\omega$  the driving frequency of the stage movement. At the same time, the position of the driven particle is recorded by the QPD and given as,  $x_P^{(dr)}(t) = A_P \sin(\omega t + \phi_P)$  with  $A_P$  and  $\phi_P$  the amplitude and phase of the trapped and driven particle. The Fourier-transformed positional information of the trapped particle and the stage are used to calculate the relaxation spectrum, defined as

$$\tilde{R}(\omega) = \frac{\tilde{x}_P^{(dr)}(\omega)}{i\omega\tilde{x}_S} = \frac{A_P}{\omega A_S} (\sin \Delta\phi - i \cos \Delta\phi). \quad (3)$$

The relaxation spectrum can therefore be extracted through the phase difference,  $\Delta\phi$ . The phase difference is given by:

$$\Delta\phi = \phi_P - \phi_S. \quad (4)$$

Steps to extract amplitude and phase of the sinusoidal movement:

9. With the same granule as in the previous passive measurement (repeat steps 2–4 if needed), drive system sinusoidally with a set amplitude. Choose the amplitude carefully (see Notes 4–6).

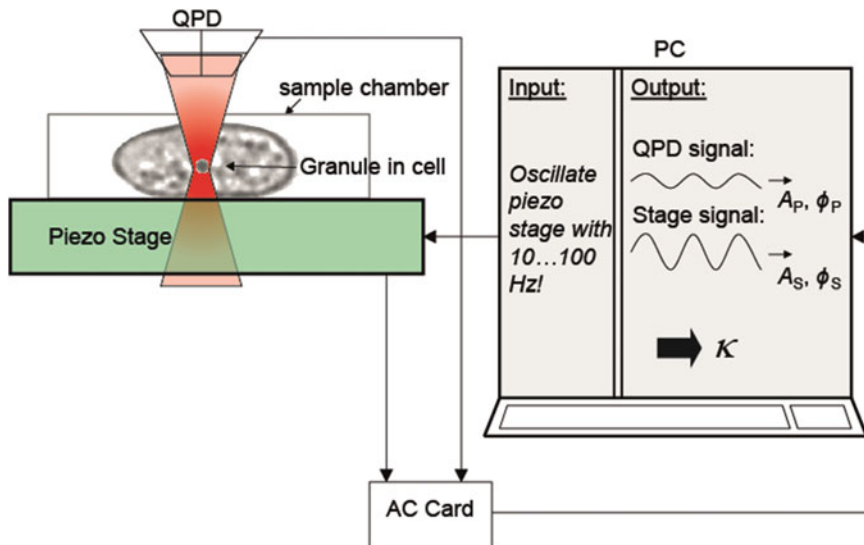


**Fig. 4** Illustration of the active force measurement. Here, the trapped particle is a lipid granule inside a cell that is moved sinusoidally by oscillating the piezo stage. The movement of the stage is recorded using a position feedback signal output from the piezo stage, and the movement of the granule is measured by the QPD. The output data is fit to the relaxation spectrum to extract the amplitude of the particle movement,  $A_P$ , and the phase difference,  $\Delta\phi$ .

$A_S = 100$  nm was used to obtain the data presented in Subheading 3.8 *Example of Experimental Data*.

10. Change frequency of the sinusoidal movement in 5 Hz decrements. The frequency has to be chosen appropriately, as it can otherwise render the FDT invalid (*see Note 3*). It is also advised to avoid frequencies corresponding to excessive instrumental noise (*see Note 7*).
11. Record the granule position with the QPD for 10 s at a sampling rate of 10 kHz [36].
12. Record sinusoidal movement of the piezo stage.
13. Check the set amplitude,  $A_S$ , by fitting the recorded positions. The amplitude and the oscillation frequency of the stage movement are in principle already known, as they are set during the experiment. Nevertheless, there might be differences between set values of the amplitude and actual motion, due to nonuniform piezo response vs. frequency (*see Note 2*).
14. Extract the amplitude of the trapped particle,  $A_P$ , and the phase difference,  $\Delta\phi$ , by fitting the relaxation spectrum given in Eq. 3 to the experimental data. Consistency checks are recommended (*see Note 8*).
15. Take an image of the trapped granule, to allow for an additional consistency check; see example in Subheading 3.8. For yet another consistency check, redo the passive measurement, steps 6–8.

### 3.6.2 Direct Positional Calibration

The direct positional calibration is an additional measurement that is needed to determine the conversion factor  $\beta$ , it is illustrated in Fig. 5.  $\beta$  translates the voltage output of the QPD,  $x_V$  (given in Volts), to SI units,  $x_{SI}$  (in meters), and is defined as the ratio

$$\beta = \frac{x_{SI}}{x_V}. \quad (5)$$

Steps to extract  $\beta$ :

16. Follow steps 1–4 from the passive measurement.
17. Drive stage for 10 s at a frequency of 2 Hz and record the movement of the trapped particle separately with the CCD camera and with the QPD. We conduct these two measurements subsequently but with identical conditions because we close the diaphragm of the condenser to increase the image contrast when recording with a CCD camera, while we leave the diaphragm open when acquiring with the QPD [49].
18. Use sampling rates of 10 kHz for the QPD and 60 Hz for the CCD camera and repeat the oscillation cycles 20 times per amplitude.

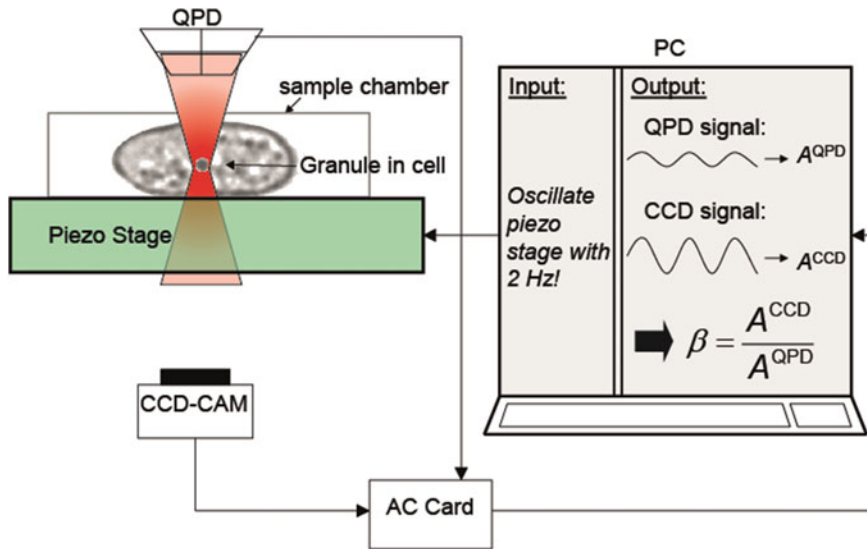


**Fig. 5** Direct positional measurement to convert the QPD voltage output to SI units. The stage is driven sinusoidally and the position of the trapped particle is recorded with both a QPD and a CCD camera. Fits of the QPD and CCD signals to sinusoidal functions are then used to extract the amplitudes to obtain the conversion factor  $\beta$

19. Fit the obtained data with a sinusoidal fit to extract the amplitudes from the two signals.
20. Calculate the conversion factor,  $\beta$ , using the extracted amplitudes.

It is advisable to check that  $\beta$  is independent of the driving amplitude as illustrated by Fig. S2 in the supplementary data of reference [36].

### 3.6.3 Pixel Size Calibration

In order to correctly determine the conversion factor,  $\beta$ , the effective pixel size,  $\alpha$ , of the camera needs to be known (in nm per pixel). This step is illustrated by Fig. 6.

Perform the following steps to extract  $\alpha$ :

21. Take 50  $\mu$ l of a bead solution and add 950  $\mu$ l millipore H<sub>2</sub>O (or a different buffer such as PBS). Mix by pipetting up and down.
22. Place bead solution into a centrifuge and spin for 15 min at 1764  $\times$   $\mathcal{g}$  (5000 rpm) (i.e. 0.35 g per rpm).
23. Resuspend in water or buffer at the desired dilution. Keep stock solution in refrigerator and vortex before use to break up aggregates.
24. Prepare sample chamber as described in Subheading 3.3, but fill the chamber with the prepared polystyrene bead solution instead of cell solution.

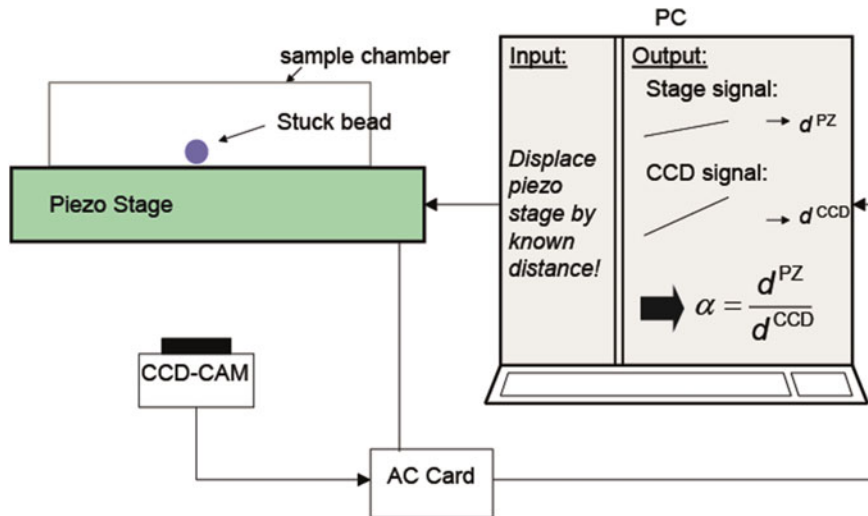


**Fig. 6** The pixel size is determined by moving a stuck bead in discrete steps in axial and lateral directions while images are continuously acquired by the CCD camera. Binary mapping is used to extract the positional change in lateral and axial directions from the images and to calculate the conversion factor  $\alpha$

25. Find a bead stuck to the bottom of the sample chamber.
26. Move the stage in predefined steps,  $d^{PZ}$ , in lateral and axial directions, while imaging simultaneously with the CCD camera.
27. Use Matlab or any software available in your lab (e.g., ImageJ) to transform the bead in the images into a bright ring on a black background using binary mapping.
28. Use your preferred software to determine the position of the center and the diameter of the ring for each image. The position of the center of the ring is interpreted as the lateral position and the diameter as the axial position of the bead. To determine the lateral position, track the position of the center of the ring by counting the number of pixels the center moved. Richardson et al. [50] found that the diameter of the ring is linearly related to the axial position with respect to the focus of the objective. The diameter of the ring can be determined by fitting a box around the ring. A custom-written program was used to extract the lateral and axial position of the bead presented in Subheading 3.8 Example of Experimental Data.
29. Plot lateral/axial position (given in pixels) as a function of the stage displacements (given in nm).
30. Extract the effective pixel size  $\alpha$  from the plot by using a linear fit.

Alternatively, freely available software such as “Video Spot Tracker” has also proven useful for tracking beads and trapped intracellular granules.

In our setup, the  $100\times$  objective together with the additional magnifying optics gives an effective pixel size of  $\alpha = (5.56 \pm 0.02)$  nm/pix for the CCD. Further information can be found in ref. [50].

### 3.6.4 Phase Correction Calibration

The voltage output of the QPD and the positional information of the piezo stage are acquired by an acquisition card. The various channels of the acquisition card allow for simultaneous read out of this data. However, when reading out channels simultaneously there is a time delay between the recording of the individual channels, which can cause systematic errors and which therefore needs to be taken into account (*see Note 1*).

As the acquisition of the bead position is delayed compared to the stage position by a delay time  $t^{(\text{del})}$ , the phase difference in Eq. (4) needs to be corrected for this delay

$$\Delta\phi^{(\text{corr})} = \Delta\phi^{(\text{fit})} - \Delta\phi^{(\text{del})}. \quad (6)$$

$\Delta\phi^{(\text{fit})}$  is found as described in Subheading 3.6.1, steps 9, 12–14 by fitting a sinusoidal function to the information obtained from the QPD and the stage position of the trapped particle, the procedure is illustrated in Fig. 7.

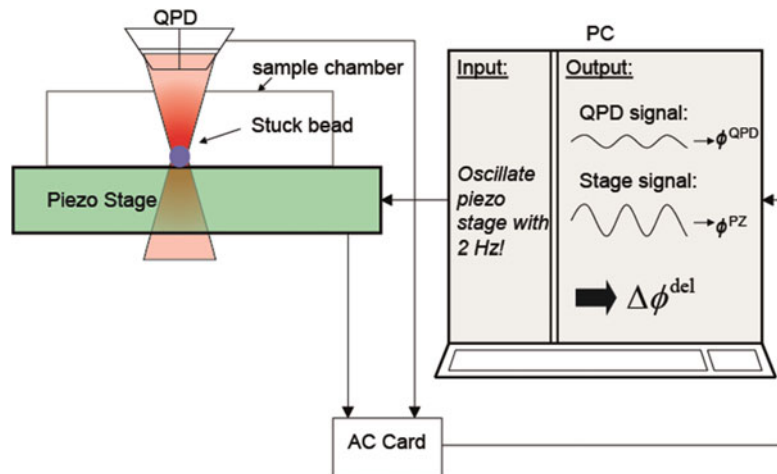


**Fig. 7** Phase correction calibration to determine the time delay between acquisition card channels. The position of a stuck bead is recorded by the QPD, while the stage is oscillated sinusoidally with 2 Hz. The phase difference between the sinusoidal fits to the QPD and stage signals gives the time delay between the channels

Steps to determine the time delay between the channels of the AC card:

31. Prepare a sample chamber with beads stuck to the bottom coverslip as in **steps 24** and **25**.
32. Follow **steps 1–4** from the passive calibration measurement.
33. Find a bead and oscillate sample sinusoidally at a frequency of 2 Hz.
34. Record the movement of the bead with the QPD and the stage position.
35. Fit both signals with a sine-wave function (since the bead is stuck to the coverslip it should move exactly like the stage).
36. Calculate the phase difference of the sinusoidal fits to the stage and QPD signals. This phase difference reveals the time lag due to the acquisition process.

This phase correction calibration procedure only needs to be performed once for a given acquisition card and is in our case determined to be  $(467 \pm 65) \mu\text{s}$  for the acquisition card used here [37] (see Note 1).

**Steps 21–36** need only be completed once, whereas **steps 1–15** can be carried out for several granuli within the same cell, providing in particular information about variations in the viscoelastic properties of the cytoskeleton at different locations within the cell. **Steps 16–20** are preferably repeated for each new sample.

### 3.7 Active–Passive Calibration to Extract Spring Constant and Viscoelastic Moduli

Using the information gained from the active and passive calibration procedures, the spring constant can be found using this equation:

$$\kappa - \omega^2 m = 2k_B T \frac{\text{Re}(\tilde{R}(\omega))}{P(\omega_S)} - \frac{2k_B T A_P}{P(\omega_S) \omega_S} \sin(\Delta\phi). \quad (7)$$

Perform the following steps to determine  $\kappa$  and the viscoelastic moduli using Eq. 7:

1. The spring constant as function of the stage oscillation frequency,  $\omega_S$ , is calculated by inserting the parameters  $A_P$ ,  $\Delta\phi$ ,  $P(\omega_S)$  and  $\omega_S$  into Eq. 7. Here  $m$  stands for the mass of the trapped particle. However, it is not necessary to know the mass of the trapped particle because the frequency  $\omega$  is so small that the term  $\omega^2 m$  can be neglected, as it is significantly smaller than the other terms in the equation.
2. Based on the obtained value for  $\kappa(\omega)$ , the elastic modulus  $G(\omega)$  can be found. This modulus consists of a real part, which characterizes the elastic response, and an imaginary part characterizing the viscous response of the medium. The real part is

also known as the shear storage modulus  $G$  and the imaginary part is the shear loss modulus  $G''$ .

$$G(\omega) = \frac{i\omega}{6\pi r} (\kappa - \omega^2 m) \frac{\tilde{R}(\omega)}{1 - i\omega\tilde{R}(\omega)}. \quad (8)$$

3. Calculate the elastic modulus  $G(\omega)$  by inserting the values for  $\kappa(\omega)$  and for the relaxation spectrum  $\tilde{R}(\omega)$ , defined in Eq. 3. The radius of the trapped particle is denoted as  $r$  and can be extracted from the bright field images. The average radius of the granules used herein was determined to be  $(0.6 \pm 0.1) \mu\text{m}$  [36].
4. The spring constant can be used to determine the linear response function (Eq. 2) of the medium:

$$\chi(\omega) = \frac{1 - i\omega\tilde{R}(\omega)}{\kappa - \omega^2 m} \simeq \frac{1 - i\omega\tilde{R}(\omega)}{\kappa}. \quad (9)$$

5. The effective spring constant, which is the spring constant that combines all elastic forces from the optical trap and from the viscoelastic medium acting on the trapped particle, is given as the inverse linear response function:

$$\kappa_{\text{eff}} = \frac{1}{|\chi(\omega)|}. \quad (10)$$

### 3.8 Example of Experimental Data

This section gives an example of an experimental data set, where lipid granules within living *S. pombe* cells were used as probes for the calibration of the optical trap. Data were acquired by focusing the trapping laser onto a chosen lipid granule and time series of the positions visited by the granule were recorded. Bright field images showing the cell and the cytoplasmic granules were acquired before and after trapping a granule, to visually ensure that other granules or organelles had not entered the trap during data acquisition (Fig. 8). A time series was disregarded, if additional objects were found or if the trapped granule changed shape.

The spring constant  $\kappa$  and the viscoelastic moduli  $G$  and  $G'$  were determined using the described active–passive calibration procedure.

The spring constant of the optical trap was calculated using Eq. 7. The viscoelastic environment within the cells can also contribute to the total effective spring constant, which describes the total elastic force acting on a lipid granule. The effective spring constant,  $\kappa_{\text{eff}}$ , which takes into account the viscoelastic environment, was determined using the linear response function,  $\chi(\omega)$  (Eq. 9), and is simply calculated from the absolute value of the linear response function (Eq. 10). Figure 9a shows  $\kappa$  and  $\kappa_{\text{eff}}$  as a function of driving frequency. The depicted asterisk in Fig. 9 is the value  $k_B T / \langle x_p^2 \rangle$ , which would be the value of the trap's spring constant in a purely viscous system. In a viscoelastic environment,

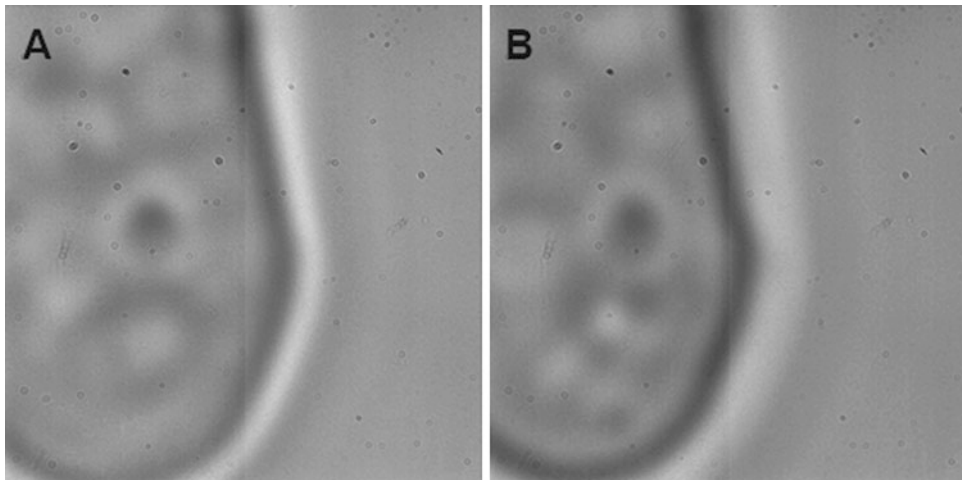


**Fig. 8** Images of a lipid granule in an *S. pombe* cell, (a) before and (b) after the calibration procedure, indicating that neither the size nor the number of trapped granules have changed

however, this value can be understood as an independent measure of a low-frequency effective spring constant. This interpretation is in agreement with the values of  $k_{\text{B}}T/\langle x_{\text{P}}^2 \rangle$  and the effective spring constant given in Fig. 9.

The viscoelastic moduli of the cells' cytoplasm were obtained from Eq. 8 using the measured average radius of the lipid granule,  $r$  ( $0.6 \pm 0.1 \mu\text{m}$ , see Subheading 3.5). Figure 9b displays the real part  $G'$ , the storage loss modulus, describing the elastic response of the system. The imaginary part  $G''$  corresponds to the viscous response of the viscoelastic modulus. Both parts are functions of the driving frequency. For example, Fig. 9b shows that the storage loss modulus increases for driving frequencies below  $\sim 40$  Hz, while it becomes largely insensitive to driving frequencies in the range of  $\sim 40$  Hz and  $\sim 70$  Hz. The observation of a plateau in the frequency response of the storage loss modulus is typical for a semi-dilute polymer solution [27].

#### 4 Notes

1. *The acquisition card has to be chosen carefully:* Several steps of the active–passive calibration procedure require the simultaneous recording of stage and particle position. However, reading out this information from different channels simultaneously comes with a time delay. This time delay introduces systematic errors to the experimental results and should therefore be taken into account. The delay time for the acquisition card used is  $(467 \pm 65) \mu\text{s}$  [36, 37]. When purchasing an acquisition card, it is therefore imperative to choose the card carefully to ensure fast readout of different channels.

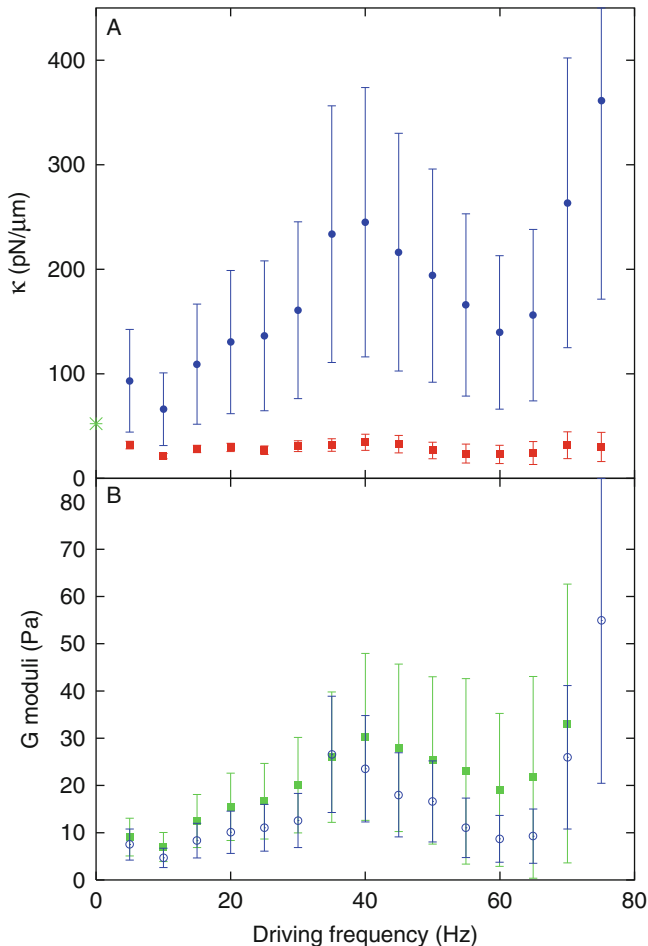


**Fig. 9** Spring constant and viscoelastic moduli as a function of driving frequency. **(a)** Spring constant,  $\kappa$ , characterizing the optical trap and **(b)** viscoelastic moduli of one lipid granule as a function of the driving frequency (5–75 Hz). **(a)** The graph depicts the effective spring constant,  $\kappa_{\text{eff}}$  (blue filled circles with error-bars), which includes contributions from the trap and the viscoelastic local environment, and the spring constant  $\kappa$  (red filled squares with error-bars), which solely characterizes the trap. The green asterisk on the ordinate axis corresponds to the value of  $k_B T / \chi_P^2$ . **(b)** Real part (storage; blue open circles) and imaginary part (loss; green filled squares) of the viscoelastic modulus  $G$  as function of driving frequency. The error bars in **(a)** and **(b)** were calculated using error propagation of systematic instrumental uncertainties and statistical errors

**2. Stage or laser driving, what to choose?** Oscillating the trapped particle with either a stage or the laser beam using an AOD has both advantages and disadvantages. Starting from a technical perspective, stage driving is easier to implement and instrumental efforts are less demanding in comparison to laser driving. However, the bandwidth of available frequencies is limited. State-of-the-art stages are capable of oscillations with frequencies in the order of hundreds of Hz [37]. We also observed that the stage in our setup does not reach the set amplitude at higher oscillation frequencies, which is a problem that should be taken into account [36]. AOD-based laser beam

oscillations on the other hand, can be driven with significantly higher frequencies (see subsequent chapter) and therefore with frequencies well above those at which active biological processes and noise occur [34] (*see Note 3*). Additionally, the use of laser driving omits the need of a separate calibration procedure to obtain the conversion factor  $\beta$  to convert from voltage to metric units, which is prone to large errors. The conversion factor can be obtained directly by the ratio between the set oscillation amplitude of the laser and the voltage output of the QPD. When using laser driving, one should still be aware and acknowledge the limitations of this method, see for example refs. [33, 35]. Finally, it is important to choose an oscillation amplitude that does not exceed the harmonic trapping region of the trap [50] and one that still ensures that the perturbations are small.

3. *Choose the best oscillating frequencies:* The active–passive calibration procedure is based on linear response theory. The perturbation caused by the active movement in the calibration procedure should therefore be small to ensure a linear response of the system. In living cells, however, active processes take place and these processes can render the fluctuation dissipation theorem (FDT) method invalid in certain frequency ranges. For example, it has been shown that the fluctuations of beads in an actin network with active molecular motors or in MLO-Y<sub>4</sub> cells violate the FDT at frequencies below 10 Hz [51, 52], implying that the system is governed by nonequilibrium processes at lower frequencies. Using only higher frequencies can help avoiding recordings in this problematic frequency range. The use of an AOD, which can operate even in the kHz range, may therefore be preferable over stage driving which is difficult to do in the kHz regime. It is worth noting, however, that the active biological processes should reveal themselves in the calibration process, as the extracted spring constant  $\kappa$  would in this case not be independent of driving frequency. We have found [36] that in our experiments  $\kappa$  does not change with the driving frequency, which validates the use of the linear response theory for the frequency range used (5–75 Hz). However, in our experiments,  $\kappa$  exhibited relatively large variations from one cell to another and at different locations within a cell. These variations are likely caused by differences in the local cellular cytoskeleton and/or differences in the size, shape and refractive index of the trapped lipid granules. Considering that these parameters will vary from one trapped particle to the next, calibration of the trap for each trapped object is necessary, especially for precise force measurements [36].
4. *Choose the best oscillation amplitude:* Larger oscillation amplitudes lead to larger deflections of the trapped particle and therefore to a better signal to noise ratio. However, the

amplitude cannot be chosen arbitrarily large, as there are constraints on the size of the amplitude. First, the trapped particle needs to stay within the linear detection region of the QPD [53]. Secondly, the trapped particle needs to stay within the harmonic trapping potential of the optical tweezers [50]. Thirdly, there are constraints given by linear response theory on which our calibration procedure is built. For the linear response theory to be upheld, the oscillatory motion must only generate a small perturbation of the equilibrium system (*see Note 3*). For this reason, only small amplitudes can be used [38]. Taking these conditions into account, the driving amplitude should be chosen in a way such that the amplitude of the trapped particle is roughly equal to the half width of the trap,  $(k_B T / \kappa)^{1/2}$ . In doing so, a linear response of the system will be ensured [37].

5. *Determine the QPD's linear regime:* The voltage output of the QPD is proportional to the distance a particle moves in the optical trap within a certain interval, which is referred to as the linear region. When executing the active–passive calibration procedure it is important that the active oscillations of the sample do not exceed this linear region of the QPD (*see Note 4*). The linear region of the QPD can be defined by moving a stuck bead through the laser focus with constant velocity. From the obtained data, the regime with a monotonic linear voltage response can be determined [36]. When staying within this linear region of the QPD, it is not necessary to obtain the conversion factor  $\beta$  to retrieve the force. Because the position measured by the QPD is given in Volts, the amplitude of the stage-driven particle motion,  $A_p$ , and the power spectrum,  $P(\omega_s)$ , are given in V and  $V^2 s^{-1}$ , respectively. If the spring constant  $\kappa$  is determined from these parameters, then the units of  $\kappa$  are given as  $N V^{-1}$ . The resulting force is then given in SI units, since the position of the trapped particle given in Volts times the spring constant gives Newtons, N. However, if absolute values for  $\kappa$  and  $G(\omega)$  are needed, determination of  $\beta$  is required [36]. In micro-rheological measurements, one needs only information about the characteristic power law for the viscoelastic moduli of the cell cytoplasm,  $G'(\omega)$ ,  $G''(\omega) \propto \omega^\delta$ . Information about the value of  $\delta$  can for example be obtained using optical tweezers without the knowledge of an absolute trap spring constant because  $\delta$  is also reflected in the mean squared displacement calculated from the positions visited by a particle [25, 48]. These types of measurements have brought insight into the diffusion of tracer particles [25, 48, 54, 55] and the viscoelastic moduli of the cytoplasm [56, 57] and of reconstituted polymer networks [40, 41].

6. *Choose the right QPD and CCD axis:* Particle trajectories normally follow the direction of the sinusoidal perturbation (laser driven or stage driven). It is convenient to have both QPD and CCD detectors positioned with one of their lateral axes parallel to the stage/laser driving direction, which reduces the calibration to a unidimensional problem. Otherwise bidimensional trajectories would need to be projected onto the active perturbation axis before sinusoidal fitting, and care should be taken in having the appropriate  $\beta$  calibrations for all axes. Moreover, once the axes are aligned, the directions of movement might be parallel or antiparallel, depending on the orientation of the stage/QPD. Note that the measurement of the conversion factor  $\beta$  (described in Subheading 3.6.2, steps 16–20), which is given by the ratio of amplitudes, yields an absolute value. The sign of  $\beta$  depends on every system and should be determined once. To determine the sign, move a stuck bead with the stage away from the trap center along the axis of interest and measure the change of the sign of the QPD signal after displacement. If the stage and QPD signals change in opposite directions, the sign of  $\beta$  should be set negative for the system, to ensure that a zero phase delay in the stage-particle sinusoidal signals corresponds to the particle and the stage moving together in the same direction.
7. *Avoid vibrations:* Vibrations in the microscope setup might arise at specific frequencies, depending on mechanical resonances of the system, and will show up as peaks in the passive power spectrum. Active–passive measurements should be avoided in the region of noise peaks, since they might mask the actual particle oscillation, and affect the measurement of the phase difference between particle and stage.
8. *Do consistency checks:* The full calibration procedure with stage driving takes about 5 min to complete, and the cellular activity does not stop. The trapped granule might interact with other elements in the cell cytoplasm during this time, and undergo unexpected movements that can affect the measurement of the trap stiffness. Hence, to make sure the experiment was not affected by unexpected movements, it is recommended to confirm the following observations: (1) no significant motion occurs perpendicular to the driving direction, (2) the mean position does not change, both during active and passive measurements, (3) the granule does not drift axially during the experiment, and (4) the particle vs. stage plot is elliptical (superposition of two sinusoidal signals with a relative phase). Deviations from the ideal elliptical behavior might indicate the presence of other organelles in close vicinity of the trapped granule, or possibly that the granule moved out of the linear region (e.g., if driving amplitude is too large). An example of such a consistency check is illustrated in Fig. 10, where panel

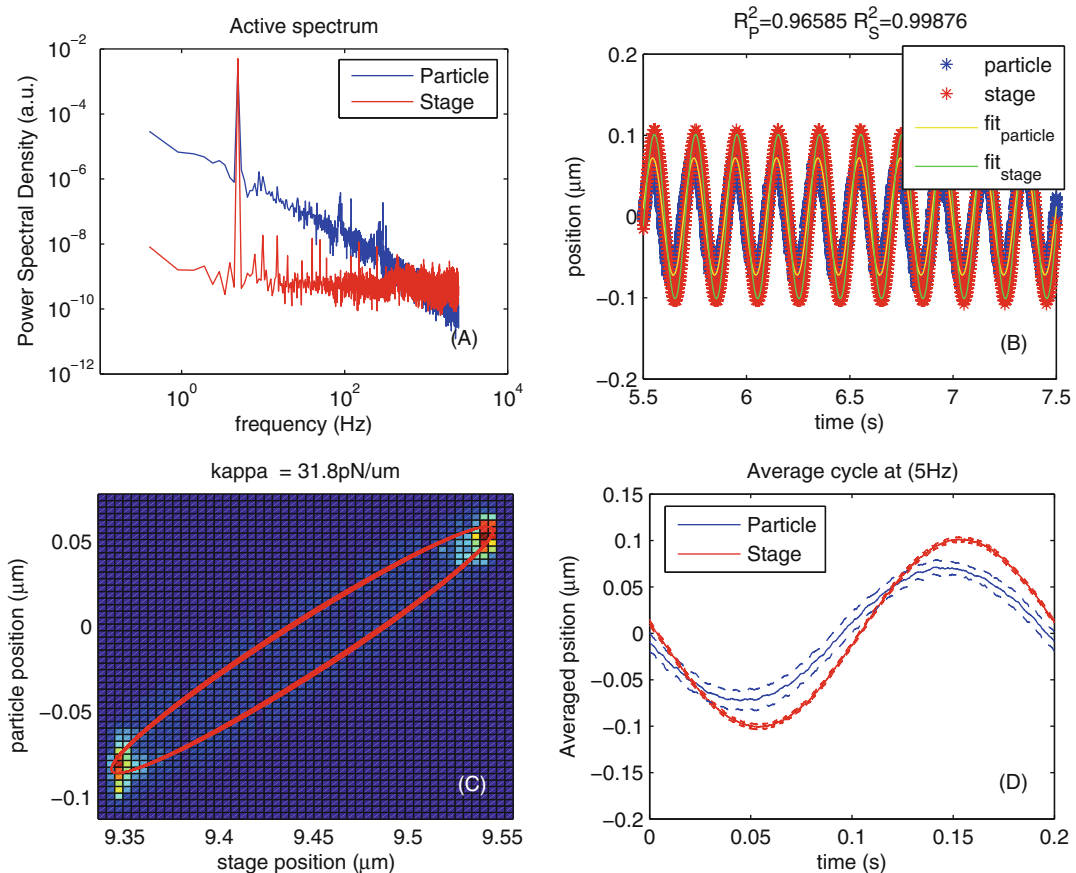


**Fig. 10** Consistency checks for the active force calibration part. **(a)** Power spectra of particle and stage obtained during active calibration. The sharp frequency peak corresponds to the 5 Hz driving frequency in that particular active measurement. **(b)** Fragment of a time series showing the sinusoidal motion imposed by the stage during the experiment and corresponding response of the trapped granulus, with their respective sinusoidal fits. **(c)** Example showing the ellipsoidal shape corresponding to an undisturbed experiment where the trapped granulus follows the stage position with a phase-difference. **(d)** Illustration of the calculated average of all periods of the oscillation from the time series shown in **(b)**. The sine wave reflecting the particle motion leads in phase relative to the sine wave corresponding to the stage motion. Even though counter intuitive, this result corresponds correctly to the situation in a non-inertial regime (low Reynolds number), where the particle position is driven by instantaneous forces, rather than responding to stage acceleration. The instantaneous forces are a combination of viscous and elastic forces. In a purely viscous media, the maximum of the particle position will correspond to the maximum of the stage speed. This point corresponds to the maximum derivative of the stage trajectory, which for a sinusoidal trajectory corresponds to the zero crossing point, just  $90^\circ$  before the stage maximum position. In a purely elastic medium (~solid) the force changes linearly with distance in respect to the equilibrium position, and the maximum in particle position is reached when the stage is at its maximum position, i.e., with a  $0^\circ$  phase difference with the stage. In a viscoelastic material on the other hand, the phase will be somewhere in between  $90^\circ$  and  $0^\circ$ , with the particle trajectory always being advanced with respect to the stage due to the viscous component, which is what we observe in **(d)**. The individual panels in this figure were created using a custom-written MATLAB program that analyses the experimental recordings

(A) shows the power spectral density of both trapped particle and stage; confirming the driving frequency of 5 Hz and no other particular noise peaks. Panel (B) and (C) illustrate the sinusoidal behavior of both particle and stage, panel (C) shows indeed the elliptical shape mentioned in point (4) above. Finally, panel (D) presents the average of all oscillations and indicate the phase difference between particle and stage.

## References

1. Fazal FM, Block SM (2011) Optical tweezers study life under tension. *Nat Photonics* 5:318–321
2. Moffitt JR, Chemla YR, Smith SB et al (2008) Recent advances in optical tweezers. *Annu Rev Biochem* 77(1):205–228
3. Greenleaf WJ, Woodside MT, Block SM (2007) High-resolution, single-molecule measurements of biomolecular motion. *Annu Rev Biophys Biomol Struct* 36:171–190
4. Neuman KC, Nagy A (2008) Single-molecule force spectroscopy: optical tweezers, magnetic tweezers and atomic force microscopy. *Nat Methods* 5(6):491–505
5. Berg-Sørensen K, Flyvbjerg H (2004) Power spectrum analysis for optical tweezers. *Rev Sci Instrum* 75(3):594–612
6. Tolić-Nørrelykke SF, Schäffer E, Howard J et al (2006) Calibration of optical tweezers with positional detection in the back focal plane. *Rev Sci Instrum* 77(10):103101
7. Neuman KC, Block SM (2004) Optical trapping. *Rev Sci Instrum* 75(9):2787–2809
8. Gittes F, Schmidt CF (1998) Signals and noise in micromechanical measurements. *Methods Cell Biol* 55:129–156
9. Veigel C, Schmidt CF (2011) Moving into the cell: single-molecule studies of molecular motors in complex environments. *Nat Rev Mol Cell Biol* 12(3):163–176
10. Sims PA, Xie XS (2009) Probing dynein and kinesin stepping with mechanical manipulation in a living cell. *ChemPhysChem* 10(9–10):1511–1516
11. Leidel C, Longoria RA, Gutierrez FM et al (2012) Measuring molecular motor forces in vivo: implications for tug-of-war models of bidirectional transport. *Biophys J* 103 (3):492–500
12. Shubeita GT, Tran SL, Xu J et al (2008) Consequences of motor copy number on the intracellular transport of kinesin-1-driven lipid droplets. *Cell* 135(6):1098–1107
13. Guet D, Mandal K, Pinot M et al (2014) Mechanical role of actin dynamics in the rheology of the Golgi complex and in Golgi-associated trafficking events. *Curr Biol* 24 (15):1700–1711
14. Oddershede LB (2012) Force probing of individual molecules inside the living cell is now a reality. *Nat Chem Biol* 8(11):879–886
15. Norregaard K, Jauffred L, Berg-Sørensen K et al (2014) Optical manipulation of single molecules in the living cell. *Phys Chem Chem Phys* 16(25):12614–12624
16. López-Quesada C, Fontaine AS, Farré A et al (2014) Artificially-induced organelles are optimal targets for optical trapping experiments in living cells. *Biomed Opt Express* 5 (7):1993–2008
17. Gross SP (2003) Application of optical traps in vivo. *Methods Enzymol* 361:162–174
18. Rasmussen MB, Oddershede LB, Siegumfeldt H (2008) Optical tweezers cause physiological damage to *Escherichia coli* and *Listeria* bacteria. *Appl Environ Microbiol* 74(8):2441–2446
19. Peterman EJG, Gittes F, Schmidt CF (2003) Laser-induced heating in optical traps. *Biophys J* 84(2):1308–1316
20. Neuman KC, Chadd EH, Liou GF et al (1999) Characterization of photodamage to *Escherichia coli* in optical traps. *Biophys J* 77 (5):2856–2863
21. Lee YJ, Patel D, Park S (2011) Local rheology of human neutrophils investigated using atomic force microscopy. *Int J Biol Sci* 7 (1):102–111
22. Wilhelm C (2008) Out-of-equilibrium micro-rheology inside living cells. *Phys Rev Lett* 101 (2):028101
23. Dufrene YF, Evans E, Engel A et al (2011) Five challenges to bringing single-molecule force spectroscopy into living cells. *Nat Methods* 8 (2):123–127
24. Jun Y, Tripathy SK, Narayananreddy BR et al (2014) Calibration of optical tweezers for

- in vivo force measurements: how do different approaches compare? *Biophys J* 107(6):1474–1484
25. Tolić-Nørrelykke IM, Munteanu E-L, Thon G et al (2004) Anomalous diffusion in living yeast cells. *Phys Rev Lett* 93(7):078102
  26. Schnurr B, Gittes F, MacKintosh FC et al (1997) Determining microscopic viscoelasticity in flexible and semiflexible polymer networks from thermal fluctuations. *Macromolecules* 30(25):7781–7792
  27. Gittes F, Schnurr B, Olmsted PD et al (1997) Microscopic viscoelasticity: shear moduli of soft materials determined from thermal fluctuations. *Phys Rev Lett* 79(17):3286–3289
  28. Mas J, Farré A, López-Quesada C et al (2011) Measuring stall forces in vivo with optical tweezers through light momentum changes. *Proc SPIE* 8097:809726
  29. Farré A, Montes-Usategui M (2010) A force detection technique for single-beam optical traps based on direct measurement of light momentum changes. *Opt Express* 18(11):11955–11968
  30. Farré A, Marsà F, Montes-Usategui M (2012) Optimized back-focal-plane interferometry directly measures forces of optically trapped particles. *Opt Express* 20(11):12270–12291
  31. Smith SB, Cui Y, Bustamante C (2003) Optical-trap force transducer that operates by direct measurement of light momentum. In: *Methods in Enzymology*. Academic, New York, NY, pp 134–162
  32. Hendricks AG, Holzbaur EL, Goldman YE (2012) Force measurements on cargoes in living cells reveal collective dynamics of microtubule motors. *Proc Natl Acad Sci U S A* 109(45):18447–18452
  33. Vermeulen KC, van Mameren J, Stienen GJM et al (2006) Calibrating bead displacements in optical tweezers using acousto-optic deflectors. *Rev Sci Instrum* 77(1):013704
  34. Blehm BH, Schroer TA, Trybus KM et al (2013) In vivo optical trapping indicates kinesin's stall force is reduced by dynein during intracellular transport. *Proc Natl Acad Sci* 110(9):3381–3386
  35. Valentine MT, Guydosh NR, Gutiérrez-Medina B et al (2008) Precision steering of an optical trap by electro-optic deflection. *Opt Lett* 33(6):599–601
  36. Mas J, Richardson AC, Reihani SN et al (2013) Quantitative determination of optical trapping strength and viscoelastic moduli inside living cells. *Phys Biol* 10(4):046006
  37. Fischer M, Richardson AC, Reihani SN et al (2010) Active-passive calibration of optical tweezers in viscoelastic media. *Rev Sci Instrum* 81(1):015103
  38. Fischer M, Berg-Sorensen K (2007) Calibration of trapping force and response function of optical tweezers in viscoelastic media. *J Opt A Pure Appl Opt* 9(8):S239–S250
  39. Atakhorrami M, Sulkowska JI, Addas KM et al (2006) Correlated fluctuations of microparticles in viscoelastic solutions: Quantitative measurement of material properties by microrheology in the presence of optical traps. *Phys Rev E* 73(6):061501
  40. Mizuno D, Head DA, MacKintosh FC et al (2008) Active and passive microrheology in equilibrium and nonequilibrium systems. *Macromolecules* 41(19):7194–7202
  41. Lee H, Ferrer JM, Nakamura F et al (2010) Passive and active microrheology for cross-linked F-actin networks in vitro. *Acta Biomater* 6(4):1207–1218
  42. Lau AWC, Hoffman BD, Davies A et al (2003) Microrheology, stress fluctuations, and active behavior of living cells. *Phys Rev Lett* 91(19):198101
  43. Robert D, Nguyen T-H, Gallet F et al (2010) In vivo determination of fluctuating forces during endosome trafficking using a combination of active and passive microrheology. *PLoS One* 5(4):e10046
  44. Andersson M, Czerwinski F, Oddershede LB (2011) Optimizing active and passive calibration of optical tweezers. *J Opt* 13(4):044020
  45. Oddershede L, Greco S, Nørrelykke SF et al (2001) Optical tweezers: probing biological surfaces. *Probe Microsc* 2:129
  46. Gittes F, Schmidt CF (1998) Interference model for back-focal-plane displacement detection in optical tweezers. *Opt Lett* 23(1):7–9
  47. Pralle A, Prummer M, Florin EL et al (1999) Three-dimensional high-resolution particle tracking for optical tweezers by forward scattered light. *Microsc Res Tech* 44(5):378–386
  48. Leijnse N, Jeon JH, Loft S et al (2012) Diffusion inside living human cells. *Eur Phys J Spec Top* 204(1):75–84
  49. Dreyer JK, Berg-Sorensen K, Oddershede L (2004) Improved axial position detection in optical tweezers measurements. *Appl Opt* 43(10):1991–1995
  50. Richardson AC, Reihani SNS, Oddershede LB (2008) Non-harmonic potential of a single beam optical trap. *Opt Express* 16(20):15709–15717
  51. Mizuno D, Tardin C, Schmidt CF et al (2007) Nonequilibrium mechanics of active cytoskeletal networks. *Science* 315(5810):370–373

52. Mizuno D, Bacabac R, Tardin C et al (2009) High-resolution probing of cellular force transmission. *Phys Rev Lett* 102(16):168102
53. Ott D, Reihani SN, Oddershede LB (2014) Crosstalk elimination in the detection of dual-beam optical tweezers by spatial filtering. *Rev Sci Instrum* 85(5):053108
54. Jeon J-H, Tejedor V, Burov S et al (2011) In vivo anomalous diffusion and weak ergodicity breaking of lipid granules. *Phys Rev Lett* 106 (4):048103
55. Selhuber-Unkel C, Yde P, Berg-Sorensen K et al (2009) Variety in intracellular diffusion during the cell cycle. *Phys Biol* 6(2):025015
56. Yamada S, Wirtz D, Kuo SC (2000) Mechanics of living cells measured by laser tracking microrheology. *Biophys J* 78(4):1736–1747
57. Wei M-T, Zaorski A, Yalcin HC et al (2008) A comparative study of living cell micromechanical properties by oscillatory optical tweezers. *Opt Express* 16(12):8594–8603
58. Czerwinski F, Richardson AC, Oddershede LB (2009) Quantifying noise in optical tweezers by allan variance. *Opt Express* 17(15): 13255–13269

# Chapter 21

## Measuring Molecular Forces Using Calibrated Optical Tweezers in Living Cells

Adam G. Hendricks and Yale E. Goldman

### Abstract

Optical tweezers have been instrumental in uncovering the mechanisms motor proteins use to generate and react to force. While optical traps have primarily been applied to purified, *in vitro* systems, emerging methods enable measurements in living cells where the actively fluctuating, viscoelastic environment and varying refractive index complicate calibration of the instrument. Here, we describe techniques to calibrate optical traps in living cells using the forced response to sinusoidal oscillations and spontaneous fluctuations, and to measure the forces exerted by endogenous ensembles of kinesin and dynein motor proteins as they transport cargoes in the cell.

**Key words** Optical trap, Optical tweezers, Kinesin, Dynein, Intracellular transport, Microtubules, Cell mechanics, Live-cell assays, Biological materials

---

### 1 Introduction

Through the ability to exert piconewton-level forces on microscopic refractile particles, such as micron-sized polymer beads, and to make precise measurements of forces and displacements, optical traps, also termed optical tweezers, have provided fundamental insights into motor protein mechanochemistry [1], microtubule dynamics [2, 3], protein folding [4], and biological materials [5, 6]. Yet how motor protein function is modulated by the cellular environment, where motor proteins operate in teams, interact with binding partners and effectors, and navigate complex cytoskeletal networks (Fig. 1), is not well understood. The use of optical traps in living cells has been limited due to the lack of methods to reliably calibrate the instrument in the cytoplasm (Fig. 1). Active processes in the cell (motor proteins, cytoskeletal dynamics, etc.) continually exert fluctuating forces on the trapped object, precluding the use of standard calibration methods based on predictable thermal fluctuations. The index of refraction of the cytoplasm varies among cell types and may depend on the local

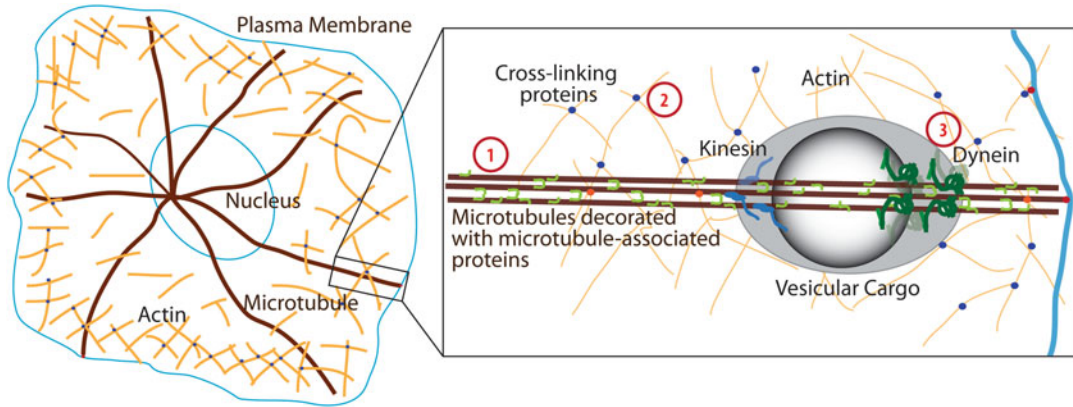


**Fig. 1** Teams of motor proteins transport cargoes along dense, cross-linked networks of cytoskeletal filaments. Many factors regulate the activity of motor proteins to direct transport in the cell: (1) the microtubule cytoskeleton is organized by microtubule-associated proteins which also directly modulate motor function, (2) the dense, dynamically cross-linked actin network constrains diffusion of cargoes, and (3) opposing teams of motor proteins interact to enable bidirectional transport. The activity of motor proteins is further regulated by interactions with binding partners and scaffolding proteins that mediate cargo binding. Note that an actual cell is much more densely packed than this cartoon

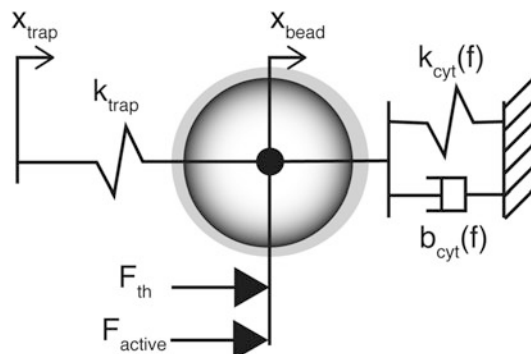


**Fig. 2** The cellular environment is viscoelastic. Forces are exerted on intracellular cargoes by the optical trap ( $k_{\text{trap}}$ ), active forces including motor proteins and cytoskeletal dynamics ( $F_{\text{active}}$ ), thermal motion ( $F_{\text{th}}$ ), and the viscoelastic cytoplasmic environment ( $k_{\text{cyt}}(f)$  and  $b_{\text{cyt}}(f)$ ). The positions of the trap and bead are indicated by  $x_{\text{trap}}$  and  $x_{\text{bead}}$

environment in different regions of a cell. In addition, due to the presence of cross-linked cytoskeletal filaments, the cellular environment is highly viscoelastic, such that the response to forces applied by the optical trap includes contributions from both the cytoplasm and the optical trap that must be resolved (Fig. 2). The elastic and viscous components of the cytoplasm are frequency-dependent, further complicating quantification.

Measurement of biophysical force using an optical trap often involves attaching the biological target specimen, such as a

molecular motor, to a small plastic bead and illuminating it with tightly focused infrared (IR) light which constrains its position near the beam waist. The position or scattering of the IR light by the bead is detected with a differential photodetector, usually a quadrant (QPD) or lateral-effect photodiode. The classical method to calibrate the force sensitivity, in units of pN per volt deflection of the detector signal, uses the frequency spectrum of thermal fluctuations of the bead within the trap [7, 8]. The power density spectrum ( $P(f)$ ) of the photodiode signal in this situation is a Lorentzian curve given by:

$$P_{\text{th}}(f) = \frac{k_B T}{\beta^2 \gamma \pi^2 (f^2 + f_c^2)}, \text{ with } f_c = \frac{k_{\text{trap}}}{2\pi\gamma},$$

where  $\beta$  is the position sensitivity of the photodiode signal in nm/V,  $k_{\text{trap}}$  is the Hookean stiffness of the optical trap [pN/nm],  $f$  is the frequency [Hz],  $f_c$  is the cutoff (half-power) frequency of the spectrum [Hz], and  $\gamma$  is the viscous drag coefficient [N s/m]. The force sensitivity of the photodiode signal,  $C$  [pN/V], is then given by  $\beta k_{\text{trap}}$ . If the radius,  $r$ , of the bead and viscosity,  $\eta$ , of the fluid are known, then  $\gamma$  is calculated using Stokes' equation ( $\gamma = 6\pi\eta r$ ). Alternatively, a sinusoidal oscillation can be applied to measure the drag coefficient [7]. Note that reliable values of  $r$  and  $\eta$  are required to define  $\gamma$ , and their uncertainties are propagated into the value of the force sensitivity.

The power spectrum method assumes that fluctuations are entirely due to thermal motion in a purely viscous fluid. To account for the actively fluctuating, viscoelastic environment in living cells, several methods have been proposed. The effect of the cellular refractive index on the stiffness of the optical trap can be approximated by performing calibrations *in vitro* using a medium that has a similar index of refraction [9, 10]. To determine the refractive index of the cytoplasm, oils of varying refractive indices are microinjected into cells [10] or the refractive index of the cytosol is measured using an Abbe-type refractometer [9]. This method is straightforward to implement and allows the calibration to be performed outside of the cell. However, refractive index matching does not account for variations in properties between cells or at different locations in a cell, and variability in the size or refractivity of the cargo must be estimated through image analysis. Cellular viscosity has also been noted to be temperature dependent [11].

An alternative method is based on the conservation of light momentum. Instead of imaging the bead on the detector, the distribution of the trap's IR light transmitted through the sample and arriving at the back-focal plane of the collecting condenser is imaged onto the photodetector. Using this back-focal plane interferometry [7], the lateral displacement of the light that is scattered and refracted by the trapped object is proportional to the

displacement of the bead from the center of the trap, i.e., proportional to the force, rather than the position. In the case that all or a large fraction of the light is collected, the force calibration is insensitive to the size of the trapped object, the refractive index and viscosity of the medium, and the absolute position of the trap [11]. The light momentum method has significant advantages, as the calibration performed in water remains valid regardless of the media in which the measurement is performed. To maximize the amount of light captured, a high numerical aperture (NA) condenser is paired with an objective of lower numerical aperture. Scattering by the media or other objects in the cell will result in errors, so measurements must be performed near the coverslip or slide surface of the flow cell closest to the condenser. One disadvantage of light momentum methods is that these constraints make them more difficult to use with total internal reflection fluorescence microscopy, which requires the use of high NA, oil-immersion objectives. Also, light momentum methods provide the calibration factor for force ( $C$ ) but not for position ( $\beta$ ), so camera-based tracking is often used in parallel to obtain or calibrate position data [11].

To explicitly account for the viscoelastic environment in living cells and enable calibration to be performed *in situ*, active calibration methods impose a series of sinusoidal oscillations through either the stage or the trap position and analyze the deflection of the trapped object [12, 13]. The correlated response to sinusoidal oscillations is insensitive to random disturbances from biological processes in the cell (motor proteins, cytoskeletal dynamics, etc.) as these occur stochastically and do not strongly or systematically affect the sinusoidal response at the frequency of the imposed oscillations. The calibration is performed in the cell on the same object that is used for measurements, thereby accounting for variations in the properties of the trapped object or the local viscoelastic environment. The relationship between the QPD signal and the position and force on the trapped object are determined by comparing the measured responses to a simple model of cellular viscoelasticity. This calibration also provides a measurement of the viscoelastic properties of the cellular environment.

Most endogenous intracellular components have refractive indices too close to the cytoplasm to be reliably trapped by laser tweezers. Lipid storage droplets in early *Drosophila* embryos are an exception that have been used to study motions and forces generated by intracellular molecular motors [9]. Some mammalian cells, such as macrophages, will readily take up plastic beads by phagocytosis. The resulting phagosomes are encased in a native lipid membrane containing endogenous motors, which transport them within the cell [14]. These latex-bead containing phagosomes are particularly amenable for studying intracellular transport by native kinesin and dynein molecular motors [10, 13, 15].

Live cell optical trapping techniques have been used to measure the forces exerted by microtubule-based motor proteins on intracellular cargoes such as lipid droplets and phagosomes. Forces indicate that motor proteins function collectively, working in teams of several motors to transport these cargoes [9, 10, 13, 15]. Teams of up to ten dynein motors drive transport from the cell cortex toward the cell center where multiple motors, each producing ~1.6 pN, are often simultaneously engaged [10, 13]. In contrast, transport towards the cell periphery is driven by kinesin motors, each of which produce ~6 pN and rarely function collectively [10, 13]. The cargoes demonstrate fast switching between plus- and minus-end-directed movements typical of bidirectional motility, suggesting that most commonly only one type of motor is engaged [13]. However, there is evidence that kinesin and dynein may sometimes oppose each other's motions during transport [15]. Future studies will focus on how motor proteins are regulated to achieve targeted trafficking of intracellular cargoes, and how transport is misregulated in disease [16–18].

The ability to perform calibrated optical trapping measurements in living cells has also enabled researchers to quantify the mechanical properties of the cellular environment [6, 13]. Unlike microrheological measurements based on tracking the spontaneous fluctuations of particles in the cytoplasm, optical tweezers-based measurements use the coherent response to known mechanical perturbations and are thus less sensitive to the stochastic active processes in the cell [12]. These measurements indicate that the cellular environment is viscoelastic, with viscosity dominating at low frequencies and elasticity becoming more prominent at higher strain rates [12, 13]. The cytoplasm of benign cells tends to be stiffer than malignant cells, suggesting that cell mechanics are perturbed in disease [6].

---

## 2 Materials

### 2.1 Cell Culture

1. J774A.1 mouse macrophage cells (ATTC).
2. Complete medium: Dulbecco's Modified Eagle Medium (DMEM) supplemented with 10 % heat-denatured newborn calf serum, 1 % glutamine.
3. Imaging medium: Complete medium supplemented with 10 mM HEPES.
4. Polystyrene beads: 0.5–1  $\mu\text{m}$ , carboxylated, 2.68 % solids (Fluorospheres, Molecular Probes). Pellet and resuspend in blocking buffer (10 mM K-PIPES, 50 mM potassium acetate, 4 mM MgSO<sub>4</sub>, 1 mM EGTA, 1 mg/ml bovine serum albumin, pH 7.0). Store for up to 2 weeks at 4 °C.
5. 50 mm  $\times$  0.17 mm glass coverslips (Biophtechs).

## **2.2 Force Measurements**

1. Optical trapping microscope (*see* Subheading 2.4).
2. Data acquisition and control instrumentation (*see* Subheading 2.5).
3. Live cell chamber (*see* Subheading 2.6).

## **2.3 Optical Trap Calibration**

1. Optical trapping microscope (*see* Subheading 2.4).
2. Data acquisition and control instrumentation (*see* Subheading 2.5).
3. Live cell chamber (*see* Subheading 2.6).

## **2.4 Optical Trapping Microscope**

A combined optical trap and Total Internal Reflection Fluorescence (TIRF) microscope is used to perform simultaneous imaging, manipulation, and force measurements (Fig. 3). Briefly, the output of a 10 W, 1064 nm laser is expanded to overfill the back aperture of an oil immersion objective. Acousto-optic deflectors, located conjugate telecentric to the back-focal plane of the objective, are used to control the position of the trap and impart sinusoidal oscillations. The light scattered and refracted by the trapped object is collected using an oil-immersion condenser. A quadrant photodiode detector is positioned conjugate to the back-focal plane of the condenser such that the output signal is proportional to displacement of the object from the trap center. For more details on the design and alignment of optical tweezers, see [8] and [19]. A live cell chamber is used to maintain cells at 37 °C in buffered medium (*see* Subheading 2.6). The thermal gradients caused by heating the sample require active stabilization of the focus to counteract drift. We monitor the reflection of a low-intensity TIRF beam using a quadrant photodiode and use a laboratory-built controller to maintain a stable focus.

Components include:

1. Inverted microscope (Nikon).
2. 1064 nm diode-pumped, solid-state laser, 10 W maximum output (Spectra Physics).
3. Acousto-optic deflectors controlled via a 30-bit direct digital synthesizer (Gooch and Housego).
4. Custom dichroic mirror mounted below the objective to couple the 1064 nm beam into the optical path (Chroma Technology Corp.).
5. 100×, oil-immersion objective (Nikon 1.49 NA, CFI APO TIRF).
6. Oil-immersion condenser lens, NA 1.4 (Nikon).
7. Quadrant photodiodes (Electro Optical Components, model JQ 50P). The QPD bias voltage is set to -150 V to narrow the electron/hole depletion layer near the P-N junctions of the photodiodes which markedly improves their frequency

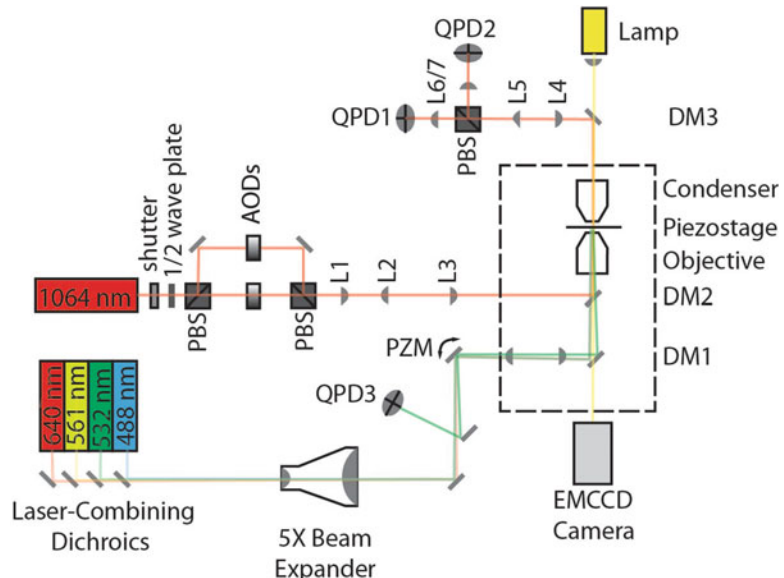


**Fig. 3** Combined optical tweezers and total internal reflection fluorescence (TIRF) microscope. The optical trap is based on a 1064 nm diode-pumped, solid-state laser. A half-wave plate and a polarizing beam splitter (PBS) are used for fine adjustments of the laser power or to divide the power between two orthogonally polarized beams. The two beams can be used to form two optical traps by recombining the light using a second polarizing beam splitter. Acousto-optic deflectors (AODs) enable fast, high-resolution control of the trap position. Achromatic lenses (L1–L3) serve to expand the beam  $\sim 3\times$  and to position a conjugate back focal plane near the AODs such that angular deflections produced by the AODs result in translation of the optical trap at the image plane. A custom dichroic mirror (DM2) mounted beneath the objective couples the optical trapping laser into the optical path. A 100 $\times$ , oil immersion objective is used to focus the laser beam to a narrow beam waist and for fluorescence and bright-field imaging. An oil immersion condenser, mounted on a custom 3D translation stage, collects the light that is transmitted, scattered and refracted by the trapped particle. The dichroic mirror (DM3) directs the IR light to quadrant photodiodes (QPD1,2). Lenses L4–L7 are used to relay the back focal plane to the quadrant photodiodes causing the photodiode signal to report force exerted on the trapped object and become insensitive to the trap position [7]. For live cell assays, a heated sample chamber is used, along with an objective heater. A custom auto-focus system monitors the position of a totally reflected beam from a low-intensity 532 nm laser using a quadrant photodiode (QPD3) and adjusting the sample position using the piezo stage

response [20]. Although the maximum specified bias voltage is 20 V, the photodiode operates stably under the high bias voltage.

8. Piezoelectric nano-positioning stage (Mad City Labs).
9. EMCCD camera (Cascade II, Photometrics).

## **2.5 Data Acquisition and Control Instrumentation**

A field-programmable gate array (FPGA) is used to control the piezoelectric nanostage via an analog voltage and an acousto-optic deflector through a 30-bit direct digital synthesizer. The signals from the nanostage and quadrant photodiode are amplified to utilize the full range of the analog-to-digital converters, low-pass filtered to avoid aliasing, and acquired using a simultaneous-sampling data acquisition card which preserves phase information between the signals. Custom LabVIEW (National Instruments) software is used to monitor signals, apply feedback control to conduct force-clamp experiments, and to apply sinusoidal oscillations over a range of frequencies to the stage and laser trap position for calibration in living cells.

Components include:

1. Field programmable gate array card (PXI-7851R, National Instruments).
2. Simultaneous-sampling data acquisition card (PXI-6143, National Instruments).
3. 8-pole Bessel low-pass filters.
4. Custom LabVIEW software.

## **2.6 Live Cell Chamber**

Cells are plated on a 50-mm diameter coverslip, then mounted in a customized live cell chamber which maintains the sample at 37 °C during imaging. The chamber consists of the 50-mm coverslip and a 1-mm thick glass disk spaced apart by a 2 mm-thick silicone gasket, allowing access for the oil-immersion imaging objective underneath (the coverslip side) and the oil-immersion condenser above. The chamber is used in combination with an objective heater to provide increased thermal stability.

Components include:

1. Live cell chamber (FCS2 with custom top plate to allow access with an oil-immersion condenser, Bioptechs Inc.).
2. 50-mm × 1-mm glass disk (Bioptechs Inc.).
3. 50-mm × 0.17 coverslips (Bioptechs Inc.).
4. 2-mm thick silicone gasket (Bioptechs Inc.).
5. Objective heater (Bioptechs Inc.).

## **3 Methods**

### **3.1 Cell Culture**

1. Maintain mouse macrophage cells (J774A.1) in 10 cm dishes in complete medium at 37 °C, 5 % CO<sub>2</sub>. Passage by scraping with a plastic policeman.
2. For optical trapping assays, plate cells on 50 mm glass coverslips and grow to ~50 % confluence.

3. On the day of the experiment, sonicate polystyrene beads for 1 min to disrupt aggregates. Dilute beads 1:50 in complete medium.
4. Replace cell medium with bead-containing medium. The concentration of beads is titrated to result in only one or two phagosomes present in each cell to avoid interference during experiments. Incubate cells at 37 °C and 5 % CO<sub>2</sub> for 10 min to allow the cells to phagocytose beads.
5. Wash cells three times with complete media to remove any beads that have not been internalized.
6. Incubate cells at 37 °C for an additional 60 min while phagosomes mature (*see Note 1*).
7. Transfer coverslip to live cell chamber and add imaging media.
8. Transport cells to the microscope in a styrofoam box filled with warm (37 °C) aluminum pellets. Once positioned on the microscope in the live cell chamber, allow 10–15 min for thermal equilibration.

### **3.2 Force Measurements**

1. Once the cells have equilibrated in the live cell chamber, select a phagosome undergoing robust bidirectional transport in a cell with extended morphology so that the direction of movement and polarity of the microtubule cytoskeleton is well defined.
2. With the optical trapping laser shuttered, adjust the stage and acousto-optic deflector to center the selected phagosome at the position the IR beam will appear and activate the focus feedback to minimize focus drift (*see Subheading 2.4*). Open the laser shutter and use the nanostage to make fine adjustments to center the trap over the phagosome, using the *x*- and *y*-photodiode signals as a reference.
3. Record quadrant photodiode signals at 2 kHz for 250 s intervals.
4. Record an image of the cell.

### **3.3 Optical Trap Calibration**

#### **3.3.1 Response to Spontaneous Fluctuations and Sinusoidal Oscillations**

1. After recording force and displacements produced by the motor proteins driving motility of the phagosome, initiate the calibration procedure. First, record the spontaneous fluctuations of the bead at 20 kHz for 25 s.
2. Apply a series of sinusoidal oscillations of position either through a piezoelectric stage (frequencies <50 Hz) or the acousto-optic deflector (frequencies ≥ 50 Hz) (Fig. 4a). To obtain accurate calibrations, frequency data must be recorded over a large enough range (~5–500 Hz) to capture the sigmoidal shape of the mechanical transfer function (Fig. 4d).
3. For each frequency, adjust the amplitude of the oscillation such that (1) the coherence, a measure of the fraction of energy in

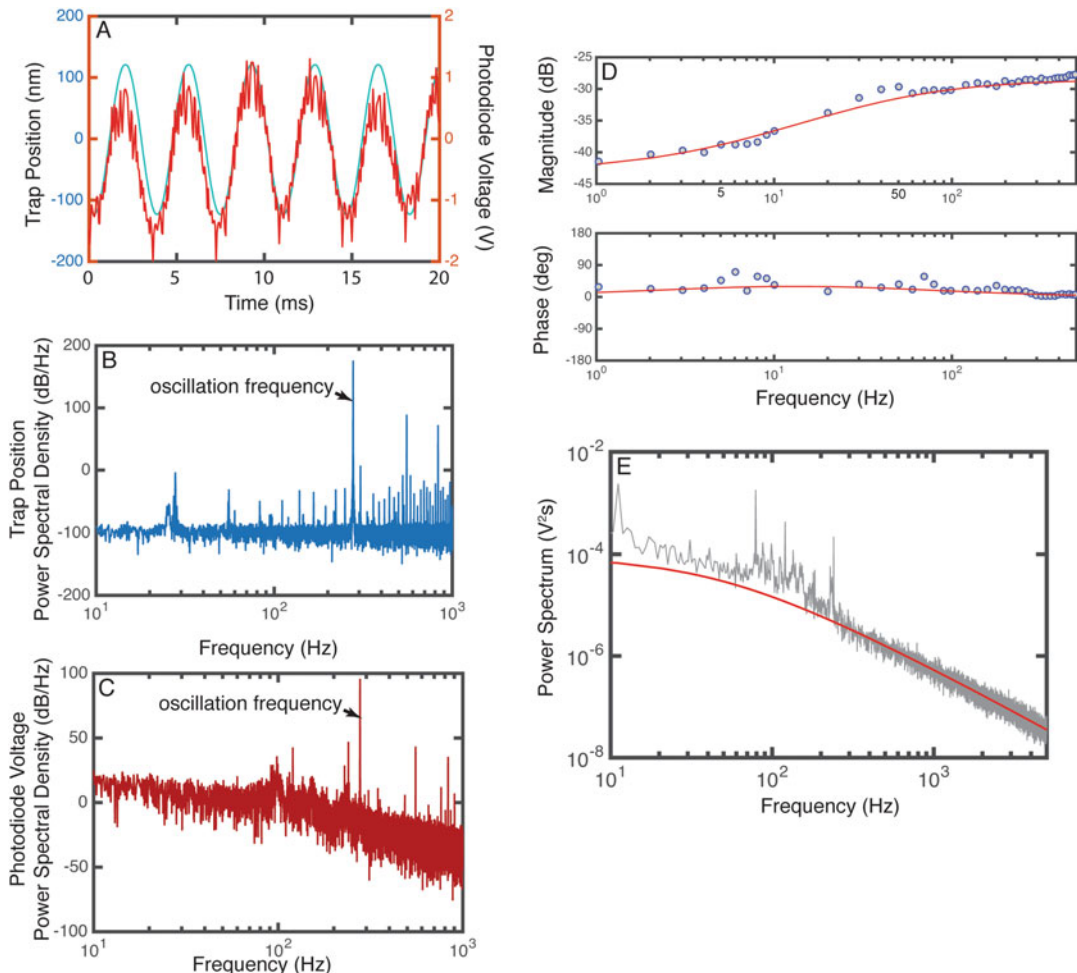


**Fig. 4** The forced response of the bead to oscillations of the stage and optical trap position enables calibration in the cellular environment. **(a)** To obtain the forced response, sinusoidal oscillations are applied using a piezoelectric stage (for frequencies  $<50$  Hz) or by moving the optical trap position using an acousto-optic deflector ( $f \geq 50$  Hz). The trace shows the trap position (blue) and the quadrant photodiode voltage (red), which corresponds to the force exerted on the trapped object, at excitation frequency 280 Hz. **(b)** The power spectral density of the trap position shows a peak at 280 Hz. **(c)** The differential photodiode voltage also shows a dominant peak at 280 Hz (see Note 2). **(d)** Forced responses were obtained for a range of excitation frequencies (blue circles). The red line indicates the fitted theoretical response (Eq. 1, see Notes 3 and 4). **(e)** The power spectrum of spontaneous fluctuations (no sinusoidal excitation) indicates that thermal motions dominate at frequencies  $>300$  Hz. At lower frequencies, the fluctuations are influenced by active processes in the cell, such as molecular motors. Vibrations of the stage also affect the passive response at low frequencies. The red line indicates a fit of Eq. 4 at  $f > 300$  Hz

the response that is correlated with the excitation signal [21], is greater than 0.98; and (2) the magnitude of harmonics in the response at multiples of the excitation frequency are less than one tenth of the response (20 dB below) that at the excitation (fundamental) frequency to obtain linearity (see Note 2;

Fig. 4b,c). Typically, excitation amplitudes that meet these constraints range from 100 to 250 nm, gradually decreasing with frequency.

4. Apply the excitation for 2 s before recording data to allow transients in the response to decay.
5. Record signals (quadrant photodiode, piezo stage position, and acousto-optic deflector position) at 20 kHz for 25 s at each frequency of excitation.
6. To test for possible degradation of motor protein function or damage due to exposure of the IR laser during the calibration procedure, remove the sinusoidal perturbations and record force and displacements of the phagosome for 250 s as in Subheading 3.2. Our measurements indicate that the calibration procedure does not substantially alter the motility and dynamics of phagosomes in the J774A.1 macrophage cell line.

### *3.3.2 Analysis of the Bead Response to Spontaneous Fluctuations and Forced Oscillations*

1. Calculate the power spectrum of spontaneous bead fluctuations recorded while the optical trap and stage are stationary using MATLAB (Natick, MA). The power spectra measured in living cells deviate significantly from power spectra obtained in buffer, particularly for frequencies <300 Hz (Fig. 4e). This excess noise has two sources: (1) Active processes in the cell including motor proteins and cytoskeletal dynamics exert forces on the phagosomes at these timescales. (2) The viscoelastic environment of the cytoplasm produces strong mechanical coupling between the bead and the coverslip, resulting in increased sensitivity to stage vibrations.
2. Calculate the frequency response of the bead to sinusoidal oscillations. The response of the bead position (measured by the quadrant photodiode), to sinusoidal perturbations of the stage or trap position, i.e., the mechanical transfer function, is characterized by the ratio of the magnitudes and the phase between the response and the sinusoidal excitation (Fig. 4, see Note 3). The magnitude and phase of the response is calculated at each frequency of excitation using MATLAB (scripts available upon request). See Tolic-Norrelykke et al. [7] for an excellent discussion of data handling and frequency domain analysis in optical trap calibration experiments.
3. To estimate trap parameters (trap stiffness, position sensitivity) and the viscoelastic properties of the cellular environment, fit the power spectrum of spontaneous fluctuations and response to sinusoidal oscillations to a simple viscoelastic model (see subheading 3.3.3 and Note 4).

### 3.3.3 Simple Model of Cellular Viscoelasticity

To interpret the viscoelastic response of the bead to spontaneous and forced oscillations, we developed a minimal dynamic model that describes the responses observed in cells [13]. The forces on the trapped object are assumed to originate from (1) the optical trap acting as a Hookean spring with stiffness  $k_{\text{trap}}$ , (2) the viscous and elastic components of the cytoplasm, (3) thermal fluctuations, and (4) random active forces from biological processes in the cell (Fig. 2). The mechanical components of the cellular environment are described by a linear elasticity ( $k_{\text{cyt},0}$ ) and viscosity ( $\gamma$ ), as well as frequency-dependent viscoelasticity ( $k_{\text{cyt},1}t^{-(\alpha-1)}$ ) characteristic of cross-linked semi-flexible polymers. At steady-state, the force response to sinusoidal oscillations ( $s \rightarrow j\omega$ ) is given by

$$\begin{aligned}\frac{\Delta X}{X_{\text{stage}}}(s) &= -\frac{\Delta X}{X_{\text{trap}}}(s) \\ &= \frac{s + \frac{1}{\gamma}(k_{\text{cyt},0} + k_{\text{cyt},1}s^\alpha/\Gamma(\alpha))}{\frac{m}{\gamma}s^2 + s + \frac{1}{\gamma}(k_{\text{cyt},0} + k_{\text{cyt},1}s^\alpha/\Gamma(\alpha) + k_{\text{trap}})} \quad (1)\end{aligned}$$

where  $\Delta X = X_{\text{bead}} - X_{\text{trap}} = \beta V_{\text{PD}}$ ,  $\beta$  is the position sensitivity of the detector in nm/V, and  $\Gamma$  is the gamma function. The force sensitivity, in pN/V, is given by  $C = \beta k_{\text{trap}}$ . The steady-state response to thermal fluctuations is

$$\frac{\Delta X}{F_{\text{th}}}(s) = \frac{1}{ms^2 + \gamma s + k_{\text{cyt},0} + k_{\text{cyt},1}s^\alpha/\Gamma(\alpha) + k_{\text{trap}}} \quad (2)$$

for spherical particles in a homogeneous medium. Stokes law relates Eq. 2 to the viscous ( $G''(\omega)$ ) and elastic ( $G'(\omega)$ ) moduli of the cellular environment [22].

$$G(\omega) = G'(\omega) + jG''(\omega) = \frac{1}{6\pi R} \left[ \frac{\Delta X}{F_{\text{th}}}(\omega) \right]^{-1} \quad (3)$$

and the power spectrum is given by [23].

$$P_{\text{th}}(\omega) = \beta^2 \langle |V_{\text{PD}}(\omega)|^2 \rangle = \frac{2k_B T}{6\pi R} \frac{G''(\omega)}{\omega |G(\omega)|^2} \quad (4)$$

Equations 1 and 4 are fit to the responses to sinusoidal perturbations (Fig. 4d, Note 4) and thermal fluctuations (Fig. 4e). The frequency response enables the contributions to the elastic response from the optical trap and the cytoplasm to be determined separately, as the critical frequency of the zero in the transfer function (see Note 3, the zero corresponds to the upward change in slope at ~5 Hz in Fig. 4d) is defined by the cellular elasticity (Fig. 5b,c), while the critical frequency of the pole in the transfer function (see Note 3, the pole corresponds to the leveling off of the slope at ~60 Hz in Fig. 4d) is defined by the total elasticity (from the optical

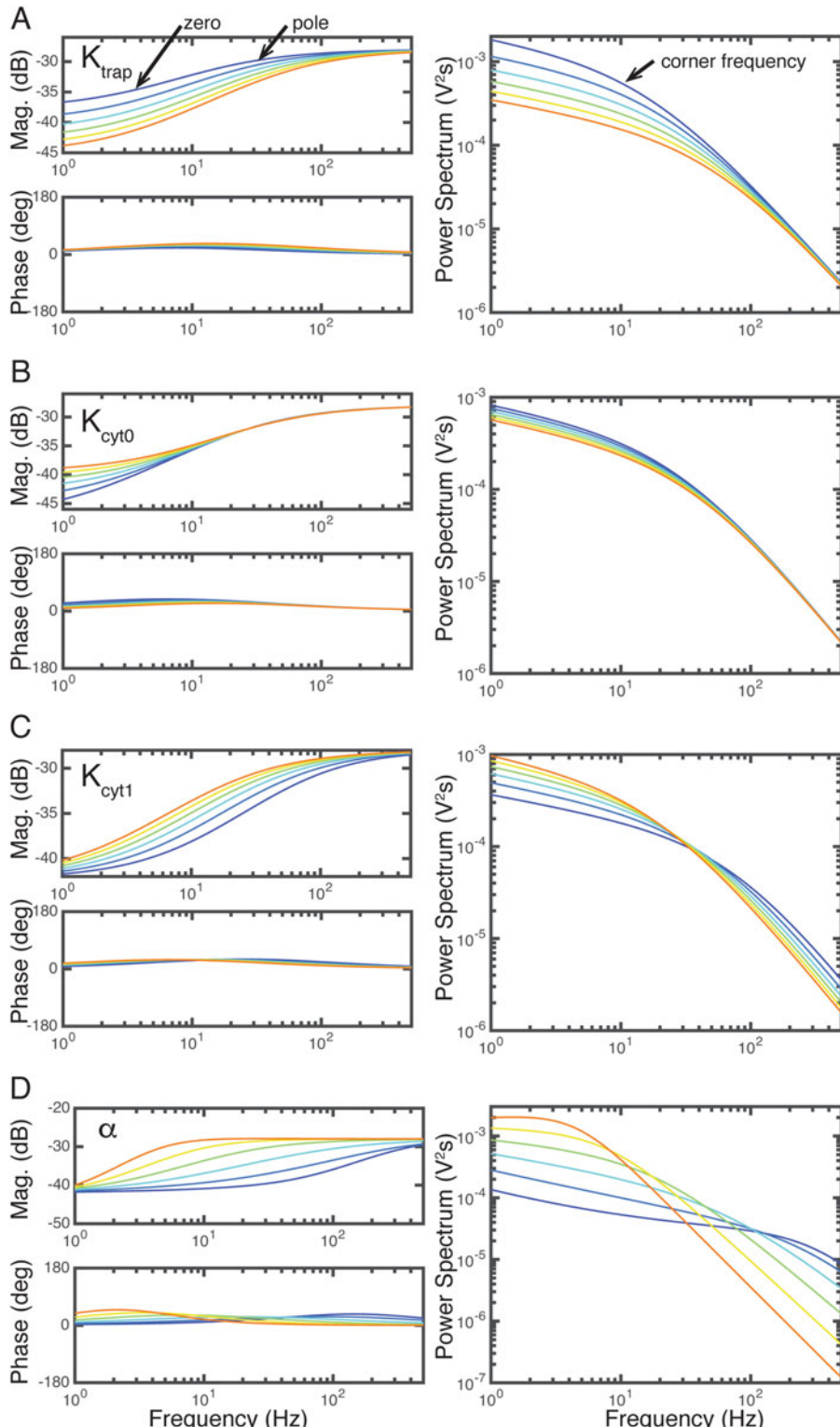


**Fig. 5** The properties of the optical trap and cellular environment influence the forced response and thermal oscillations. Each plot shows the effect of changing the parameter by  $\pm 50\%$  (blue to red) from the

trap and cellular components, Fig. 5a–c). The exponent  $\alpha$  determines the slope of the response to sinusoidal oscillations for frequencies between the zero and the pole, as well as the downward slope of the thermal response at high frequencies (Fig. 5d). The slope of the thermal response is 2 (when plotted on a log-log) in the familiar situation that  $\alpha = 1$ .

## 4 Notes

1. Phagosomes undergo a series of biochemical changes as they are internalized and ultimately fuse with lysosomes. These biochemical changes correlate with changes in motility and motor protein activity [24].
2. The calibration procedure requires that the response to sinusoidal oscillations is in the linear range, i.e., the magnitude of the response (Eq. 1) does not depend on the amplitude of the excitation. Nonlinear effects, as evidenced by the presence of harmonics in the response (Fig. 4c) become more pronounced at high amplitudes of excitation. For this reason, and to minimize perturbing the cellular components near the phagosome, the minimum amplitude of excitation needed to obtain a coherent response is used.
3. In minimum phase systems (no distributed transport components), a zero in a transfer function is defined as a root of its numerator (see Eq. 1), and a pole is a root of the denominator, i.e., the power density is zero at that frequency. In the frequency response, or Bode diagram, a zero corresponds to a change in the asymptotic slope of the magnitude of +20 dB/decade and a change in phase of +90°. A pole corresponds to a change of –20 dB/decade in slope of the magnitude and –90° in phase (Fig. 5).

**Fig. 5** (continued) nominal value  $k_{\text{trap}} = 0.17 \text{ pN/nm}$ ,  $k_{\text{cyt},0} = 0.04 \text{ pN/nm}$ ,  $k_{\text{cyt},1} = 0.005 \text{ pN/nm}$ ,  $\alpha = 0.73$ . (a) Increasing optical trap stiffness (blue to red) causes the pole (see Note 3) of the forced response to move to higher frequencies, while the zero is unaffected. The corner frequency of the thermal fluctuations increases with increasing trap stiffness. (b) The elasticity of the cellular environment affects the zero in the forced response, and only weakly influences the thermal response. (c) Increasing the frequency-dependent viscoelasticity of the cytoplasm shifts the zero and pole of the forced response and the corner frequency of the thermal response rightward. (d) The exponent alpha describes the scaling of the viscoelasticity with frequency. As alpha increases, the viscous component dominates such that the total elasticity in the system is decreased and the zero and pole in the forced response occur at lower frequencies. Alpha also determines the slope of the thermal response at high frequencies, such that subdiffusive behavior is observed at low values of alpha, while  $\alpha = 1$  corresponds to pure diffusion

4. To determine the model parameters that result in the best fits of Eqs. 1 and 4 to the forced and spontaneous responses, use a Levenberg–Marquardt algorithm (implemented in MATLAB using the lsqcurvefit() function) to perform a global fit of the model responses to the magnitude of the full sinusoidal frequency response (Fig. 4d) and the power spectrum of spontaneous oscillations (Fig. 4e) at frequencies of 300 Hz and above. The random fluctuations are driven primarily by thermal motions in this range. A weighting function is used to account for differences in the number of data points between the forced and spontaneous responses. Initial estimates of  $\alpha$ ,  $k_{\text{cyt},0}$ ,  $k_{\text{trap}}$ , and  $\beta$  are calculated based on estimating the corner frequencies in the frequency response and the slope of the power spectrum.

## Acknowledgements

The authors thank Mr. Pritish Agarwal for developing custom software to control the optical trap, Mr. Pete Cainfrani for building the custom focus stabilization system, and Ms. Mariko Tokito for sharing her wealth of knowledge on cell culture and protein purification. This work was supported by the Natural Sciences and Engineering Research Council of Canada (Discovery Grant to AGH) and the National Institutes of Health (P01-GM087253 to YEG).

## References

1. Neuman KC, Nagy A (2008) Single-molecule force spectroscopy: optical tweezers, magnetic tweezers and atomic force microscopy. *Nat Methods* 5:491–505
2. Gardner MK, Charlebois BD, Janosi IM et al (2011) Rapid microtubule self-assembly kinetics. *Cell* 146:582–592
3. Kerssemakers JW, Munteanu EL, Laan L et al (2006) Assembly dynamics of microtubules at molecular resolution. *Nature* 442:709–712
4. Cecconi C, Shank EA, Bustamante C et al (2005) Direct observation of the three-state folding of a single protein molecule. *Science* 309:2057–2060
5. Mizuno D, Tardin C, Schmidt CF et al (2007) Nonequilibrium mechanics of active cytoskeletal networks. *Science* 315:370–373
6. Guo M, Ehrlicher AJ, Jensen MH et al (2014) Probing the stochastic, motor-driven properties of the cytoplasm using force spectrum microscopy. *Cell* 158:822–832
7. Tolic-Norrelykke SF, Schaffer E, Howard J et al (2006) Calibration of optical tweezers with positional detection in the back focal plane. *Rev Sci Instrum* 77:103101
8. Nicholas MP, Rao L, Gengerich A (2014) An improved optical tweezers assay for measuring the force generation of single kinesin molecules. *Methods Mol Biol* 1136:171–246
9. Leidel C, Longoria RA, Gutierrez FM et al (2012) Measuring molecular motor forces in vivo: implications for tug-of-war models of bidirectional transport. *Biophys J* 103:492–500
10. Rai AK, Rai A, Ramaiya AJ et al (2013) Molecular adaptations allow dynein to generate large collective forces inside cells. *Cell* 152:172–182
11. Jun Y, Tripathy SK, Narayananreddy BR et al (2014) Calibration of optical tweezers for in vivo force measurements: how do different approaches compare? *Biophys J* 107:1474–1484

12. Mas J, Richardson AC, Reihani SN et al (2013) Quantitative determination of optical trapping strength and viscoelastic moduli inside living cells. *Phys Biol* 10:046006
13. Hendricks AG, Holzbaur ELF, Goldman YE (2012) Force measurements on cargoes in living cells reveal collective dynamics of microtubule motors. *Proc Natl Acad Sci* 109:18447–18452
14. Blocker A, Severin FF, Burkhardt JK et al (1997) Molecular requirements for bi-directional movement of phagosomes along microtubules. *J Cell Biol* 137:113–129
15. Blehm BH, Schroer TA, Trybus KM et al (2013) In vivo optical trapping indicates kinesin's stall force is reduced by dynein during intracellular transport. *Proc Natl Acad Sci U S A* 110:3381–3386
16. Verhey KJ, Hammond JW (2009) Traffic control: regulation of kinesin motors. *Nat Rev Mol Cell Biol* 10:765–777
17. Hirokawa N, Niwa S, Tanaka Y (2010) Molecular motors in neurons: transport mechanisms and roles in brain function, development, and disease. *Neuron* 68:610–638
18. Maday S, Twelvetrees AE, Moughamian AJ et al (2014) Axonal transport: cargo-specific mechanisms of motility and regulation. *Neuron* 84:292–309
19. Lee WM, Reece PJ, Marchington RF et al (2007) Construction and calibration of an optical trap on a fluorescence optical microscope. *Nat Protoc* 2:3226–3238
20. Berg-Sorensen K, Oddershede L, Florin EL et al (2003) Unintended filtering in a typical photodiode detection system for optical tweezers. *J Appl Phys* 93:3167–3176
21. Bendat JS, Piersol AG (2000) Random data: analysis and measurement procedures. Wiley series in probability and statistics, 3rd edn. Wiley, New York, NY
22. Gittes F, Schnurr B, Olmsted PD et al (1997) Microscopic viscoelasticity: shear moduli of soft materials determined from thermal fluctuations. *Phys Rev Lett* 79:3286–3289
23. Lau AWC, Hoffman BD, Davies A et al (2003) Microrheology, stress fluctuations, and active behavior of living cells. *Phys Rev Lett* 91:198101
24. Loubéry S, Wilhelm C, Hurbain I et al (2008) Different microtubule motors move early and late endocytic compartments. *Traffic* 9:492–509

# INDEX

## A

- AAA+protease ..... 317, 318, 320–323  
Absolute calibration ..... 25–38  
Active stabilization ..... 77–106, 542  
Actomyosin ..... 498–504  
Angular trapping ..... 168, 174  
Anti-reflection coating ..... 92  
ATPase ..... 295, 317, 318, 320, 321, 343–345, 348, 349, 353, 483

## B

- Back-focal plane interferometry ..... 10, 19, 45–50, 112, 130, 193, 265, 266, 280, 358, 425  
Biological materials ..... 288  
Birefringence ..... 142, 151, 158, 161, 166, 167, 169, 172

## C

- Centroid tracking ..... 452  
ClpXP ..... 317–339  
Confocal microscopy ..... 196, 241, 269  
Core–shell particles ..... 138  
Cytoplasm ..... 111, 318, 514, 515, 519, 527, 528, 531, 532, 537–541, 547, 548, 550  
Cytoskeleton ..... 417, 505, 526, 530, 538, 545

## D

- Differential interference contrast (DIC) ..... 5, 142, 416, 424, 425, 438–442, 447–449, 452, 455, 459, 461, 462  
DNA tether ..... 122, 226, 241, 243, 254, 258, 308, 313, 319, 323, 329, 332, 334, 337, 351, 354, 364, 374, 392, 470, 472–475  
Dual DNA manipulation ..... 277  
Dual trap ..... 111, 183–254, 258, 260, 264, 269, 275, 325, 345, 346, 351, 362, 364  
Dynein ..... 4, 111, 318, 412–415, 417–419, 421–424, 427, 429, 430, 438, 471, 540, 541

## E

- Energy landscape ..... 380, 382–384, 386

## F

- Fleezers ..... 183–254  
Fluorescence ..... 5, 124, 178, 183–254, 259, 260, 262–264, 268, 269, 276, 278, 295, 296, 303, 304, 306, 308–313, 319, 358, 437–465, 477, 479, 496, 506, 540, 542, 543  
Fluorescence localization ..... 296  
Focus correction ..... 439  
Force clamp ..... 109–134, 262, 267, 268, 333–338, 393, 404, 408, 428, 544  
Force detection ..... 260, 262–266, 269, 270, 286, 290–292, 424  
Force generation ..... 344, 412, 417, 427–430, 469, 483–507  
Force measurements ..... 5, 48, 59, 140, 471, 513, 514, 521, 530, 542, 545  
Force spectroscopy ..... 502  
Förster resonance energy transfer (FRET) ..... 185, 186

## G

- Gating ..... 202  
Glycoprotein 41 (gp41) ..... 359, 364, 366–370, 373–380, 382, 383, 386  
Gold coated barriers ..... 413, 418–419

## H

- Helicase ..... 186, 295–314  
Hidden Markov modeling ..... 376, 379–382

## I

- Interhead coordination ..... 469  
Intracellular transport ..... 540  
Intramolecular distance ..... 444  
In vivo ..... 18, 358, 439, 452, 463, 514, 515

## K

- Kinesin ..... 4, 77, 110, 111, 115, 116, 121, 122, 124, 126–131, 133, 141, 438, 440, 450, 454, 455, 458, 459, 464, 469–478–480, 540, 541  
Kinetics ..... 257, 319, 322, 357–359, 364, 375–378, 392, 408, 483–506  
Kinetochore ..... 411, 430, 437–465

**L**

- Light momentum method ..... 540  
 Liquid crystalline birefringent particles ..... 141, 151  
 Live-cell assays ..... 541

**M**

- MCM-41 ..... 148  
 Mechanochemistry ..... 537  
 Micro-fabrication ..... 412, 413  
 Microfluidics ..... 98, 259, 260, 263, 267, 268, 275–292, 344, 346, 349, 350, 363, 373–376, 518  
 Micron-sized dielectric objects ..... 157  
 Microspheres ..... 26, 28–30, 32–38, 44, 48, 51, 57, 58, 61, 62, 64, 72, 109–111, 114–116, 120–132, 137–152, 185, 206, 208, 230, 231, 257, 298, 486, 492  
 Microtubule(s) ..... 4, 19, 110, 115, 116, 121, 122, 126, 127, 131, 133, 134, 318, 411–433, 437–465, 471, 538, 541, 545  
 ends ..... 411–433  
 cell mechanics ..... 115  
 Molecular motor ..... 4, 111, 120, 126, 134, 141, 158, 257, 258, 262, 343, 344, 391, 530, 539, 540, 546

**N**

- Nanodiamonds ..... 139–141, 143, 148–151, 153  
 Nanonewton ..... 4, 261  
 NS3 ..... 296

**O**

- Optical torque ..... 142, 157–180, 184  
 Optical trap/trapping ..... 4–8, 12, 17–19, 42, 66, 72, 74, 110, 113, 116, 124, 126, 133, 148, 157, 163, 166, 178, 183–188, 191, 193, 196, 212, 216, 217, 230, 231, 238–242, 252–271, 276–278, 280, 281, 302–304, 312–314, 319, 320, 325, 326, 337, 345, 358, 362, 363, 373, 374, 378, 385, 392–407, 412, 413, 417, 424, 427–430, 439, 446, 448, 459, 460, 469, 470, 472, 473, 476–477, 484–489, 491, 493–496, 499, 501, 503, 506, 513–534, 537–551  
 forces ..... 4, 5, 42  
 Optical tweezers ..... 3, 25, 41, 109, 137, 157, 183, 257, 275, 295, 319, 343, 357, 397, 411, 438, 469, 483, 513, 537

**P**

- Passive force clamp ..... 334–338  
 Polarization ..... 7, 8, 11, 15, 19, 29, 30, 32, 71, 79, 80, 82, 85, 88, 91–93, 104, 129, 142, 145,

- 159–179, 188, 190, 260, 263–265, 270, 280, 292, 362, 440, 447, 495

- Proportional-integral-derivative (PID)  
 controller ..... 111–113, 116–120, 123, 131, 244  
 Proportional-integral-derivative (PID) tuning ..... 112, 113, 116

- Proteasome ..... 317, 320  
 Protein folding ..... 5, 357–388, 537  
 Protein-mediated inter-DNA bridging ..... 279

**Q**

- Quadruple-trap optical tweezers ..... 257–271, 275–292

**R**

- Ring ATPase ..... 320  
 RNA polymerase ..... 77, 111, 391–408  
 RNA polymerase II ..... 392–395, 397, 399, 400, 403–406  
 Rotation ..... 29, 91, 122, 137, 141–143, 158, 160–163, 168, 169, 171, 172, 174, 175, 179, 194, 197, 215, 276, 345, 444  
 Rupture forces ..... 471

**S**

- Single molecule ..... 41, 77, 79, 112, 115–116, 118, 121, 122, 124, 126, 140, 153, 157, 158, 183–254, 257, 259, 261, 267, 278, 295, 296, 301, 313, 318–321, 337, 343–349, 351–354, 357–388, 392, 394, 397, 399–400, 403–404, 406, 438, 440, 453, 484, 489, 495, 498, 500, 501, 514  
 biophysics ..... 77  
 degradation ..... 337  
 fluorescence ..... 124, 183–254, 295, 438  
 force spectroscopy ..... 257  
 manipulation ..... 257, 343, 387  
 SNARE assembly ..... 364  
 SNARE proteins ..... 365–367  
 Spring constant ..... 43, 75, 109, 121, 362, 427, 433, 514, 515, 519, 520, 526–531  
 SU8 barriers ..... 413, 417, 425, 426, 428, 430  
 Super-resolution ..... 3, 437–465  
 Surface passivation ..... 288, 301, 453, 456, 463

**T**

- Tetraethyl orthosilicate (TEOS) ..... 141, 144, 148, 150, 153  
 TIRF. *See* Total internal reflection fluorescence (TIRF)  
 Titania ..... 137–152  
 Torque ..... 18–19, 140–142, 157–179, 184  
 Total internal reflection fluorescence (TIRF) ..... 296, 298, 302–304, 306, 310, 313, 438, 440–443, 446, 447, 452–454, 458, 462, 477, 542, 543  
 microscopy ..... 296, 302–304

- Transcription ..... 141, 184, 391–395, 397, 399–408  
Translocation ..... 111, 296, 309, 310, 317, 319,  
320, 322, 336, 337, 345, 392, 408
- U**
- Unfolding ..... 111, 258, 317–323, 334, 336,  
337, 357, 358, 365, 366, 375–380, 382, 387
- V**
- Unwinding ..... 184, 186, 296, 307, 310, 311  
Uvrd ..... 186, 296, 307–311
- Viral DNA packaging ..... 343  
Viscoelasticity ..... 18, 513–534